FOSSIL ENERGY

DOE/MC/21136-28
(DE91002245)

IMPROVEMENT OF CO_2 FLOOD PERFORMANCE

Final Report for the Period
April 1, 1984-March 1, 1991

By
F. D. Martin
J. P. Heller

June 1991

Performed Under Contract No. DE-FC21-84MC21136

New Mexico Institute of Mining and Technology
Petroleum Recovery Research Center
Socorro, New Mexico

National Petroleum Technology Office
U.S. DEPARTMENT OF ENERGY
Tulsa, Oklahoma

DISCLAIMER

This report was prepared as an account of work sponsored by an agency of the United States Government. Neither the United States Government nor any agency thereof, nor any of their employees, makes any warranty, expressed or implied, or assumes any legal liability or responsibility for the accuracy, completeness, or usefulness of any information, apparatus, product, or process disclosed, or represents that its use would not infringe privately owned rights. Reference herein to any specific commercial product, process, or service by trade name, trademark, manufacturer, or otherwise does not necessarily constitute or imply its endorsement, recommendation, or favoring by the United States Government or any agency thereof. The views and opinions of authors expressed herein do not necessarily state or reflect those of the United States Government.

This report has been reproduced directly from the best available copy.

DOE/MC/21136-28
Distribution Category UC-122

Improvement of CO_2 Flood Performance

Final Report for the Period
April 1, 1984-March 1, 1991

By
F. David Martin
John P. Heller

June 1991

Work Performed Under Contract No. DE-FC21-84MC21136

Prepared for
U.S. Department of Energy
Assistant Secretary for Fossil Energy

Royal J. Watts, Project Manager
Morgantown Energy Technology Center
P. O. Box 880
Morgantown, WV 26505

Prepared by
New Mexico Institute for Mining and Technology
Petroleum Recovery Research Center
Socorro, New Mexico

ABSTRACT

This is the final report of a six-year research project devoted to the study of processes of oil displacement using dense carbon dioxide. The topics studied have included phase behavior and physical properties of mixtures of crude oil with CO_2, the phenomena involved in the displacement of oil through reservoir rock under oilfield conditions, the influence of stabilized lamella or CO_2-foam on this displacement and the development of computer programs to simulate the displacement. In addition, the occurrence of nonuniformities in the displacement pattern has also been considered. The effect on displacement of permeability heterogeneities in the reservoir have been studied geostatistically and by direct numerical modelling. Displacement nonuniformities that are induced by viscosity and density differences between displaced and displacing fluids have also been considered, and efforts are described for the development of two different types of additive for purposes of mobility control of CO_2 floods. One of these is the so-called CO_2-foam, formed by simultaneous flow through the formation of dense CO_2 with a water solution of a special surfactant. The second type under development in the project is known as direct thickener, and consists of a polymer that is soluble in dense CO_2 and able to viscosify it. Significant progress is reported on all of the topics mentioned above.

TABLE OF CONTENTS

ABSTRACT iii

LIST OF FIGURES viii

LIST OF TABLES xix

ACKNOWLEDGEMENTS xxii

EXECUTIVE SUMMARY xxiii

INTRODUCTION xxiv

HISTORY OF PROJECT xxxi

I. DISPLACEMENT WITH PURE AND IMPURE CO_2 . . . . . I-1

A. PHASE BEHAVIOR AND FLUID PROPERTY STUDIES: DEVELOPMENT OF A VISCOSITY/ DENSITY/COMPOSITION DATABASE FOR PURE AND IMPURE CO_2/CRUDE OIL MIXTURES I-1
1. Viscosity, Density, and Composition Measurement I-5
2. Effect of Solution Gas on Fluid Properties I-14
3. Effects of Contamination of CO_2 on Fluid Properties I-19
4. Conclusions I-26

B. DEVELOPMENT OF A VISCOSITY CORRELATION I-27
1. Review of Related Literature I-29
2. Viscosity/Density/Composition Data I-32
3. Comparison of Viscosity Data to the Lohrenz, Bray, and Clark Correlation . . . I-32
4. Correlation Development I-37
5. Summary of the Calculation Procedure I-41
6. Results and Conclusions I-44
7. Nomenclature I-57

C. EFFECT OF SOLUTION AND FREE GAS ON THE DEVELOPMENT OF MISCIBILITY I-58
1. Modeling of Wasson crude oil with the Peng-Robinson EOS I-61
2. Characterization of Pseudocomponents I-65
3. Binary Interaction Parameters I-67

D. MECHANISTIC STUDIES OF HIGH PRESSURE GAS/FOAM FLOW: MICROMODEL VISUALIZATION EXPERIMENTS I-80
1. Apparatus I-80
2. Descriptions of Experiments I-84
3. Mechanisms Associated with In-situ Foam Generation and Propagation. I-84

4. Effects of CO_2 Miscibility and Injection Mode I-89
a. Pure CO_2 Displacements I-89
b. Water-Alternating-Gas (WAG) Displacements I-92
c. Surfactant-Alternating-Gas (SAG) Displacements I-96
5. Effect of Gas-Liquid Volumetric Ratio I-101
6. Effect of Pregenerated Foam I-106
7. Conclusions I-115

E. MECHANISTIC STUDIES OF HIGH PRESSURE GAS/FOAM FLOW: COREFLOOD EXPERIMENTS I-116
1. Apparatus I-116
2. Description of the Experiment I-118
3. Results and Discussion I-118
4. Conclusions I-138
5. Future Work I-138

F. MECHANISTIC MODELING OF HIGH PRESSURE GAS/FOAM FLOW I-141
1. Model Description I-141
2. Results and Discussion I-144
3. Conclusions I-169
4. Future Work I-169

G. REFERENCES I-172

II. CO_2 MOBILITY CONTROL AND FLOW HETEROGENEITIES II-1

A. HETEROGENEITY OF RESERVOIR ROCK II-1
1. Assessment of Geostatistical Parameters II-2
2. Application of Geostatistics to Characterize Reservoir Heterogeneity II-3
a. Variography II-7
b. Validation of the Parameters II-9
c. Influence of Scale on Variance and Correlation Length II-9
d. Conditioned Log-Permeability Field II-11
3. Small-Scale Heterogeneity II-16
a. Analysis of The CT-Scanned Images of a Carbonate Rock Sample II-16
b. The Accuracy of the Rephotographed Images II-21
c. Investigated Parameters From The CT-Scanned Images II-22
d. Local Vug Density Distribution II-22
e. Distribution of Light Intensity II-25
f. Contribution of Vugs To Measured Porosity II-25
g. Vug Size Distribution II-30
h. Spatial Distribution of Vugs II-32
i. Vug Connectivity II-32
4. Mobility Control II-41

B. DEVELOPMENT OF DIRECT THICKENERS II-41
1. Introduction II-41
a. Research Objectives II-42

b. Research Accomplishments II-42
2. Overview II-42
3. Method I Polymers II-43
4. Method III Organotin Fluorides II-44
5. Method II Ionomers II-47
a. Exploratory Work II-47
i. Experimental Procedures and Characterization II-52
ii. Solubility Measurements of Copolymers and Ionomers in Dense CO_2 . II-57
iii. Solution Properties of Copolymer and Ionomers II-57
b. Rationale of Method II-Telechelic Ionomers II-63
i. Preliminary Experiments of Living Polymerization of Isobutylene . . . II-65
ii. Incremental Monomer Addition (IMA) Technique II-66
iii. All-Monomer-In (AMI) Technique II-68
iv. Inifer Methods II-68
v. New Initiators II-72
vi. Polymer Characterization II-78
vii. Dehydrochlorination II-82
viii. Sulfonation of Dehydrochlorinated Polyisobutylenes II-89
ix. Neutralization of Sulfonated Telechelic Polyisobutylenes by Acid-Base Titration II-93
x. Solution Viscosity Behavior of Mono Telechelic Prepolymers II-93
6. High-pressure Solubility Measuring Apparatus II-96
7. The High-pressure Capillary Tube Viscometer II-101
8. Conclusions II-106

C. MOBILITY CONTROL BY USE OF CO_2 FOAMS II-107
1. CO_2-Foam Mobility Measurements II-108
a. Effect of Rock Permeability II-111
b. Effect of Surfactant Concentration II-113
c. Effect of Flow Rate II-113
2. Foam Durability Experiment II-118
3. Dynamic Adsorption Experiment II-144
4. Description of the Experiment and Apparatus II-145

D. FOLLOW-ON PROJECT—FIELD VERIFICATION OF CO_2 FOAM II-154

E. SUMMARY AND CONCLUSIONS II-155

F. REFERENCES II-157

APPENDIX A

APPENDIX B

LIST OF FIGURES

Figure 1. Effect of surfactant concentration xxxviii

Figure 2. Effect of foam quality xxxix

Figure 3. Apparent viscosity vs. rock permeability xl

Figure I-1. Schematic of continuous phase equilibrium (CPE) apparatus I-2

Figure I-2. Schematic of pressure-temperature projection of CO_2/n-Hexadecane systems I-11

Figure I-3. Schematic diagrams of Gibbs free energy/composition surface for a binary system exhibiting three-phase liquid-liquid-vapor (L_1-L_2-V) immiscibility I-12

Figure I-4. Pseudoternary phase behavior representation with corresponding density and viscosity for the RO-B/CO_2 system at 1700 psia and 116°F I-15

Figure I-5. Pseudoternary phase behavior representation with corresponding density and viscosity for the RO-B1/CO_2 system at 1700 psia and 116°F I-16

Figure I-6. Phase viscosities vs. CO_2 mole fraction for the RO-A, RO-B, RO-B1, and RO-B2 systems I-17

Figure I-7. Phase viscosities vs. phase densities for the RO-A, RO-B, RO-B1, and RO-B2 systems I-18

Figure I-8. Pressure/composition phase diagrams for mixtures of CO_2 with STO-A (Orr and Taber[8]) I-20

Figure I-9. Pressure/composition phase diagrams for mixtures of STO-A with CO_2 containing 10 mole% N_2 (Orr and Taber[8]) I-21

Figure I-10. Pseudoternary phase behavior representation with corresponding density and viscosity for the STO-A/CO_2 system at 1500 psia and 109°F I-22

Figure I-11. Pseudoternary phase behavior representation with corresponding density and viscosity for the STO-A/CO_2 + N_2 system at 1500 psia and 109°F I-23

Figure I-12. Phase viscosities vs. CO_2 mole fraction for the RO-A systems I-24

Figure I-13. Phase viscosities vs. phase densities for the RO-A systems I-25

Figure I-14. Relationship between the residual viscosity modulus, $(\mu - \mu^*)\xi$, and the reduced density, ρ_r, for normally behaving substances I-35

Figure I-15. Comparison of LBC-predicted and measured viscosities for CO_2/crude oil systems I-38

Figure I-16. Relationship between the difference of the LBC-predicted and experimental viscosity and the reduced density I-39

Figure I-17. Comparison of the modified LBC-predicted vs. experimental viscosities I-45

Figure I-18. Comparison of predicted vs. experimental viscosities as a function of CO_2 concentration for single-phase mixtures of $CO_2/n\text{-}C_7$ binary system I-48

Figure I-19. Comparison of predicted vs. experimental viscosities as a function of phase densities for single-phase mixtures of $CO_2/n\text{-}C_7$ binary system I-49

Figure I-20. Comparison of predicted vs. experimental viscosities as a function of CO_2 concentration for single-phase and equilibrium vapor-phase mixtures of the CO_2 + C_1/Amoco Oil A system I-54

Figure I-21. Schematic diagram of the high pressure CO_2 flooding apparatus I-59

Figure I-22. Cumulative recovery at breakthrough and at 1.2 pore volumes of CO_2 injected for Oil-A, Oil-B, and Oil-C at 160°F I-62

Figure I-23. Density of CO_2 with 0, 10, and 30 mole% C_1 contamination at 160°F I-63

Figure I-24. Pressure-composition phase diagram for methane/Wasson STO at 105°F I-64

Figure I-25. Peng-Robinson Equation of State match of Wasson oil/CO_2 pressure-composition diagram I-73

Figure I-26. Cumulative recovery at breakthrough and at 1.2 pore volumes of CO_2 injected for Oil-D and Oil-F I-76

Figure I-27. Effluent/initial concentration ratio curves for C_1 component in Oil-D at 105°F and five different pressures I-77

Figure I-28. Effluent/initial concentration ratio curves for C_1 component in Oil-F at 105°F and five different pressures I-78

Figure I-29. Density of CO_2 with 0%, 10%, and 30% C_1 contamination at 105°F for Oil-D and Oil-F I-79

Figure I-30. Schematic of high-pressure micromodel apparatus I-81

Figure I-31. Micromodel pattern and pore size distribution of modified layered micromodel (MLAY) I-82

Figure I-32. Micromodel pattern and pore size distribution of modified heterogeneous micromodel (MHE) I-83

Figure I-33. Effect of CO_2 miscibility on oil recovery I-90

Figure I-34. Effect of CO_2 miscibility on oil recovery I-93

Figure I-35. Effect of CO_2 miscibility on pressure drop I-94

Figure I-36. Effect of CO_2 miscibility on average pressure drop I-95

Figure I-37. Effect of CO_2 miscibility on oil recovery I-97

Figure I-38. Effect of CO_2 miscibility on pressure drop I-98

Figure I-39. Effect of CO_2 miscibility on average pressure drop I-99

Figure I-40. Effect of CO_2 miscibility on average pressure drop I-100

Figure I-41. Effect of injection ratio on oil recovery I-102

Figure I-42. Effect of injection ratio on oil recovery after breakthrough I-103

Figure I-43. Effect of injection ratio on pressure drop I-104

Figure I-44. Effect of injection ratio on average pressure drop I-105

Figure I-45. Effect of injection ratio on pressure drop I-107

Figure I-46. Effect of injection ratio on average pressure drop I-108

Figure I-47. Effect of injection ratio on pressure drop I-109

Figure I-48. Effect of injection ratio on average pressure drop I-110

Figure I-49. Effect of injection ratio on average pressure drop I-111

Figure I-50. Effect of injection mode on oil recovery at 2.00 cm^3/hr I-113

Figure I-51. Effect of injection mode on pressure drop at 2.00 cm^3/hr I-114

Figure I-52. Schematic of CO_2/foam coreflood apparatus I-117

Figure I-53. Concentric core for heterogeneous coreflood studies I-123

Figure I-54. Critical gas fraction and interstitial gas velocity for stable foam formation I-125

Figure I-55. Effect of interstitial gas velocity on pressure drop I-126

Figure I-56. Effect of interstitial gas velocity on pressure drop I-127

Figure I-57. Effect of interstitial gas velocity on pressure drop I-128

Figure I-58. Effect of gas-liquid ratio on pressure drop I-129

Figure I-59. Effect of gas-liquid ratio on pressure drop I-130

Figure I-60. Effect of gas-liquid ratio on pressure drop I-131

Figure I-61. Effect of gas fraction and interstitial gas velocity on gas mobility in CO_2/Alipal CD-128 foam I-132

Figure I-62. Liquid production history for brine displacement from a homogeneous core by (a) CO_2 and brine (HOWAG-1) and (b) CO_2 and surfactant solution (HOSAG-1) I-134

Figure I-63. Pressure drop history for brine displacement from a homogeneous core by (a) CO_2 and brine (HOWAG-1) and (b) CO_2 and surfactant solution (HOSAG-1) I-135

Figure I-64. Oil recovery performance for oil displacement from a homogeneous core by (a) CO_2 and brine (HOWAG-2) and (b) CO_2 and surfactant solution (HOSAG-2) I-136

Figure I-65. Pressure drop history for oil displacement from a homogeneous core by (a) CO_2 and brine (HOWAG-2) and (b) CO_2 and surfactant solution (HOSAG-2) I-137

Figure I-66. Oil recovery performance for oil displacement from a heterogeneous core by (a) CO_2 and brine (HEWAG-1) and (b) CO_2 and surfactant solution (HESAG-1) I-139

Figure I-67. Pressure drop history for oil displacement from a heterogeneous core by (a) CO_2 and brine (HEWAG-1) and (b) CO_2 and surfactant solution (HESAG-1) I-140

Figure I-68. Flow diagram for the modification of gas-phase mobility I-143

Figure I-69. History match of liquid production and pressure drop I-145

Figure I-70. Comparison of simulation with experimental results I-149

Figure I-71. Effect of K_2 on the pressure drop history I-150

Figure I-72. Effect of C_{sref} on the pressure drop history I-151

Figure I-73. Effect of e_2 on the pressure drop history I-152

Figure I-74. Effect of U_{ref2} on the pressure drop history I-153

Figure I-75. Effect of c_2 on the pressure drop history I-154

Figure I-76. Effect of K_1 on the pressure drop history I-155

Figure I-77. Effect of n_c on the pressure drop history I-156

Figure I-78. Effect of e_1 on the pressure drop history I-157

Figure I-79. Effect of U_{ref1} on the pressure drop history I-158

Figure I-80. Effect of c_1 on the pressure drop history I-159

Figure I-81. Water relative permeability curves for k^o_{rw} = 1.0, 0.8, 0.6, 0.4, respectively, and gas relative permeability curve used in the calculations I-163

Figure I-82. The effect of k^o_{rw} on the pressure drop across the system I-164

Figure I-83. The effect of n_w on the pressure drop across the system I-165

Figure I-84. Water relative permeability curves for n_w = 2, 3, 4, 5, respectively, and gas relative permeability curve used in the calculations I-166

Figure I-85. The effect of k^o_{rg} on the pressure drop across the system I-167

Figure I-86. Gas relative permeability curves for k^o_{rg} = 1.0, 0.8, 0.6, 0.4, respectively, and water relative permeability curve used in the calculations I-168

Figure I-87. The effect of n_g on the pressure drop across the system I-170

Figure I-88. Gas relative permeability curves for n_g = 2, 3, 4, 5, respectively, and water relative permeability curve used in the calculations I-171

Figure II-1. Locations of weller for a section of reservoir-B II-6

Figure II-2. Variograms for reservoir-B II-8

Figure II-3. The effect of scales on variance for reservoir-B II-10

Figure II-4. Variograms for reservoir-B at different scales II-12

Figure II-5. The effect of scale on correlation length for reservoir-B II-13

Figure II-6. Reservoir-B, unconditioned log-permeability field II-14

Figure II-7. Reservoir-B, conditioned log-permeability field II-15

Figure II-8. Schematic view of the vuggy core sample II-17

Figure II-9. Photograph of the CT-scanned image of the cross-section of the Canadian limestone reef II-18

Figure II-10. Schematic representation of individual pixel size in the generated data file II-19

Figure II-11. Colored image of the generated data file for the CT-scanned image shown in Fig. II-9 . . . . . II-20

Figure II-12. Vug distribution in the generated file of the CT-scanned image shown in Fig. II-9 . . . . . II-23

Figure II-13. Variation of the local vug density along the sample length II-24

Figure II-14. Schematic representation of the expected pattern in the core sample II-26

Figure II-15. Histogram of the light intensity of 91 images II-27

Figure II-16. Histogram of vug size less than 100 pixels II-28

Figure II-17. Schematic view showing principle of estimating minimum vug contributions II-29

Figure II-18. Histogram of all vug sizes of 91 images II-31

Figure II-19. Three dimensional semivariogram of the vug size II-33

Figure II-20. Semivariogram of the local vug density II-34

Figure II-21. Schematic view of the synthesized cross-section in the Z direction II-35

Figure II-22. Synthesized cross-section showing the vug distribution II-36

Figure II-23. Synthesized cross-section showing vugs and high porosity matrix regions (light intensity < 5) II-38

Figure II-24. Relationship of the local vug density and high porosity matrix II-39

Figure II-25. Synthesized cross-section showing vugs and matrix region having light intensity < 20 . . . . . II-40

Figure II-26. Schematic representation of the formation of chains of trialkyltin fluoride through penta coordination of tin in nonpolar solvents II-45

Figure II-27. Schematic of syntheses of silylorganotin fluorides II-46

Figure II-28. Viscosity as a function of concentration of tris(trimethylsilylpropyl)tin fluoride (PTF) and of dibutyl(trimethylsilylpropyl)tin fluoride (BTF) in *n*-hexane at 25°C (the number at each data point indicates approximate shear rate at the wall) II-49

Figure II-29. Viscosity of solutions of tris(trimethylsilylpropyl)tin fluoride (PTF) in CO_2 . . . . II-50

Figure II-30. Types of ionic associations in ionomers II-51

Figure II-31. FTIR spectrum of poly(1-hexene-co-1,4-hexadiene) II-54

Figure II-32. FTIR spectrum of sulfonated poly(1-hexene-co-1,4-hexadiene) II-55

Figure II-33. Effect of sulfonation upon relative viscosity for (○) poly(1-hexene-co-1,4-hexadiene) and (●) sulfonated poly(1-hexene-co-1,4-hexadiene) II-56

Figure II-34. FTIR spectrum of potassium ionomer II-58

Figure II-35. FTIR spectrum of zinc ionomer II-59

Figure II-36. FTIR spectrum of barium ionomer II-60

Figure II-37. Comparison of relative viscosities of poly(1-hexene-co-1,4-hexadiene) (▲), potassium ionomer (○), zinc ionomer (●), and barium ionomer (△) in *n*-hexane at 25°C II-61

Figure II-38. Comparison of reduced viscosities of poly(1-hexene-co-1,4-hexadiene) (▲), potassium ionomer (○), zinc ionomer (●), and barium ionomer (△) in *n*-hexane at 25°C II-62

Figure II-39. Synthesis of two-arm linear sulfonated polyisobutylene telechelic ionomers with *binifers* II-64

Figure II-40. GPC traces of α,ω-Di(*tert*-chloro)polyisobutylenes using 1,4-bis(1-hydroxy-1-methy-lethyl)benzene (DiCumOH)/IB/BC_3/CH_2Cl_2 at -65°C for 15 minutes: (a) In the absence of electron-pair donor: [DiCumOH] = 0.00178 moles/L, [IB] = 0.06675 moles/L, [BCl_3] = 0.0224 moles/L and (b) In the presence of electron-pair donor: [DiCumOH] = 0.00143 moles/L, [IB] = 0.0534 moles/L, [BCl_3] = 0.0179 moles/L, and [DMA] = 0.00286 moles/L II-67

Figure II-41. M_n vs. weight W_p and N vs. W_p plots of α-ethyl-ω-(*tert*-chloro)polyisobutylenes formed using *tert*-amyl alcohol/ IB/BCl_3/DMA/CH_2Cl_2 system at -40°C by IMA technique [(a), (b), and (c) refer to three incremental monomer additions]. Solid line indicates the theoretical values II-70

Figure II-42. Synthesis of α-ethyl-ω-(*tert*-chloro)polyisobutylenes using *tert*-amyl alcohol/IB/BCl_3/1-methyl-2-pyrrolidinone initiating system II-71

Figure II-43. Synthesis of 1,4-di(2-propyl-2-acetate)benzene II-76

Figure II-44. ^1H, ^{13}C-NMR and ^1H-^{13}C COSY of 1,4-di(2-propyl-2-acetate)benzene II-77

Figure II-45. GPC traces if α-ethyl-ω-(*tert*-chloro)polyisobutylenes [(a), (b), and (c) indicate the polymers formed by three incremental additions of monomer by IMA technique, see Fig. II-16] II-79

Figure II-46. GPC traces of (a) α-methyl-ω-(*tert*-chloro)polyisobutylene formed in the *tert*-butanol/IB/BCl_3/CH_2Cl_2 system at -40°C, (b)α-methyl cyclohexyl-ω-(*tert*-chloro) polyisobutylene formed in the 1-methylcylohexanol/IB/BCl_3/DMA/CH_2Cl_2 system at -40°C, and (c) α-ethyl -ω-(*tert*-chloro)polyisobutylene formed in the *tert*-amyl alcohol/IB/ BCl_3/DMA/CH_2Cl_2 system at -40°C II-80

Figure II-47. GPC trace of α,ω-di(*tert*-chloro)polyisobutylene formed in the 2,4-dimethyl-2,4-pentanediol/IB/BCl3/DMA/CH_2Cl_2 system at -40°C II-81

Figure II-48. GPC trace of α,ω-di(*tert*-chloro)polyisobutylene formed in the 2,4-dimethyl-2,4-pentanediol/IB/$TiCl_4$/DMA/CH_2Cl_2 system at -40°C II-82

Figure II-49. FTIR spectrum of α-ethyl-ω-(*tert*-chloro)polyisobutylene II-84

Figure II-50. FTIR spectrum of α-methyl-ω-(*tert*-chloro)polyisobutylene II-85

Figure II-51. FTIR spectrum of α,ω-di(*tert*-chloro)polyisobutylene formed in the 2,4-dimethyl-2,4-pentanediol/IB/BCl_3/DMA/CH_2Cl_2 system at -40°C II-86

Figure II-52. FTIR spectrum of α,ω-di(*tert*-chloro)polyisobutylene (polymer #1) formed in the 1,4-dicumyl alcohol/IB/BCl3/DMA/CH_2Cl_2 system at -60°C II-87

Figure II-53. FTIR spectrum of α,ω-di(*tert*-chloro)polyisobutylene (polymer #2) formed in the 1,4-dicumyl alcohol/IB/BCl3/DMA/CH_2Cl_2 system at -60°C II-88

Figure II-54. FTIR spectrum of α,ω-di(isopropenyl)polyisobutylene II-90

Figure II-55. FTIR spectrum of α,ω-di(isopropenyl)polyisobutylene (obtained by the dehydrochlorination of the prepolymer formed in the 2,4-dimethyl-2,4-pentanediol/IB/BCl_3/DMA/CH_2Cl_2 system) II-91

Figure II-56. FTIR spectrum of α-ethyl-ω-(isoprepenyl)polyisobutylene II-92

Figure II-57. FTIR spectrum of sulfonated telechelic polyisobutylene (obtained by the sulfonation of α,ω-di(isopropenyl)polyisobutylene) II-94

Figure II-58. FTIR spectrum of sulfonated telechelic potassium ionomer II-95

Figure II-59. Relative viscosity vs. concentration profiles of (a) α-methyl-ω-(*tert*-chloro) polyisobutylene, (b) α-ethyl-ω-(*tert*-chloro)polyisobutylene, and (c) α-methyl cyclohexyl-ω-(*tert*-chloro)polyisobutylene in *n*-hexane at 25°C II-96

Figure II-60. Effect of sulfonation upon relative viscosity for α,ω-di(isopropenyl)polyisobutylene (formed in the 1,4-dicumyl alcohol binifer system) in *n*-hexane at 25°C II-98

Figure II-61. Relative viscosity vs. concentration profiles of (a) α,ω-di(*tert*-chloro)polyisobutylene (formed in the 2,4-dimethyl-2,4-pentanediol binifer system), (b) α,ω-di (isopropenyl)polyisobutylene, (c) sulfonated α,ω-di(isopropenyl)polyisobutylene, and (d) zinc ionomer of sulfonated telechelic polyisobutylene in *n*-hexane at 25°C II-99

Figure II-62. Effect of sulfonation and KOH neutralization upon relative viscosity for (a) α,ω-di(*tert*-chloro)polyisobutylene (formed in the 1,4-dicumyl alcohol, *binifer*, system), (b) α,ω-di(isopropenyl)polyisobutylene, (c) sulfonated α,ω-di(isopropenyl)polyisobutylene, and (d) potassium ionomer of sulfonated telechelic polyisobutylene in *n*-hexane at 25°C II-100

Figure II-63. Modified high-pressure solubility measuring apparatus (a) CO_2 syringe pump, (b) thermostated water bath, (c) tubing to achieve temperature equilibrium, (d) sapphire mixing tube chamber (e) magnet, (f) spiral extension, (g) pressure transducer, (h) Whitey 3-way valve, (i) test tube, (j) cotton, (k) needle tube, (l) assay chamber, and (m) N_2 syringe pump, and valve (10 allows the addition of cosolvent) II-102

Figure II-64. Modified high-pressure capillary tube viscometer II-105

Figure II-65. Simplified diagram of the apparatus for measuring steady-state/CO_2 mobility . . II-109

Figure II-66. Foam mobility measurement system II-110

Figure II-67. Apparent viscosity of CO_2-foam for different rock permeabilities II-112

Figure II-68. Effect of surfactant concentration (Witcolate 1276) on CO_2-foam mobility II-114

Figure II-69. Effect of surfactant concentration (Chevron CD1050) on CO_2-foam mobility . . . II-115

Figure II-70. Effect of surfactant concentration (Enordet X2001) on CO_2-foam mobility II-116

Figure II-71. Effect of flow rate on CO_2-foam mobility II-117

Figure II-72. Foam durability test system II-119

Figure II-73. High-pressure cell for foam durability test II-120

Figure II-74. Interfacial tension between dense CO_2 and Witcolate 1276/1 wt% brine solution II-123

Figure II-75. Interfacial tension between dense CO_2 and Witcolate 1259/1 wt% brine solution II-124

Figure II-76. Interfacial tension between dense CO_2 and Enordet X2001/1 wt% brine solution II-125

Figure II-77. Interfacial tension between dense CO_2 and Chevron CD1040/1 wt% brine solution II-126

Figure II-78. Interfacial tension between dense CO_2 and Chevron CD1050/1 wt% brine solution II-127

Figure II-79. Interfacial tension between dense CO_2 and Chevron CD1040/4 wt% brine solution II-128

Figure II-80. Interfacial tension between dense CO_2 and Chevron CD1050/4 wt% brine solution II-129

Figure II-81. Foam decay of Witcolate 1276/1 wt% brine in dense CO_2 . . . . . II-131

Figure II-82. Foam decay of Witcolate 1259/1 wt% brine in dense CO_2 . . . . . II-132

Figure II-83. Foam decay of Enordet X2001/1 wt% brine in dense CO_2 . . . . . II-133

Figure II-84. Foam decay of Chevron CD1040/1 wt% brine in dense CO_2 . . . . . II-134

Figure II-85. Foam decay of Chevron CD1050/1 wt% brine in dense CO_2 . . . . . II-135

Figure II-86. Foam decay of Chevron CD1040/4 wt% brine in dense CO_2 . . . . . II-136

Figure II-87. Foam decay of Chevron CD1050/4 wt% brine in dense CO_2 . . . . . II-137

Figure II-88. Interfacial tension and foam decay of a Chevron CD1040 desktop-aged sample in dense CO_2 . . . . . II-138

Figure II-89. Interfacial tension and foam decay of a Chevron CD1040 oven-aged sample in dense CO_2 . . . . . II-139

Figure II-90. Interfacial tension and foam decay of a Chevron CD1040 fresh-acidified sample in dense CO_2 . . . . . II-140

Figure II-91. Interfacial tension and foam decay of a Chevron CD1050 desktop-aged sample in dense CO_2 . . . . . II-141

Figure II-92. Interfacial tension and foam decay of a Chevron CD1050 oven-aged sample in dense CO_2 . . . . . II-142

Figure II-93. Interfacial tension and foam decay of a Chevron CD1050 fresh-acidified sample in dense CO_2 . . . . . II-143

Figure II-94. Effluent profile of 1 wt% brine solution without a pulse dampener II-146

Figure II-95. Effluent profile of 1 wt% brine solution with a pulse dampener II-147

Figure II-96. Schematic of the modified drop-weight method apparatus II-148

Figure II-97. The calibration curve for Enordet X2001/1 wt% brine solution II-152

Figure II-98. The calibration curve for Chevron CD1050/4 wt% brine solution II-153

LIST OF TABLES

Table I-1. Components of the Continuous Phase Equilibrium Apparatus I-3

Table I-2. Calculated Densities and Viscosities (from SUPERTRAPP) for Binary and Certain Ternary Mixtures of CO_2 with C_1-C_4 Pure Hydrocarbon Components at 1500 psia and 105°F I-9

Table I-3. List of Hydrocarbon Systems used in the Database I-33

Table I-4. Ranges of Variables for all the Analyses Used in the Determination of the Fitting Parameters I-34

Table I-5. Summary of Average Absolute Percentage Deviations† I-46

Table I-6. Comparison of MLBC, LBC, and Pedersen *et al.* Predicted vs. Experimental Viscosities and PREOS Predicted vs. Experimental Densities for the CO_2/nC_7 Binary System at 1500 psia and 100°F I-50

Table I-7. Summary of Average Absolute Percent Deviations Between Experimental and Predicted Viscosities for the CO_2/nC_7 Binary System I-51

Table I-8. Summary of Average Absolute Percent Deviations Between Experimental and Predicted Densities for the CO_2/nC_7 Binary System I-52

Table I-9. Comparison of MLBC, LBC, and Pedersen *et al.* Predicted vs. Experimental Viscosities for the CO_2 + C_1/Amoco Oil A System at 1200 psia and 106°F I-55

Table I-10. Summary of the Average Absolute Percent Deviations between Experimental and Predicted Viscosities for the CO_2 + C_1/Amoco Oil A System I-56

Table I-11. Resulting Composition of the Five Oil Mixtures Used in the Displacement Experiments I-60

Table I-12. Heavy Components of the Wasson Crude Oil (C_7 - C_{37+}) Lumped into Five Pseudocomponent Groups Using Whitson Method I-66

Table I-13. Initial Characterizing Parameters Obtained from the Lin-Chao and The Katz-Firoozabadi Correlations I-68

Table I-14. Adjusted Critical Parameters and Acentric Factors for the PREOS Calculations . . I-70

Table I-15. Binary Interaction Coefficients (Δ_{ij}) for the Wasson Reservoir Fluid, Used in PREOS Calculations I-71

Table I-16. Summary of the Experimental and the PREOS Predicted BPP for the Wasson Reservoir Oil Plus CO_2 . . . . . I-72

Table I-17. Flash Calculation for Oil-F at 105°F Performed Using PREOS I-74

Table I-18. Recovery Efficiency of Oil-D and Oil-F After 1.2 Pore Volumes (PV) of CO_2 Injected at Constant Temperature of 105°F I-75

Table I-19. Summary of Flow Visualization Results I-85

Table I-20. Liquid Composition of Maljamar STO Obtained by Gas Chromatographic Analysis I-87

Table I-21. Properties of the Fluids I-88

Table I-22. Coreflood Experimental Parameters (Simultaneous Injection into 1% NaCl Solution) I-119

Table I-23. Experimental Conditions and Core Properties I-120

Table I-24. Experimental Conditions I-121

Table I-25. Properties of Homogeneous Core I-122

Table I-26. Properties of Concentric (Heterogeneous) Core I-124

Table I-27. Parameters Used in the History Match I-146

Table I-28. Gas Density and Viscosity Data I-147

Table I-29. Water-Gas Relative Permeability and Capillary Pressure Data I-148

Table I-30. Parameters Used in the Sensitivity Analysis I-160

Table I-31. Data and Parameters Used in the Calculations I-162

Table II-1. Solubilities of Silicon-Containing Triorganotin Fluorides at 25°C II-48

Table II-2. Reaction Conditions of Cationic Copolymerization of 1-Hexane with 1,4-Hexadiene II-53

Table II-3. Polymerization of Isobutylene by the *tert*-Amyl Alcohol/BCl_3/DMA/CH_2Cl_2 System II-69

Table II-4. Polymerization of Isobutylene with Minifers II-73

Table II-5. Living Polymerization of Isobutylene with 2,4-Dimethyl-2,4-pentanediol/BCl_3 or $TiCl_4$/DMA Initiating Systems II-74

Table II-6. Living Polymerization of Isobutylene with 1,4-Dicumyl Alcohol/BCl_3 or $TiCl_4$/DMA Initiating Systems II-75

Table II-7. Solubility Measurements of a Slightly Soluble α-Ethyl-ω-(*tert*-chloro)polyisobutylene with Cosolvents in Dense CO_2 . . . . . II-103

Table II-8. Solubility Measurements of α-Ethyl-ω-(*tert*-chloro)polyisobutylenes in Dense CO_2 . . . . . II-104

Table II-9. Composition of 4 wt% Brine II-122

Table II-10. Summary of the Foam Durability Experiment II-130

ACKNOWLEDGEMENTS

Many different research scientists and technicians have been involved in the completion of this six-year research project; however, their work could not have been fully accomplished without the efforts of a host of others.

First among these are the sponsoring agencies and companies who have contributed financially to support this project. These are the Morgantown Energy Technology Center of the U.S. Department of Energy, the State of New Mexico, as represented by the New Mexico Research and Development Institute, and the following oil companies who have been supporters of our consortium during all or part of the six years: Abu Dhabi National Reservoir Research Foundation, Amoco Production Company, Arco Oil and Gas Company, BP Exploration Company, Chevron Oil Company, Cities Service Oil Company, Conoco Inc., Elf Aquitaine, Gulf Oil Company, Japan National Oil Company, Japex Research Center, Marathon Oil Company, Mobil Research and Development Corporation, Oxy USA, Petro Canada Inc., Phillips Petroleum Company, Shell Oil Company, Sun Exploration Company, Tenneco Oil Company, and Texaco USA.

In addition to these organizations and the individuals within them, there are many dedicated persons here at the Petroleum Recovery Research Center who have exerted tremendous efforts so that this work could be properly described and reported. Mentioning their names here does not begin to discharge our indebtedness to them for their dedication and hard work. Even the casual reader of this final Annual will be able to see the quality of the product they have generated. They are:

K. Allbritton (editor)
Karen Bohlender
Bob Emery (computer administrator)
Cathy Lambert
Brenda Parson
Janet Golding
Monica Ferdig
Cliff Polston
Scott Thompson (student assistant editor)
Jason Weiss

We also express our great appreciation to other members of the staff of New Mexico Tech who have extended their efforts in various ways to help produce this report on our activities.

EXECUTIVE SUMMARY

This is the Final Annual Report of "Improvement of CO_2 Performance." In its six years, we have subjected to careful scrutiny many individual facets important to the use of dense CO_2 for oil recovery. These topics have ranged from measurements that are extremely specific to CO_2 and to particular crude oils to more general research questions that also apply to different fields and recovery processes besides CO_2. Because of the diversity of this large range of topics, the entire project is divided into Task I and Task II, which are described in separate paragraphs below. The report contains a lengthy Introduction, an extensive historical section that reviews earlier results, two other sections that give details of research accomplishments during this final year, and a concluding section in which a follow-on project, the "Field Verification of CO_2-Foam," is described.

One primary aim in Task I was to increase our understanding (and the body of relevant data) concerning the complicated interaction between injected high-pressure CO_2 and *in situ* fluids. The local displacement efficiency of a CO_2 flood depends on the phase behavior and fluid properties of the phases that evolve for the particular CO_2/crude oil system. For this purpose, experiments have continued throughout the project with the continuous phase equilibrium (CPE) apparatus that was invented and developed in our laboratory. This computerized device enables the continuous measurement of the changes in phases and properties that occur as the components are mixed—and this corresponds, to some extent, to the range of mixtures that exist in the transition zone where crude oil is displaced by CO_2. We have also performed laboratory floods and computer simulations to study the effects of a number of variables on the displacement process. These variables include the phase behavior, the density and viscosity of the fluids, the porous system, dispersion, and viscous fingering. The high-pressure laboratory measurements were conducted in slim tubes, cores, and micromodels, whereas the simulations have ranged from the computation of particular experiments to the broader subject of CO_2-foam flooding in reservoirs.

The major emphasis in Task II has been on the effects of the nonuniformity of displacement—especially in miscible CO_2 displacements. We have considered the causes of the nonuniformity, its assessment, and the possible responses that can be made by the reservoir engineer. Displacement in the reservoir (and often in cores) occurs nonuniformly for two reasons, both of which are often present at the same time. The first of the reasons is the heterogeneity of the rock itself. The report contains measurements of small scale heterogeneities, geostatistical descriptions of permeability distributions on a reservoir scale, and simulations of the effect of these heterogeneities on miscible displacement and on tracer flow. The second reason for displacement nonuniformity is the low viscosity of the CO_2 displacing fluid. The report contains extensive descriptions of our work in developing two remedies for this situation. The first of these has been a search for polymers that are soluble in dense CO_2 and raise its viscosity sufficiently to eliminate frontal instability during CO_2 displacement of crude oil. Although the search is not over, a class of polymers has been found that offers great promise and is worthy of further effort. A second *mobility control* agent is CO_2-foam, which is a mixture of dense CO_2 and an aqueous surfactant solution. This offers a more immediate solution. We believe that CO_2-foam can be used to improve the recovery in many of today's CO_2-based EOR projects. The report also describes, briefly, the status of a follow-on project in which the usefulness of CO_2-foam is to be attempted in a New Mexico oil field.

INTRODUCTION

The New Mexico PRRC Research Project "Improvement of CO_2 Flood Performance" has reached its end. Over the past six years, a large number of topics have been investigated, and it is the purpose of this introduction to give brief but informational descriptions of them all. A separate section on the history of the project goes into greater depth on some of the earlier aspects of the research. A separate, extensive treatment in yet another section covers the principal research results of the project and its current status.

A. TASK I—PHASE BEHAVIOR AND SIMULATION

The research program on the "Improvement of CO_2 Flood Performance" at the New Mexico Petroleum Recovery Research Center has reached its final phase. The program is a comprehensive study aimed at developing an understanding of the fundamental aspects of carbon dioxide flooding. For the past six years, a coordinated agenda of experimental and theoretical work has produced a level of comprehension that facilitates the characterization and proper interpretation of CO_2 flooding in laboratory experiments. Much of what has been learned in the interim is now being utilized in a recently initiated Proof of Concept project entitled "Field Verification of CO_2 Foam."

The introduction of carbon dioxide in an oil reservoir results in a complicated interaction between the injected CO_2 and the *in situ* fluids. The local displacement efficiency of a CO_2 flood is determined by the phase behavior and fluid properties (viscosity and density) of the phases that evolve for a particular CO_2/crude oil system. The phase behavior and fluid properties, together with viscous and gravitational instabilities, porous media heterogeneity, and hydrodynamic dispersion, account for the competing factors during a CO_2 flood, the sum of which determines the overall recovery efficiency. Although a complete decoupling of these factors is not possible, laboratory CO_2 floods, if properly designed and interpreted, can provide valuable information for setting the grounds for evaluating the effects of the competing mechanisms.

Laboratory floods depend on a number of factors as well. These are: (1) the phase behavior of the CO_2/crude oil system, (2) the fluid properties (density and viscosity) of the phases that evolve during the flood, (3) the wettability and interfacial tension of the phases present, (4) the porous medium properties, (5) dispersion, (6) viscous fingering, (7) gravity segregation, and (8) the phase relative permeabilities. The correct identification of the dominant displacement mechanism requires the independent measurement of these factors.

By now, it is well known that the phase behavior of CO_2/crude oil systems accounts for the high displacement efficiency that is characteristic of slim tube displacements. The extraction efficiency of a dense CO_2-rich phase has been known to produce a high local-displacement efficiency. Static phase equilibria measurements with CO_2 and its mixture with synthetic and naturally occurring hydrocarbon systems have shown a rich and complex phase behavior topography. Although these findings have resulted in an excellent understanding of the phase behavior of CO_2/hydrocarbon system under a wide range of conditions, there is still a need to address the impact of phase behavior in a dynamic setting, such as those encountered in coreflood experiments.

CO_2 flooding projects have frequently experienced poor sweep efficiency because of rock heterogeneity, unfavorable mobility ratio, and adverse density ratio. The mobility of a gas flowing through a porous medium is lowered when it is dispersed within a liquid as a foam. Consequently, foams can improve sweep in recovery processes that use gases such as CO_2. CO_2-foam is a better displacing fluid than CO_2 alone because it can lessen the effect of fingering and reduce the severity of channels.

The research philosophy adapted over the past six years is described briefly in the following paragraphs. Details of each of the research areas are provided in the pertinent sections of the report.

1. Viscosity, Density, and Composition Measurements

The reduction of crude oil viscosity by dissolved CO_2 during a CO_2 flood is a well known and beneficial effect. The CO_2 flooding literature, nevertheless, contain very little viscosity data. In a developed miscibility CO_2 process, the properties as well as compositions of phases in equilibrium are needed hopes to obtain an accurate prediction of CO_2 floods. Information on the viscosity of CO_2-rich phases, in particular, are needed to assess the effect of viscosity on local mixing at the leading edge of the transition zone.

An apparatus was developed that provides the simultaneous measurement of fluid properties and composition for single and coexisting phases. The apparatus has provided a fast and efficient method of generating information on CO_2/hydrocarbon mixture viscosities along with densities and phase compositions. Measurements performed with a variety of synthetic oils and a number of naturally occurring crudes (mostly from West Texas) have produced a comprehensive database of viscosity data. The injection gases used ranged from pure CO_2 to mixtures of CO_2 as well as several light hydrocarbon and nonhydrocarbon gases. A viscosity correlation has been developed based on the data obtained.

2. Effect of Solution Gas on Miscibility Development

The effect of solution gas on the development of miscibility is a controversial topic in CO_2 flooding. The light hydrocarbon components (C_1-C_4) dissolved in the oil have been shown to have little effect on the pressure required to generate miscibility (the so-called minimum miscibility pressure [MMP]). The same, however, cannot be said when the C_1-C_4 components are present as free gas (i.e., when the reservoir pressure is below the oil bubble point pressure). Our investigation was, therefore, concerned with whether high displacement efficiency is possible at pressures below the bubble point. The standard description of multiple-contact miscibility development rules out such a possibility. The question of how miscibility could be generated in the above scenario is of more than academic interest. Several reservoirs have gas caps that are large enough so that the reservoir pressure cannot be raised substantially to force the free gas into solution. If the displacement efficiency is high at the bubble point pressure, then there is a possibility that a favorable efficiency can also be realized for pressures in the two-phase region. The results of our investigation are presented in the report.

3. Mechanistic Modeling of High-Pressure Gas/Foam Flow

The results of both experimental and theoretical studies of gas-foam behavior in the literature have led to models of foam generation and propagation, which have been incorporated in several

mechanistic foam simulators. These models are based on a population balance description of the foam texture, which is one of the important variables governing foam mobility. A generalized, two-dimensional mechanistic foam-flood simulator was developed. Foam is generated by the following mechanisms: snap-off, lamella division, and leave-behind, all of which are included in the simulator. In addition, foam coalescence and trapping mechanisms are incorporated in the model. This simulator is able to model many of the processes associated with channel blockage by foam and diversion of flow into the bypassed oil matrix. Results from CO_2-foam corefloods were matched with the simulator, and a good agreement was obtained.

4. Mechanistic Studies of High-Pressure Gas/Foam Flow: Coreflood Experiments

Numerical simulation of foam flow in porous media requires knowledge of the relationship between gas mobility in the presence of foam and surfactant concentration, fluid saturations, pressure, and interstitial gas velocity. Coreflood experiments can be correlated with the micromodel studies to develop empirical relationships for gas mobility. Under simultaneous injection of CO_2 and surfactant solution, foam is formed inside the core when conditions favorable for foam formation are met. Our investigations were, therefore, concerned with what happens when the gas encounters surfactant solution in the porous medium. This was investigated in terms of surfactant concentration, presence of an oil phase, gas-liquid volumetric ratio, and flow rate.

5. Mechanistic Studies of High-Pressure Gas/Foam Flow: Micromodel Visualization Experiments

The visualization of high-pressure gas/oil/surfactant solution flow through glass micromodels helps determine principal mechanisms at the pore level during CO_2-foam displacements at reservoir conditions. A qualitative analysis of glass micromodel experiments was used to help explain physical results from high pressure foam coreflood displacements. The information was also utilized in the development of a mechanistic foam flood simulator. The mechanisms associated with CO_2 mobility reduction were investigated in terms of microscopic heterogeneity, presence of an oil phase, gas-liquid volumetric ratio, and displacement efficiency in miscible and immiscible CO_2 floods.

B. TASK II—FLOW NONUNIFORMITY

In our recent work, this task has been divided into three subtasks that are concerned with two major features of the nonuniformity of flow, displacement in reservoirs, and in samples of porous rock. These features are the nonuniformities that are caused by heterogeneities of the porous matrix itself and flow nonuniformities that are caused or aggravated by the differences between the mobilities and the densities of the displaced and displacing fluids.

Both of these situations have been considered primarily as they apply to the miscible displacement by CO_2. It is, of course, realized that CO_2 is not 'first contact miscible' with most crude oils; indeed, the 'conditions for miscibility' with mixtures of dense CO_2 and other gases have been substantially clarified in Task I of this project. It has become apparent that even when the system pressure is well above the 'minimum miscibility pressure' (MMP), when the details of the displacement can be understood as a single-phase flow situation, the transfer of material into and out of the flowing phase cannot be

completely ignored. This transfer occurs principally by molecular diffusion in two different types of pore-scale environments. The first of these types lie completely within the irregular boundaries of the nonaqueous hydrocarbon/CO_2 phase. The oil in these regions is eventually gathered up into an 'oil bank.' The second environment directly involves the phase boundaries between the nonpolar flowing phase and regions occupied by the mobile or immobile water in the rock. The principal component transported across these phase boundaries is CO_2 going into solution in the aqueous phase.

In spite of the complex nature of the actual system, it is possible, as a first approximation, to view a CO_2 flood as a miscible displacement that can be described in terms of two principal variables. These variables are the Darcy velocity of the hydrocarbon/dense CO_2 phase and, within that phase, the concentration of the CO_2. A convenient representation of the latter is the family of 'isoconcentration surfaces' that describes the location of the injected CO_2 and of the 'front' between it and the oil. The surfaces are especially close to each other in localities where the concentration gradient is large; this measure, therefore, gives practical ways to envisage the extent of the transition zone as well as the degree to which the injected fluid is dissipated into 'fingers.' Further, the evolution of the displacement process can be viewed in terms of the motion of the isoconcentration surfaces.

Considering such a picture, we divide the causes of displacement nonuniformity into two types. The first type of irregularities can occur and grow on the isoconcentration surfaces, even if the displaced fluid is not hydrodynamically different from the injected fluid. The irregularities arise and become larger as flow proceeds because of differences in the effective permeability or porosity from place to place in the rock. These differences may be due to permanent features of the rock structure, the result of geological processes that took place during the long history of the rock, starting with its deposition. The differences might also be caused by more recent variations from place to place in the value of the oil saturation. In either case, these nonuniformities in the ability of the rock to support flow will cause the continued growth of the amplitude of distortions of the front as the flood proceeds.

We have focused our research on the effects of heterogeneity primarily on the influence on displacement of variations in permeability. We have studied, in particular, the situation that arises when the positions of the permeability heterogeneities are not correlated with each other over long distances. It has become clear that the effect on displacement is closely linked with the degree of spatial correlation of the permeability variations, and, consequently, the detailed statistical study of permeability fields has become quite important. Fortunately, the relatively new mathematical discipline known as geostatistics has made its appearance in the past two decades, with much of the associated research centering around Dr. Allan Gutjahr of the New Mexico Tech Mathematics Department. As will become apparent, we have made use of our proximity to him, and have considered in some detail the extent and statistics of permeability fields as well as the consequent growth of irregularities on displacement fronts.

A second class of situations that cause the growth of irregularities or distortions on the isoconcentration surfaces are those that are related to the contrast in hydrodynamic properties of displaced and displacing fluids. The analysis of such 'fingers' and their growth during displacement is less complex in the miscible displacement situation. Furthermore, the work is well described in terms of the motions of the isoconcentration surfaces discussed above. Early in our research project, a theoretical and experimental analysis was conducted to determine the conditions under which *frontal instabilities* will continue to grow. It was shown that, in a core or unconsolidated pack of circular cross section, the length to which fingers will grow in single phase flow is limited by the transverse dispersion of concentration, and that the limiting length is inversely proportional to the square of the tube diameter.

Thus, a miscible flood in a narrow tube gives a much better approximation of a 'one-dimensional' experiment, even in an unstable situation, than does a similar flood in a larger diameter pack or core.

In a reservoir environment in which the extent of the porous medium is large in the transverse direction (perpendicular to the average flow), instability fingers can grow without the limitation they encounter in laboratory experiments. Transverse dispersion is able to stop the growth of these fingers with shorter wavelengths, of the order of the transition zone width or less, but is unable to prevent the continued linear growth of larger-scale fingers or irregularities, the length of which increases in proportion to the overall distance travelled by the front. The most unfavorable result of such fingers is that they open up passageways from injection to production wells, along which the fluid velocity is higher than in the rest of the reservoir. These passageways (along which the velocity is correlated) can have a much more serious effect on production efficiency than is caused by natural variations in permeability, the positions of which may not be correlated in such a consistently harmful way with well positions.

Because of the deleterious effect of finger growth on displacement efficiency, a constant goal of our research has been the development of effective thickeners or mobility control agents for CO_2 floods. Our purpose has been the long-term design of means by which CO_2 floods can be *stabilized* against the growth of frontal instabilities. Stabilized miscible floods promise displacement performance in reservoirs comparable to that which is experienced in small-diameter laboratory packs or cores, and will increase the crude oil reserves of the Nation far beyond the usual EOR targets. This is in contrast to most[1] current CO_2 and other miscible floods, which have only been able to increase oil recovery by a relatively small fraction.

Two types of thickeners were considered as possible targets when we initiated our research six years ago. Since that time we have made significant progress in our research of the thickeners; however, significant technical questions concerning both of these possible types of additives remain uninvestigated.

The first possibility that we have worked on, as a conceivable mobility control additive in CO_2 floods, is called the 'direct thickener.' These materials are polymers, which are soluble in dense CO_2, that will increase the viscosity of the solution sufficiently so that a stabilized CO_2 flood in a horizontal direction can be undertaken. Early during this work, we examined a variety of commercially available polymers, and we realized that the class of polymers that are soluble in water is nonintersecting with the set of polymers soluble in nonpolar fluids such as dense CO_2. Lists of known polymers[2] that are soluble in CO_2, and of those that are not, were published. These lists have guided our research and that of others who have researched this topic. In particular, our list contains the polymer polymethylsiloxane that was recently used in conjunction with an aromatic cosolvent a recent successful demonstration of the effectiveness of a direct thickener in CO_2 corefloods by Bae and Irani.[3]

---

[1]The exceptions are a few reservoirs with substantial vertical extent, where it was possible to operate gravitationally stable miscible displacements. During periods when it was economically possible to operate these projects at the requisite low flow rate, the flooding efficiency was upwards of 95%.

[2]Heller, J.P., Dandge, D.K., Card, R.J., and Donaruma, L.G.: "Direct Thickeners for Mobility Control of CO_2 Floods," *SPEJ* (Oct. 1985) 679-686.

[3]Bae, J.H. and Irani, C.A.: "A Laboratory Investigation of Thickened CO_2 Process," paper SPE 20467 presented at the Annual Technical Conference and Exhibition, New Orleans, Sept. 23-26, 1990.

The main objective of our work has been to discover single polymers that will accomplish the required viscosification of dense CO_2 at low concentration so as to satisfy the economic constraints for use in EOR. It has become apparent that dense CO_2, even at high pressure, is a poor solvent. Our search for a 'Method I' direct thickener—that is, for a simple polymer that would be both soluble and capable of sufficiently increasing solution viscosity—was limited by the fact that in order to be soluble at the percent level, the molecular weight of the polymer could not be larger than a few thousand. On the other hand, to produce sufficient viscosification, such a polymer would need to consist of a much longer molecular chain—that is, it would need to have a much larger molecular weight. In the course of our investigation, a variety of polymers were synthesized, characterized, and examined for possible use as direct thickeners. Many different types of hydrocarbon polymers of different molecular weight have been synthesized using different polymerization methods. Testing of their viscosity-building properties were accomplished with a variety of instruments, many of them designed and constructed in our laboratory. Our research has progressed to the synthesis and testing of Method II and Method III materials, which are capable of producing 'associative' polymeric solutions that promise to bypass the fundamental difficulty previously described—that beset the Method I polymers. In the fuller section on our research on direct thickeners, we describe the extensive progress that we have made. We have not yet achieved our goal, however, of a simple and inexpensive polymer that can be used at low concentration to stabilize CO_2 floods.

A second possibility for the thickening of CO_2 has been to use a two-phase mixture of CO_2 with an aqueous surfactant solution. Although this accomplishes no change in the properties of the dense CO_2 itself, the addition of the surfactant changes the ordinary two-phase flow regime that would otherwise be expected to govern the simultaneous flow of water and dense CO_2 in the porous system. Apparently, the difference arises because of the stability of aqueous 'lamellae' that separate CO_2 into groups of pores in the rock, restricting its flow. The effect depends on the population of these lamellae or bubble-films, which is in turn a function not only of the surfactant concentration and stability but of characteristics of the rock as well. Although much of the theoretical and experimental research on the flow of foam has focused on the microscopic conditions under which lamellae form and break, we have concerned ourselves largely with the macroscopic or larger-scale measurements of the increased resistance to foam in reservoir rock.

During the course of the research project, different features of this 'CO_2-foam' were investigated experimentally at reservoir pressures, and, more recently, at the slightly elevated temperatures characteristic of the Permian Basin reservoirs. The major property of CO_2-foam that was studied was the mobility—that is, the ratio of the superficial or Darcy flow velocity through a core sample to the pressure gradient required to maintain that flow. This is a steady-state measurement in which the net fluid content of the core is not changed during the test. It is presumed that the core sample tested is in a situation similar to that of rock in the 'flushed' portion of the reservoir, from which essentially all of the oil has been displaced and through which both dense CO_2 and surfactant solution are flowing. The lowered mobility in this region is needed for mobility control—to prevent the creation of correlated flow-paths for the injected CO_2. Our experiments were designed to show the influence on mobility of surfactant concentration and type, CO_2 to total fluids ratio ('quality'), and flow rate. Another important independent variable was the type of rock used in the test.

It was discovered that the influence of rock type is quite important, and may be stated simply in terms of the brine permeability of the rock. Our results show that the relative mobility of foam, the reciprocal of which can be considered the effective viscosity of the CO_2-foam as a reservoir fluid, is quite dependent on the permeability of the rock. Furthermore, the variation in apparent viscosity is in the exact

direction that is needed—a higher apparent viscosity is observed in higher permeability rock. Although the effect is nonlinear, it is significant over a useful range of permeability. Consequently, the use of mixtures of CO_2 and surfactant solution holds even greater promise than anticipated because CO_2-foam can be expected to compensate to some degree for the effect of natural heterogeneities.

In the area of surfactant interaction with reservoir rock material, perhaps the most important practical question concerns the quantity that will be adsorbed on the rock. This quantity may be separated into a reversible and a permanent component on the basis of the time required for equilibration. Both of these characteristics may be evaluated in a dynamic adsorption experiment in which the surfactant concentration in a brine effluent is continuously measured. The report details the method that we developed for the real-time measurement of surfactant concentration in the fluid emerging from test core.

We are also investigating the properties of bubble films in a reservoir conditions visual cell. Dense CO_2 is bubbled into this cell, which contains the chosen surfactant/brine at high pressure, and forms a foam layer in the upper portion of the cell. In addition to the lifetime of this foam, we are also able to compute the interfacial tension (IFT) between the two fluids from the size of the bubbles. This device has given us a means to compare the apparent stability of films formed by different surfactants, as well as an accurate measure of the IFT and the critical micelle concentration (CMC) under reservoir conditions.

Many of the properties of the mixture of dense CO_2 with aqueous surfactant solution have been investigated and are detailed in the following pages. A follow-on project has been developed in which the utility of CO_2-foam will be evaluated in collaboration with the operator of a large, unitized New Mexico oil field and the interest owners. This latter project, the "Field Verification of CO_2-Foam," is also described in a later section.

HISTORY OF PROJECT

A. PRECEDING RESEARCH

The PRRC research project "Improvement of CO_2 Flood Performance" was started in 1983 as an outgrowth of two independent research projects that were concerned with related EOR problems. These projects were entitled "Displacement of Oil by Carbon Dioxide" (DOE BC10331, NMRDI 3306) and "The Development of Mobility Control Methods to Improve Recovery by CO_2" (DOE MC 10689, NMRDI 3307).

The first project, "Displacement of Oil by Carbon Dioxide," had pioneered the representation of the CO_2 displacement of crude oil on pseudoternary diagrams, showing the importance of oil composition and pressure to the phase behavior. This research emphasized both experimental measurements of the properties of mixtures of CO_2 and various crude oils and the development of numerical models for the displacement process. In this early project, the idea of a "continuous multi-contact experiment" was first developed in order to trace the properties of near equilibrium mixtures of displaced and displacing fluids. Early concerns also included the effect of water at different saturations on the displacement process.

The second project, "The Development of Mobility Control Methods to Improve Recovery by CO_2," surveyed the literature concerning the problems that develop during the displacement of a more-viscous fluid by a less-viscous one, and the means that had been proposed for alleviating these problems, especially in the case of CO_2 floods. The project examined these means and identified two as offering promise for effectively thickening the injected CO_2. The first method is the use of so-called CO_2-foam, consisting of a mixture of dense CO_2 and aqueous surfactant solution, and the second is the use of direct thickeners, which consist of CO_2-soluble polymers. Many of the experimental procedures developed in this early project, as well as some of the concepts on which the subsequent research has been based, are still in use.

Thus, these two projects developed many of the early ideas and procedures that formed the basis of the subsequent and more extensive research in the six-year project discussed here. Although the two preceding PRRC CO_2 research projects were combined into the new one, many of the historic divisions were maintained. With the above as background, the further evolution and expansion of the various research topics in this project, "Improvement of CO_2 Flood Performance," will now be discussed in more detail.

B. PROJECT PERSONNEL

Every effort has been made to make the following lists complete. Some of the people on the lists have been with the project since it started, some were with us for several years, and a few were here only a relatively short time. It will be noticed that some of the personnel are listed in several places. The purpose of this is to indicate that they have contributed to both projects or in more than one capacity.

1. **Task I**

Principal Investigators:
F.M. Orr, J.J. Taber, Frank Kovarik, F. David Martin
Research Collaborators:
Robert Bretz, Eric Chang, Dae Gee Huh, Robbie Lansangan, Chris Lien, Larry Owusu, Matthew Silva, Jim Smith, Mark Taylor
Technicians:
David Berridge, Sean French, David Fritchman, John Oelfke, Tony Onimole, Mickey Pelletier, Tracy Spence
Graduate Students:
Naveed Akram, Ibraham Bahralolom, Tom Cochrane, Min Huang, L.L. Larsen, G.J. Ruskauff, Tanvir Sadiq, C. Thomas, Hossein Yaghoobi, Zahid Md. Zain
Undergraduate Student Technicians:
David Berridge, Elloitt Boyle, Brian Deen, Cynthia Hutter, Sandy Ishmael, Eric Jacobson, Todd Mueller, A.R. Tabaei, Jung-Ming Tarng, T. Vogelei, Wendy Weiss, S.L. Welch

2. **Task II**

Principal Investigator:
John Heller
Research Collaborators:
Dileep Dandge, Pratap Gullapalli, Murty Kuntamukkula, Hae Ok Lee, Chris Lien, Jyun-Syung Tsau
Technicians:
Brent Gordon, Kirk Hollis, Jim McLemore, Andrew Rosenthal, Ron Sandoval, Rita Singh, Sandy Svec, Susan Weber, Ann Westerberg-Hoefer, Kennard Wilson
Graduate Students:
Elhassan Abdalla, Ibrahim Bahralolom, Saleem Ghori, Saral Ghosh, Naser Heravi, Kirk Hollis, Marilyn Moore, Sufi Mustafa, Pradeep Singh, Junaid Sultan, Craig Taylor, Sunil Tehwari, Jian Wang, Kennard Wilson
Undergraduate Student Technicians:
Tariq Ahsan, Chris Anderson, Jon Becker, Rodney Blount, Martin Brueggemann, Nannette Brumley, Dana Hite, Jesse Lawson, Richard Liddle, Charlene Matlock, Ali Maqsood, G. McColpin, Tony Onimole, Urban Ronellenfitsch, Mustafa Sadeq, Robert Sumpter, Bob Svec, Mike Thach, Mike Turner, Bob Wooten

C. DEVELOPMENT OF RESEARCH TOPICS

1. Task I — Measurement of Reservoir Condition Mixture Properties

The first of the continuous multi-contact (CMC) experiments was assembled from separate components on a laboratory bench, which were maintained at reservoir temperature by wrappings of heater tape and hot-water filled tubing. Although inconvenient to operate and plagued by problems stemming from uneven temperatures, these experiments produced useful data. As a result, the 'separate

component' design was continued during the early work. One of the first subtasks of the new project was the improvement of this situation, converting the assemblage of disparate apparatus into a single-integrated system with a wider and more-stable range of operating conditions.

Accomplishment of this goal was secured in several steps. Perhaps the most important of these resulted from the final perfection of an early inspiration—the inclusion in the experiment of on-line, high-pressure, high-temperature viscosity measurement. In the method used for this measurement, no pressure drop is involved. Thus, viscosity measurements made by this method, unlike those made by a capillary tube system, are each representative of a single fluid density. This is vital for measurements in the neighborhood of the critical point, where density varies strongly with pressure. The method used measures the damping of torsional oscillations that are induced in a quartz crystal cut into a cylindrical shape by the viscous friction in the surrounding fluid. This technique was first used in the 1930s and, in the mid-80s, was used by physicists at the National Institute for Science and Technology (NIST, formerly NBS) for measuring the viscosity of gases at near atmospheric pressure. The effectiveness of this method is a consequence of the extremely low internal friction in quartz crystals. As a result, measured damping, which can be measured with great precision by electronic means, is largely due to the viscosity of the fluid in which the crystal is immersed.

Several major developments of the NBS technique were needed to adapt it for use in this project. The method would first of all need to operate on-line as a flow-through instrument. Since the fluid composition would be changing during the course of the experiment, the annulus surrounding the crystal would have to be small and completely flushed while fluid was flowing through the instrument. The fluid, and the crystal itself, would have to be contained in a specially designed vessel—capable of withstanding high pressures and temperatures. The pressure vessel should also contain facilities for securely mounting the crystal at nodes of the vibration. These goals were attained after the solution of many agonizingly difficult problems. These ranged from the design and construction of secure mounting points in a designated nodal groove cut into the crystal through the fabrication of an electrode assembly installed in a machinable-glass insert, to the identification of parasitic modes of oscillation of the cylindrical crystal-fluid system.

Before the quartz crystal viscometer could be used in the CMC experiment, it was necessary to develop a method to measure quickly and accurately the damping parameter. In the NBS system, this was performed by laboriously balancing an alternating current bridge; an operation that requires the simultaneous adjustment of two parameters. This adjustment requires great patience and can only be performed by a very experienced experimenter. In contrast, for the PRRC instrument to operate at the same rate as the other instruments connected to the system, it would be necessary to automate the measurement so that viscosity readings could be obtained 'on-line,' at a rate of one per minute without the operator's attention. This goal was attained by using a commercial instrument (a Hewlett-Packard Impedance Analyzer), which was capable of making electrical impedance measurements at programmable frequencies under computer control. A BASIC subroutine was written that automatically sought out the resonance frequency and, by measuring the half-width of the resonance curve, computed the damping of the crystal's oscillations and, therefore, the viscosity of the fluid passing through the crystal holder. This subroutine was then incorporated into the existing control program.

A third vital task in upgrading the CMC system was to design and construct a heated and insulated enclosure that would enable all necessary parts—the mixing chamber, the two viscometers, and the two densitometers—to be maintained at a chosen temperature with a minimum variation in time or temperature difference between the components. This goal was achieved by the use of a triple-wall, insulated box

equipped with two blowers, two heaters, and a commercial, thermocouple-based control system. This enabled experiments to be performed at controlled temperatures from room temperature up to 250°F.

The use of this system has exceeded our expectations in its operational characteristics, with virtually no further modifications. During the course of the research project, a large number of crude-oil/displacing gas-systems were examined with this unique tool, which has come to be known by the more descriptive name "Continuous (Pseudo) Equilibrium Experiment."

2. Task II — Use of CO_2-foam for a Displacement Fluid

Our early research activity in the development of CO_2-foam as a mobility control additive consisted primarily in the choice and development of apparatus and procedures for performing the critical experiments and of the concepts that lay behind them.

The foam of ordinary, atmospheric-pressure experience is a two-phase mixture in which the aqueous phase, though continuous, represents only a minor part of the overall volume. It is this low fractional volume of the continuous phase (less than about 26% for three-dimensional, and less than about 10% for 2-D foams) that is responsible for the high apparent viscosity of foam-like dispersions. It was expected that in porous media, the mixture that we conveniently call foam would exist in about the same volume fraction range and would show other similar properties, despite its confinement in the multiply-connected pore space.

The classical definition of 'viscosity' is not concerned with the size-scale of the volume element subjected to shear, and the measured viscosities of even non-Newtonian fluids are independent of the size of the viscometer. Because of this, the concept of viscosity is strictly applicable only to continuous fluids and cannot be expected to provide consistent results if used blindly to compute the resistance to foam flow in fluid-conducting channels of different sizes relative to the bubble size of the foam. This fact has been demonstrated in many experiments and was discussed by us in an early literature review.[4]

In reservoir rock, the importance of the relative size of the 'bubbles' of non-polar fluid to the pore space was also clear, yet the nature of the relationship is difficult to discern from theory. This is because the pore spaces of interest cover such a wide range of sizes and shapes and because there is such a variety of wall material. Thus, the channels through which flow proceeds are extremely varied. It was evident from previous research that successful use of foam, in the displacement of oil, could not be assured without a more-basic understanding of the process of foam flow in reservoir rock and of the chemical behavior of the surfactant in contact with different varieties of reservoir rock.

As in the current work, three themes can be traced through the earlier research. These are the screening of surfactants for their compatibility and effectiveness with dense CO_2, the extent of the adsorptive loss of surfactant to be expected as foam flows through the reservoir, and the mobility of the two-phase mixture of aqueous surfactant solution with the liquid-like CO_2 in porous material. The research during the first five years of the project, and the changing status of knowledge in each of these areas, are briefly discussed in the three sections below.

---

[4]Kuntamukkula, M.S. and Heller, J.P.: "Critical Review of the Foam Rheology Literature," *Ind. & Eng. Chem. Res.* (1987) **26**, 318-325.

a. Surfactant Screening

It was recognized early that, whatever the microscopic geometry at the pore level, the characteristics of the interfaces between CO_2 and surfactant solution were of great importance. These interfaces could not *a priori* be expected to have the same properties as air-surfactant surfaces or even as CO_2-surfactant surfaces at atmospheric pressure. In addition to the possibly different arrangement of surfactant molecules at such an interface, other work had made us quite aware of the solvent power of dense CO_2, which made this fluid capable of greatly influencing the molecular distribution in operational use. It was decided that measurements of foam stability and surface tensions between surfactant solutions and air would not fill our needs. At the same time, the difficulty of performing the experiments with liquid or supercritical CO_2 apparently precluded such high-pressure measurements for the screening of surfactants.

For the purposes of screening, then, it was decided to simulate the major characteristics of dense CO_2 by a nonpolar, light hydrocarbon liquid, which could be handled under ambient conditions of temperature and pressure. It seemed that several of the alkanes would meet this need, and isooctane was selected. A device, and a procedure for its use, was developed to enable surfactant solutions to be shaken with isooctane in a closed test tube. The shaking action was quite mild, consisting of periods in which the test tube was quickly inverted alternating with longer periods during which the droplets or bubbles of isooctane could float upwards to collect in a layer simulating the CO_2-foam. We recorded the thickness of the layer of foam-like dispersion that was built up and the length of time it persisted after the repeated inversions were stopped.

This test, as well as the measurements of both surface tensions against air and interfacial tensions against isooctane (measured with a conventional Wilhelmy plate apparatus), was performed on many different commercial surfactants. 'Foamability' assessments made on eighty-eight surfactants were presented in the Project's Third Annual Report.[5]

Although the applicability of these atmospheric pressure screening measurements (made against isooctane) has remained credible to us, it has not been universally accepted. Accordingly, and responding to continued questions about the possible uniqueness of dense CO_2, a procedure was developed by which repeated high pressure measurements could be made using different surfactant solutions without excessive turn-around time. The apparatus by which this can be accomplished was developed in 1989. A section describing the operation of the apparatus, including diagrams, appears in the Fifth Annual Report[6] of the project. Only minor improvements have been made in the apparatus and procedure since its first construction. It has been used to give measurements of interfacial tension (IFT) with sufficient precision, which reveal dependable values for the critical micelle concentrations (CMC) of many different surfactants.

---

[5]Heller, J.P., Kovarik, F.S., and Taber, J.J.: "Improvement of CO_2 Performance," Third Annual Report, DOE/MC/21136-17 (Jan. 1989).

[6]Kovarik, F.S. and Heller, J.P.: "Improvement of CO_2 Performance," Fifth Annual Report, Oct. 1, 1988-Sept. 30, 1989, PRRC Report No. 89022, New Mexico Petroleum Recovery Research Center, Feb. 1990.

In addition, the 'foam durability apparatus' described above has also made more-quantitative measurements of the foamability of the surfactant materials with dense CO_2 possible. Although the exact manner in which the numerical values for this latter quantity can be used in our application is not entirely clear, they certainly measure in some (probably non-linear) fashion the relative usefulness of different surfactants for this task. In order for a surfactant to be at all valuable in stabilizing bubble-films or lamella to keep the CO_2 in smaller bubbles or packets, the foam layers produced in this apparatus must endure more than a few minutes. On the other hand, a foam layer that lasts longer than a few hours, or even tens of hours, is probably overly durable, so that the foam would impede the flow of the CO_2 in most reservoir rock by too great a factor.

Along with these direct tests of bubble-film properties in the foam durability apparatus, we have been concerned with the thermal and chemical stability of the surfactants. Our screening tests have, accordingly, been made with the surfactant dissolved in a 'standard brine' of 0.5% NaCl and 0.5% $CaCl_2$ solution. The tests have also been made on samples both before and after they were held at reservoir temperatures for a month.

b. Surfactant Adsorption

A second category of tests was aimed at the measurement of the adsorption to be experienced by the surfactant in the reservoir. For these tests, it was deemed especially important that the procedure should measure the adsorption on typical reservoir rock during flow and in the presence of a brine similar to that present in the field. Thus, a dynamic test was designed to measure both the amount remaining from an injected slug of surfactant solution and the relative rate at which the slug is propagated. This test was described in the Third Annual Report,[2] along with an early implementation of it that used a refractive index method to measure surfactant concentration. Because of a difficulty pointed out with this procedure, a search was instituted for a means by which surfactant concentration could be measured more convincingly than with refractive index. As will be seen in the body of the report, such a means has been found, which is particularly effective at lower surfactant concentrations.

c. Mobility Measurements

The third and most direct group of tests that have been required in research on CO_2-foam concern the flow of CO_2-foam through reservoir rock. In this area, the critical measurement, as far as mobility control is concerned, is that of the mobility of the two-phase mixture called foam in the swept part of the reservoir. We have focussed our investigation on this type of flow tests because of our perception of the mechanism by which frontal instabilities lead to the formation and growth of fingers in miscible displacements. In terms of displacement efficiency, the most damaging fingers are those which have long wavelengths; that is, distances (perpendicular to the flow direction) between the instability-generated higher flow rate regions. These long wavelength perturbations result from changes in the flow velocity that extend for correspondingly longer distances behind as well as in front of the displacement front. As a result, only those procedures that increase the pressure gradient associated with flow of the displacing fluid in a large region of the reservoir can retard the propagation of such long wavelength fingers. The continued growth of fingers with short wavelengths, on the other hand, can be prevented by smaller quantities of thickener and even by the presence of the graded transition zone that develops naturally through the operation of dispersion.

The pressure gradient associated with flow is proportional to the flow itself and to the mobility. The latter quantity, in accord with Darcy's equation, is usually considered to be simply the ratio of the rock permeability (or relative permeability) to the fluid viscosity. In this case, in which it is not clear what is the appropriate permeability to use, and where the 'viscosity of foam' is known to depend on size scale in other flow environments, it has seemed safer to report our measurements of *mobility* (in darcy/cp, or md/cp) itself. In view of observations that the mobility of CO_2-foam is indeed quite variable, this seems to have been a wise choice. For reference purposes, we have also reported the ratio of measured mobility to the brine permeability of the rock (calling this ratio the *relative mobility*, measured in units of cp^{-1}). The reciprocal of relative mobility is then given in units of centipoise, and we have called it the *apparent viscosity*.

In our experiments, we have measured the variation of mobility as a function of the combined fluid superficial velocity (Darcy velocity), surfactant type, surfactant concentration, volumetric ratio of CO_2 (*quality*), and rock type. In most of the tests, we have used the *standard brine* referred to above, containing 0.5% each of sodium and calcium chloride and acidified to pH 3 (which according to recent evidence may be more acid than needed). Results of these measurements have been published in earlier reports of this project and in publications of the American Chemical Society (ACS) and Society of Petroleum Engineers (SPE). The following graphs summarize these results. In many of the plots, variation of the Darcy velocity is represented along the X axis, ranging from 1 to 10 ft/day. The Y axis represents either mobility, relative mobility, or apparent viscosity.

Figure 1 shows some of the data we have accumulated on the effect of surfactant type and concentration. Mobility, measured at a foam quality of about 80% and at a Darcy velocity of about six ft/day in Berea sandstone, is plotted against surfactant concentration for two different surfactants. These are the zwitterionic compound Varion CAS from Sherex, and the anionic Enordet X2001 from Shell. It can be seen that in both cases the mobility decreases with increasing surfactant concentration. The decrease is not without limit, however, in either direction. For very low concentrations, the mobility does not increase beyond that to be expected for a two-phase mixture of dense CO_2 and water without surfactant (this value is apparently that which would be predicted by the ordinary relative permeability relationship). At very high concentrations, however, the mobility does not decrease below a lower level that is apparently dependent on the properties of the surfactant.

Figure 2 shows the effects on mobility of foam quality and of the Darcy velocity for foam flow of Enordet X2001 at 0.05% concentration through Berea sandstone. It can be seen that the mobility is lower for low quality and that in this circumstance the mobility is essentially constant at all of the velocities in the range. Not only does the average mobility increase in the experiments at a higher foam fraction, but also a *shear-thinning* behavior becomes apparent, in which the mobility increases (linearly, over the velocity range of the tests) with velocity. The same effect has also been observed in Baker dolomite, but generally shows less than a factor of two increase in mobility from the lowest to the highest of the velocities we have investigated.

The most arresting observation of our experiments, however, has been the dependence of mobility on rock type. We have performed these measurements on cores ranging in brine permeability from 0.4 md (dolomite from the West Jordan Field in the Permian Basin) to 305 md Berea, and have found that the mobility of CO_2-foam in these rocks varies by a factor of less than three. Thus, the apparent viscosity of CO_2-foam increases markedly from low to high permeability rocks. The effect is shown in Fig. 3 at several different concentrations of the surfactant Enordet X2001. Note that although in the middle range of permeability the slope of the curves is near 45°, the apparent viscosities increase at a

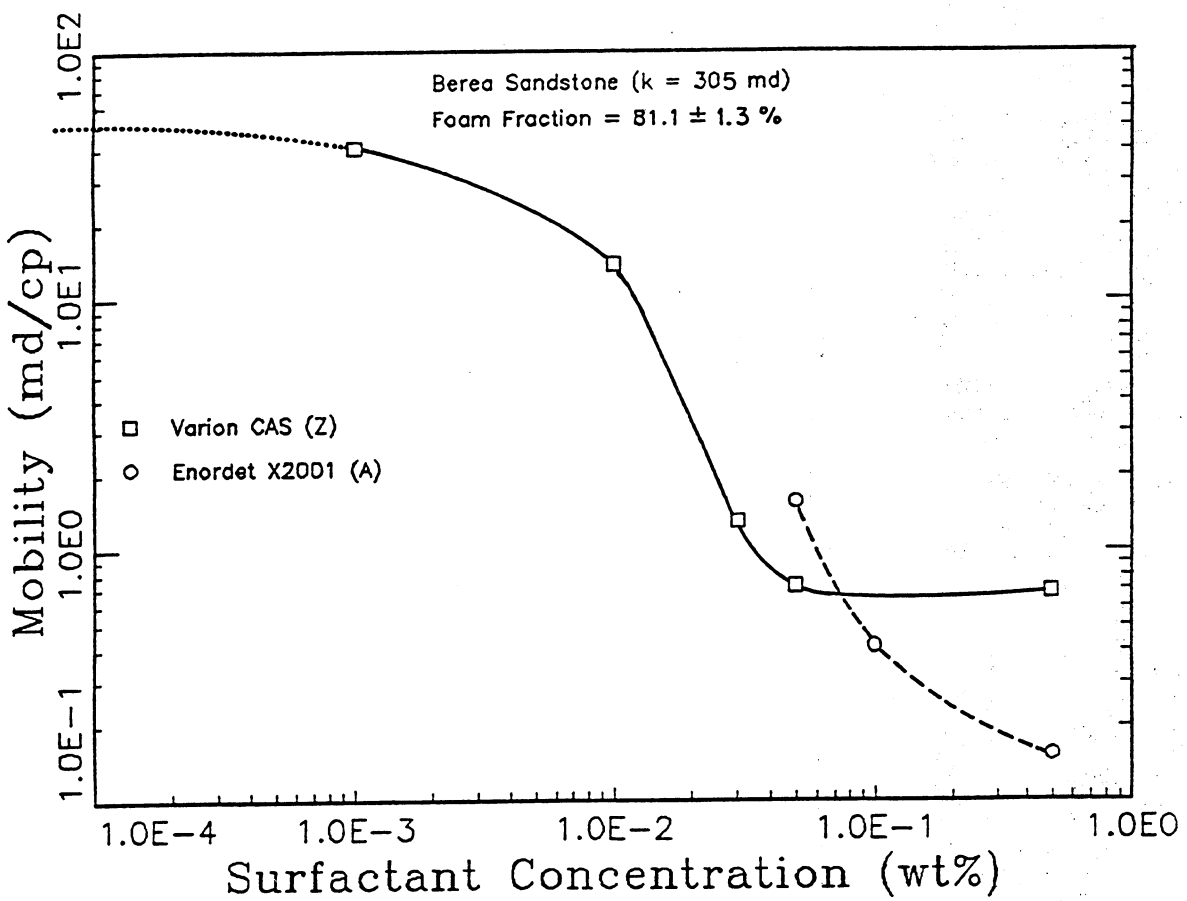

Figure 1. Effect of surfactant concentration.

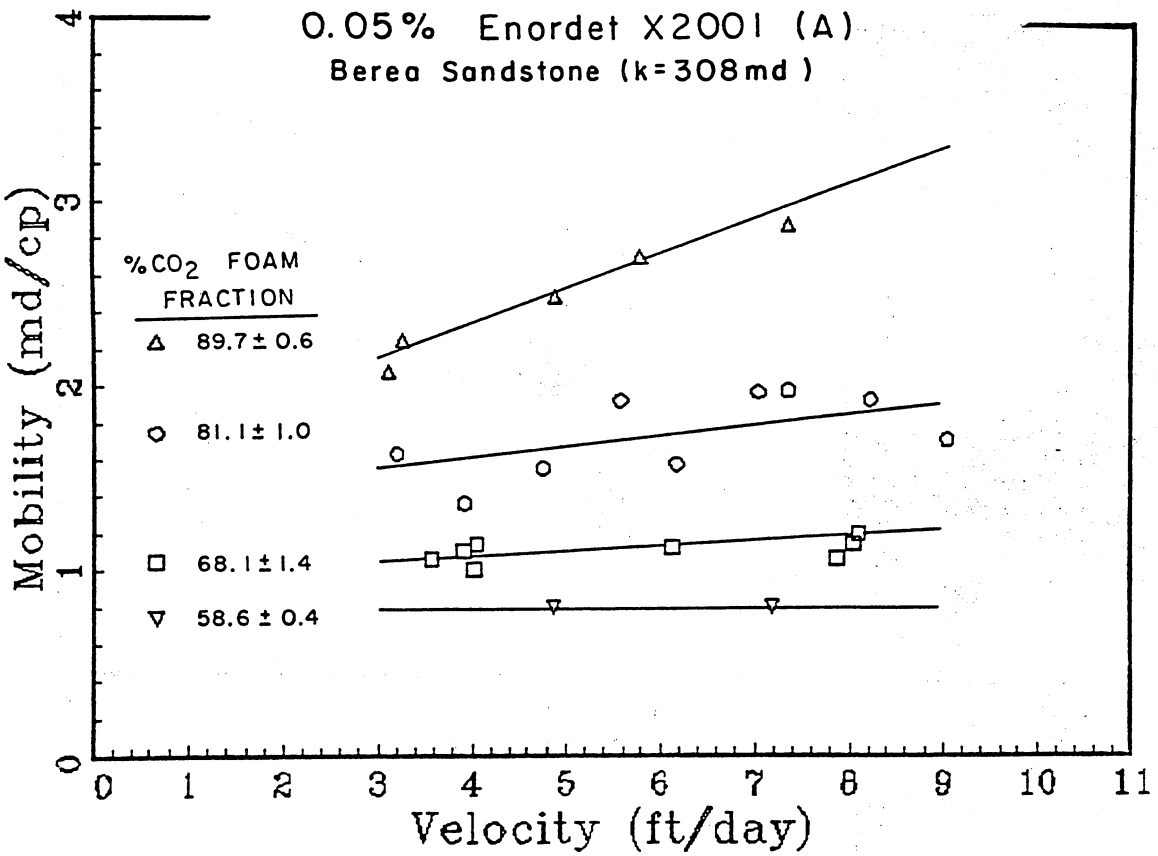

Figure 2. Effect of foam quality.

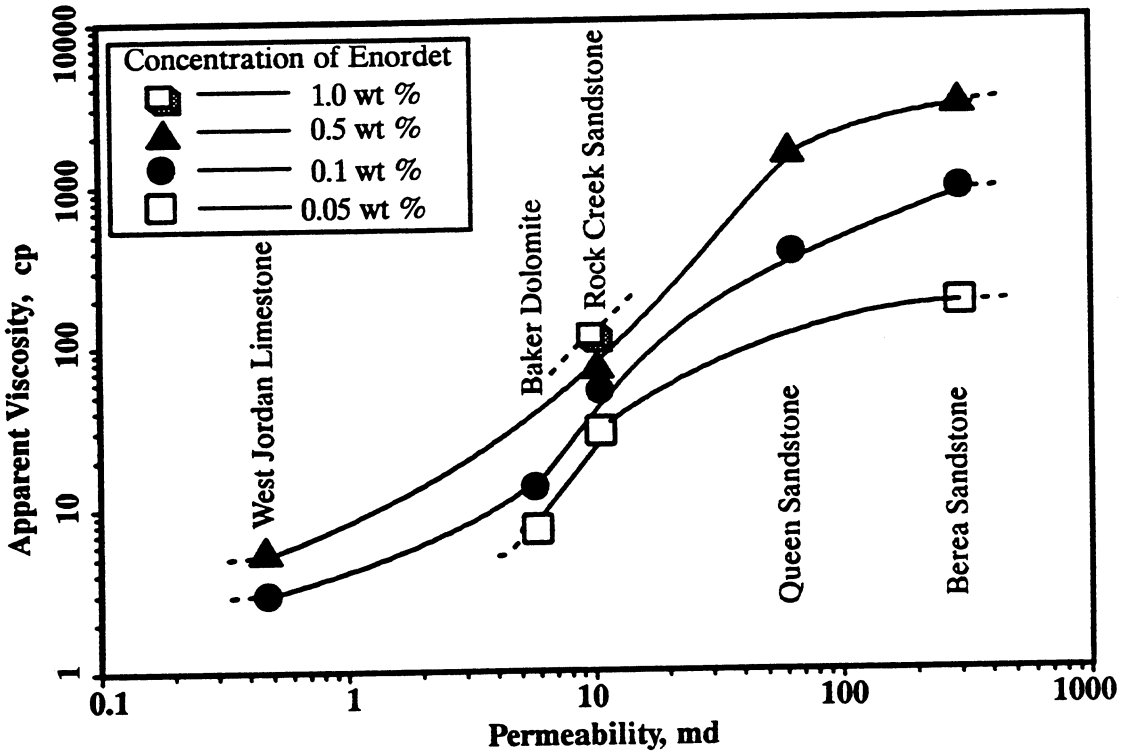

Figure 3. Apparent viscosity vs. rock permeability.

much lower rate with rock permeability at both ends of the permeability range shown. While the effect is definitely nonlinear, it seems to operate strongly over a range that is of great importance in CO_2 flooding.

Within certain limitations, this latter result suggests strongly that CO_2-foam can be expected to partially compensate for spatial variations of the reservoir permeabilities. The limitations are that only rock in the permeability range of from 0.4 to 400 md has been examined and that only one type of surfactant has been studied. Current experiments are intended to reduce the latter of these two restrictions.

3. Task II — Development of Direct Thickeners

We have performed a great deal of experimental work in the development of direct thickeners and have gained valuable information about the types of polymers needed to fulfill the goals defined early in the work. In the preceding research, an initial version of the high-pressure solubility measuring apparatus was designed and constructed. This device was refined during the latter course of the project to include an automatic magnetic stirring facility as well as the facility to include cosolvents with the polymer. This latter addition made it possible to measure the solubility of polymers in mixtures of dense CO_2 with small percentages of various liquid solvents. The collection system, by which the actual determination of solubility takes place was also improved in two ways. The first of these was the substitution of clean, dry cotton for the glass beads in the collection tube, and the second was a change of equipment and procedure by which two piston transfer pumps and a differential pressure transducer are used for the transfer.

The first of these changes has increased the precision of the measurement by a factor of about ten. This is possible because of the decreased tare involved in weighing the formerly dissolved polymer. It has also proved necessary, for the highest accuracy, to bake the cotton used to collect the sample to remove small traces of adsorbed water from it. The second change noted above has made it possible to maintain constant and equal pressures on the CO_2-polymer solution and on the nitrogen gas surrounding the collection tube during the transfer operation. With these two changes, we have been able to increase our confidence in our solubility measurements, so that they can more effectively guide our synthesis efforts.

The effectiveness of a direct thickener should now be apparent to all, as a result of paper SPE 20467,[7] which was presented at the Fall 1990 meeting. As noted in the Introduction of this report, the paper by Bae and Irani of Chevron demonstrates that a solution (albeit quite concentrated) of poly(dimethylsiloxane) and toluene in dense CO_2 has a sufficiently high viscosity, which enables it to displace SACROC oil efficiently from both Berea and reservoir core material. Although this mixture is far from economic to use in an oilfield, the experiments should make clear that the stabilization of field CO_2 displacements could greatly increase their effectiveness.

Our own program has concentrated on the development of polymers likely to be economical enough to be usable in the oilfield. After surveying commercially available polymers for their solubility in dense

---

[7]Bae, J.H. and Irani, C.A.: "A Laboratory Investigation of Thickened CO_2 Process," paper SPE 20467 presented at the Annual Technical Conference and Exhibition, New Orleans, Sept. 23-26, 1990.

CO_2, we targeted atactic hydrocarbon polymers as the most promising candidates. We expected that the tacticity would strongly influence the solubility of the polymer in such a weak, nonpolar solvent as dense CO_2. This expectation was partially fulfilled, but not to a sufficient extent, and it became apparent that the molecular weight of polymers such as poly(1-hexene) was of overwhelming importance in determining their solubility.

Furthermore, it also became apparent that our efforts were caught in a dilemma for all polymers of this class. While the solubility decreases markedly with increasing molecular weight, the power of a solute to increase the viscosity of the solvent increases with molecular weight. Thus, in order for a polymer of this type to be effective as a direct thickener, the chain length has to be great. In that case, however, its solubility would be so low that one could not dissolve enough of it in the CO_2.

As a result of these experiments, the likelihood of obtaining the required properties in any of the above 'Method I' polymers became more remote. However, another route to direct thickeners was apparent, based on a different molecular mechanism for viscosification. In ordinary polymer solutions, the increase of viscosity arises as a result of solvent-solute interactions. There exists another type of polymeric solution, known as associative, in which interactions between solute molecules are dominant as a major basis of viscosification. As a result of association, transient combinations of molecules are formed in the solvent. When such combinations can form long chains, they are particularly effective in building viscosity in the solvent.

We, therefore, targeted two types of associative viscosifiers. 'Method II' represents the class of *ionomers*, polymers that include ionic groups by which they can interact with each other in a nonpolar solution. The name 'Method III' was chosen to symbolize associative polymeric solutions based on the more subtle interaction caused by differences in *electronegativity*. A molecule that contains atoms that differ greatly in this characteristic will display a much greater dipole moment because of the unbalanced bond strengths present in the molecule.

One of these latter compounds, which has been known to support particularly strong attractive interactions between molecules is the organometallic tributyltin fluoride (TBF). This compound is available commercially (it is sold as an anti-fouling additive for marine paints). Certain unusual properties of TBF have been noted in several papers. These associative properties have been ascribed to the presence of tetravalent tin and fluorine in the molecule, which lie near opposite ends of the electronegativity scale. They include very high viscosity of solutions of TBF in light hydrocarbons such as n-octane and n-decane (the solubility of TBF in higher hydrocarbons, and in water, is extremely small). We speculated that TBF should have sufficient solubility in pentane, and in liquified butane and propane, making it very effective in building viscosity in these hydrocarbons. Experiments proved this conjecture to be correct, and we decided that other compounds of this type could be useful models for associative viscosity-building behavior.

Our Method III program consisted of the synthesis of a number of previously unknown trialkyltin fluorides. We attempted to modify these molecules through substitution of less-expensive atoms or complexes for tin and to secure adequate solubility in dense CO_2. Although as little as 0.4% by weight of, for instance, butyldiamyltin fluoride would thicken condensed propane to the 10cp range, we were not able to synthesize any of these compounds that had any more than 0.15% or so of solubility in dense CO_2. In addition to the characterization of these new compounds, we verified an important characteristic of associative thickening. The increase in viscosity with concentration follows a different course, in these cases, than it does with polymer solutions thickened by the ordinary solute-solvent interactions.

Whereas, in the ordinary polymer solution, the viscosity increases at a rate that is nearly linear with increasing concentration, associative thickening is marked by a more nearly power-law type of behavior in which the increase of viscosity is much more rapid beyond some concentration threshold. This behavior of associative compounds suggests that a successful direct thickener is more likely to be found in this class, which has increased our conviction that an economical direct thickener for CO_2 can be found.

Because we have been unable to find an effective substitute for tin in the electronegativity-based Method III compounds, and because their solubilities in CO_2 are too low to reach the threshold for large viscosification, we have reduced our efforts in this method and have been concentrating for the past year on Method II. In this work, much of our experience in Methods I and III has been useful in guiding our synthesis, characterization, and testing of new polymers and ionomers.

In early work in Method II, we converted some of the poly(1-hexene)s of different molecular weights (which we had synthesized in Method I) into *ionomers* by chlorosulfonation and neutralization methods. The results were detailed in the Fifth Annual Report.[3] These results indicated that the increase in viscosity largely depends on ionic content and the position of these groups in addition to the molecular weight of the base polymer. In order to optimize all of these conditions, we have, therefore, designed the synthesis of perfect *telechelic* (terminally functionalized polymers with reactive groups) polymers. The literature survey of these polymers indicated that the introduction of the ionic groups primarily facilitates substantial changes in the physical properties, which are due to the *ion-pair* interactions, leading to the exceptional *thickening behavior*. A great deal of research along these lines is currently underway, the results of which are presented in the major section of this report devoted to direct thickeners.

4. Task II — Displacement Nonunformity in Porous Columns

A research topic addressed midway through this project concerned a problem often encountered in laboratory work, the question of whether the fingers that grow on an unstable miscible front would reach a limiting length and, if so, what this length would be, and what it would depend on.

Briefly, our analysis showed that this question involves a balance between the transverse dispersion and the convective forces of instability. If the fluid is confined in directions transverse to the flow, then the wavelength (spacing) of instability fingers will be restricted and a limiting length of the fingers will exist. This is the case whether the source of the instability is viscous (i.e., a thin fluid displacing a viscous one) or gravitational (i.e., a heavy fluid above a less dense one in a vertical column or core), or a combination of the two. For the case where the cross-section of the core is circular, the formula for the limiting length δ_{DS} is:

$$\delta_{DS} = \left(U \ell n M + kg \frac{(\varrho_u - \varrho_\ell)}{\mu} \right) \frac{a^2}{(\phi D_T \lambda^2)}$$

In this equation,

U is the Darcy velocity
$\ln M$ is the logarithm of the mobility ratio
k is the permeability
g is the acceleration due to gravity
ϱ_u, ϱ_l are the densities of the upper and lower fluids
μ is the mean viscosity of the fluid
a is the radius of the core or column
D_T is the transverse dispersion
$\lambda \approx 1.84$ arises from the solution of Bessel's equation for the fastest growing perturbation.

The variables must be expressed in a consistent set of units, such as meter kilogram seconds.

The formula shows why even an unstable flood in a slim tube (for which the radius, a, is often no more than 0.3 cm.) generally gives a much greater flood efficiency at, say, 1.2 pore volumes, than does one conducted in a core of 1.2 cm. radius or greater. More detailed physical descriptions of this problem, as well as mathematical particulars, are given in the Second and Third Annual Reports of the project.[2]

5. Task II — Flow Nonuniformity Caused by Rock Heterogeneities

In the latter part of this project, we have included in this Task an additional broad topic—the significance of reservoir heterogeneity on the efficiency of displacement. The majority of the work in this subarea was done by a number of graduate students who have studied these questions in work for the Petroleum, Computer Science, and Mathematics Departments at New Mexico Tech. Their research topics have ranged from the influence of permeability variations on laboratory measurements of dispersion to the mathematical representation of spatial variation and the effect of gravity on the distribution of miscible fluids in a simple geometry.

In an early master's thesis (granted in 1987), Junaid Sultan examined the apparent dispersion that would be computed in the laboratory for a core that contained several parallel segments with different permeabilities. The dispersion in each segment was treated as a sum of a diffusive and a velocity-dependent term, and diffusion between each pair of segments was accounted for. Because of the different permeabilities, the initial spreading of an injected concentration step-change increased linearly with volume injected. At greater distances from the injection plane, the mass transfer between segments became important and caused the overall transition zone vs. volume injected curve to assume the square-root-of-time shape that is observed in a miscible displacement for a more uniform sample.

A relatively new mathematical discipline known as *geostatistics* is devoted to the study of *spatially random* distributions. These are sometimes called *random fields* or *regionalized variables*. Geostatistics deals with the functional dependence of the correlations between the values of a variable and the positions at which it is measured. Geostatistically well-behaved fields are called *statistically homogeneous* if their mean value and the variance are independent of position. Several procedures have been developed for the synthesis of such spatially random distributions or fields, in which the correlation structure can be varied independently by some parameter. Among these are the *Turning-Band Method*, the *Fast Fourier Transform Method*, and the *Source Point Method*. A random field such as that generated by any of these

methods can be characterized by a graph depicting the correlation behavior—that is, that depicts how the correlation varies with the *lag distance* between points of measurement. An example of these graphs is the *(semi)variogram* $\gamma(h)$, which is defined by:

$$\gamma(h) = \left(\frac{1}{2N_h}\right) \sum_{i=1}^{N_h} (U(x_i) - U(x_i + h))^2$$

In the equation, h is the lag distance, and the sum is over all pairs of points x_i that are a distance h apart. The variable is denoted $U(x)$. Generally, the variogram starts from zero or near zero and rises over a more-or-less well-defined *correlation length*, to an asymptote at a *limiting variance* or *sill*.

The topic of flood efficiency in a simple miscible displacement was examined in a master's thesis by Naser Heravi,[8] who completed his work for the degree in 1988. He generated a set of random permeability fields in a five-spot pattern. He then computed the pressure distribution, the positions of the streamlines, the successive positions of a 'sharp front' between a displacing and displaced fluid of the same mobility. Finally, Naser obtained from these results the production cut and overall efficiency after breakthrough. He utilized the source point method for the generation of the original random fields, which allowed him to vary both the overall variance of the log permeability and the correlation length.

Naser found that there was a noticeable decrease in flooding efficiency in heterogeneous formation from that obtained in uniform formations. The correlation length seemed to be more important in this decrease than the value of the limiting variance. There still remained several questions concerning details of the methods and the effect of possible variations between different *realizations* of fields with the same geostatistical parameters (In other words, were there other effects of heterogeneity on flood efficiency, over and above those that could be described in terms of geostatistics?).

A more recent master's degree thesis (completed in 1990) by Elhassan Abdalla pursued these questions further. In particular, he generated a random field in a larger region than the five-spots to be studied, and then performed the rest of the computations on *subrealizations* in smaller regions within it. He verified that the variations in flooding efficiency among these realizations were small and performed statistical analyses to show that they were not significant. He also examined several mathematical details concerning the computation methods including alternative methods for some of the steps, such as the use of the finite-element procedure to compute the pressure field. A still unanswered question concerns the range of correlation lengths over which the geostatistical description is sufficient to characterize efficiency of miscible floods. If the correlation distance is an appreciable fraction of the well-to-well spacing, one would expect that the particular heterogeneity pattern would become more important than the geostatistical description in determining flooding efficiency.

A master's degree in Petroleum Engineering was also awarded to Saleem Ghori in 1988 for thesis research dealing with a hypothetical uniform reservoir for developing some of the mathematical and numerical techniques used later in heterogeneous formations. These techniques concerned the means of following distinct isoconcentration lines that describe an injected tracer slug in a five-spot pattern. For

---

[8]Heravi, N.E.: "Five-Spot Displacement at Unit Mobility Ratio in Reservoirs with Heterogeneous Permeability," MS thesis, New Mexico Inst. of Mining and Technology, Socorro, NM (Sept. 1988).

this work, not only does the effect of dispersion need to be taken into account in increasing the distance between isoconcentration lines (or in preventing the early convective velocity change from bringing them too close together), but also the extreme variation in the direction of the Darcy velocities. Saleem's thesis shows the effects of both transverse and longitudinal dispersion on the output concentration profile from single, homogeneous layers in the five-spot configuration.

In addition to the above master's research, the project also includes the work of three students, two of the above-mentioned students and one other, who are currently in the last stages of their Ph.D. programs. Their projects are given in greater detail in the main section of this report. Briefly, they deal with the heterogeneity of laboratory-size samples (Ibrahim Bahralolom), the details of synthesis, testing, and conditioning of random fields (Junaid Sultan), and the diagnosis of field-scale heterogeneity by the use of well-to-well tracer studies (Saleem Ghori).

6. Summary of Project History

The above review is presented as a relatively brief description of the background of the research performed in this last year of the project. It is certainly not a complete summary; this would be better given by the sum of all of the reports and published papers that have been written and circulated from the project. As an aid to those caring to dig deeper, those reports and papers, which originated from our research, are marked by an asterisk in the References section of this report.

I. DISPLACEMENT WITH PURE AND IMPURE CO_2

A. PHASE BEHAVIOR AND FLUID PROPERTY STUDIES: DEVELOPMENT OF A VISCOSITY/DENSITY/COMPOSITION DATABASE FOR PURE AND IMPURE CO_2/ CRUDE OIL MIXTURES

This section of the report covers the phase behavior and fluid property aspect for mixtures of CO_2/crude oils and a number of CO_2/synthetic oil mixtures. It includes a summary of the results over the past six years with emphasis on the results of the previous year. The bulk of the experimental data was generated with the Continuous Phase Equilibrium (CPE) apparatus (originally called the Continuous Multiple Contact [CMC] apparatus). A schematic diagram of the CPE is shown in Fig. I-1 and a list of the components is given in Table I-1. A brief description of the system will be given here. The history of the CPE from its conception to the present configuration is outlined in the "History of Projects" section of this report. The detailed characterization of the apparatus, including the experimental procedure, the analytic techniques, and the associated uncertainties, can be found in previous annual reports and published papers.[1-6*]

The CPE apparatus is an assembly of mechanical and electronic equipment designed for the measurement of phase behavior and fluid properties of high-pressure fluid mixtures. The apparatus has the capability of measuring the viscosities, densities, and compositions of a single phase or near-equilibrium vapor (or dense fluid) and liquid phases under isobaric and isothermal conditions. Conventional static cell experiments measure phase volumes under isothermal conditions by traversing a path of constant overall mixture composition at varying pressures. A series of measurements performed under different overall compositions maps out a pressure/composition (P-x) phase diagram. Unlike conventional experiments, the CPE apparatus measures physical properties and compositions of a single phase or two coexisting phases at constant temperature and pressure but with a continuously changing overall mixture composition. The data generated from these measurements is most conveniently depicted in terms of a pseudoternary phase diagram. When the pseudoternaries obtained from measurements at different pressures are "stacked" vertically in increasing pressure, a three-dimensional P-x diagram is generated that shows the region of partial miscibility for the particular system of interest at a given temperature. The saturation pressure loci defined by the static measurements are simply those at which a plane, drawn from the pure CO_2 apex to the original oil composition, intersect the surface bounding the multiple-phase region. Thus, the CPE apparatus can provide not only fluid properties but also the entire phase behavior topography of a particular system at a given temperature.

The use of carbon dioxide to recover residual oil left behind by conventional recovery methods has become the dominant contributor to the domestic enhanced oil production, eclipsing other methods of enhanced oil recovery (EOR). Part of the reason for the phenomenal success of the process is the large supply of natural CO_2 gas in the continental United States. A major advantage of using CO_2 over other injection gases (such as natural gas, flue gas, or nitrogen) is the achievement of developed miscibility at moderate pressures, which makes it suitable for a broad class of reservoirs. A 1988 survey by the *Oil and Gas Journal*[7] revealed a 29% increase in the number of CO_2 flooding projects (miscible) despite a 28.5% decrease in the total number of active EOR projects in the United States (the only other type of project that posted an increase was "hot water" injection, which was initiated in 1986). Orr and Taber[8]

---

*References for Task I start on page I-172.

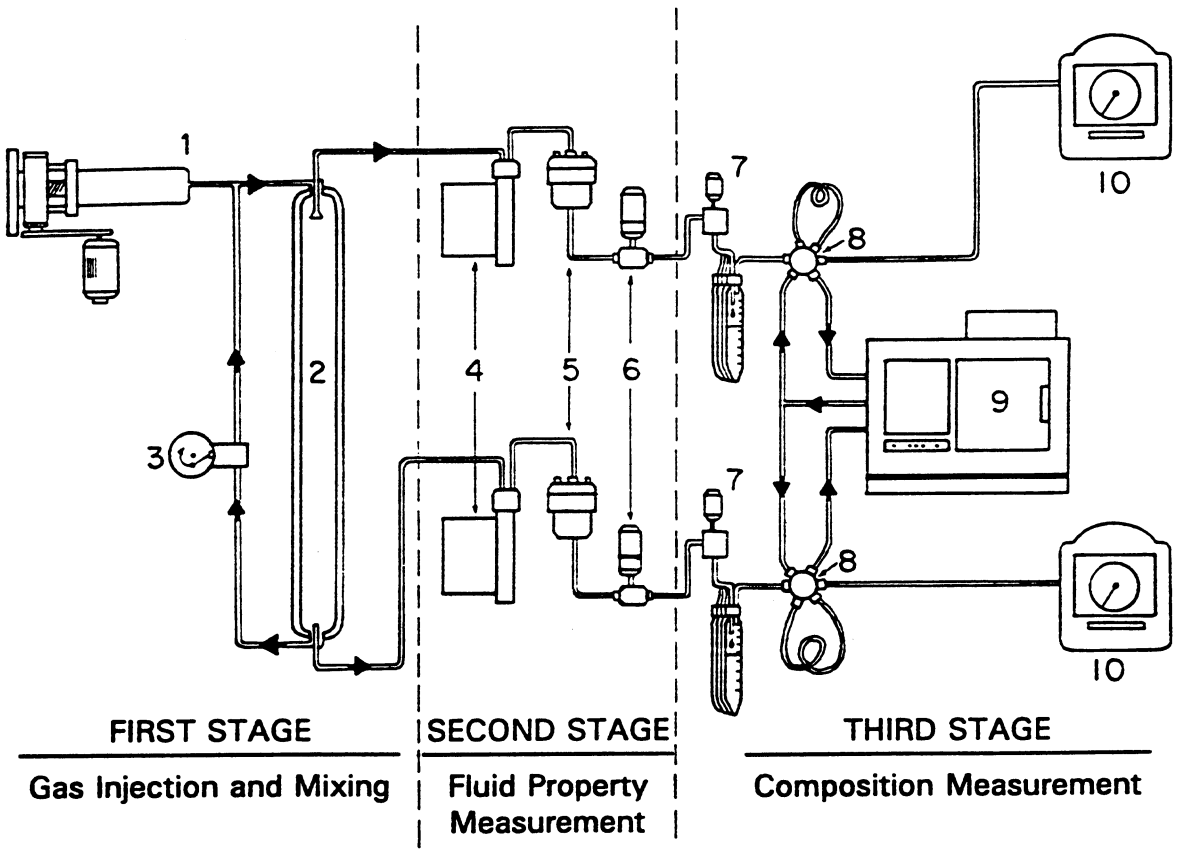

Figure I-1. Schematic of continuous phase equilibrium (CPE) apparatus.

TABLE I-1. COMPONENTS OF THE CONTINUOUS PHASE EQUILIBRIUM APPARATUS

NO.	COMPONENT
1	Ruska positive displacement motorized pump
2	134 cm^3 mixing vessel
3	Eldex high-pressure circulating pump (450 cm^3/hr)
4	Mettler-Paar DMA 512 densitometer
5	Torsional crystal viscometer
6	Motorized back pressure regulators
7	Multi-port sample valve and sample vials
8	Air-actuated gas sample valve
9	Hewlett-Packard 5840 gas chromatograph
10	GCA 63125 wet test meter

commented that supercritical CO_2 would play a large role in EOR, and this certainly has been the case. The potential exists to recover about 75% of the roughly 400 billion barrels of oil discovered in the U.S. that will be left behind by standard recovery methods.

The study of phase behavior of CO_2/crude oil mixtures has accounted for a major part of research in the field in comparison to other aspects of CO_2 flooding. The proper interpretation of flow experiments and consistent compositional material balance calculations require thermodynamic and transport property data. Furthermore, the complexity of the phase behavior topography for mixtures of CO_2 and most naturally occurring crude oils, especially around the CO_2 critical point vicinity, has attracted much interest: scholars want to gain a fundamental understanding of the underlying physics of the phenomena. The concoction of prototype systems has led to the understanding of the occurrence and evolution of liquid-liquid (L_1-L_2), liquid-liquid-vapor (L_1-L_2-V), and solid-liquid-liquid-vapor (S-L_1-L_2-V) phase behavior. This has led to the extensive mapping and equation-of-state modeling of these behaviors for mixtures of CO_2 and crude oils.

It has long been established that phase behavior of CO_2/crude oil systems, through the generation of multiple contact miscibility, is responsible for the high recovery efficiency observed in slim tube displacements where the effects of viscous and gravitational instabilities are minimized. Dense supercritical CO_2 has the ability to extract a broad range of hydrocarbon components, possibly through the C_{35} range. This phenomenon leads to the high local displacement efficiency that is characteristic of CO_2 floods. It has also been shown that the extraction efficiency is directly related to the density of the CO_2 at the reservoir conditions. Orr, Silva, and Lien[9] have demonstrated the efficacy by which a dense fluid or liquid CO_2-rich phase extracts hydrocarbons compared to a low-density CO_2-rich vapor phase. Nevertheless, the complex interaction of phase behavior and hydrodynamic mixing in a porous medium under dynamic flow conditions makes the prediction of a CO_2 flood performance rather challenging.

These combined efforts have resulted in a solid understanding of how phase behavior impacts the displacement efficiency of CO_2 floods, at least in a slim tube setting. Research during the six-year project has been directed toward complementing established knowledge of CO_2 floods with the aim of improving the prediction of the process' behavior. There are at least three research areas where significant contributions have been made. These are:

(1) Viscosity, density, and composition measurements for pure and impure CO_2/hydrocarbon mixtures. Development of a viscosity correlation for pure and impure CO_2/hydrocarbon mixtures.

(2) Effects of the presence of light hydrocarbon (C_1, C_2, and C_3) and nonhydrocarbon (N_2) components in the CO_2 on fluid properties.

(3) Effects of solution gas on the development of miscibility. Investigation of displacement below the bubble-point pressure.

The major results of the study in each of these areas are discussed in a semi-chronological manner. The simultaneous measurement of phase behavior and fluid properties essentially results in a degree of overlap between Tasks 1 and 2.

1. Viscosity, Density, and Composition Measurement

One of the beneficial effects of CO_2 when it dissolves in the oil is the drastic reduction of the viscosity of the single-phase mixtures. The CO_2 flooding literature, however, contains very little published data of viscosities. The scarce data that is available is often limited to undersaturated oil or equilibrium oil-rich liquid phases. In a developed miscibility process, viscosity data for the CO_2-rich phases in particular, are required to estimate the effect of phase viscosities on mixing at the leading edge of the transition zone. Thus, what is needed is the measurement of fluid properties both in the single-phase and two-phase regions that are tied in with phase compositions. These simultaneous measurements would provide a means for estimating the effects of viscous and gravitational instabilities in a reservoir setting. The data generated can also be used to test and develop a viscosity correlation applicable to CO_2/crude oil systems.

A number of viscosity measurement techniques that would meet the above requirements were surveyed. The torsionally vibrating quartz crystal viscometer[10] offered the flexibility of viscosity measurement over a wide range of values with very low dead-volume requirement. The first two years of the project involved the design of a high-pressure containment for the quartz crystals. After a successful design was made, two viscometers (one each for the upper and lower sample ports) were incorporated to the existing apparatus configuration. The apparatus also includes two on-line high-pressure oscillating tube densitometers with ± 0.001 g/cm^3 estimated accuracy.[6]

Here, the two torsionally vibrating quartz-crystal viscometers used in the study will be described briefly. Details of the theory, construction, and operation of the viscometers are found elsewhere.[11-15] The quartz crystal viscometer was first introduced by Mason in 1947. The lack of any macroscopically moving components makes this type of viscometer suitable for application to the high-pressure region.

The quartz viscometers implicitly measure viscosity via an energy balance equation that relates the product of viscosity and density, ($\mu \bullet \rho$), to the energy lost by viscous dissipation when the crystal is driven by an external energy source. The energy balance equation accounts for two possible energy sinks in the system: (1) the viscous shearing of the fluid surrounding the crystal, and (2) the support system of the crystal. The energy lost to the support system can be measured when the crystal is in a vacuum. Any additional energy loss in the presence of a fluid is assumed to be caused by viscous energy dissipation. Viscosities were obtained from the following expression:

$$\mu = \frac{\pi f}{\rho}\left(\frac{M_q}{S_q}\right)^2\left[\frac{\Delta f}{f} - \frac{\Delta f_{vac}}{f_{vac}}\right]^2 \qquad \text{(I-1)}$$

where ρ is the density of the fluid, (M/S) is the mass-to-surface area ratio of the crystal, f is the resonant frequency, and Δf is the half conductance bandwidth; f_{vac} and Δf_{vac} are frequencies which are measured in a vacuum.

The next step involved the testing and validation of the viscometers by comparing measured viscosity values against published data. The Second Annual Report[2] presented the results of validation tests against pure substances and a binary mixture. The range of conditions were 100°F to 220°F and from atmospheric pressure to 4000 psia. The average errors for methane, ethane, carbon dioxide, and normal

decane were better than 4%. The measurements performed with the binary CO_2/n-C_{10} system covered a range of compositions from 100 mole% n-C_{10} to 93 mole% CO_2. The average error was estimated to be better than 5%.

Further validation tests were performed with mixtures of CO_2 and a four-component synthetic oil system. The range of conditions covered 100-190°F and 1300-2000 psia. Details of the results were given in the Third Annual Report.[3] The average viscosity measurement errors fell within the earlier established range. A comparison of the CPE- and static cell-measured CO_2 bubble-point concentrations yielded an average error of -3.2%. The report also included the results of the first run attempted with a crude oil. A run labeled CPE 210 was conducted with the Maljamar separator oil at 90°F and 1200 psia. Initial comparison of the measured viscosities against the prediction of the Lohrenz, Bray, and Clark correlation (LBC)[16] yielded large deviations, which are unacceptable.

The dynamic nature of the experiments performed with the CPE apparatus is accomplished through the continuous introduction of a high-pressure injection gas. The gas is injected into a vertically oriented mixing vessel initially charged with the oil at the run conditions. There was a bit of concern for whether near-equilibrium conditions could, in fact, be realized with denser and more viscous crude oils. A second circulation pump was added to the system to allow fluids to be circulated at a maximum rate of 400 cm^3/hr, which is large compared to the nominal CO_2 injection rate of 10-15 cm^3/hr. Additional refinements to the viscometer pressure vessels were also done to facilitate the cleaning of the crystals. Modifications to the airbath extended the upper range of operating temperatures, to 250°F.

The Fourth Annual Report[4] included a second run with a crude oil from the Wasson field in West Texas and a highly asphaltic oil from Northwest New Mexico. The viscosity measurements showed that asphaltene precipitation occurred under high overall CO_2 concentration for the New Mexico crude. The precipitate presumably deposited on the crystal surface, which caused erroneously high viscosity readings. Although the study of asphaltene precipitation under miscible flooding conditions is more than an academic interest, the CPE apparatus configuration is not capable of the task since it was not a consideration in the original design of the system. A screening procedure was adopted to ensure that asphaltene precipitation would not occur in the course of the run. Crude oils were filtered through a high-pressure filtration apparatus to rid the oil of any suspended particles or loose sand grains greater than 10 microns in diameter. Visual experiments with a static PVT cell were then performed to confirm whether asphaltene dropout occurred.

The validation runs performed on the well-defined systems as well as the initial attempts with crude oils resulted in a complete characterization of the CPE apparatus. Procedures were modified, analytic techniques were refined, experimental accuracies were established, and data acquisition and handling protocols were set up. The CPE apparatus now allows rapid determination of phase densities and viscosities together with compositions. The experiment is certainly not without limitations. The inherent differences between the CPE and conventional static-equilibrium apparatuses are presented elsewhere.[6,17] The major advantages of the experimental approach over the conventional static cell method are its simplicity and speed in generating data. The large sample volumes that are obtained allow ample flexibility in the type of chemical analyses that can be performed. This feature, coupled with the fluid property measurement ability, provided valuable information that has contributed to the understanding of compositional and fluid property behavior in CO_2/crude oil systems. These results are presented in the following paragraphs.

Crude oil samples were requested and subsequently received from the consortium members. All the oils were recombined to yield, as closely as possible, the reported reservoir composition. An extensive experimental program was initiated in the third quarter of 1988. The purpose of the study was the development of a comprehensive data base of viscosity, density, and composition of single and near-equilibrium phases for mixtures of pure and impure CO_2 with crude oils. The data, through its proper interpretation, could provide valuable insight on the effects of viscous and gravitational instabilities in corefloods and in a reservoir flow regime. It could also be used to develop a viscosity correlation that can be used in numerical reservoir simulations. The latter has, in fact, been achieved and is the topic of the next section of this report.

The Fifth Annual Report[5] presented the results of the phase behavior and fluid property measurements for CO_2 and a number of crude oils from West Texas. Equilibrium phase compositions, densities, and viscosities were reported for all the crude oils using pure CO_2 as the injection gas. The experiments were performed at the slim-tube measured minimum miscibility pressure (MMP) and the corresponding reservoir temperature. Selected experiments were conducted to delineate the effects of small amounts of nitrogen (N_2) in the CO_2 stream on phase compositions (the extraction of hydrocarbon by CO_2) and the properties of the impure CO_2/crude oil mixtures. The composition of an oil was altered to assess the effect of solution gas on phase behavior and fluid properties. The range of conditions were 105-165°F and 1200-2350 psia.

The results were presented in terms of pseudoternary phase diagrams with data points along the dilution path (single-phase region) and in the two-phase region together with the phase densities and viscosities. A number of unique features of CO_2/crude oil mixtures were revealed by the experiments. These characteristic patterns in phase behavior and fluid properties are summarized in the following paragraphs.

For the runs with pure CO_2 injection, the dilution paths were such that the coexistence envelopes were entered from the bubble-point side. These were apparent from the sudden drop in the density values recorded by the upper port densitometer at the onset of phase separation. The upper phases that evolved were dense CO_2-rich fluid phases (F) that contained anywhere from 10-30 mole% hydrocarbons with components as heavy as a boiling point cut corresponding to a carbon number 30 in the normal alkane series. Measured phase viscosities were plotted as a function of phase densities and CO_2 concentrations. These plots revealed fluid property trends that are unique to CO_2/hydrocarbon systems.

The μ vs. x_{CO_2}/y_{CO_2} (Figs. I-6, I-13, I-17, and I-21 in the Fifth Annual Report[5]) and the μ vs. ρ plots (Figs. I-7, I-14, I-18, and I-22 in the Fifth Annual Report[5]) reveal fluid property trends unique to CO_2/hydrocarbon mixtures. One of the beneficial effects of CO_2 when it dissolves in the oil, from the standpoint of improved oil recovery, is the drastic reduction of the viscosity of the single-phase mixtures. This behavior certainly helps to improve the unfavorable mobility ratio during a CO_2 flood. The μ vs. x_{CO_2}/y_{CO_2} plots show the dependence of viscosity in the single-phase and two-phase regions on CO_2 concentration. The single-phase CO_2/crude oil viscosities reach a minimum at the bubble-point CO_2 concentration, after which the viscosity curve becomes discontinuous, separating into dense fluid- and liquid-phase viscosity branches. The equilibrium liquid-phase viscosities increase monotonically as a result of the continued depletion of the extractable C_5-C_{30} hydrocarbon range. Most of the CO_2/crude oil systems used in the study show liquid phase viscosity values that are higher when compared to the original oil for mixtures that have been considerably depleted of the extractable hydrocarbons. This phenomenon occurs in spite of the continued rise in the solubility of CO_2 in the oil-rich liquid phase.

The viscosity-reduction-effect of CO_2 has, presumably, reached a point of diminishing returns such that the heavy-hydrocarbon contribution dominate the liquid phase viscosity.

The equilibrium CO_2-rich fluid phase viscosities, however, reveal a slightly more-complicated pattern with the continued dilution of the two-phase mixture with CO_2. The fluid phase that appears at the onset of phase separation contains a high concentration of the natural gas components (C_1 and C_2) of the solution gas with very little to trace amounts of components with carbon number greater than three. The high concentration of C_1 and C_2 mixed with the supercritical CO_2 cause a reduction of the dense-fluid phase viscosity and density relative to that of pure CO_2 at the run conditions. Table I-2 shows the effect of the presence of C_1-C_4 in binary and ternary mixtures with CO_2 at 1500 psia and 105°F. The density and viscosity values were calculated using SUPERTRAPP (Transport Properties Prediction Program), a transport property correlation based on an extended Corresponding States Principle.[18] Note that 90%:10% (mol) CO_2:C_1, CO_2:C_2, and CO_2:C_3 mixtures have viscosities that are 48%, 21%, and 2.4% lower, respectively, compared to that of pure CO_2. The presence of the C_4 results in an increased mixture viscosity as shown in Table I-2. Thus, the C_1-C_3-effect dominates the fluid-phase viscosities resulting in lowered density and viscosity values relative to pure CO_2 for early post phase-split samples. The trend is then reversed when enough of the C_{4+} components are present in the dense fluid phase resulting in increased viscosity and density values. One would expect that the asymptotic fluid phase values would be that of the pure CO_2 if the solvent injection was carried on indefinitely. For the experiments with pure solvent injection, the magnitude of the viscosity values of the dense fluid-phase samples are approximately 100% greater than that of pure CO_2, even at CO_2 concentrations in excess of 90 mole%.

A closer inspection of the μ vs. ρ plots reveals the dependence of viscosity on density for the CO_2/crude oil systems. The addition of CO_2 to the oil results in a rapid decrease in viscosity of the single-phase mixtures with the attendant increase in the mixture density. This behavior shows an abnormal dependence of liquid viscosity on density where we expect $(\partial\mu/\partial\rho)_{T,P} > 0$ for a multicomponent mixture. The equilibrium dense fluid and liquid phase viscosities, however, show normal viscosity/density dependence.

The unexpected increase in the density of the single-phase CO_2/crude oil mixtures, when compared to the original oil before the addition of CO_2, suggests that the initial introduction of CO_2 molecules into the liquid phase causes the hydrocarbon molecules to reorient themselves, on average, in closer proximity to each other. This phenomenon can perhaps be explained if one considers the supercritical fluid behavior of CO_2 at the run conditions. It is by now well recognized that anomalies in certain thermodynamic properties exist in dilute binary mixtures of a nonvolatile solute and a near- or supercritical solvent in the vicinity of the solvent's critical point.[19-25]

Several investigators[26-32] have reported large negative solute partial molar volumes at infinite dilution for a number of organic liquids in the vicinity of the solvent critical point. Eckert *et al.*[33,34] reported large negative solute partial molar volumes at infinite dilution for a variety of non-volatile solute/supercritical solvent systems. Eckert and his co-workers have qualitatively interpreted these results in terms of a positive "clustering" effect whereby a large number of solvent molecules "condense" around a single solute molecule when the latter is added to a highly compressible fluid (solvent).

Debenedetti[35] used fluctuation theory and derived fluctuation-explicit expressions for the solute partial molar volumes at infinite dilution for dilute binary mixtures where the solvent is in super- or near-critical conditions. The mathematical expressions are explicit in a parameter (cluster size) which, in

TABLE I-2. CALCULATED DENSITIES AND VISCOSITIES (FROM SUPERTRAPP) FOR BINARY AND CERTAIN TERNARY MIXTURES OF CO_2 WITH C_1-C_4 PURE HYDROCARBON COMPONENTS AT 1500 PSIA AND 105°F

CO_2	C_1 Mole	C_2 Fractions	C_3	C_4	ρ (g/cm^3)	μ (cp)
1.0	-	-	-	-	0.6374	0.05030
0.9	0.1	-	-	-	0.3315	0.02691
0.9	-	0.1	-	-	0.5022	0.03888
0.9	-	-	0.1	-	0.6218	0.05349
0.9	-	-	-	0.1	0.6929	0.06724
0.8	0.1	0.1	-	-	0.3070	0.02588
0.8	0.1	-	0.1	-	0.3970	0.03154
0.8	0.1	-	-	0.1	0.5123	0.04298
0.8	-	0.1	0.1	-	0.5440	0.04666
0.8	-	0.1	-	0.1	0.6176	0.05926
0.8	-	-	0.1	0.1	0.6617	0.06983

general, is a measure of the statistical correlations between the solute and solvent concentration fluctuations at infinite dilution. The same parameter, however, acquires a mechanistic interpretation for super- or near-critical systems, i.e., the collapse of solvent molecules around a solute molecule (positive clustering phenomenon) upon isobaric, isothermal solute addition. This phenomenon was also shown to be a necessary and sufficient condition for the negative divergence of the solute partial molar volume at infinite dilution. The attraction or "condensation" of solvent molecules around a solute molecule will cause a pressure decrease at constant volume. Thus, for a high compressibility solvent, a decrease in volume must accompany the isothermal, isobaric addition of solute, which translates to an increase in the resulting mixture density.

The CO_2/crude oil systems studied here are certainly far removed from conditions of infinite dilution. The supercritical CO_2 solvent is added to a complex hydrocarbon mixture under isothermal, isobaric, and isochoric conditions until the saturation point is reached at the existing temperature and pressure upon which the system separates into a dense CO_2-rich fluid phase and an oil-rich liquid phase. Levelt Sengers *et al.*[22] pointed out, that for dilute binary mixtures of a nonvolatile solute and a supercritical solvent, the partial molar properties of the solute in the supercritical phase diverge *only* at the solvent's critical point. In the presence of a second phase (the oil-rich liquid phase for these cases), the partial molar properties will be finite even at a critical end point. The partials, however, can still manifest anomalous values if the critical end point is in the vicinity of the solvent's critical point. These observations, nonetheless, seem insufficient to rationalize the observed density increase (negative partial molar volumes) upon the addition of small amounts of CO_2 (the solvent) to a hydrocarbon mixture (the solute).

Kobayashi and his co-workers[36,37] have hypothesized that the presence of multiple condensed phases such as liquid-liquid-vapor (L_1-L_2-V) or solid-liquid-vapor (S-L-V) immiscibility at some temperatures lower than the critical temperature of the more volatile component in the case of a binary mixture is essential to the occurrence of supercritical extraction (i.e., the enhancement in solubility that is related to the anomalies in the partial molar properties discussed above) at higher pressures and temperatures. Here the L_1 and L_2 are the heavy hydrocarbon-rich and light hydrocarbon- or CO_2-rich liquid phases, respectively. The data of Lin *et al.*[38] on the binary system methane/toluene as well as the binary system CO_2/n-Hexadecane[39-41] was cited by Kobayashi *et al.* as prototype systems that support their contention. The CH_4/C_6H_9 and CO_2/n-C_{16} systems exhibit similar phase diagram projections in pressure/temperature space, shown schematically in Fig. I-2, for the latter binary pair. For these systems, the L_1-L_2-V locus is terminated at a lower temperature by a quadruple point (S-L_1-L_2-V, not shown in the figure) and at an upper temperature by a critical end point (a type K point) where the CO_2-rich liquid phase (L_2) goes critical with the vapor phase (L_1-L_2=V). The pressure and temperature at which the K-point occurs is in close proximity to the critical point of the more volatile component (methane and CO_2) in both systems.

Lansangan *et al.*[42] suggested that based on Gibbs' phase space topography, shown schematically in Fig. I-3, the Kobayashi hypothesis is born out of the presence and eventual disappearance of the L_2 "lobe" in the thermodynamic phase space. For the systems they studied (L-V isotherms for certain binary CO_2/n-alkylbenzene systems at temperatures below and above the critical temperature of CO_2), consider the case where the three-phase L_1-L_2-V locus, which lies close to the CO_2 vapor pressure curve in pressure/temperature space, is terminated at its highest temperature (which is close to the CO_2 critical point) by an upper critical end point (i.e., L_1-L_2=V). The vapor phase for a supercritical isotherm for this system is replaced by a merger of the L_2 and the V phases, shown in Fig. I-3d, which, while not decreasing the CO_2 concentration, can cause the hydrocarbon concentration (and phase density) to

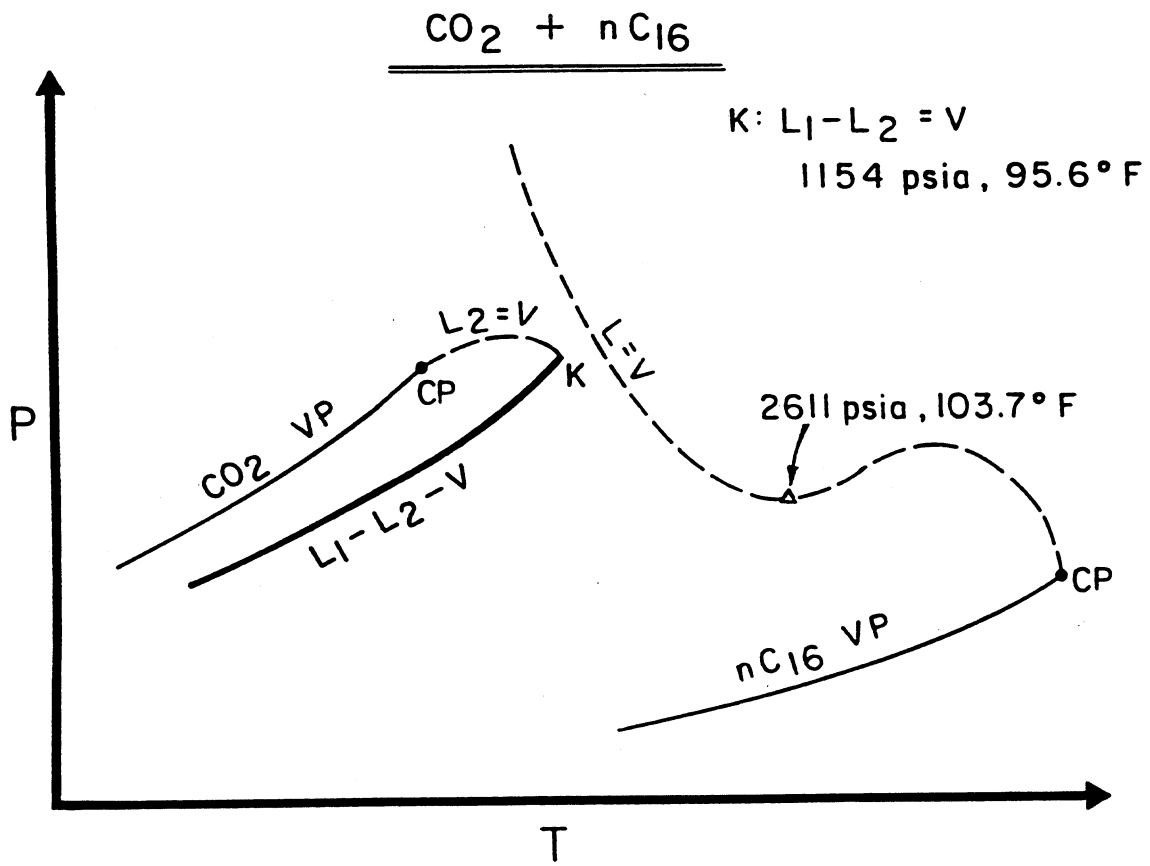

Figure I-2. Schematic of pressure-temperature projection of CO_2/n-Hexadecane systems.

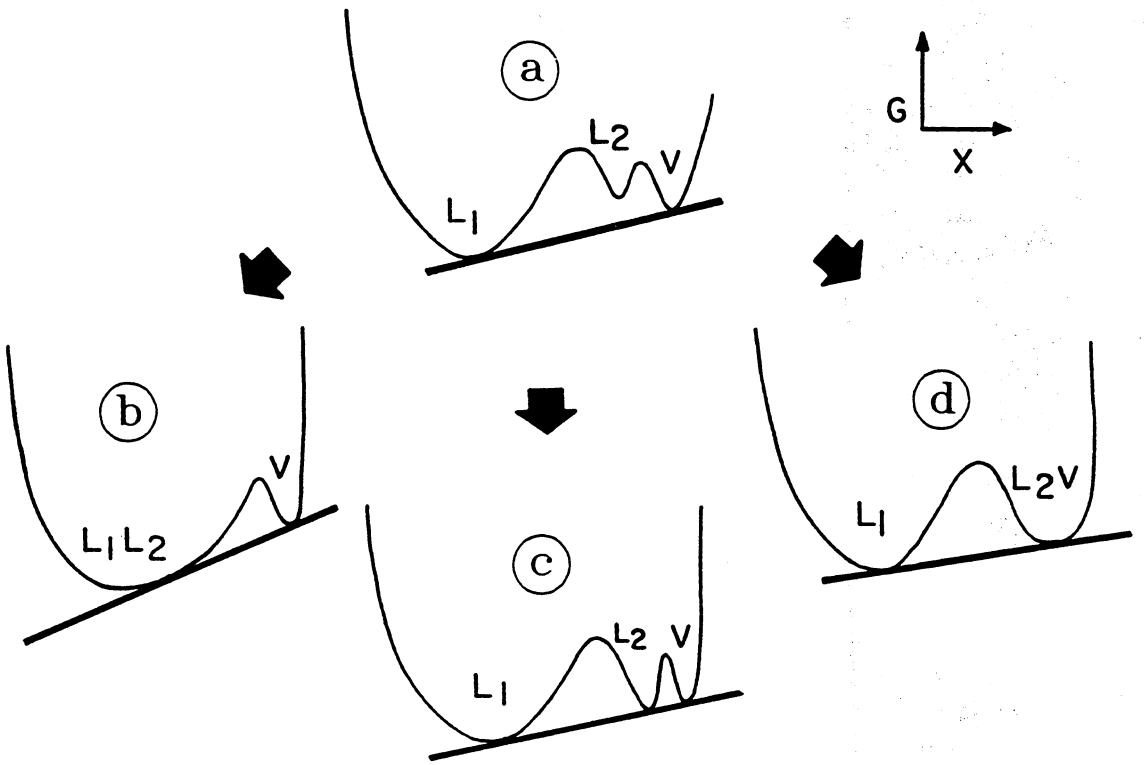

Figure I-3. Schematic diagrams of Gibbs free energy/composition surface for a binary system exhibiting three-phase liquid-liquid-vapor (L_1-L_2-V) immiscibility.

increase dramatically when compared to its prior vapor phase value. This effect is the well-known solubility enhancement phenomenon in supercritical extraction. Thus, the requirement that a critical end point be close to the solvent's critical point is topographically analogous to the occurrence of L_1-L_2-V immiscibility behavior at some lower temperature for the occurrence of supercritical solubility enhancement (with the attendant thermodynamic anomalies in partial molar properties), at least for the CO_2/hydrocarbon systems cited here.

The recombined oil E (RO-E) exhibits L_1-L_2-V immiscibility behavior with CO_2 at 90°F,[10] the extent of which is expected to persist at temperatures below 87.9°F, the critical temperature of CO_2, and terminate at a critical end-point below 105°F. Thus, the RO-E/CO_2 system is a prototype system that meets the above requirements for the occurrence of supercritical extraction phenomenon with its attendant anomalies in certain partial molar properties. A corollary to the above hypothesis is that the CO_2/crude oil systems used in this study exhibit L_1-L_2-V immiscibility at some lower temperatures.

Another possible contributor to the increase in the single-phase CO_2/crude oil mixture densities is the solute-solvent interaction through an induced dipole-quadrupole interaction, which is always attractive in nature. CO_2 is a linear molecule with no permanent dipole moment but possesses a strong quadrupolar moment. The permanent quadrupole is sufficiently strong to affect its thermodynamic properties, which are significantly different compared to other nonpolar molecules of similar size and/or molecular weight (propane, for instance). Several investigators have calculated the induction effects on excess thermodynamic properties for binary systems where one of the constituents is either a polar or quadrupolar molecule.[43-45] Their results reveal large deviations from ideal behavior when the induction forces are accounted for in the model.

An idealization of a complex crude oil is a multicomponent mixture whose constituents are strictly members of the homologous normal alkane series. Normal alkanes are nonpolar symmetric molecules that have no permanent dipoles, but whose electron clouds can be displaced from their normal position under the influence of an electric field giving rise to induced dipole moments. Thus, the CO_2 molecules serve as "catalysts" that polarize the hydrocarbon molecules resulting in attractive Coulombic forces that are superimposed on the London dispersion forces. A qualitative interpretation on the microscopic level is a denser packing of molecules in a quasi-lattice structure whose macroscopic manifestation is an increase in density.

The effect that this behavior will have on the initiation of gravitational instabilities during a CO_2 flood is debatable. Coreflood experiments are routinely performed with the less dense CO_2 injected from the top of a vertically-oriented core, contacting the denser oil at the bottom and, thus, gravity stabilizing the flood front. Once the CO_2 goes into solution, however, the density contrast is reversed, the more dense CO_2/oil solution rises above the less dense oil, potentially negating any gravity stabilization effects. The initiation of gravitational induced instabilities in the oil phase close to the CO_2/oil interface can be determined in part by the size of the pores and the mass transfer rate of CO_2 in the oil phase. Very small pores could give rise to capillary effects that could balance (if not exceed) the downward gravitational forces and, thus, arrest the convective currents. The mass transfer rate, on the other hand, will determine how fast large concentration gradients can be dissipated relative to the time required for the instabilities to form. The extent to which this phenomenon occurs in a porous medium and the effect it has on the displacement efficiency of a CO_2 flood is not known and certainly leaves the question open for now.

2. Effect of Solution Gas on Fluid Properties

The effect of solution gas on the development of miscibility (i.e., on MMP) is not well understood.[46-49] No consensus on the effect exists in the literature.

Orr *et al.*[50] conducted phase behavior measurements of a CO_2/crude oil system with and without the presence of solution gas to find an explanation for the apparent insensitivity of slim-tube displacement efficiency to the presence of the dissolved, light hydrocarbon components in the stock tank oil. They concluded from their study that the addition of solution gas enlarges the region of partial miscibility in composition space. This rather obvious effect would immediately suggest that pressure would have to be increased (i.e., MMP) in order to achieve developed miscibility based on the Hutchinson-Braun[51] concept. A concomitant effect of the two-phase region enlargement, however, is the dislocation of the critical point of the system to lower CO_2 concentrations. The displacement of the critical point also modifies the slopes of the tie lines such that the critical tie line extension becomes more parallel to the CO_2-heavy hydrocarbon side of a pseudoternary diagram. What this means in terms of equilibrium phase compositions is that the CO_2-rich phase now contains relatively equal amounts of light extractable hydrocarbons compared to the oil-rich liquid phase; i.e., an increase in extraction efficiency of the dense CO_2-rich phase even at a lowered overall CO_2 concentration. The addition of solution gas to the oil, at the same time, shifts the oil composition point towards the CO_2-light hydrocarbon side, moving it further away from the already receded critical tie line extension. Both effects combine to offset the adverse impact of the two-phase region enlargement, and thus presumably explain the apparent insensitivity of slim-tube displacement efficiency to the presence of solution gas in the oil, at least based on pseudoternary diagram arguments.

Probably, fewer studies have been done on the effect of solution gas on the physical properties of CO_2/oil mixtures; so, we performed experiments to address this phenomenon. Two recombined oil mixtures were prepared from a stock tank oil with varying amounts of methane. The recombined oil B (RO-B) and recombined oil B1 (RO-B1) have methane concentrations of 21 mole% and 34 mole%, respectively. The RO-B/CO_2 systems served as the baseline case for comparing the fluid properties with the methane-enriched oil/CO_2 system.

The results of phase behavior and fluid property measurements for the two systems are shown in Figs. I-4 and I-5 in terms of pseudoternary phase diagrams. Figures I-6 and I-7 show the dependence of phase viscosities on phase densities and overall CO_2 concentrations. Both measurements were conducted at 1700 psia and 116°F. A comparison of Figs. I-4 and I-5 reveals all the manifestations of the effects of solution gas on phase behavior as depicted on a pseudoternary diagram. Phase separation occurred at a much lower overall CO_2 concentration for RO-B1 as a result of the enlargement of the coexistence envelope. The tie lines, especially at lower overall CO_2 concentrations, are unmistakably closer to being parallel to the CO_2-C_{7+} side of the triangle than those of RO-B as shown in Fig. I-4. The apparent location of the critical point for the RO-B1/CO_2 system is approximately 48 mole% CO_2 and 41 mole% C_{6-} compared to 62 mole% CO_2 and 26 mole% C_{6-} for the baseline case. Thus, the CO_2/methane-enriched oil critical mixture is much richer in the extractable hydrocarbon components at a much lower overall CO_2 concentration. The critical tie line extension intersects the base of the triangle at a lower C_{6-} composition, moving it away from the original oil composition point.

When the measured densities and viscosities of the equilibrium CO_2-rich fluid phases of the RO-B/CO_2 and RO-B1/CO_2 systems are compared, as shown in Figs. I-6 and I-7, the latter show an average increase of 6% for density and 135% for viscosity, respectively. The properties of the CO_2-rich phase

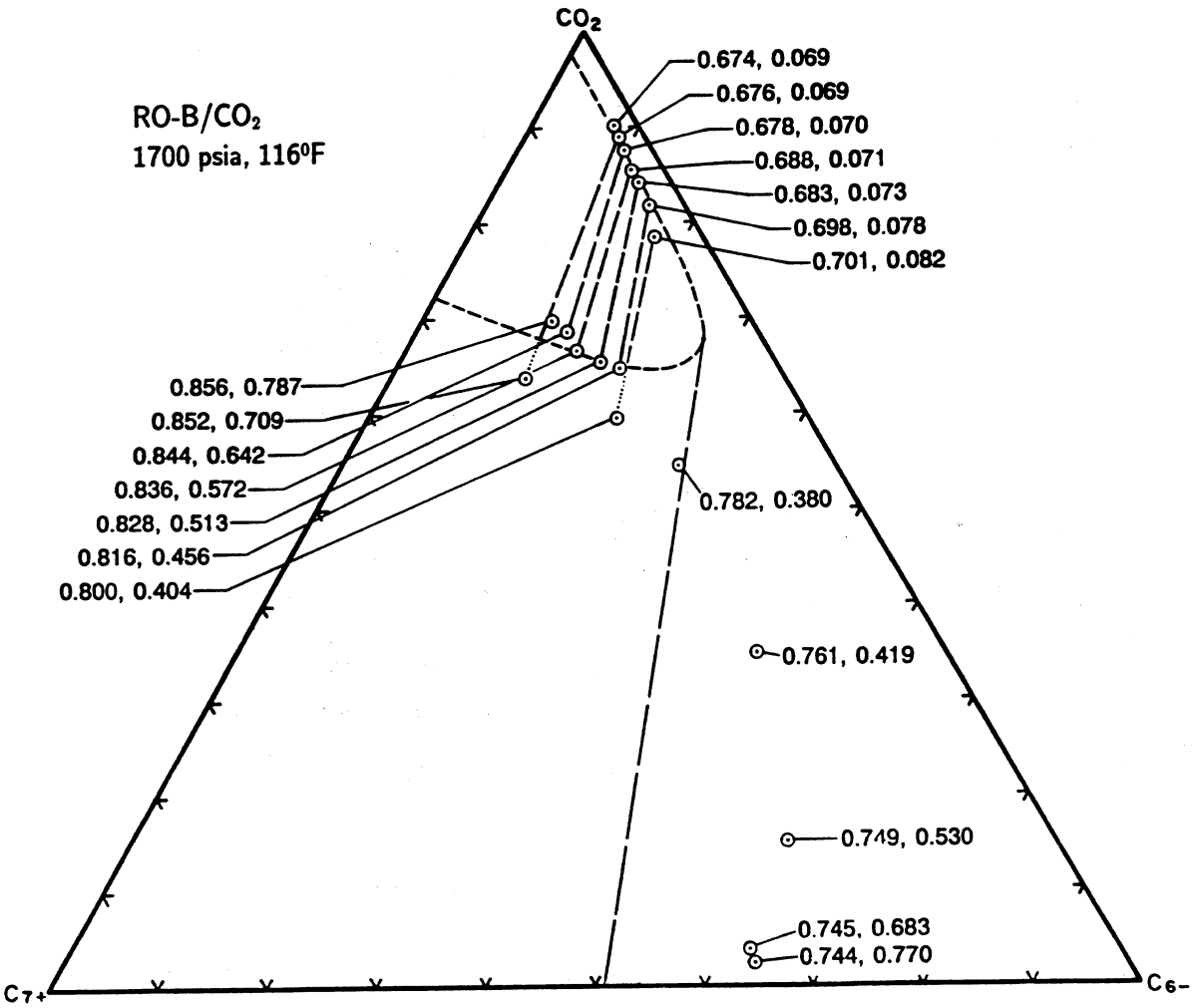

Figure I-4. Pseudoternary phase behavior representation with corresponding density and viscosity for the RO-B/CO_2 system at 1700 psia and 116°F.

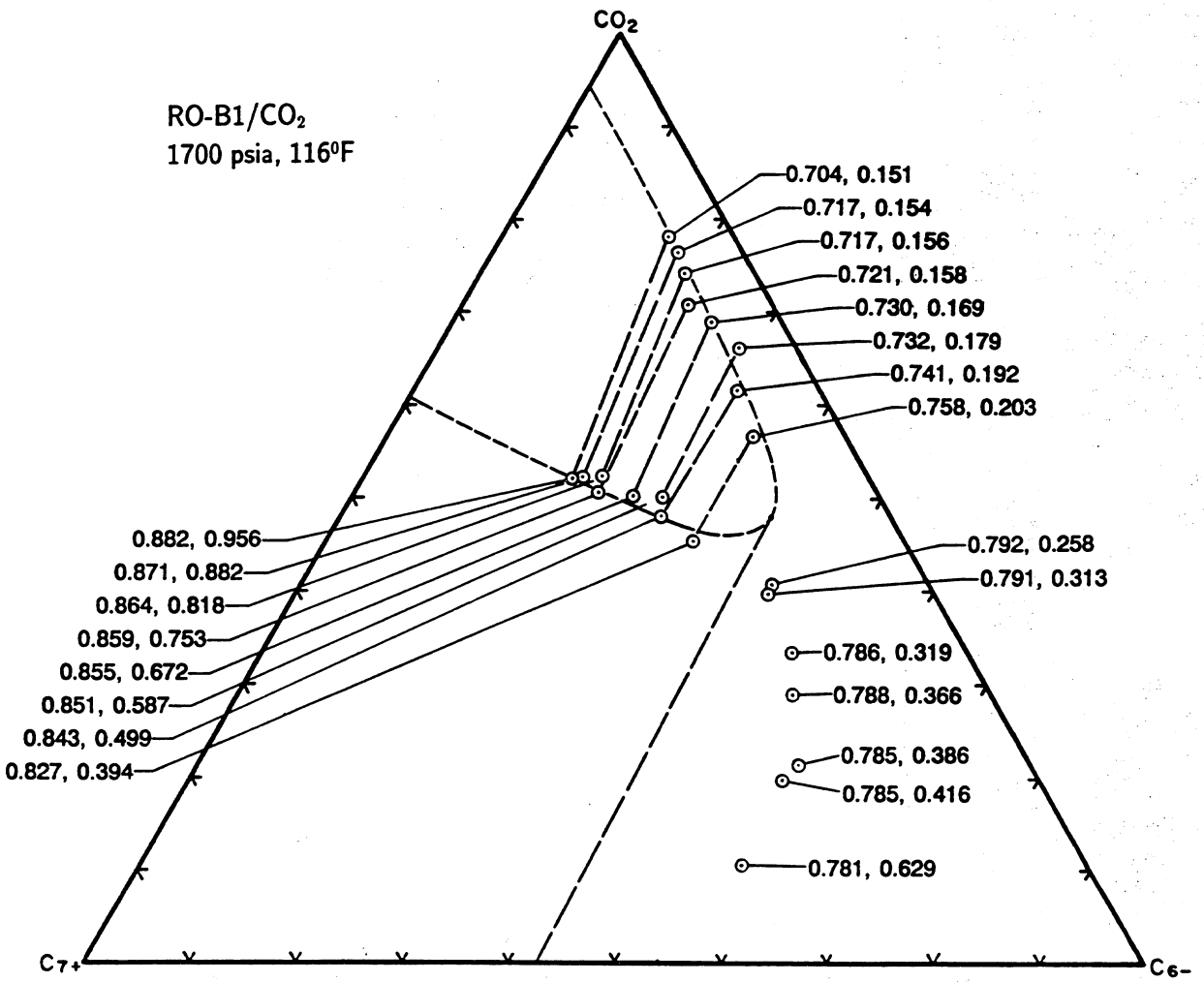

Figure I-5. Pseudoternary phase behavior representation with corresponding density and viscosity for the RO-B1/CO_2 system at 1700 psia and 116°F.

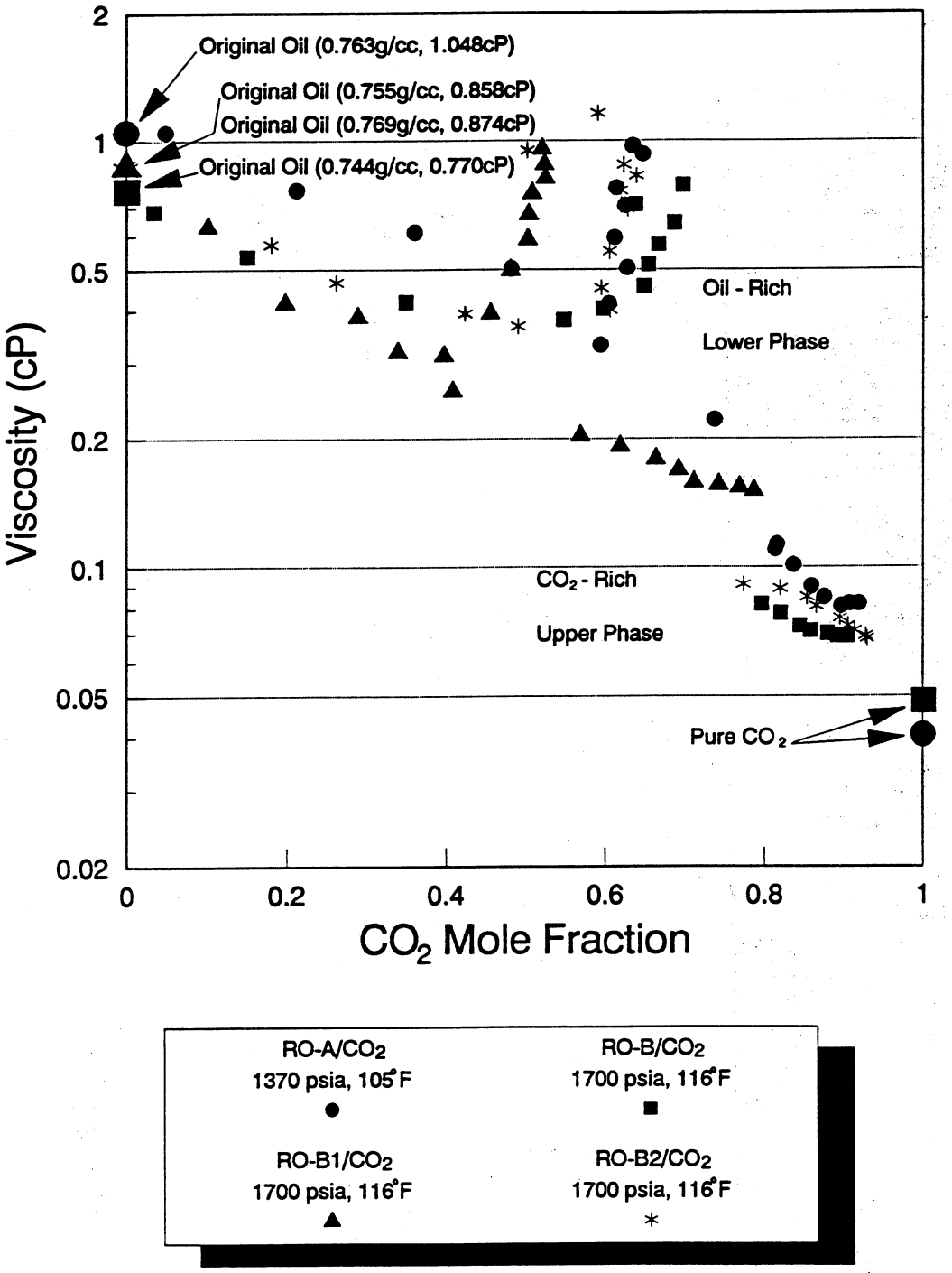

Figure I-6. Phase viscosities vs. CO_2 mole fraction for the RO-A, RO-B, RO-B1, and RO-B2 systems.

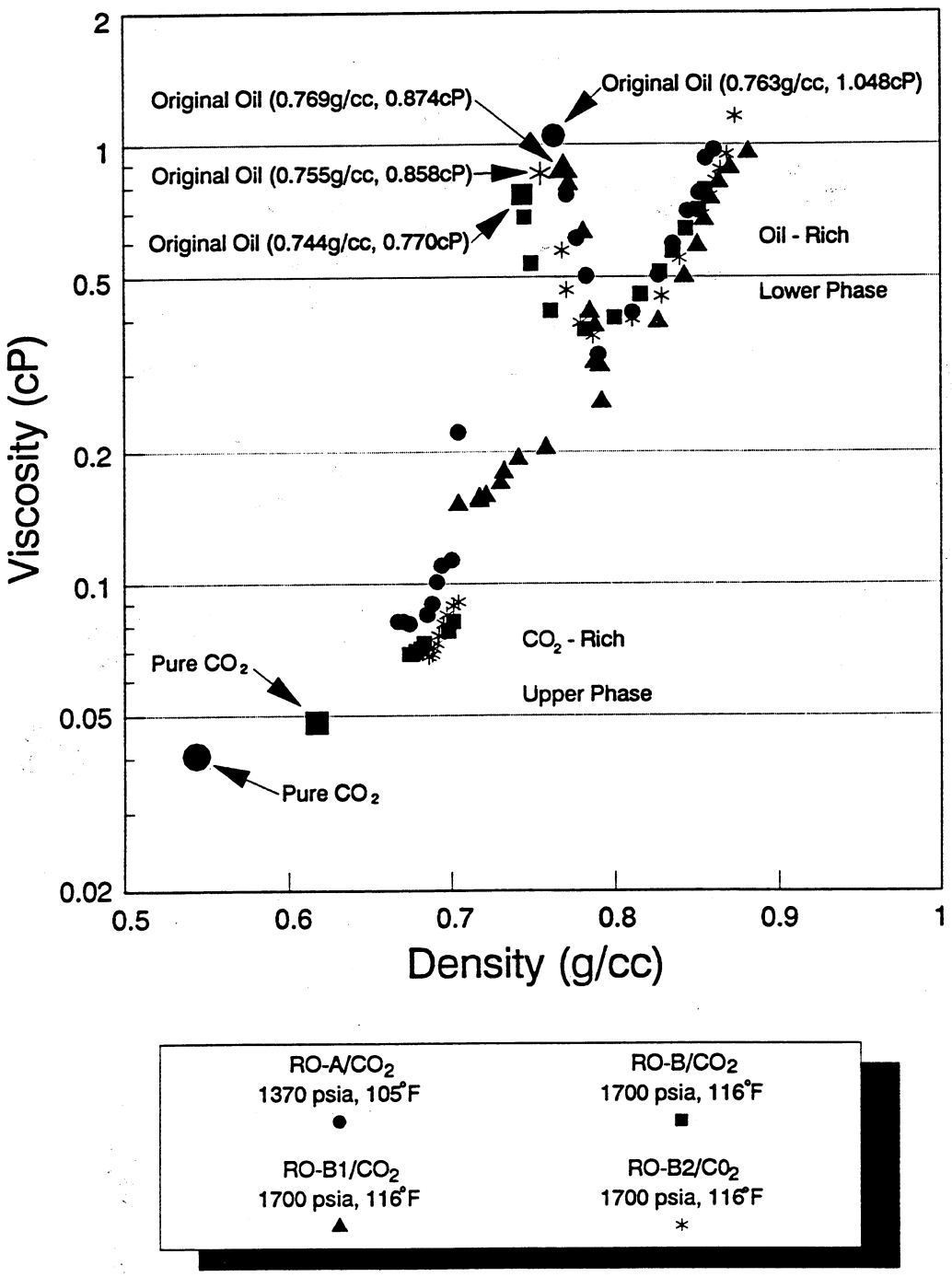

Figure I-7. Phase viscosities vs. phase densities for the RO-A, RO-B, RO-B1, and RO-B2 systems.

for the methane-enriched oil are similar to those of the original oil. The equilibrium liquid phase properties, also, show the same trend, yet to a lesser degree. On the average, the measured liquid-phase density values for the RO-B1/CO_2 system are 3% higher, while the viscosities are 20% higher. The increased densities and viscosities of the equilibrium phases that evolve with an increased amount of solution gas (methane, in this case) are due to the efficient extraction of hydrocarbons (or to the nonmutually exclusive decrease of CO_2 concentration, depending on how it is viewed) from the oil-rich liquid phase. The CO_2-rich phase viscosity enhancement that occurs when solution gas is present could have some beneficial impact on the unfavorable mobility ratio between the CO_2-rich phase in the front of the transition zone and the oil bank. The beneficial effects of the changes in the physical properties of the equilibrium dense fluid and liquid phases, at least from the standpoint of mobility control, could conceivably offset the adverse phase behavior effect (if it exists at all) that can result in a moderate increase in MMP in the presence of solution gas. The slight increase in MMP observed by several investigators[46-49] who studied the effect of solution gas were mostly performed in a slim-tube flow regime where the adverse effects of viscous instabilities and heterogeneities were minimized to isolate the impact of phase behavior on displacement efficiency. Displacement experiments in a porous medium that allowed for the occurrence of flow instabilities would have to be performed to assess the effect, if any, of the observed property changes of the equilibrium dense fluid and liquid phase mixtures in the presence of solution gas.

3. Effects of Contamination of CO_2 on Fluid Properties

Orr and Taber[10] presented results of static cell equilibrium tests on a stock tank oil (STO-A) from the Wasson field in West Texas at three different temperatures (90, 105, and 120°F). The pressure/composition phase diagrams shown in Fig. I-8 and I-9 (from Orr and Taber[8]) detail the complex phase behavior exhibited by this system. Figure I-9 shows the results of tests with a 10 mole% N_2 + 90 mole% CO_2 injection gas.

The STO-A/CO_2 system exhibits three-phase (L_1-L_2-V) immiscibility at 90 and 105°F. The three-phase region occurs in the pressure range of around 1000-1300 psia and bulk CO_2 concentrations in excess of 72 mole%. It pinches at the bubble-point curve and, thus, separates the L_1-V and L_1-L_2 bubble-point loci.

Phase behavior and fluid property measurements were performed on the STO-A oil using pure CO_2 and 9.8 mole% N_2-contaminated CO_2 injection gases. The measurements were conducted at 1500 psia and 109°F (above the three-phase pressure). The results are shown in Figs. I-10 through I-13. The constant-pressure slice in pressure/composition space cuts through the liquid-liquid (L_1-L_2) region and should yield a bubble-point CO_2 concentration of around 72 mole%, based on Fig. I-8. The two-phase liquid-liquid bifurcation occurred at around 70.5 mole% CO_2 along the dilution path for the STO-A/CO_2 system. The difference in the bubble-point compositions, although certainly well within the established uncertainties, could be partly caused by temperature effect. The temperature of 109°F for these experiments could have caused a slight enlargement of the phase envelope compared to the results of Orr and Taber[8] at 105°F. Figure I-10 reveals that a very narrow portion of the two-phase L_1-L_2 region was traversed in composition space during the dilution of STO-A with CO_2 because of the lack of intermediate hydrocarbon components in the oil.

The adverse effect of the presence of small amounts of nitrogen (N_2) in the CO_2 stream on the pressure required for the development of multiple-contact miscibility is well established. The presence

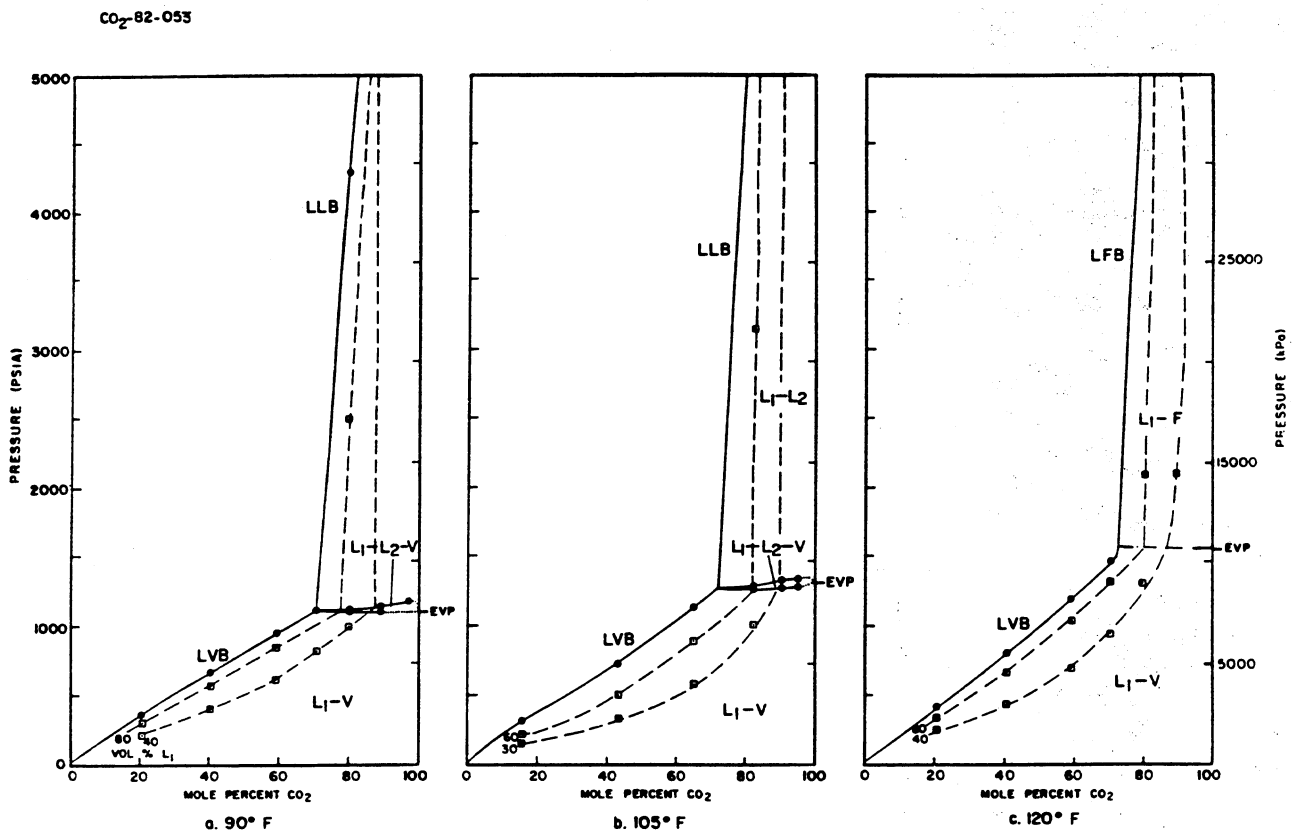

Figure I-8. Pressure/composition phase diagrams for mixtures of CO_2 with STO-A (Orr and Taber[8]).

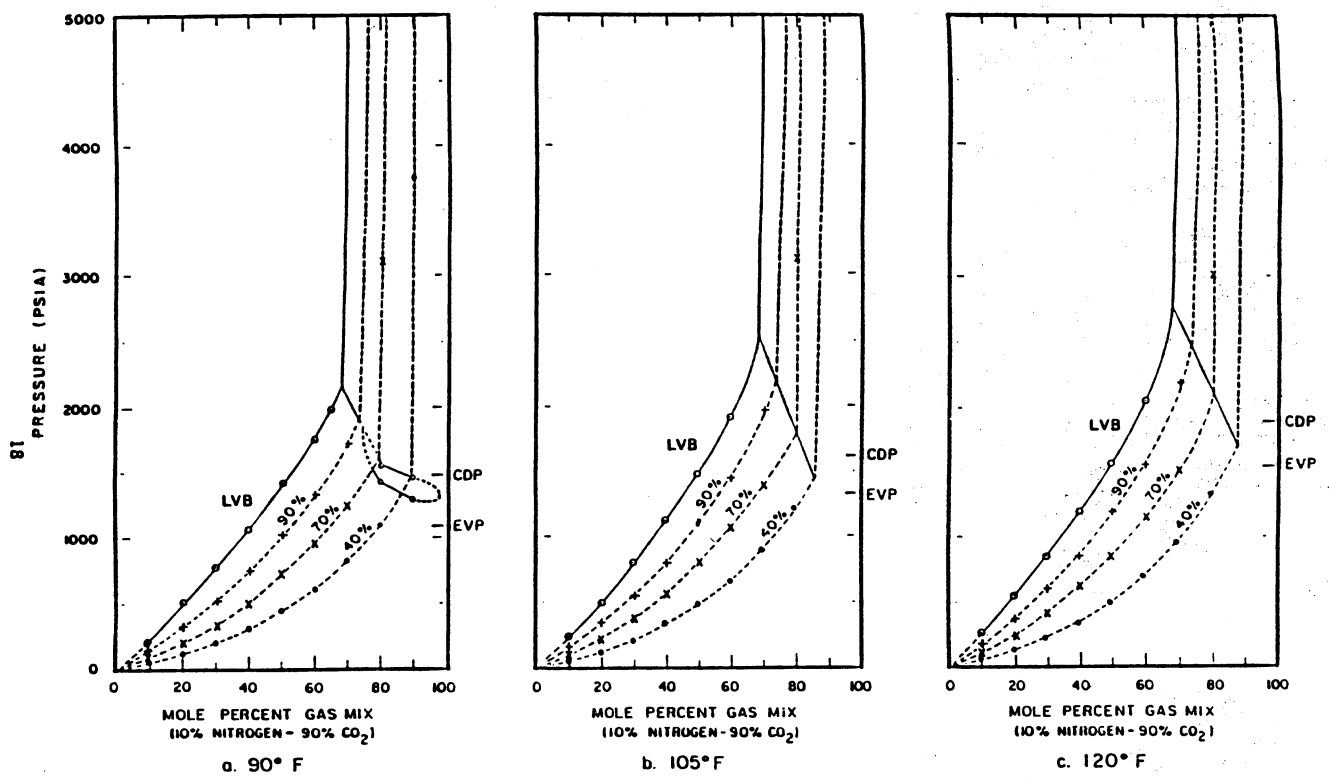

Figure I-9. Pressure/composition phase diagrams for mixtures of STO-A with CO_2 containing 10 mole% N_2 (Orr and Taber[8]).

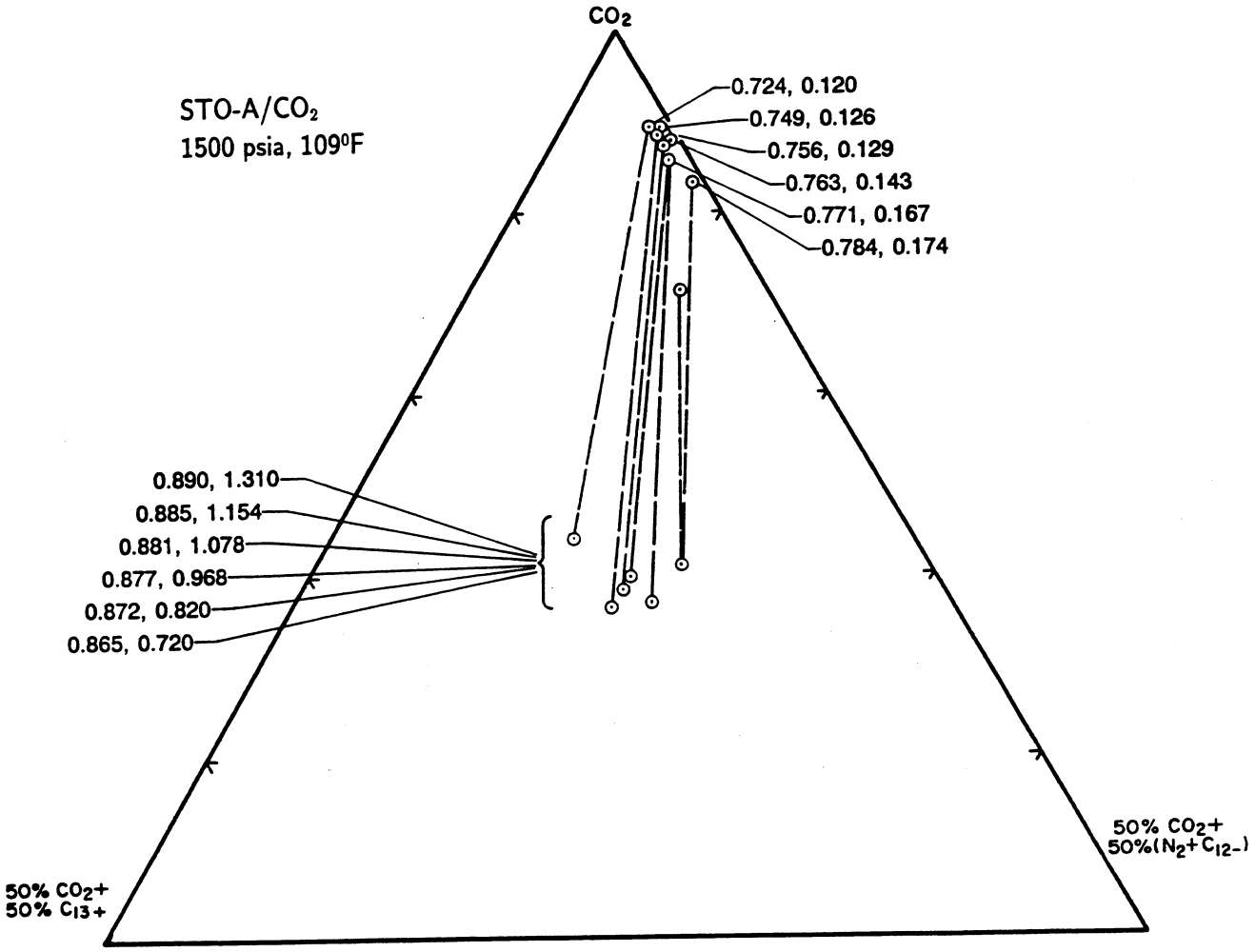

Figure I-10. Pseudoternary phase behavior representation with corresponding density and viscosity for the STO-A/CO_2 system at 1500 psia and 109°F.

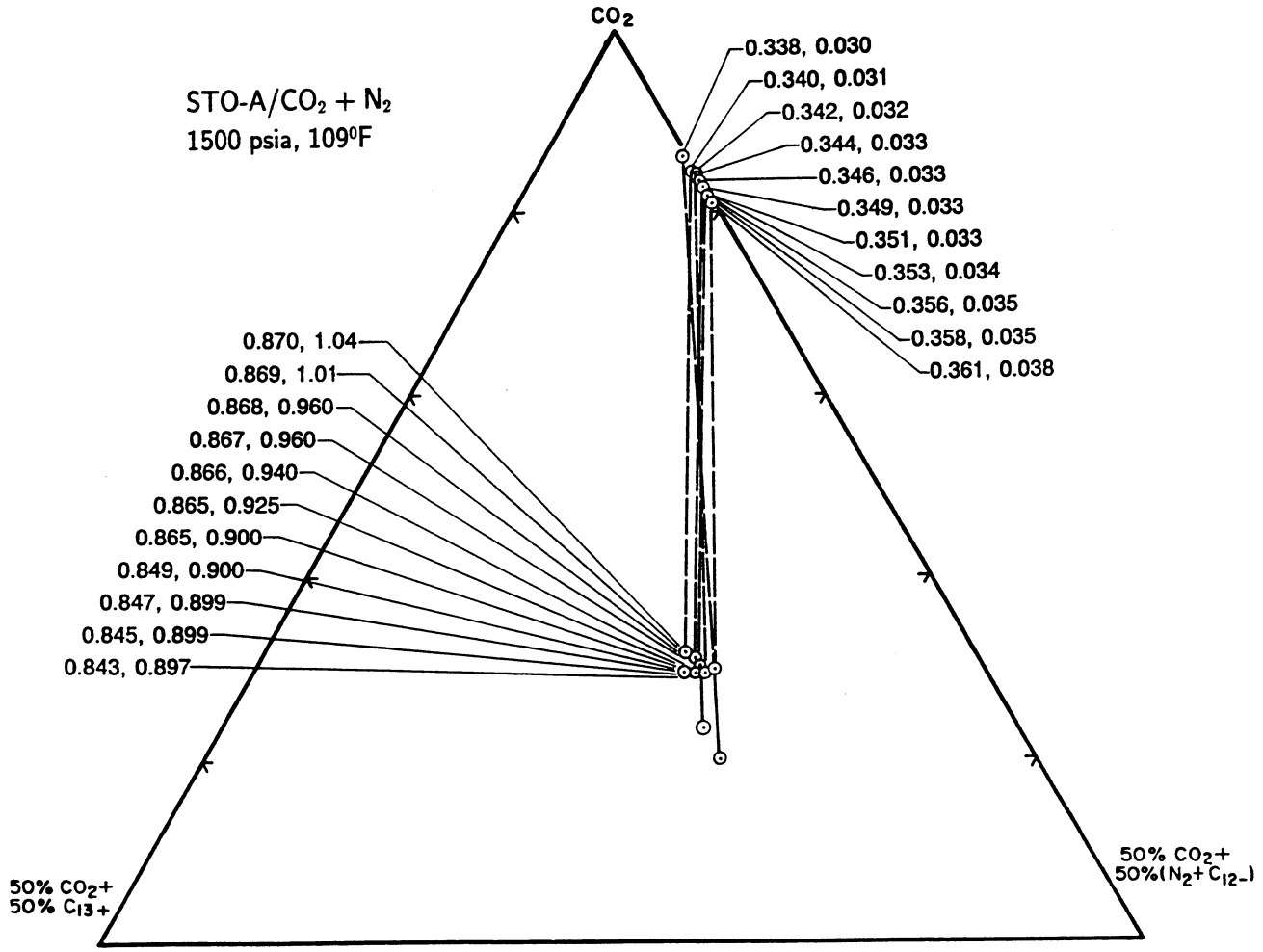

Figure I-11. Pseudoternary phase behavior representation with corresponding density and viscosity for the STO-A/CO_2 + N_2 system at 1500 psia and 109°F.

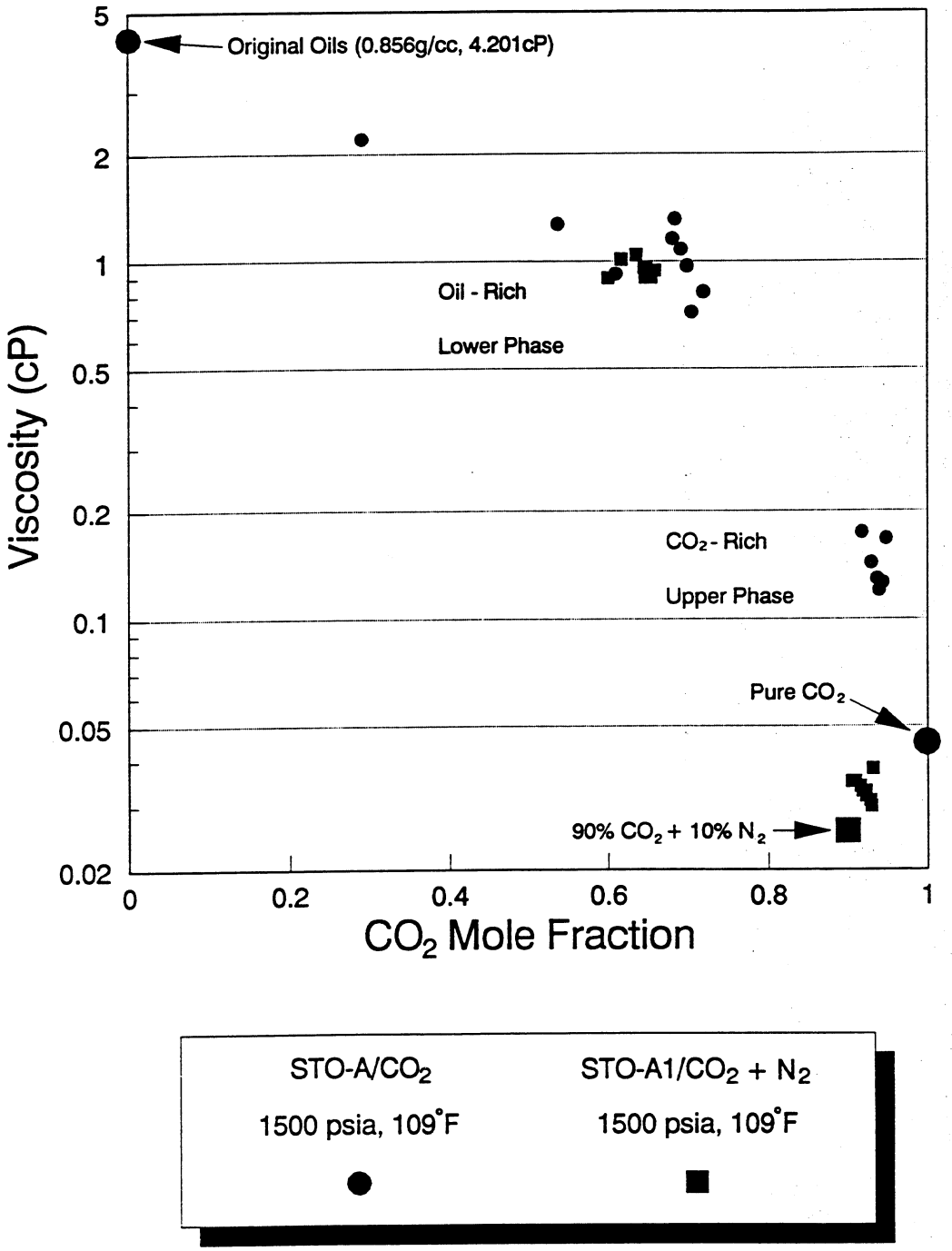

Figure I-12. Phase viscosities vs. CO_2 mole fraction for the RO-A systems.

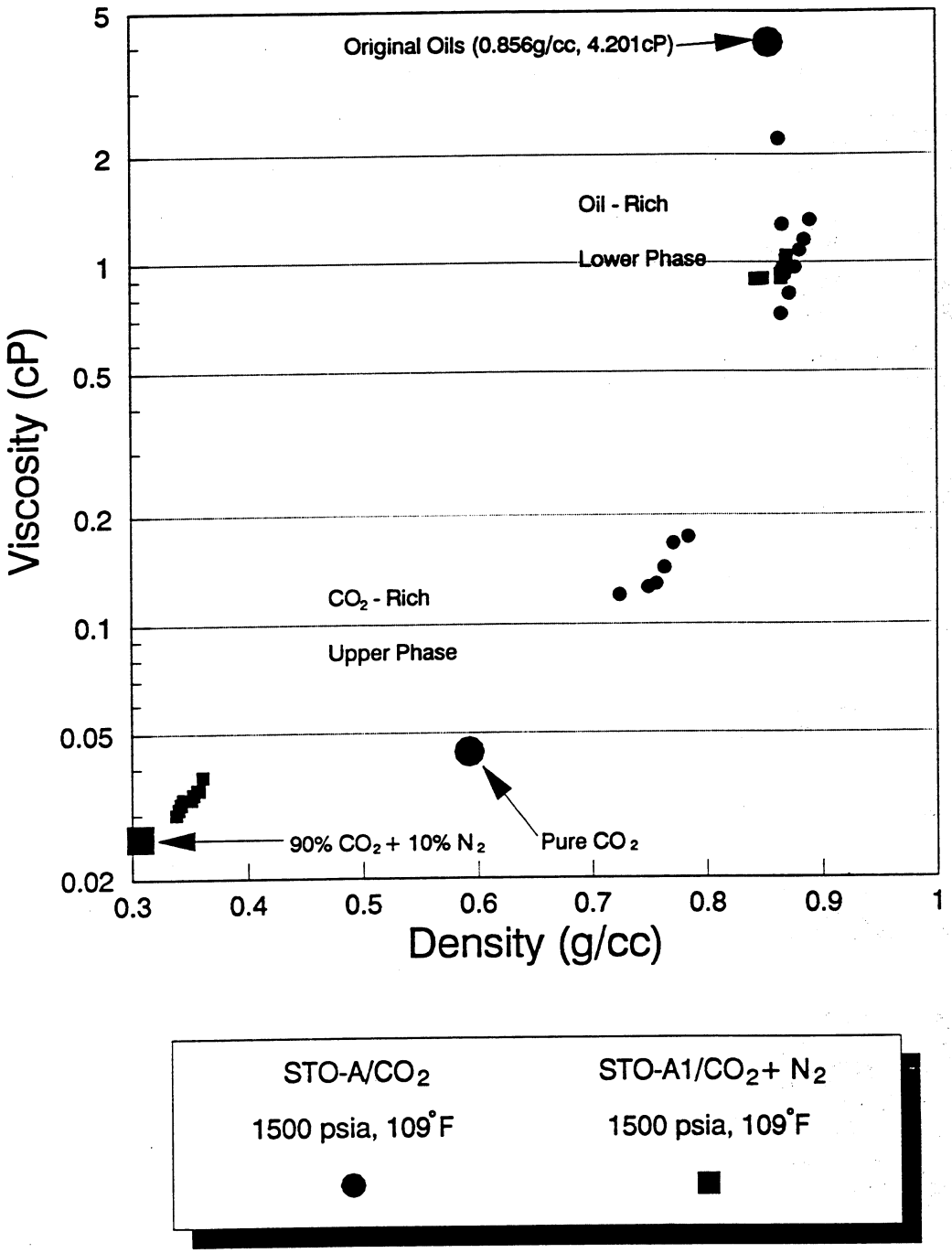

Figure I-13. Phase viscosities vs. phase densities for the RO-A systems.

of N_2 raises the MMP considerably in comparison to that of pure CO_2. The effect is larger at low temperatures. Since natural (and industrial) sources of CO_2 are rarely pure, it is unfortunate that few MMP correlations that take into account impurities in the CO_2 stream[52-55] have been published in comparison to those for pure CO_2.

A comparison of the results of the nitrogen-contaminated run with the baseline case revealed the following:

- The solubility of CO_2 in the oil-rich liquid phase is lowered (shown in the tables in Appendix A of the Fifth Annual Report[5]) with the addition of N_2. This is shown as an enlargement of the two-phase region in a pseudoternary diagram (Figs. I-10 and I-11).

- The densities of the CO_2-rich upper phase mixtures are, on average, 55% lower in the presence of N_2, resulting in poor hydrocarbon extraction efficiency.

- The viscosities of the upper phase mixtures are decreased by an average of 76%.

The adverse impact of N_2 on the viscosity of the CO_2-rich phase can have a drastic effect on the flood-front mobility ratio. The low solubility of N_2 in crude oils at typical CO_2 flooding pressures could result in a buildup of N_2 in the vapor phase. Lansangan[56] studied the effect of N_2 on the mass transfer rate of CO_2 into a vertical packed column of quiescent normal decane system. A drastic reduction of the rate of mass transfer was observed compared to the case where pure CO_2 was used under identical conditions. He concluded that the presence of N_2 creates a stagnant phase through which CO_2 must diffuse before contacting the oil, thus, lowering the interfacial equilibrium CO_2 concentration, which results in a decreased rate of mass transfer even at low N_2 concentrations. This adverse effect can persist even if the pressure (i.e., MMP) is increased enough to produce a dense CO_2-rich phase because of the relative insensitivity of fluid viscosity to changes in pressure at constant temperature. On the other hand, the increased density of the CO_2-rich phase could result in better hydrocarbon extraction efficiency, which could presumably account for an increase in the viscosity of the CO_2-rich phase when N_2 is present.

4. Conclusions

The experimental results presented in this paper can be summarized as follows:

a. Mixtures of CO_2 and crude oil systems show an abnormal dependence of viscosity on density in the single-phase region. The viscosities decrease monotonically, while the densities increase with the continued dilution of the oil with CO_2 along the composition path. The mixtures in the two-phase region exhibit normal viscosity/density dependence, i.e., $(\partial\mu/\partial\rho)_{TP} > 0$.

b. The presence of extracted hydrocarbons in the dense CO_2-rich phase can result in increased viscosities relative to pure CO_2 even at CO_2 concentrations greater than 90 mole%.

c. The increased amount of solution gas resulted in an increase in densities and viscosities of the equilibrium dense fluid and liquid phases when compared to the same oil but with

a lower solution gas/oil ratio. The viscosity enhancement could presumably have a favorable effect on phase mobilities during a CO_2 flood.

d. The presence of small amounts of nitrogen mixed with the CO_2 stream resulted in a drastic reduction of the CO_2-rich phase viscosities compared to the values obtained using pure CO_2 solvent. The adverse impact of N_2 on phase behavior and fluid properties could have dramatic effects on a nitrogen-contaminated CO_2 flood, which would result in poor recovery efficiencies.

B. DEVELOPMENT OF A VISCOSITY CORRELATION

Accurate simulation and performance prediction of multiple-contact miscibility processes require, among other information, the viscosities of the injected solvent, the *in situ* reservoir fluid, and the two mixed together. The literature on CO_2 flooding contains numerous correlations for prediction of viscosities of hydrocarbon mixtures in both the gaseous (low pressure) and dense fluid (high pressure) phases. For the prediction of CO_2/reservoir oil mixture viscosities, however, an accurate and consistent correlation covering a wide range of conditions is highly desired.

This section of the report presents a correlation for predicting viscosities of single phase and equilibrium vapor (dense fluid) and liquid phases of CO_2/synthetic oil and CO_2/reservoir oil mixtures. The database of viscosity and density tied in with composition was used to estimate the pertinent correlation parameters. A high temperature crude oil/lean gas system was also included in the database. The experimental error in viscosity measurement was determined to be less than 5% over a 0.04 cp to 4.0 cp range. Crude oils from West Texas, Northeastern New Mexico, and the Middle East as well as certain synthetic oils of varying complexity were used in the study. The LBC correlation[16] was modified using the Corresponding States Principle coupled with new mixing rules to include mixtures with CO_2 concentrations of up to 98 mole%. Experimental conditions covered a range of 90°F to 247°F and pressures up to 5000 psia. The new correlation showed about a 70% improvement in average absolute deviation compared to the Lohrenz, Bray, and Clark correlation. The new correlation is expected to improve, in many cases, our ability to predict oil recovery performance both in the laboratory and in the field.

The oil industry has not been spared from the exponential growth of computer use in the last decade. Numerical modeling of reservoir processes to estimate field performance, i.e., oil production over a period of years, has presently become a standard tool used by oil company management to assess the viability of potential projects and to make economic projections based on a forecasted market price. Mathematical models used to predict the field performance of a carbon dioxide flood employ viscosity correlations based on viscosity databases where the maximum CO_2 concentration is generally less than 10 mole%.[16] The oil recovery efficiency of a CO_2 flood, however, is often determined by a CO_2-rich phase having CO_2 concentrations that can be in excess of 50 mole%. Viscosity correlations in the literature are well over 100% off in their predictions [57,58] and, thus, can greatly affect the calculated phase mobilities in the simulation. A large phase-mobility contrast produces an unstable displacement front, resulting in early gas breakthrough (yielding a conservative oil production estimate), while an artificially-favorable mobility ratio would result in an overly optimistic production estimate. Both are artifacts caused in part by viscosity-estimation errors that can render the simulation meaningless. A common practice in industry is to "fine tune" certain parameters in the viscosity correlation employed in individual simulators to match the company's own field data. This procedure, however, does not

guarantee an accurate viscosity prediction for processes different than those from which the matched data were obtained. Furthermore, even with the same oil and the same process, one can have an entirely different set of conditions.

The viscosities of crude oils and their mixture with a variety of solvents are also of importance in various aspects of reservoir engineering analysis. Typical PVT analyses of oils generally report the viscosity at reservoir conditions. In most cases, however, the viscosity value is needed at some other temperature and/or pressure, during a flash or differential liberation process, or after the dilution of the oil with some solvent. Even if only a selected set of laboratory measurements are conducted, this process can still be very costly and time consuming. A correlational package that would allow for the estimation of viscosity over a wide range of conditions with reasonable accuracy is highly desirable. Thus, the need for a better viscosity estimation procedure for CO_2/crude oil systems is apparent.

A correlation package has been developed for estimating CO_2/reservoir oil viscosities, covering a wide range of CO_2 concentrations, for both single-phase and equilibrium liquid- and vapor-phase mixtures from a single, internally consistent equation. The new procedure is a modification of the LBC correlation,[16] which uses the viscosity, density, and composition database obtained in our laboratories.

The LBC method was published in 1964 and became accepted as an industry-wide standard for estimating the viscosity of crude oils and natural gas/crude oil mixtures, requiring only input data that are readily available, thereafter. The procedure was developed by adapting a pure-component viscosity correlation[59] for mixtures via combinatorial rules to obtain the correlation parameters for a multicomponent system. A comparison between our results and the LBC prediction reveals deviations that can be on the order of 100% or more for the CO_2/crude oil systems used in this work. Kovarik *et al.*[58] also reported large deviations between predicted and measured viscosities, even for well-defined CO_2/synthetic oil mixtures at high CO_2 concentrations. This is not surprising considering that the database used by Lohrenz and his co-workers has CO_2 concentrations of 5 mole% or less.

Several authors have pointed out numerous shortcomings associated with the LBC correlation. Pedersen *et al.*[60] reported that the accuracy of the LBC correlation is strongly dependent on the density correlation used. Emanuel[57] also pointed out the sensitivity of the LBC predictions to the mixture critical density because of the fourth power dependence of the correlation to the reduced density. These findings are corroborated by the results of Kovarik *et al.*;[58] they measured (using the CPE apparatus) the viscosities of a well-defined, four-component hydrocarbon system and its mixtures with CO_2 at varying conditions. The result of their comparison with the LBC prediction revealed that for pure hydrocarbon components heavier than C_7, the critical molar volume correlation presented by Lohrenz *et al.*[16] resulted in a lower average absolute deviation (AAD) than the calculations achieved while using the reported critical molar volume of the pure component. Recent advances in the area of crude oil characterization have, perhaps, made the use of cubic equations of state (EOS) more popular for the correlation of fluid properties. The Peng-Robinson EOS[61] (PREOS), tuned to match a few experimental data, has been shown to yield fairly accurate density predictions. The strong density dependency of the LBC correlation would probably not pose severe limitations when used in an EOS-based compositional simulator.

Saeedi and Rowe[62] reported unstable and inconsistent vapor-phase viscosity predictions for a number of hydrocarbon systems by the LBC correlation, although they reported excellent liquid-phase viscosity predictions from the same method. More taxing, from the standpoint of compositional simulation, is the lack of convergence of the vapor- and liquid-phase viscosities as the two phases approach criticality,[63] a behavior shown by the LBC correlation as reported by Saeedi and Rowe. This is not surprising if the

fact that the original LBC correlation consists of separate procedures for equilibrium liquid and vapor phases is taken into consideration. Lohrenz *et al.*[16] commented, however, that the liquid-phase viscosity estimation procedure could be used for gas viscosity predictions, given a reliable density prediction method for reservoir gases (which they deemed unavailable at that time). Our calculations reveal stable (albeit inaccurate) LBC-predicted vapor-phase viscosities when employing the liquid-phase procedure and the measured vapor-phase densities as input data for the calculations. The use of a single estimation procedure, applicable to both equilibrium vapor and liquid phases, affords the convergence of the phase viscosities at the critical point.

The modification to the LBC correlation is obtained by introducing a deviation function correlated against the reduced mixture density and employing nontraditional mixing rules for the mixture pseudocritical properties. The modified LBC (MLBC) is then compared to the Pedersen *et al.*[64] viscosity correlation, which is based on a "hindered-molecular-rotation" theory in the liquid phase[65] and is shown to be more accurate in estimating CO_2/crude oil mixture viscosities. The correlation presented in this work is based on 393 viscosity/density/composition data points. The database includes single-phase and equilibrium vapor- and liquid-phase mixtures with CO_2 concentrations ranging from 0 mole% in the liquid phase to around 98 mole% in the vapor phase. The new procedure of viscosity estimation resulted in an average absolute percentage deviation (AAPD) of 12.5%. The original LBC and the Pedersen *et al.* correlations were 40.5% and 23.4%, respectively.

1. Review of Related Literature

The coefficient of shear viscosity (or simply viscosity), μ, is one of the essential physical properties used in petroleum reservoir engineering. Numerous correlations for the estimation of viscosities of crude oils and their mixtures with a variety of light gases have appeared in the literature since the publication of the generalized reduced viscosity plots of Uyehara and Watson.[16,57,60,63,66-78] These correlations can be roughly classified (not mutually exclusive) as empirical, semi-empirical, composition-based, and noncomposition-based. A few appear in graphical form, which makes them unsuitable for digital process simulations.

Correlations that were designed to estimate the viscosities of crude oils and their mixtures with different solvents or natural gases possess a certain feature that sets them apart from viscosity correlations designed for pure components or for simple, well-defined mixtures. The inherent uncertainty in the makeup of the oil for carbon numbers greater than seven sets a limit to the generality of any proposed viscosity estimation procedure for crude oils. Until a universal characterization scheme is found, any correlation will be dependent on the procedure it employs to determine the correlation parameters for the heavy fraction in the complex hydrocarbon mixture. A majority of the published correlations were, in fact, originally developed for pure substances. Combinatorial rules were essentially incorporated in the correlation to obtain the parameters for a mixture. These shortcomings are often circumvented by regressing the correlation parameters against a large volume of data. This procedure certainly expands the range of the correlations' applicability, but their database dependency cannot be denied.

Notwithstanding the analytical problems associated in identifying the components of such a complex mixture, the lack of a rigorous mathematical model for the condensed phase of matter has precluded the understanding of the mechanism of momentum transfer in the liquid state, even for the simplest case of Newtonian flow behavior.[79,80] These factors have certainly hindered the formulation of a general predictive theory for the viscosity of simple liquids. Thus, any attempt at arriving at a prediction method

for the viscosity of crude oils will always encounter the unavoidable recourse to empiricism. But as Brush[81] commented, there is no reason why an empirical formulation should not be judged with regard to its accuracy in fitting experimental data and the ease of its application. What should be avoided is the temptation to attach theoretical significance to the correlation.

The highlights of the Pedersen *et al.*[60,64] viscosity correlation, to which the correlation presented in this paper was compared, are discussed briefly in the following paragraphs.

The correlation of Pedersen *et al.* is an extension of the model proposed by Tham and Gubbins[65] for the prediction of thermal conductivities and viscosities of both vapor- and liquid-phase mixtures. The Tham and Gubbins' model, in turn, is an extension of the corresponding states principle, which incorporates the theory that free molecular rotation is not possible in the liquid phase (or dense fluid phase). The model introduces a parameter called the rotation coupling coefficient, α_{TG}, which accounts for the hindered molecular rotation; it appears in the following viscosity equation, which is based on a modified, simple correspondence principle

$$\mu(P,T) = \left(\frac{T_c}{T_{co}}\right)^{-\frac{1}{6}} \left(\frac{P_c}{P_{co}}\right)^{\frac{2}{3}} \left(\frac{M}{M_o}\right)^{\frac{1}{2}} \left(\frac{\alpha_{TG}}{\alpha_{TG_o}}\right) \times \mu_o\left[\frac{P \bullet P_{co}\alpha_{TG,o}}{P_c\alpha_{TG}}, \frac{T \bullet T_{co}\alpha_{TG,o}}{T_c\alpha_{TG}}\right] \tag{I-2}$$

Pedersen *et al.* extended the above model to crude oil systems by adapting mixing rules for $T_c, P_c, M,$ and α_{TG}. These are

$$T_{cm} = \frac{\sum_i \sum_j x_i x_j \left[\left(\frac{T_{c_i}}{P_{c_i}}\right)^{\frac{1}{3}} + \left(\frac{T_{c_j}}{P_{c_j}}\right)^{\frac{1}{3}}\right]^3 \left[T_{c_i} T_{c_j}\right]^{\frac{1}{2}}}{\sum_i \sum_j x_i x_j \left[\left(\frac{T_{c_i}}{P_{c_i}}\right)^{\frac{1}{3}} + \left(\frac{T_{c_j}}{P_{c_j}}\right)^{\frac{1}{3}}\right]^3} \tag{I-3}$$

$$P_{cm} = \frac{8\sum_i \sum_j x_i x_j \left[\left(\frac{T_{c_i}}{P_{c_i}}\right)^{\frac{1}{3}} + \left(\frac{T_{c_j}}{P_{c_j}}\right)^{\frac{1}{3}}\right]^3 \left[T_{c_i} T_{c_j}\right]^{\frac{1}{2}}}{\left(\sum_i \sum_j x_i x_j \left[\left(\frac{T_{c_i}}{P_{c_i}}\right)^{\frac{1}{3}} + \left(\frac{T_{c_j}}{P_{c_j}}\right)^{\frac{1}{3}}\right]^3\right)^2} \tag{I-4}$$

$$M_m = 1.304 \times 10^{-4}\left(\bar{M}_w^{2.303} - \bar{M}_n^{2.303}\right) + \bar{M}_n \tag{I-5}$$

$$\bar{M}_n = \sum_i x_i M_i \tag{I-6}$$

$$\bar{M}_w = \frac{\sum_i x_i M_i^2}{\sum_i x_i M_i} \tag{I-7}$$

$$\alpha_{TG_m} = 1 + 7.378 \times 10^{-3} \rho_r^{1.847} M_m^{0.5173} \tag{I-8}$$

$$\alpha_{TG_o} = 1 + 3.100 \times 10^{-2} \rho_r^{1.847} \tag{I-9}$$

In Eqs. (I-8) and (I-9), ρ_r is the reduced density of the reference substance and is given by

$$\rho_r = \frac{\rho_o(P^*, T^*)}{\rho_{co}} \tag{I-10}$$

where

$$T^* = \frac{T \bullet T_{co}}{T_{cm}} \tag{I-11}$$

$$P^* = \frac{P \bullet P_{co}}{P_{cm}} \tag{I-12}$$

Methane is used as the reference substance and the equation of state employed to calculate the reference substance density is given by McCarty.[82] The EOS is a modified Benedict-Webb-Rubin formulation and is given by

$$P = \sum_{n=1}^{9} a_n(T)\rho^n + \sum_{n=10}^{15} a_n(T)\rho^{2n-17}\exp(-\gamma\rho^2) \tag{I-13}$$

where the coefficients $a_n(T)$ are evaluated as a function of temperature.

The reference viscosity correlation of Hanley, McCarty, and Haynes,[83] extended by Pedersen *et al.*[64] below the freezing point of methane, is used to calculate μ_0. This is given by

$$\mu(\rho,T) = \mu_0(T) + \mu_1(T)\rho + F_1\Delta\mu'(\rho,T) + F_2\Delta\mu''(\rho,T) \tag{I-14}$$

2. Viscosity/Density/Composition Data

The CPE apparatus was employed to generate a database relating phase viscosities to densities and compositions for mixtures of CO_2 and crude oils of West Texas, Northeastern New Mexico, and the Middle East. Certain synthetic oil mixtures were included in the database as well. These mixtures include a single phase and equilibrium vapor and liquid phases. A list of the hydrocarbon systems included in the database is given in Table I-3. The ranges of pertinent variables from all the analyses used in the correlation development are presented in Table I-4. In this list, the extent of CO_2 content, which ranges from pure hydrocarbon mixture to almost pure CO_2 in contrast to the Lohrenz *et al.* database (which has a reported maximum CO_2 concentration of about 4 mole%), is worth noting. Kovarik *et al.*[58] performed extensive error analysis based on the CPE apparatus configuration and the analytic techniques used in the study. They determined the experimental error associated with the viscosity measurements to be generally less than 5% within the 0.04 cp to 4.0 cp range.

3. Comparison of Viscosity Data to the Lohrenz, Bray, and Clark Correlation

The viscosity data were compared to the LBC correlation,[16] the highlights of which are described briefly in this section. The backbone of the LBC procedure is the Jossi, Stiel, and Thodos viscosity correlation[59] developed for pure nonpolar fluids in the dense gaseous- and liquid-phase regions. The latter correlation was developed using the residual viscosity concept coupled with the corresponding states principle. Figure I-14 is a plot of the quantity $(\mu - \mu^*)\xi$ versus ρ_r reproduced from the Jossi *et al.*[59] Here, μ^* is the low-pressure gas viscosity, ξ is the inverse viscosity parameter, and ρ_r is the reduced mixture density. Note that for all the substances included in their study, all the data points essentially fall on the same curve in the reduced density range of about 0.02 to 3.0. The best-fit curve for all the data points is given by

$$\begin{aligned}[(\mu - \mu^*)\xi + 10^{-4}]^{\frac{1}{4}} &= 0.1023 + 0.023364\rho_r + 0.058533\rho_r^2 \\ &\quad -0.040758\rho_r^3 + 0.0093324\rho_r^4\end{aligned} \tag{I-15}$$

TABLE I-3. LIST OF HYDROCARBON SYSTEMS USED IN THE DATABASE

$nC_5 + nC_{10} + nC_{16} + nC_{30}$
Wasson Stock Tank Oil
Wasson Oil + C_1
Maljamar Stock Tank Oil
Abu Dhabi Stock Tank Oil
Abu Dhabi Enriched Reservoir Oil
Amoco Oil A
Amoco Oil B
Oxy Oil B
Texaco Oil 1
Texaco Oil 2
Texaco Oil 2A
Texaco Oil 2B

TABLE I-4. RANGES OF VARIABLES FOR ALL THE ANALYSES USED IN THE DETERMINATION OF THE FITTING PARAMETERS

VARIABLE	RANGE
Total number of data points	393
Carbon dioxide mole fraction	.0000 to 0.9810
Methane mole fraction	.0000 to .8869
C_{7+} mole fraction	.0035 to .9028
C_{7+} specific gravity	.6873 to .8163
C_{7+} average molecular weight	100 to 341
Temperature (°F)	90 to 247
Pressure (psia)	1200 to 5000
Original oil API gravity	30.0 to 38.4
Experimental density (g/cm^3)	.1361 to .8900
Experimental viscosity (cp)	.025 to 4.4

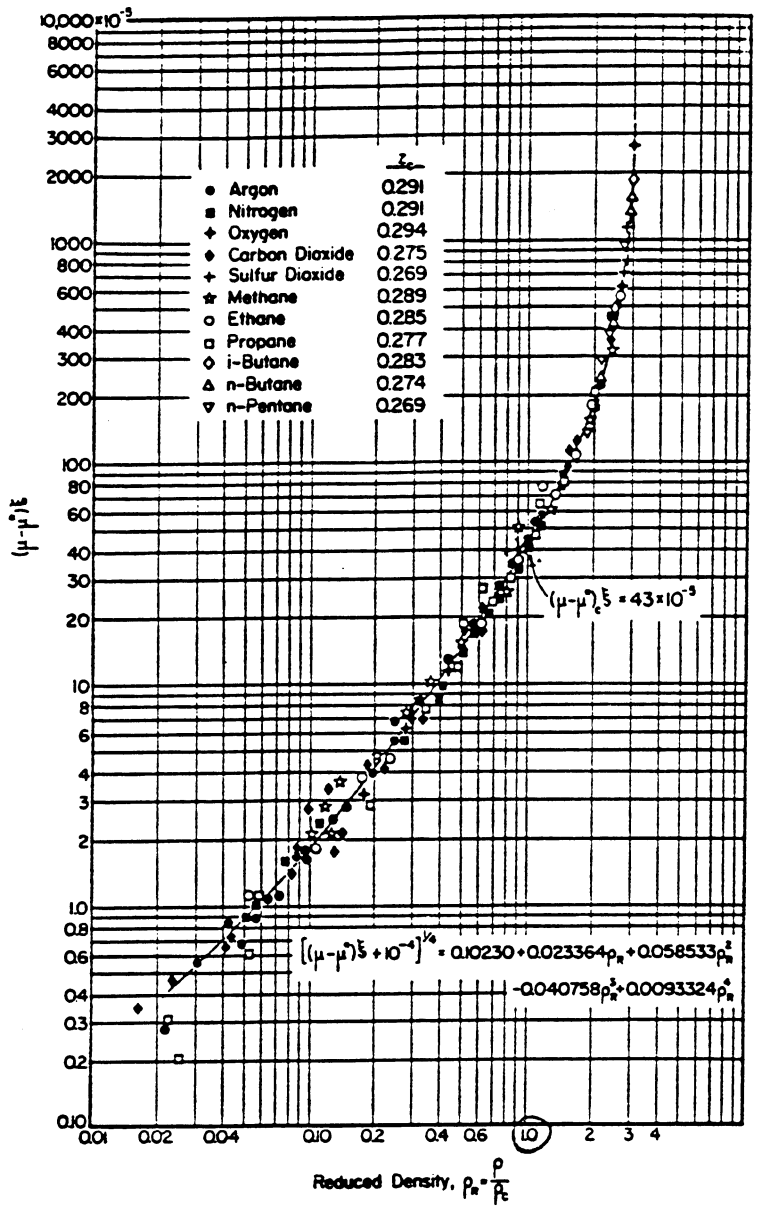

Figure I-14. Relationship between the residual viscosity modulus, $(\mu - \mu^*)\xi$, and the reduced density, ρ_r, for normally behaving substances.

where

$$\xi = \frac{T_{c_i}^{1/6}}{M_i^{1/2} P_{c_i}^{2/3}} \tag{I-16}$$

Lohrenz *et al.*[16] extended the Jossi *et al.* equation[59] to mixtures by defining mixing rules to obtain μ^* and the pseudocritical mixture properties. These are given by

$$\mu_m^* = \frac{\sum_i x_i \mu_i^* M_i^{1/2}}{\sum_i x_i M_i^{1/2}} \tag{I-17}$$

$$T_{c_m} = \sum_i x_i T_{c_i} \tag{I-18}$$

$$P_{c_m} = \sum_i x_i P_{c_i} \tag{I-19}$$

$$V_{c_m}' = \sum_{i \neq C_{7+}} x_i V_{c_i} + x_{C_{7+}} V_{cC_{7+}} \tag{I-20}$$

$$M_m = \sum_i x_i M_i \tag{I-21}$$

The C_{7+} critical molar volume was correlated in terms of its mole fraction-averaged molecular weight and specific gravity. This is given by

$$V_{cC_{7+}} = 21.573 + 0.015122 M_{C_{7+}} - 27.656 \gamma_{C_{7+}} + 0.070615 M_{C_{7+}} \gamma_{C_{7+}} \tag{I-22}$$

A correlation was also adopted to estimate the mixture density. In our calculations, the mixture density correlation in the original LBC procedure was relinquished in favor of the experimentally measured value for that parameter. The extraction of hydrocarbons in the C_5-C_{30} range by the CO_2-rich phase when the CO_2/crude oil mixture enters the two-phase region alters the overall hydrocarbon composition in the oil-rich phase, thereby modifying its physical and critical properties. The correlations of Lin and Chao[84] and Hankinson *et al.*[85,86] were used to estimate the C_{7+} critical properties and specific gravity, respectively, for mixtures in the two-phase region.

The results of the calculations using the LBC correlation for 393 data points of the single phase, the equilibrium vapor, and liquid phases are presented as calculated versus measured viscosity, as shown in Fig. I-15. Note the general trend of increasing deviations with increasing values of viscosity. The average absolute percent deviation (AAPD) for all data points was 40.5% with a maximum of 194%.

The liquid-phase LBC viscosity predictions are generally higher than the measured values, while the vapor-phase calculated viscosities show the opposite trend when compared to the corresponding measured value. One of the physical changes that occurs when CO_2 is added to hydrocarbon mixtures is the drastic reduction of the viscosity of the resulting CO_2/oil mixture compared to the original oil compressed to the same state. In the two-phase region, the vapor-phase (dense fluid phase) mixtures exhibit an increased viscosity relative to pure CO_2 at the same conditions because of the presence of extracted hydrocarbons in the CO_2-rich phase. The LBC correlation apparently cannot account for these associated phenomena in a satisfactory manner.

The high density of data points along the 45° line for viscosity values less than about 0.3 cp may result for a number of possible reasons. First, the LBC method has been documented to be more accurate with light oils[57,62] having low viscosities. Second, these data points fall well within the reduced density range for which the Jossi *et al.*[59] equation was developed. Third, there is also a large number of the high-temperature oil/lean gas system data points below 0.5 cp. Outside of this very narrow range, however, it is apparent that the LBC correlation is inaccurate for predicting the viscosities of CO_2/crude oil mixtures.

4. Correlation Development

The viscosity correlation presented in this work is a modification of the LBC correlation: a deviation function and new set of mixing rules for the mixture pseudocritical temperature and pressure are used.

Figure I-16 is a plot of the difference between the LBC-calculated and experimental viscosity values ($\mu^{LBC} - \mu^{exp}$) versus the reduced mixture density for 393 mixtures. Several features of this plot are noteworthy. At reduced density values of less than about 2.8, the values of ($\mu^{LBC} - \mu^{exp}$) are practically zero (the lean-gas system data points fall within this range). Above this value, the deviations start to increase rapidly. This behavior may result because of the reduced density limitations of Eq. (I-15). The data points, as plotted in Fig. I-16, suggest that a functional dependence of the quantity($\mu^{LBC} - \mu^{exp}$) to ρ_r can be expressed mathematically. The choice of ρ_r allows for smooth interpolation in the critical region and assures the convergence of the vapor and liquid phase viscosities at the critical point, both of which are important considerations in digital simulation.

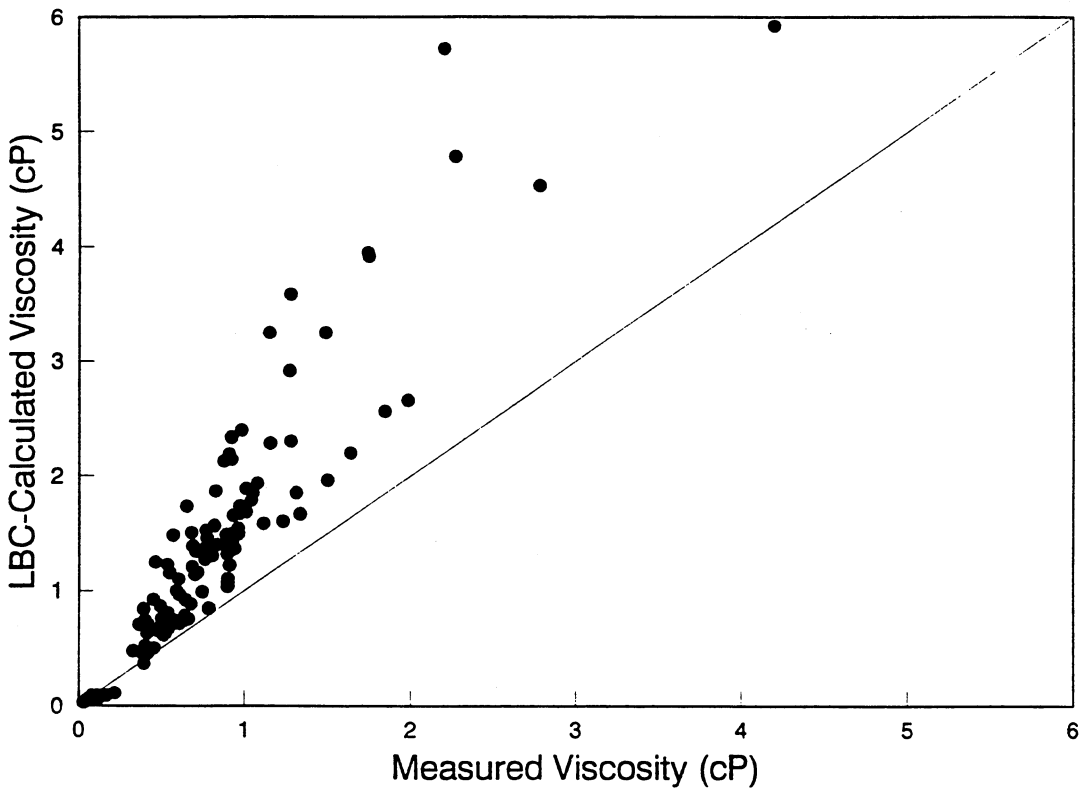

Figure I-15. Comparison of LBC-predicted and measured viscosities for CO_2/crude oil systems.

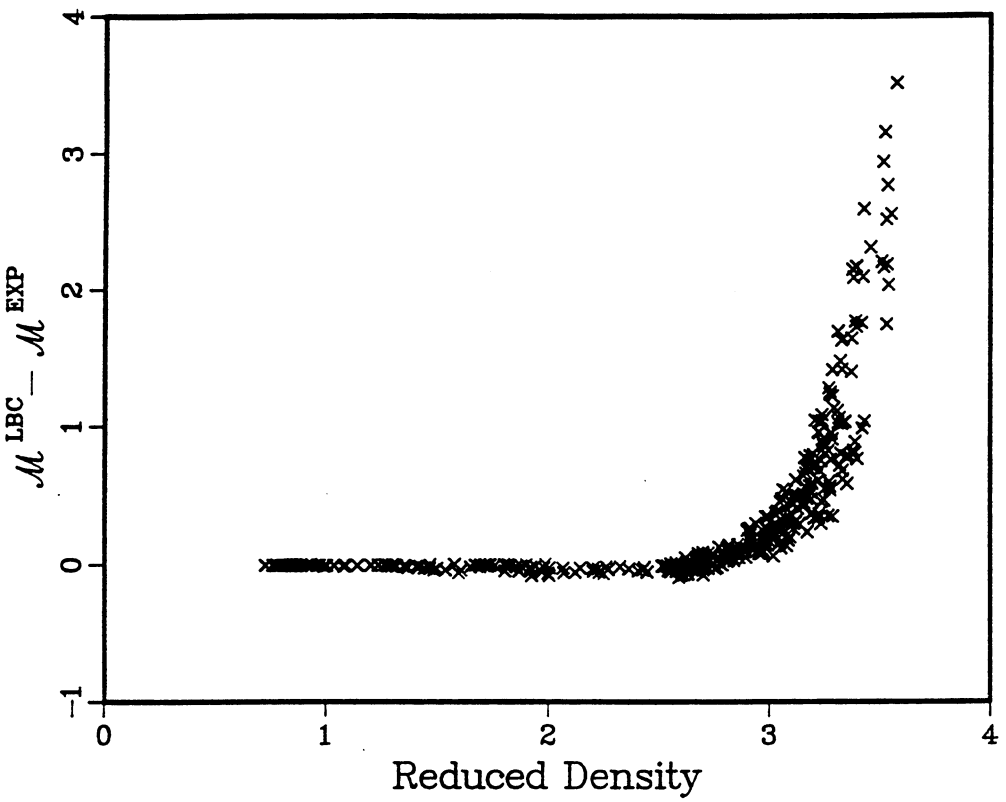

Figure I-16. Relationship between the difference of the LBC-predicted and experimental viscosity and the reduced density.

The present form of the viscosity correlation for CO_2/hydrocarbon systems is a modification of the LBC viscosity prediction. The LBC was modified by adding a deviation function $\Im(\rho_r)$; i.e.,

$$\mu = \mu^{LBC} + \Im(\rho_r) \tag{I-23}$$

where $\Im$ is given by

$$\Im(\rho_r) = \psi \rho_r^{\lambda} \tag{I-24}$$

The constants α and β were determined using a least-squares-errors fit to the experimental data. The resulting values were:

$$\psi = -1.8366 \times 10^{-8}$$

$$\lambda = 13.992$$

The mixing rules of Teja *et al.*,[76] which are based on semitheoretical arguments, were used to obtain the mixture pseudocritical temperature and pressure. These are:

$$T_{c_m}/P_{c_m} = \sum_i \sum_j x_i x_j \left(T_{c_{ij}}/P_{c_{ij}}\right) \tag{I-25}$$

$$T_{c_m}^2/P_{c_m} = \sum_i \sum_j x_i x_j \left(T_{c_{ij}}^2/P_{c_{ij}}\right) \tag{I-26}$$

where the cross-terms are given by

$$T_{c_{ij}} = \zeta_{ij} \left(T_{c_{ii}} T_{c_{jj}}\right)^{1/2} \tag{I-27}$$

and

$$P_{c_{ij}} = \frac{8 T_{c_{ij}}}{\left[\left(\frac{T_{c_{ii}}}{P_{c_{ii}}}\right)^{\frac{1}{3}} + \left(\frac{T_{c_{jj}}}{P_{c_{jj}}}\right)^{\frac{1}{3}}\right]^3} \tag{I-28}$$

where ζ_{ij} is the binary interaction parameter.

5. Summary of the Calculation Procedure

The calculation of the viscosity of any given mixture may be carried out in the following manner. The data obtained from a CPE run reports the following information for a mixture:

$\{z_i\}$ → mixture composition in terms of nonhydrocarbon and hydrocarbon mole fractions up to C_{36}, the balance being lumped into a C_{37+} fraction;

ρ_m → measured mixture density;

μ_m → measured mixture viscosity;

T, P → run temperature and pressure.

a. The C_{7+} fraction is characterized as follows:

1) Average molecular weight

$$\bar{M}_{C_{7+}} = \sum_{i=7}^{37+} \tilde{x}_i M_i \tag{I-29}$$

where

$$\tilde{x}_i = \frac{x_i}{\sum_{i=7}^{37+} x_i} \tag{I-30}$$

2) Pseudocritical pressure and temperature

$$P_{cC_{7+}} = P_c\left(\bar{M}_{C_{7+}}\right) \tag{I-31}$$

and

$$T_{cC_{7+}} = T_c\left(\bar{M}_{C_{7+}}\right) \tag{I-32}$$

where Eqs. (I-31) and (I-32) are given by the Lin-Chao[84] correlation.

3) C_{7+} specific gravity

$$\gamma_{C_{7+}} = \gamma\left(\{x\}_{i=7}^{37+}, T\right) \tag{I-33}$$

where Eq. (I-33) is given by the Hankinson-Brobst-Thomson[85,86] correlation.

4) Pseudocritical molar volume

$$V_{cC_{7+}} = f\left(\bar{M}_{C_{7+}}, \gamma_{C_{7+}}\right) \tag{I-34}$$

where Eq. (I-34) is given in the LBC correlation, Eq. (I-22).

b. Low-pressure, pure-component and mixture gas viscosity calculations:

The following calculations are performed for i = CO_2, N_2, C_1, ..., C_{7+}:

$$T_{r_i} = \frac{T}{T_{c_i}} \tag{I-35}$$

$$\xi_i = \frac{T_{c_i}^{1/6}}{M_i^{1/2} P_{c_i}^{2/3}} \tag{I-36}$$

$$\mu_i^* \xi_i = \begin{cases} 34.0 \times 10^{-5} T_{r_i}^{0.94}, & T_{r_i} < 1.5 \\ 17.78 \times 10^{-5} (4.58 T_{r_i} - 1.67)^{5/8}, & T_{r_i} > 1.5 \end{cases} \tag{I-37}$$

$$\mu_m^* = \frac{\sum_i x_i \mu_i^* M_i^{1/2}}{\sum_i x_i M_i^{1/2}} \tag{I-38}$$

c. Mixture pseudocritical properties:

$$T_{c_m}/P_{c_m} = \sum_i \sum_j x_i x_j \left(T_{c_{ij}}/P_{c_{ij}}\right) \tag{I-39}$$

$$T_{c_m}^2/P_{c_m} = \sum_i \sum_j x_i x_j \left(T_{c_{ij}}^2/P_{c_{ij}}\right) \tag{I-40}$$

where the cross-terms are given by

$$T_{c_{ij}} = \zeta_{ij} \left(T_{c_{ii}} T_{c_{jj}}\right)^{1/2} \tag{I-41}$$

and

$$P_{c_{ij}} = \frac{8 T_{c_{ij}}}{\left[\left(\frac{T_{c_{ii}}}{P_{c_{ii}}}\right)^{\frac{1}{3}} + \left(\frac{T_{c_{jj}}}{P_{c_{jj}}}\right)^{\frac{1}{3}}\right]^3} \tag{I-42}$$

$$V'_{c_m} = \sum_{i \neq C_{7+}} x_i V_{c_i} + x_{C_{7+}} V_{cC_{7+}} \tag{I-43}$$

$$M_m = \sum_i x_i M_i. \tag{I-44}$$

d. Mixture reduced density and inverse viscosity parameter calculation

$$\rho_r = \rho_m V'_{c_m} \tag{I-45}$$

$$\xi = \frac{T_{c_m}^{1/6}}{M_m^{1/2} P_{c_m}^{2/3}} \tag{I-46}$$

e. Mixture viscosity calculation:

$$\left[(\mu^{LBC} - \mu^{*}) - 10^{-4}\right]^{\frac{1}{4}} = \sum_{n=0}^{4} \varphi_n \rho_r^n \tag{I-47}$$

where Eq. (I-47) is given by the Jossi *et al.*[59] viscosity equation, Eq. (I-15).

$$\mu = \mu^{LBC} + \Im(\rho_r) \tag{I-48}$$

where

$$\Im(\rho_r) = -1.8366 \times 10^{-8} \rho_r^{13.992} \tag{I-49}$$

The calculation procedure outlined above is noniterative and may be carried out using a calculator.

6. Results and Conclusions

An experimental apparatus that yields rapid measurements of viscosity, density, and composition of single-phase or of two near-equilibrium coexisting phases (vapor-liquid or liquid-liquid) with acceptable engineering accuracy was developed. A large volume of data can be generated in a considerably less time with the apparatus than in a conventional static equilibrium experiment.

The viscosities of the 393 mixtures were recalculated with the modified LBC correlation and compiled in a database. The results are summarized in Fig. I-17. The binary interaction parameters for unlike components were set to unity in all the calculations. The statistical comparison of the LBC,[16] the Pedersen *et al.*,[60] and the present correlation in terms of AAPD is summarized in Table I-5. The average absolute deviation (AAD) reported here is calculated as the absolute value of the difference between the calculated and the measured values divided by the measured value. The correlation presented in this work is clearly superior to both the LBC[16] and the Pedersen *et al.*[60] correlations.

Lohrenz *et al.*[16] reported the insensitivity of the viscosity predictions of their procedure to the mixing rules used to obtain the mixture pseudocritical properties. Our calculations using the LBC correlation, incorporating the mixing rules defined in Eqs. (I-25) through (I-28), resulted in an AAPD of 25.0%, a dramatic improvement over the original LBC method. The regression parameters in Eq. (I-24) were determined based on the difference between the measured viscosities and the LBC-predicted viscosities, which uses the new mixing rules.

An *a priori* prediction of viscosities was performed for two CO_2/hydrocarbon systems to test the accuracy of the present correlation (MLBC) relative to the LBC and Pedersen *et al.* correlations.

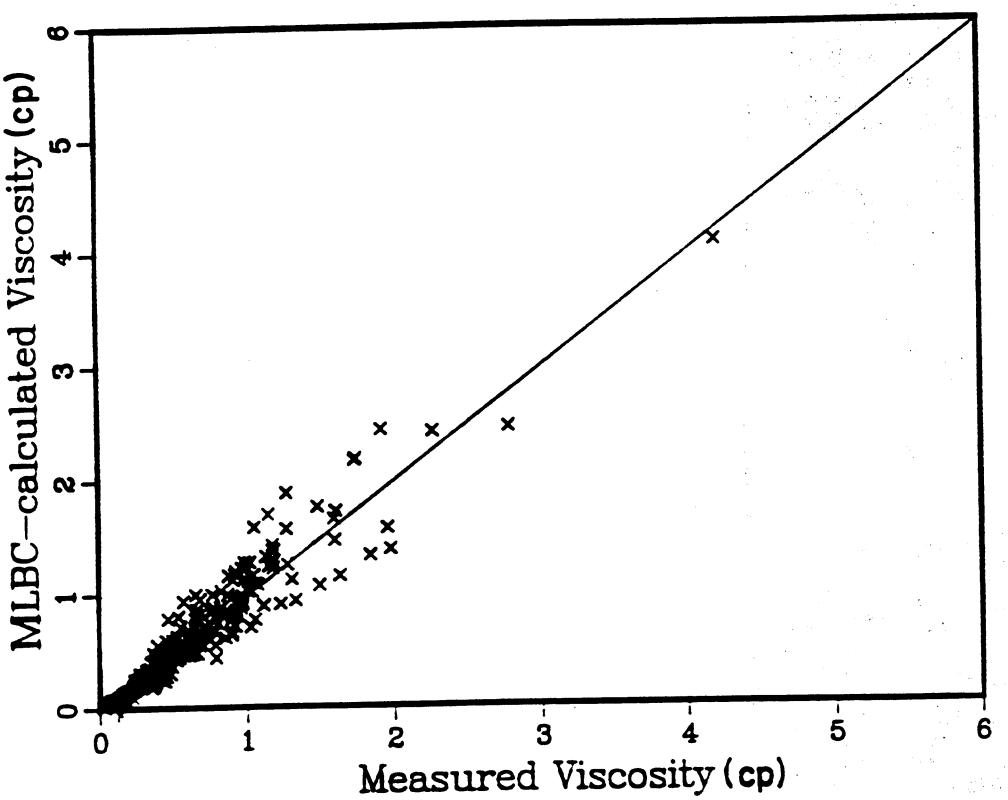

Figure I-17. Comparison of the modified LBC-predicted vs. experimental viscosities.

TABLE I-5. SUMMARY OF AVERAGE ABSOLUTE PERCENTAGE DEVIATIONS†

CORRELATION	AAPD
LBC	40.5%
Pedersen	23.4%
This Work	12.5%

†Based on 393 data points

Further comparisons were made with a correlation based on a modified Corresponding States Principle (SUPERTRAPP[18]) for the well-defined $CO_2/n\text{-}C_7$ binary system.

A continuous phase equilibrium experiment, labeled CPE 232 (reported in the Fourth Annual Report[4]) was performed using pure CO_2 as an injection fluid and pure normal heptane ($n\text{-}C_7$) as the hydrocarbon component. The run was conducted at 1500 psia and 100°F, where CO_2 and $n\text{-}C_7$ are miscible in all proportions. A summary of the results as well as comparisons of experimental and predicted values of viscosities and densities are presented in Figs. I-18 and I-19 and Tables I-6 through I-8. The literature values (interpolated) of viscosity and density[87] for pure CO_2 and $n\text{-}C_7$ are also plotted in Figs. I-18 and I-19, respectively. These values are as follows:

For CO_2 (1500 psia, 100°F):

$$\rho = 0.6910 \text{ g/cm}^3$$
$$\mu = 0.05193 \text{ cP}$$

For $n\text{-}C_7$ (1500 psia, 100°F):

$$\rho = 0.6791 \text{ g/cm}^3$$
$$\mu = 0.3855 \text{ cP}$$

The corresponding experimental values for density and viscosity of pure $n\text{-}C_7$ are 0.683 g/cm^3 and 0.391 cP, yielding relative errors of 0.57% and 1.43%, respectively. A casual inspection of Table I-6 (or Fig. I-18) shows that the MLBC correlation provides a slightly conservative estimate of viscosities for the $CO_2/n\text{-}C_7$ binary mixtures in the range of concentrations from pure hydrocarbon to almost pure CO_2. The worst predicted values were those of SUPERTRAPP (values not reported in Table I-6). This is not surprising if one considers that SUPERTRAPP is based on the Conformal Solution, One-Fluid Model[88,89] and thus, works well for conformal mixtures (e.g., mixtures of hydrocarbons). The presence of CO_2 in hydrocarbon mixtures produces some anomalies in thermodynamic and physical properties (the higher density of the resulting solution compared to that of the mixture before the addition of CO_2, for instance), especially at conditions close to the critical point of CO_2. The empirical correlations (MLBC, LBC,[16] and Pedersen *et al.*[60]) apparently perform better for a well-defined system than a theoretically-based model.

The measured densities were also compared to the predictions of SUPERTRAPP and the Peng-Robinson equation of state[61] (PREOS). The latter calculations were performed using values of critical parameters and a "default" binary interaction parameter found in the literature. Both methods provided accurate density predictions for pure $n\text{-}C_7$, while SUPERTRAPP yielded a better density estimate for pure CO_2. The PREOS density predictions are consistently lower, while those of SUPERTRAPP are always higher for mixtures of the two pure components. The inadequacy of SUPERTRAPP in predicting properties of nonconformal mixtures is again evident. The statistical comparison of all the correlations in terms of the average absolute percent deviations is summarized in Table I-7 for viscosity and in Table I-8 for density.

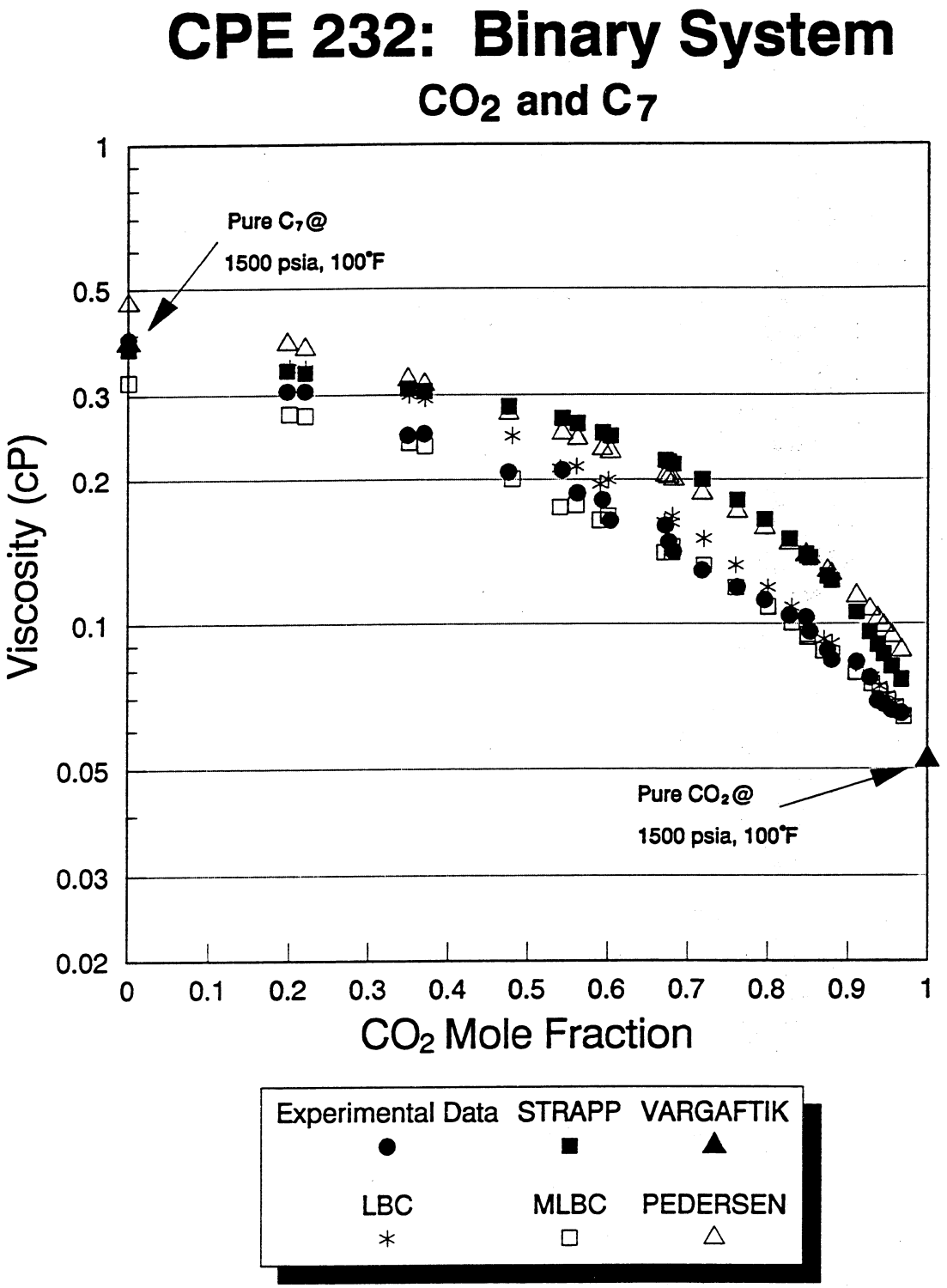

Figure I-18. Comparison of predicted vs. experimental viscosities as a function of CO_2 concentration for single-phase mixtures of $CO_2/n\text{-}C_7$ binary system.

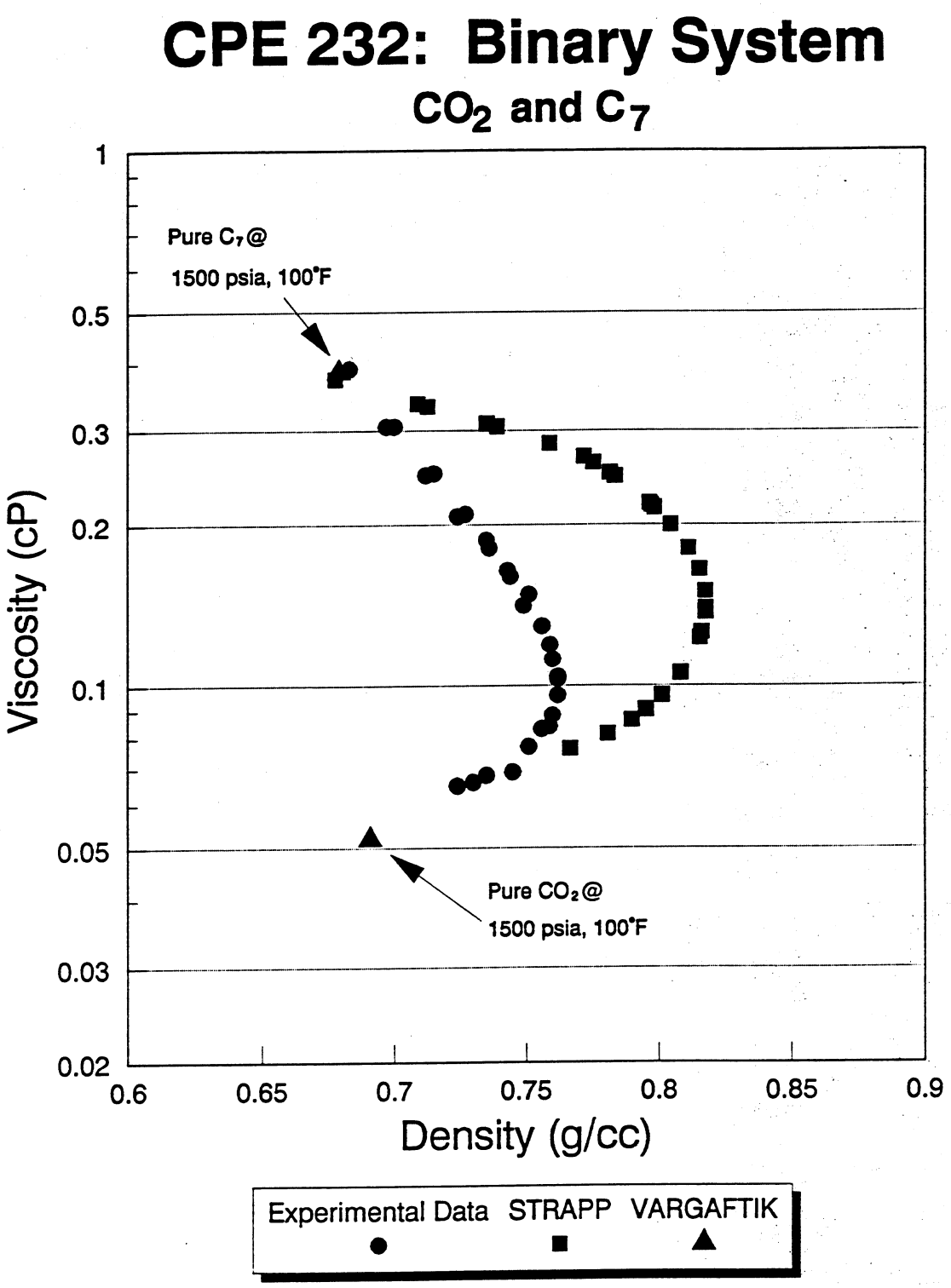

Figure I-19. Comparison of predicted vs. experimental viscosities as a function of phase densities for single-phase mixtures of $CO_2/n\text{-}C_7$ binary system.

TABLE I-6. COMPARISON OF MLBC, LBC, AND PEDERSEN *ET AL.* PREDICTED VS. EXPERIMENTAL VISCOSITIES AND PREOS PREDICTED VS. EXPERIMENTAL DENSITIES FOR THE CO_2/nC_7 BINARY SYSTEM AT 1500 PSIA AND 100°F.

CO_2 MOLE FRACT.	EXPERIMENTAL		MLBC		LBC		PEDERSEN		PREOS	
	ρ (g/cc)	μ (cp)	μ (cp)	Δ%	μ (cp)	Δ%	μ (cp)	Δ%	ρ (g/cc)	Δ%
.0000	.683	.391	.319	-18.4	.374	-4.3	.467	19.4	.676	-1.0
.1972	.697	.305	.274	-10.2	.341	11.9	.383	25.6	.690	-1.0
.2195	.700	.305	.272	-11.0	.340	11.4	.374	22.6	.692	-1.1
.3483	.712	.247	.239	-3.4	.300	21.1	.323	30.6	.703	-1.2
.3689	.715	.249	.235	-5.7	.294	18.2	.315	26.4	.705	-1.4
.4753	.724	.207	.200	-3.2	.247	19.1	.274	32.6	.715	-1.2
.5427	.727	.209	.175	-16.3	.211	0.9	.250	19.4	.722	-0.7
.5615	.735	.187	.177	-5.6	.213	13.7	.243	29.8	.723	-1.6
.5931	.736	.181	.164	-9.3	.195	7.9	.231	27.8	.726	-1.3
.6030	.743	.164	.168	2.2	.199	21.6	.228	38.9	.727	-2.2
.6715	.744	.160	.141	-12.1	.163	1.5	.203	27.0	.732	-1.6
.6757	.751	.148	.145	-2.3	.167	13.1	.202	36.3	.733	-2.4
.6816	.749	.141	.141	-0.2	.162	15.1	.200	41.5	.733	-2.1
.7178	.756	.129	.132	2.5	.150	16.5	.187	44.7	.735	-2.8
.7616	.759	.119	.119	-0.2	.132	11.2	.171	43.6	.736	-3.0
.7960	.760	.112	.108	-3.2	.119	6.1	.158	41.4	.736	-3.2
.8271	.762	.104	.100	-3.6	.108	4.3	.147	41.2	.733	-3.8
.8478	.762	.103	.095	-7.9	.102	-1.4	.139	34.9	.731	-4.1
.8527	.762	.096	.094	-2.5	.100	4.2	.137	42.8	.730	-4.2
.8745	.760	.088	.088	-0.2	.093	5.5	.129	46.2	.726	-4.5
.8799	.759	.084	.086	2.7	.091	8.4	.127	50.6	.724	-4.6
.9108	.756	.083	.079	-4.8	.082	-1.0	.114	37.1	.714	-5.5
.9275	.751	.077	.075	-2.8	.077	0.3	.107	38.5	.706	-6.0
.9376	.745	.069	.072	4.3	.074	7.1	.102	47.9	.700	-6.0
.9450	.733	.070	.069	1.6	.071	4.0	.099	45.0	.695	-5.4
.9550	.730	.066	.067	1.0	.068	3.0	.094	42.1	.687	-5.9
.9671	.724	.065	.064	-1.6	.065	-0.2	.088	34.8	.676	-6.6

TABLE I-7. SUMMARY OF AVERAGE ABSOLUTE PERCENT DEVIATIONS BETWEEN EXPERIMENTAL AND PREDICTED VISCOSITIES FOR THE CO_2/nC_7 BINARY SYSTEM.

CORRELATION	AAPD
MLBC	5.1%
LBC	8.6%
PEDERSEN	35.9%
SUPERTRAPP	35.3%

TABLE I-8. SUMMARY OF AVERAGE ABSOLUTE PERCENT DEVIATIONS BETWEEN EXPERIMENTAL AND PREDICTED DENSITIES FOR THE CO_2/nC_7 BINARY SYSTEM.

CORRELATION	AAPD
SUPERTRAPP	6.1%
PREOS	3.3%

Comparisons of predicted and measured viscosities were also performed for a recombined oil system with methane-contaminated CO_2 as the injection gas. Phase behavior and fluid property measurements for the CO_2 + C_1/Amoco Oil A system, to which the comparisons were made, are presented in PRRC Report 90-17.[90]

The occurrence of three-phase L_1-L_2-V immiscibility with this system, which resulted in the entrainment of the two liquid phases, precluded the prediction and comparison for the equilibrium liquid-phase viscosities. The single-phase and equilibrium vapor-phase data, however, should still be valid.

A comparison of the experimental and predicted viscosities for the single-phase and equilibrium vapor-phase mixtures is presented in Fig. I-20 and Table I-9. Note that the Pedersen *et al.* predictions are consistently lower than the measured values, while the MLBC and LBC predictions show the opposite trend. A statistical comparison of the three correlations in terms of average absolute percent deviations are presented in Table I-10. Notice the slightly better performance of the Pedersen *et al.*[60] method compared to the MLBC correlation for this system. The poor performance of the LBC method is, nevertheless, apparent for this as well as for the rest of the CO_2/hydrocarbon systems used in our study.

In conclusion, we have developed an improved viscosity correlation applicable to single-phase and equilibrium vapor- and liquid-phase CO_2/hydrocarbon mixtures. The present correlation extends the upper limit of reduced density of the LBC correlation to about 3.6. The viscosity behavior encountered when CO_2 is mixed with hydrocarbons, both in the single-phase and equilibrium vapor- and liquid- phase regions, is better represented through the use of the deviation function. The proposed correlation can be easily incorporated into digital reservoir simulation studies and is expected to help improve our ability to predict oil recovery performance both in the laboratory and in the field. The new mixing rules allow for the flexibility of tuning the correlation for a particular system via the binary interaction parameter. A correlation (Pedersen *et al.*[60]) based on a modification of a simple correspondence principle, performed much better than the LBC correlation[16] when compared to the experimental data. The deviations between the Pedersen *et al.* predictions and experimental viscosities can certainly be attributed to the database dependency of a correlation.

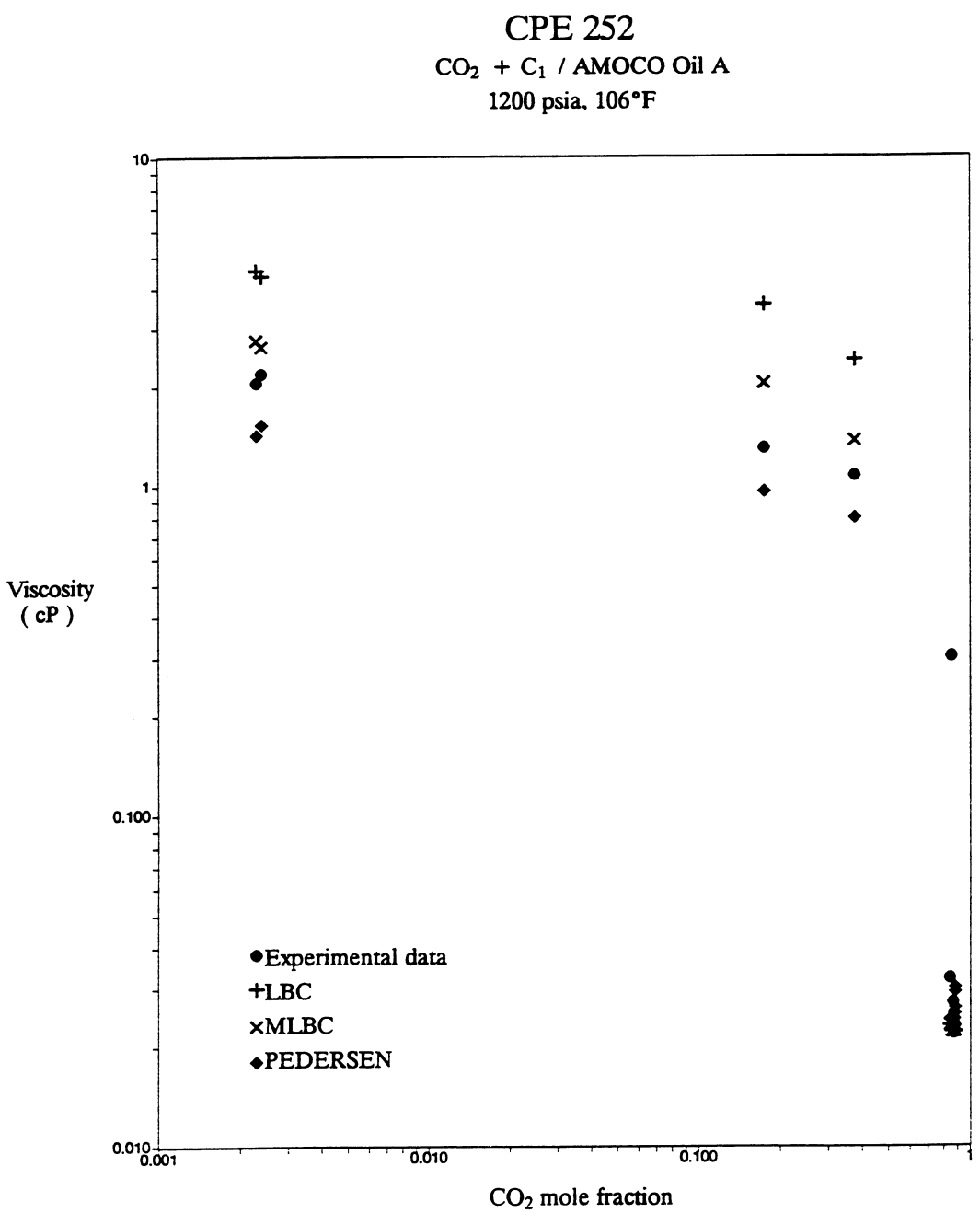

Figure I-20. Comparison of predicted vs. experimental viscosities as a function of CO_2 concentration for single-phase and equilibrium vapor-phase mixtures of the CO_2 + C_1/Amoco Oil A system.

TABLE I-9. COMPARISON OF MLBC, LBC, AND PEDERSEN *ET AL.* PREDICTED VS. EXPERIMENTAL VISCOSITIES FOR THE CO_2 + C_1/AMOCO OIL A SYSTEM AT 1200 PSIA AND 106°F.

CO_2 MOLE FRACT.	EXPERIMENTAL		MLBC		LBC		PEDERSEN	
	ρ (g/cm^3)	μ (cp)	μ (cp)	Δ%	μ (cp)	Δ%	μ (cp)	Δ%
.0024	.815	2.180	2.637	20.9	4.364	100.2	1.532	-29.7
.0023	.816	2.050	2.757	34.5	4.533	121.1	1.423	-30.6
.1753	.818	1.300	2.044	56.2	3.553	173.3	.960	-26.2
.3759	.827	1.070	1.367	27.7	2.400	124.3	.796	-25.6
.8466	.244	.032	.023	-29.7	.023	-29.5	.024	-9.0
.8600	.240	.300	.022	-25.8	.022	-25.6	.024	-11.1
.8707	.236	.027	.022	-18.3	.022	-18.1	.024	-12.1
.8760	.232	.025	.022	-12.5	.022	-12.3	.024	-2.9
.8764	.229	.024	.022	-9.4	.022	-9.2	.025	-3.5
.8781	.229	.023	.022	-5.5	.022	-5.2	.025	-2.4
.8796	.229	.023	.022	-5.5	.022	-5.3	.025	-2.4
.8803	.228	.023	.022	-5.7	.022	-5.4	.025	-2.2
.8815	.227	.022	.022	-1.6	.022	-1.3	.025	-3.0
.8840	.227	.022	.022	-1.7	.022	-1.4	.025	-5.3
.8829	.227	.022	.022	-1.6	.022	-1.3	.026	-0.6
.8823	.227	.022	.022	-1.1	.022	-0.7	.029	8.2
.8830	.227	.022	.022	-0.6	.022	-0.3	.030	11.7

TABLE I-10. SUMMARY OF THE AVERAGE ABSOLUTE PERCENT DEVIATIONS BETWEEN EXPERIMENTAL AND PREDICTED VISCOSITIES FOR THE CO_2 + C_1/AMOCO OIL A SYSTEM.

CORRELATION	AAPD
MLBC	15.1%
LBC	37.3%
PEDERSEN	11.0%

7. Nomenclature

$a_n(T)$ = coefficients in the BWR-EOS for methane, n = 1, 2, ..., 15

f, f_{vac} = quartz crystal viscometer resonant frequency

F_1, F_2 = coefficients in the viscosity equation for methane

M_q = mass of quartz crystal viscometer

M = molecular weight

n = number of components in the mixture

P = pressure

P_{c_i} = critical pressure of component i

P_{c_m} = mixture pseudocritical pressure

P_{c_o} = reference substance critical pressure

P^* = defined in Eq. (11)

S_q = quartz crystal viscometer surface area

T = temperature

T_{c_i} = critical temperature of component i

T_{c_m} = mixture pseudocritical temperature

T_{c_o} = reference substance critical temperature

T^* = defined in Eq. (10)

V_c' = pseudocritical molar volume of a mixture

V_{c_i} = pure component critical molar volume

$V_{cC_{7+}}$ = pseudocritical molar volume of the C_{7+} fraction

x_{c7+} = mole fraction of the C_{7+} fraction

$\Im$ = general function

Subscripts

c = critical state

i, j = component i or j

m = mixture

o = reference substance

r = reduced property

C_{7+} = heptanes-plus fraction

Superscripts

LBC = Lohrenz, Bray, and Clark viscosity correlation calculated value

EXP = experimental value

Greek Letters

TG = rotation coupling coefficient

α, β = regression parameters

$\gamma_{C_{7+}}$ = C_{7+} specific gravity

μ = mixture viscosity

μ^* = viscosity of a gas mixture at low pressure, defined in Eq. (17)

ϵ = viscosity parameter of a mixture, defined in Eq. (16)

ρ = mixture density

ρ_r = reduced density

π = constant pi

C. EFFECT OF SOLUTION AND FREE GAS ON THE DEVELOPMENT OF MISCIBILITY

The effects of solution gas on the minimum miscibility pressure (MMP) has been a controversial issue. For example, Rathmell *et al.*[46] argued that the addition of methane to a reservoir oil should increase the MMP, and that a methane-rich bank ahead of the CO_2 is evidence of an immiscible process. Holm and Josendal[47] stated that the presence of methane in the reservoir oil reduces the efficiency of oil extraction by CO_2 and extends the distance of the immiscible zone. They also reported that the presence of methane in the reservoir oil does not change the MMP appreciably. However, Metcalfe and Yarborough[91] reported that changing methane concentration from 0 mole% to 25 mole% in a synthetic oil has an insignificant effect on the MMP. Yellig and Metcalfe[48] showed that addition of C_1 to an oil has not changed the MMP appreciably.

The first phase of this project planned for a detailed experimental study (slim-tube displacement) to answer the contradiction about the solution-gas effect on the MMP. A high-pressure CO_2 flooding apparatus was designed to conduct a series of slim-tube experiments using two oil systems (synthetic oil, $C_1 + C_4 + C_{10}$ and Crude Oil, C_1 + Maljamar STO). A detailed description of these oils is given in Tables 1.7 and 1.9 in the Third Annual Report.[3] A schematic diagram of the oil-displacement apparatus used for these experiments is depicted in Fig. I-21. Oil mixtures and injection gas (CO_2) are stored in two high-pressure floating piston accumulators. These fluids are driven by an HPLC metering pump. At the effluent end, a sight glass is installed to view the transition zone. The produced fluids are blown down through a back-pressure regulator and separated into liquid and vapor phases. The liquid phase is captured in a multiport sampler, and the vapor phase passes through a gas chromatograph and a wet test meter for a volumetric measurement. A detailed experimental procedure, as well as a description of the apparatus, is given in the Third Annual Report[3] and Yaghoobi's MS thesis.[92] A summary of slim tube runs for these oil systems at various pressure is given in Tables 1.7 and 1.9 in the Third Annual Report.[3] Plots of fractional recovery vs. pressure for these runs at breakthrough and at 1.2 pore volumes of CO_2 injected are depicted in Figs. 2.29 and 2.39 of the Third Annual Report.[3] From these curves, the MMPs of both Oil A and Oil B were at 1600 psia, whereas the MMP of Oil C with 30 mole% methane was at 1700 psia. These result showed that changing methane concentration in synthetic oils ($C_1 + C_4 + C_{10}$) from 10 mole% to 30 mole% increased the MMP by 6.25% while maintaining a constant C_4-C_{10} ratio. On the other hand, Kovarik[54] showed an increase of 57% in MMP when the methane composition in the CO_2 stream changed from 10 mole% to 30 mole%. This comparison suggests that the effect of methane on the MMP is more pronounced in the CO_2 stream than in an oil. Results of the crude oil runs indicated that the recovery at 1200 psia using Maljamar with 20% methane was almost the same as the recovery of the Maljamar STO at the same pressure. These results suggest no significant increase in MMP with the addition of up to 30 mole% methane in the crude oil systems.

The possibility of high recovery efficiency below the bubble-point pressure (BPP) is reported in the literature. Monroe *et al.*[93] stated that high recovery performance is possible even when the original oil composition is in the two-phase region. Slim-tube displacement results reported in the Third Annual Report[3] indicated the possibility of efficient oil displacement below BPP. A study of the effect of solution gas, as well as free gas on the development of miscibility, was extended by performing a series of core flood experiments to investigate this hypothesis. The displacement runs were conducted above and below the BPP of five oil mixtures in a high-pressure apparatus (Fig. I-21). Descriptions of these oil mixtures with different methane composition are given in Table I-11.

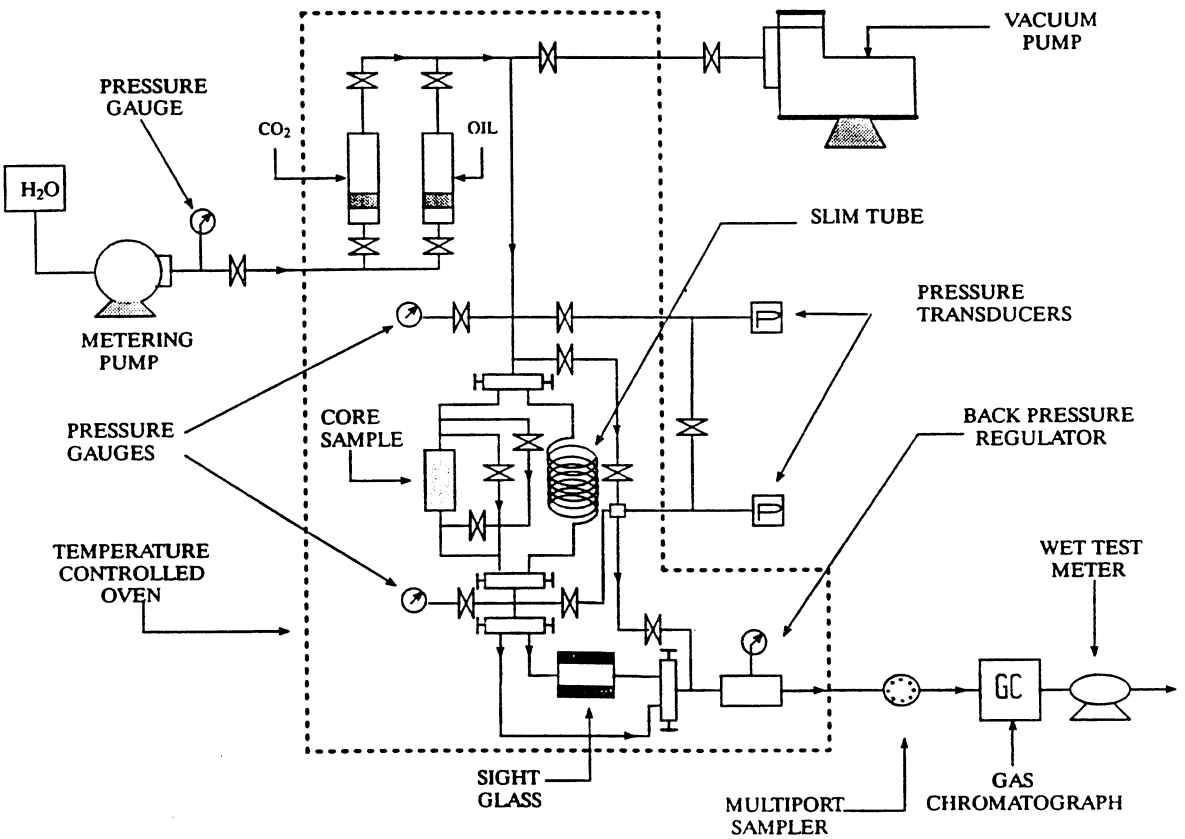

Figure I-21. Schematic diagram of the high pressure CO_2 flooding apparatus.

TABLE I-11. RESULTING COMPOSITION OF THE FIVE OIL MIXTURES USED IN THE DISPLACEMENT EXPERIMENTS

OIL MIXTURE	COMPOSITION (mole %)			
	CRUDE OIL	C_1	C_4	C_{10}
Oil-A	-	-	43.2	56.8
Oil-B	-	28.5	27.8	43.7
Oil-C	-	46.5	21.4	32.1
Oil-D	Wasson STO	26.3	-	-
Oil-E	Wasson STO	33.8	-	-

Displacements of a ternary (Oil-A) and the two quaternary (Oil-B and Oil-C) oil systems were conducted in a one foot vertical consolidated Berea sandstone core using pure CO_2 as a displacing fluid. Critical flow velocity calculations were performed prior to each displacement run, using Hill's flow rate equation,[94] whereby the CO_2 injection rate used was below the calculated critical flow rate in order to maintain gravity stabilized displacement during the course of an experiment.

Plots of recovery factors vs. displacement pressure for these three oils at breakthrough (BT) and at 1.2 pore volumes of CO_2 injected are depicted in Fig. I-22. The experimental MMPs obtained for these three oils indicated that MMP increases with increasing solution gas methane. These results show that the MMP values increased from 1655 psig for Oil-A to about 1810 psig for Oil-B, when 28 mole% methane was added to the system. This is an increase of 9% in the MMP value. However, changing the solution gas methane concentration from about 28 mole% to 46 mole% increased the MMP from 1810 psig to 2025 psig, respectively. This means that adding 18 mole% methane to Oil-B increased the MMP by 11%.

Orr and Silva[95] used the CO_2 density criteria suggested by Holm and Josendal[49] for an MMP prediction for C_1 and N_2 contaminated CO_2. They reported that the effects of contamination and temperature changes on the MMP can be estimated with an accuracy of $\pm$ 1.5 MPa ($\pm$ 217 psi). Holm and Josendal presented a correlation in which the required CO_2 density is empirically correlated to the extractable portion of the crude oil, $(C_5\text{-}C_{30})/C_{5+}$. The MMP is then found by determining the pressure required at reservoir temperature to obtain that density. Fig. I-23 shows the change in solvent density as a function of pressure at a given temperature for a 0 mole% to 30 mole% C_1 contamination in the CO_2 stream. Using the minimum density criteria of 0.42 g/cm^3 for an MMP prediction gives the MMP value of 2255 psig for 10 mole% C_1 in the CO_2 stream and 3170 psig with the presence of 30 mole% in the CO_2 stream. This indicates an increase of about 40% in MMP over an increase of 20 mole% methane in CO_2 stream. This comparison suggests that the effect of solution gas methane on the development of miscibility is relatively small compared to the effect of methane present in the injection gas.

Displacement experiments of the two crude oil systems, Oil-D and Oil-F, as listed in Table I-11, were conducted at a constant temperature (105°F) and at an injection rate of 8 cm^3/hr and 4 cm^3/hr, respectively. Fluid properties of these oils, such as BPP and density at various pressures, were required to process the experimental data. A description of how these properties were obtained as is presented in the following paragraphs.

A series of pressure-volume experiments were conducted in a PVT static cell apparatus to obtain the pressure-composition (P-x) diagram for the methane/Wasson STO mixture at 105°F. Fig. I-24 depicts the P-x curve by which the BPP of Oil-D and Oil-F were obtained. Other properties of this oil system were obtained by modeling the Wasson oil, using a modified GPA-Peng Robinson Equation of State[61] (PREOS).

1. Modeling of Wasson Crude Oil with the Peng-Robinson EOS

The GPA-Peng Robinson Equation of State was used to model the phase behavior and the fluid properties of the Wasson crude oil. The approach used in this work included adjusting the EOS parameters to provide an optimal match between the PREOS calculations and the available experimental data.

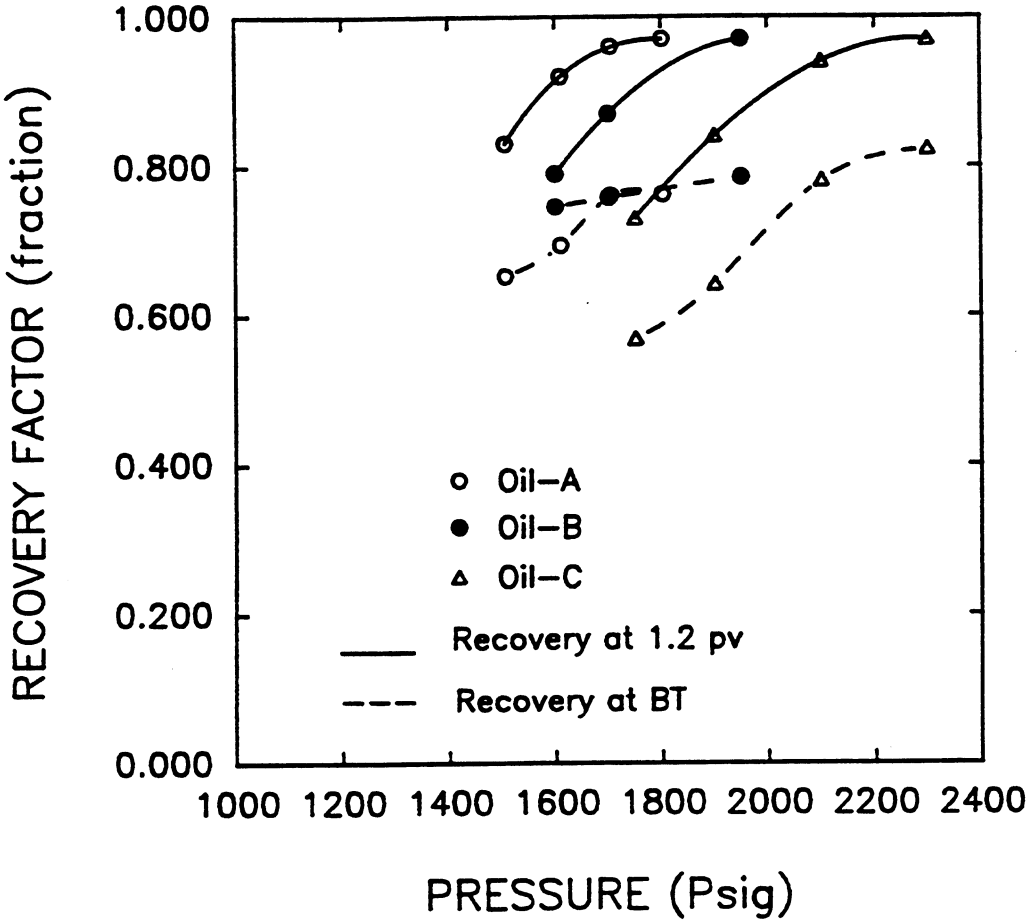

Figure I-22. Cumulative recovery at breakthrough and at 1.2 pore volumes of CO_2 injected for Oil-A, Oil-B, and Oil-C at 160°F.

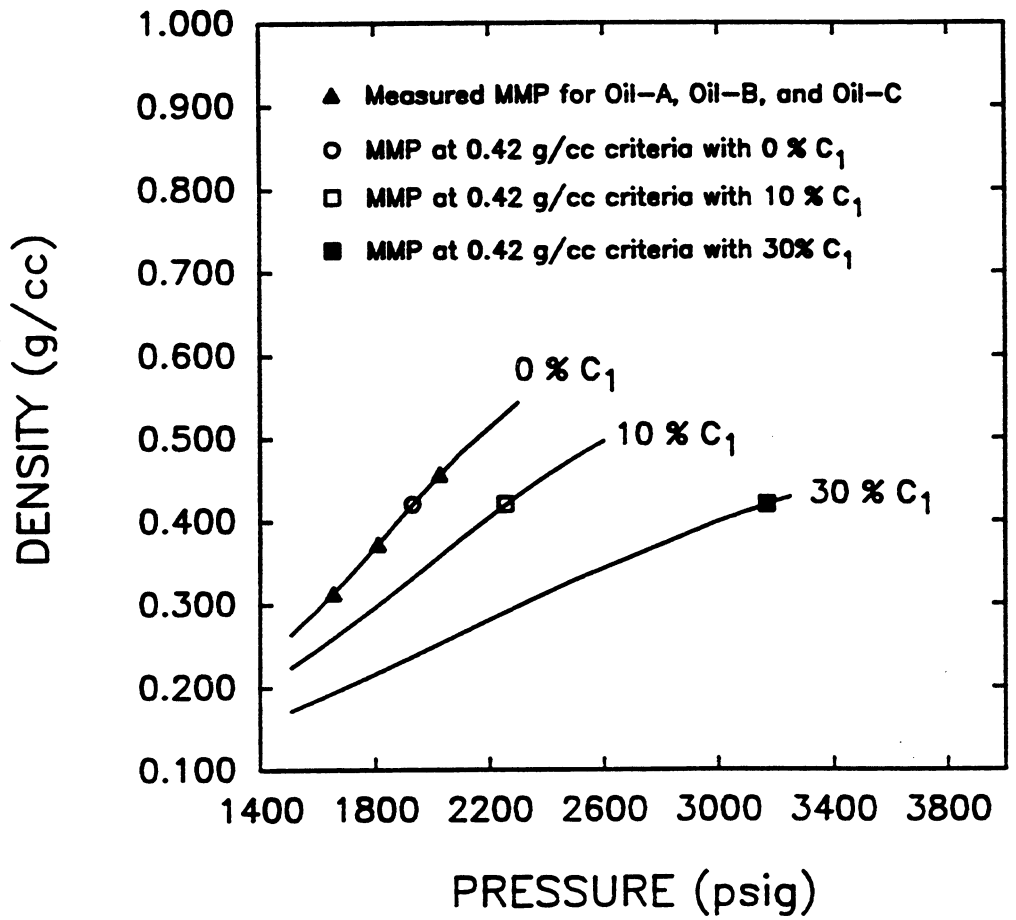

Figure I-23. Density of CO_2 with 0, 10, and 30 mole% C_1 contamination at 160°F.

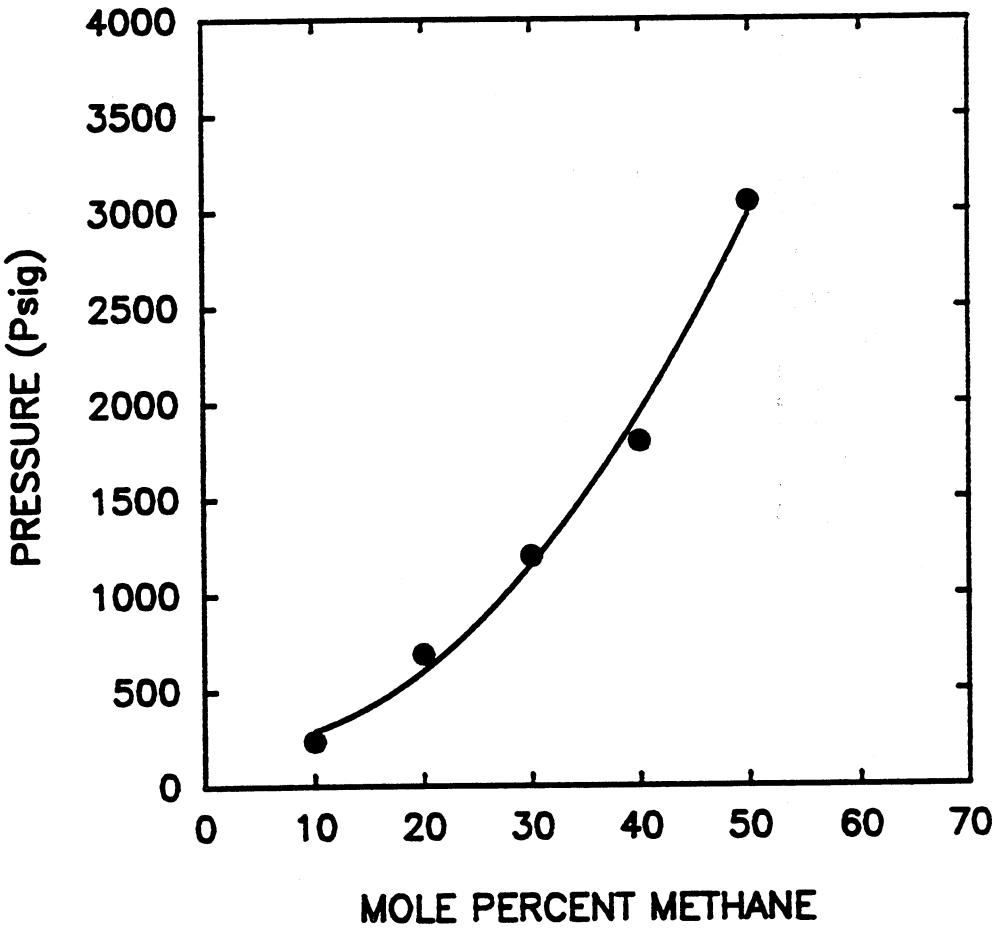

Figure I-24. Pressure-composition phase diagram for methane/Wasson STO at 105°F.

The chromatographic analysis performed on Wasson crude oil detailed its composition in terms of the components, C_5 to C_{36} and the C_{37+} fraction. The molecular weights and the mole fractions of these components are listed in Table I-1 from the Second Quarterly Report in 1990.[90] Since the PREOS is not well suited for consideration of such a large number of components, the heptanes plus (C_{7+}) components were therefore grouped into five pseudocomponents using the technique presented by Whitson.[96] The molecular weight ranges of each pseudocomponent group was obtained from the following equation:

$$M_i = M_L \left[\frac{M_H}{M_L} \right]^{i/N} \quad , \; i = 1,2,\ldots,N \tag{I-50}$$

where M_L and M_H are the molecular weights of the lightest and the heaviest components in the crude oil (i.e., M_L = 100.2 for C_7, and M_H = 563.2 for C_{37+}). N is the number of pseudocomponent groups, which was selected to be five in this case. The substitution of the values of M_L, M_H, and N into the Eq. (I-50) for i from 1 to 5 gives the range of the molecular weight in each pseudocomponent group. Thus, if the molecular weight of each pure component falls between the values of the M_i and M_{i+1}, that component would be included in the ith pseudocomponent. The average molecular weight of a pseudocomponent was then evaluated from the mole fractions of the individual components within a given pseudocomponent. The five pseudocomponent groups with their corresponding average molecular weights are summarized in Table I-12.

2. Characterization of Pseudocomponents

Several different empirical correlations were used to obtain the starting values for the critical pressure (P_c), critical temperature (T_c), acentric factor (ω), and the binary interaction parameters (δ_{ij}). These values were assigned for each pseudocomponent group from which adjustments were made to improve the PREOS predictions. The Lin-Chao correlations[84] (Eq. I-51 through I-53) were used to obtain the starting values for critical parameters and acentric factors as a function of the molecular weight of each pseudocomponent group. The equations are as follows:

$$\begin{aligned} \ln P_c = {} & 1.77645 - 1.0182\times10^{-2} M_w + 2.51106\times10^{-5} M_w^2 \\ & - 3.73775\times10^{-8} M_w^3 + 3.50737/M_w \end{aligned} \tag{I-51}$$

$$\begin{aligned} T_c = {} & 272.697 + 3.91999 M_w - 1.17706\times10^{-2} M_w^2 \\ & + 1.48679\times10^{-5} M_w^3 - 2277.89/M_w \end{aligned} \tag{I-52}$$

TABLE I-12. HEAVY COMPONENTS OF THE WASSON CRUDE OIL (C_7 - C_{37+}) LUMPED INTO FIVE PSEUDOCOMPONENT GROUPS USING WHITSON METHOD

PSEUDOCOMPONENTS	COMPONENTS LUMPED	MW (g/g-mole)
PsC_1	C_7 - C_9	114.0
PsC_2	C_{10} - C_{14}	165.1
PsC_3	C_{15} - C_{20}	245.3
PsC_4	C_{21} - C_{28}	338.9
PsC_5	C_{29} - C_{37+}	531.9

$$\omega T_c = -15.6752 + 1.22751\, M_w + 9.96848\times10^{-3}\, M_w^2 - 2.04742\times10^{-5}\, M_w^3 - 69.0883/M_w \quad \text{(I-53)}$$

where

M_w = Average molecular weight of pseudocomponent
P_c = Critical pressure (Mpa)
T_c = Critical temperature (K)
ω = Acentric factor

The values of acentric factors obtained from the Lin-Chao correlation (Eq. I-53) were not satisfactory for pseudocomponent groups whose molecular weights exceeded 300. However, the last two pseudocomponent groups (PsC_4, PsC_5) were adjusted using extrapolations for the series of normal alkanes. These initial characterizing properties for the five pseudocomponents are summarized in Table I-13.

3. Binary Interaction Parameters

Binary interaction coefficients are used to model the intermolecular forces of attraction between light and heavy molecules. The use of δ_{ij} generally has been limited to zero values for hydrocarbon-hydrocarbon pairs and a small set of values for nonhydrocarbon-hydrocarbon pairs.[61]

The starting values for binary interaction coefficients between methane and pseudocomponents (δC_1-PsC) were calculated using the following correlation developed by Katz and Firoozabadi.[97] These calculated coefficients are also tabulated in Table I-13.

$$\delta_{C_1-PsC} = -6.091\times10^{-3} + \sqrt{(1.37\times10^{-5} M_w - 1.83\times10^{-4})} \quad \text{(I-54)}$$

The binary interaction coefficients between nitrogen and pseudocomponents were fixed to be 0.12 in all of the cases. Even though this value was only a rough approximation, and a small amount of nitrogen was present in the oil, no significant effect was found on the results. The binary interaction coefficients between carbon dioxide and pseudocomponent groups were initially fixed to be 0.10. These coefficients were found to be more sensitive, especially at a higher CO_2 concentration. However, a sensitivity analysis was performed later on these coefficients in order to adjust them to the best possible value that would give a better match with the experimental P-x data.

The parameters in Table I-13 were initially used to predict the bubble point pressure (BPP) using the PREOS calculations. The results obtained from these calculations were lower than the experimental results. Thus, the critical parameters and acentric factors of each pseudocomponents as well as the binary interaction coefficients were systematically adjusted until a selected set of

TABLE I-13. INITIAL CHARACTERIZING PARAMETERS OBTAINED FROM THE LIN-CHAO AND THE KATZ-FIROOZABADI CORRELATIONS

PSEUDOCOMPONENTS	P_c (atm)	Tc (K)	ω	δC_1-PsC
PsC_1	24.71	568.59	0.392	0.031
PsC_2	18.58	652.20	0.562	0.040
PsC_3	12.71	736.13	0.792	0.050
PsC_4	7.80	821.32	1.110	0.061
PsC_5	1.14	1260.85	1.450	0.078

δCO_2-PsC = 0.10
δN_2-PsC = 0.12

parameters was obtained to provide the best match with the experimental P-x data. Table I-14 shows the adjusted values for critical parameters, acentric factors, and pseudocomponent groups.

The binary interaction coefficients between CO_2 and pseudocomponents were also adjusted for a better performance of the PREOS calculations. Table I-15 includes the nonhydrocarbon-hydrocarbon and hydrocarbon-hydrocarbon δ_{ij} values.

The predicted BPP obtained by the PREOS using the adjusted parameters in Tables I-14 and I-15 are in agreement with the experimental data. The measured and calculated BPP for the four different CO_2 concentrations with the Wasson reservoir oil are tabulated in Table I-16.

The average absolute deviation of 2.97% was obtained by comparing the experimental P-x curve and the predicted results. The PREOS match to the experimental P-x data for the Wasson reservoir oil at 107°F is shown in Fig. I-25. The average difference between the measured and the calculated BPP for all the points tabulated in Table I-16 is about ± 35 psi.

A total of ten displacements were performed using Oil-D and Oil-F. Five displacements for Oil-D were conducted above its original BPP, while three runs for Oil-F were conducted below BPP and two above the BPP. Table I-17 shows a flash calculation for Oil-F at three different pressure (below BPP) using PREOS. A summary of crude oil runs is given in Table I-18. The recovery factors for the runs below BPP are relatively low compared to the synthetic oil runs (Oil-C) conducted below BPP. The presence of the intermediate hydrocarbons (C_2-C_4) in the CO_2 stream as well as in the reservoir oil is reported to be beneficial in CO_2 miscible flooding. Intermediate components become miscible with the CO_2 and form a long transition zone, which improves the extraction of hydrocarbons and enhances the displacement efficiency. However, it seems that the absence of these intermediates, particularly in Oil-F, which was conducted at lower pressures (below BPP), caused poor displacement efficiency. The recovery data at BT and at 1.2 pore volumes plotted in Fig. I-26 indicate displacement performance of Oil-D and Oil-F over a range of run pressures from 1200 to 1900 psig. The MMPs for Oil-D and Oil-F were found to be 1650 psig and 1700 psig, respectively. The recovery curve for Oil-F started poorly at 43% efficiency at 1200 psig, and it increased with increasing pressure. The effluent/initial concentration ratio curves for Oil-D and Oil-F are shown in Figs I-27 and I-28, respectively. There are obvious indications of a methane bank in these figures. Fluctuations are more pronounced for runs below BPP in Fig I-28. A detailed description of the concentration histories of these runs are given in Yaghoobi's thesis.[92]

Figure I-29 shows the density-pressure curves for CO_2 with 0, 10, and 30 mole% C_1 contaminant over a range of 1200 psig to 1900 psig. Oil-D and Oil-F were displaced with a dense CO_2 (0.72 g/cm^3) at and above their MMPs (1650 and 1700 psig). This shows that a CO_2 density of 0.42 g/cm^3 is not high enough to extract the heavy hydrocarbon components efficiently. A reservoir pressure must be able to compress CO_2 to a density that dissolves enough hydrocarbons to promote miscibility with the reservoir fluid. This explains the low displacement efficiency in the F-1 and F-2 runs below BPP (Table I-18). However, the recovery efficiency below BPP is expected to be improved for lighter oils.

The results concerned with the effect of solution and free gas methane on the development of miscibility suggests the following:

TABLE I-14. ADJUSTED CRITICAL PARAMETERS AND ACENTRIC FACTORS FOR THE PREOS CALCULATIONS.

PSEUDOCOMPONENTS	P_c (atm)	T_c (K)	ω	δC_1-PsC
PsC_1	24.78	655.72	0.4515	0.016
PsC_2	18.50	672.19	0.6954	0.016
PsC_3	17.20	706.13	0.9615	0.016
PsC_4	15.25	791.32	1.1109	0.016
PsC_5	13.45	875.85	1.4338	0.016

TABLE I-15. BINARY INTERACTION COEFFICIENTS (Δ_{ij}) FOR THE WASSON RESERVOIR FLUID, USED IN PREOS CALCULATIONS

NAME	C_1	C_2	C_3	C_4	C_5	C_6	N_2	CO_2
C_1	.0000							
C_2	.0000	.0000						
C_3	.0000	.0000	.0000					
C_4	.0000	.0000	.0000	.0000				
C_5	.0000	.0000	.0000	.0000	.0000			
C_6	.0000	.0000	.0000	.0000	.0000	.0000		
N_2	.0360	.0500	.0800	.0950	.0900	.0950	.1000	.100
CO_2	.1000	.1300	.1350	.1300	.1300	.0500	.0500	-.02
PsC_1	.0160	.0000	.0000	.0000	.0000	.0000	.1000	.085
PsC_2	.0160	.0000	.0000	.0000	.0000	.0000	.1000	.085
PsC_3	.0160	.0000	.0000	.0000	.0000	.0000	.1000	.085
PsC_4	.0160	.0006	.0003	.0002	.0001	.0001	.1000	.085
PsC_5	0.016	.0008	.0006	.0009	.0007	.0006	0.100	.085

TABLE I-16. SUMMARY OF THE EXPERIMENTAL AND THE PREOS PREDICTED BPP FOR THE WASSON RESERVOIR OIL PLUS CO_2

MOLE FRACTION CO_2	P (psia) MEASURED	P (psia) CALCULATED	Δ%
0.00	870	909	4.48
0.25	1218	1170	3.94
0.50	1545	1512	2.14
0.60	1755	1778	1.31
Average Absolute Percentage Deviation = 2.97 %			

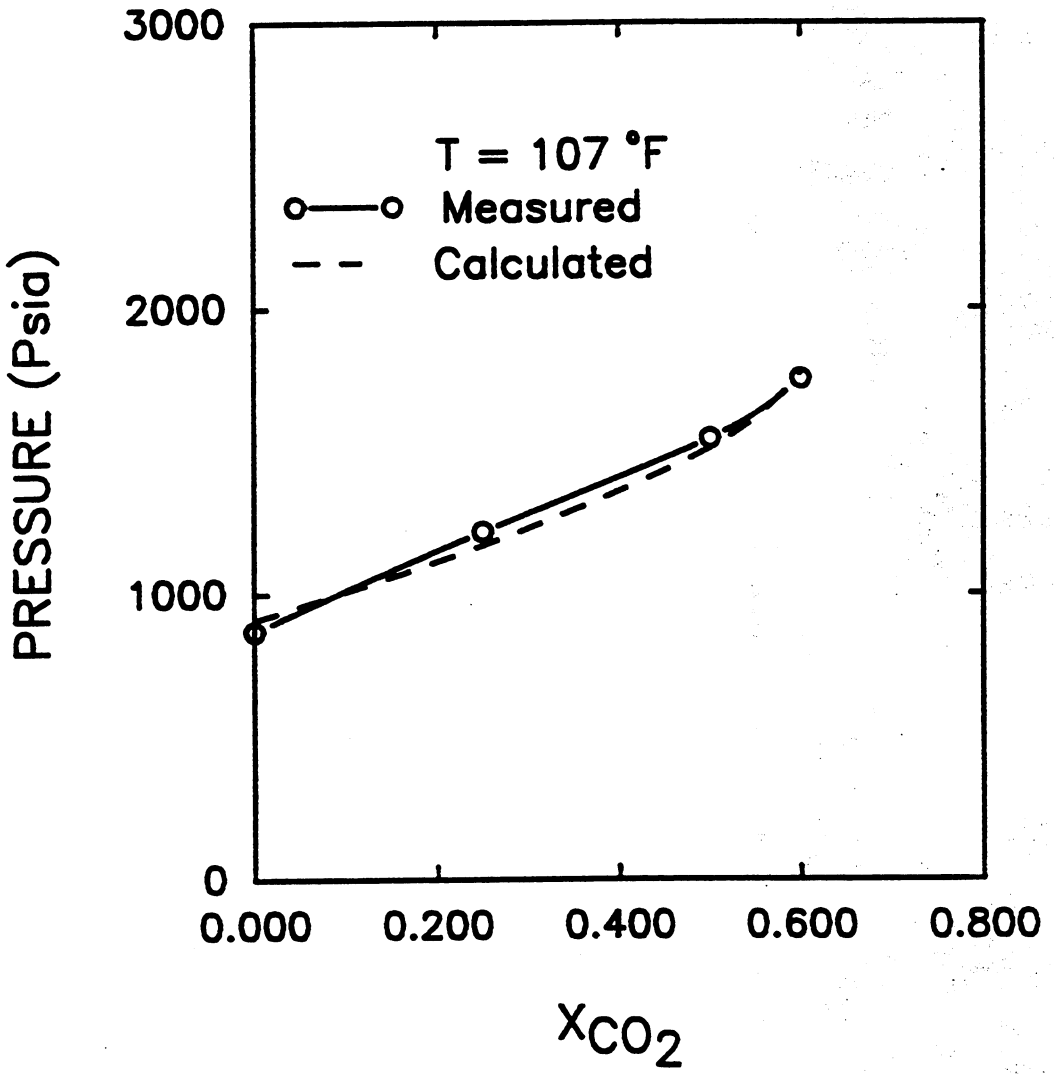

Figure I-25. Peng-Robinson Equation of State match of Wasson oil/CO_2 pressure-composition diagram.

TABLE I-17. FLASH CALCULATIONS FOR OIL-F AT 105°F PERFORMED USING PREOS

P (psig)	LIQUID			VAPOR		
	COMPOSITION (mole %)		ρ (g/cm^3)	COMPOSITION (mole %)		ρ (g/cm^3)
	C_1	C_{2+}		C_1	C_{2+}	
1200	0.2602	0.7398	0.8400	0.9877	0.0123	0.0605
1300	0.2727	0.7273	0.8289	0.9596	0.0404	0.0706
1400	0.2924	0.7076	0.8327	0.9867	0.0133	0.0717

TABLE I-18. RECOVERY EFFICIENCY OF OIL-D AND OIL-F AFTER 1.2 PORE VOLUMES (PV) OF CO_2 INJECTED AT CONSTANT TEMPERATURE OF 105°F

OIL MIXTURE	PRESSURE (psig)	DENSITY (g/cm^3)	RECOVERY (fraction)
D-1	1400	0.830	0.79
D-2	1500	0.832	0.84
D-3	1600	0.833	0.89
D-4	1700	0.820	0.92
D-5	1900	0.829	0.95
F-1	1200	-	0.42
F-2	1300	-	0.54
F-3	1400	-	0.63
F-4	1600	0.783	0.81
F-5	1700	0.795	0.92

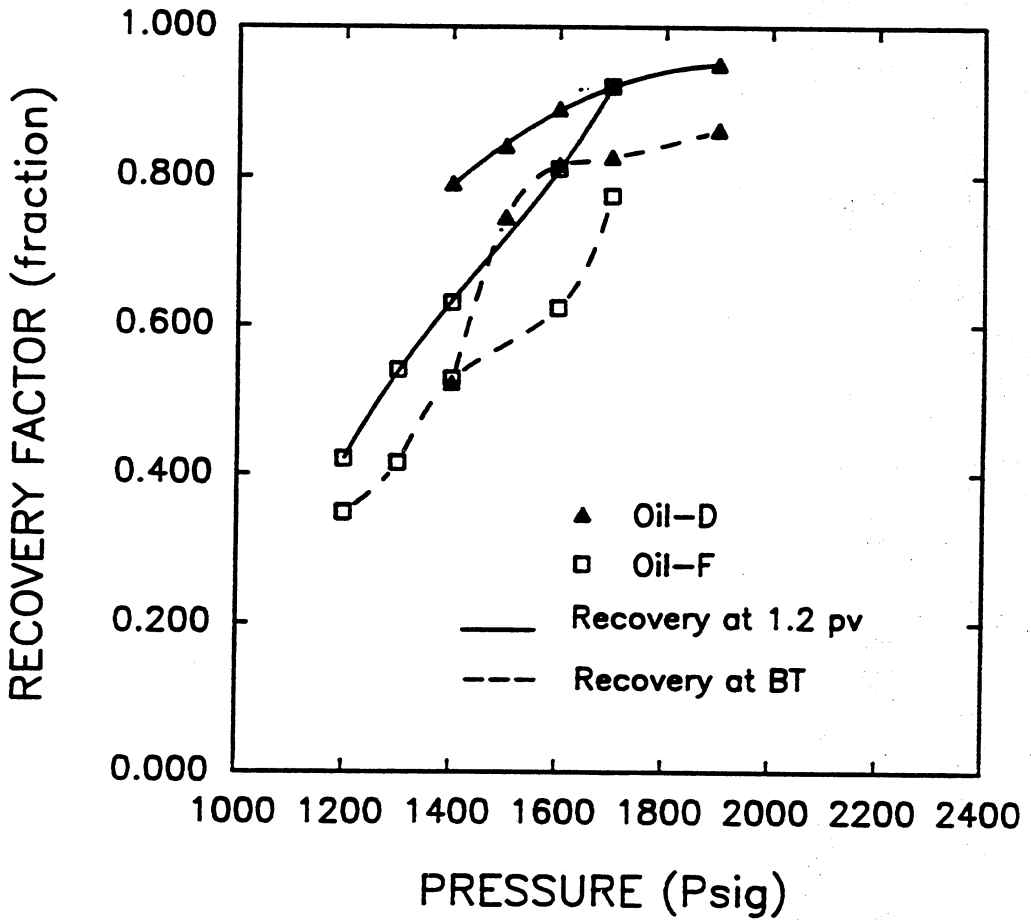

Figure I-26. Cumulative recovery at breakthrough and at 1.2 pore volumes of CO_2 injected for Oil-D and Oil-F.

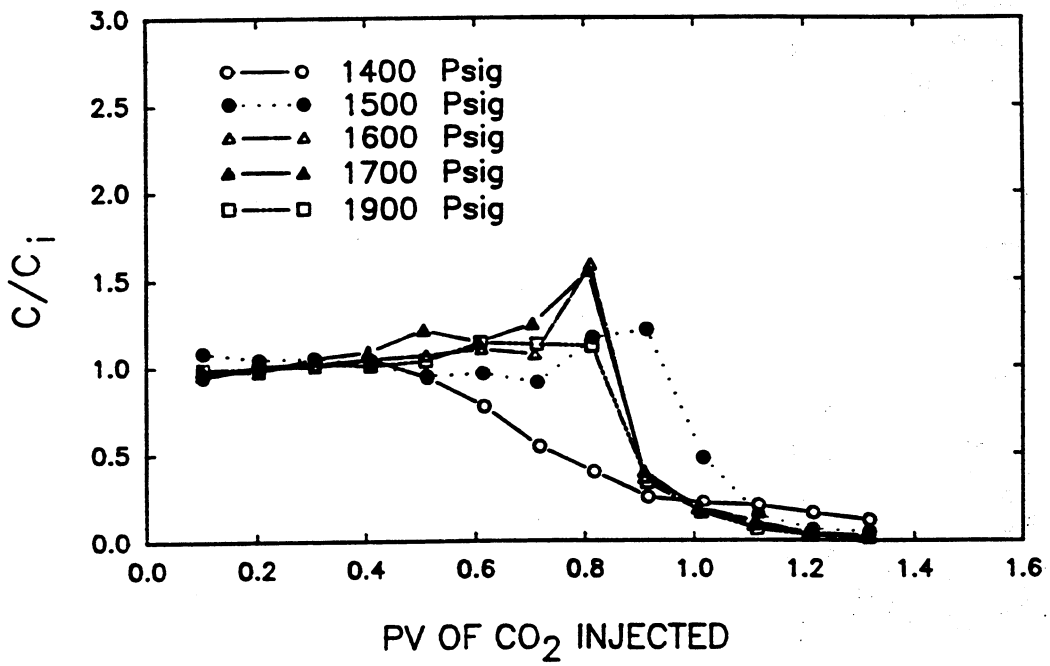

Figure I-27. Effluent/initial concentration ratio curves for C_1 component in Oil-D at 105°F and five different pressures.

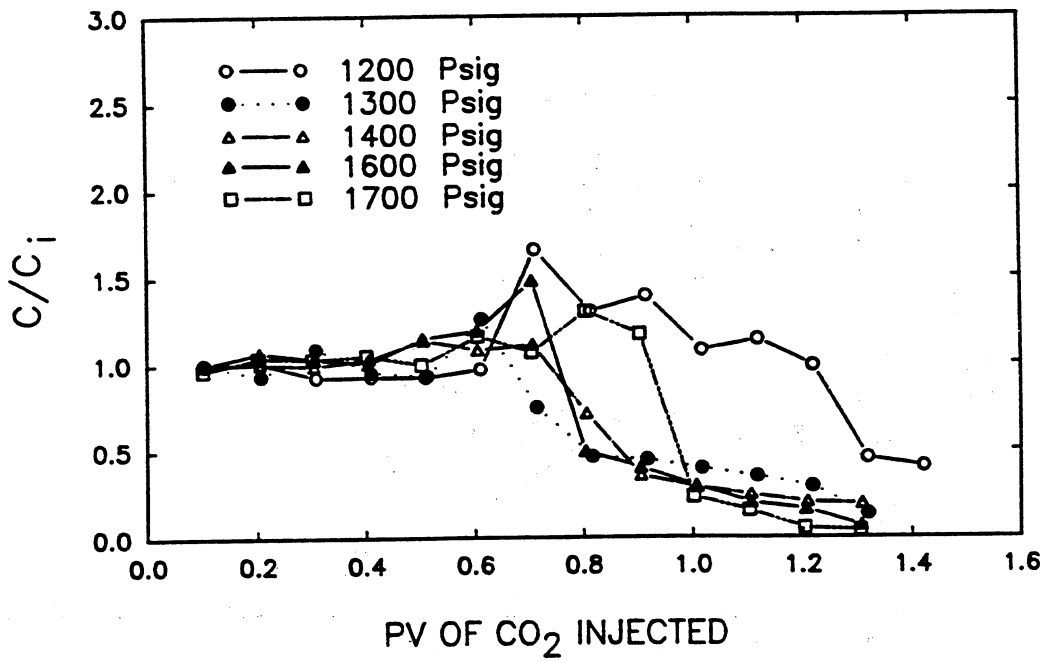

Figure I-28. Effluent/initial concentration ratio curves for C_1 component in Oil-F at 105°F and five different pressures.

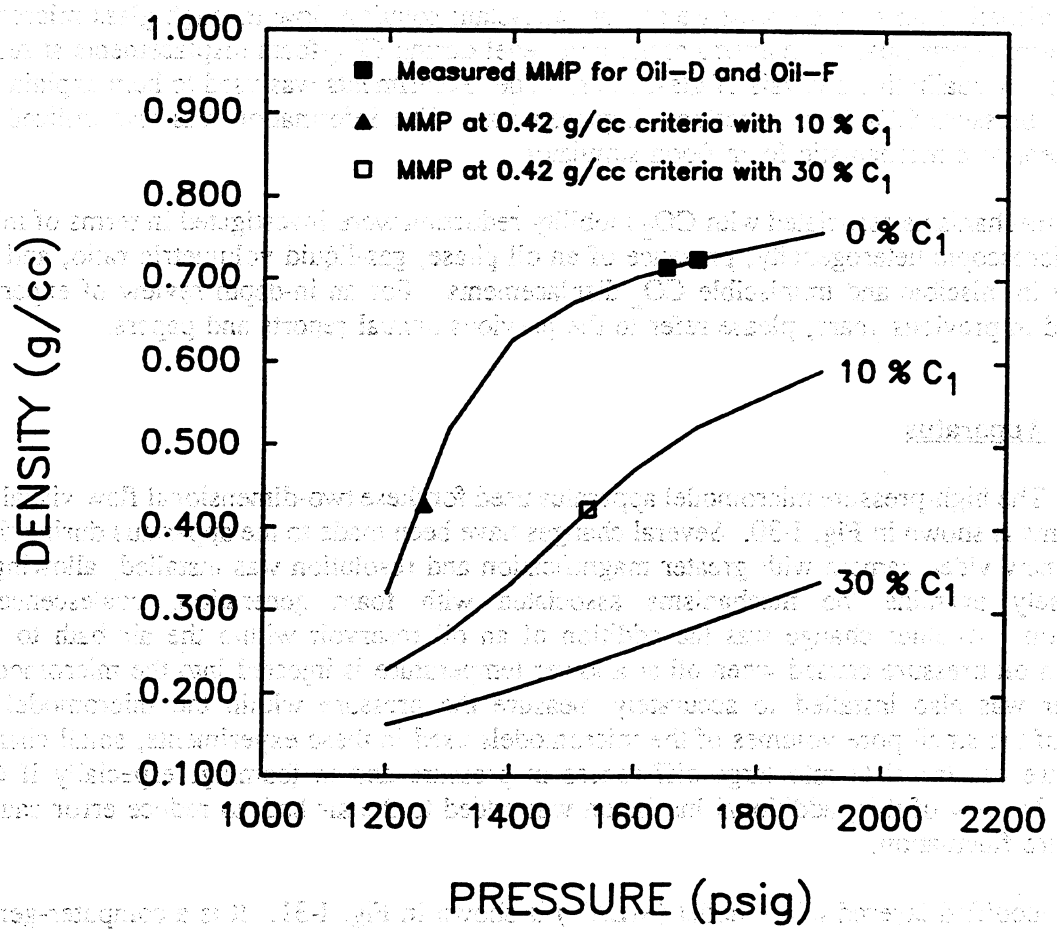

Figure I-29. Density of CO_2 with 0%, 10%, and 30% C_1 contamination at 105°F for Oil-D and Oil-F.

Recovery efficiency in the CO_2 oil displacement for pressures below the BPP are likely to be improved if intermediate hydrocarbons are present in the oil. Displacement efficiency could be higher for lighter oils. The increase in the MMP for solution gas methane in an oil is rather small compared to that in the CO_2 stream. The pure and contaminated CO_2 density value of 0.42 g/cm^3 for MMP predictions is a fast and reasonable criterion for lighter oils. However, for heavier oils, higher CO_2 density is required to dissolve enough hydrocarbons and promote miscibility.

D. MECHANISTIC STUDIES OF HIGH PRESSURE GAS/FOAM FLOW: MICROMODEL VISUALIZATION EXPERIMENTS

The visualization of high-pressure gas/oil/surfactant solution flow through glass micromodels helps determine principal mechanisms at the pore level during CO_2-foam displacements at reservoir conditions. A qualitative analysis of glass micromodel experiments was used to help explain results from high-pressure CO_2-foam coreflood displacements. The information was also utilized in the development of a mechanistic foam flood simulator.

The mechanisms associated with CO_2 mobility reduction were investigated in terms of injection mode, microscopic heterogeneity, presence of an oil phase, gas-liquid volumetric ratio, and sweep efficiency in miscible and immiscible CO_2 displacements. For an in-depth review of experiments performed in previous years, please refer to the previous annual reports and papers.

1. Apparatus

The high-pressure micromodel apparatus used for these two-dimensional flow visualization experiments is shown in Fig. I-30. Several changes have been made to the apparatus during the past year. A new video camera with greater magnification and resolution was installed, allowing us to more-closely examine the mechanisms associated with foam generation, coalescence, and propagation. Another change was the addition of an oil reservoir within the air bath to reduce changes in oil pressure caused when oil at a lower temperature is injected into the micromodel. A transducer was also installed to accurately measure the pressure within the micromodel itself. Because of the small pore volumes of the micromodels used in these experiments, small changes in temperature can translate into large differences in pressure and in foaming, especially if CO_2 is injected. In view of this, additional insulation was added to the air bath to reduce error caused by temperature fluctuation.

The modified layered micromodel (MLAY) is shown in Fig. I-31. It is a computer-generated model developed to study both aspect ratio and layer effect with crossflow. Although this model does not represent the geometric complexity found in reservoir rock, its regular geometric shape makes it possible to calculate displacement efficiency with some degree of accuracy. Its high aspect ratio, especially in the widest pore body zones, promotes bubble generation by downstream snap-off and aids in fluid diversion into the smaller pore matrix. The MLAY model has a pore volume of 0.378 cm^3 and a length of 6.45 cm.

The modified heterogenous micromodel (MHE) was developed from a thin section of a San Andreas rock and is shown in Fig. I-32. This model is approximately 10 times larger than the actual thin section. The widest pores near the inlets to the preferential flow path have been blocked. This

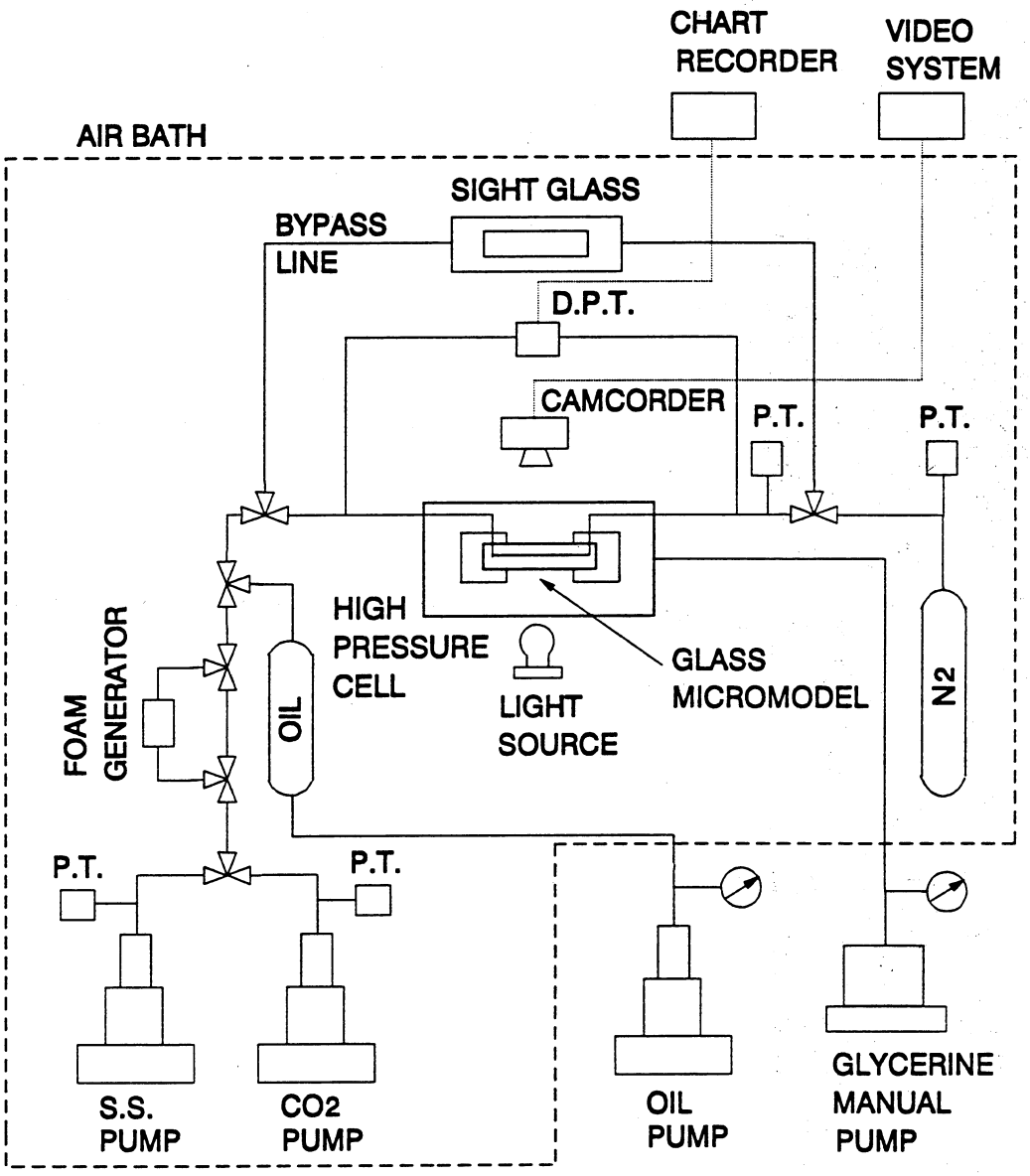

Figure I-30. Schematic of high-pressure micromodel apparatus.

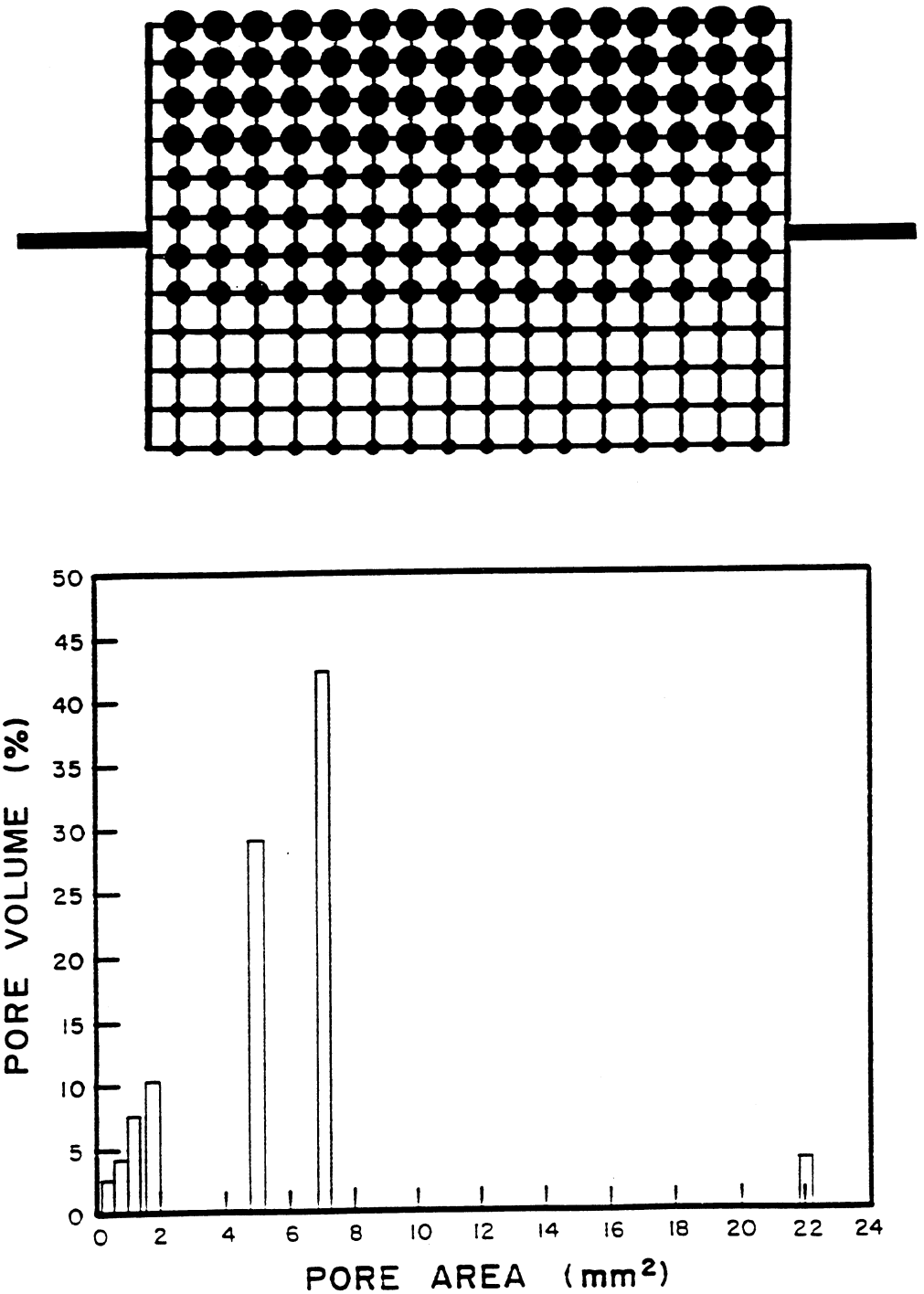

Figure I-31. Micromodel pattern and pore size distribution of modified layered micromodel (MLAY).

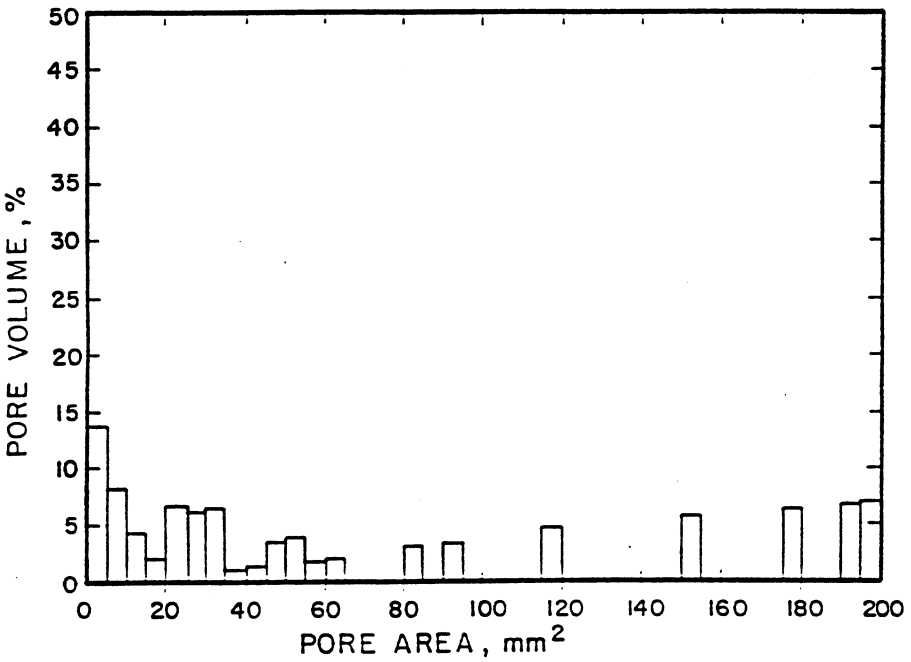

Figure I-32. Micromodel pattern and pore size distribution of modified heterogeneous micromodel (MHE).

promotes bubble generation because of high aspect ratio. The pore volume of the MHE model is 0.505 cm^3 and the length is 7.0 cm.

It is important to note that the micromodels used in this year's study are not necessarily the same as the models used in previous years' studies. The MHE micromodel used in last years research broke and it was necessary to make a new one. While the pore structure of both micromodels is the same, differences in pore volume and permeability may result in slight differences in foaming and sweep efficiency. The MLAY micromodel was used in research conducted over the last two years.

2. Descriptions of Experiments

Fifty-seven experiments were conducted at the conditions outlined in Table I-19. Injection mode, run pressure, and gas liquid volumetric ratio were varied. The initial saturation in these experiments was Maljamar stock tank oil with and without connate water. A liquid composition of the Maljamar sample for components C_5 through C_{37+} was obtained by gas chromatographic analysis and is listed in Table I-20. Also, the density and viscosity of the fluids used in these experiments is given in Table I-21. The properties of CO_2 were obtained from the Transport Properties Prediction Program (SUPERTRAPP) of the National Institute of Standards and Technology.[18]

All experiments were conducted at 90°F $\pm$ 0.1°F. Pressure drop across the micromodel was measured with a Honeywell STD-120 differential pressure transducer, which has an accuracy of 0.1% of the calibrated span. Calibrated span in these experiments ranged from 0.05 to 2.0 psid and the pressure drop was recorded as a function of time on a chart recorder. Flow rates in the displacements were 2.47 cm^3/hr for the MHE micromodel and 2.00 cm^3/hr for the MLAY micromodel. These flow rates corresponded to an interstitial velocity of 27 ft/D in both cases. The surfactant solution used was 1% Alipal CD-128 in 1% brine solution. All experiments were filmed to allow oil recovery to be estimated.

3. Mechanisms Associated with In-situ Foam Generation and Propagation.

Two primary mechanisms were shown to be the main cause of foam generation: snap-off and bubble subdivision.[98] Previous investigators[99,100] observed bubble generation by snap-off at the bubble generation site and bubble subdivision at the branching pores. The foam generation sites here refer to the pore structure that has a certain aspect ratio (pore body to pore throat ratio). This type of snap-off is called downstream snap-off because bubbles are generated only at the exit of the constriction.

For bubble generation by downstream snap-off to occur, the following requirements must be satisfied.[101] First, the porous medium should be a water-wet system and sufficient surfactant solution must be available at the bubble generation site. Second, the wetting phase should backflow to generate a collar at the pore constriction. Third, a high pressure drop must be present, so that the nonwetting phase can invade the bubble generation site. Roof[99] calculated the minimum distance that a nonwetting phase must advance before snap-off can occur in a toroidal constriction. This minimum distance is 7.07 times the pore throat radius at static condition. For dynamic conditions, this distance is expected to be smaller.

TABLE I-19. SUMMARY OF FLOW VISUALIZATION RESULTS

MODEL RUN	INJECT. MODE	C_s (wt %)	q TOTAL (cm^3/hr)	GAS LIQUID RATIO	INIT. SAT.	PRESS. (psia)	RECOVERY
MLAY5-19	PRE	1	2.00	4	MeSWi	1320	95
MLAY5-20	S	1	2.00	3	MeSWi	1320	80
MLAY5-21	S	1	2.00	5	MeSWi	1320	95
MLAY5-22	PRE	1	2.00	5	MeSWi	1320	-
MLAY5-23	PRE	1	2.00	3	MeSWi	1320	99
MLAY5-24	PRE	1	2.00	5	MeSWi	1320	99
MLAY5-28	S	1	2.00	3	MeSWi	1320	90
MLAY5-29	S	1	2.00	5	MeSWi	1320	95
MLAY5-30	S	1	2.00	6	MeSWi	1320	99
MLAY5-31	S	1	2.00	6	MeSWi	1320	95
MLAY5-32	P	0	2.00	Pure	MeSWi	1320	90
MLAY5-33	S	1	2.00	4	MeSWi	1320	90
MLAY5-34	SS	1	2.00	Pure	MeSWi	1320	75
MLAY5-35	SS	1	2.00	Pure	MeSWi	1320	80
MLAY5-36	S	1	2.00	4	MeSWi	1320	90
MLAY5-37	P	0	2.00	Pure	MeSWi	1320	95
MLAY5-38	P	0	2.00	Pure	M	1320	95
MLAY5-39	SS	1	2.00	Pure	M	1320	65
MLAY5-40	P	0	2.00	Pure	M	1085	90
MLAY5-41	P	0	2.00	Pure	M	1000	90
MLAY5-42	P	0	2.00	Pure	M	800	42
MLAY5-43	P	0	2.00	Pure	M	1110	90
MLAY5-44	S	1	2.00	4	M	1100	95
MLAY5-45	S	1	2.00	4	M	1000	95
MLAY5-46	S	1	2.00	4	M	800	-
MLAY5-47	W	0	2.00	4	M	1320	90
MLAY5-48	W	0	2.00	4	M	1320	90
MLAY5-49	S	1	2.00	4	M	1320	95
MLAY5-50	S	1	2.00	4	M	1320	95
MLAY5-51	S	1	2.00	4	M	1110	95

TABLE I-19 (CONT.)

MODEL RUN	INJECT. MODE	C_s (wt %)	q TOTAL (cm^3/hr)	GAS LIQUID RATIO	INIT. SAT.	PRESS. (psia)	RECOVERY
MLAY5-52	S	1	2.00	4	M	1110	90
MLAY5-53	W	0	2.00	4	M	1110	90
MLAY5-54	W	0	2.00	4	M	1110	-
MLAY5-55	W	0	2.00	4	M	1000	88
MLAY5-56	W	0	2.00	4	M	800	73
MLAY5-57	S	1	2.00	4	M	1110	95
MLAY5-58	S	1	2.00	4	M	1000	90
MLAY5-59	S	1	2.00	4	M	800	82
MHE2-1	S	1	2.47	4	M	1320	-
MHE2-2	S	1	2.47	4	M	1320	-
MHE2-3	P	0	2.47	Pure	M	1320	-
MHE2-4	P	0	2.47	Pure	M	1320	-
MHE2-5	S	1	2.47	3	M	1320	-
MHE2-6	S	1	2.47	5	M	1320	-
MHE2-7	S	1	2.47	6	M	1320	-
MHE2-8	S	1	2.47	6	M	1320	-
MHE2-9	S	1	2.47	4	M	1320	-
MHE2-10	SS	1	2.47	Pure	M	1320	-
MHE2-11	S	1	2.47	4	SS	1320	-
MHE2-12	S	1	2.47	6	SS	1320	-
MHE2-13	S	1	2.47	5	SS	1320	-
MHE2-14	S	1	2.47	3	SS	1320	-
MHE2-15	S	1	2.47	3	SS	1320	-
MHE2-16	S	1	2.47	3	SS	1320	-
MHE2-17	S	1	2.47	5	SS	1320	-
MHE2-18	S	1	2.47	6	SS	1320	-
MHE2-19	P	0	2.47	Pure	SS	1320	-

M = Maljamar Stock Tank Oil
McSWi = Maljamar Stock Tank Oil with Connate Water
P = Single Phase Pure CO_2 Injection
S = Simultaneous Injection of CO_2 and Surfactant Solution
SS = Surfactant Solution
W = Simultaneous Injection of CO_2 and Brine
Surfactant = Alipal CD-128

TABLE I-20. LIQUID COMPOSITION OF MALJAMAR STO OBTAINED BY GAS CHROMATOGRAPHIC ANALYSIS

COMPONENTS	MW	WT. FRACTION	CUMULATIVE	MOLE FRACTION	CUMULATIVE
C_5	72.15	0.0575	0.0575	0.1496	0.1496
C_6	86.18	0.0415	0.0990	0.0903	0.2399
C_7	100.21	0.0673	0.1663	0.1261	0.3660
C_8	114.23	0.0528	0.2191	0.0867	0.4526
C_9	128.60	0.0488	0.2679	0.0712	0.5239
C_{10}	142.29	0.0429	0.3108	0.0566	0.5805
C_{11}	156.31	0.0370	0.3478	0.0444	0.6248
C_{12}	170.34	0.0306	0.3784	0.0338	0.6586
C_{13}	184.37	0.0267	0.4051	0.0272	0.6858
C_{14}	198.39	0.0353	0.4404	0.0333	0.7191
C_{15}	212.42	0.0260	0.4664	0.0230	0.7421
C_{16}	226.45	0.0256	0.4920	0.0212	0.7633
C_{17}	248.48	0.0202	0.5121	0.0157	0.7790
C_{18}	254.50	0.0259	0.5380	0.0191	0.7981
C_{19}	268.53	0.0187	0.5568	0.0131	0.8112
C_{20}	282.56	0.0182	0.5750	0.0121	0.8233
C_{21}	296.58	0.0177	0.5926	0.0112	0.8345
C_{22}	310.61	0.0177	0.6104	0.0107	0.8452
C_{23}	324.64	0.0169	0.6272	0.0098	0.8549
C_{24}	338.66	0.0164	0.6436	0.0091	0.8640
C_{25}	352.69	0.0112	0.6548	0.0060	0.8700
C_{26}	366.72	0.0161	0.6709	0.0082	0.8782
C_{27}	380.75	0.0165	0.6874	0.0081	0.8863
C_{28}	394.77	0.0113	0.6987	0.0054	0.8917
C_{29}	408.80	0.0117	0.7104	0.0054	0.8971
C_{30}	422.83	0.0115	0.7219	0.0051	0.9022
C_{31}	436.85	0.0170	0.7390	0.0073	0.9095
C_{32}	450.88	0.0116	0.7506	0.0048	0.9143
C_{33}	464.91	0.0117	0.7623	0.0047	0.9191
C_{34}	478.94	0.0122	0.7745	0.0048	0.9238
C_{35}	492.96	0.0123	0.7868	0.0047	0.9285
C_{36}	506.00	0.0118	0.7986	0.0044	0.9329
C_{37+}	563.20	0.2014	1.0000	0.0671	1.0000

TABLE I-21. PROPERTIES OF THE FLUIDS

FLUID (@ 90°F)	DENSITY (gm/cm^3)	VISCOSITY (cp)
CO_2 (1320 psia)	0.718	0.060
CO_2 (1110 psia)	0.536	0.039
CO_2 (1000 psia)	0.225	0.021
CO_2 (800 psia)	0.141	0.019
Maljamar Crude Oil	0.838	3.6
Alipal CD-128 (1.0%)	0.988	0.85

A different type of snap-off mechanism was also observed. When a slug of surfactant solution is injected into a CO_2 swept zone, the surfactant solution flows along the wall of the pore body. Then this wetting phase (surfactant solution) pinches off the nonwetting phase (gas) at the leading edge of the surfactant solution. This type of snap-off mechanism is called upstream snap-off. The size of the bubbles generated by upstream snap-off is usually larger than the bubbles generated by downstream snap-off. A minimum aspect ratio is not a necessary condition for the upstream snap-off mechanism.

One important point to remember is that when the nonwetting phase (CO_2) is injected into the wetting phase (surfactant solution) porous medium, most snap-off is downstream snap-off. While the simultaneous injection of CO_2 and surfactant solution, or the injection of a surfactant solution slug into a CO_2 saturated zone, usually results in upstream snap-off.

Bubble subdivision at branching pores is another important foam generation mechanism. Large bubbles are subdivided into smaller bubbles both at the inlet and outlet of branching pores. Bubble division at the inlet of the branching pores occurs when the flow velocity in one channel is much lower than in the other channel. When a large bubble approaches the branching pores, it stretches into both channels, and is then pinched off by the following bubble at the branch point. Smaller bubbles continue to be generated as this process is repeated until the channel is completely blocked.

4. Effects of CO_2 Miscibility and Injection Mode

Flow visualization experiments were performed in the high pressure micromodel apparatus to investigate CO_2 phase behavior on displacement efficiency during the simultaneous injection of CO_2 and brine (WAG), the simultaneous injection of CO_2 and surfactant solution (SAG), and the injection of pure CO_2 into the MLAY micromodel. The initial saturation in these experiments was Maljamar stock tank oil without connate water present. Four different run pressures were studied: 800, 1000, 1110, and 1320 psia, and the gas-liquid volumetric ratio was 4:1.

a. Pure CO_2 Displacements

Figure I-33 compares oil recoveries in pure CO_2 displacements at the pressures given above. These displacements were conducted to provide a reference point for the more complex displacements attempted later. The minimum miscibility pressure (MMP) for a CO_2-Maljamar crude oil system at 90°F was reported by Orr and Taber[102] to be approximately 1160 psia. Thus, the displacement of oil by CO_2 at 1320 psia exhibited multi-contact miscibility. In displacements conducted at pressures close to and well below the MMP, CO_2 was soluble to some extent in Maljamar, but was not multi-contact miscible with oil.

Phase behavior experiments conducted in a static cell by Orr *et al.*[103] helped us understand the effect of various types of phase behavior on CO_2-Maljamar crude oil systems. Results of these experiments indicate that at 90°F and 800 psia (a pressure well below the CO_2 vapor pressure) CO_2 and Maljamar crude oil form two distinct phases: a vapor phase and a liquid phase. When the pressure is raised to around 1000 psia, a vapor phase, a CO_2 rich liquid phase, and an oil rich liquid phase are produced. Upon an additional increase in pressure to 1200 psia, an oil rich liquid phase and a CO_2 rich liquid phase, which are highly efficient at extracting hydrocarbons, are produced.

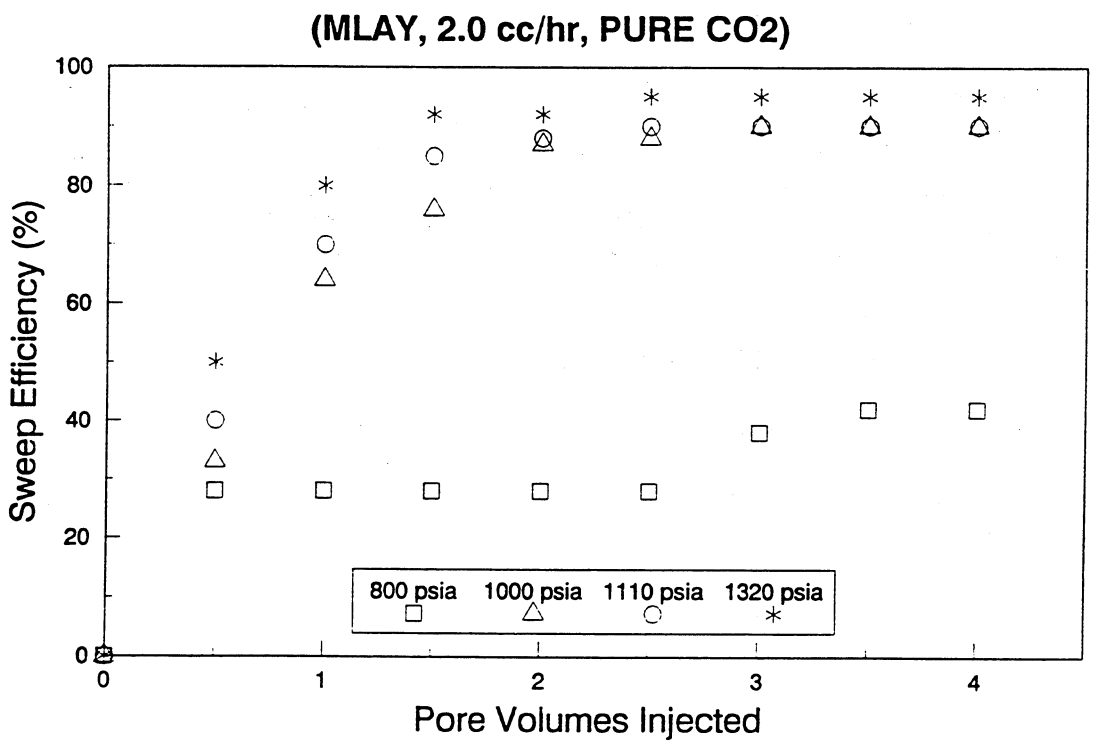

Figure I-33. Effect of CO_2 miscibility on oil recovery.

Flow visualization experiments conducted with Maljamar stock tank oil by Bahralolom[104] at a lower temperature (77°F) provide direct visual evidence of the effect of phase behavior on displacement efficiency in both homogeneous and heterogeneous micromodels. Results of these experiments show a distinct improvement in hydrocarbon extraction and displacement efficiency by CO_2 at pressures close to and well above the MMP as compared to immiscible conditions.

Direct observation of the displacement conducted at 1320 psia showed a noticeable lack of CO_2 slugs in the pore matrix. Instead, CO_2 dissolved into the crude and lightened it until the oil was no longer visible. However, a significant amount of dark particulate matter comprised of what are presumably heavier hydrocarbons the CO_2 failed to extract, was left in the pore spaces and especially the pore throats of the micromodel. Much of the particulate matter had undoubtably formed in the flow line upstream where mixing of the CO_2 and crude initially took place, and was observed entering the micromodel along with a single phase mixture of CO_2 and crude oil. Some of this matter was also generated within the micromodel itself. It is believed that CO_2-contacting oil in the flow line upstream led to the development of a CO_2 rich liquid phase, which moved into the micromodel as a transition zone. This observed behavior is consistent with flow visualization results obtained by Campbell[105] and Bahralolom,[104] in a CO_2-Maljamar system at 77°F and 1200 psia.

The displacement conducted at 1110 psia was similar to that at 1320 psia in that a transition zone consisting of a CO_2 rich liquid phase was created in the flow line upstream, indicating that extraction of oil by CO_2 was taking place. Also, a stream of black particulate matter was observed entering the micromodel. Displacement efficiency was somewhat lower than at 1320 psia. However, it caught up to within 5% of it after 1.5 PVI. A higher residual oil content was responsible for the lessened displacement efficiency at this pressure. (For this study, residual oil content is defined as oil left within the micromodel after breakthrough of injection fluid.) Another difference between these displacements was the appearance of CO_2 slugs moving within the oil rich phase, indicating perhaps that CO_2 extracts hydrocarbons less efficiently at this pressure. The vapor pressure of CO_2 at 90°F is 1095 psia. Thus, liquid/liquid phase behavior was most likely observed.

The displacement conducted at 1000 psia was intended to determine the effect of a liquid/liquid/vapor phase on displacement efficiency through Maljamar oil. Phase behavior experiments conducted in a static cell by Orr *et al.*[103] indicated that at pressures ranging from 1000 to 1110 psia, a three phase region consisting of two liquid and one vapor phase will develop when CO_2 is mixed with Maljamar crude at 90°F. A visual analysis of this experiment reveals that a CO_2 meta-stable phase was produced but disappeared quickly in the dynamic environment within the micromodel. As in the other experiments, a CO_2 rich liquid phase entered the micromodel first. However, as this phase passed through the micromodel and gave way to a vapor phase, an interface developed between the vapor and the CO_2 rich phase which preceded it. As the vapor invaded this phase through pore constrictions, distinct bubbles immiscible with the denser CO_2 were generated. These bubbles began to shrink and disappear almost immediately as phases of different densities sought to establish equilibrium with each other. Displacement efficiency was slightly less than at 1110 psia, but managed to equal it after 1.5 PVI. Residual oil at 4 PVI was left in the model to about the same degree as that left in the 1320 psia displacement.

The displacement at 800 psia varied significantly with the previous displacements in that no CO_2 rich liquid phase was produced in the upstream flow line and no dark particulate matter was observed entering the micromodel. Instead, there was a distinct interface between the CO_2 and crude oil. This and the lack of any change in the oil color shows that there was probably very little extraction

of hydrocarbons by CO_2 taking place. Displacement efficiency was significantly less than that of the previous displacements. Approximately 40% of the oil in place was swept from the micromodel and very little additional oil was recovered after breakthrough. At 800 psia, a mixture of CO_2 and crude oil forms two phases Orr *et al.*[103] The very low density and viscosity of CO_2 (well below the vapor pressure) creates a high interfacial tension between the CO_2 and oil.[104] As a result, CO_2 displaced the oil in a piston like fashion, pushing oil ahead of it pore by pore until breakthrough was achieved. After breakthrough, the CO_2 simply followed the same flow path through the micromodel.

b. Water-Alternating-Gas (WAG) Displacements

Figure I-34 compares displacement efficiency in experiments involving the simultaneous injection of brine and CO_2 into Maljamar stock tank oil. This data shows that, up to 2 PVI, the multi-contact miscible displacement at 1320 psia had the highest recovery. However, after 2 PVI, oil recovery at 1000, 1110, and 1320 psia was virtually the same. Displacement efficiency at 800 psia was significantly lower at 4 PVI than at higher pressures. From 0 to 1.5 PVI, though, it matched up quite well with displacements at 1000 and 1110 psia. Pressure drop data shown in Figs. I-35 and I-36 indicate that a higher pressure drop was created as run pressure was decreased. This can be explained, in part, that due to high interfacial tension between CO_2 and oil at low pressure, CO_2 becomes less efficient at partitioning into the oil phase and lowering its viscosity.

No CO_2 rich liquid phase was observed entering the micromodel at 1320 psia. Instead, brine entered the micromodel first, so it was possible to directly observe the initial contact between CO_2 and crude oil. The CO_2 did not flow through the brine to contact fresh oil, but bypassed it by forming a flow channel between the brine and the edge of the pore spaces. The CO_2 was instantly miscible with the crude upon contact, lightening it to a pale yellow and causing dark particulate matter to drop out and adhere to the pore walls almost immediately. Brine flowing through the pore matrix did a fairly good job of clearing it out of the micromodel by picking it up and pushing it out at its leading edge. However, a good deal of oil was also surrounded and trapped within the pore throats by the brine. As brine began to fill the micromodel, CO_2 formed a channel through the matrix and followed it through the rest of the run.

The displacement conducted at 1110 psia was initially similar to that of pure CO_2. A CO_2 rich liquid phase formed in the flow line upstream and entered the micromodel as a light, single phase mixture of dense CO_2 and extracted hydrocarbons. When brine entered the micromodel, the CO_2 again bypassed it and contacted oil. However, it didn't dissolve into the crude quite as readily. In pores only partly filled with brine, an angle formed between the pore wall and the brine into which crude was injected. When CO_2 flowing between the brine and the pore wall hit the oil rich phase, tiny bubbles were generated, which almost immediately coalesced with each other and formed a larger bubble. Sometimes they travelled as distinct bubbles through the oil rich phase until they reached a CO_2-rich phase and dissolved into it. About the same amount of residual oil was found in this displacement at 4 PVI as in that of 1320 psia.

A CO_2 meta-stable phase was observed in the WAG injection conducted at 1000 psia and continued to be seen throughout the duration of the experiment. Brine entered the micromodel first, so it was again possible to directly observe the initial contact between the CO_2 and crude oil. The oil was lightened somewhat by CO_2 upon contact, but not nearly to the extent it was at 1320 psia.

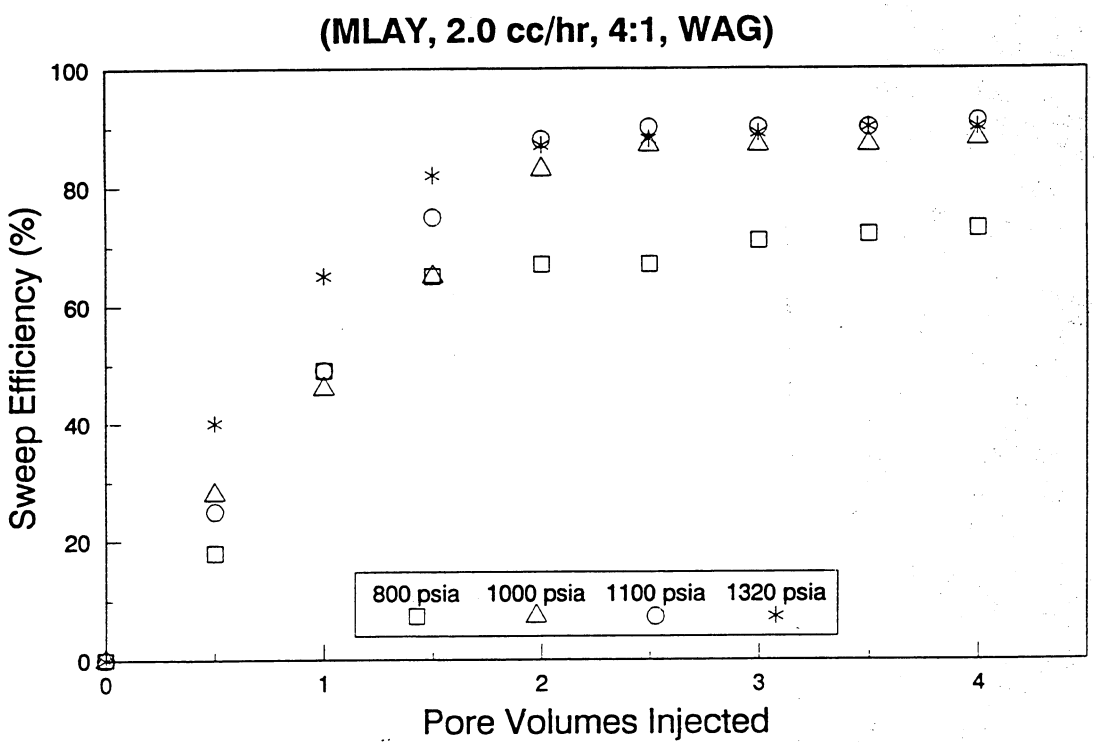

Figure I-34. Effect of CO_2 miscibility on oil recovery.

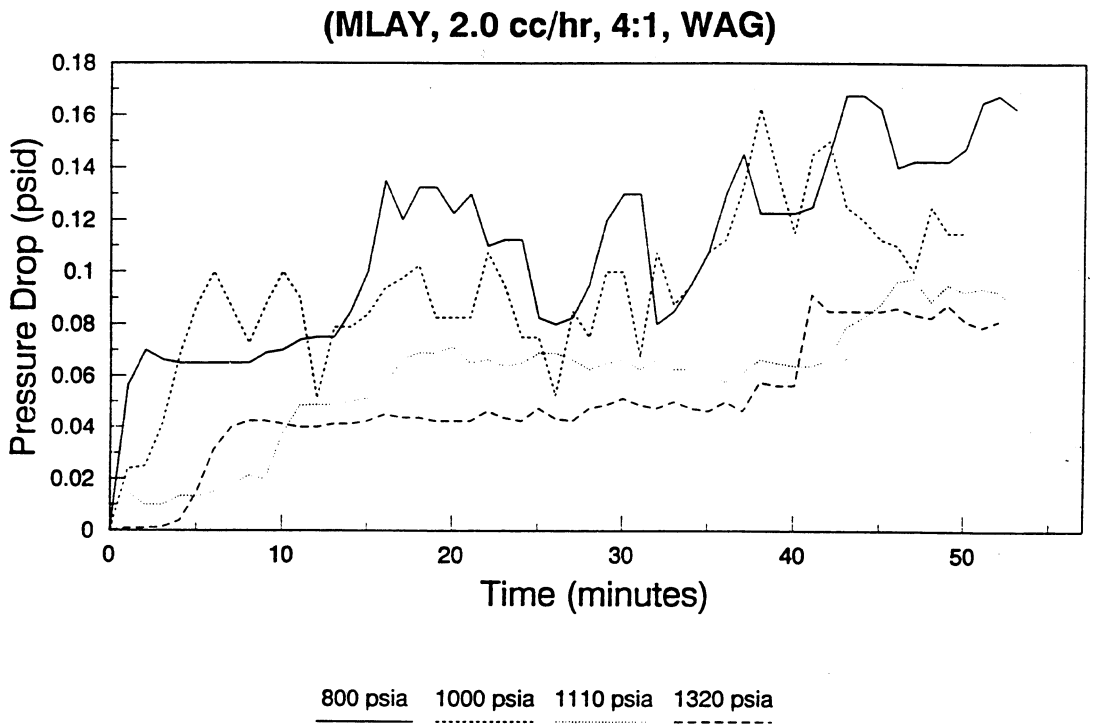

Figure I-35. Effect of CO_2 miscibility on pressure drop.

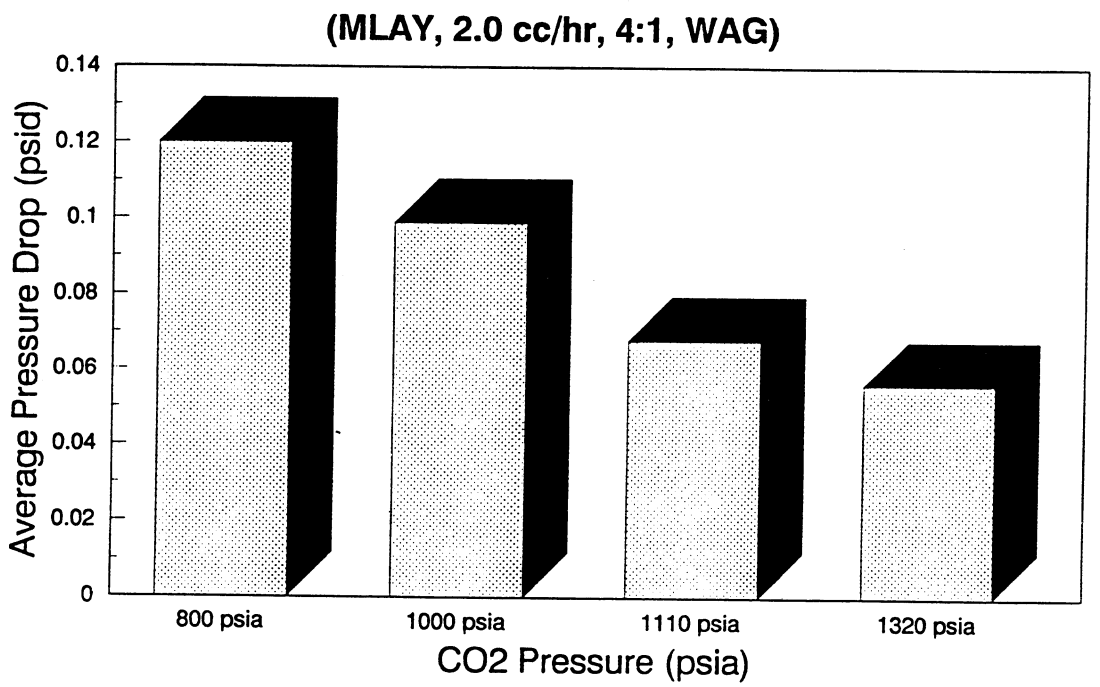

Figure I-36. Effect of CO_2 miscibility on average pressure drop.

There seemed to be a large amount of residual oil left behind. Recovery was calculated to be slightly lower at 4 PVI than that of the previous WAG displacements.

The WAG displacement performed at 800 psia was characterized by a very high initial pressure drop and what seemed to be a stoppage of flow at 0.5 PVI and again at 1 PVI. This is reinforced by the fact that breakthrough didn't occur until 1.5 PVI, an obvious impossibility since if breakthrough didn't occur, the entire model would be swept at 1 PVI. Also, there was no decrease in pressure drop until breakthrough, which indicated that there was no backflow. The most logical explanation for this phenomenon is that it took a considerable amount of pressure build up to overcome the capillary forces that seem to dominate the system. There was very little oil recovered after breakthrough of injection fluid. As in the pure CO_2 displacement at the same pressure, CO_2 formed a distinct interface with the oil. No lightening of the oil was observed, again indicating that very little hydrocarbon extraction was occurring.

c. Surfactant-Alternating-Gas (SAG) Displacements

Figure I-37 compares oil recoveries in experiments involving the simultaneous injection of surfactant solution and CO_2 into Maljamar stock tank oil. These results indicate that displacement efficiency is virtually the same at pressures of 1110 and 1320 psia after 1.5 PVI. The displacement conducted at 800 psia had a higher recovery at all points when compared to its complement WAG displacement and twice as high as that conducted with the pure CO_2 displacement. Displacement efficiency at 1000 psia, while still quite high, was slightly lower when compared to the higher run pressures. Pressure drop data for these runs are found in Figs. I-38 and I-39. Average pressure drop in all cases was much lower in the SAG displacements when compared to the WAG displacements at the same pressure (Fig. I-40). The lower surface tension of the surfactant solution may have contributed to the lower pressure drop. A lower run pressure translated into a higher average pressure drop in the SAG displacements with the exception of that at 800 psia. Again, this is probably due to the higher interfacial tension between CO_2 and oil at lower pressure, which prevents CO_2 from partitioning into the oil phase and lowering its viscosity. The average pressure drop at 800 psia, while higher than 1110, psia was lower than at 1000 psia. There was a noticeable lack of bubble formation at 4 PVI, even when a considerable amount of surfactant had entered the micromodel and was available at bubble generation sites. This lack of bubbles within the pore matrix may have contributed to the lower pressure drop. Additional experiments at this ratio and pressure are being planned to further investigate this phenomenon.

The movement of CO_2 through the micromodel at 1320 psia was much different when compared to the WAG displacements, where CO_2 formed a flow channel between the brine and the edge of the pore spaces. Instead, it flowed directly through the surfactant as a travelling lamellae until it reached oil. It mixed vigorously with the oil upon contact, resulting in very small bubbles of CO_2 being formed within the surfactant solution. Also, what seemed like an oily emulsion was formed at the mixing sites and adhered to the glass surface within each pore space. The excellent recovery at 4 PVI was due to two factors: the appearance of bubbles within the large pore spaces of the micromodel, which diverted flow into the tighter pore matrix, and the fact that surfactant seemed to be much better at mobilizing residual oil than brine. It was reported last year that dark particulate matter found within the micromodel could have been caused by surfactant solution concentration. Further visual evidence indicates that this is not the case. However, surfactant does displace the residual oil by pushing and concentrating it at its leading edge. Residual oil surrounded and trapped

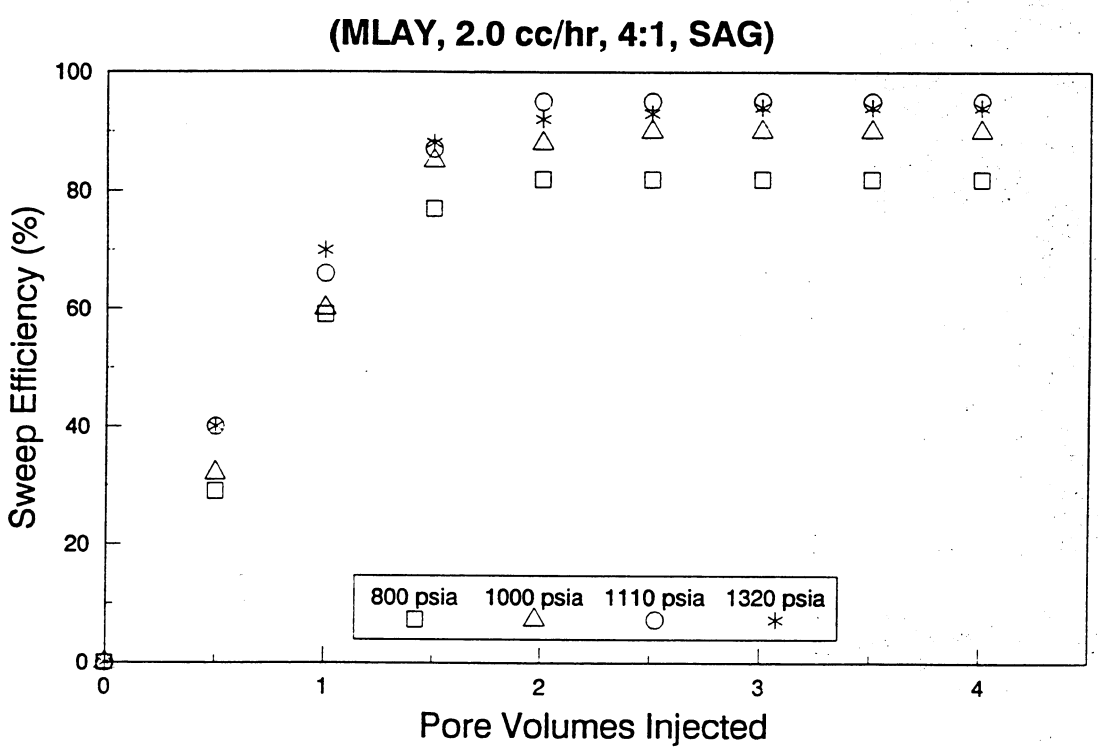

Figure I-37. Effect of CO_2 miscibility on oil recovery.

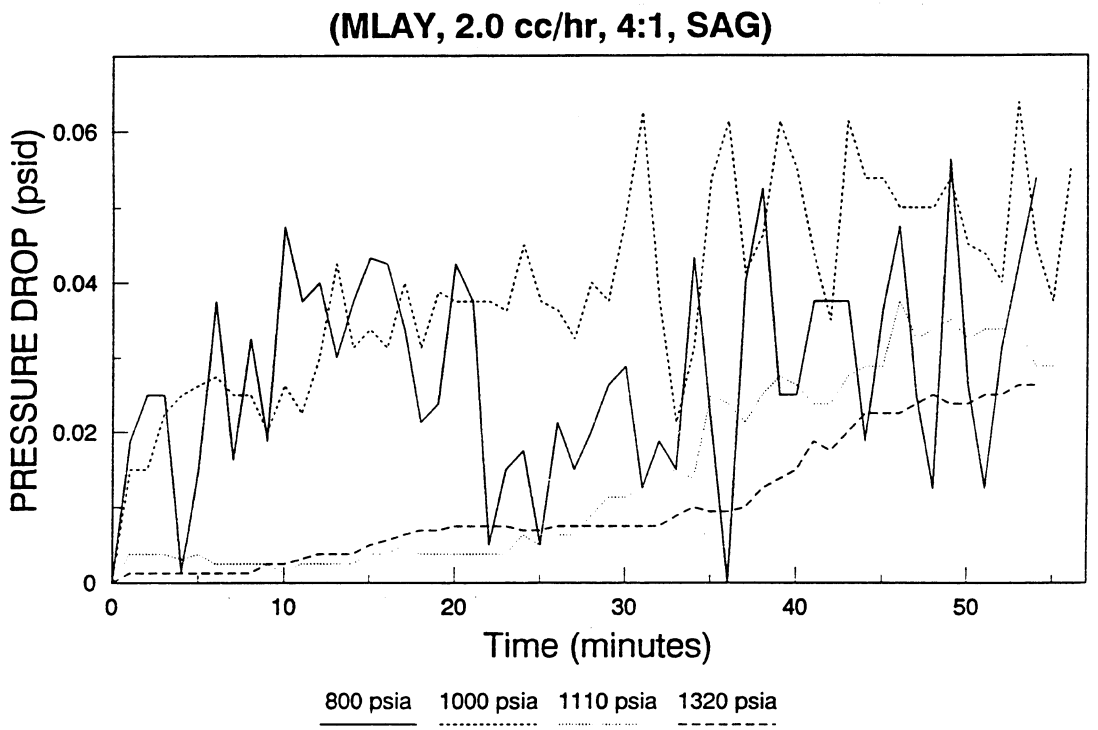

Figure I-38. Effect of CO_2 miscibility on pressure drop.

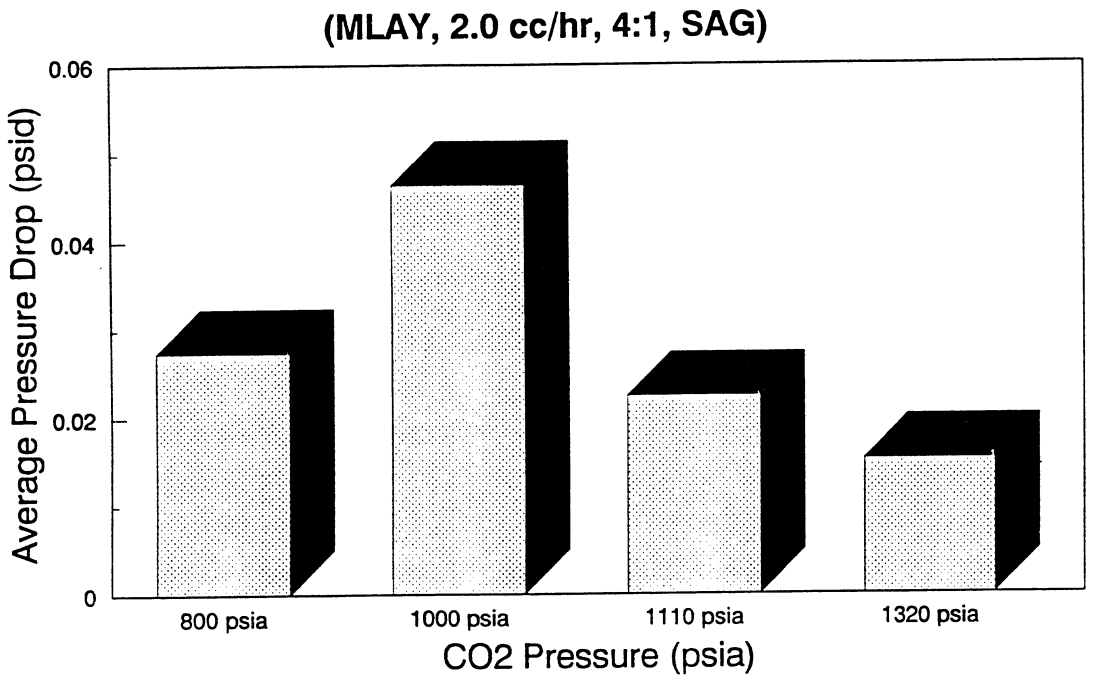

Figure I-39. Effect of CO_2 miscibility on average pressure drop.

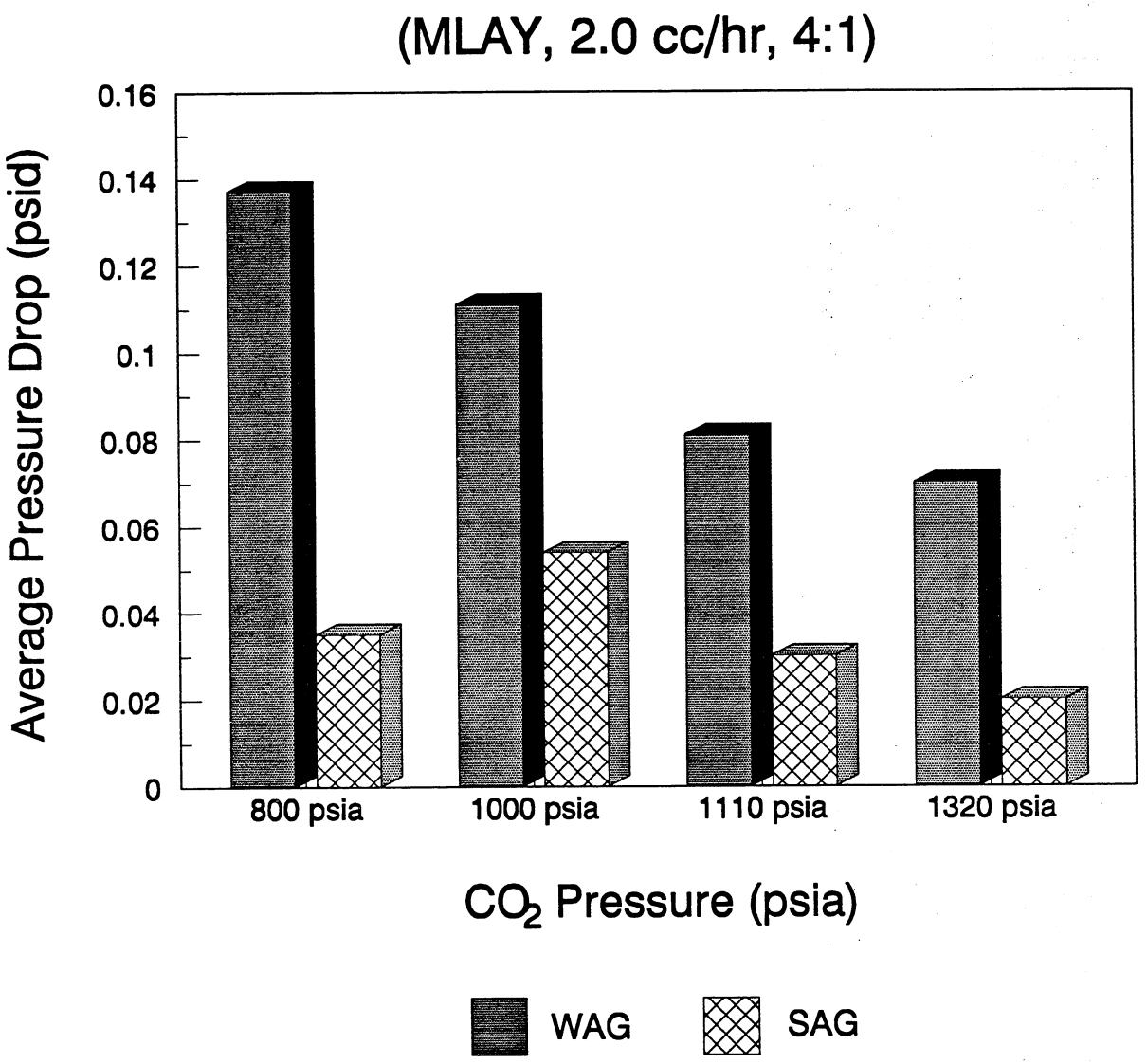

Figure I-40. Effect of CO_2 miscibility on average pressure drop.

by surfactant may still be displaced by CO_2 diverted by foam in the large pore spaces. When a travelling CO_2 lamellae contacted residual oil, it spread along the CO_2 surfactant interface and moved it through the micromodel.

The slightly lower recovery, up to 1.5 PVI at 1110 psia, is attributed to the fact that CO_2 at immiscible conditions was less efficient at displacing oil than it was at the multi-contact miscible condition in the previous run. Upon surfactant breakthrough, however, the mechanisms described above were equally efficient at displacing oil. Very small CO_2 bubbles, as well as the oil emulsion described earlier, were also seen within the surfactant solution.

Direct visual observation of the displacement conducted at 1000 psia shows a decreased displacement efficiency at each half PVI when compared with runs at higher pressure. CO_2 at this pressure was less efficient at displacing the oil than it was at 1110 psia. As was observed in the pure CO2 and WAG displacements, the CO_2 lightened the crude less, indicating decreased hydrocarbon extraction. This resulted in an area within the small pore spaces not contacted by CO_2 and surrounded by surfactant solution. While there was good bubble formation after surfactant breakthrough, it didn't divert fluid flow enough to displace the oil. The presence of a CO_2 meta-stable phase in this experiment did not seem to increase displacement efficiency in any way. There was also a significant decrease of small CO_2 bubbles or oil emulsion within the micromodel.

The displacement performed at 800 psia differed quite a bit with the previous displacements. In addition to the decreased pressure drop and lack of bubble formation, some residual oil found within the micromodel took the form of individual blobs of oil floating in the surfactant solution or adhering to the pore walls. Unlike the residual oil found in displacements conducted at higher pressures, it didn't change to a darker color and very little was found in the pore throats. Also, very little of this oil was displaced by spreading along the CO_2 surfactant solution interface. For the most part, these residual oil blobs remained intact as they were pushed along by the CO_2 lamellae. One possible explanation for this phenomenon is that since CO_2 extracts hydrocarbons poorly at this pressure, the oil managed to retain its integrity when it came into contact with CO_2.

5. Effect of Gas-Liquid Volumetric Ratio

Displacements with simultaneous injection of CO_2 and surfactant solution were conducted into both the MLAY and MHE micromodels at four different gas-liquid volumetric ratios; 3:1, 4:1, 5:1, and 6:1. The MLAY micromodel was initially saturated with Maljamar stock tank oil with connate water, and the MHE micromodel with either surfactant solution or just Maljamar stock tank oil.

Figure I-41 compares oil recovery for SAG displacements into the MLAY micromodel. This figure shows a slightly better recovery after 1.5 PVI in displacements conducted at higher gas-liquid volumetric ratios, with 6:1 having the highest recovery. Displacements with lower gas-liquid volumetric ratios result in higher initial recovery of oil before breakthrough, but may have no bearing on a particular ratio's ability to produce foam, divert fluid, and ultimately recover oil. Figure I-42 shows total oil recovery after breakthrough of injection fluid at 4 PVI of each of the ratios tested. In this case, total oil recovery after breakthrough increased sharply through 5:1, then dropped slightly at 6:1. Corresponding pressure drop data for these experiments is shown in Figs. I-43 and I-44. The highest pressure drop was found in the 3:1 displacement and the lowest at 6:1.

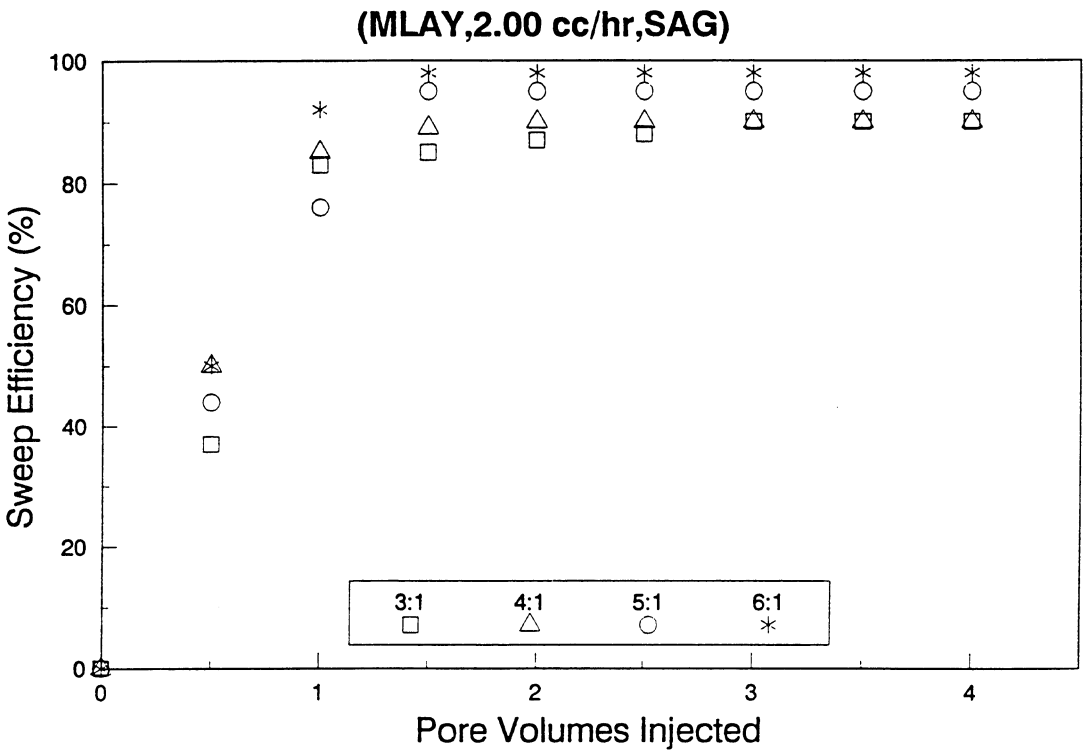

Figure I-41. Effect of injection ratio on oil recovery.

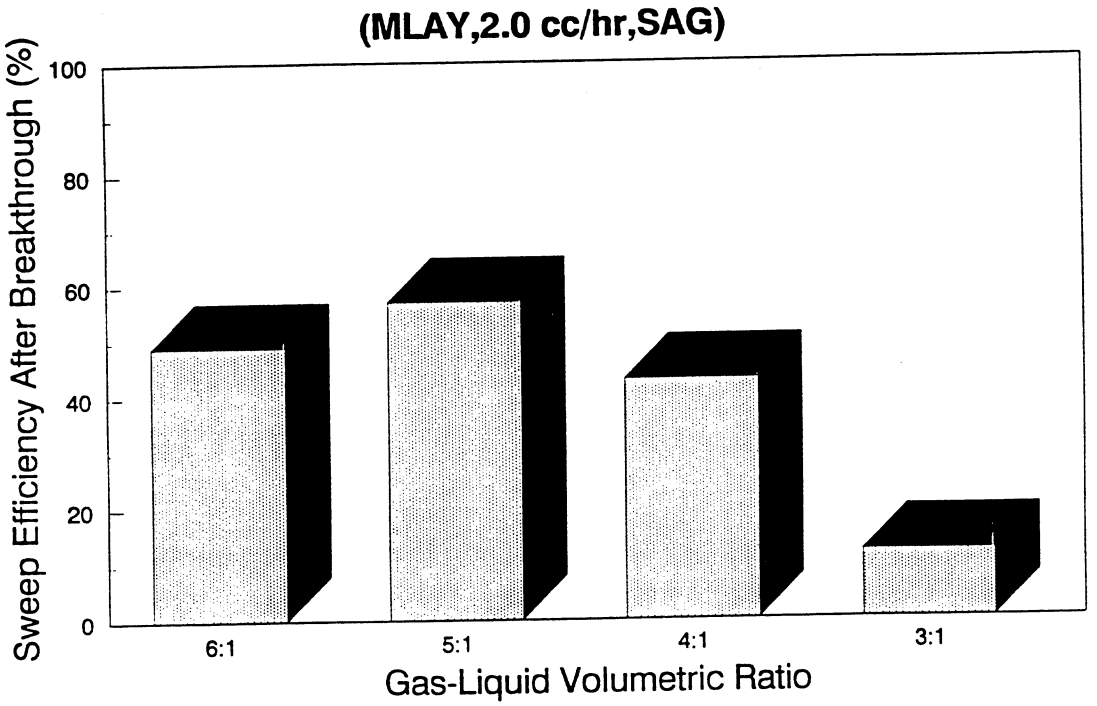

Figure I-42. Effect of injection ratio on oil recovery after breakthrough.

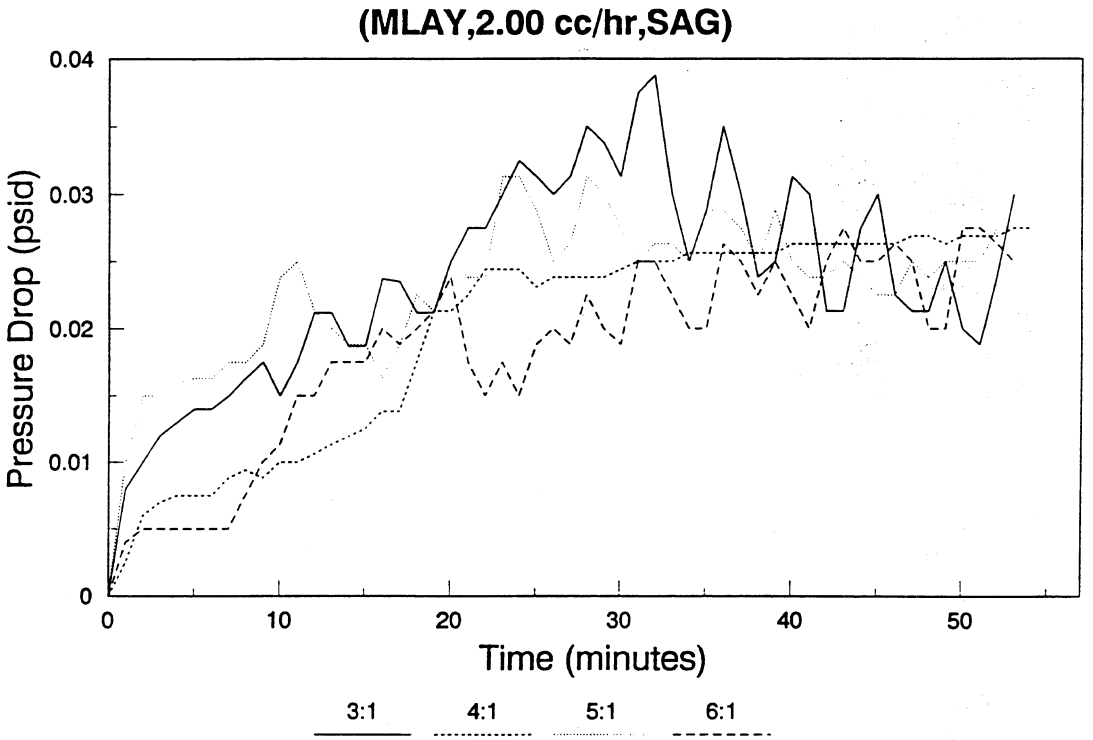

Figure I-43. Effect of injection ratio on pressure drop.

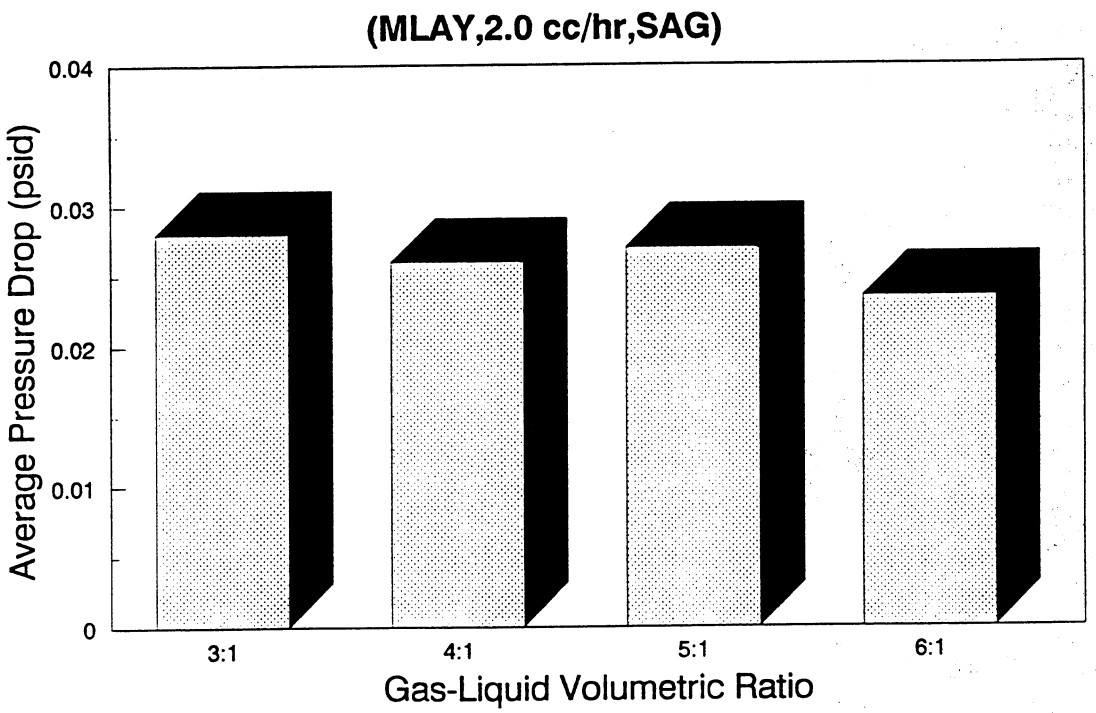

Figure I-44. Effect of injection ratio on average pressure drop.

The pressure drop at 5:1 was higher than at 4:1, so no definite trend defining the effect of gas-liquid volumetric ratio on differential pressure was found.

Usually, a CO_2 rich phase entered the micromodel first, dissolving into the crude and lightening it. Very few travelling lamellae were observed until after 0.5 PVI, and bubbles generated were generally on the order of the pore spaces in the micromodel (1.0-2.5 mm). However, there were times when as many as four or five CO_2 bubbles generated by downstream snap-off would form in one of the larger pore spaces. When this happened, fluid flow would be diverted into the smaller pore matrix. As in several of the previous experiments, several small CO_2 bubbles were produced at foam generation sites in the large pore spaces.

Experiments involving the simultaneous injection of surfactant solution and CO_2 into the MHE micromodel were conducted. Due to its complexity, we were unable to estimate displacement efficiency in the MHE micromodel accurately. However, by careful observation of each displacement, we were able to get a general idea of how well each ratio was able to recover oil.

In most cases, CO_2 entered the micromodel first and travelled along the preferential flow path (PFP). Once surfactant solution entered the PFP, much of the CO_2 chose to bypass it and flow into the tighter pore matrix. Upon surfactant solution breakthrough, however, the CO_2 again reverted almost exclusively to the PFP and moved as travelling lamellae through the micromodel. Bubbles generated were on the order of the pore spaces (0.1-1.5 mm) and were produced by either downstream snap-off or bubble subdivision. When viewed closely, what appeared to be an emulsion of CO_2, surfactant, and crude oil was observed. Bubbles within this emulsion were very stable and were much smaller than the pore spaces in the micromodel. The greater amount of foam was found in the 3 and 4:1 displacements, and the least in the 6:1 displacement. Oil recovery by 4 PVI in all of the displacements was very good. However, recovery up to 2 PVI was highest in the 3 and 4:1 displacements. The pressure drop data in Figs. I-45 and I-46 shows that differential pressure increases as the gas-liquid volumetric ratio decreases. This is in contrast with the somewhat skewed pressure drop data for the MLAY micromodel, where the 5:1 ratio had a higher pressure drop than 4:1. It seems clear in this case that higher surfactant concentrations create a higher pressure drop.

Figures I-47 and I-48 compare pressure drop data in experiments involving the simultaneous injection of surfactant solution and CO_2 into the MHE micromodel saturated with surfactant solution. A quite definite trend was observed showing an increasing pressure drop corresponding to a decreasing gas-liquid volumetric ratio. When compared to the average pressure drops of displacements into the MHE micromodel saturated with crude oil (Fig. I-49), it is easy to see the deleterious effect oil has on foam generation. Surfactant loss owing to partitioning into the oil phase and foam coalescence upon contact with oil are two major factors contributing to lower pressure drop when oil is present. In this case, however, bubbles are formed almost immediately and are more stable. There was also an increase in foam generation and fluid diversion at higher surfactant concentrations.

6. Effect of Pregenerated Foam

Pregenerated foam displacements into the MLAY micromodel were conducted at gas-liquid volumetric ratios of 3, 4, and 5:1. Pregenerated foam was produced by the simultaneous injection of CO_2 and surfactant solution into a three-by-five inch Berea sandstone core with a pore volume of

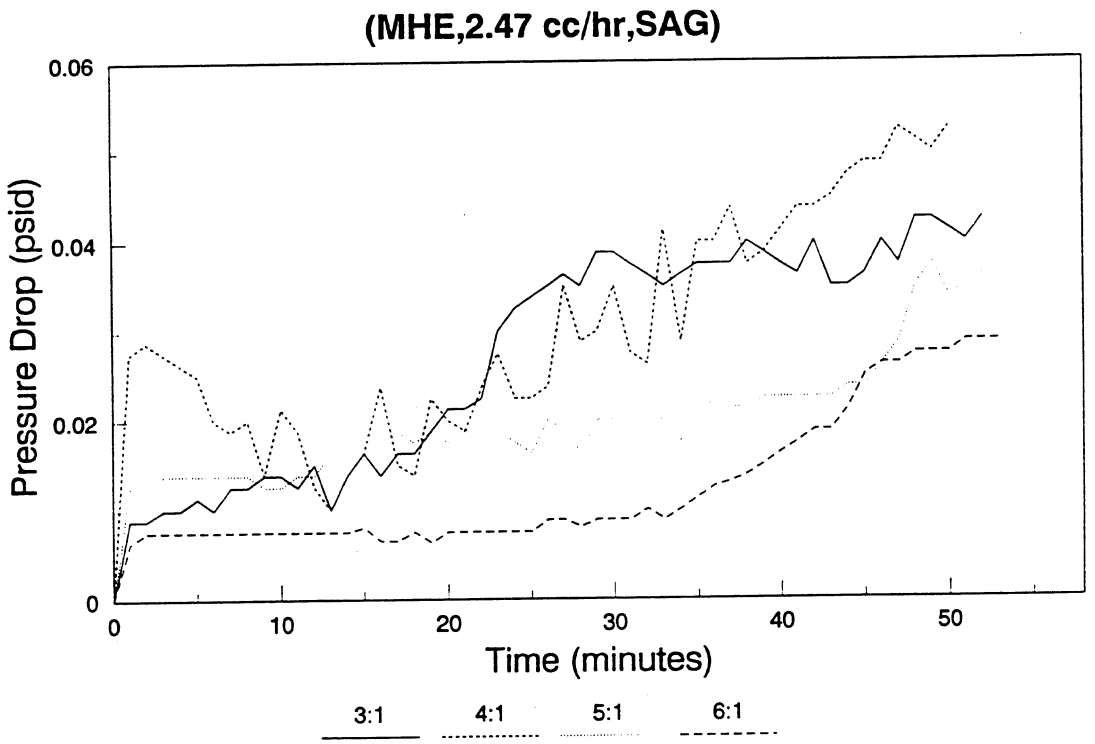

Figure I-45. Effect of injection ratio on pressure drop.

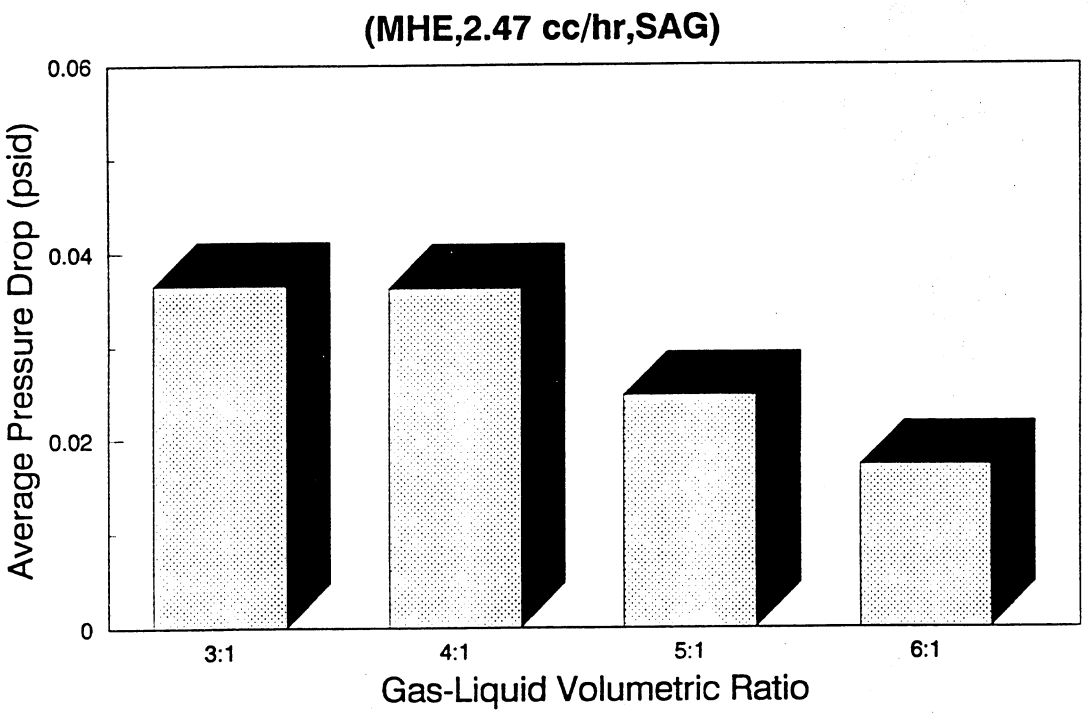

Figure I-46. Effect of injection ratio on average pressure drop.

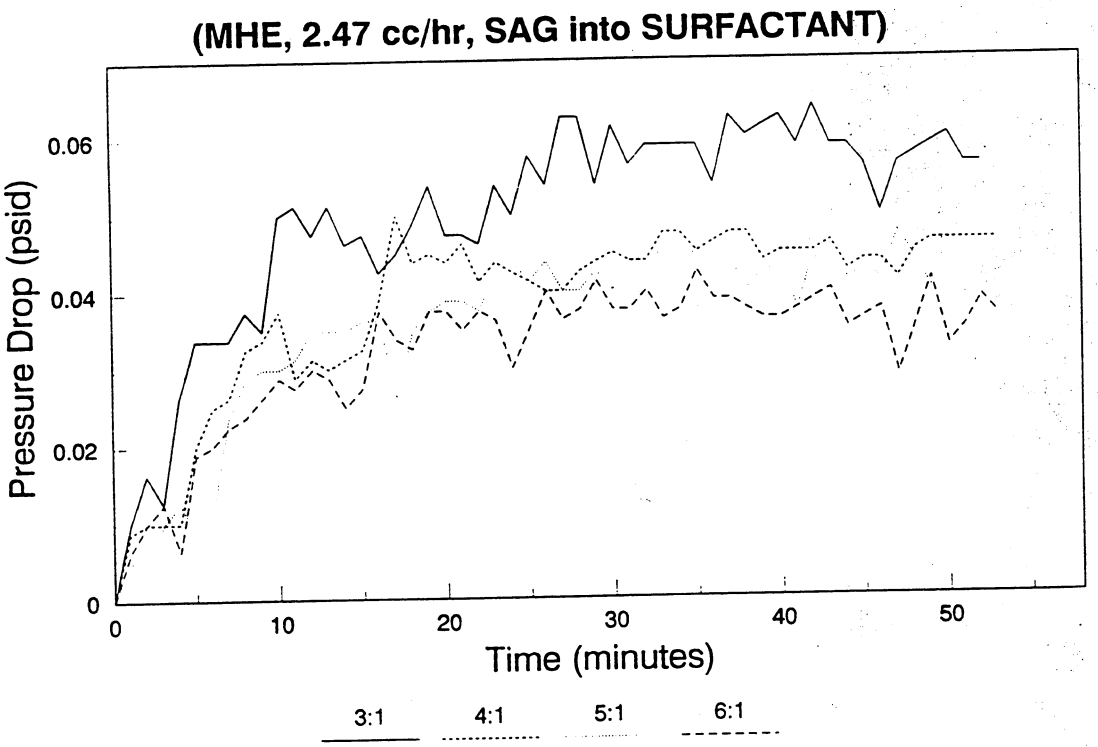

Figure I-47. Effect of injection ratio on pressure drop.

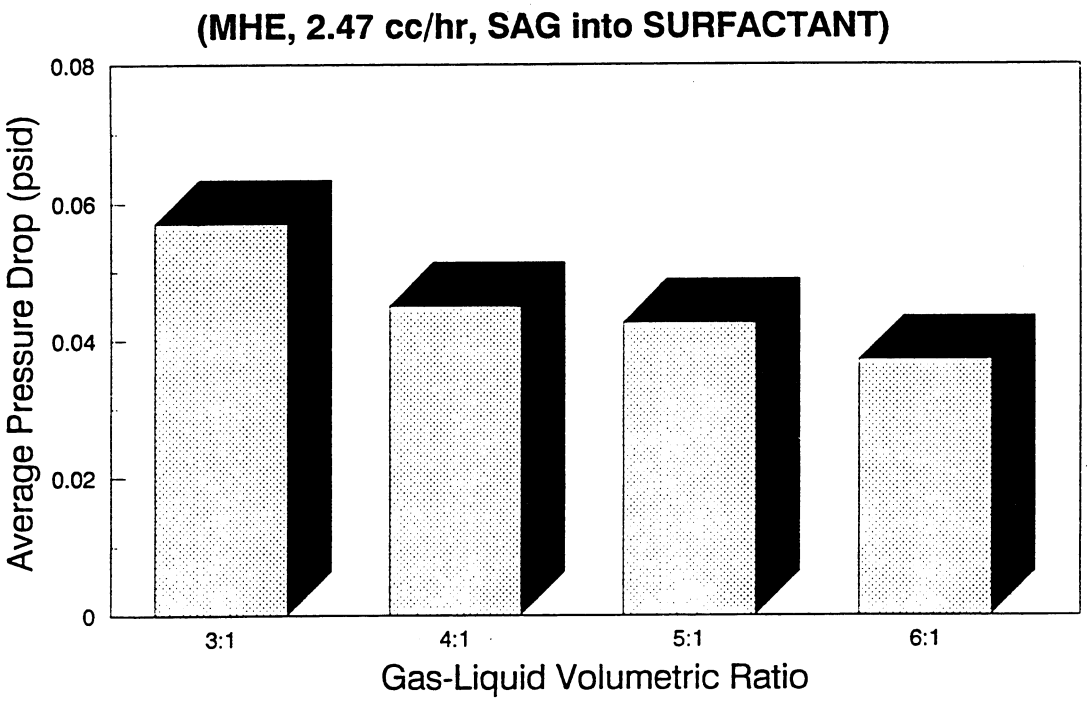

Figure I-48. Effect of injection ratio on average pressure drop.

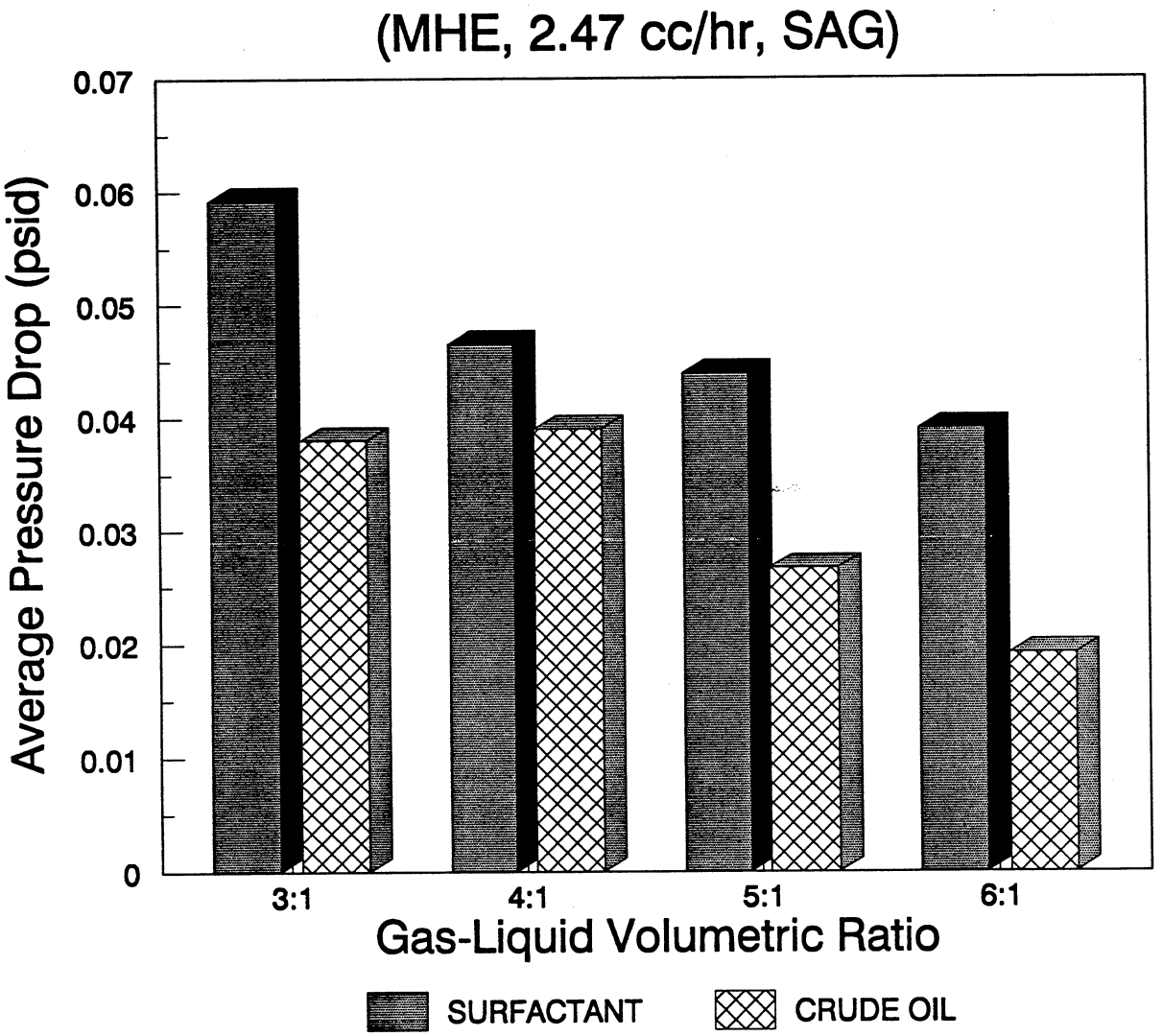

Figure I-49. Effect of injection ratio on average pressure drop.

approximately 12 cm^3. The resulting CO_2-surfactant solution foam was then injected into the micromodel. Initial saturation in these displacements was Maljamar stock tank oil with connate water.

Pregenerated foam entered the micromodel as a high-density foam of very small bubbles (on the order of the pore size of the core used in the foam generator). In previous experiments, there was some coalescence of foam upon initial contact with oil in the micromodel, which caused the foam to break down into individual phases of CO_2 and surfactant solution. In this set of experiments, the injection rate was high enough that there was always enough new foam being introduced into the model to overcome foam coalescence. The result was a stable foam front throughout the micromodel. Upon analysis of these experiments, there did not seem to be an optimum gas-liquid volumetric ratio. A 3:1 gas-liquid ratio produced slightly better recovery up to 1.5 PVI, but after 1.5 PVI, all three ratios exhibited similar results, with over 95% recovery after 2.5 PVI.

Figure I-50 compares sweep efficiency of a pregenerated foam displacement in the MLAY micromodel saturated with oil with connate water. The gas-liquid volumetric ratio was constant at 4:1. In these experiments, the PRE displacement had a higher recovery than the SAG displacement. Improved recovery in the PRE displacement was caused by the high density foam, which consistently blocked pores and caused excellent fluid diversion. Bubble size in the SAG displacements was on the order of the size of the pores in the micromodel (1.0-2.5 mm) and, while the bubbles did block pores and cause diversion, they were not as efficient as the high density foam in the PRE displacement. Figure I-51 shows the pressure drop history of these displacements. The larger pressure drop in the PRE displacement may have been caused by the high-density foam formed of very small bubbles. The high density foam may have affected pressure drop in three ways. First, the texture of the foam in the PRE displacements has an inherent effect on pressure drop because the high density of small bubbles has a higher viscosity than *in situ* generated foams. Second, the dense foam acts to reduce the amount of mixing that occurs between CO_2 and crude oil. When CO_2 and crude oil mix, as in SAG displacements, there is a reduction in viscosity of the oil in the micromodel. The lower viscosity of crude oil in the micromodel causes lower pressure drop. And third, as a result of the superior blocking properties of the foam, much of the injection fluid is diverted into the smaller pores.

While preliminary reports on pregenerated foam are encouraging, an analysis of pressure drop, oil recovery, and entry time of injection fluid into the micromodel reveals that injection fluid may have been flowing into the micromodel at a higher than expected flow rate. This may have been caused by the foam generator creating a pressure gradient, which resulted in fluid flowing faster out of the core than it was flowing in. While the micromodel apparatus is a closed system and the flow rate will eventually stabilize, we do not feel that we had flow stabilized through the bypass line long enough to overcome this increase in flow rate before we injected fluid into the micromodel. As a result, we cannot be sure if the improved oil recovery and higher pressure drop in the PRE displacements was caused by the superior pore blocking ability of the foam or the increased flow rate. Our operating procedure is currently being reviewed to determine a way to achieve more consistent flow into the micromodel.

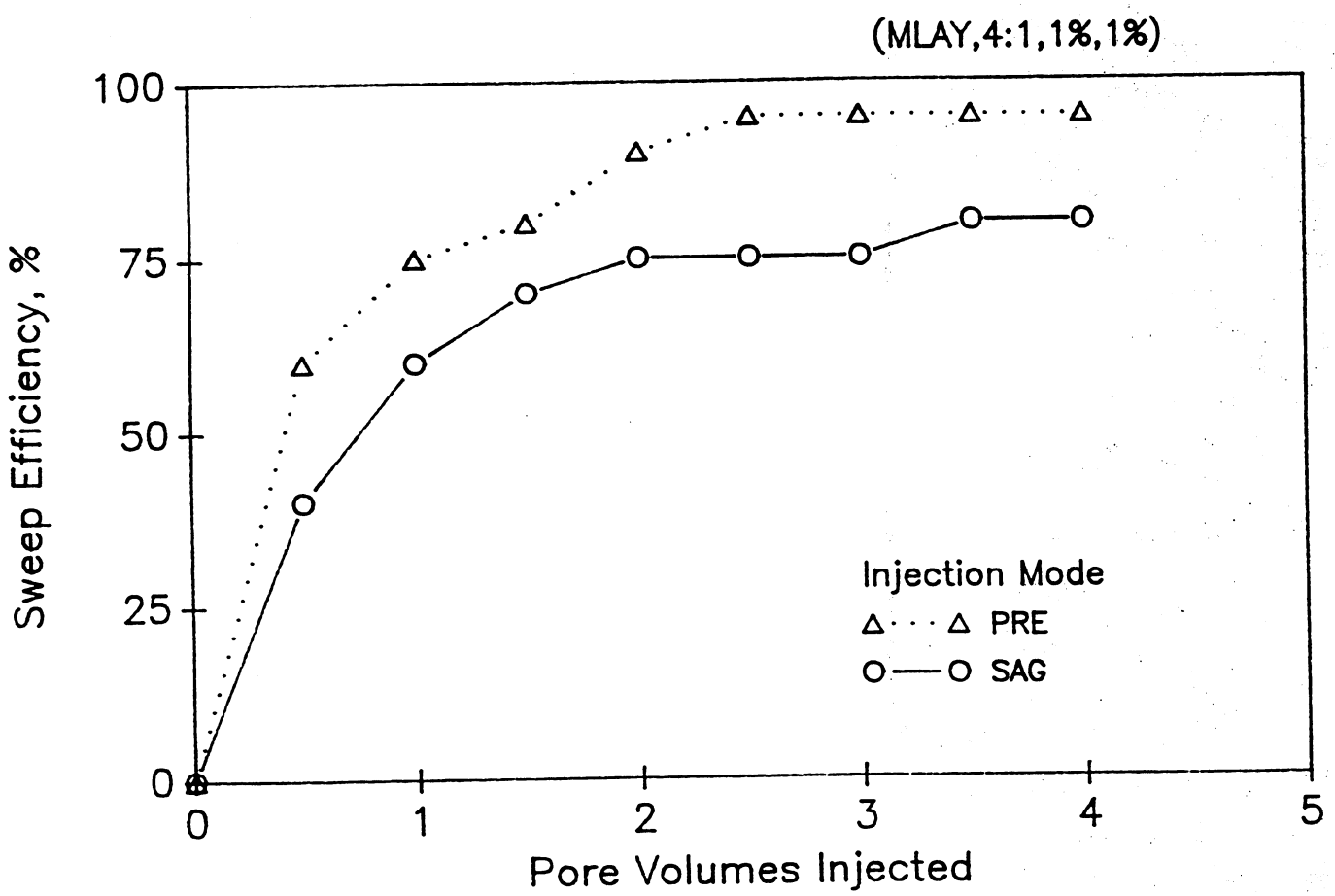

Figure I-50. Effect of injection mode on oil recovery at 2.00 cm^3/hr.

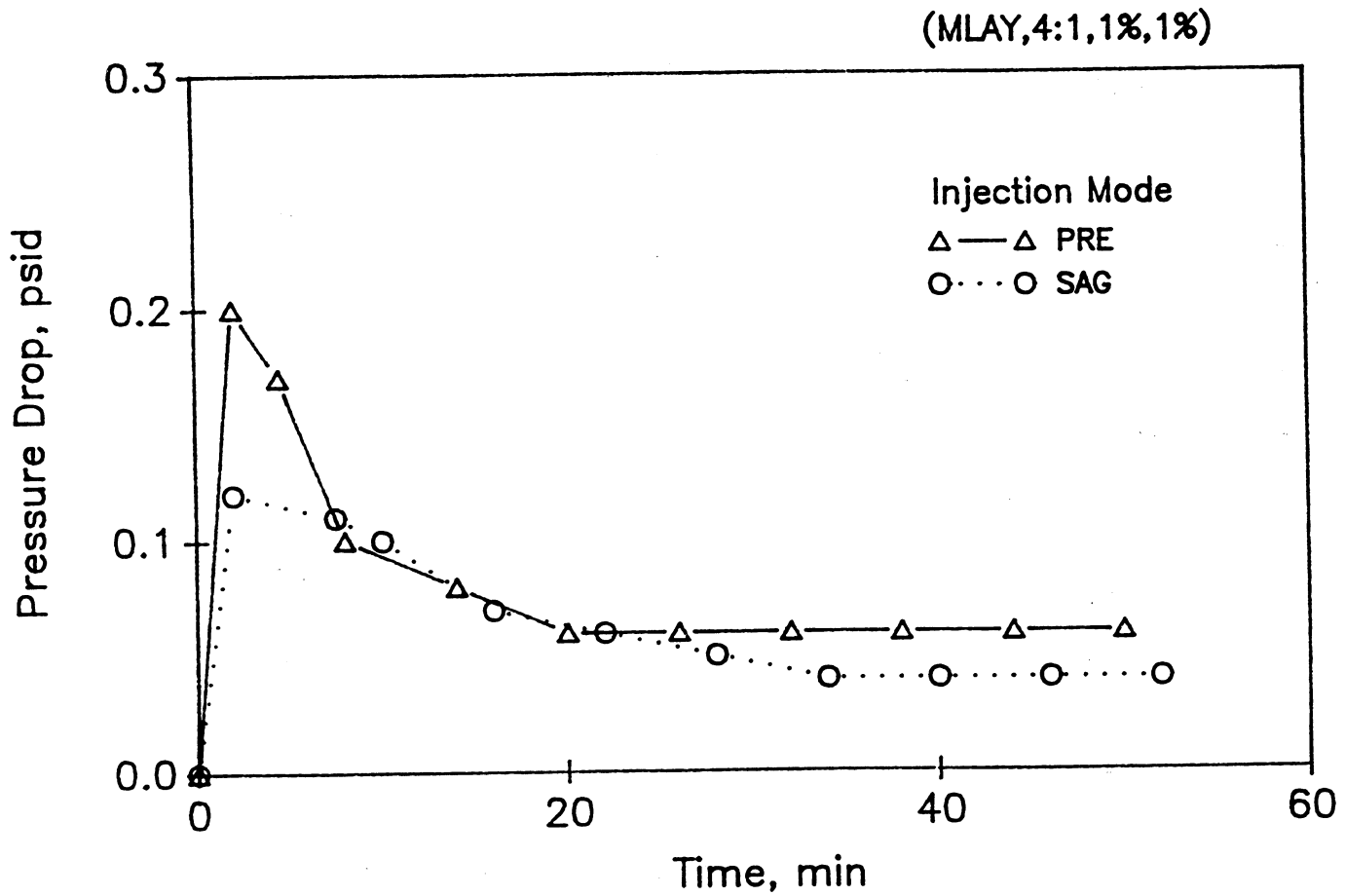

Figure I-51. Effect of injection mode on pressure drop at 2.00 cm^3/hr.

7. Conclusions

a. Residual oil was mobilized more effectively in SAG displacements than in WAG or pure CO_2 displacements in the MLAY micromodel.

b. With pure CO_2 displacements into the MLAY micromodel saturated with Maljamar oil, an increase in CO_2 pressure resulted in improved sweep efficiency.

c. With SAG displacements into the MLAY micromodel saturated with Maljamar oil, there did not appear to be as strong a dependency of CO_2 pressure on sweep efficiency as in the WAG and pure CO_2 displacements.

d. With SAG displacements into the MHE micromodel saturated with Maljamar oil or surfactant solution, a decrease in gas-liquid volumetric ratio created an increase in pressure drop.

e. In the MLAY micromodel saturated with Maljamar oil, WAG displacements had higher pressure drops than SAG displacements at all pressures tested.

f. In both WAG and SAG displacements conducted into the MLAY micromodel saturated with Maljamar oil, a decrease in CO_2 pressure generally resulted in an increased pressure drop and decreased sweep efficiency.

In addition to the conclusions stated above, several other conclusions were drawn from research conducted previously.

g. Foam bubbles coalesced, and foam generation was inhibited when foaming agents flowed into an oil saturation. However, if there is a large enough water barrier between the oil and the foam, the oil may not cause coalescence. So, in systems where waterflooding is an important mechanism, the dissolvability effect that oil has on foam may be reduced.

h. Foam was generated at the front of both CO_2 and surfactant slugs.

i. Higher surfactant concentrations improved foamability over the range of concentrations tested.

j. Fluid diversion can be caused by not only foam and lamellae, but also by multiple interfaces of oil, CO_2, surfactant solution, and multiphase microemulsions.

k. In the absence of a discontinuous CO_2 phase (foam), surfactant solution inhibited oil/CO_2 contact and oil recovery because the CO_2 preferentially flowed through the surfactant solution phase.

l. Foam was generated by upstream snap-off as well as downstream snap-off and bubble subdivision, which are equally important foam generation mechanisms.

m. The mixing of fluids and the aspect ratio of the porous media are the most important factors in foam generation.

n. A wider distribution of pore sizes can promote better mixing between fluids, hence enhancing the generation of foam.

o. In preferential flow path systems, the upstream aspect ratio (flow inlet to the preferential flow path) can have a large effect on zone blockage.

p. Simultaneous injection of CO_2 and surfactant solution is more effective in high permeability channel blockage than single phase CO_2 injection into a surfactant solution.

q. In the MHE micromodel saturated with Maljamar oil, WAG displacements had a lower sweep efficiency than SAG displacements at pressures above the MMP.

r. With SAG displacements in the presence of Maljamar oil, an increase in flow rate resulted in improved sweep efficiency in the MHE micromodel. For WAG displacements, an increase in flow rate can have the opposite effect on recovery.

E. MECHANISTIC STUDIES OF HIGH PRESSURE GAS/FOAM FLOW: COREFLOOD EXPERIMENTS

Modeling of foam flow through porous media requires the relationship between gas mobility in the presence of foam and surfactant concentration, fluid saturations, pressure, and interstitial gas velocity. Coreflood experiments can be correlated with micromodel studies to develop empirical relationships for gas mobility.

Under simultaneous injection of CO_2 and surfactant solution, foam is formed inside the core when conditions favorable for foam formation are met. Our investigations were therefore concerned with what happens when the gas encounters surfactant solution in the porous medium. We wanted to know the conditions favorable for foam formation and the gas mobility in the presence of foam.

1. Apparatus

The coreflood apparatus is shown in Fig. I-52. The original design of the apparatus as well as experimental procedures were described in the paper of Chang *et al.*[106] Several changes have been made to the apparatus during the past year. The Honeywell and Sensotec pressure transducers were moved inside the constant temperature oven. A chart recorder was installed to record the pressure drop across the core. A Cheminert Multiport Rotary Valve was also installed to collect the effluent. To prevent the injection of rust into the core and the corrosion of the pump, floating piston accumulators were added within the oven.

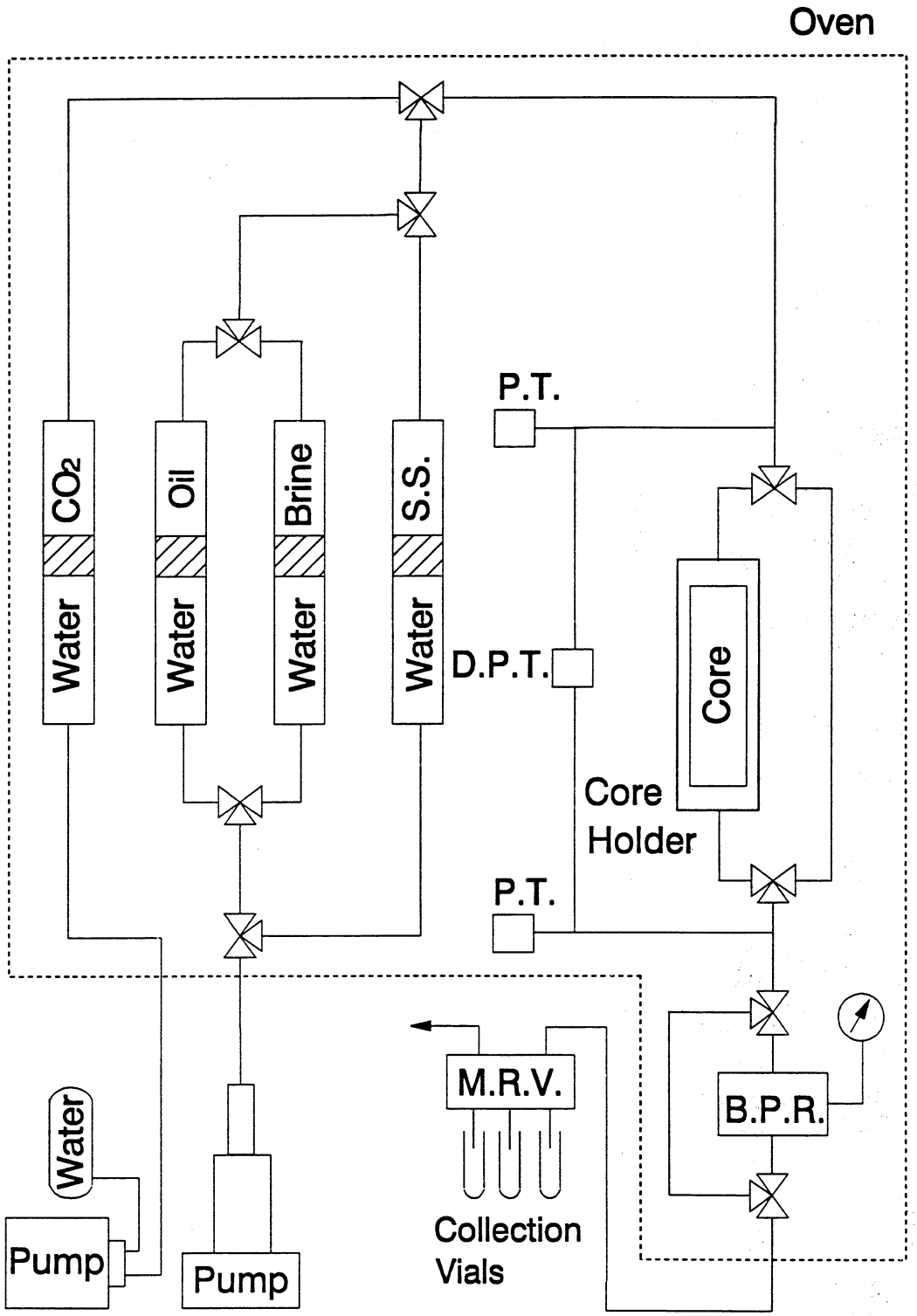

Figure I-52. Schematic of CO_2/foam coreflood apparatus.

2. Description of the Experiment

Eighteen experiments have been performed in the absence of oil with various gas and liquid injection rates as shown in Table I-22. These experiments were intended to determine the maximum mobility reductions as a result of foaming without the deleterious effect of oil. The core was initially saturated with brine. The experimental conditions are shown in Table I-23.

Six experiments were run for the purpose of displacing oil from the cores, as shown in Table I-24. The first two experiments were run without oil because we started using cores from a new Berea sandstone block that has different core properties (Table I-25) than those used in the previous set of experiments. The core was initially saturated with brine. These are the base case experiments. In the next two experiments, oil was displaced from a homogeneous core with simultaneous injection of CO_2 and brine (HOWAG-2), and then with simultaneous injection of CO_2 and surfactant solution (HOSAG-2). In the last two experiments, the corefloods were performed with a heterogenous core, which consists of a Berea sandstone core with a concentric hole in the middle filled with a sand pack (Fig. I-53). The properties of this core are shown in Table I-26. In these experiments, oil was displaced from the core by simultaneous injection of CO_2 and brine (HEWAG-1), and also by simultaneous injection of CO_2 and surfactant solution (HESAG-1).

The cores in the oil displacement experiments were initially saturated with Texaco II oil at irreducible water saturation. The brine used in all the experiments is 1% NaCl solution and the surfactant solution is 1% Alipal-CD 128 in 1% NaCl solution. All the experiments were conducted at a constant temperature of 100°F with the core outlet back-pressure regulator set at 1000 psig.

3. Results and Discussion

Figure I-54 shows that the critical interstitial gas velocity (V_{gc}) increases with increasing gas fraction. The relationship between the critical gas fraction (F_{gc}) and V_{gc} is given by

$$F_{gc} = \beta\, V_{gc}^{m} \tag{I-55}$$

where β and m are constants determined experimentally. For this study, β and m are 65.5 and 0.0896, respectively. This is in agreement with the results of Friedmann *et al.*[107] Figures I-55 through I-57 show the effect of gas interstitial velocities on pressure drop for gas-liquid volumetric ratios of 10, 4, and 2, respectively. Figures I-58 through I-60 show the effect of gas-liquid volumetric ratio on the pressure drop for interstitial gas velocities of 14.3, 28.6, and 52.7 ft/D, respectively. As expected, when conditions were favorable for foam formation, the steady-state pressure drop increased with increasing gas velocity and decreasing gas-fraction or gas-liquid volumetric ratio. In Figs. I-59 and I-60, the curves for $Q_g/Q_l = 2$ and $Q_g/Q_l = 4$ cross over during the transition period. This probably is due to the effects of trapped gas and relative permeability. Further investigations will be conducted to ascertain the reasons for this phenomenon. The plot of the gas mobility vs. interstitial gas velocity for gas volume fractions of 66.7 and 80.0% shows shear-thinning behavior (Fig. I-61). The relationship between gas mobility, $\lambda_g = kk_{rg}/\mu_g$, and gas volume fraction, interstitial gas velocity, surfactant concentration, and saturations, is given by

$$\lambda_g = (k_1 F_g + k_2 V_g^{n})\,[1 + k_3 C_s\,(S_w - S_{wr})]\,[1 + k_4\,(S_o - S_{or})] \tag{I-56}$$

TABLE I-22. COREFLOOD EXPERIMENTAL PARAMETERS (SIMULTANEOUS INJECTION INTO 1% NaCl SOLUTION)

RUN NUMBER	LIQUID RATE (cm^3/hr)	GAS RATE (cm^3/hr)	Q_g/Q_l	V_g (ft/D)	INJECTION MODE
1	50.0	200.0	4.0	57.2	CO_2/Br
2	20.0	200.0	10.0	57.2	CO_2/Br
3	10.0	200.0	20.0	57.2	CO_2/Br
4	25.0	100.0	4.0	28.6	CO_2/Br
5	10.0	100.0	10.0	28.6	CO_2/Br
6	12.5	50.0	4.0	14.3	CO_2/Br
7	5.0	50.0	10.0	14.3	CO_2/Br
8	12.5	25.0	2.0	7.2	CO_2/Br
9	6.3	25.0	4.0	7.2	CO_2/Br
10	50.0	200.0	4.0	57.2	CO_2/S.S.
11	20.0	200.0	10.0	57.2	CO_2/S.S.
12	10.0	200.0	20.0	57.2	CO_2/S.S.
13	25.0	100.0	4.0	28.6	CO_2/S.S.
14	10.0	100.0	10.0	28.6	CO_2/S.S.
15	12.5	50.0	4.0	14.3	CO_2/S.S.
16	5.0	50.0	10.0	14.3	CO_2/S.S.
17	12.5	25.0	2.0	7.2	CO_2/S.S.
18	6.3	25.0	4.0	7.2	CO_2/S.S.

Br = 1% NaCl Solution
S.S. = 1% Alipal CD-128 in 1% NaCl Solution

TABLE I-23. EXPERIMENTAL CONDITIONS AND CORE PROPERTIES

Core Description	=	Berea Sandstone
Length	=	15.16 cm
Diameter	=	3.88 cm
Porosity	=	23.3%
Pore Volume	=	41.75 cm^3
Brine Permeability	=	242 md
Air Permeability	=	467 md
Temperature	=	100°F
Pressure, P_2	=	1000 psig

TABLE I-24. EXPERIMENTAL CONDITIONS

RUN ID	DISPLACING FLUIDS	DISPLACED FLUIDS	TYPE OF CORE
HOWAG-1	CO_2 + Brine	Brine	Homogeneous
HOSAG-1	CO_2 + S.S.	Brine	Homogeneous
HOWAG-2	CO_2 + Brine	Oil	Homogeneous
HOSAG-2	CO_2 + S.S.	Oil	Homogeneous
HEWAG-1	CO_2 + Brine	Oil	Heterogeneous
HESAG-1	CO_2 + S.S.	Oil	Heterogeneous

Q_g = 100 cm^3/hr
Q_l = 25 cm^3/hr
V_g = 2.86 ft/D
T = 100°F
P_2 = 1000 psig
Brine = 1% NaCl Solution
S.S. = 1% Alipal CD-128 in 1% NaCl Solution

TABLE I-25. PROPERTIES OF HOMOGENEOUS CORE

Material	=	Berea Sandstone
Length	=	14.6 cm
Diameter	=	3.88 cm
Brine Permeability	=	119 md
Porosity	=	20.0%
Pore Volume	=	34.5 cm^3

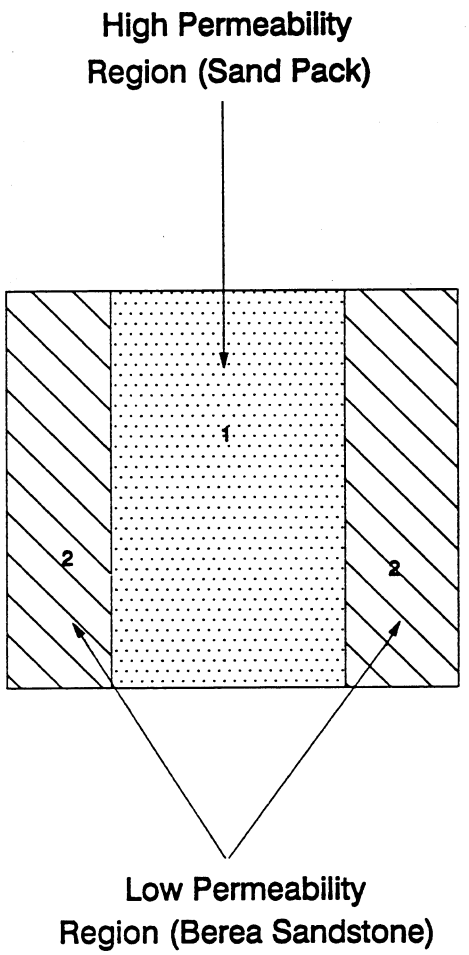

Figure I-53. Concentric core for heterogeneous coreflood studies.

TABLE I-26. PROPERTIES OF CONCENTRIC (HETEROGENEOUS) CORE

Material of Inner Zone	=	Sand Pack
Material of Outer Zone	=	Berea Sandstone
Length	=	14.1 cm
Inner Diameter, d_1	=	1.6 cm
Outer Diameter, d_2	=	3.87 cm
Inner Zone Permeability, k_1	=	15 darcys
Outer Zone Permeability, k_2	=	117 md
Inner Zone Porosity, ϕ_1	=	40.4%
Outer Zone Porosity, ϕ_2	=	20.1%
Pore Volume of Inner Zone	=	11.54 cm^3
Pore Volume of Outer Zone	=	27.5 cm^3

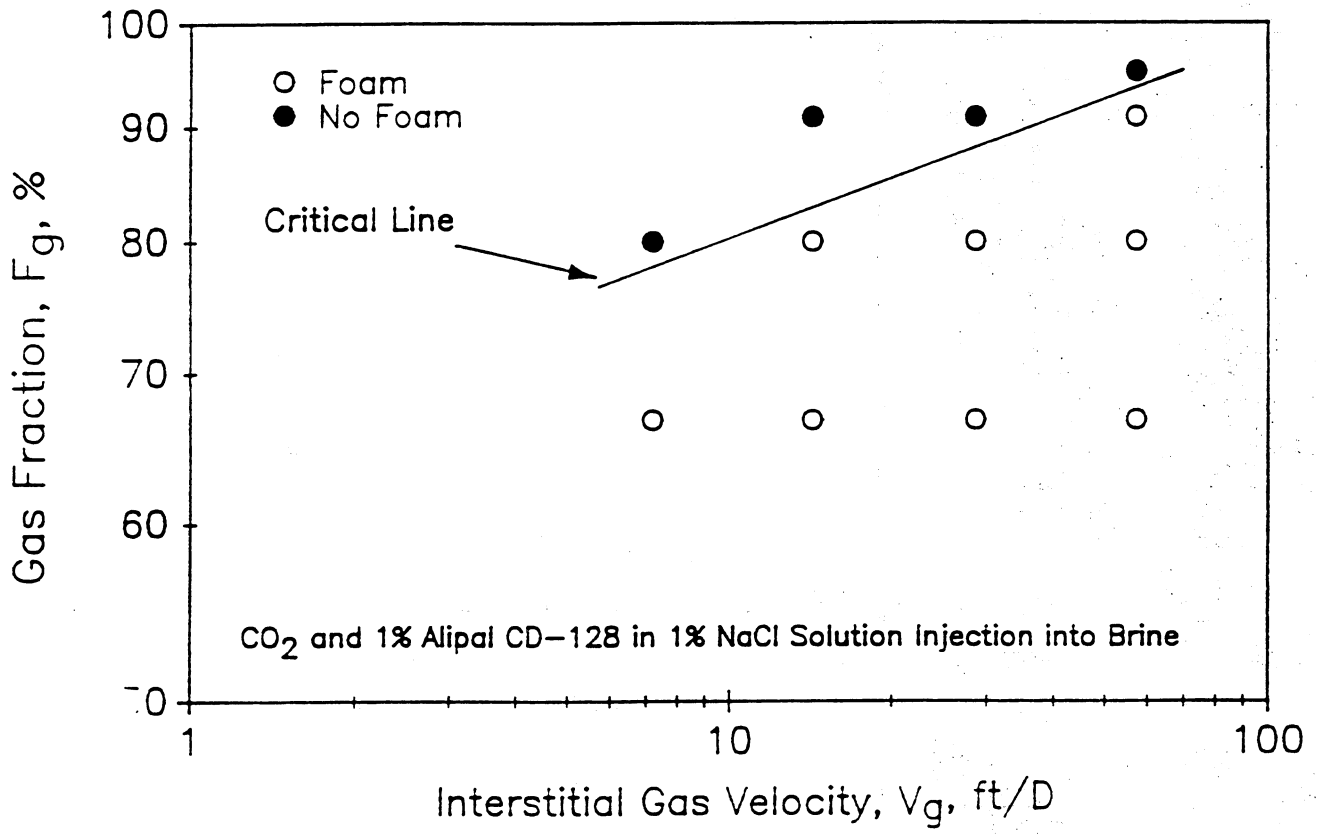

Figure I-54. Critical gas fraction and interstitial gas velocity for stable foam formation.

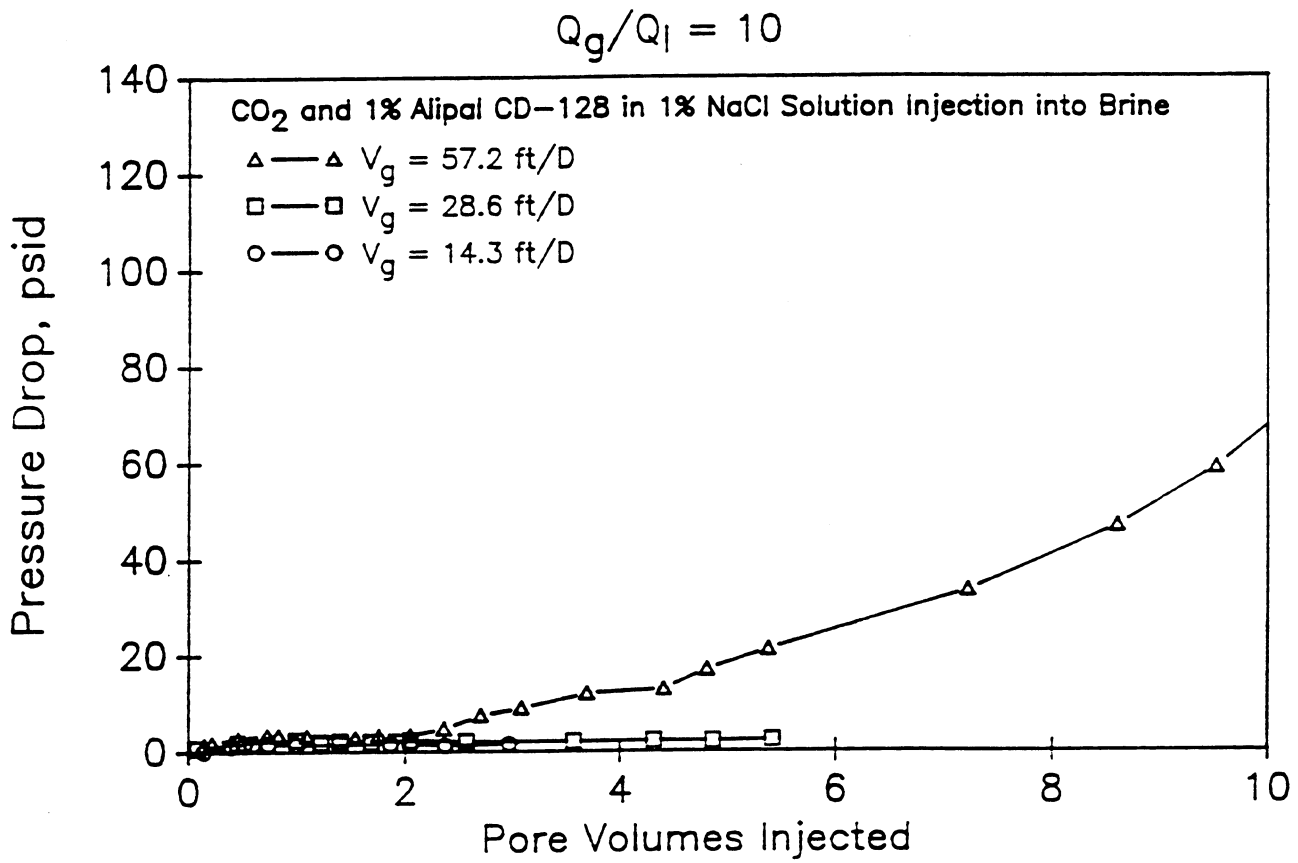

Figure I-55. Effect of interstitial gas velocity on pressure drop.

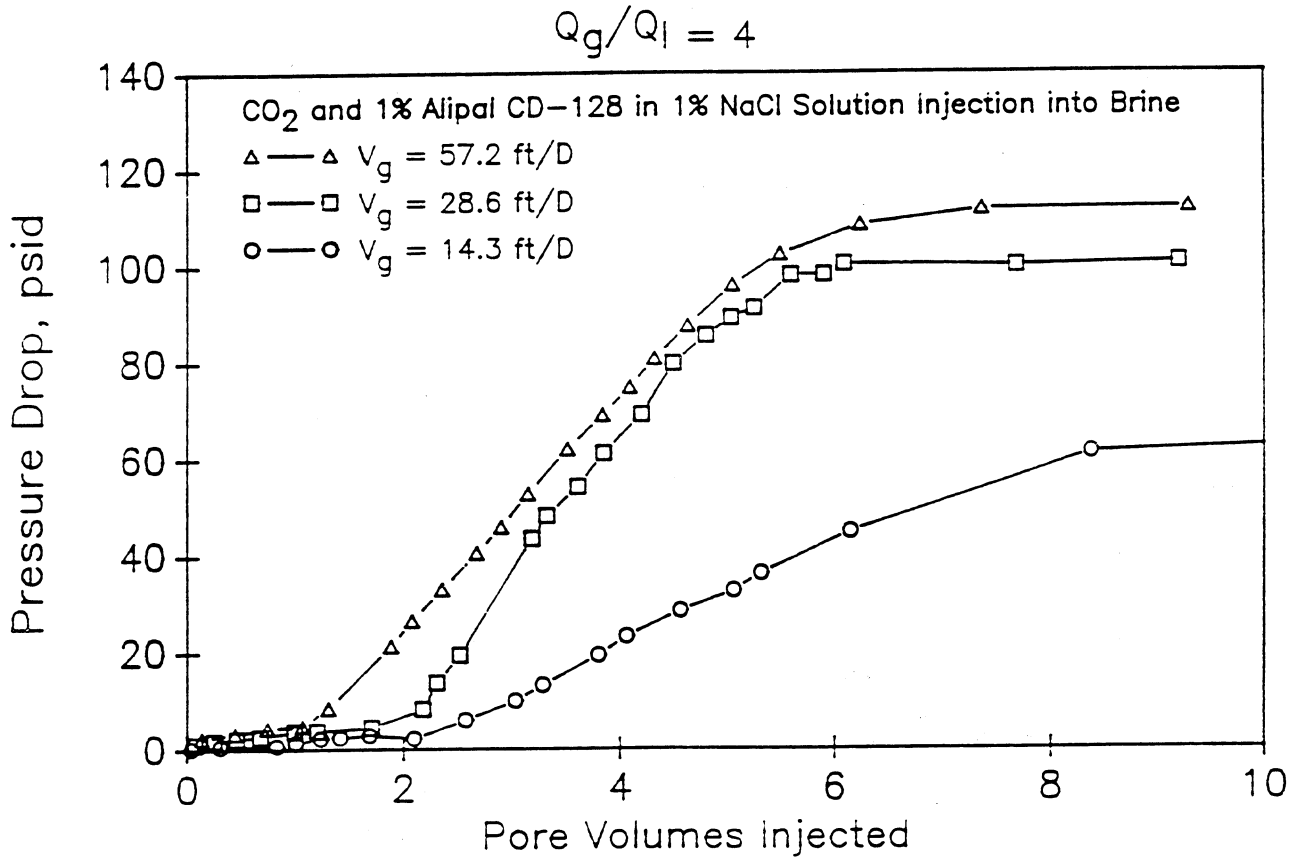

Figure I-56. Effect of interstitial gas velocity on pressure drop.

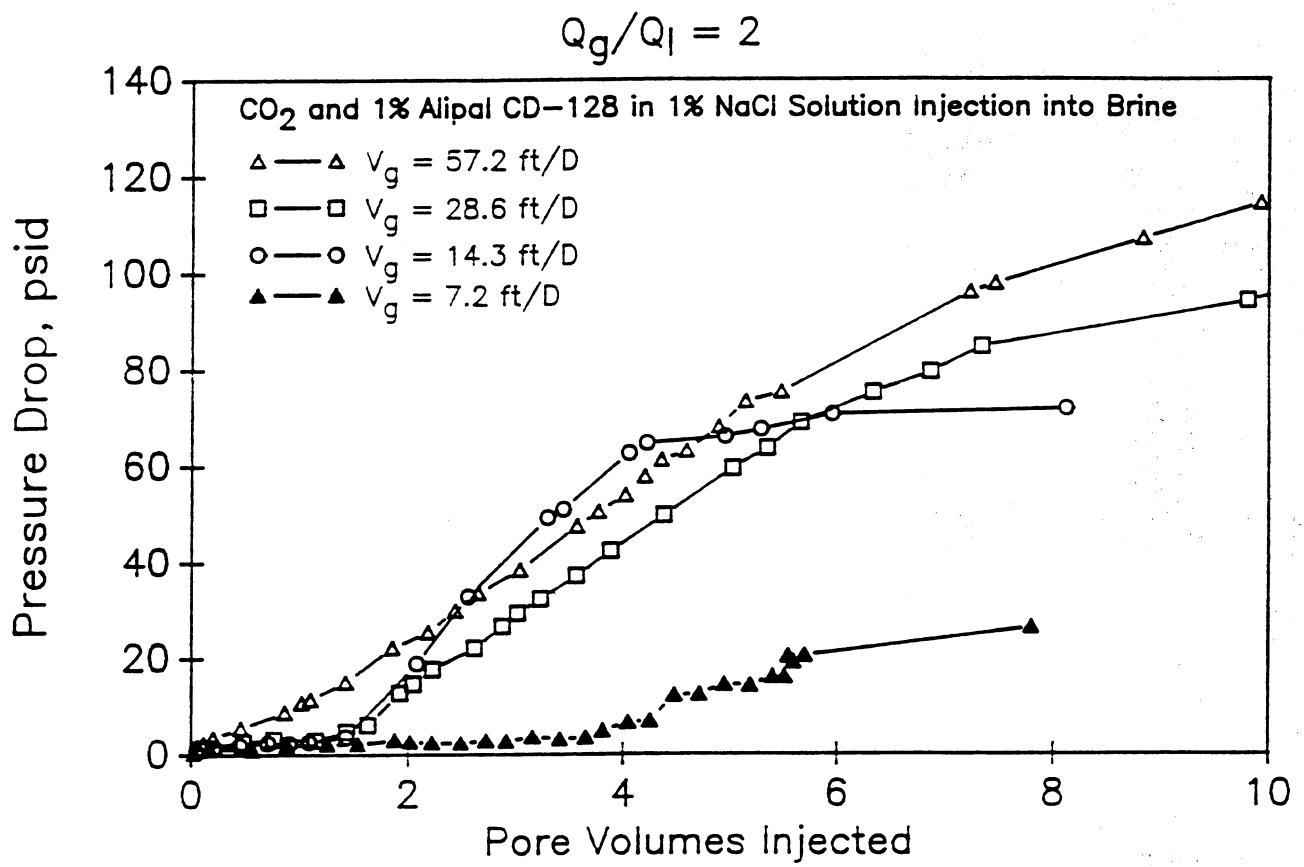

Figure I-57. Effect of interstitial gas velocity on pressure drop.

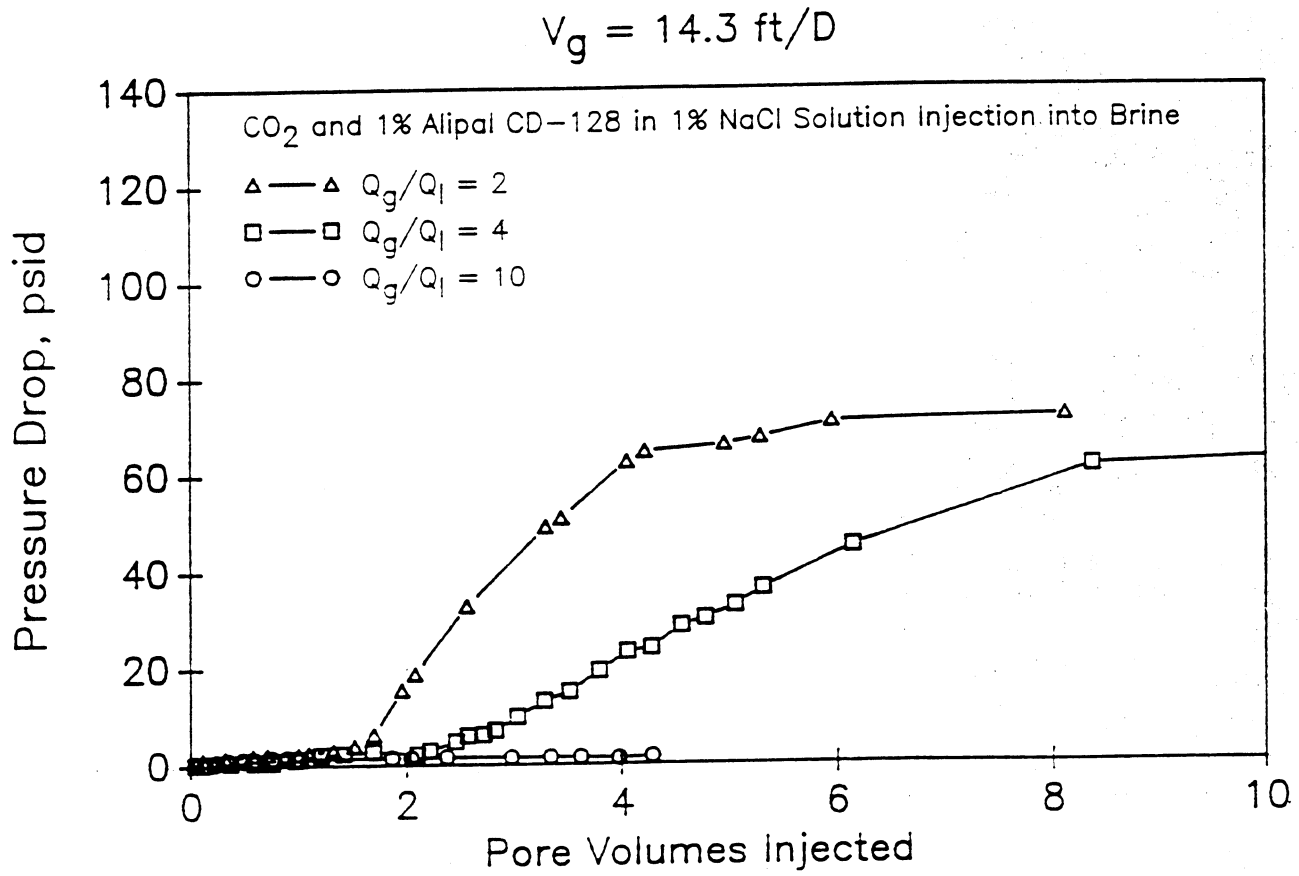

Figure I-58. Effect of gas-liquid ratio on pressure drop.

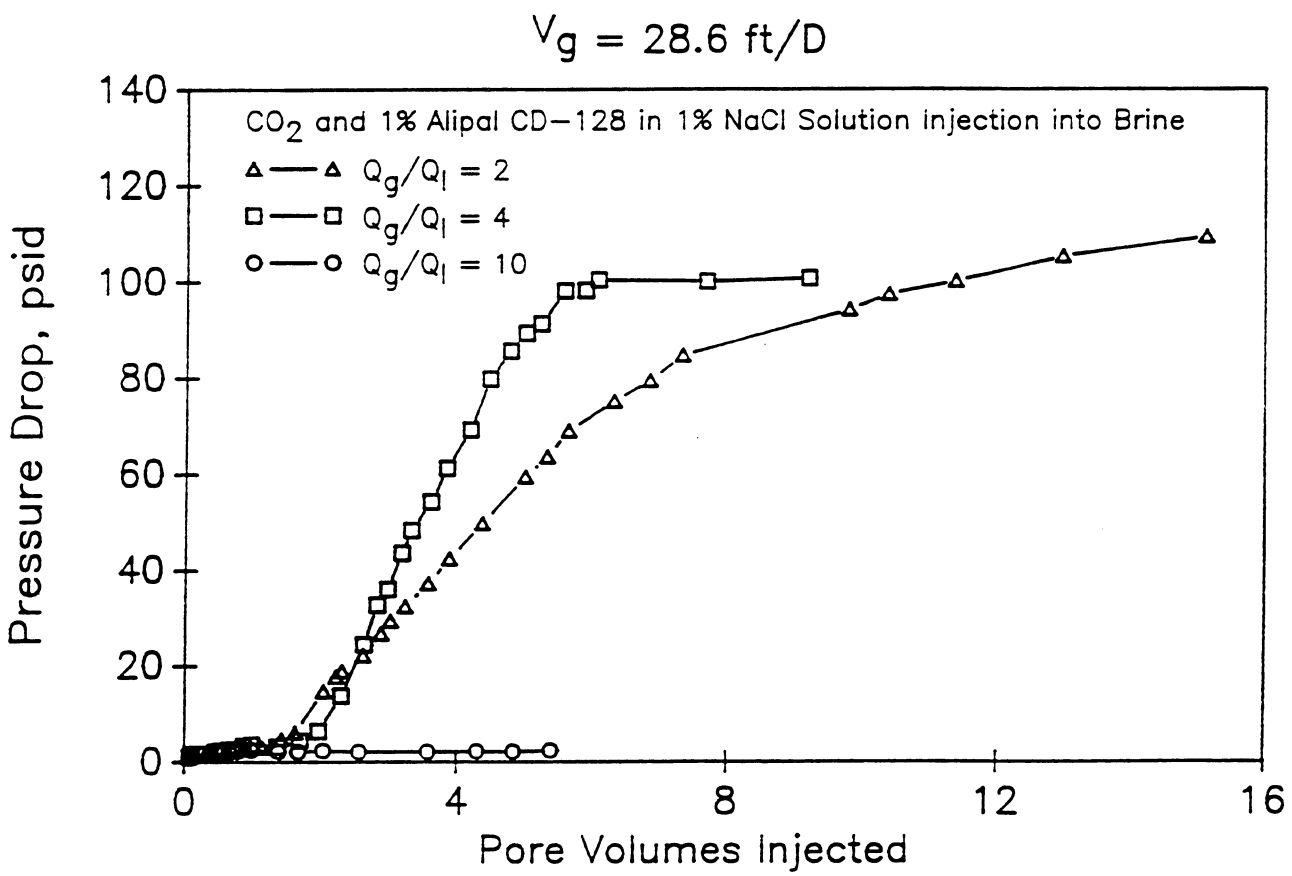

Figure I-59. Effect of gas-liquid ratio on pressure drop.

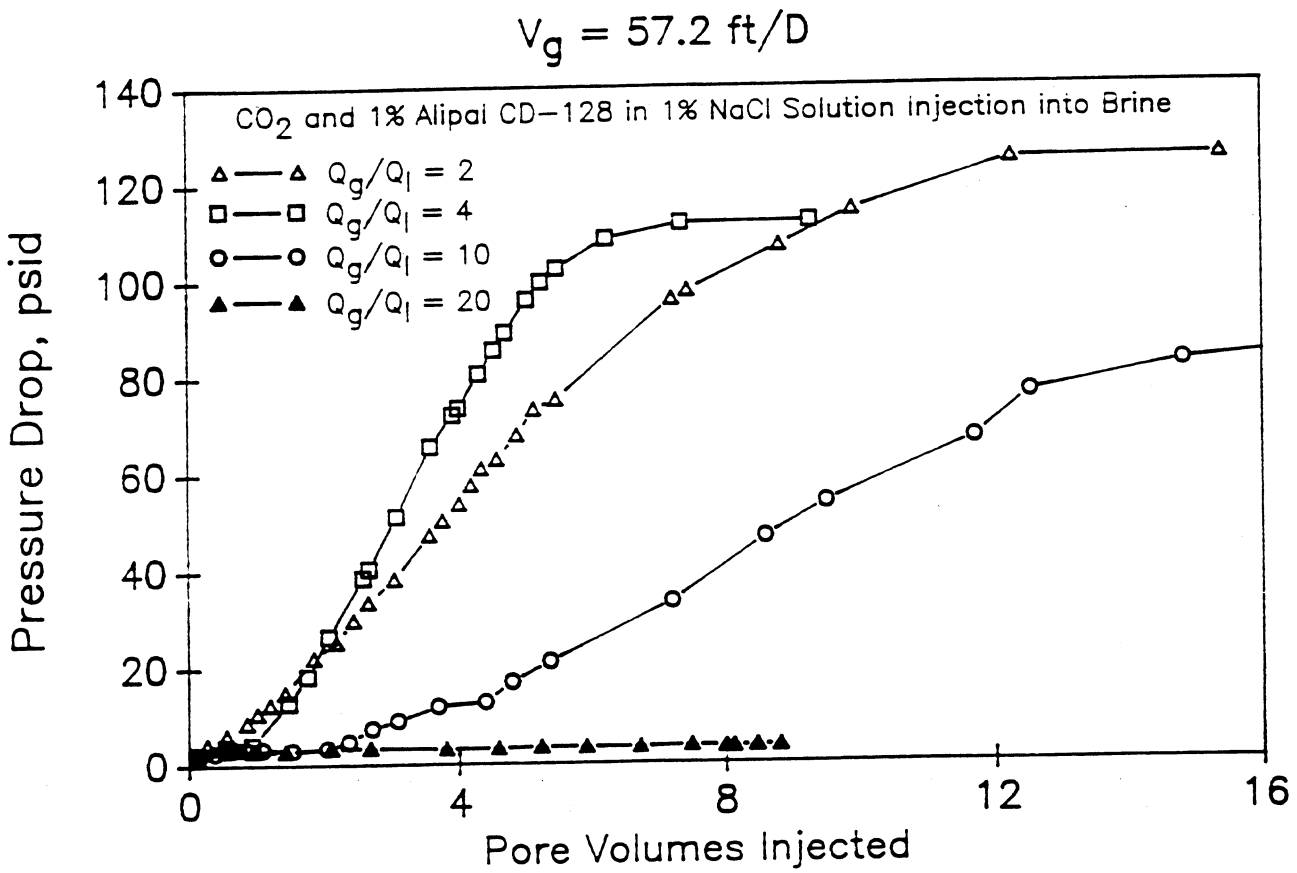

Figure I-60. Effect of gas-liquid ratio on pressure drop.

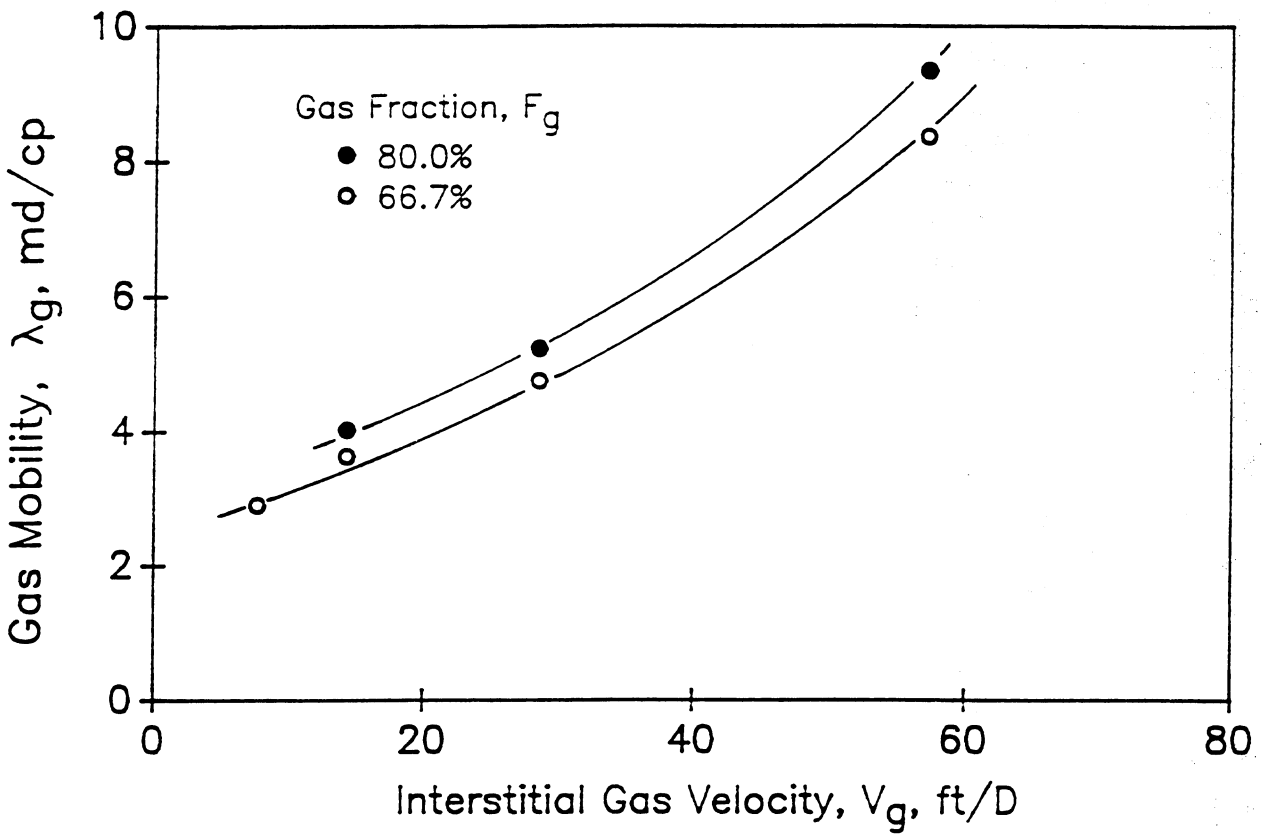

Figure I-61. Effect of gas fraction and interstitial gas velocity on gas mobility in CO_2/Alipal CD-128 foam.

where k_1, k_2, k_3, k_4, and n are constants determined experimentally. For this study, k_1, k_2, and n are 0.015, 0.66, and 0.68, respectively. Experimental results[98,108] have shown that when critical surfactant concentration for foam formation has been reached, k_3 is small. Friedmann *et al.*[107] assume that once the oil saturation is less than the critical oil saturation, k_4 is negligible. We believe that, in practice, a surfactant with negligible or small k_4 should be selected for CO_2-foam flooding of oil reservoirs. A similar approach was presented by Marfoe *et al.*[109] for estimating the apparent gas viscosity. In their model, a separate expression is required to calculate gas relative permeability.

The CO_2-foam experimental results show shear-thinning behavior in the cores. This is in agreement with the coreflood studies of Lee and Heller[108] and Sharma *et al.*[110] Additionally, Falls *et al.*[111] have shown, theoretically and experimentally from their studies with bead-packs, that shear-thinning behavior is exhibited. Similarly, Hirasaki and Lawson[112] have also shown, both theoretically and experimentally by using smooth capillaries, the shear-thinning behavior of foam. However, the CO_2-foam mechanistic studies[98] have at times shown shear-thickening behavior. We believe that in reservoir rocks, high gas velocity promotes gas and surfactant mixing as well as bubble division, and increases the fraction of flowing foam as compared with trapped foam.

Figure I-62 shows the plots of liquid production vs. pore volume of fluids injected in the cases where brine was displaced by simultaneous injection of (a) CO_2 and brine (HOWAG-1) and (b) CO_2 and surfactant solution (HOSAG-1). It is evident that the reduction in gas mobility as a result of the formation of foam in the case HOSAG-1 resulted in higher displacement efficiency. The plots of pressure drop across the core vs. pore volume of fluids injected for the cases HOSAG-1 and HOWAG-1 are shown in Fig. I-63. As would be expected, the pressure drop in HOWAG-1 reached a steady-state value of about 32 psid (66.8 psi/ft) after 3.5 pore volumes of fluids injection. In the case of HOSAG-1, the pressure began to rise slowly initially. During this period very coarse foam (large bubbles) was observed at the core outlet. As the experiment progressed, thicker foam was observed and correspondingly, higher pressure drops were recorded. The dense CO_2 that was formed when the pressure drop reached 400 psid (i.e., core inlet pressure = 1400 psig) resulted in the formation of a much denser foam, which almost blocked the pores of the core. This is reflected in the rapid rise in the pressure drop. When the experiment was stopped, because of the maximum pressure limitation of the pressure transducer, the pressure drop had risen to a value of 1040 psid (2171 psi/ft). The important result here is the total blockage of the pores that resulted from the dense foam formation. It remains to be seen whether such a blockage is possible selectively in only the high permeability regions of heterogeneous systems and in the presence of oil.

Figure I-64 shows the oil recovery performance plots of the cases in which oil was displaced from a homogeneous core by simultaneous injection of (a) CO_2 and brine (HOWAG-2) and (b) CO_2 and surfactant solution (HOSAG-2). It appears that the ultimate recovery in HOWAG-2 (60%) is higher than in HOSAG-2 (53%). However, it should be pointed out that oil continued to be produced in HOSAG-2 after the 53% oil recovery, but it came out in the form of emulsion that could not be separated. Figure I-65 shows the pressure drop history of the HOWAG-2 and HOSAG-2 cases. The pressure drop in HOWAG-2 stabilized at about 78 psid (162.8 psi/ft), while in HOSAG-2, the pressure drop was 145 psid (303.4 psi/ft) and still rising after nearly 30 pore volumes of fluids injected. The experiment was stopped because of the depletion of CO_2 in the accumulator. At this time, only coarse foam was observed at the outlet. As mentioned earlier, oil production was followed by a rather long transition period during which emulsion was produced. It would be expected that if the experiment had been carried out much longer, the oil in the core would have been cleaned out, forming thicker foam, and resulting in a higher pressure drop. The result from HOSAG-2 shows the deleterious effect of oil on foam formation. Yang and

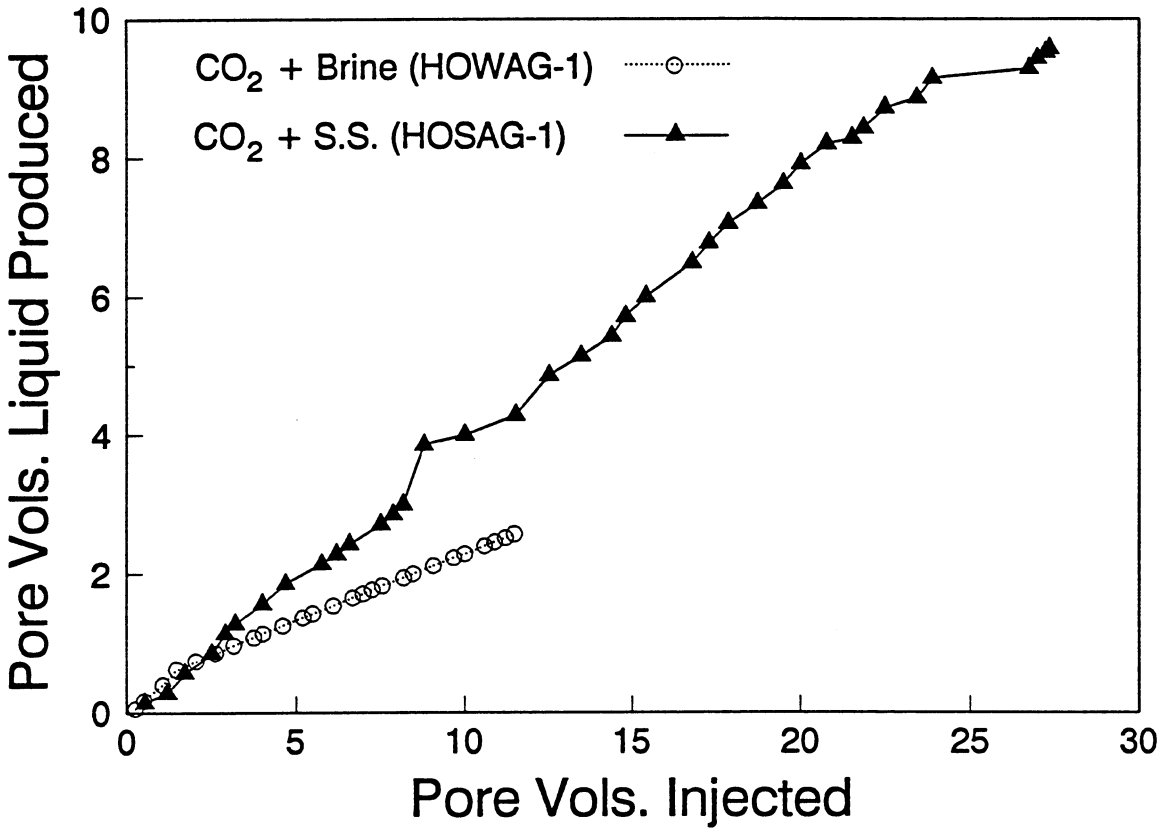

Figure I-62. Liquid production history for brine displacement from a homogeneous core by (a) CO_2 and brine (HOWAG-1) and (b) CO_2 and surfactant solution (HOSAG-1).

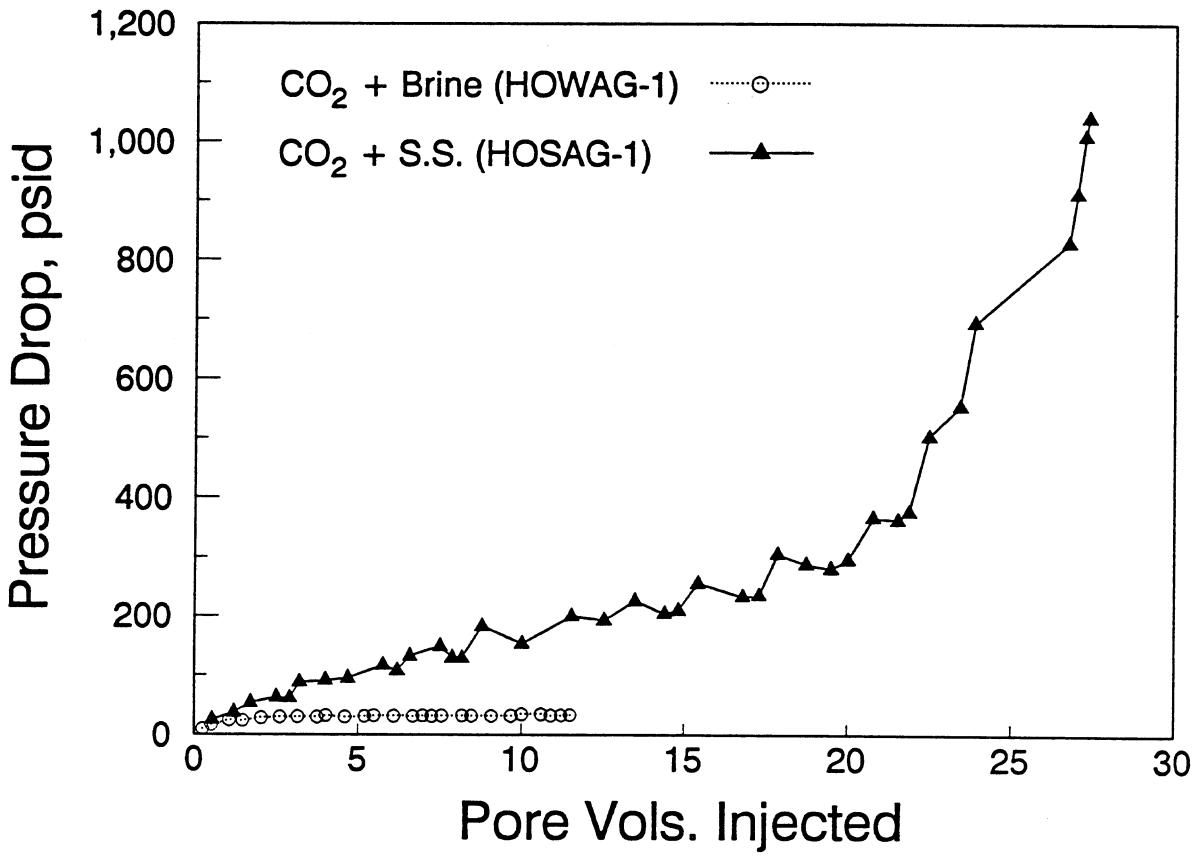

Figure I-63. Pressure drop history for brine displacement from a homogeneous core by (a) CO_2 and brine (HOWAG-1) and (b) CO_2 and surfactant solution (HOSAG-1).

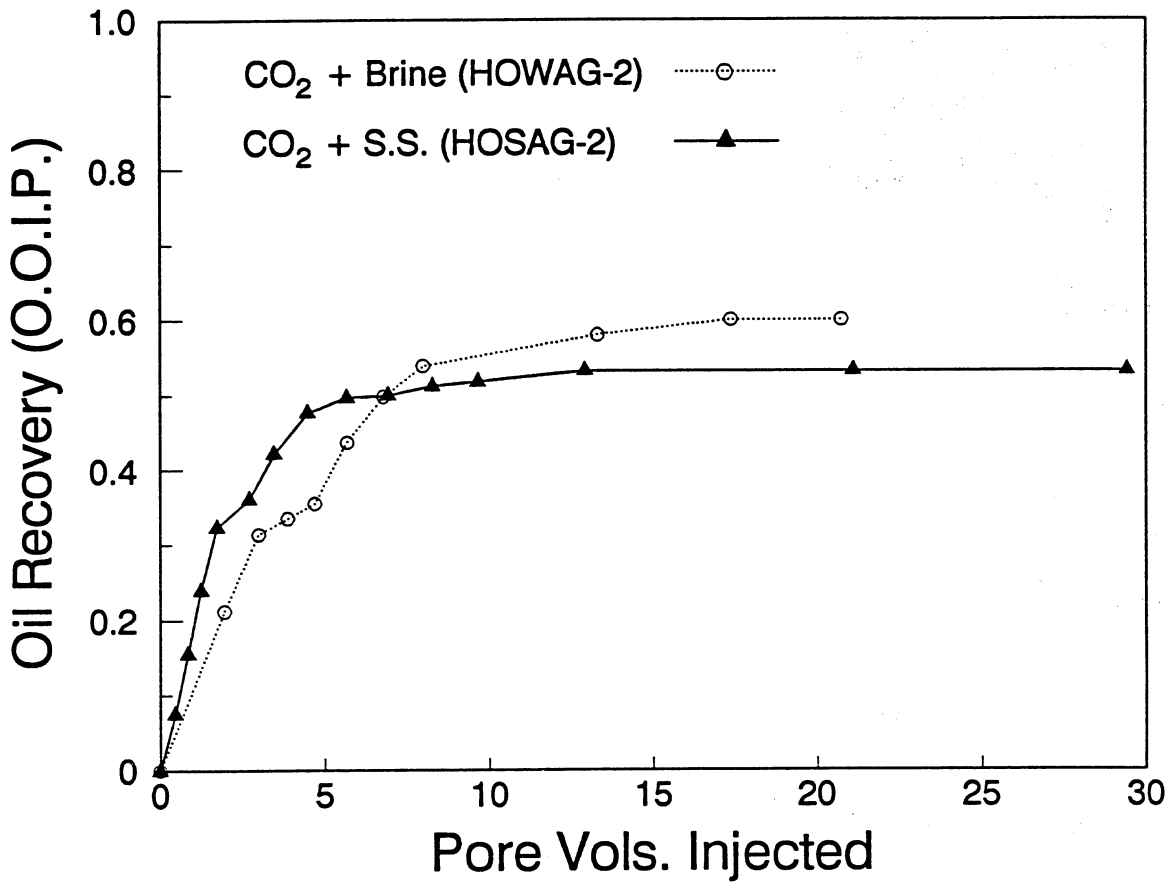

Figure I-64. Oil recovery performance for oil displacement from a homogeneous core by (a) CO_2 and brine (HOWAG-2) and (b) CO_2 and surfactant solution (HOSAG-2).

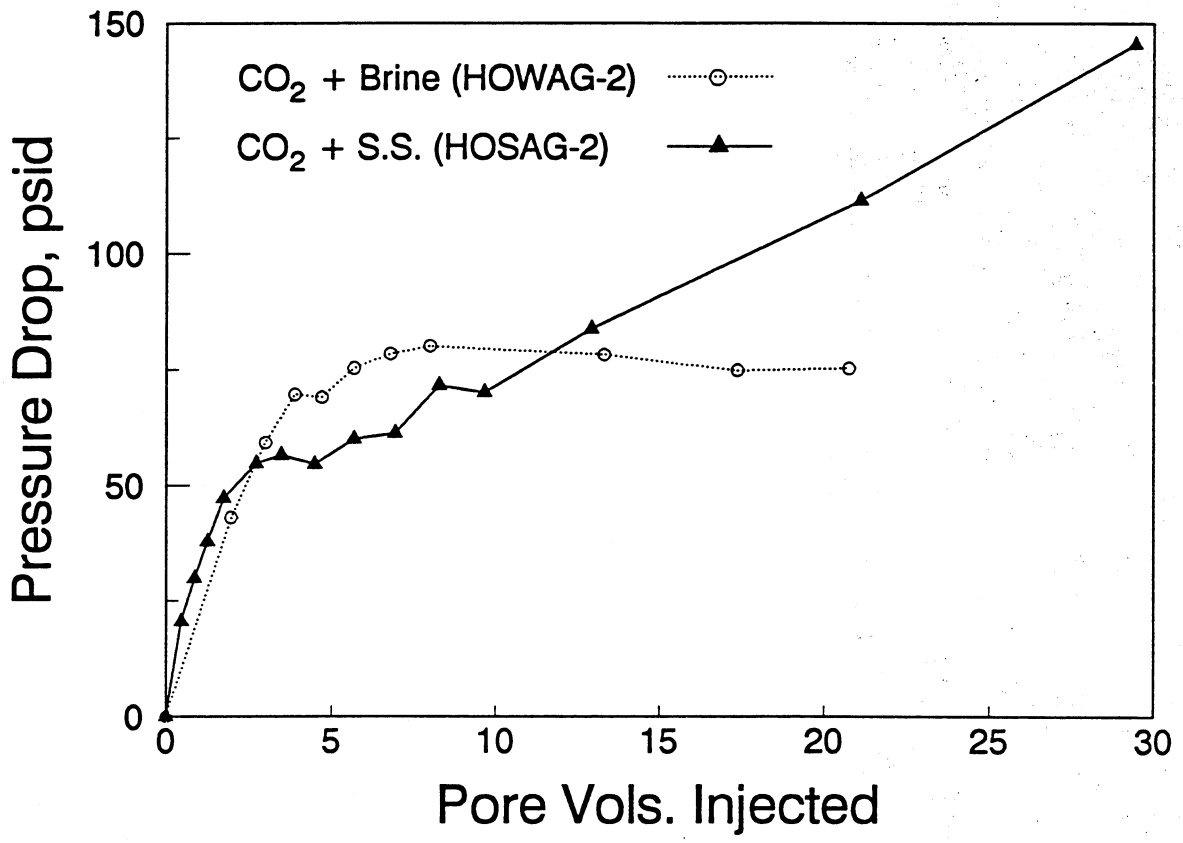

Figure I-65. Pressure drop history for oil displacement from a homogeneous core by (a) CO_2 and brine (HOWAG-2) and (b) CO_2 and surfactant solution (HOSAG-2).

Reed[113] investigated the impact of oil-water emulsions on *in situ* generated foams and report as low as 10% maximum oil saturation (S_{orm}) below which foam can be formed. The maximum oil saturation for foam formation (S_{orm}) was not measured in this experiment, but from the results it is expected to be low. In the selection of a surfactant for foam generation in the presence of a particular oil, it is important to select one with a high S_{orm}.

Figure I-66 shows the oil recovery performance in the cases where oil was displaced from a heterogeneous core by simultaneous injection of (a) CO_2 and brine (HEWAG-1) and (b) CO_2 and surfactant solution (HESAG-1). Oil recovery rate is rather high initially, in both cases because of the recovery from the high permeability zone, but reached ultimate recoveries of 56% for HEWAG-1 and 53.7% for HESAG-1 soon thereafter. It is interesting to note that the equilibrium pressure drop was higher in HEWAG-1 (3.24 psi/ft) than in HESAG-1 (1.9 psi/ft), as shown in Fig. I-67. As in the case of HOSAG-2, oil production in the HESAG-1 was followed by a long period of emulsion production, but no foam was formed. It is probable that foam would have been formed after a prolonged injection period.

4. Conclusions

a. The relationship between critical gas velocity and gas fraction has been established for the CO_2-foam reservoir rock system. The critical velocity increases with increasing gas fraction.

b. At constant gas interstitial velocity, the pressure drop at steady state increases with decreasing gas/liquid injection ratios. A shear-thinning behavior of the foam is exhibited in the CO_2-foam reservoir rock system, and a correlation between the gas mobility, interstitial gas velocity, and gas fraction has been proposed for simulation of CO_2-foam flow in reservoirs. This is simpler than the current method of using separate correlations for gas relative permeability and apparent viscosity.

c. Simultaneous injection of CO_2 and surfactant solution into a homogeneous core initially saturated with oil at irreducible water saturation resulted in less oil recovery than expected because of oil-in-water emulsion formation.

d. Simultaneous injection of CO_2 and surfactant solution into a heterogeneous core initially saturated with oil at irreducible water saturation resulted in a high initial rate of recovery and rapid decline in the rate as expected. But generation of foam in the high permeability region to block that region, and thereby resulting in improved oil recovery, did not occur because of oil-in-water emulsion formation.

5. Future Work

It is our intent to perform the following tasks in the future:

a. Conduct further investigations to develop the relationship between gas mobility and surfactant concentration, gas velocity, and saturations, using different surfactants and reservoir oils and rocks.

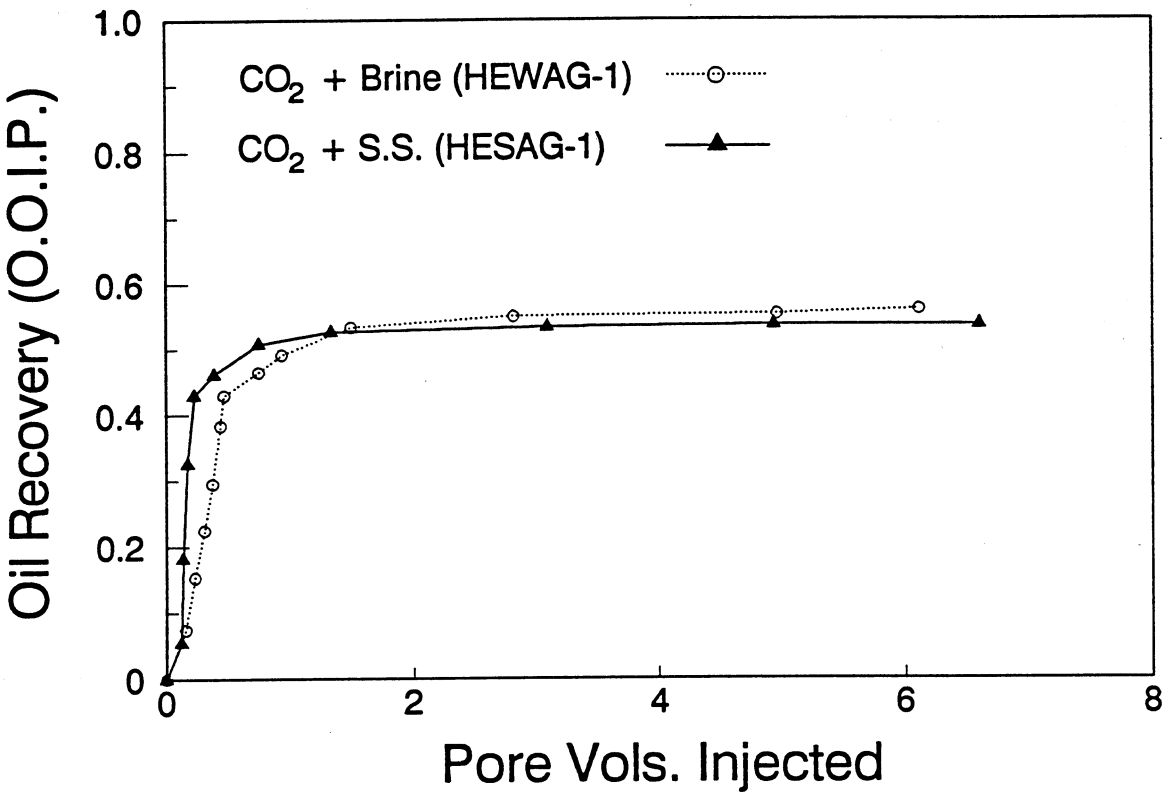

Figure I-66. Oil recovery performance for oil displacement from a heterogeneous core by (a) CO_2 and brine (HEWAG-1) and (b) CO_2 and surfactant solution (HESAG-1).

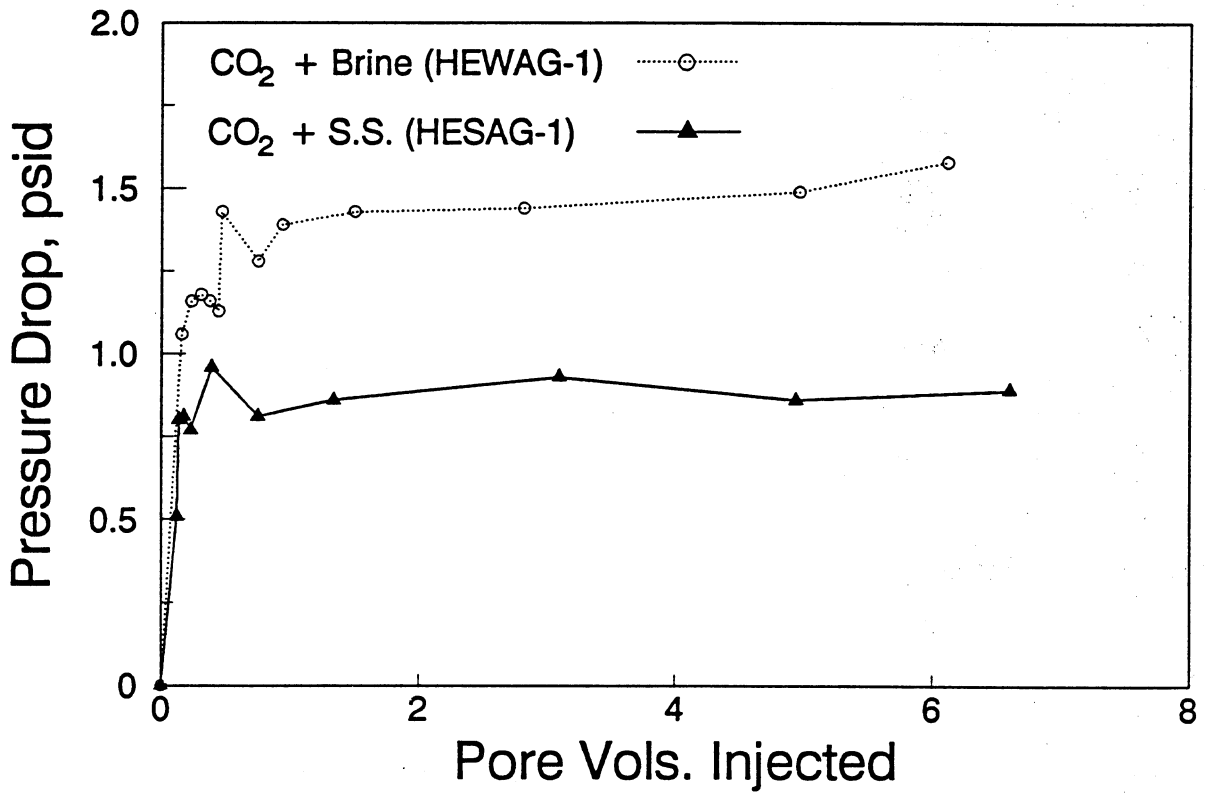

Figure I-67. Pressure drop history for oil displacement from a heterogeneous core by (a) CO_2 and brine (HEWAG-1) and (b) CO_2 and surfactant solution (HESAG-1).

b. Investigate the mechanisms for foam blockage, gas diversion, and crossflow, and their influence on oil recovery in naturally fractured reservoirs.

F. MECHANISTIC MODELING OF HIGH PRESSURE GAS/FOAM FLOW

The mobility of a gas flowing through a porous medium is lowered when it is dispersed within a liquid as a foam.[114] Consequently, foams can improve sweep in recovery processes that use gases such as CO_2.[115] The behavior of gas-foam has been studied both theoretically and experimentally.[100,101,111,112,117] The results of these studies have led to models of foam generation and propagation, which have been incorporated in several mechanistic foam simulators.[107,118] These models are based on a population balance description[119] of the foam texture, which is one of the important variables governing foam mobility.[112]

1. Model Description

A generalized, two-dimensional mechanistic foam-flood simulator was developed by combining the results of micromodel and core displacement studies with the results of prior studies.[107,118] The model description as well as the user's manual for the mechanistic foam simulator (MFS 2.1) have been completed and combined as a separate report,[106] which has been distributed to the supporters of this project and appended with this report. Therefore, the model will only be briefly described here. Foam is generated by the following mechanisms: snap-off, lamella division, and leave-behind, all of which are included in the simulator. In addition, foam coalescence and trapping mechanisms are incorporated in the model.

The simulator was formulated by adding a conservation equation for the surfactant and a population balance equation[119] for the foam texture to the basic three-phase conservation equations. The assumptions used in the model include:

a. There are four components—oil, gas, water, and surfactant—and three phases—oil, gas, and water.

b. The amount of surfactant in the oil and gas phases is negligible.

c. Loss of surfactant by foam formation is negligible.

d. Surfactant concentration adsorbed on the rock is in equilibrium with the surfactant concentration in the water phase.

e. Surfactant does not affect the mobility of the water phase.

f. Foam affects only the gas-phase mobility.

g. The Darcy's equation applies for the gas phase in the presence of foam.

h. Foam cannot exist if the oil saturation is larger than a limiting oil saturation or if the surfactant concentration is less than a limiting surfactant concentration.

i. Snap-off or lamella division only occurs above a critical gas velocity.

j. The flowing and trapped foams do not discriminate between pores of different size.

k. The process of foam trapping is instantaneous, and the bubble density of trapped foam is in equilibrium with the bubble density of flowing foam.

l. The mass transfer among the bubbles has a negligible effect on the average bubble density.

m. Dispersion is negligible.

New correlations for the rate of bubble consumption by coalescence and the rate of bubble generation by snap-off and lamella division were proposed and incorporated into the simulator. The rate of bubble consumption by coalescence is modeled as follows:

$$C_f = K_2 n_f \left(\frac{C_{sref}}{C_s}\right)^{e_2} \left(\frac{|U_g|}{U_{ref2}}\right)^{c_2} \tag{I-57}$$

where K_2 is the coalescence rate constant, n_f is the bubble density of the flowing foam, C_s is the surfactant concentration in the water phase, C_{sref} is the reference surfactant concentration, U_g is the Darcy's velocity of the gas phase, $|U_g|$ is the magnitude of U_g, U_{ref2} is the reference velocity, and e_2 and c_2 are the exponents. Equation (I-57) is based on the work of Khatib *et al.*,[117] which indicates that the limiting capillary pressure for coalescence varies with gas velocity. In addition, the rate of coalescence is proportional to the number of bubbles, and the higher the surfactant concentration, the more stable the bubbles. In the region where foam cannot exist, the rate of coalescence is infinite.

The rate of bubble generation by snap-off and lamella division is given as:

$$G_f = K_1 \left[1 + \left(\frac{n_f}{n_c}\right)^{e_1}\right]^{-1} \left(\frac{|U_g|}{U_{ref1}}\right)^{c_1} \tag{I-58}$$

where K_1 is the generation rate constant, n_c is the critical bubble density such that the generation rate approaches zero when n_f is much larger than n_c, U_{ref1} is the reference velocity, and e_1 and c_1 are the exponents. The use of the velocity term in Eq. (I-58) is based on other studies,[107,120] which indicate that steady foam flow resistance decreases with increasing gas velocity and by Eq. (I-57), which, in turn, indicates that the coalescence rate is a function of gas velocity. When the critical velocity is not exceeded, the rate of generation is zero.

In the simulator, the gas-phase mobility is modified according to the flow diagram shown in Fig. I-68. The first decision is whether or not foam is flowing. If foam is flowing, the gas-phase mobility is modified. Next, conditions need to be assessed to determine if foam can occur. If there is no gas

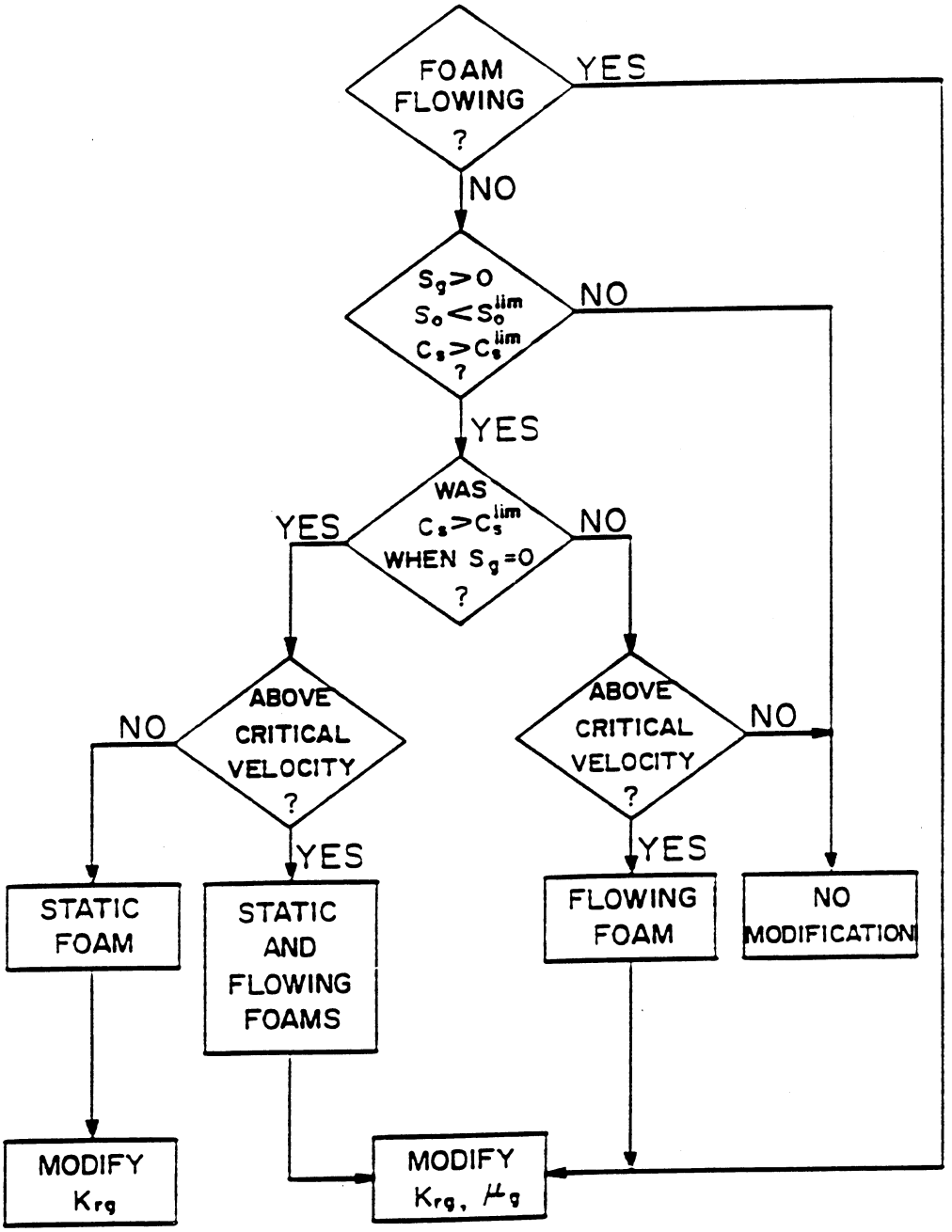

Figure I-68. Flow diagram for the modification of gas-phase mobility.

saturation, or if the oil saturation is above some limiting valve, or if the surfactant concentration is below some limiting valve, foam will not occur and the gas-phase mobility is not modified. If foam can occur, the conditions to generate the static and flowing foams are checked. For static foam to occur, surfactant needs to be present in the water phase prior to gas invasion. In this case, only the gas-phase relative permeability is modified. For flowing foam to occur, the gas velocity should be above a critical value, and then the gas-phase mobility is modified. When conditions permit the existence of both static and flowing foams, the modification method yielding the lowest mobility is selected. When both static and flowing foams cannot occur, no modification is made in gas-phase mobility.

The implicit pressure explicit saturation (IMPES) method is used to solve the multiphase equations. Surfactant concentration and foam bubble density from the previous time step are used to modify the gas-phase mobility. After the solution converges, the surfactant and population balance equations are solved for the current time.

2. Results and Discussion

The mechanistic foam flood simulator was used to perform a history match with one of the CO_2 coreflood experiments to determine the model parameters. This experiment, labeled #20, was conducted at 100°F and 1000 psig with a flow rate of 75 cm^3/hr. The core was a 15.16-cm long Berea sandstone with a diameter of 3.88 cm and was initially saturated with 1% NaCl brine. Both CO_2 (gas phase) and surfactant solution (water phase) were simultaneously injected into the core with a volumetric ratio of 2:1. The surfactant solution was 1% Alipal CD-128 surfactant in 1% NaCl brine. The experimental results, the experimental conditions, and the core properties were reported in the Fifth Annual Report of this project. Figure I-69 shows the matching results for this experiment. The solid line and the dashed line represent the pressure drop and the liquid production calculated by the simulator, respectively. The solid circles and the triangles correspond to the experimental data. The simulation results matched well with the experimental results. The matched parameters are listed in Table I-27. The data used in the history match are given in Tables I-28 and I-29.

The mechanistic foam simulator can be verified by history matching coreflood performance, and then predicting coreflood performance under other conditions. Using the matched parameters, the simulator was then used to predict liquid production and pressure drop history for comparison with the foam coreflood experimental data. The experiment, labeled #21, was performed at a flow rate of 62.5 cm^3/hr with a gas-liquid volumetric ratio of 4:1 (other conditions remained the same as the matched experiment). Simulation and experimental results were in good agreement for pressure drop and liquid production, as shown in Fig. I-70.

Ten unknown parameters arise from Eqs. (I-57) and (I-58): K_2, C_{sref}, e_2, U_{ref2}, c_2, K_1, n_c, e_1, U_{ref1}, and c_1. A sensitivity analysis for each of these parameters was performed. Figures I-71 through I-80 show the effects of these parameters on the pressure drop history. The effects of these parameters on the liquid production history are not significant. The system used in the analyses is a 15.16-cm long Berea sandstone core with a diameter of 3.88 cm, which is initially saturated with brine. The system temperature is 100°F. Both gas and surfactant solution are injected into the system simultaneously with a volumetric ratio of 2:1. The surfactant solution is 1% surfactant in brine. The total flow rate is 75 cm^3/hr and the production pressure is 1000 psig. The data and parameters used in the analyses are listed in Tables I-28 through I-30.

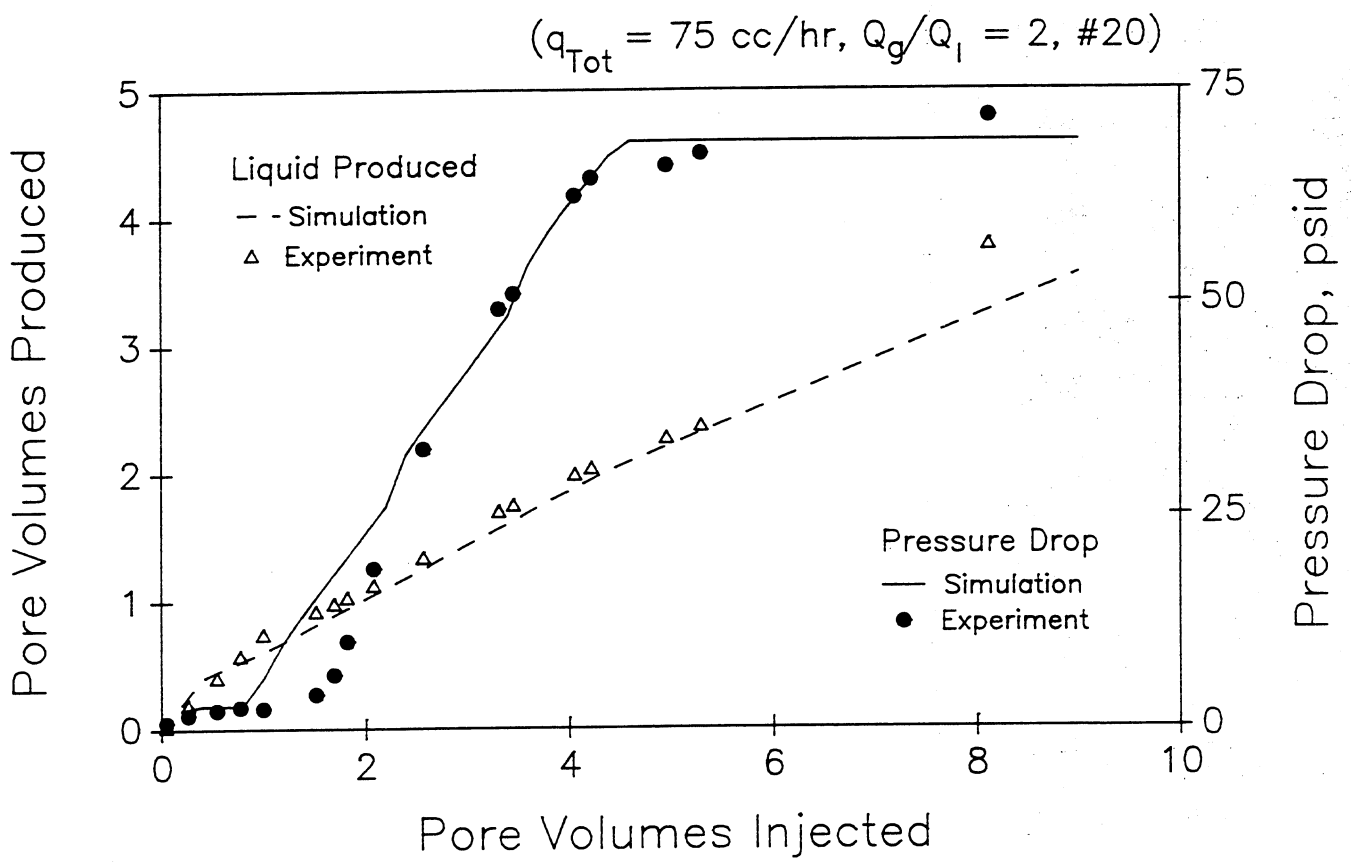

Figure I-69. History match of liquid production and pressure drop.

TABLE I-27. PARAMETERS USED IN THE HISTORY MATCH

A_f:	7.5×10^6 #/cm^3
A_s:	2.52×10^{-7} g/cm^2
b:	25.345
C_{sI}:	0.01 g/g
C_s^{lim}:	0.00999 g/g
C_{sref}:	0.01 g/g
c_1:	0.333333333
c_2:	1
c_3:	0.29
d:	5.5×10^{-5} cm/sec
e:	1.54
e_1:	5
e_2:	1.4
K_f:	1.0×10^{-4} cm^3/#
K_s:	793.0 g/g
K_1:	1.0218×10^6 #/sec/cm^3
K_2:	2.0436×10^{-2} cm^3/cm^3/sec
K_3:	1.9×10^8
n_c:	2.0×10^6 #/cm^3
n_{fI}:	0.0 #/cm^3
S_o^{lim}:	1.0
U_{ref1}:	0.03916 cm/sec
U_{ref2}:	0.03916 cm/sec
U_{ref3}:	0.03916 cm/sec
X_f:	0.175
δ:	3000 cm^2/g
ρ_r:	2.66 g/cm^3

TABLE I-28. GAS DENSITY AND VISCOSITY DATA

PRESSURE (psia)	DENSITY (g/cm^3)	VISCOSITY (cp)
995	0.1955	0.0203
1020	0.2062	0.0207
1050	0.2205	0.0212
1075	0.2338	0.0217
1100	0.2499	0.0224
1130	0.2737	0.0235

TABLE I-29. WATER-GAS RELATIVE PERMEABILITY AND CAPILLARY PRESSURE DATA

WATER SATURATION	WATER REL. PERM.	GAS REL. PERM.	CAPILLARY PRESSURE (psi)
0.40	0.00	0.8	8.5
0.55	0.03	0.15	1.5
0.65	0.08	0.025	0.5
0.70	0.12	0.010	0.4
0.75	0.30	0.007	0.25
0.80	0.53	0.001	0.15
0.85	0.80	0.0003	0.10
0.90	1.00	0.0000	0.05

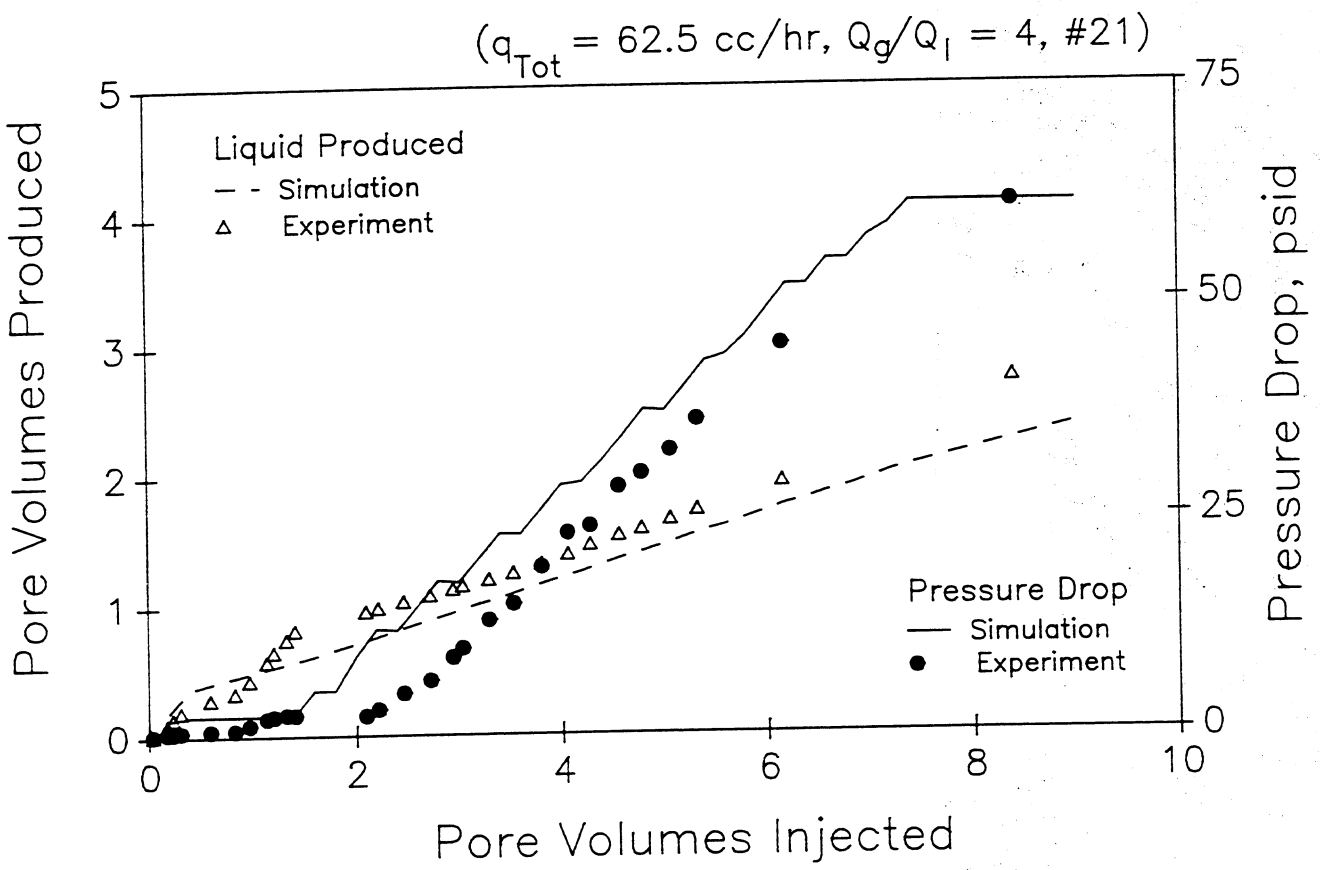

Figure I-70. Comparison of simulation with experimental results.

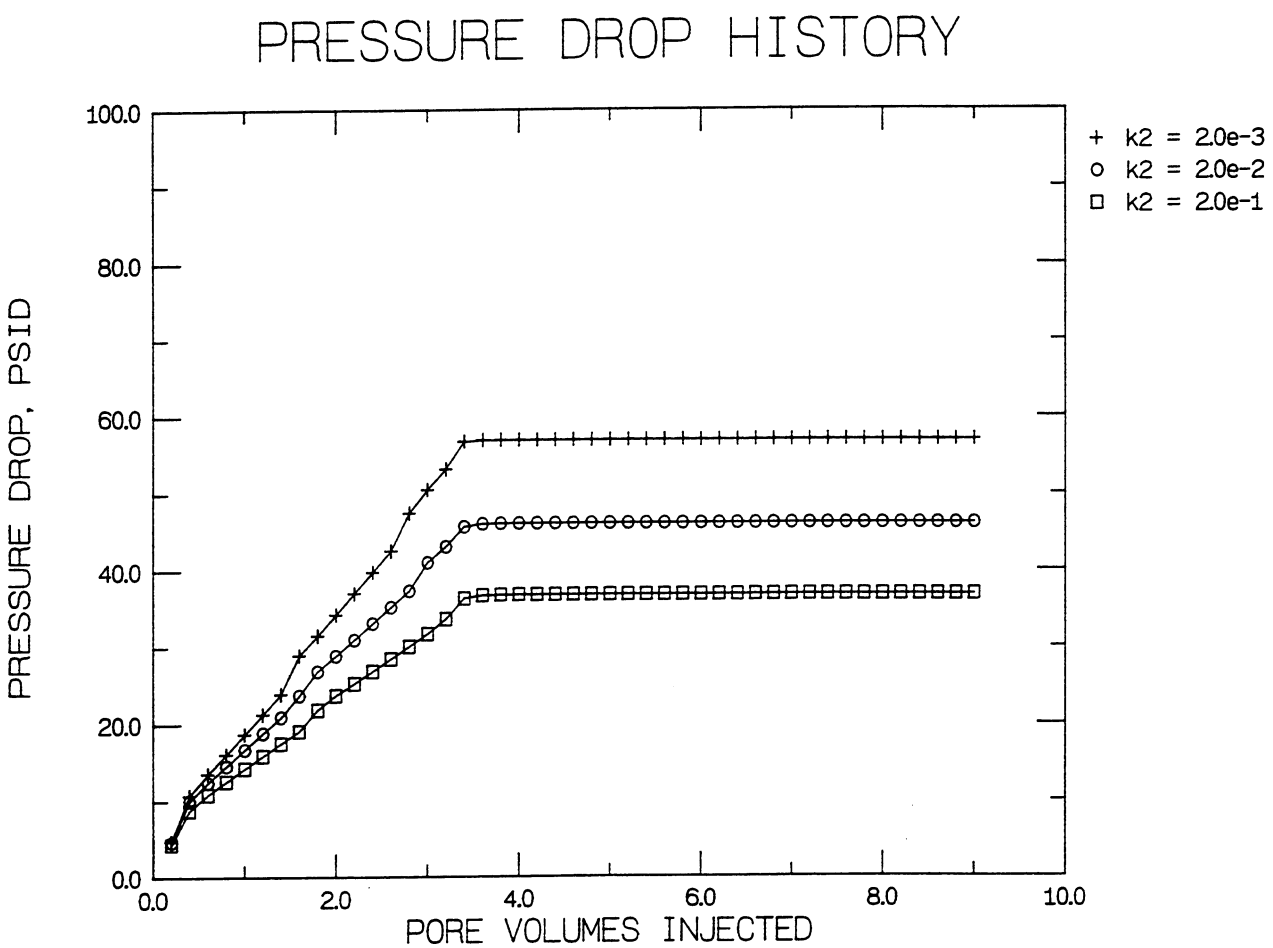

Figure I-71. Effect of K_2 on the pressure drop history.

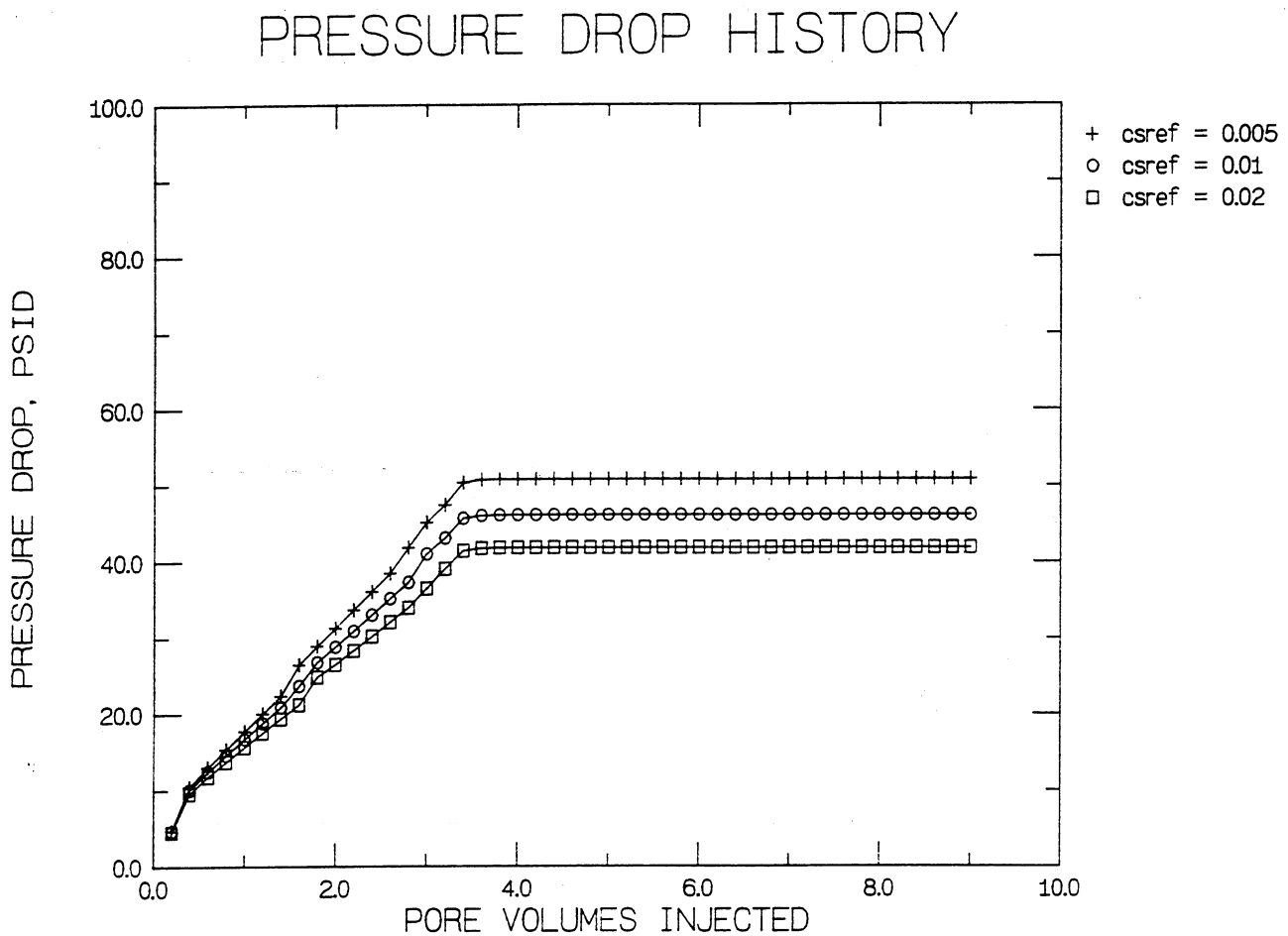

Figure I-72. Effect of C_{sref} on the pressure drop history.

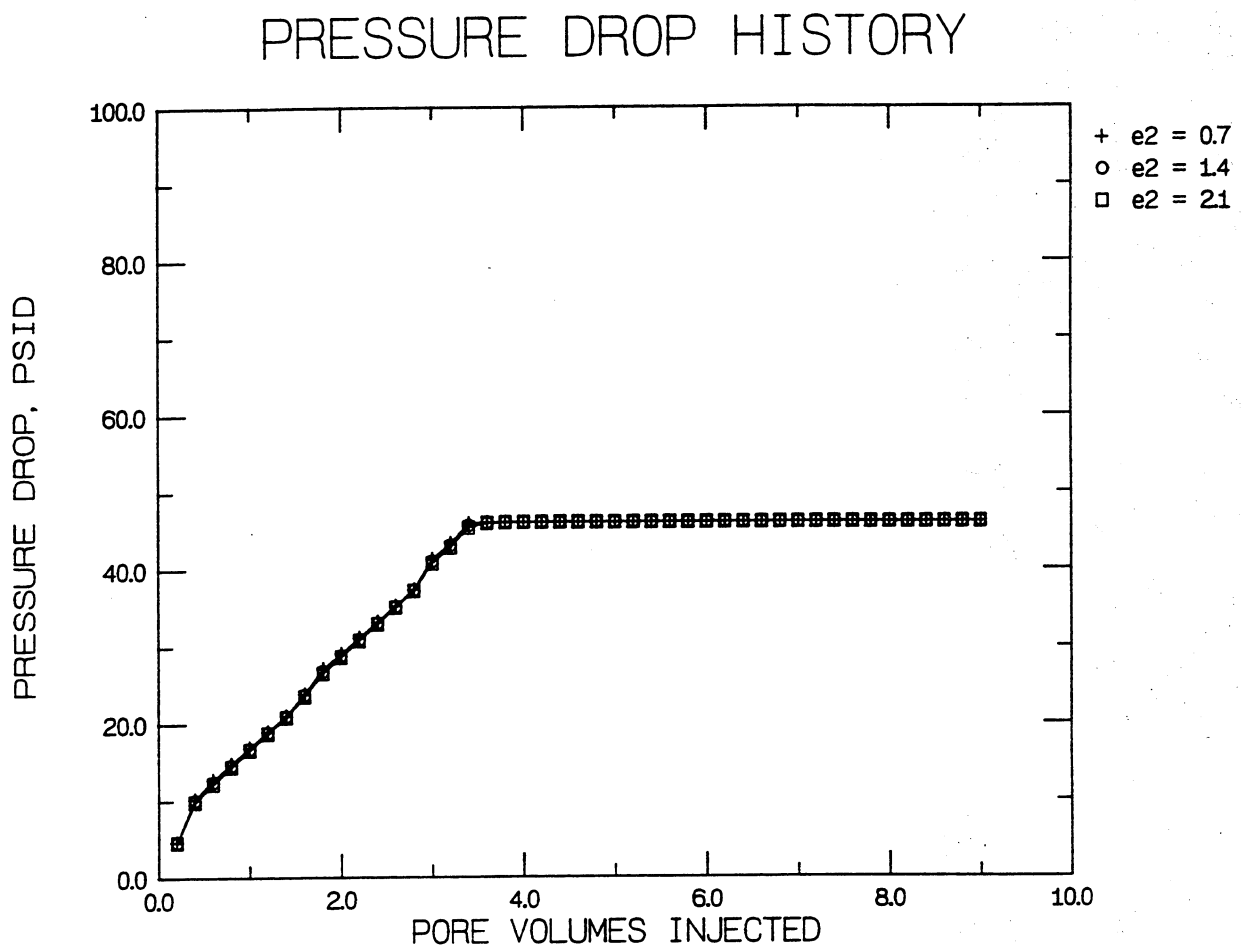

Figure I-73. Effect of e_2 on the pressure drop history.

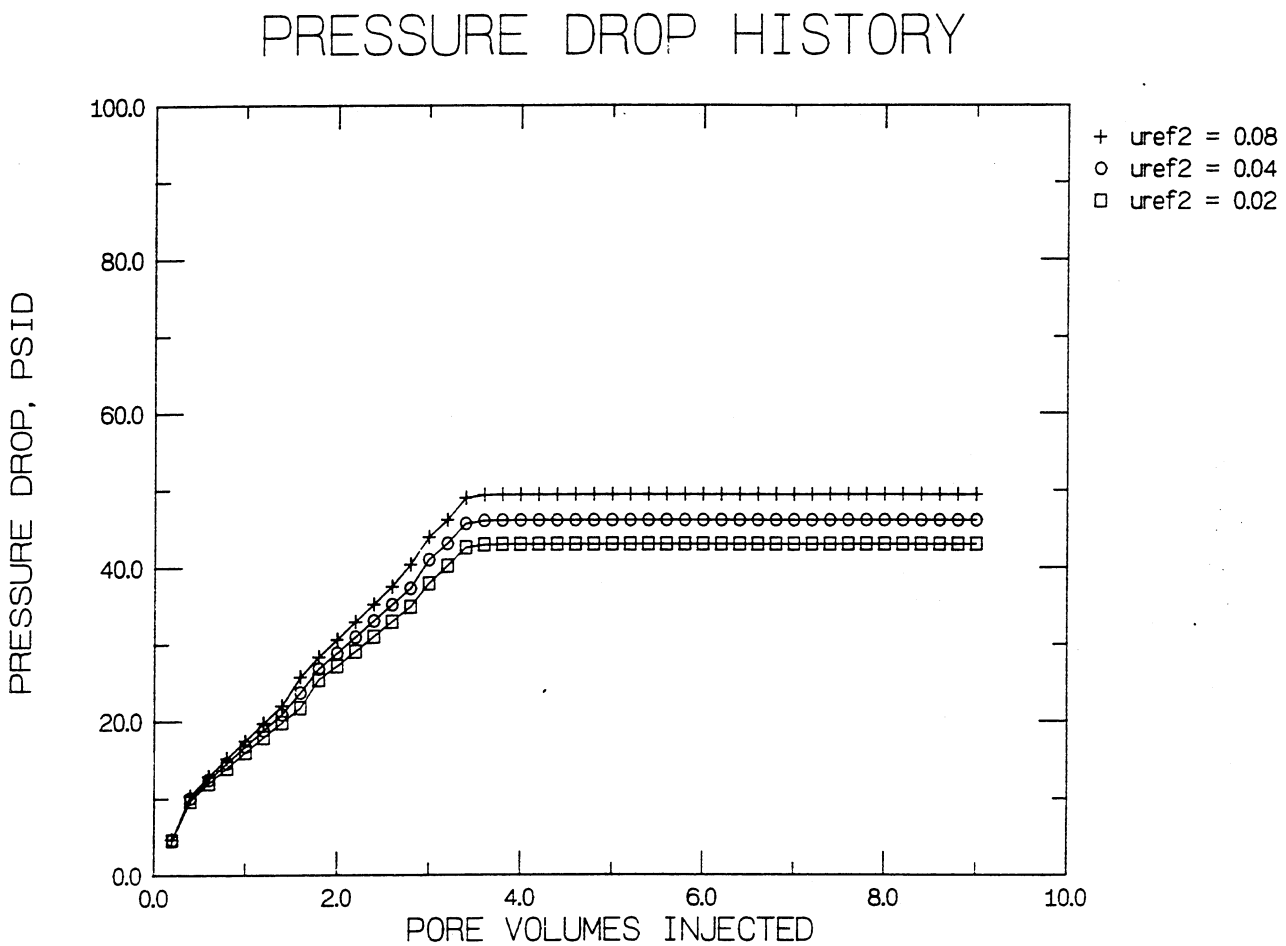

Figure I-74. Effect of U_{ref2} on the pressure drop history.

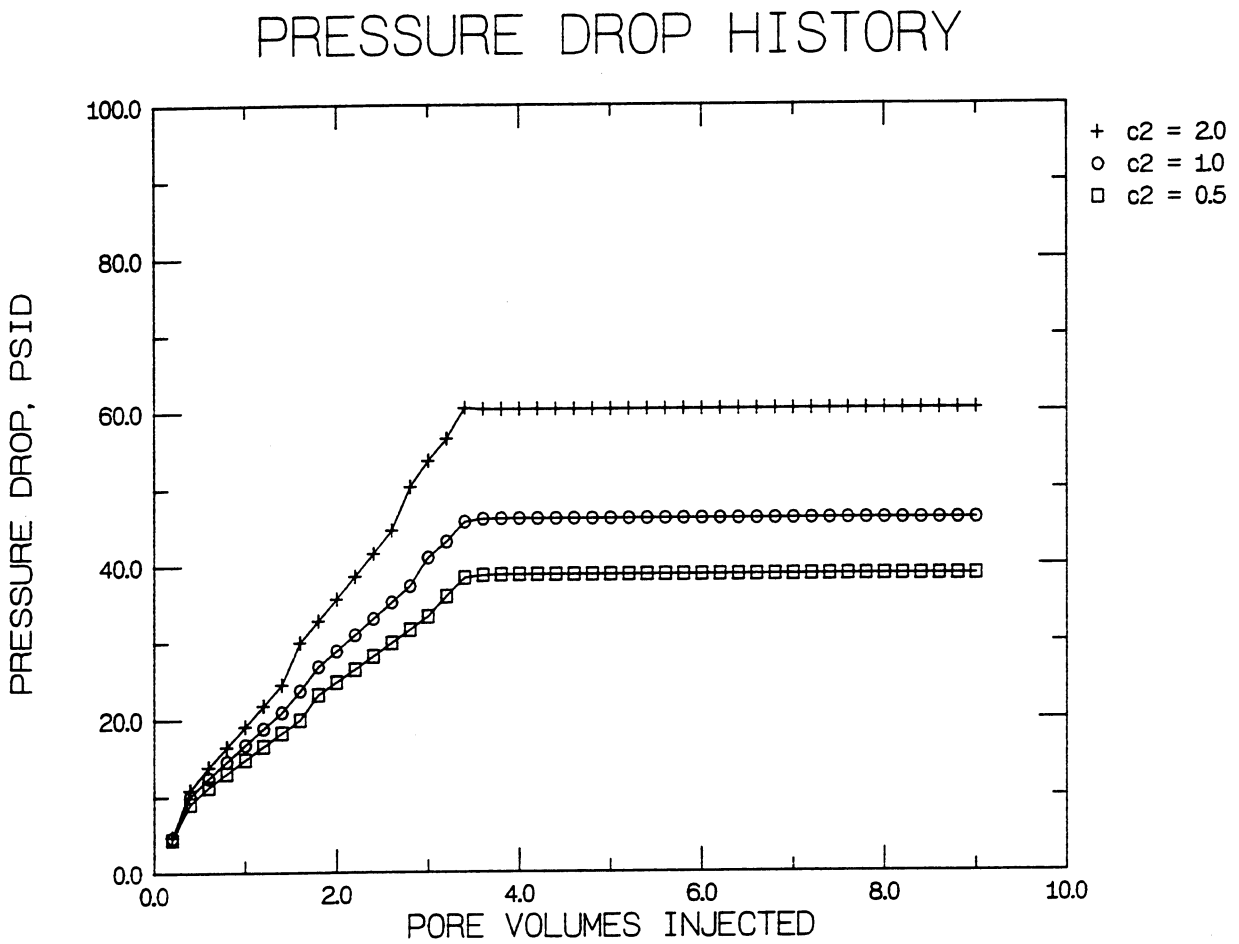

Figure I-75. Effect of c_2 on the pressure drop history.

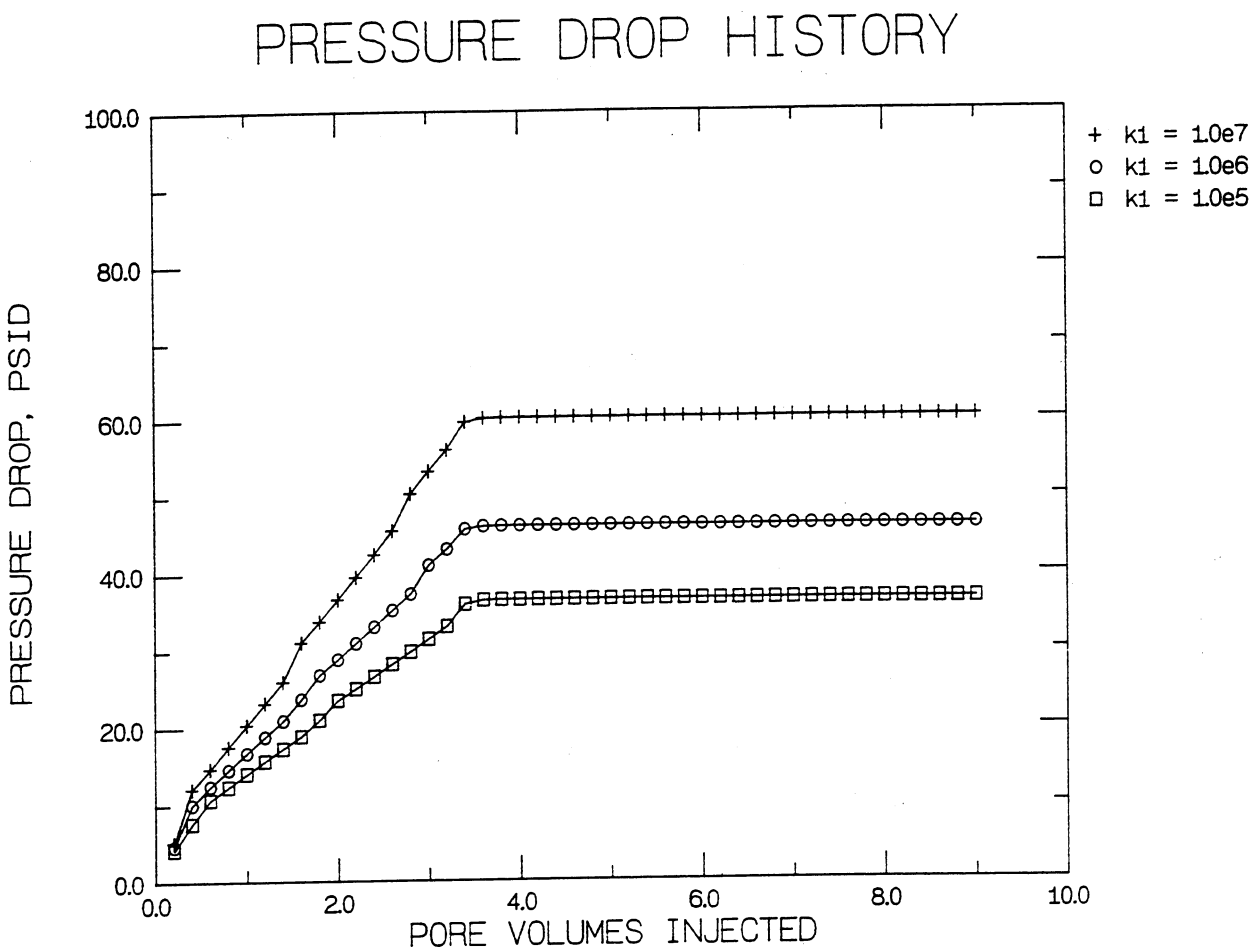

Figure I-76. Effect of K_1 on the pressure drop history.

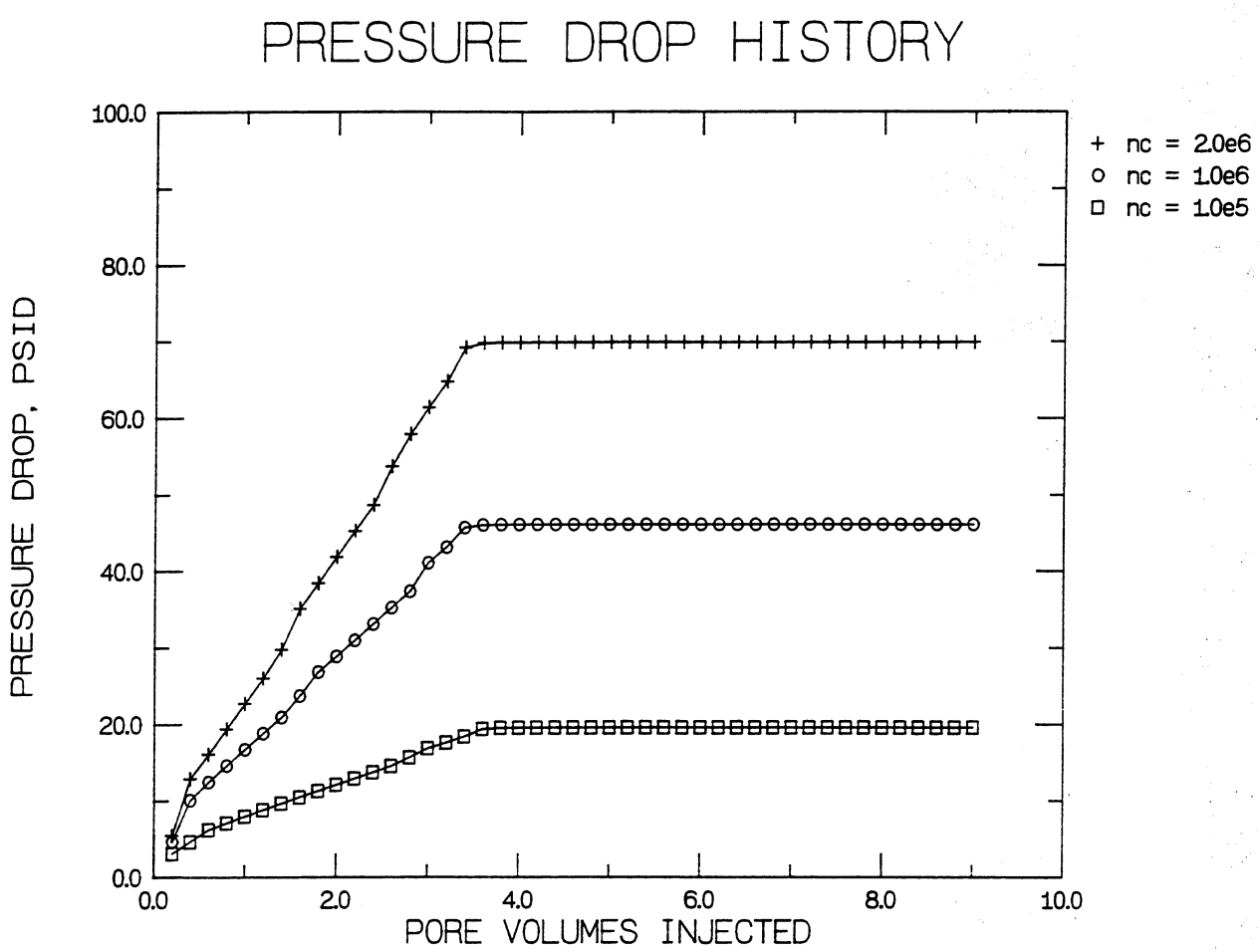

Figure I-77. Effect of n_c on the pressure drop history.

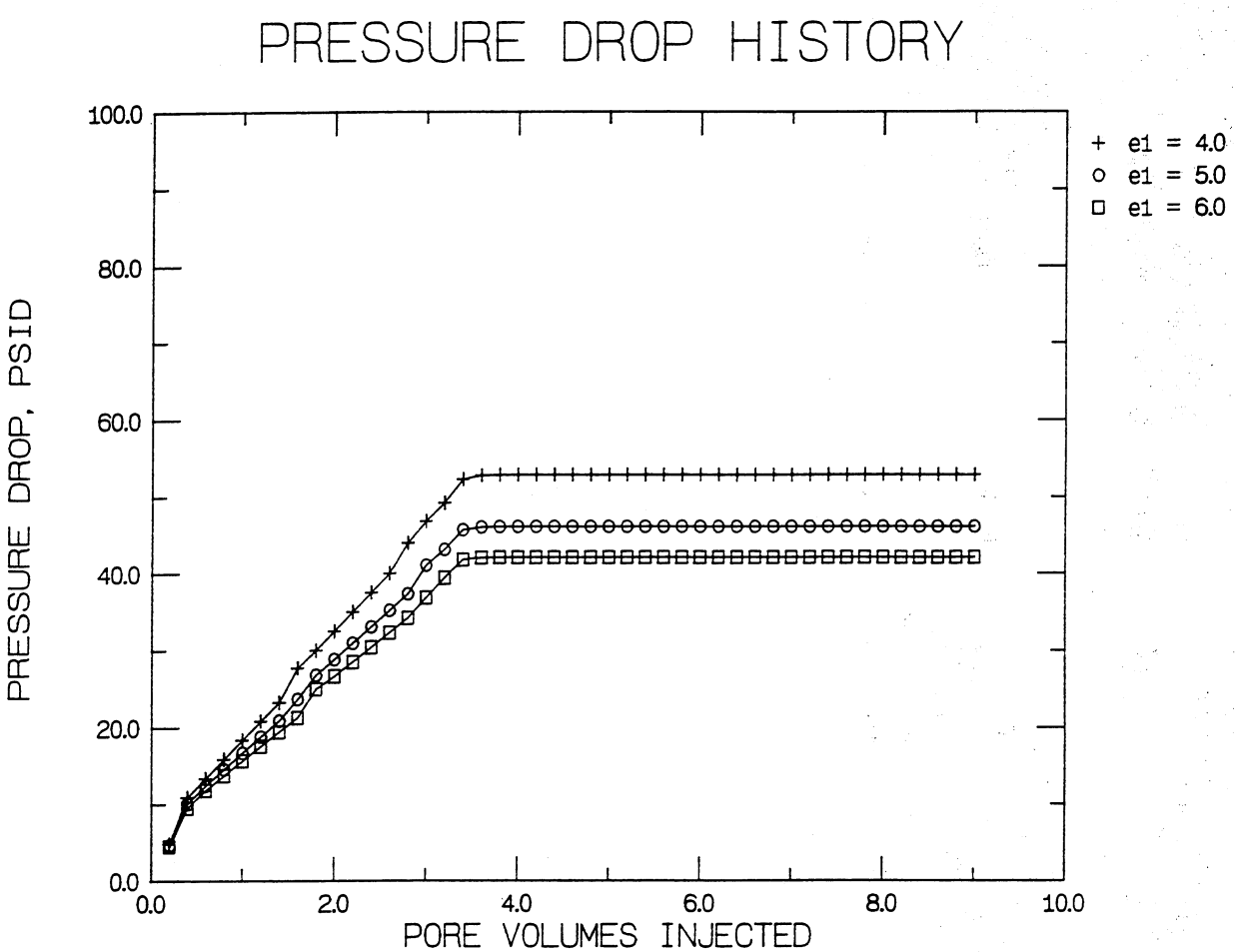

Figure I-78. Effect of e_1 on the pressure drop history.

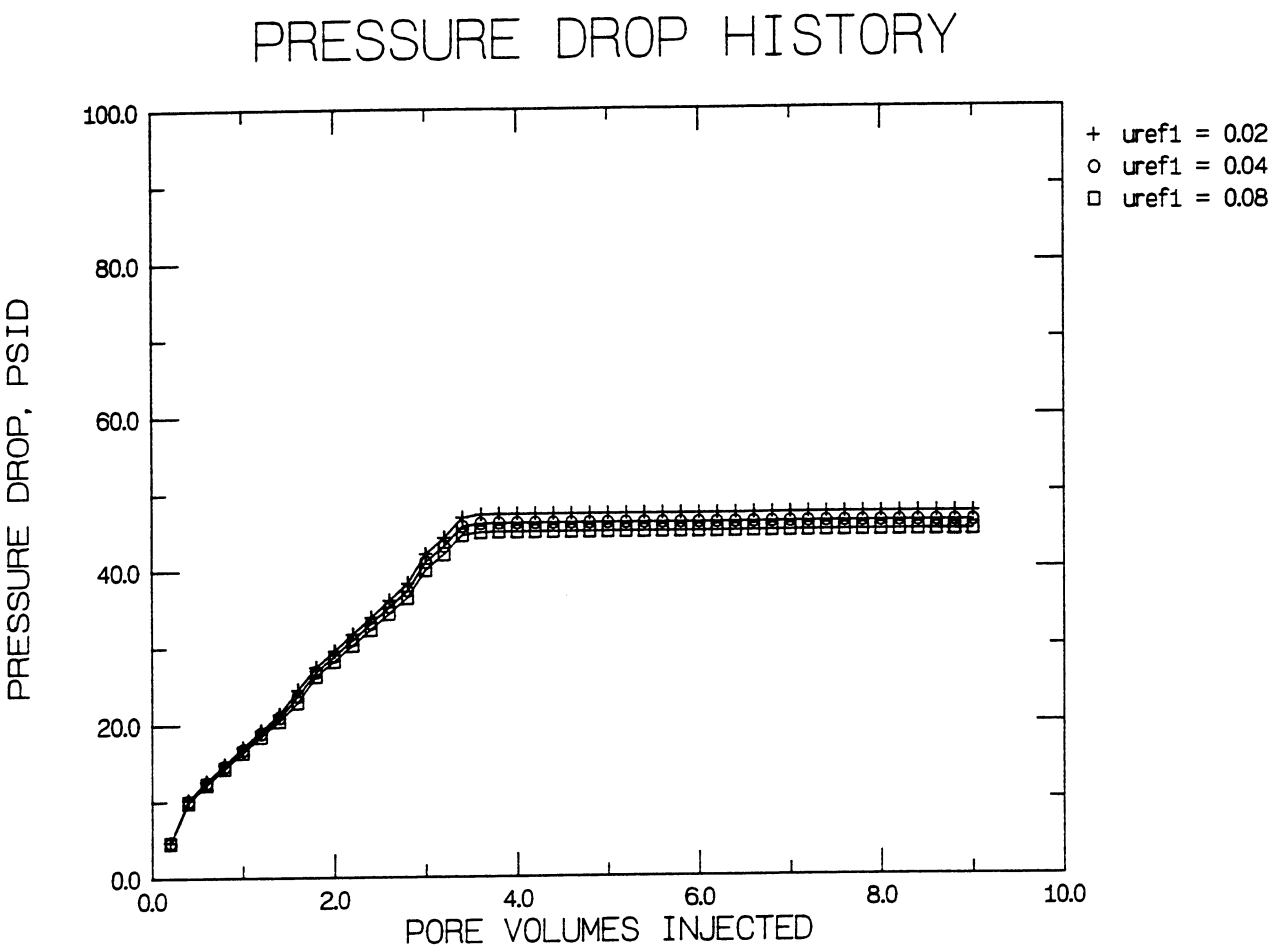

Figure I-79. Effect of U_{ref1} on the pressure drop history.

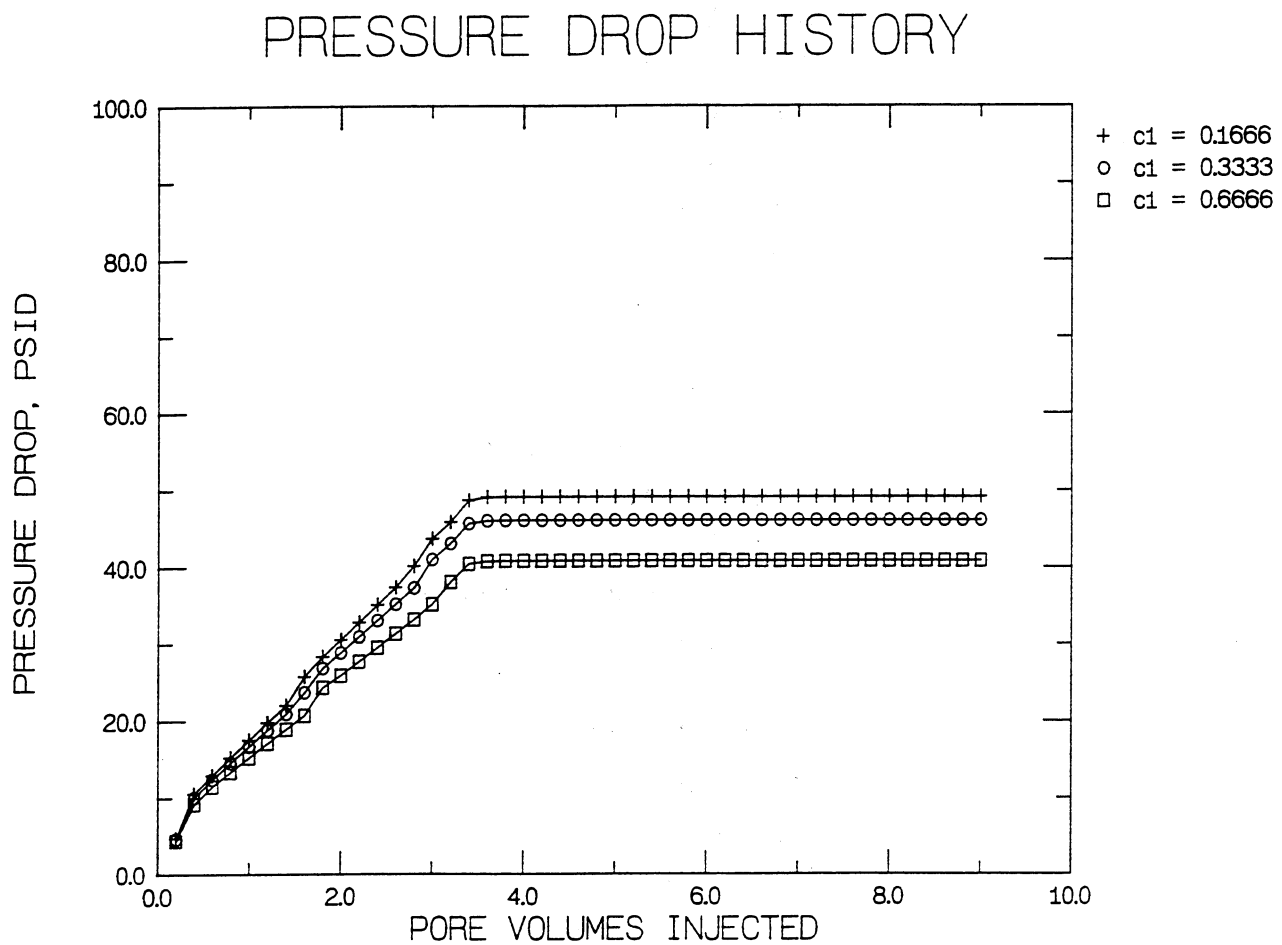

Figure I-80. Effect of c_1 on the pressure drop history.

TABLE I-30. PARAMETERS USED IN THE SENSITIVITY ANALYSIS

A_f:	7.5×10^6 #/cm^3
A_s:	2.52×10^{-7} g/cm^2
b:	25.345
C_{sI}:	0.01 g/g
C_s^{lim}:	0.001 g/g
C_{sref}:	0.01 g/g
c_1:	0.3333
c_2:	1
c_3:	0.29
d:	5.5×10^{-5} cm/sec
e:	1.54
e_1:	5
e_2:	1.4
K_f:	1.0×10^{-4} cm^3/#
K_s:	793.0 g/g
K_1:	1.0×10^6 #/sec/cm^3
K_2:	2.0×10^{-2} cm^3/cm^3/sec
K_3:	1.9×10^8
n_c:	1.0×10^6 #/cm^3
n_{fI}:	0.0 #/cm^3
S_o^{lim}:	1.0
U_{ref1}:	0.04 cm/sec
U_{ref2}:	0.04 cm/sec
U_{ref3}:	0.03916 cm/sec
X_f:	0.175
δ:	3000 cm^2/g
ρ_r:	2.66 g/cm^3

The mechanistic foam simulator was used to match experiment #20 again by reducing both valves of K_1 and K_2 (old values are shown in Table I-27) according to the results of the sensitivity analyses. The simulation results matched with the experimental results were as good as those using the old values. The coreflood performance of experiment #21 was then predicted using the new values, 1.0 x 10^5 #/sec/cm^3 for K_1 and 7.0 x 10^{-4} cm^3/cm^3/sec for K_2. The predictions were in agreement with the experimental data and better than those using the old values.

The mechanistic foam flood simulator was used to investigate the effect of relative permeability on the performance of CO_2-foam flood. The following equations are used for relative permeability calculations.

$$k_{rw} = k_{rw}^{o}\left(\frac{S_w - S_{wr}}{1 - S_{gr} - S_{wr}}\right)^{n_w} \tag{I-59}$$

$$k_{rg} = k_{rg}^{o}\left(\frac{S_g - S_{gr}}{1 - S_{gr} - S_{wr}}\right)^{n_g} \tag{I-60}$$

Here k_{rw} and k_{rg} are the relative permeability to the water phase and to the gas phases, respectively; k_{rw}^{o} and k_{rg}^{o} are the endpoints; S_w is the water saturation; S_g is the gas saturation; S_{wr} is the residual water saturation; S_{gr} is the residual gas saturation; and n_w and n_g are the exponents through which the curvature of the relative permeability curve can be changed.

The system used in the calculations is a 15.16-cm Berea sandstone core with a diameter of 3.88 cm that is initially saturated with 1% brine. Both CO_2 (gas phase) and surfactant solution (water phase) are simultaneously injected into the core with a volumetric ratio of 2:1. The total flow rate is 75 cm^3/hr. The surfactant solution is 1% surfactant in 1% brine. The viscosity and density of the fluids are assumed to be constant. The data and parameters used in the calculations are given in Table I-31.

To study the effect of the relative permeability endpoint of the water phase on the performance of CO_2-foam flood, four values of k_{rw}^{o} were chosen. The corresponding water relative permeability curves are shown in Fig. I-81 for k_{rw}^{o} = 1.0, 0.8, 0.6, 0.4, respectively. The gas relative permeability data used in the calculations are also shown in Fig. I-81. The calculated pressure drop history for these four cases are shown in Fig. I-82. The lower the value of the endpoint, the higher the pressure drop across the system. By varying the value of the exponent in Eq. (I-59), n_w, the curvature of the water relative permeability curve can be changed. The effect of the relative permeability curvature of the water phase on the pressure drop across the system is shown in Fig. I-83. The higher the value of the exponent, the higher the pressure drop across the system. The corresponding water relative permeability curves are shown in Fig. I-84 for n_w = 2, 3, 4, 5, respectively.

Figure I-85 shows the effect of the relative permeability endpoint of the gas phase, k_{rg}^{o}, on the pressure drop across the system. The lower the value of the endpoint, the higher the pressure drop across the system. The corresponding gas relative permeability curves are shown in Fig. I-86 for k_{rg}^{o} = 1.0,

TABLE I-31. DATA AND PARAMETERS USED IN THE CALCULATIONS

A_f:	7.5×10^6 #/cm^3
A_s:	2.52×10^{-7} g/cm^2
b:	25.345
C_{sI}:	0.01 g/g
C_s^{lim}:	0.00999 g/g
C_{sref}:	0.01 g/g
c_1:	0.333333333
c_2:	1
c_3:	0.29
d:	5.5×10^{-5} cm/sec
e:	1.54
e_1:	5
e_2:	1.4
K_f:	1.0×10^{-4} cm^3/#
K_s:	793.0 g/g
K_1:	1.0218×10^6 #/sec/cm^3
K_2:	2.0436×10^{-2} cm^3/cm^3/sec
K_3:	1.9×10^8
n_c:	2.0×10^6 #/cm^3
n_{fI}:	0.0 #/cm^3
S_o^{lim}:	1.0
U_{ref1}:	0.03916 cm/sec
U_{ref2}:	0.03916 cm/sec
U_{ref3}:	0.03916 cm/sec
X_f:	0.175
δ:	3000 cm^2/g
ρ_g:	0.205 g/cm^3
ρ_r:	2.66 g/cm^3
ρ_w:	0.8536 g/cm^3
μ_g:	0.0206 cp
μ_w:	0.09772 cp

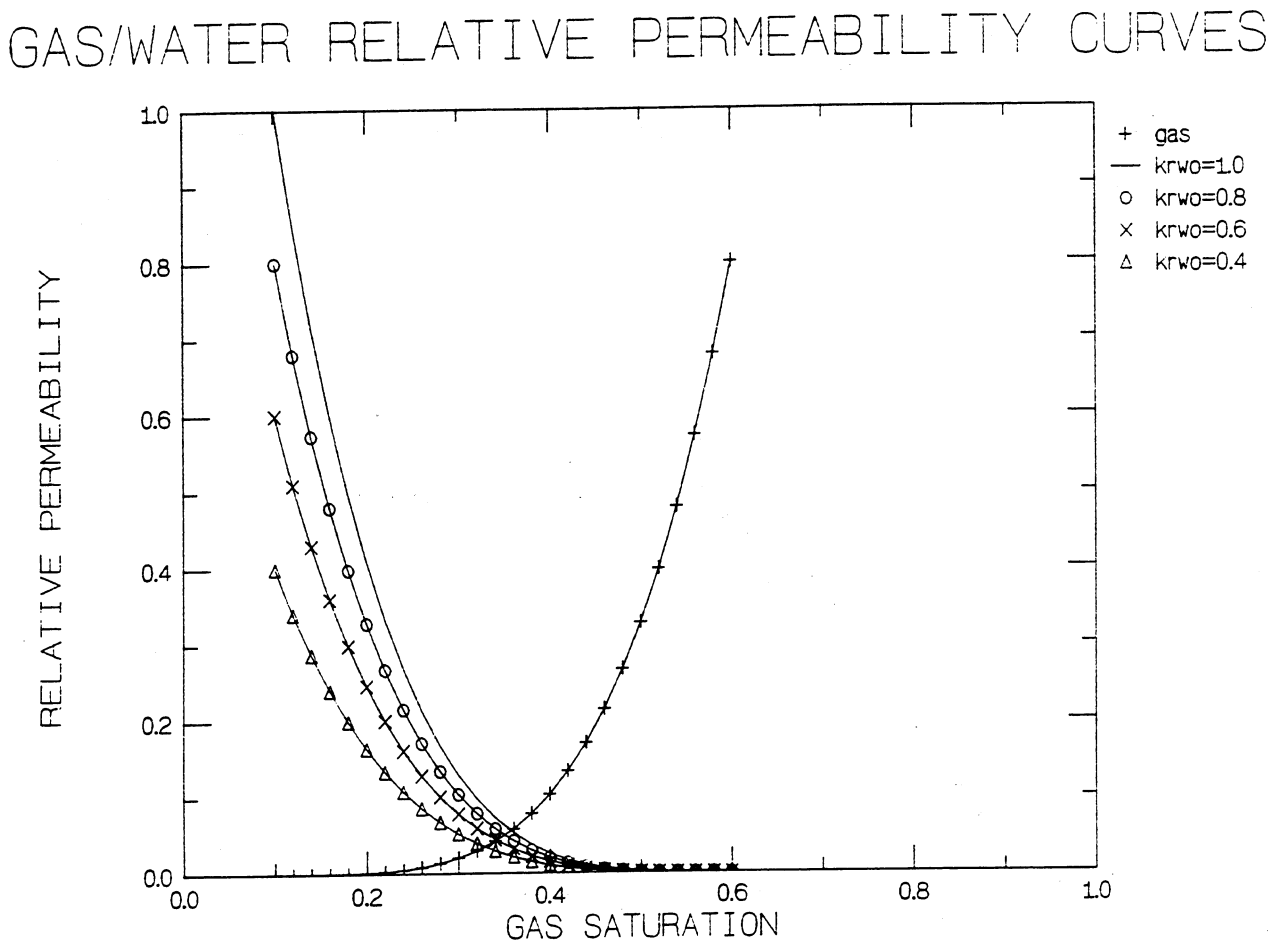

Figure I-81. Water relative permeability curves for k^o_{rw} = 1.0, 0.8, 0.6, 0.4, respectively, and gas relative permeability curve used in the calculations.

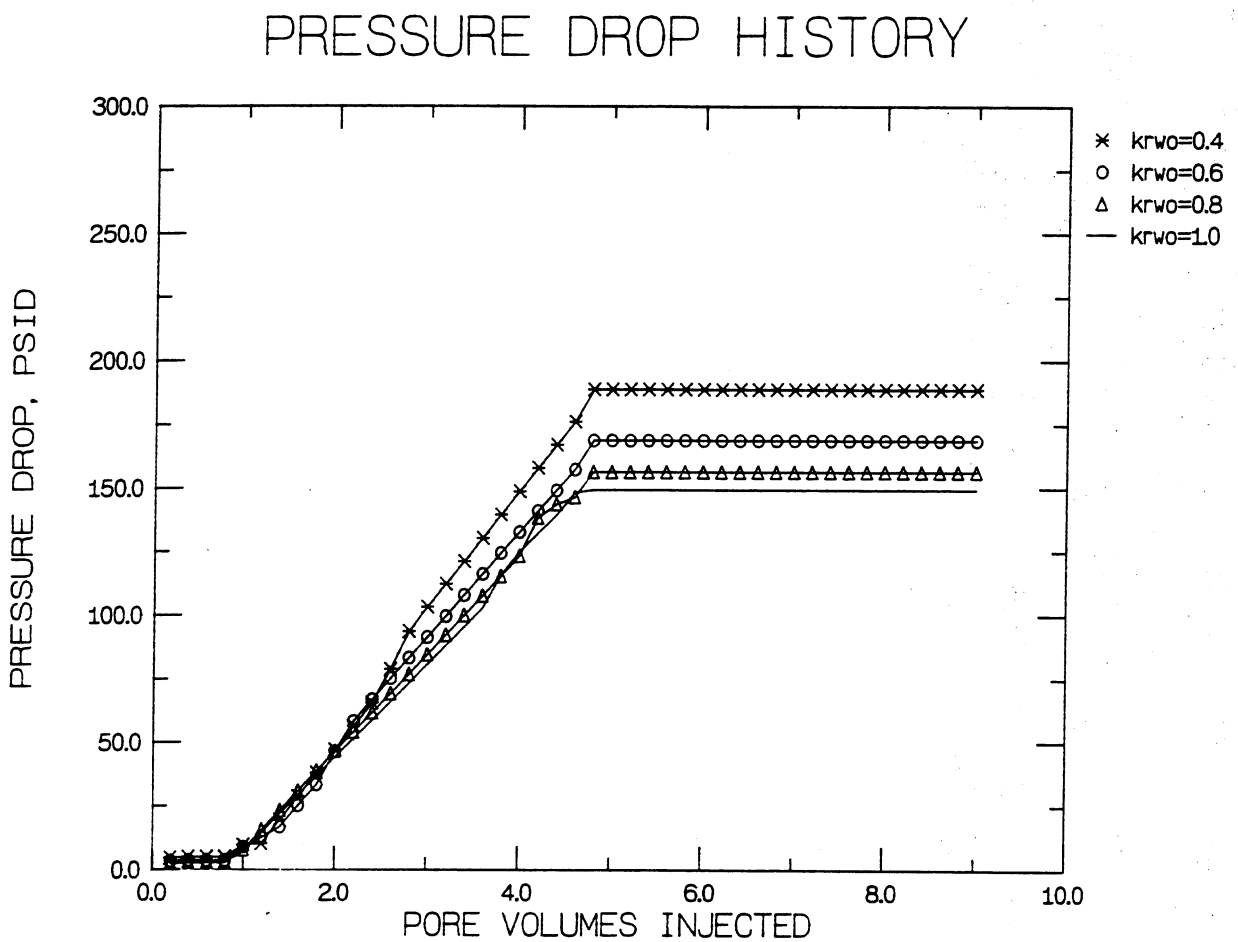

Figure I-82. The effect of k^o_{rw} on the pressure drop across the system.

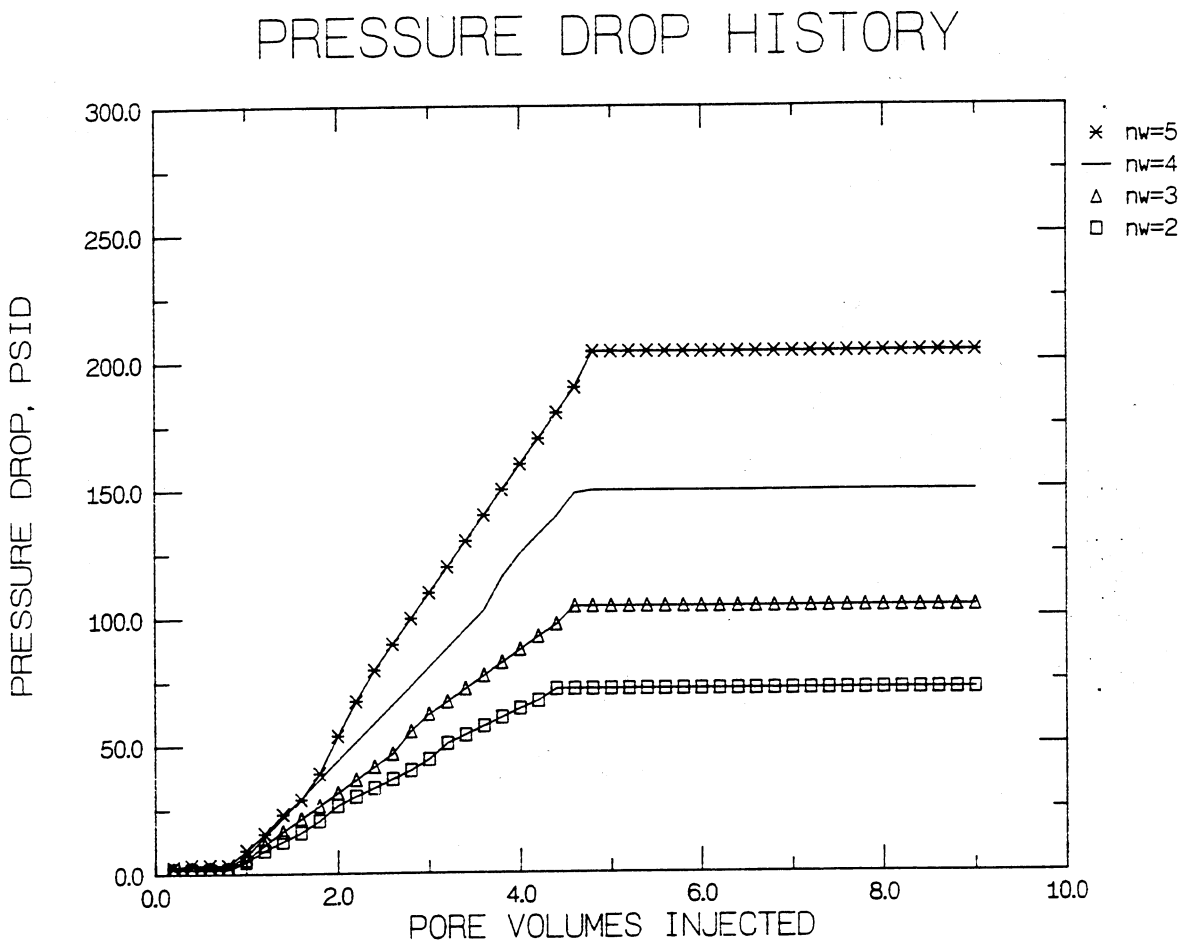

Figure I-83. The effect of n_w on the pressure drop across the system.

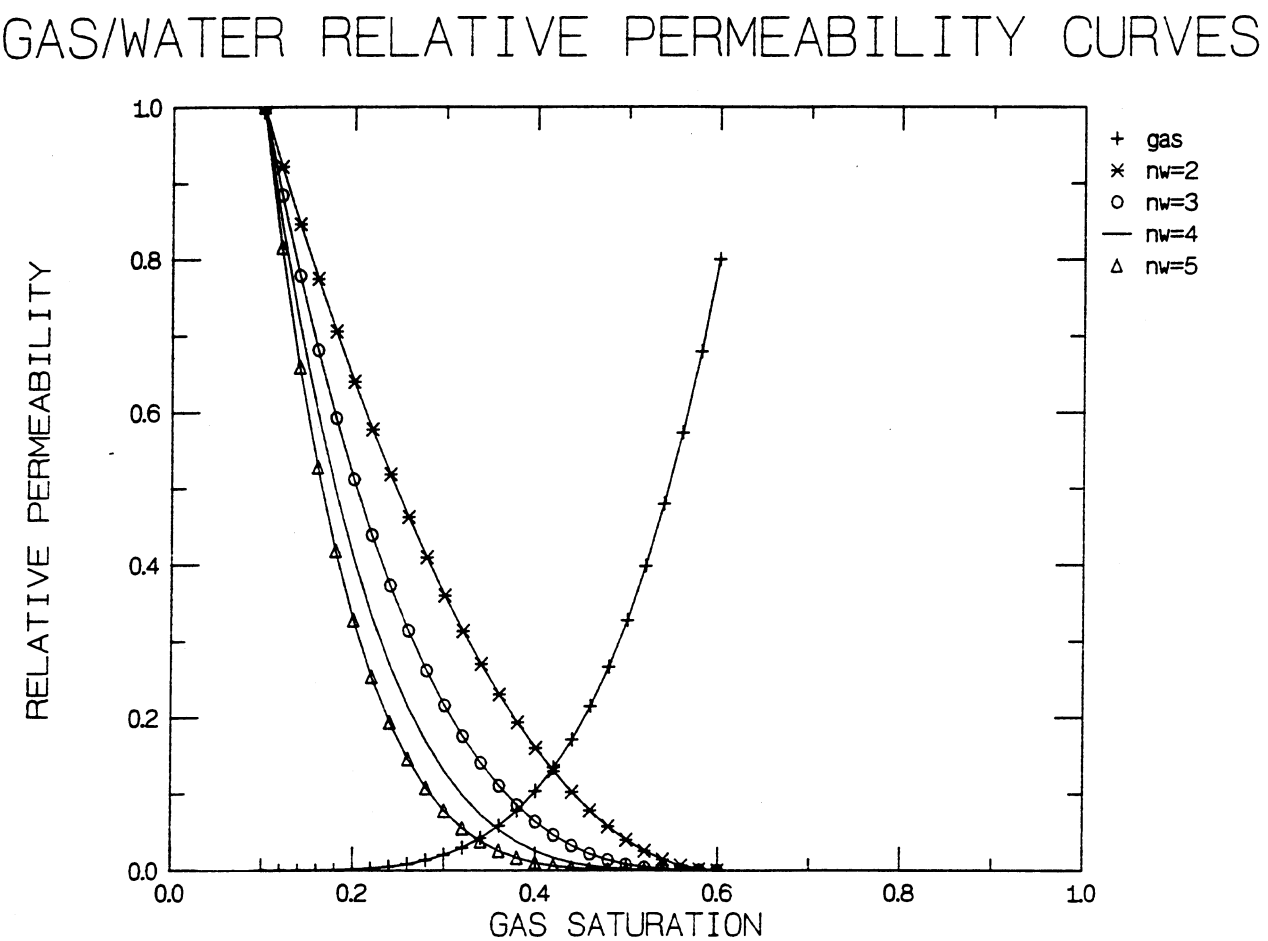

Figure I-84. Water relative permeability curves for n_w = 2, 3, 4, 5, respectively, and gas relative permeability curve used in the calculations.

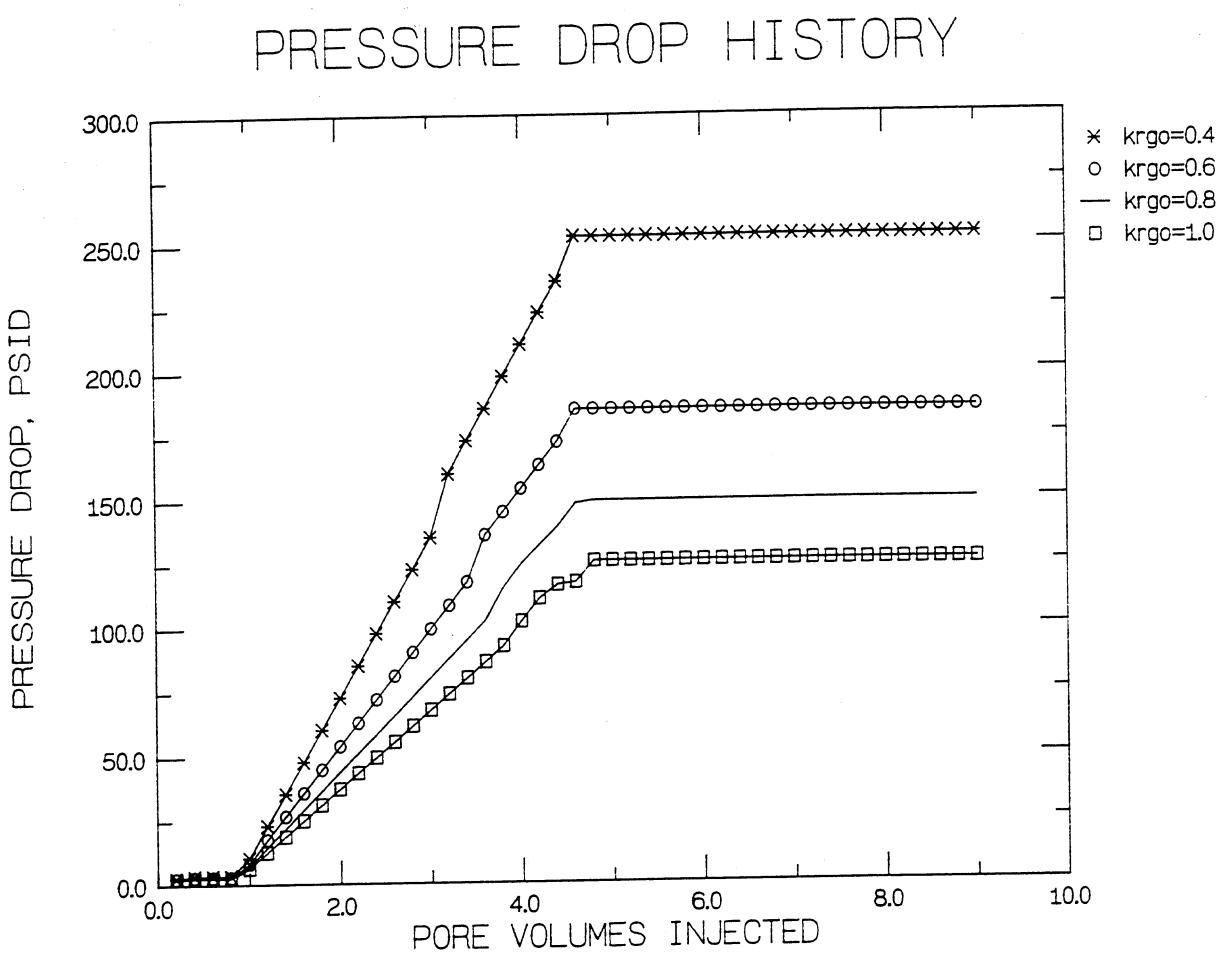

Figure I-85. The effect of k_{rg}^{o} on the pressure drop across the system.

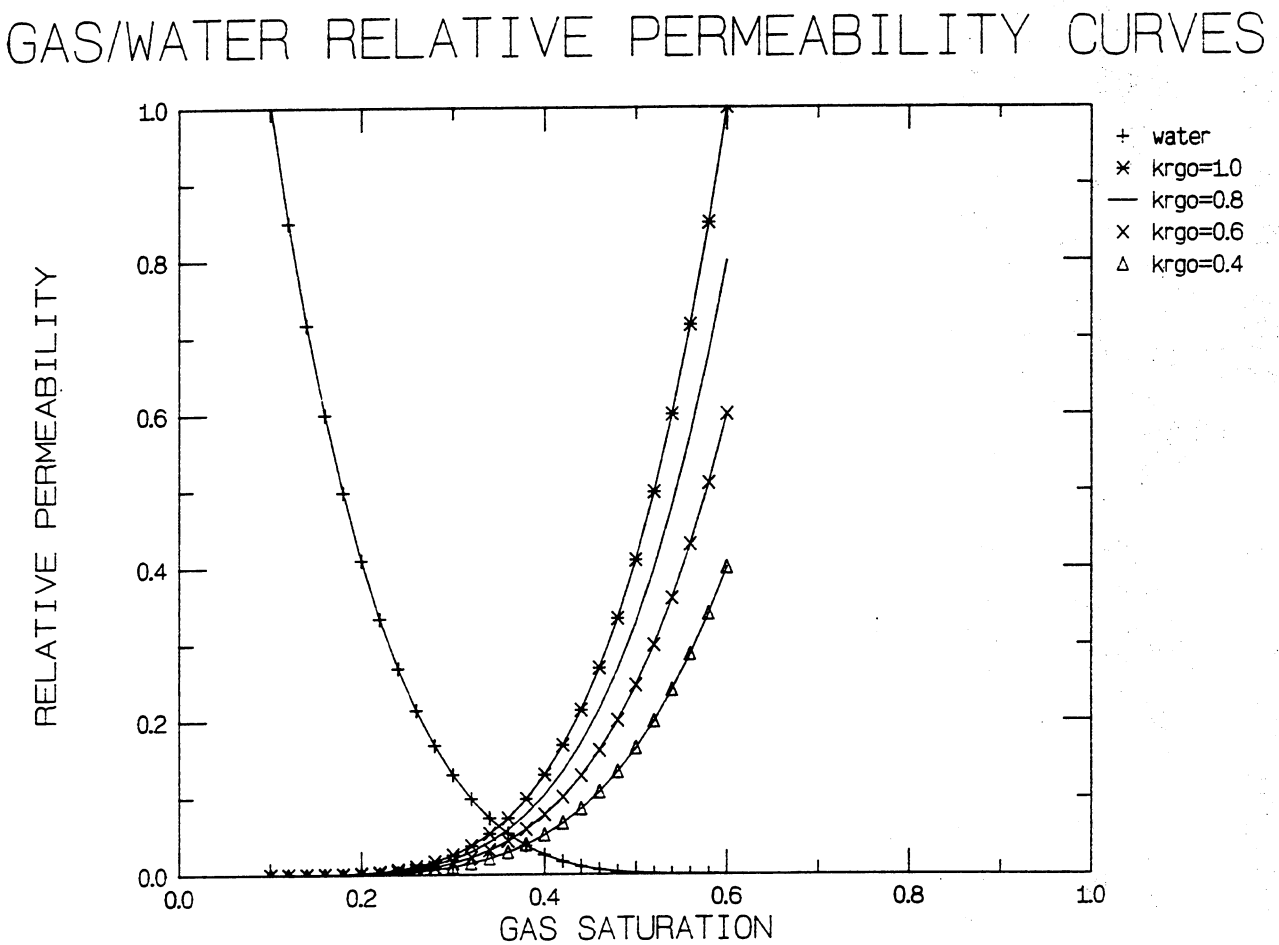

Figure I-86. Gas relative permeability curves for k^o_{rg} = 1.0, 0.8, 0.6, 0.4, respectively, and water relative permeability curve used in the calculations.

0.8, 0.6, 0.4, respectively. The water relative permeability data used in the calculations are also shown in Fig. I-86. The effect of the relative permeability curvature of the gas phase on the pressure drop across the system is shown in Fig. I-87. The higher the value of the exponent, the higher the pressure drop across the system. The corresponding gas relative permeability curves are shown in Fig. I-88 for n_g = 5, 4, 3, 2, respectively.

The gas relative permeability endpoint affects the pressure drop across the system more significantly than does the water relative permeability endpoint, as shown in Figs. I-82 and I-85. However, the water relative permeability curvature affects the pressure drop across the system more significantly than does the gas relative permeability curvature, as shown in Figs. I-83 and I-87. The effect of relative permeability on the liquid production history is not significant.

3. Conclusions

a. A two-dimensional simulator with newly proposed correlations for foam generation and coalescence has been developed. This simulator is able to model many of the processes associated with channel blockage by foam and diversion of flow into the bypassed oil matrix.

b. The predictions for pressure drop and liquid production by the simulator agree well with the experimental results.

c. The free parameters used in modeling foam generation and coalescence affect the pressure drop across the system more significantly than the liquid production.

d. The gas relative permeability endpoint affects the pressure drop across the system more significantly than does the water relative permeability endpoint. However, the water relative permeability curvature affects the pressure drop across the system more significantly than does the gas relative permeability curvature.

e. The effect of relative permeability on the liquid production history is not significant.

4. Future Work

a. The correlations will be modified regularly to incorporate results that are observed in the micromodel and core mechanistic studies.

b. A limited compositional foam flood simulator is under development by refining the four-component reservoir simulator, which was supplied by the Department of Energy, with the mechanistic foam-flood simulator.

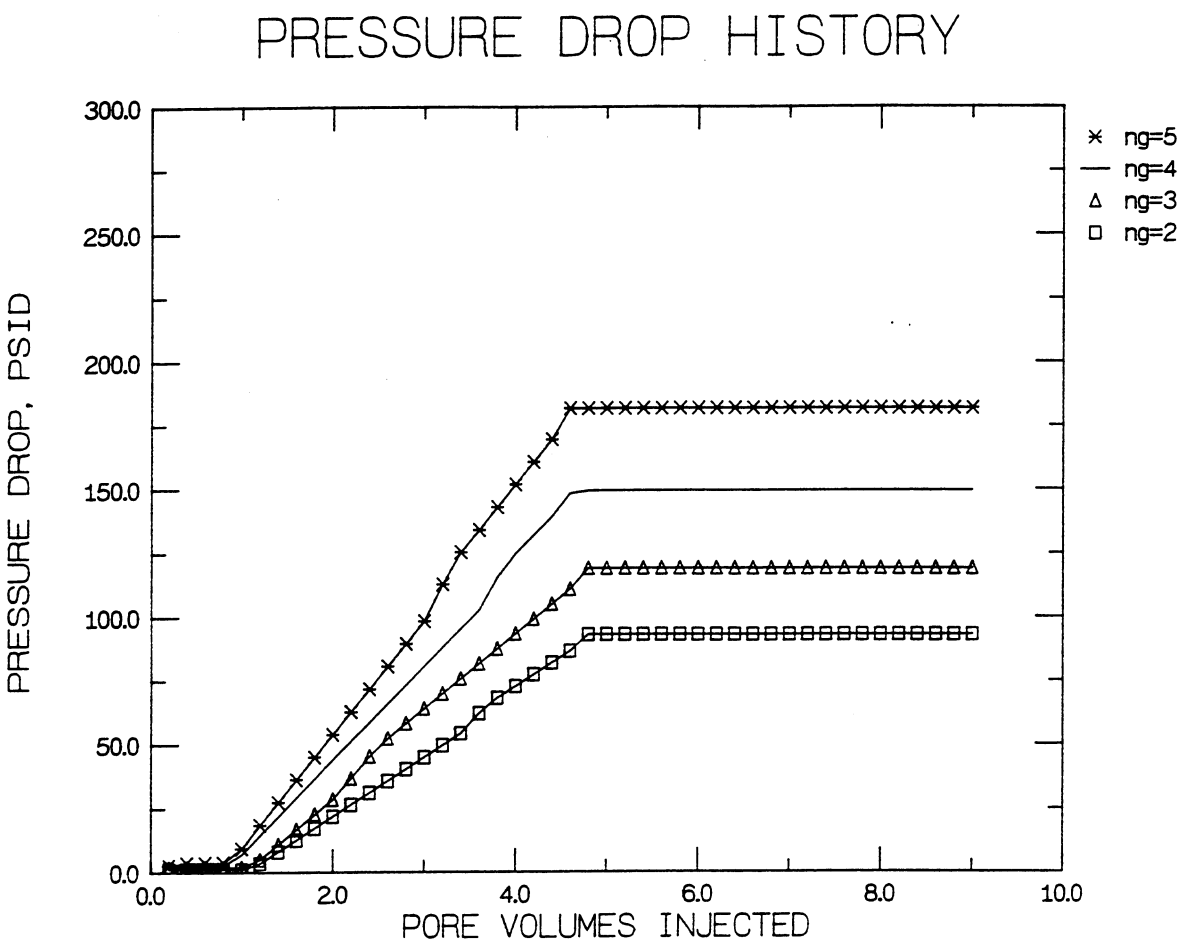

Figure I-87. The effect of n_g on the pressure drop across the system.

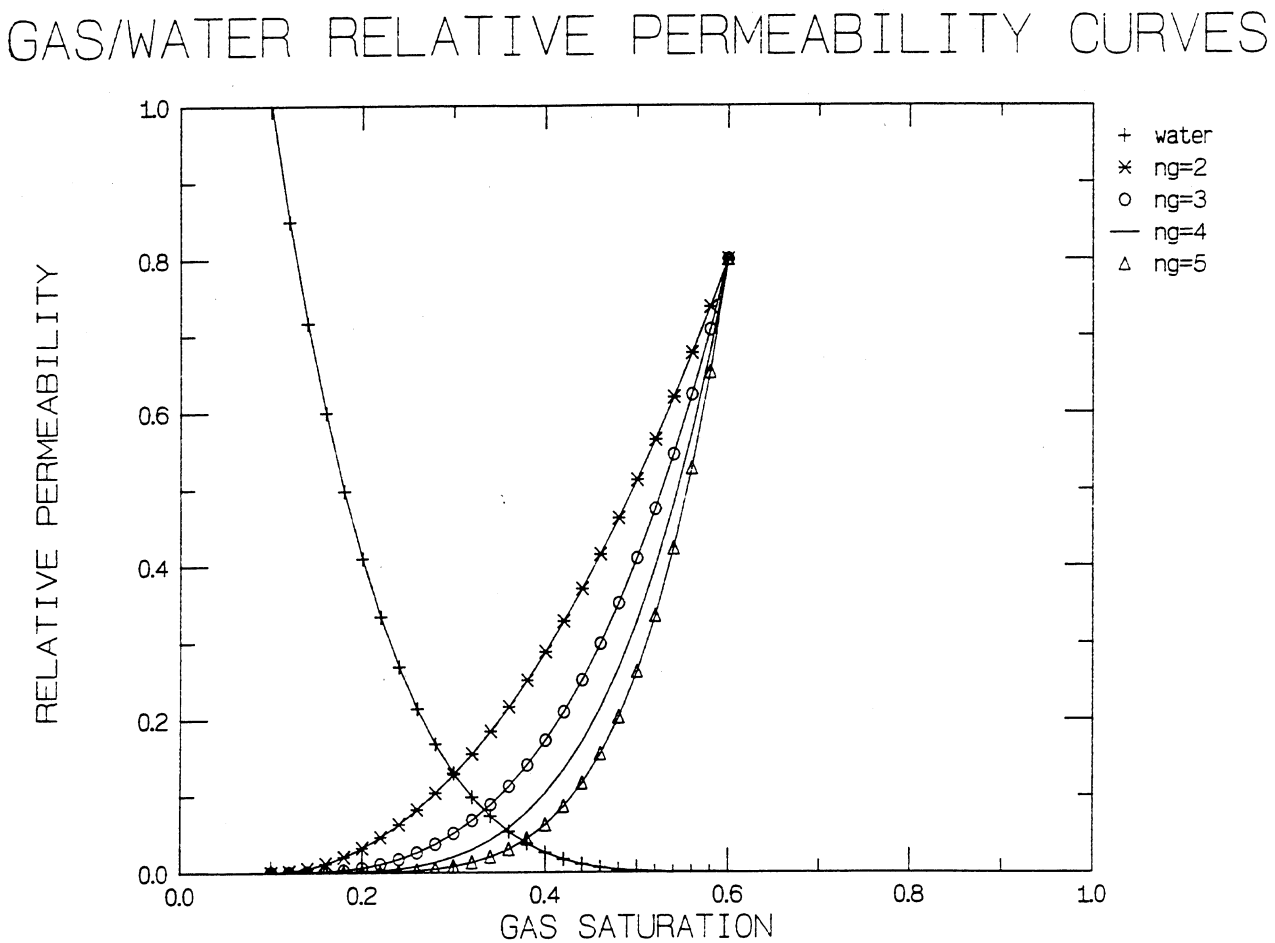

Figure I-88. Gas relative permeability curves for n_g = 2, 3, 4, 5, respectively, and water relative permeability curve used in the calculations.

G. REFERENCES

1. Heller, J.P. and Taber, J.J.: "Improvement of CO_2 Performance," First Annual Report, DOE/MC/21136-6 (June 1986).

2. Heller, J.P., Kovarik, F.S., and Taber, J.J.: "Improvement of CO_2 Performance," Second Annual Report, DOE/MC/21136-10 (May 1987).

3. Heller, J.P., Kovarik, F.S., and Taber, J.J.: "Improvement of CO_2 Performance," Third Annual Report, DOE/MC/21136-17 (Jan. 1989).

4. Heller, J.P. and Kovarik, F.S.: "Improvement of CO_2 Performance," Fourth Annual Report, DOE/MC/21136-21 (July 1989).

5. Kovarik, F.S. and Heller, J.P.: "Improvement of CO_2 Performance," Fifth Annual Report, Oct. 1, 1988-Sept. 30, 1989, PRRC Report No. 89-22, New Mexico Petroleum Recovery Research Center, Feb. 1990.

6. Orr, F.M. and Silva, M.K.: "Equilibrium Phase Compositions of CO_2-Hydrocarbon Mixtures —Part I: Measurement by a Continuous Multiple Contact Experiment," *SPEJ* (Apr. 1983) 272-280.

7. Aalund, L.R.: "EOR Projects Decline, but CO_2 Pushes Up Production," OGJ Annual Production Report, *Oil & Gas J.* (Apr. 1988) 33-47.

8. Orr, F.M., Jr. and Taber, J.J.: "Use of Carbon Dioxide in Enhanced Oil Recovery," *Science* (1984) **224**, 563-569.

9. Orr, F.M., Jr., Silva, M.K., and Lien, C.L.: "Equilibrium Phase Compositions of CO_2/Crude Oil Mixtures—Part 2: Comparison of Continuous Multiple-Contact Slim-Tube Displacement Tests," *SPEJ* (Apr. 1983) 272-280.

10. Orr, F.M., Jr. and Taber, J.J.: "Displacement of Oil by Carbon Dioxide," Final Report to the U.S. Department of Energy and the New Mexico Energy Research and Development Institute (1984).

11. Mason, W.P.: "Measurement of Viscosity and Shear Elasticity of Liquids by Means of a Torsionally Vibrating Crystal," *Trans.*, AIME (May 1947) **69**, 359-370.

12. Welber, B.: "Damping of a Torsional Oscillating Cylinder in Liquid Helium at Various Temperatures and Densities," *Physical Review* (1960) **119**, No. 6, 1816-1822.

13. Haynes, W.M.: "Viscosity of Gaseous and Liquid Argon," *Physica* (1973) **67**, 440-447.

14. Diller, D.E.: "Measurements of the Viscosities of Compressed Gaseous and Liquid Nitrogen," *Physica* (1983) 119A, 92-100.

15. Taylor, M.A., Heller, J.P., and Hutter, C.: "Design and Application of the Torsional Crystal Quartz Viscometer for the Continuous Phase Equilibrium Apparatus," PRRC Report 87-2, New Mexico Petroleum Recovery Research Center, 1987.

16. Lohrenz, J., Bray, B.G., and Clark, C.P.: "Calculating Viscosities of Reservoir Fluids From Their Compositions," *JPT* (Oct. 1964) 1171-1176.

17. Lansangan, R.M., Taylor, M.A., Smith, J.L., and Kovarik, F.S.: "An Improved Viscosity Correlation for CO_2/Reservoir Oil Systems," paper SPE/DOE 20209 presented at the Seventh Symposium on Enhanced Oil Recovery, Tulsa, Apr. 22-25, 1990.

18. Ely, J.F. and Huber, M.L.: "NIST Thermophysical Properties of Hydrocarbon Mixtures Database," Version 1.0, National Institute of Standards and Technology, Standard Reference Data Program (1990).

19. Chang, R.F., Morrison, G., and Levelt Sengers, J.M.H.: "The Critical Dilemma of Dilute Mixtures," *J. Phys. Chem.* (1984) **88**, 3389-3391.

20. Morrison, G., Levelt Sengers, J.M.H., Chang, R.F., and Christensen, J.J.: "Thermodynamic Anomalies in Supercritical Fluid Mixtures," *Supercritical Fluid Technology*, J.M.L. Penninger, M. Radosz, M.A. McHugh, and V.J. Krukonis (eds.), Elsevier Science Publishers, Amsterdam (1985).

21. Sengers, J.V. and Levelt Sengers, J.M.H.: "Thermodynamic Behavior of Fluids Near the Critical Point," *Ann. Rev. Phys. Chem.* (1986) **37**, 189-222.

22. Levelt Sengers, J.M.H., Morrison, G., Nielson, G., Chang, R.F., and Everhart, C.M.: "Thermodynamic Behavior of Supercritical Fluid Mixtures," *Int. J. Thermophys.* (1986) **7**, No. 2, 231-243.

23. Chang, R.F. and Levelt Sengers, J.M.H.: "Behavior of Dilute Mixtures Near the Solvent's Critical Point," *J. Phys. Chem.* (1986) **90**, 5921-5927.

24. Debenedetti, P.G. and Kumar, S.K.: "The Molecular Basis of Temperature Effects in Supercritical Extraction," *AIChE J.* (1988) *34*, No. 4, 645-657.

25. Brennecke, J.F. and Eckert, C.A.: "Phase Equilibria for Supercritical Fluid Process Design," *AIChE J.* (1989) **35**, No. 9, 1409-1427.

26. Benson, S.W., Copeland, C.S., and Pearson, D.: "Molar Volumes and Compressibilities of the System NaCl-H_2O Above the Critical Temperature of Water," *J. Chem. Phys.* (1953) **21**, No. 12, 2208-2212.

27. Chappelear, D.C. and Elgin, J.C.: "Phase Equilibria in the Critical Region," *J. Chem. Eng. Data* (1961) **6**, No. 3, 415-420.

28. Tsekhanskaya, Y.V., Roginskaya, N.G., and Mushkina, E.V.: "Volume Changes in Naphthalene Solutions in Compressed Carbon Dioxide," *Russ. J. Phys. Chem.* (1966) **40**, No. 9, 1152-1156.

29. Ehrlich, P. and Fariss, R.H.: "Negative Partial Molar Volumes in the Critical Region. Mixtures of Ethylene and Vinyl Chloride," *J. Phys. Chem.* (1969) **73**, No. 4, 1164-1167.

30. Ehrlich, P.: "Partial Molar Volume Anomaly in Supercritical Mixtures and the Free Radical Polymerization of Ethylene," *J. Macromol. Sci. Chem.* (1971) **A5**(8), 1259-1263.

31. Wu, P.C. and Ehrlich, P.: "Volumetric Properties of Supercritical Ethane-*n*-Heptane Mixtures: Molar Volumes and Partial Molar Volumes," *AIChE J.* (1973) **19**, No. 3, 533-540.

32. Abraham, K. P. and Ehrlich, P.: "Partial Molar Volume of a Polymer in Supercritical Solution," *Macromol.* (1975) **8**, No. 6, 944-946.

33. Eckert, C.A., Ziger, D.H., Johnston, K.P., and Ellison, T.K.: "The Use of Partial Molar Data to Evaluate Equations of State for Supercritical Fluid Mixtures," *Fluid Phase Equil.* (1983) **14**, 167-175.

34. Eckert, C.A., Ziger, D.H., Johnston, K.P., and Kim, S.: "Solute Partial Molar Volumes in Supercritical Fluids," *J. Phys. Chem.* (1986) **86**, 2738-2746.

35. Debenedetti, P.G.: "Clustering in Dilute, Binary Supercritical Mixtures: A Fluctuation Analysis," *Chem. Eng. Sci.* (1987) **42**, No. 9, 2203-2212.

36. Hwang, S.C., Lin, Y.N., and Kobayashi, R.: "Relation of Liquid-Liquid Equilibrium Behavior at Low Temperatures to Vapor-Liquid Equilibria Behavior at High Temperatures and Elevated Pressures," *Proc.*, 57th Ann. GPA Conv. (1978) 7-12.

37. Charoensombut-amon, T.: "Application of a Generalized Multiproperty Apparatus to the Measurement of Thermodynamic and Transport Properties to Measure Phase Equilibria and Vapor Phase Densities of Supercritical Carbon Dioxide in n-Hexadecane System," Ph.D Dissertation, Rice University (1985).

38. Lin, Y.N., Hwang, S.C., and Kobayashi, R.: "Vapor-Liquid Equilibria of the Methane-Toluene System at Low Temperatures," *J. Chem. Eng. Data* (1978) **23**, 231-234.

39. Stewart, W.C. and Nielsen, R.F.: "Phase Equilibria for Mixtures of Carbon Dioxide and Several Normal Saturated Hydrocarbons," *Prod. Monthly* (1954) **18**, 27-32.

40. Schneider, G.M.: "Phase Equilibria in Binary Fluid Systems of Hydrocarbons with Carbon Dioxide, Water, and Methane," *AIChE Symp. Series* (1968) **64**, 9-15.

41. Schneider, G.M.: "Phase Equilibria in Fluid Mixtures at High Pressures," *Adv. Chem. Phys.* (1970) **17**, 1-42.

42. Lansangan, R.M., Jangkamolkulchai, A., and Luks, K.D.: "Binary Vapor-Liquid Equilibria Behavior in the Vicinity of Liquid-Liquid-Vapor Loci," *Fluid Phase Equil.* (1987) **36**, 49-66.

43. Gubbins, K.E. and Twu, C.H.: "Thermodynamics of Polyatomic Fluid Mixtures - I. Theory," *Chem. Eng. Sci.* (1978) **33**, 863-878.

44. Twu, C.H. and Gubbins, K.E.: "Thermodynamics of Polyatomic Fluid Mixtures - II. Polar, Quadrupolar, and Octopolar Molecules," *Chem. Eng. Sci.* (1978) **33**, 879-887.

45. Venkatasubramanian, V., Gubbins, K.E., Gray, C.G., and Joslin, C.G.: "Induction Effects in Polar-Polarizable Liquid Mixtures—Calculation of Thermodynamic Properties Using Renormalized Perturbation Theory," *Mol. Phys.* (1984) **52**, No. 6, 1411-1429.

46. Rathmell, J.J., Stalkup, F.I., and Hasinger, R.C.: "A Laboratory Investigation of Miscible Displacement by Carbon Dioxide," paper SPE 3483 presented at the SPE Annual Tech. Conf. and Exhib., New Orleans, Oct. 3-6, 1971.

47. Holm, L.W. and Josendal, V.A.: "Mechanisms of Oil Displacement by Carbon Dioxide," *JPT* (Dec. 1974) 1427-1438.

48. Yellig, W.F. and Metcalfe, R.S.: "Determination and Prediction of CO_2 Minimum Miscibility Pressures," *JPT* (Jan. 1980) **32**, 160-168.

49. Holm, L.W. and Josendal, V.A.: "Effect of Oil Composition on Miscible-Type Displacement by Carbon Dioxide," *SPEJ* (Feb. 1982) **22**, 87-98.

50. Orr, F.M., Jensen, C.M., and Silva, K.M.: "Effect of Solution Gas on the Phase Behavior of CO_2-Crude Oil Mixtures," presented at the International Energy Agency Workshop on Enhanced Oil Recovery, Winfrith, U.K., Sept. 24, 1981.

51. Hutchinson, C.A., Jr. and Braun, P.H.: "Phase Relations of Miscible Displacements and Oil Recovery," *AIChE J.* (Mar. 1961) **7**, 64-72.

52. Johnson, J.P. and Pollin, J.S.: "Measurement and Correlation of CO_2 Miscibility Pressures," paper SPE/DOE 9790 presented at the 1981 SPE/DOE Second Joint Symp. on Enhanced Oil Recovery, Tulsa, Apr. 5-8.

53. Metcalfe, R.S.: "Effects of Impurities on Minimum Miscibilty Pressures and Minimum Enrichment Levels for CO_2 and Rich-Gas Displacements," *SPEJ* (Apr. 1982) 219-225.

54. Kovarik, F.S.: "A Minimum Miscibility Pressure Study Using Impure CO_2 and West Texas Oil Systems: Data Base, Correlations, and Compositional Simulation," paper SPE 14689 presented at the 1985 Production Tech. Symp., Lubbock, Nov. 11-12.

55. Alston, R.B., Kokolis, G.P., and James, C.F.: "CO_2 Minimum Miscibility Pressure: A Correlation for Impure CO_2 Streams and Live Oil Systems," *SPEJ* (Apr. 1985) 268-274.

56. Lansangan, R.M.: "Gravitationally Induced Mass Transfer of Carbon Dioxide in Hydrocarbon Liquids," Ph.D. Dissertation, University of Tulsa (1986).

57. Emanuel, A.S.: "A Mixing Rule Method for Calculating the Viscosity of CO_2 and Low-Gravity Reservoir Oil," paper SPE 14229 presented at the 1985 Annual Technical Conference and Exhibition, Las Vegas, Sept. 22-25.

58. Kovarik, F.S., Taylor, M.A., and Lansangan, R.M.: "Viscosity Measurements of High-Pressure CO_2/Hydrocarbon Systems," presented at the 1987 AIChE Annual Meeting, New York, Nov. 15-20; submitted for publication, 1989.

59. Jossi, J.A., Stiel, L.I., and Thodos, G.: "The Viscosity of Pure Substances in the Dense Gaseous and Liquid Phases," *AIChE J.* (1962) **8**, No. 1, 59-63.

60. Pedersen, K.S., Fredenslund, A., Christensen, P.L., and Thomassen, P.: "Viscosity of Crude Oils," *Chem. Eng. Sci.* (1984) **39**, No. 6, 1011-1016.

61. Peng, D.Y. and Robinson, D.B.: "A New Two-Constant Equation of State," *Ind. Eng. Chem., Fund.* (1976) **15**, No. 1, 59-64.

62. Saeedi, J. and Rowe, A.M.: "Viscosity Correlations for Compositional Reservoir Simulator," paper SPE 9643 presented at the 1981 Middle East Technical Conference, Manama, Bahrain, Mar. 9-12.

63. Coats, K.H.: "An Equation of State Compositional Model," *SPEJ* (Oct. 1980) 363-376.

64. Pedersen, K.S. and Fredenslund, A.: "An Improved Corresponding States Model for the Prediction of Oil and Gas Viscosities and Thermal Conductivities," *Chem. Eng. Sci.* (1987) **42**, No.1, 182-187.

65. Tham, M.J. and Gubbins, K.E.: "Correspondence Principle for Transport Properties of Dense Fluids. Nonpolar Polyatomic Fluids," *Ind. Eng. Chem. Fund.* (1970) **9**, No. 10, 63-70.

66. Uyehara, O.A. and Watson, K.M.: "A Universal Viscosity Correlation," *Natl. Pet. News* (1944) **36**, R714-R720.

67. Beal, C.: "The Viscosity of Air, Water, Natural Gas, Crude Oil and its Associated Gases at Oil Field Temperatures and Pressures," *Trans.* AIME (1946) **165**, 94-115.

68. Chew, J. and Connally, C.A.: "A Viscosity Correlation for Gas-Saturated Crude Oils," *Trans.* AIME (1959) **216**, 23-25.

69. Standing, M.B.: "Oil-System Correlations," *Petroleum Production Handbook*, McGraw-Hill Book Co., New York (1962).

70. Simon, R. and Graue, D.J.: "Generalized Correlations for Predicting Solubility, Swelling, and Viscosity Behavior of CO_2-Crude Oil Systems," *JPT* (1965) 102-106.

71. Little, J.E. and Kennedy, H.T.: "A Correlation of the Viscosity of Hydrocarbon Systems With Pressure, Temperature, and Composition," *SPEJ* (1968) 157-162.

72. Beggs, S.D. and Robinson, J.R.: "Estimating the Viscosity of Crude Oil Systems," *JPT* (1975) 1140-1141.

73. Houpeurt, A.H. and Thelliez, M.B.: "Predicting the Viscosity of Hydrocarbon Liquid Phases From Their Composition," *JPT* (1976) 223-231.

74. Baltatu, M.E.: "Prediction of the Liquid Viscosity for Petroleum Fractions," *Ind. Eng. Chem. Proc. Des. Dev.* (1982) **21**, 192-195.

75. Brule, M.R. and Starling, K.E.: "Thermophysical Properties of Complex Systems: Applications of Multiproperty Analysis," *Ind. Eng. Chem. Proc. Des. Dev.* (1984) **23**, 833-845.

76. Teja, A.S., Thurner, P.A., and Pasumarti, B.: "Calculation of Transport Properties of Mixtures for Synfuels Process Design," *Ind. Eng. Chem. Proc. Des. Dev.* (1985) **24**, 344-349.

77. Twu, C.H.: "Generalized Method For Predicting Viscosities of Petroleum Fractions," *AIChE J.* (1986) **32**, No. 12, 2091-2094.

78. Lawal, A.S.: "Prediction of Vapor and Liquid Viscosities From the Lawal-Lake-Silberberg Equation of State," paper SPE/DOE 14926 presented at the Fifth Symposium on Enhanced Oil Recovery of the SPE and the DOE in Tulsa, Apr. 20-23, 1986.

79. Goodstein, D.L.: *States of Matter*, Dover Publications, Inc., New York (1985).

80. Kreuzer, H. J.: *Nonequilibrium Thermodynamics and its Statistical Foundations*, Clarendon Press, Oxford (1981).

81. Brush, S.G.: "Theories of Liquid Viscosity," *Chem Rev.* (1962) **62**, 513-548.

82. McCarty, R.D.: "A Modified Benedict-Webb-Rubin Equation of State for Methane Using Recent Experimental Data," *Cryogenics* (May 1974) 276-280.

83. Hanley, H.J.M., McCarty, R.D., and Haynes, W.M.: "Equations for the Viscosity and Thermal Conductivity Coefficients of Methane," *Cryogenics* (May 1974) 413-417.

84. Lin, H.M. and Chao, K.C.: "Correlation of Critical Properties and Acentric Factor of Hydrocarbons and Derivatives," *AIChE J.* (Nov. 1984) **30**, No. 6, 981-983.

85. Hankinson, R.W. and Thomson, G.R.: "A New Correlation for Saturated Densities of Liquids and Their Mixtures," *AIChE J.* (1979) **25**, No. 4, 653-663.

86. Thomson, G.H., Brobst, K.R., and Hankinson, R.W.: "An Improved Correlation for Densities of Compressed Liquids and Liquid Mixtures," *AIChE J.* (1982) **28**, No. 4, 671-676.

87. Vargaftik, N.B.: *Handbook of Physical Properties of Liquid and Gases* (2nd ed.) Hemisphere Publishing Corp., New York (1975).

88. Mo, K.C. and Gubbins, K.E.: "Conformal Solution for Viscosity and Thermal Conductivity of Mixtures," *Mo. Phys.* (1976) **31**, No. 3, 825-847.

89. Ely, J.F. and Hanley, H.J.M.: "Prediction of Transport Properties. 1. Viscosities of Fluids and Mixtures," *Ind. Eng. Chem. Fund.* (1981) **20**, 323-332.

90. Martin, F.D. and Heller, J.P.: "Improvement of CO_2 Flood Performance," Quarterly Report to DOE, NMRDI, and Industry (Jan. - Mar. 1990) PRRC Report No. 90-20, New Mexico Petroleum Recovery Research Center, June 1990.

91. Metcalfe, R.S. and Yarborough, L.: "The Effect of Phase Equilibrium on the CO_2 Displacement Mechanism," *SPEJ* (Aug. 1979) 242-52.

92. Yaghoobi, H.: "Effect of Solution and Free Gas on the Development of Miscibility," MS Thesis, NMIMT Petroleum Dept., Socorro, NM (Dec. 1990).

93. Monroe, W.W., Silva, M.K., and Larsen, L.L.: "The Effect of Dissolved Methane on CO_2 Flood Performance in One Dimension," paper SPE 16712 presented at the 62nd Annual Technical Conference and Exhibition of the Society of Petroleum Engineers held in Dallas, Sept. 27-30, 1987.

94. Hill, S.: "Channelling in Packed Columns," *Chem. Eng. Sci.* (1952) **6**, No. 1, 247-253.

95. Orr, F.M., Jr., and Silva, M.K.: "Effect of Oil Composition on Minimum Miscibility Pressure Part 2: Correlation," paper SPE 14150 presented at the 1985 Annual Fall Meeting, Las Vegas, Sept. 22-25.

96. Whitson, C.H.: "Characterizing Hydrocarbon Plus Fractions," *SPEJ* (Aug. 1983) 683-694.

97. Katz, D.L. and Firoozabadi, A.: "Predicting Phase Behavior of Condensate/Crude-Oil Systems Using Methane Interaction Coefficients," *JPT* (Nov. 1978) 1649-55.

98. Huh, D.G., Cochrane, T.D., and Kovarik, F.S.: "The Effect of Microscopic Heterogeneity on CO_2-Foam Mobility: Part 1—Mechanistic Study," *JPT* (Aug. 1989) 872-879.

99. Roof, J.G.: "Snap-Off of Oil Droplets in Water-Wet Pores," *SPEJ* (Mar. 1970) 85-90; *Trans.*, AIME, 249.

100. Mast, R.F.: "Microscopic Behavior of Foam in Porous Media," paper SPE 3997 presented at the 1972 SPE Annual Meeting, San Antonio, Oct. 8-11.

101. Radke, C.J. and Ransohoff, T.C.: "Mechanisms of Foam Generation in Glass-Bead Packs," *SPERE* (May 1988) 573-85.

102. Orr, F.M., Jr. and Taber, J.J.: "Displacement of Oil by Carbon Dioxide," Annual Report to the U.S. DOE, DOE/BC/10331-4 (Apr. 1982).

103. Orr, F.M., Jr., Yu, A.D., and Lien, C.L.: "Phase Behavior of CO_2 and Crude Oil in Low-Temperature Reservoirs," *SPEJ* (Aug. 1981) 480-492.

104. Bahralolom, I.: "Flow Visualization of CO_2-Crude Oil Mixtures," M.S. Thesis, NMIMT Petroleum Dept., Socorro, NM (May 1985).

105. Campbell, B.T. and Orr, F.M., Jr.: "Flow Visualization for CO_2-Crude Oil Displacements," *SPEJ* (Oct. 1985) 665-678.

106. Chang, S-H., Owusu, L.A., and French, S.B.: "The Effect of Microscopic Heterogeneity on CO_2-Foam Mobility: Part 2—Mechanistic Foam Simulation," paper SPE/DOE 20191 presented at the Seventh SPE/DOE Symposium on EOR, Tulsa, Apr. 22-25, 1990.

107. Friedmann, F., Chen, W.H., and Gauglitz, P.A.: "Experimental and Simulation Study of High-Temperature Foam Displacement in Porous Media," paper SPE/DOE 17357 presented at the 1988 SPE/DOE Enhanced Oil Recovery Symposium, Tulsa, Apr. 17-20.

108. Lee, H.O., and Heller, J.P.: "Laboratory Measurements of CO_2-Foam Mobility," paper SPE/DOE 17363 presented at the 1988 SPE/DOE Enhanced Oil Recovery Symposium, Tulsa, Apr. 17-20.

109. Marfoe, C.H., Kazemi, H., and Ramirez, W.F.: "Numerical Simulation of Foam Flow in Porous Media," paper SPE 16709 presented at the 1987 SPE Annual Technical Conference and Exhibition, Dallas, Sept. 27-30.

110. Sharma, M.K., Shah, D.O., and Brigham, W.E.: "Effect of Mixed-Chain-Length Surfactants on Fluid Displacement in Porous Media by In-Situ Foaming Process," *SPERE* (May 1986) 253-260.

111. Falls, A.H., Musters, J.J., and Ratulowski, J.: "The Apparent Viscosity of Foams in Homogeneous Bead Packs," *SPERE* (May 1989) 155-164.

112. Hirasaki, G.J., and Lawson, J.B: "Mechanisms of Foam Flow in Porous Media: Apparent Viscosity in Smooth Capillaries," *SPEJ* (Apr. 1985) 176-190.

113. Yang, S.H. and Reed, R.L.: "Mobility control Using CO_2 Foams," paper SPE 19689 presented at the 1989 SPE Annual Technial Conference and Exhibition, San Antonio, Oct. 8-11.

114. Bernard, G.G., Holm, L.W., and Jacobs, W.L.: "Effect of Foam on Trapped Gas Saturation and on Permeability of Porous Media to Water," *SPEJ* (Dec. 1965) 295-300.

115. Holm, L.W., and Garrison, W.H.: "CO_2 Diversion With Foam in an Immiscible CO_2 Field Project," *SPERE* (Feb. 1988) 112-118.

116. Friedmann, F. and Jensen, J.A.: "Some Parameters Influencing the Formation and Propagation of Foams in Porous Media," paper SPE 15087 presented at the 1986 SPE California Regional Meeting, Oakland, Apr. 2-4.

117. Khatib, Z.I., Hirasaki, G.J., and Falls, A.H.: "Effects of Capillary Pressure on Coalescence and Phase Mobilities in Foams Flowing Through Porous Media," *SPERE* (Aug. 1988) 919-926.

118. Falls, A.H., Hirasaki, G.J., Patzek, T.W., Gauglitz, D.A., Miller, D.D., and Ratulowski, T.: "Development of a Mechanistic Foam Simulator: The Population Balance and Generation by Snap off," *SPERE* (Aug. 1988) 884-892.

119. Patzek, T.W.: "Description of Foam Flow in Porous Media by the Population Balance Method," *Surfactant-Based Mobility Control*, D.H. Smith, (ed.), ACS Symposium Series #373, Washington, D.C. (1988) 326-341.

120. Persoff, P., Radke, C.J., Benson, S.M., and Witherspoon, P.A.: "A Laboratory Investigation of Foam Flow in Sandstone at Elevated Pressure," paper SPE 18781 presented at the 1989 SPE California Regional Meeting, Bakersfield, Apr. 5-7.

II. CO_2 MOBILITY CONTROL AND FLOW HETEROGENEITIES

A. HETEROGENEITY OF RESERVOIR ROCK

This Section of Task II presents the research of three doctoral candidates in Petroleum Engineering, all of whom are in the final stages of writing their theses. They have been investigating different aspects of the subject now widely known as *reservoir characterization*. Because our interest has been particularly in the effects of rock nonuniformities on miscible displacement, we have focussed especially on those rock parameters that primarily affect single-phase flow and displacement—porosity and, usually to the largest extent, permeability. As an introduction to their work, the following additional background is offered.

In the historical section of this report, we discussed the earlier work of Naser Heravi[1*] on computing the displacement from five-spot patterns in reservoirs in which the permeability varied randomly from place to place. He initiated the use of a calculation method to determine the effect of the two major geostatistical parameters on unit viscosity ratio on miscible displacements. His work indicated that the value of these parameters do indeed seem to determine the broad features of the displacement process. Whereas the particular numerical *realization* of a spatial permeability distribution determines the details of successive positions of the miscible front, the natural integrals of those fronts, which are obtained automatically at the production well, are more indicative of the overall geostatistical parameters of the permeability distribution.

That section of this report also describes the more-recent research of Elhassan Abdalla. He followed similar lines to pursue this question further—to what extent are the geostatistical parameters *sufficient* to define the miscible displacement efficiency? His results, described at greater length above and in his masters thesis,[2] are that, if the correlation length is sufficiently short in comparison with the well-to-well spacing, the specification of the correlation length and the limiting variance are indeed sufficient to define the displacement efficiency and recovery curve, within a precision fixed by the parameters themselves.

It is evident that in many reservoirs, the heterogeneity pattern is such that permeabilities are correlated over longer distances. Where the correlation length is long, a geostatistical description is less useful. In this case, the particular well placement would be most important in determining the displacement history, and given the layered structure of sedimentary basins, this would often be bad news. A long correlation length coupled with a high value of limiting variance usually means that the field will be plagued with early breakthrough problems associated with the consistently higher permeabilities of layers that are identifiable over long distances.

In other cases, though, the correlation distances are shorter, because the layered structure is not so prominent, because the sediments may pinch out, as a result of an areally variable fraction of the fines component in the original deposit or because of the variability of subsequent diagenesis. In these cases, the geostatistical parameters of the permeability structure can apparently be taken as reliable indicators of well and field behavior in miscible displacement processes such as CO_2 floods.

The following subsections present the recent research of Saleem Ghori, Junaid Sultan, and Ibrahim Bahralolom. The first depicts a promising method for assessing the geostatistical parameters of a

---

*References for Task II start on page II-156.

reservoir, the second discusses the application of geostatistical data in reservoir simulation, and the third is concerned with the analysis of small-scale heterogeneities that can be observed in laboratory samples.

1. Assessment of Geostatistical Parameters

The doctoral research of Saleem Ghori consists of the determination of reservoir heterogeneity from well-to-well tracer tests. It is known that the variability of permeability within a field is the most important aspect of the heterogeneity for miscible and near miscible floods. This is because the variations in permeability are large compared to those of the porosity. Permeability variations have a direct and, in principle, calculable effect on flow of fluids through porous media. Although it is not possible to quantify the actual values or the particular variations of permeability in a reservoir by direct measurements at more than a few locations, the spatial distribution of this variability can be described in terms of statistical parameters. The problem is to find a way of estimating the statistical parameters of the permeability distribution from available information. One of the few possible methods of discovering the properties of the underground reservoir properties is to run well-to-well tracer tests. Operating engineers often use output concentration at the production well to predict the behavior of the reservoir, such as directional flow trends, flow barriers, relative velocities of the injected fluid and sweep efficiency, etc. In Saleem's research, the attempt is made to use the data from tracer tests to make quantitative, statistical estimates of the permeability distribution.

The objective of his research is to assess the geostatistical parameters of the spatial permeability distribution from the tracer production curves. As might be expected, these curves also depend on the type of flooding pattern (e.g. five-spot pattern, staggered line drive, and direct line drive) into which the field is divided. A very efficient numerical technique has made it possible to produce output tracer profiles for different sets of spatial permeability distributions. The source point method (SPM) was used to generate various permeability distributions. These distributions can be characterized by two parameters, the limiting variance and the correlation length. A catalogue of the tracer output concentration curves was produced to see the effect of these two geostatistical parameters, and the influence of the microscopic dispersivity was also observed. Results have shown that the tracer output concentration from a heterogeneous reservoir shows multiple peaks even in a single layered reservoir. A detailed description of the methodology and the results are given in the paper "Computed Effect of Heterogeneity on Well-to-Well Tracer Results," which was presented at the American/Canadian Conference on Hydrology at Calgary in September 1990. Another useful result of this work has been the assignment of the correlation length in the SPM.

The catalogue of the tracer output concentration is beneficial in attacking the inverse problem: the two geostatistical parameters of the permeability and the microscopic dispersivity, given the output concentration profile. One possible method for making these determinations is to take the spectral density of these curves and relate the important frequencies to the parameters of the permeability distribution. A base case can be obtained by using the spectral density of the tracer profile from a homogeneous formation. This work is in progress and useful generalizations are expected. These will enable the interpretation of produced tracer concentration curves in terms of the statistical parameters of the formation layer.

An attempt was also made to take into account the theory of conditional probability and conditional covariances of the permeabilities generated from the SPM. The conditional covariance of the generated permeability field can be evaluated by computing the covariance of LnK at the location of one source

point, given the locations of the rest of the source points in the manner suggested by Dr. Allan Gutjahr.[3] Because the locations of the source points change from one realization to the other, the above conditional covariance was calculated for several realizations. The average value of these gave the desired covariance function. The correlation lengths were calculated for different numbers of source points (N_{sp}) by taking the "e-fold" drop, that is, as the lag distanced for which the variograms reach $(1 - \frac{1}{e})$ of their limiting variance values. The correlation lengths of the different realizations were then plotted against the quantity $\sqrt{\text{area}/N_{sp}}$, which produced a straight line with slope approximately equals to one. This confirms that the correlation length in the SPM can be prespecified by the relationship

$$\text{correlation length} = \sqrt{\frac{\text{area}}{N_{sp}}}$$

In other words, this means that the correlation length of a field produced by the SPM, and calculated by the above method, is equal to the average spacing between the source points.

Verification of both the numerical simulation and of the rules for obtaining the permeability heterogeneity from the tracer output concentration can be performed by laboratory experiments. For this purpose, rock samples, shaped to represent a quarter of a five-spot pattern, will be used in flooding experiments. An already built mini-permeameter is used to measure the permeabilities at specified grids of the rock. Geostatistical parameters are obtained from the measured permeabilities. A tracer experiment also will be performed to obtain the tracer output concentration at some specified locations. The work in this area is also underway.

2. Application of Geostatistics to Characterize Reservoir Heterogeneity

In his doctoral research, A. Junaid Sultan has considered the geological origins of reservoir heterogeneity, the applicability of "random" geostatistical distributions to reservoirs, and a few of the accepted means of generating such fields. Most recently, and in this report, Sultan has turned his attention to the mathematical problem of *conditioning* such fields so as to be consistent with (or "honor") known data.

Several types of nonuniformity may be found on different scales of length. They are all considered to be the result of environmental variability during one or more of the three different processes by which the rock develops. These processes are: sedimentary (when the original grains were laid down), diagenetic (the gradual chemical and physical changes that occurred after deposition), and tectonic (modification caused by changes since deposition of the geological environment). The details of these geological aspects, which are the reasons for the heterogeneity of petroleum reservoirs, have been discussed in a topical report of this project by Sultan and Heller.[4]

Different rock properties may assume different degrees of significance in miscible and immiscible displacements through a porous medium. In miscible displacements, rock permeability has been found to be the most important parameter. Furthermore, the assignment of a proper permeability distribution to the grid blocks in a reservoir simulation becomes more important when the permeability variance is greater.

A common deficiency of most of the existing methods is the lack of correlation among the nearby permeability values. In other words, the permeability values have been taken to be independent of each other. Traditional statistical procedures are based on the concept of random observations of independent members of a distribution without evaluation of the spatial relationships that may exist.

The use of statistical procedures is made necessary by the joint circumstances of nonuniform reservoir rock properties and the scarce availability of data. It is impossible to visualize the details of the entire formation, because of the very limited data that are available about the reservoir rock properties. In this situation, the best description will be one that specifies only the probabilities of finding particular values. Consequently, it is frequently asserted (and perhaps the assertion is too crude an approximation) that the reservoir parameters exhibit random spatial fluctuations. However, the mathematical theory of random events is well developed and has proved its usefulness in a number of very practical applications in which modern statistics and probability theory have been applied.

To deal with the apparent randomness of petrogeological parameters, and with the uncertainty arising from insufficient information about their spatial distribution, we attempt to describe these variations stochastically instead of deterministically. This can be achieved by treating each parameter as a random variable whose spatial fluctuations are the realizations of a stochastic process. In this study, we are concentrating on the distribution of the permeability in a petroleum reservoir and, therefore, will generate the realizations of permeability distributions.

It is only because the details of natural processes are too numerous, inaccessible, and complex for direct analysis that the stochastic approach becomes a realistic way to take the extreme variability into consideration. We are driven to the stochastic approach by the lack of specific information about the values of permeability or other values. Despite this, we can anticipate that a purely statistical description will be useful in deriving overall properties of the formation.

The random nature and the spatial correlation of rock properties can be modeled by employing geostatistical techniques that have been developed as the application of modern probability theory and statistical methods to a major practical problem of earth science. The discipline has already been used with some success in characterizing the variability of mineral deposits. A good reference to these techniques is given by Journel and Huijbregts.[5]

Three methods have been considered in this study for generating random fields to represent the spatial variability of permeability for use in reservoir simulation. Heller[6] suggested the Source Point Method (SPM) to generate a random permeability distribution in a two-dimensional region. This procedure resulted in a distribution which, though random in both the location and the magnitude of "permeability extrema," was continuous in the mathematical sense. In addition, the range and form of the frequency distribution of permeability values, and the correlation length characterizing the spatial distribution, could be adjusted a priori. Heller reported that a simple transformation yielded a frequency distribution not far from log-normal that is consistent with those statistical studies that have discovered log-normal distributions of permeability values in actual fields. In subsequent years, other mathematical or numerical procedures have been developed by which random permeability distributions of similar properties can also be produced. These include the Turning Bands Method (TBM) which was originated by Matheron[7] and further developed by Montoglou and Wilson;[8] and the Fast Fourier Transform Method (FFTM) developed by Gutjahr.[9] The advantages of the last two methods are that they give the user the ability to prespecify both the correlation length and a mathematical function for the covariance shape.

The testing of generated fields by the above-mentioned three methods have been detailed in a paper by Sultan *et al.*[10]

The assumption of second-order stationarity is required to use these methods that generate unconditioned but spatially correlated permeability fields. According to this assumption, the mean of permeability is constant all over the field, and the covariance function depends only on the separation distance between points at which permeability is evaluated.

If $U_{(\underline{x})} = ln\ K(\underline{x})$ is a statistically homogeneous random permeability field, then the function

$$c(\underline{h}) = cov(U(\underline{x} + \underline{h}), U(\underline{x})) \qquad \text{(II-1)}$$

is called the covariance function for the field. The $|\underline{h}|$ would be the separation distance between the two locations of the field. The underbar indicates that $\underline{x}$ and $\underline{h}$ are considered to be vectors.

The simulations considered here are of random permeability fields. In an *unconditioned* simulation, an attempt is made to generate a possible representation of the field that has the desired random behavior (mean value and covariance function) to match those statistical properties of data given at a particular set of points.

Although an unconditioned permeability field has the same statistical character, the values it specifies for the field variable at the locations of the original data points will probably not coincide with the actual data. In other words, the unconditioned realization does not necessarily pass through the data points. In a *conditioned* simulation this defect is remedied, at the cost of some additional calculation, by combining the generation of an unconditioned field with another geostatistical technique known as *kriging*. A two-dimensional conditioned simulator has been developed that uses the unconditioned random permeability field generated by the Fast Fourier Transform method. The theoretical developments of the conditioned simulator will be reported in the forthcoming dissertation by Sultan.

This conditioned simulator takes into account permeability data obtained from the well tests, and generates a conditioned log-permeability field. There are other sources of permeability data such as cores, logs, etc. Well-test data is selected because of their reliability as measures of the average permeability surrounding the wellbore, and because of the availability of such data.

Well-test data give permeability values that are averages over a fairly large region. The geostatistical parameters of a field computed from such data, and especially the variance, may differ from those of a field computed from point values or from permeabilities averaged over smaller grid blocks. It is possible, though, to transform such large scale data to a smaller scale. An inter-scale transformation of variogram parameters has been developed in this study.

An example of field well-test permeability data is included here to demonstrate the above-mentioned methodology. The locations of tested wells of a real reservoir, identified here only as "B," are depicted in Fig. II-1. An arbitrary origin was selected from which the location of wells is referenced. The values of the permeabilities from these tests are taken to be representative of the production zones of the reservoir.

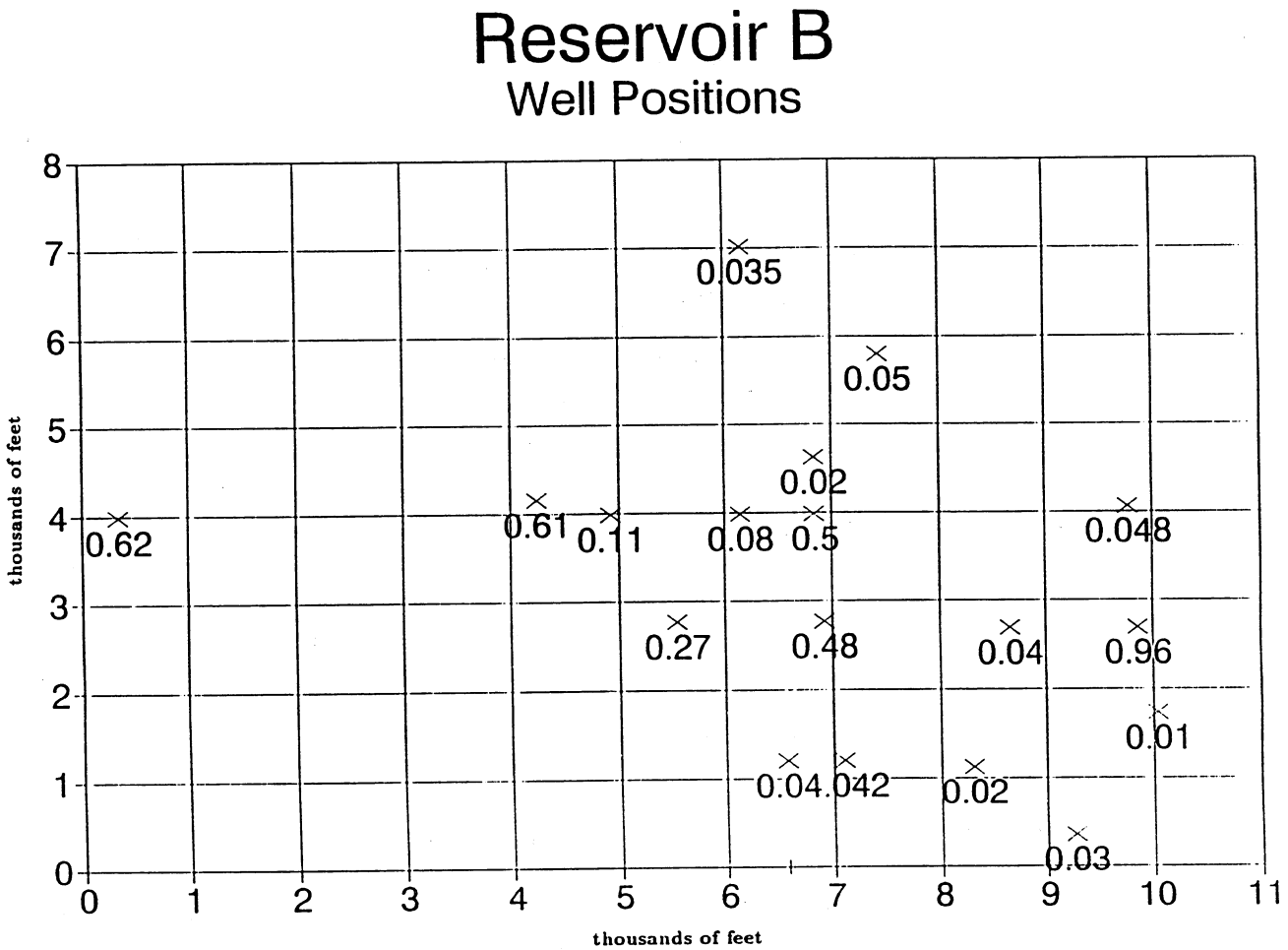

Figure II-1. Locations of weller for a section of reservoir-B.

a. Variography

The analysis should be performed on data that are as reliable as possible. The permeability values found from well-tests in reservoir-B are assumed to belong to a regionalized variable that is spread out in space and also shows a certain structure. This variable has two apparently contradictory characteristics: a random characteristic (erratic behavior from point to point) and a structural characteristic, reflecting the degree of correlation among points.

The character of the covariance function is often expressed in terms of the major geostatistical descriptor known as a variogram. The curve is usually complementary to a covariance function. The variogram is a function of lag distance h, and is defined as any value of h at one half of the expected value of the square of the difference between log-permeability at points separated by that distance

$$\gamma(h) = 1/2E\left[\{U(\underline{x}) - U(\underline{x}+h)\}^2\right] \tag{II-2}$$

The calculation formula for $\gamma^*(h)$, an approximation of $\gamma(h)$, is given as follows:

$$\gamma^*(h) = \frac{1}{2N_h}\sum_{i=1}^{Nh} [U(\underline{x}_i - U(\underline{x}_i + h)]^2 \tag{II-3}$$

where h is the distance between points, $U(\underline{x}_i)$ is the measured value at location $\underline{x}_i$, and N_h is the number of pairs of points separated by distance h.

Variograms are computed in different directions to check for anisotropy and for any trend that might exist in the region. Such a trend could be accommodated in a model by conditioning the known data (log-permeability in this study). The magnitude of the trend that could be handled by conditioning needs to be investigated. Although it is generally important to study the data in different directions to find if an anisotropy exists, an overall variogram is considered in this study because of the preexisting assumption of second order stationarity.

The variogram constructed from log-permeability data of the well-test for reservoir-B is shown in Fig. II-2. The limiting variance (σ^2), or sill, an important parameter of a variogram, can be estimated from this figure. It is, however, difficult to guess a value of correlation length (λ) from this variogram of reservoir-B because the known data are far apart from each other and/or are not great enough in number for the large area considered. The data do indicate the correlation length to be between 200-600 ft, however.

An exponential model is selected to fit this variogram. The variance of log-permeability for reservoir-B was found to be 1.893 and the value of the correlation length (λ) needs to be refined from the estimated range. A validation procedure has been adopted to estimate the best set of parameters for the chosen model of the variogram.

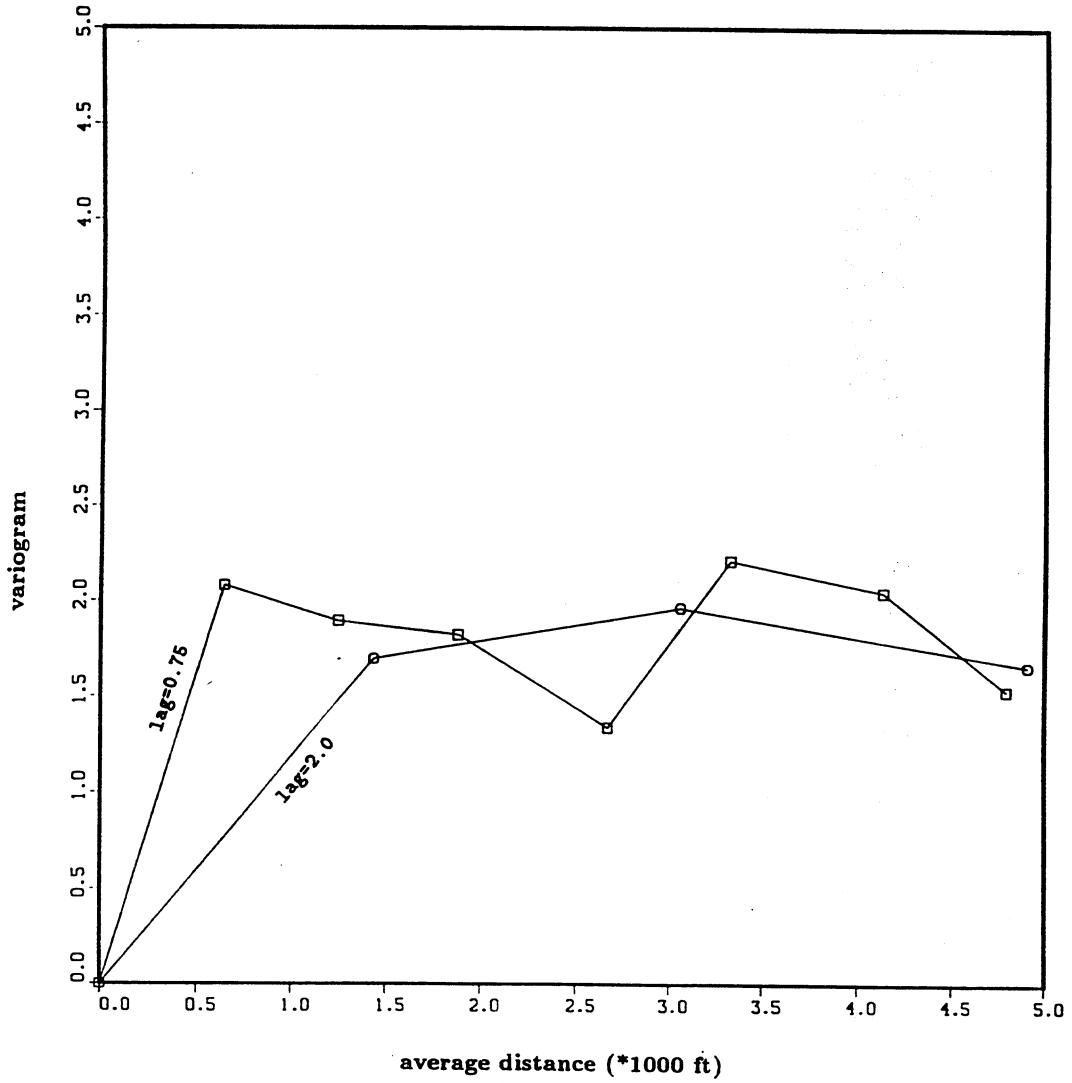

Figure II-2. Variograms for reservoir-B.

b. Validation of the Parameters

As noted, an exponential model was selected to fit the constructed variogram of reservoir-B, and a reasonable value of variance determined from the variogram. An acceptable correlation length is next decided from the estimated range by application of a validation program. This program performs N successive kriging calculations, in each one of which a different one of the data points is ignored. Thus, the program produces a set of estimated values, U_i^*, which are compared with the log-permeability values, U_i, for each point.

Several possible correlation length values, in the range determined from the variogram, are used in order to evaluate the best fit to the exponential model. This best fit occurs when two basic conditions are satisfied: the mean error vanishes and the reduced quadratic mean error approaches unity. With the choice of an exponential model, the following parameters have been estimated for reservoir-B data from the validation procedure.

$$\lambda = 250 \text{ ft and } \sigma^2 = 1.893. \tag{II-4}$$

The quality of the validation program can be appreciated from the parameters that resulted from the computation. The mean error, which the program tries to make vanish, came out to -0.00018, and the final value of the reduced quadratic mean error, which was driven toward unity in the program, was 1.084. A structural model for the correlation, which was speculated from the variogram of reservoir-B and refined by the validation program, has been expressed in an analytical form.

c. Influence of Scale on Variance and Correlation Length

Once the decisions have been made as to the analytic form of a variogram model and its parameters, then the need arises for a relationship of these parameters at various scales. Up to this point, well-test data have been considered. The permeability values obtained in such tests represent some sort of average of the permeabilities throughout a large region comparable to the surrounding drainage area. All the developments of the variogram have been done at this large scale. What would be the appropriate variogram parameters to use when the model is expressed in the smaller grid block scale used in simulation? A relationship has been established of variance and the correlation length with different sizes of grid blocks. This was done in the following manner, in which the sizes of grid blocks are referred to as different scales. A regionalized variable field with an exponential model, having known variance and correlation length, was first generated with the Fast Fourier Transform Method (FFTM).

A number of variance values for large grid blocks were evaluated, from the field generated for small grid blocks, with the help of a special program called "avgb." As the size of the large grid blocks is increased, more of the smaller grid blocks are included in it. A block average value, which is evaluated from the weighted small grid blocks from the center of the large block, is assigned to the large block.

In the small grid block field generated from FFTM, the value of the variance was 1.0, and the correlation length was .606. For various sizes of large grid blocks, variances were evaluated and the results are shown in Fig. II-3. The variance reduces as the size of large grid blocks is increased. Similar conclusions of support-scale effects for block-averaged-transmissivities have been made by Desbarats.[11]

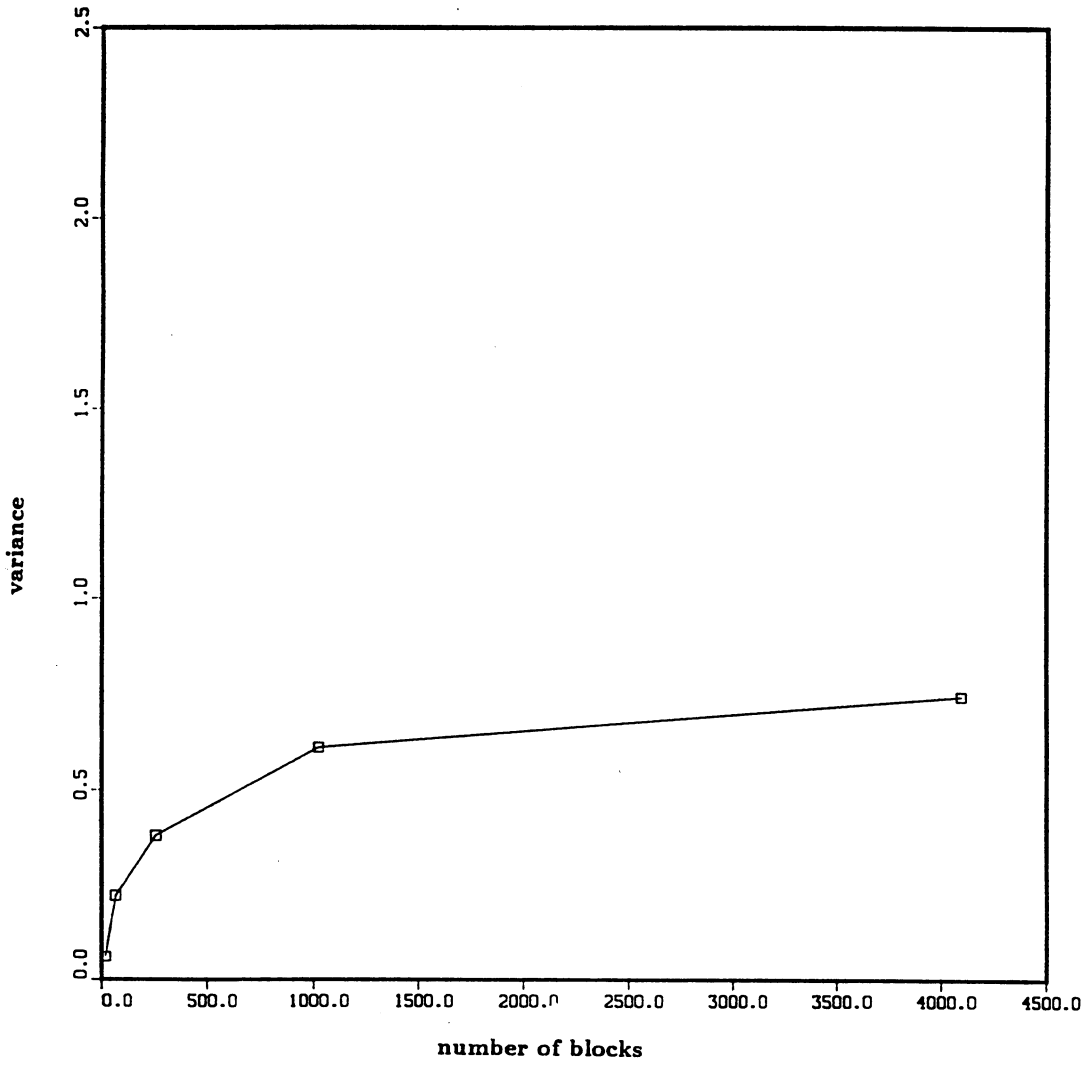

Figure II-3. The effect of scales on variance for reservoir-B.

This exercise demonstrates a relationship of variance with the grid block size. The value of variance for the well-test data of reservoir-B was found to be 1.893. Scaling the relationship (shown in Fig. II-3), small grid blocks variance is calculated to be 4.965. A numerical experiment was performed to show the effect of scale on the correlation length and the results are presented in Fig. II-4. The variograms depicted in this figure have been constructed from various grid block sizes. The change in correlation length (λ) is not significant with various scales, which have been varied from the scale of well-test data to the scale of simulation small grid blocks size. This small variation of correlation length is presented in Fig. II-5. The value of the correlation length of λ, suggested by this figure, is close to 3.1 compared to the 3 (in units of small grid-blocks) estimated by the validation procedure.

d. Conditioned Log-Permeability Field

The relationships of the important variogram parameters at various scales have been established. Reservoir properties, such as permeability, can be transformed from one scale to another scale. Various sources of data of reservoir permeability can, in this way, be taken into account in conditioning studies.

Permeability values calculated from the well-test data of reservoir-B have been used to generate conditioned correlated log-permeability fields for simulation. These fields are at smaller grid blocks than the size of the grid blocks of well-tests. The large grid blocks size (660 ft) is equivalent to double the average radius of investigation of well-tests for reservoir-B.

The reservoir-B area is divided into 16 $\times$ 16 large grid blocks (660 $\times$ 660 ft) and 128 $\times$ 128 small grid blocks of the size of 82.5 ft. The variance of log-permeability distribution for small grid blocks is calculated to be 4.965 and the correlation length is estimated to be 250 ft. For simulation, the small grid block size is taken to be 0.2 in x and y direction and the λ equals 0.606.

The small scale correlated log-permeability field has been conditioned to the known permeability data of reservoir-B. Because of the involvement of cross-covariance (relationship between small and large grid blocks) in the development of the conditioning procedure, the permeability of the known locations does not match exactly with the calculated permeability for the small scale conditioned field. In contrast, the known data coincide exactly in the case of the ordinary conditioning process. The magnitudes of the log-permeability, at given locations in the conditioned small scale field, differ by only a few percent from those of the known well-test permeability data.

The synthetic unconditioned log-permeability field was generated by the FFTM. The transformed parameters from large scale (well-test) to simulation scale of reservoir-B were used to generate this field. An example of this field is shown in Fig. II-6. Black color corresponds to low log-permeability regions, white designates high log-permeability areas, and the intermediate ranges have been depicted with different shades. The order of these shades is shown in the upper left corner of this figure. A conditioned field of reservoir-B is represented in Fig. II-7. The advantages of a conditioned field are that it maintains the statistical properties of the known data and retains the same order of magnitude of the known data at the locations of measurement. It also preserves existing trends, if any, in the field. This latter property is very important for regionalized, variable fields that are to be used for simulation purposes.

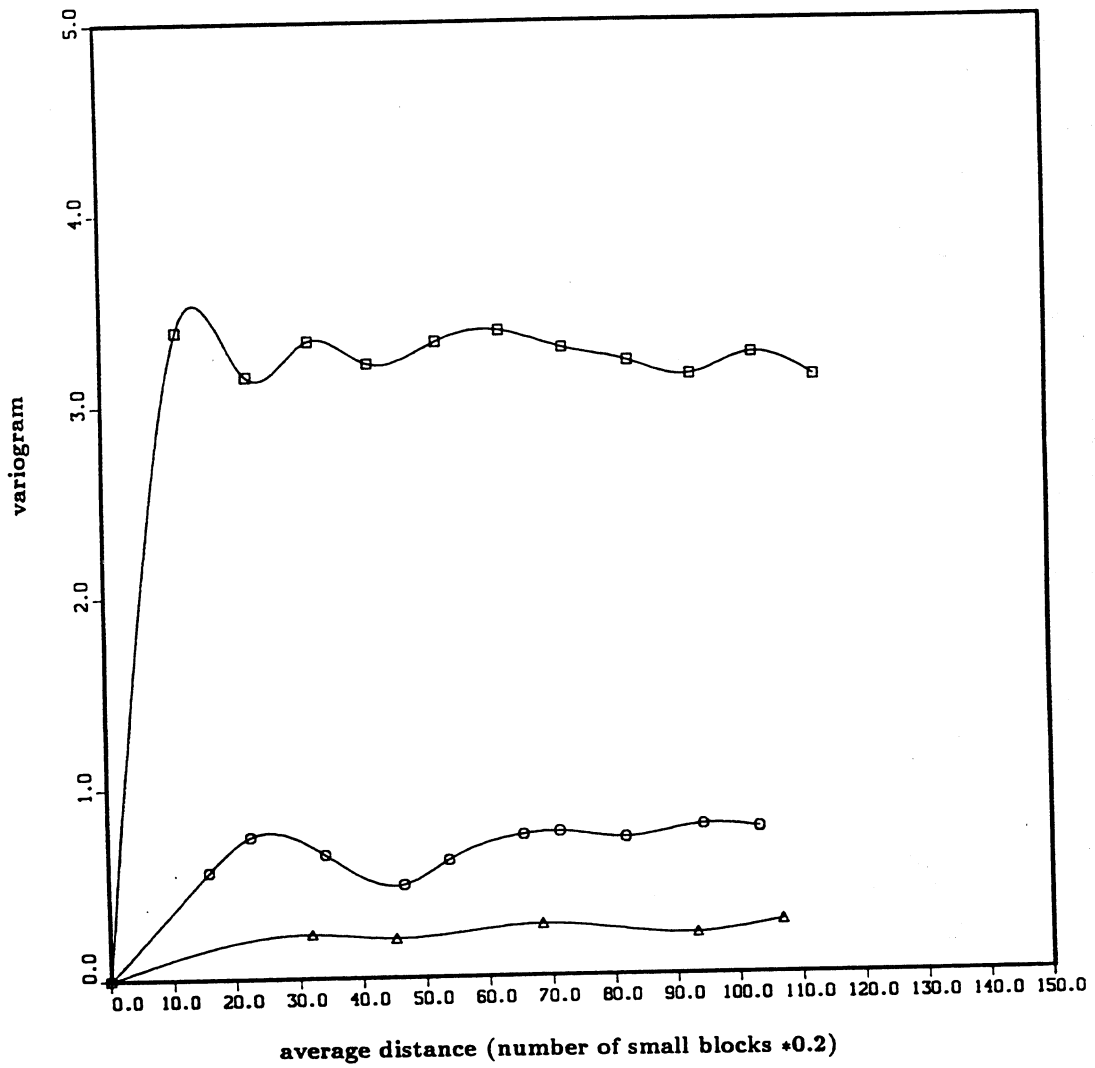

Figure II-4. Variograms for reservoir-B at different scales.

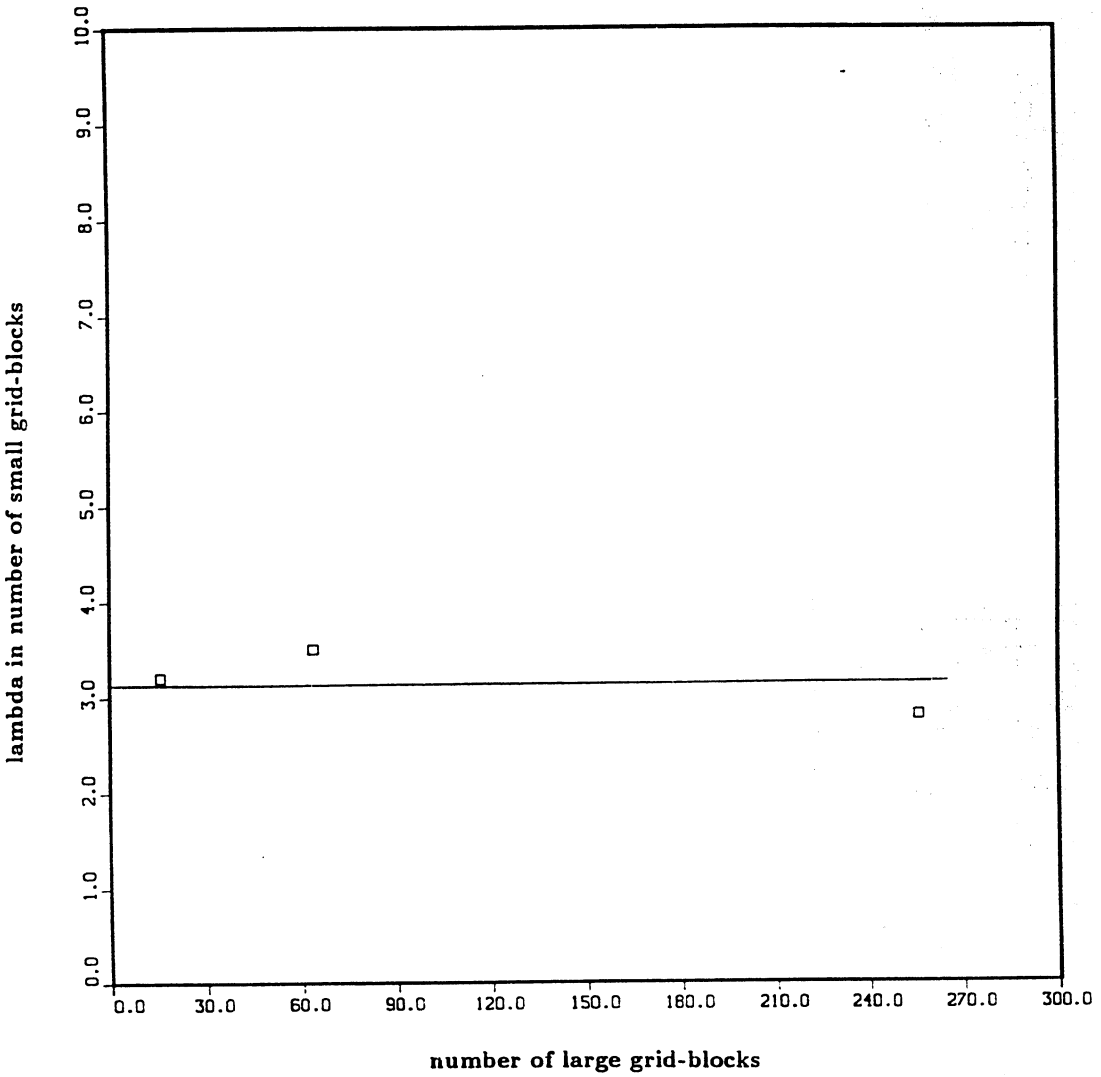

Figure II-5. The effect of scale on correlation length for reservoir-B.

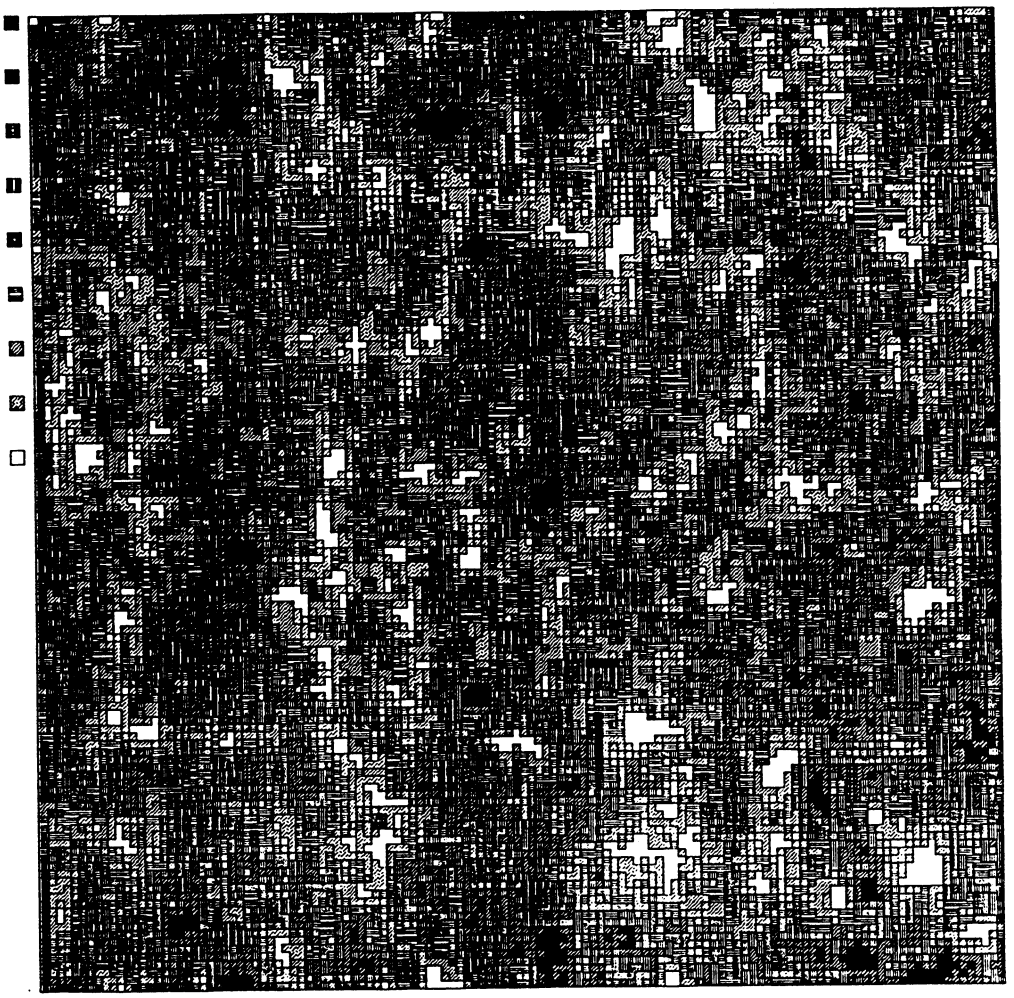

Figure II-6. Reservoir-B, unconditioned log-permeability field.

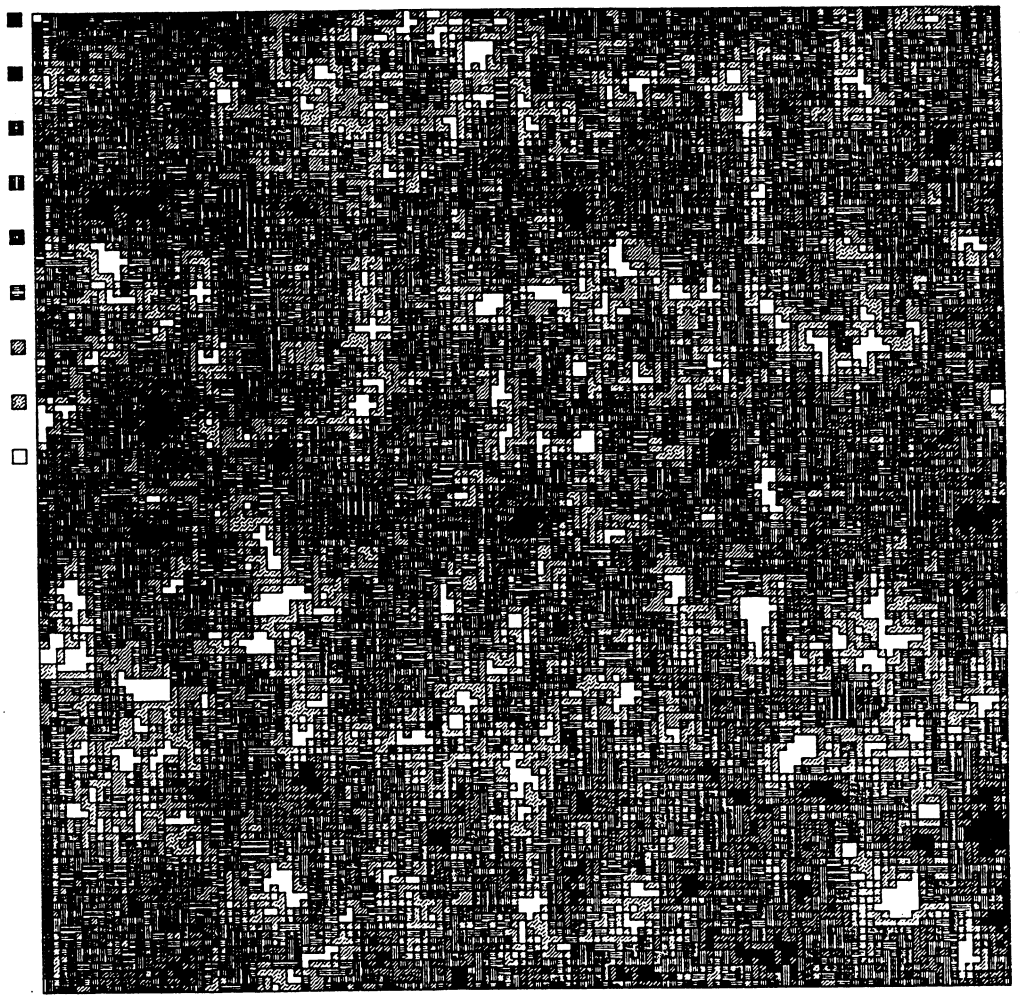

Figure II-7. Reservoir-B, conditioned log-permeability field.

3. Small-Scale Heterogeneity

Previous portions of Ibrahim Bahralolom's doctoral research weigh the impact of small-scale heterogeneities on displacement, and consider variations of both permeability and porosity. In this portion of the work, results produced by another CT-scan technique are presented to measure small scale heterogeneity of the rock. In this case, the technique does not involve any flow experiments. The influence of nonuniformities of on displacement performance can not be directly evaluated without using flow models. The different data set presented here consists of successive CT-scanned images of a full core from a vuggy carbonate formation. Estimation of the heterogeneity scale is based on a quantitative analysis of vug geometry from reconstructed CT-scanned images of the rock sample, and this is compared where possible to the results of whole-core measurements made by a service laboratory.

a. Analysis of The CT-Scanned Images of a Carbonate Rock Sample

The subject of these photographs, which were graciously supplied by an international oil company, is a vuggy limestone sample from a Canadian reef formation. The sequence consists of 91 photographs of CT-scanned cross-sectional "slices" of the core sample. They were taken when the core sample was empty, at successive intervals of 2 mm along the axis of the 180 mm sample length as shown schematically in Fig. II-8. The gross cross-section area is 62 cm^2, and the average porosity of the sample is reported to be around 14.3%. The vertical and horizontal permeabilities were measured to be 0.082 and 6.5 md, respectively.

Figure II-9 shows a photograph of the CT-scanned image of the cross-section of the reef core sample at location 90. The intensity of light in these images is taken as an indicator of the rock density. For instance, the black and white areas represent vugs and impervious matrix, respectively. The gray areas represent a matrix with different levels of porosity. If the black color or high density areas in these images represent the vugs, then a major measurable feature of the photographs is the abundance of vugs in the core sample. Because most of the oil resides in these voids, examination of the vug characteristic becomes important as one type of heterogeneity, which is frequently encountered in carbonate rock.

Quantitative examination of the vug characteristic directly from the photograph of the CT-scanned images would have been impossible were it not for secondary computer data files that were generated for these images. The technique used to generate these data files is presented in the next few paragraphs.

To assess the quantitative features of the core sample, data files of the photographs of the CT-scanned images were generated and stored digitally. The imaging computer system, which was initially designed for performing the output concentration experiments, is used to generate these data files. The process consists of rephotographing the CT-scanned images and digitizing them. A suitable light system was used for photographing the images with a video camera. The captured images were digitized by a Data Translator Frame Grabber to 64 intensities (each pixel is represented by a 6-bit number) with a resolution of 256 columns by 256 rows of pixel, or picture elements, and stored in the computer.

Ninety-one data files were generated. Each data file consists of 256 x 256 pixels. The portion of the file image that contains the entire cross-section of the core is about 150 x 190 pixels, and the portion of the core cross-section represented by an individual pixel is approximately 0.59 x 0.46 mm. Figure II-10 is a schematic representation of an individual size of the pixel element in the generated data file for a CT-scanned image of the vuggy carbonate sample rock. For comparison, Fig. II-11 is a computer-

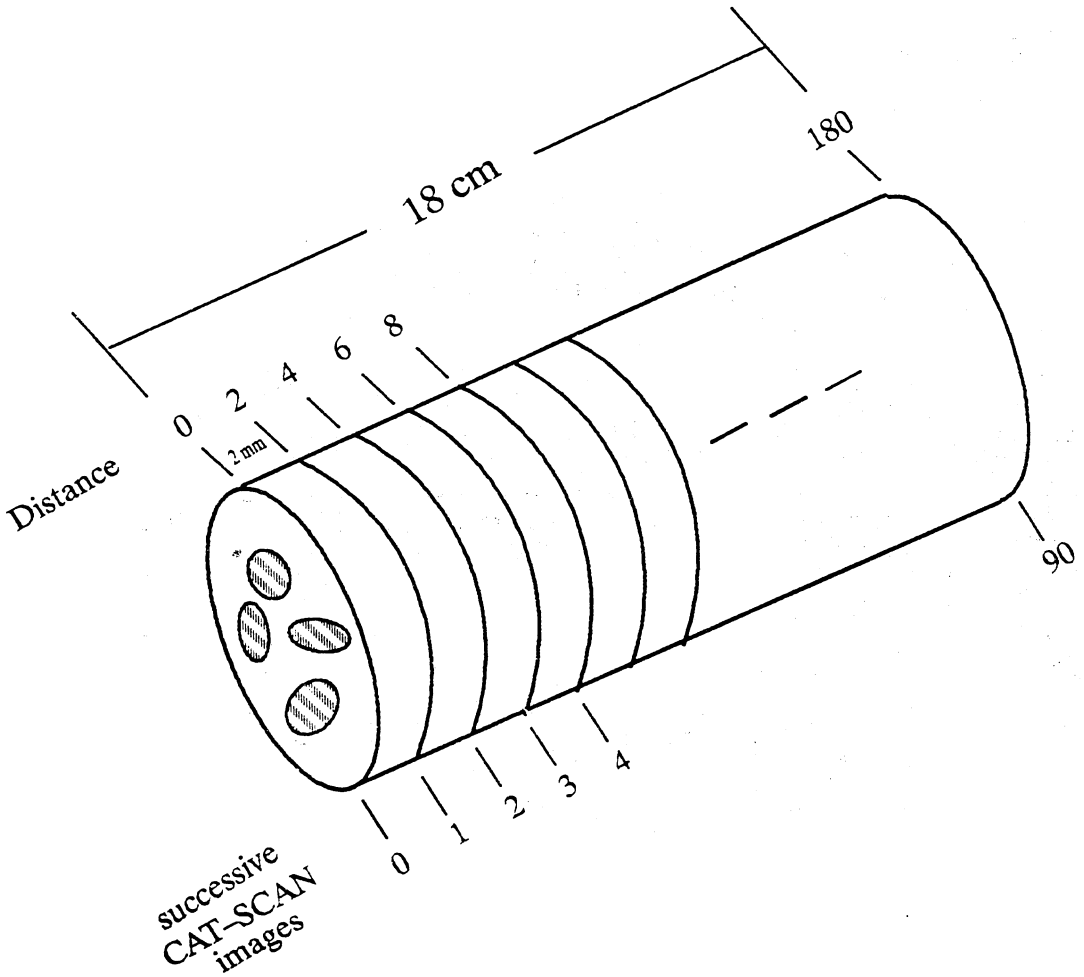

Figure II-8. Schematic view of the vuggy core sample.

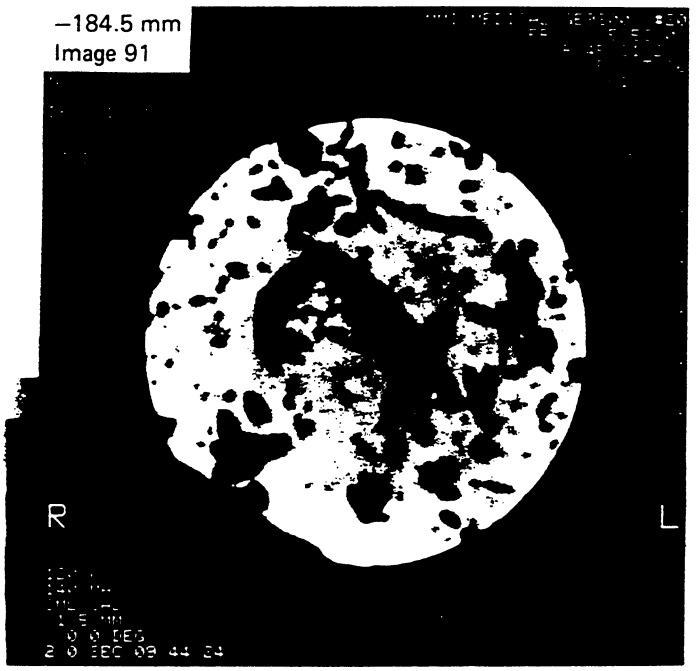

Canadian limestone reef full diameter core CAT-scanned cross-sections

Figure II-9. Photograph of the CT-scanned image of the cross-section of the Canadian limestone reef.

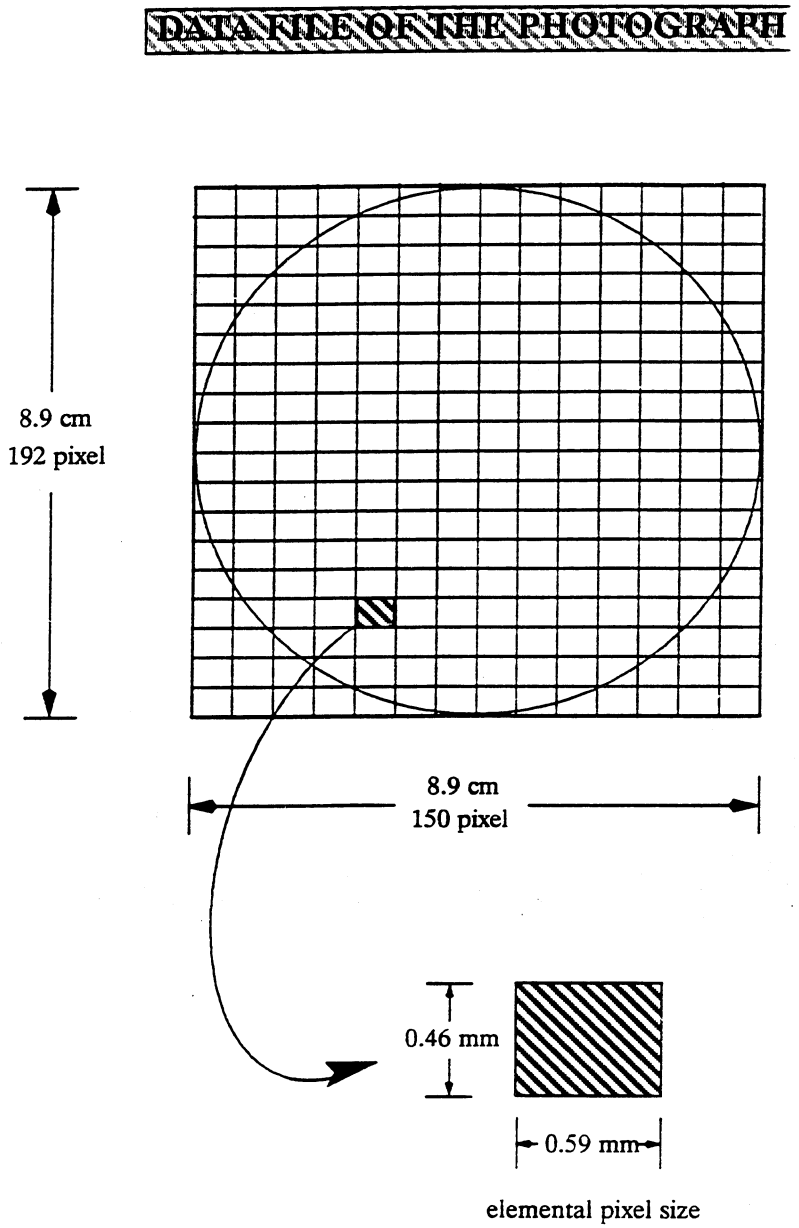

Figure II-10. Schematic representation of individual pixel size in the generated data file.

Figure II-11. Colored image of the generated data file for the CT-scanned image shown in Fig. II-9.

generated image of the generated data file for the CT-scanned image shown in Fig. II-9. The light intensity of the CT-scanned image was rescaled to 16 different colors. Figure II-11 is a black and white representation of that image. It is possible to distinguish gray areas, which represent a matrix with a different porosity. For instance, the dark areas in Fig. II-11 might be a representative of a matrix with a relatively high porosity; one notes that these are mostly located next to the vug areas. On the other hand, the light areas are most likely to be a representative of a matrix with a very low porosity and are adjacent to the solid matrix (white). The quality and accuracy of the generated data file for these CT-scanned images are discussed in the following section.

b. The Accuracy of the Rephotographed Images

A comparison of Figs. II-9 and II-11 indicates that the quality of the generated data files is acceptable. However, there are some limitations that might affect the accuracy of the quantitative analysis of the vug characteristic. Light uniformity and repositioning of the CT-scanned images in the photographing process are among the major limitations. Efforts were made to assure both a consistent and uniform light system, and similar boundary image locations for all images.

The uniformity of light over the CT-scanned images assures the equivalency of light intensity assigned to each image in the data file of the CT-images. Such uniformity is important, particularly in the gray density region of the images, while the high and low density regions (black and white areas) are likely less affected by the nonuniformity of the light. As the main purpose of this portion of our research is to study the vug geometry, the impact of the light nonuniformity would not be expected to be of primary significance. More discussion on the uniformity of a light system and its impact on the results are presented in the latter sections.

The other possible problem, which might affect analysis of vug connectivity along the sample length, is the repositioning of CT-scanned images during the photographing. Although care was taken to place the individual photographs of the CT-scanned images at the same position during the photographing process, slight movements in the vertical or horizontal direction, and slight angular rotations could not be completely avoided.

The possibility of small vertical or horizontal movements of these images from one photograph to the next was considered and allowed for as follows. A computer program was written to detect the boundaries of the cross-section of the core sample in a data file image. Pixels of the individual data file images were then renumbered according to the detected boundaries, so the images can be compared without worries for possible vertical or horizontal movement. On the other hand, the possibility of small angular rotations from image to image was not taken into account in the analysis of the vug connectivity. That computation is based on the assumption that there is no angular rotation in the CT-scanned images during the photography process. Because most of the vug sizes in the core sample are large, the assumption will not introduce a noticeable error as long as the rotation of the CT-scanned images was less than a few degrees. However, a small angular placement error might affect the analysis of the connectivities of very small vugs.

As mentioned before, the light intensity is represented by a 6-bit number. Such representation imposes yet another limitation on the accuracy of analysis. For instance, some areas will be counted as parts of the vugs, which are very close to the vug, and may show very low intensity, slightly greater than zero but less than one. This error will increase the apparent vug density. In general, however, these

limitations would not dramatically reduce the accuracy of results presented in the following sections. The main concern of this study is the vug geometry, which is less affected by these limitations.

c. Investigated Parameters From The CT-Scanned Images

It is not possible to investigate quantitatively all of the variations of rock properties of the vuggy core sample because of the limited quantity of data available. Our generated data files of the images contain information about the light intensity reflected from the photographs of the CT-scanned images. These images are of the cross-sections of the dry core sample at successive locations. The main feature of the reef formation from which the core sample was taken is the abundance of the vugs. The important issues in the dual porosity system concern the vug characteristic. For instance, the cross-sectional vug density, the spatial distribution of the vug density along the sample length, the contribution of the vugs to the measured porosity of the core sample, and spatial connectivity based on the vug size are among the main parameters that can be measured from the images. These are presented in the following sections to present a more quantitative description of the heterogeneity in the vuggy core sample.

d. Local Vug Density Distribution

One of the informative parameters that can be investigated with a reasonable degree of certainty is local vug density. This parameter is defined as the percent of the vugs in the generated CT-scanned file and it can be expressed as follows:

$$\textit{Local Vug Density} = \frac{\textit{Area occupied by vugs}}{\textit{Cross-sectional area of the image}} \qquad \text{(II-5)}$$

Where 'area occupied by vugs' is the number of pixels having a digit 0 in the generated image file and 'cross-sectional area of the image' is the total number of pixels that are contained in the cross-section of the core sample in the data file. Figure II-12 is the computer printout of the vugs that are detected in the generated CT-scanned file for the image shown in Fig. II-11. Each pixel vug in the CT-scanned image is represented in the figure by a square symbol. Using Eq. II-5, the local vug density at this location is 35% or 7,000 pixels out of 20,000 pixels having zero light intensity. Since the cross-sectional area of the core sample in all the generated data files is the same, the local vug density can be expressed either in percent or in frequency numbers. However, such parameters do not provide any information about the size of the individual vug or the vug connectivity in the cross-sectional plane. As shown in Fig. II-11, there is a great variation in the vug size. They vary from hundreds of pixels down to a pixel in size. Some of the vugs are connected with others in the plane and some of these vugs are apparently isolated and might be connected through another plane. It is also clear from the figure that there are a large number of vugs that are located around the edge of the core. Some of the external vugs are considered as an extension of the other internal vugs.

The local vug density was calculated at every 2 mm along the sample length, based on the generated image files. Figure II-13 shows the variation of vug density along the sample length. The local vug density varies from 3% to 35% with an arithmetic average about 13.3%. A great variation in the local

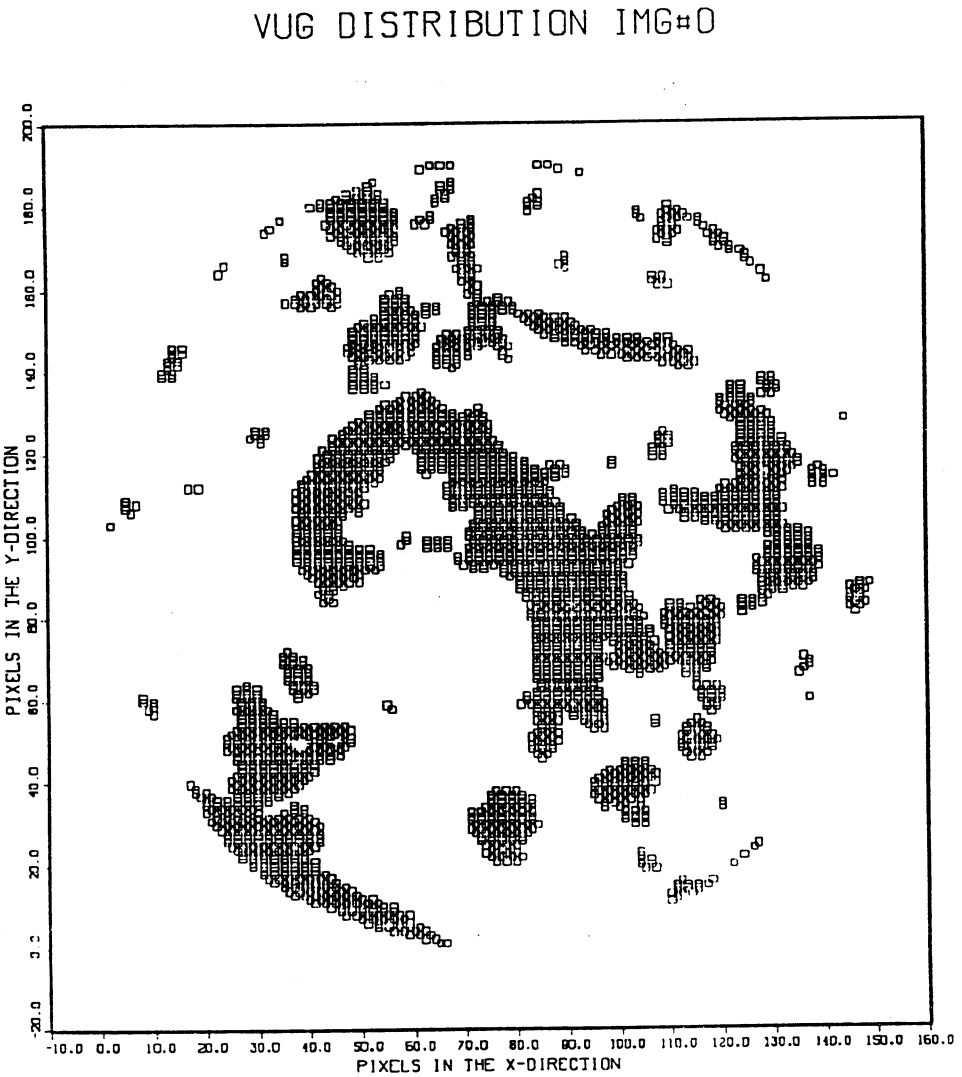

Figure II-12. Vug distribution in the generated file of the CT-scanned image shown in Fig. II-9.

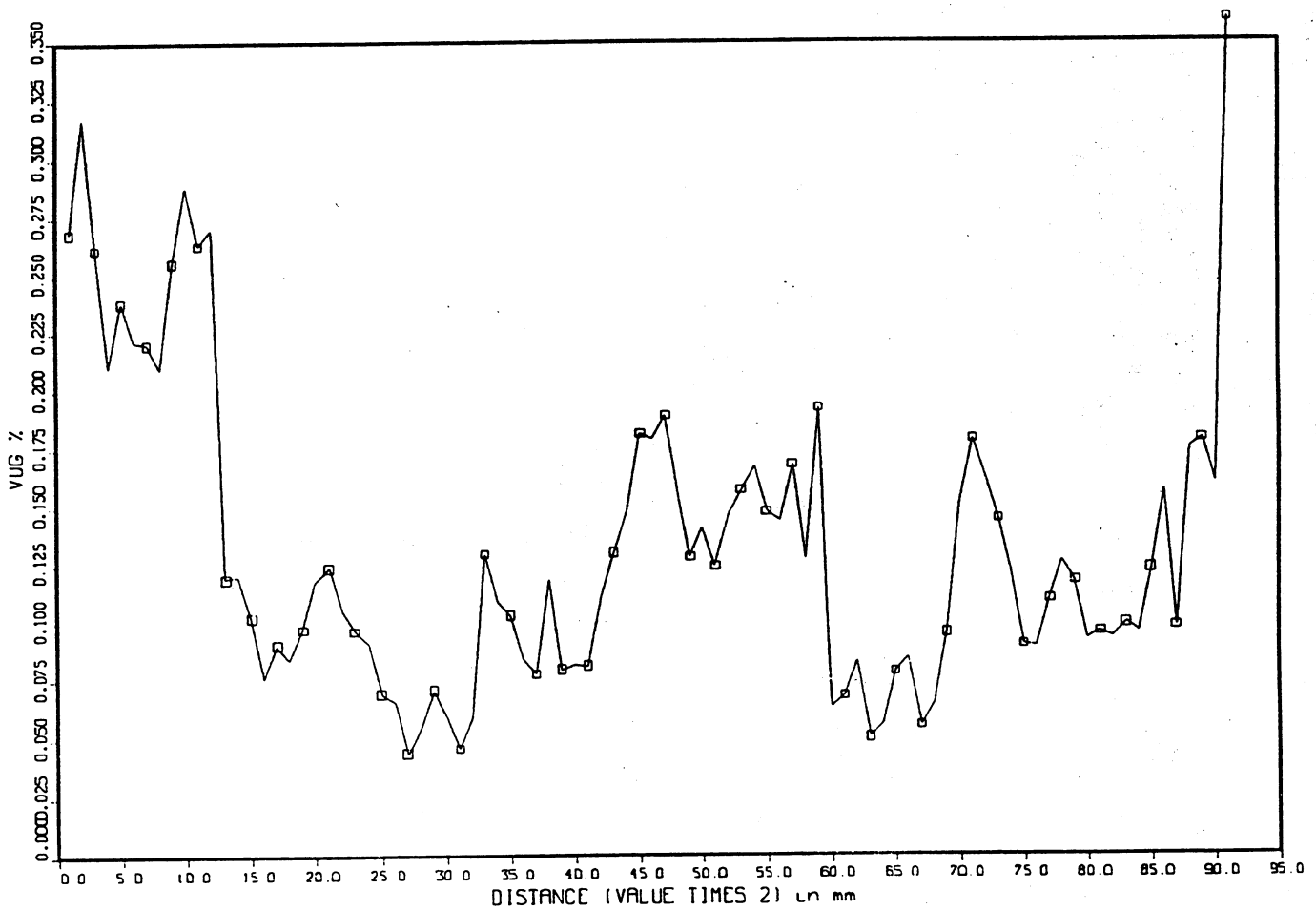

Figure II-13. Variation of the local vug density along the sample length.

vug density is anticipated from the core sample, which was cut perpendicular to the bedding plane. Although there is considerable spatial variation, it is possible to recognize a sort of layering pattern along the sample length. Figure II-14 is a schematic representation of the expected pattern in the core sample based on the smoothed values of the local vug density. Such a pattern may indicate significant changes in the depositional environment that affected the vug characteristic. Further evidence of this will be seen in the later sections.

e. Distribution of Light Intensity

A histogram of the light intensity for 91 CT-scanned images (as shown in Fig. II-15) has been constructed to determine the percentage of the total of the cross-sectional areas representing vug in the whole core. The x-axis of the figure represents the class interval of the light intensity ranging from 0 to 63, while the y-axis represents the frequency distribution of more than two million pixels. It is clear from the figure that the percentage of the vugs in the sample is higher than that of any other class interval frequencies with light intensity greater than zero. The frequency of the pixels with zero light intensity is about 13.4%. The distribution of the light intensity for values greater than zero might be taken as an indication of the matrix porosity. Pixels with high light intensity may be considered as representing a tight matrix, while pixels with low light intensity represent high matrix porosity. The distribution of matrix light intensity is not normal, but instead is skewed slightly toward the right (i.e., lower porosity) as shown in the figure. However, it is not clear whether such deviation from normality is natural, or perhaps might have been caused by some artifact in the observation system.

f. Contribution of Vugs To Measured Porosity

Another important issue to be discussed is the contribution of vugs to the total porosity. The porosity of the core sample was measured in the commercial laboratory by a method using Boyle's law; the result presented was 14.4%. The estimation of the vug density based on the histogram of all images (Fig. II-12) is about 13.4%, representing almost 93% of the measured porosity. This percentage is based on the assumption that all the vugs in the core sample, regardless of their size, contributed to the measured porosity. However, some of these vugs are small and isolated and may not have been counted in the porosity measured in the lab, because the gas would have taken a long time to reach them during the relatively short duration of the porosity experiment. Figure II-16 shows that the percent of the small vugs (size less than 2 pixels) is about 2.5%. Further, the connectivity analysis (presented in the next section) indicates that a large number of these smaller vugs are isolated. Excluding some of these small vugs from the calculated vug density would thus seem to be realistic. Even with this exclusion, though, the contribution of vugs to the total porosity must still be at least 80-85%.

Another conservative method to estimate the contribution of the vugs to the measured porosity is based on a direct comparison between the successive images. Figure II-17 is a schematic view showing the principle by which the minimum contribution of vugs could be estimated. In such a straightforward method, each vug pixel is compared with the pixels with the same x and y coordinates at the preceding and succeeding images. For instance, the vug pixel in the image (Z) is compared with the same pixels in the image (Z-1) and image (Z+1). The vug located at (i,j) in the image (Z) is considered in the porosity calculation if the other pixels at the same location in the images (Z-1) and (Z+1) are vugs, too. A computer program was written to run these calculations. The results of the estimated porosity, based on the direct connectivity, showed that at least 50% of the vug pixels contribute directly to the porosity

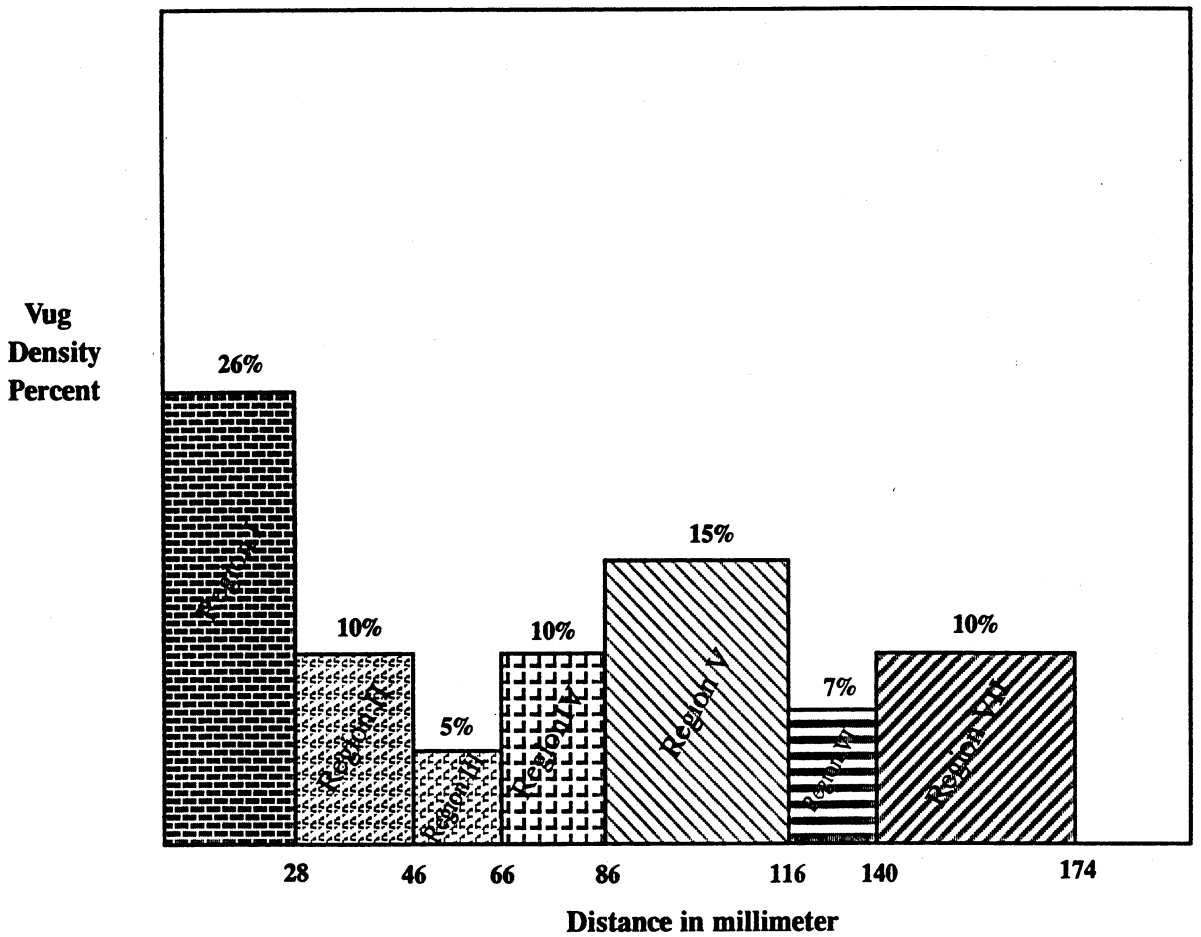

Figure II-14. Schematic representation of the expected pattern in the core sample.

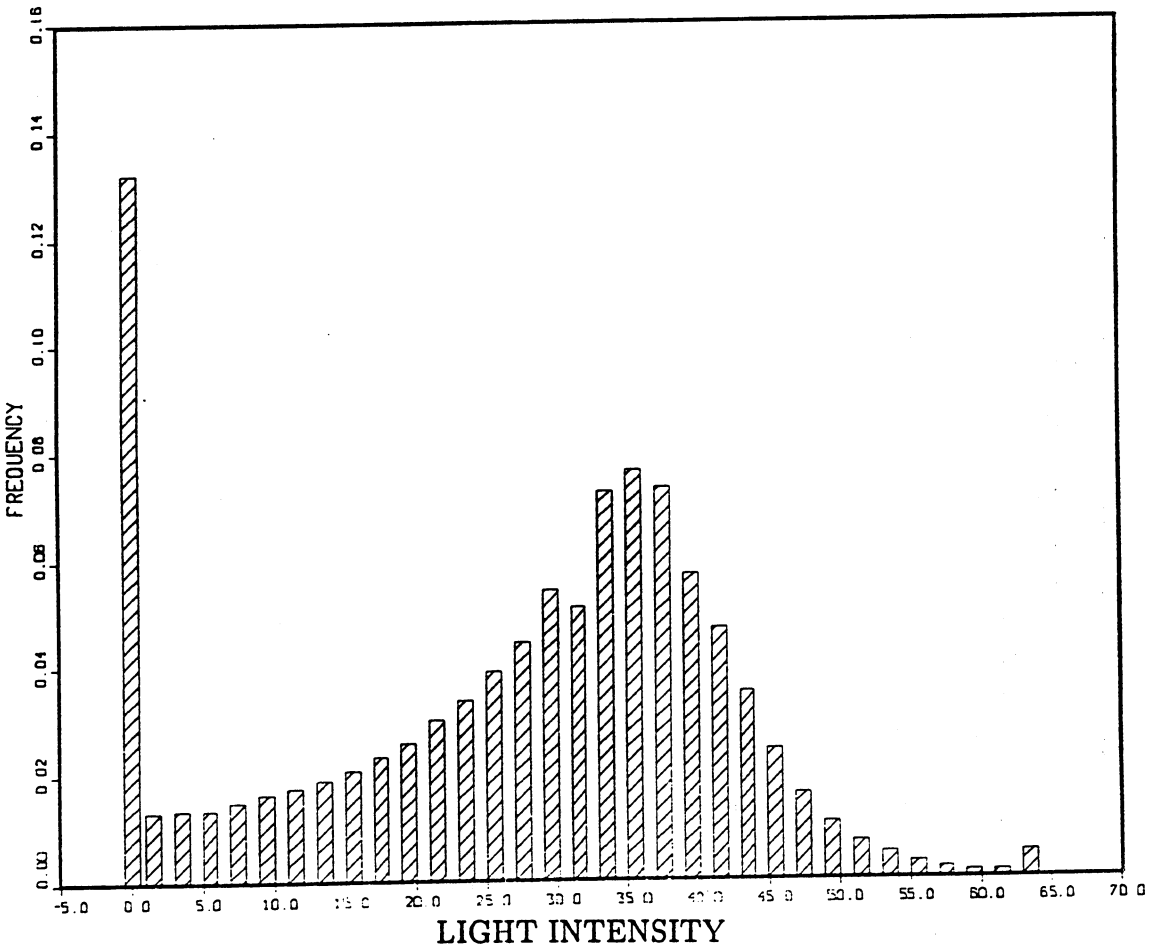

Figure II-15. Histogram of the light intensity of 91 images.

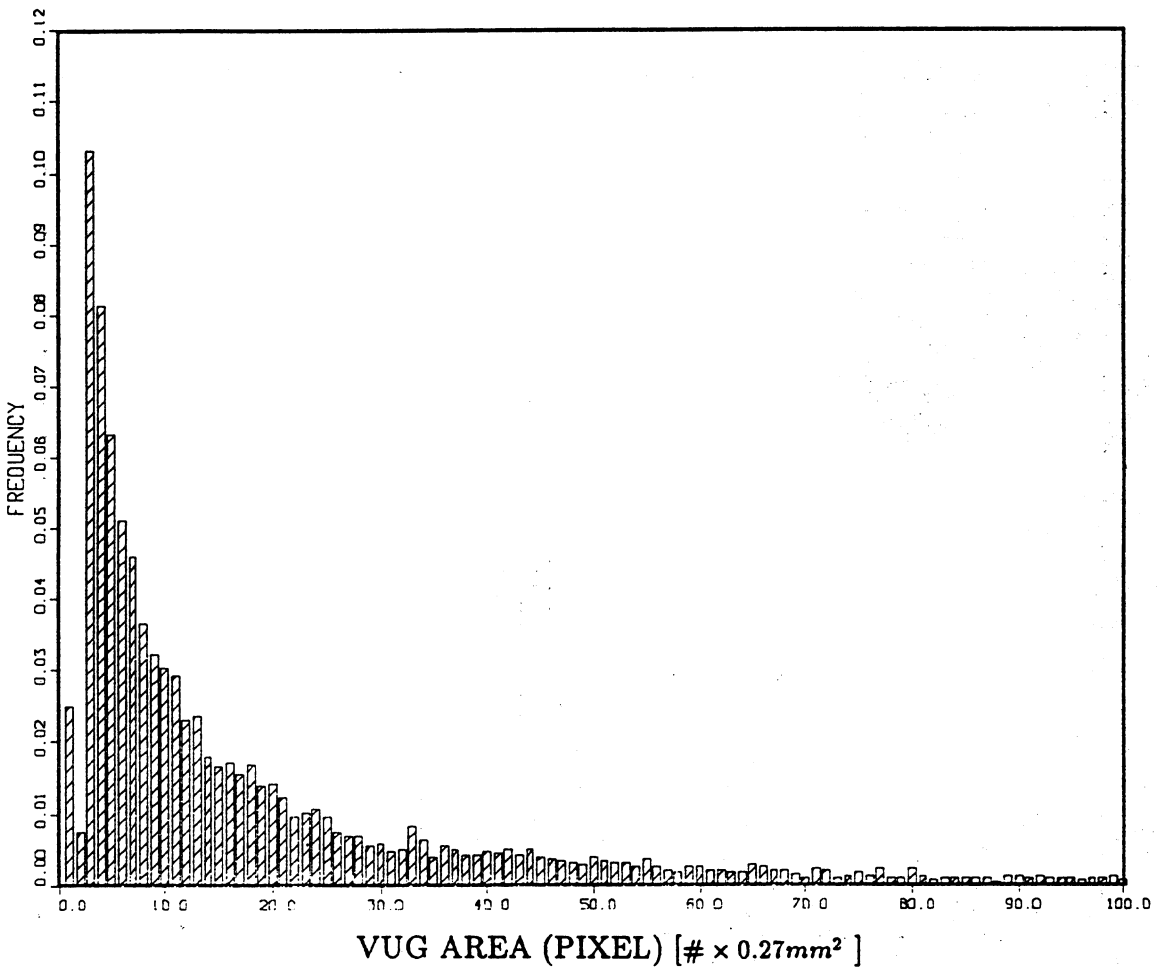

Figure II-16. Histogram of vug size less than 100 pixels.

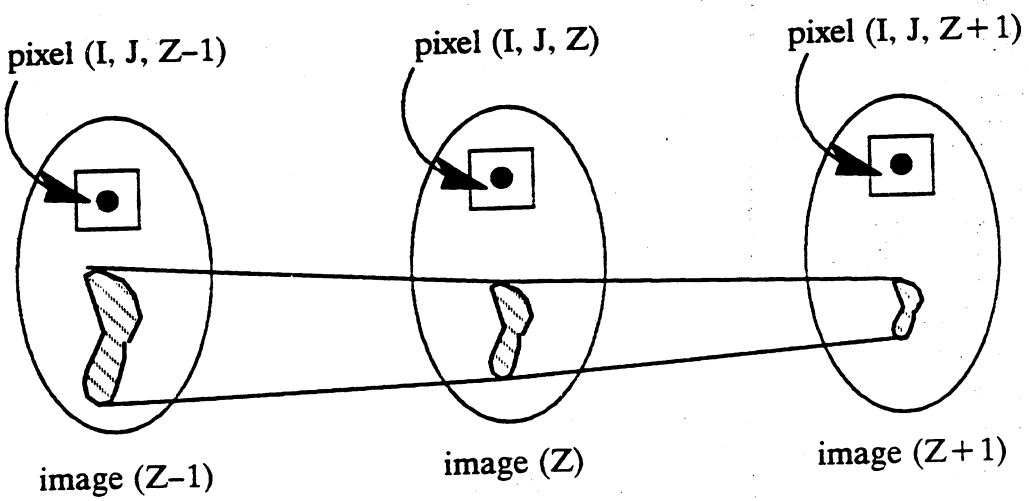

Figure II-17. Schematic view showing principle of estimating minimum vug contributions.

measurement. The percentage would be expected to have been higher than 50% if the comparison had been based on the vug boundaries. However, such great contribution of the vugs to the porosity supports the conclusion of McCaffery, Sigmund, and Fosity.[12] They reported that, based on an extensive study of different core samples taken from an Alberta carbonate reef reservoir, the vug porosity contributed to 50%, and in some cases, to about 80% of the effective porosity.

If the vugs contribute 80-85% of the measured porosity, then from the information at hand, the matrix porosity may not exceed more than 15-20% of the total porosity. There is no direct way to confirm the estimation of the vug and matrix porosity in a particular core, however. The direct porosity determination from CT-scans would require successive images to be taken with the core fully saturated with fluid. This second set of images should be taken at precisely the same positions as images of the dry core. The only available data in this research are the photographs of the CT-scanned images from the dry core, and this information is not sufficient to determine the matrix porosity. However, the amount of light at those points reflected from the CT-scanned images at the nonvug positions can be taken as an indicator of the porosity at those points. A formula of an exponential form may be suggested to estimate the porosity from the light intensity. The base line for the formula should be based on the fact that pixels with light intensity 63 (the maximum light intensity scale) means zero porosity, and those with zero light intensity (vugs) represent 100% porosity. The following type of possible relationship can be proposed for converting the light intensity to porosity:

$$\phi_{(i,j,z)} = \left(1 - a\left(\frac{I(i,j,z)}{63}\right)^b\right) EXP\left(\frac{-I(i,j,z)}{63}\right)^c \qquad \text{(II-6)}$$

Where $I(i,j,z)$ is the light intensity observed at location (i,j) in the image (z) and $a,b,$ and c are constants. Reasonable values for these constants may be determined by trial and error based on the measured porosity value of the core sample and the local vug density.

g. Vug Size Distribution

The local vug density value does not provide any information about the number and the size of the vug. A computer code was written to count the number of vugs, as well as measure their size, from the generated data image files. The program first searches for each vug by sending the pixels horizontally. If the vug is found, then it will be given a number and the search continues horizontally, then vertically to delineate the vug boundaries. The program goes back to the horizontal line, where the first pixel of the vug boundary was detected, to check for other vugs and their sizes in a similar way. Since the shape of the vugs are not uniform, as seen in Fig. II-9, the program computes, in addition to the area, the centroid point of the individual vug to be used in examination of the spatial distribution of the vugs.

Figure II-18 is a histogram of the vug size for 91 images. The x and y axes represent the calculated vug area in pixels and their frequency, respectively. As shown in the figure, there is a great variation in the vug size. The size of the vug ranges from one to one thousand pixels. Each increasing vug area level is less common than the preceding one. The majority of the vugs have an area of less than 25 pixels (about 5 mm^2). It is possible to identify a few vugs having an area greater than 1000 pixels (200

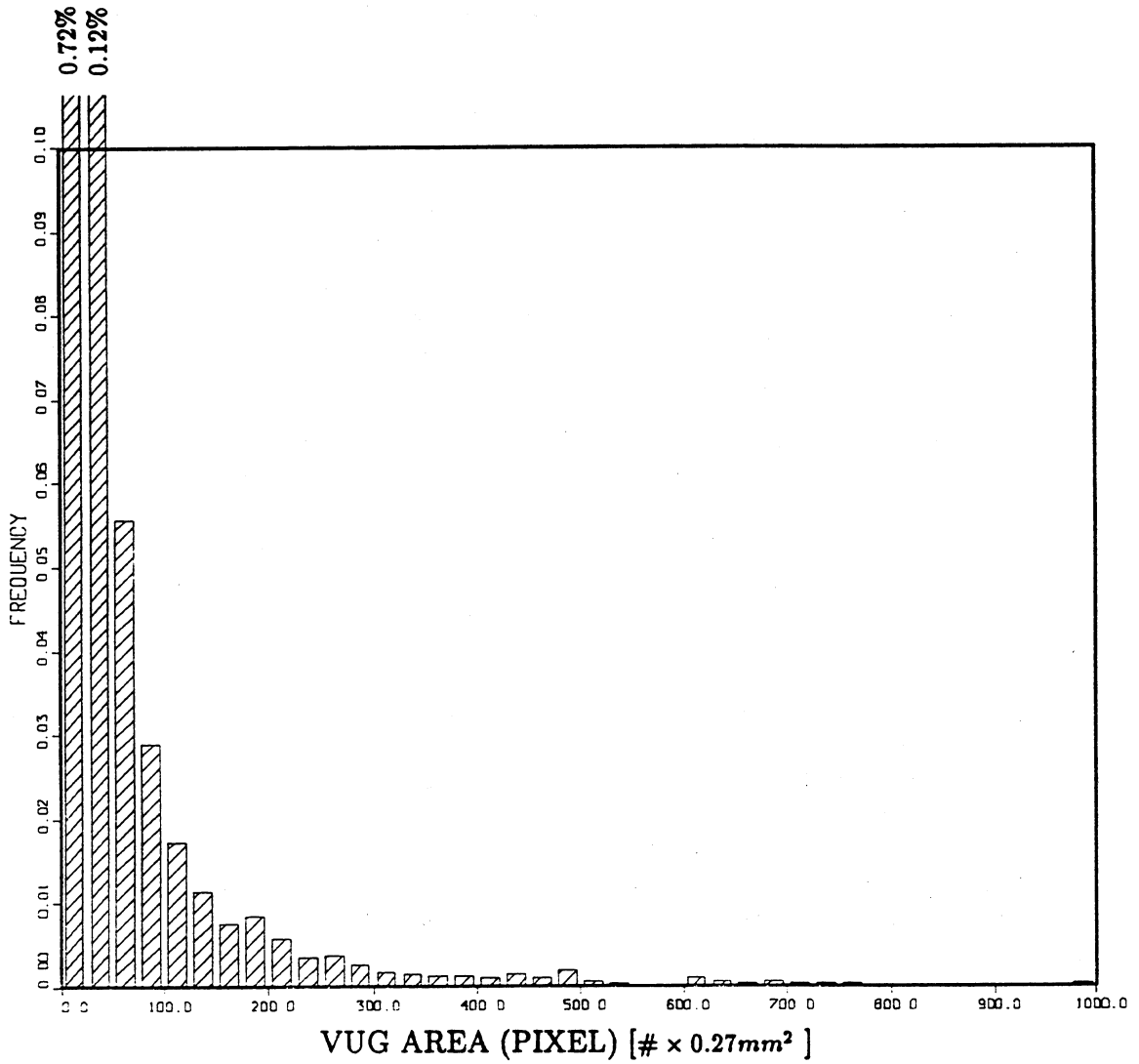

Figure II-18. Histogram of all vug sizes of 91 images.

mm^2). However, the distribution of the vug size could be following an exponential distribution. To get a better idea about the majority of vug sizes, another histogram (shown in Fig. II-16) is constructed for the class of vug size ranging from 1 to 100 pixels. The average area of these vugs is about 3 pixels (0.6 mm^2). The distribution of small vugs is similar to that of the total size distribution, in that they both follow an exponential trend.

h. Spatial Distribution of Vugs

Although the size of vugs is one of the important characterizes of a vug distribution, it is also necessary to investigate spatial distribution of the vugs. To investigate the spatial distribution of the vug sizes, a semivariogram is computed. The variability of the vug size is examined not only in the cross-sectional plane but also along the sample length. Such an investigation requires a 3-D semivariogram in order to identify the length over which the vugs are correlated. Figure II-19 presents the 3-D semivariogram of the vug size in the core sample. The vertical axis represents the mean difference squared of the vug sizes as a function of the lag distance. The computed values of γ with lag distance indicates that the vug sizes are correlated over a considerable distance. The closer together the vugs are, the higher is the correlation in their sizes. The vugs that are at a greater distance from each other are less correlated. The lag distance at which the dependency vanishes is about 2.7 cm, where a clear sill exists. The schematic representation of the layering pattern shown in Fig. II-14 indicates that the approximate thickness of the most identifiable layers is in the same range of the estimated correlation length. The coincidence suggests that the vug size is a characteristic of the depositional environment, in which they are more highly correlated.

The spatial variability of the vugs is also investigated from the local vug density values. The local vug density semivariogram is presented in Fig. II-20. In this figure, the variance in the percentage of the vugs as a function of the lag distance is computed. The semivariogram-computed values rise regularly with the lag distance from the origin, and reach a maximum at about 75 pixels, after remaining for several millimeters at a plateau. The value then drops off steadily to a minimum at 175 pixels. It again rises linearly to a large lag distance. The estimation of the correlation length is about 2.0 cm, which supports the idea that the vug sizes is a function of the environmental deposition.

i. Vug Connectivity

One of the important features of the reef formation from which the core sample was taken is the permeability anisotropy. The measured permeability is very low in the vertical direction of the core, compared to that measured in the horizontal direction. The ratio of the vertical to the horizontal permeability, as measured in the commercial lab, exceeds 100. Analysis of the vug porosity presented in the previous sections indicated that most of the oil probably resides in the vugs. In this section, quantitative analysis is presented to explore the connectivity of these vugs in the vertical and horizontal direction of the core sample.

One way to investigate the vug connectivity is to construct a cross-section along the major diameter of the core sample as schematically shown in Fig. II-21. The synthesized lengthwise cross-section of the vuggy core sample is presented in Fig. II-22. The coordinates of the latter figure represent the pixel location. The z-axis represents the distance along the sample length, while the y-axis represents the distance in along a major diameter of the core, perpendicular to the sample axis. The cross-section

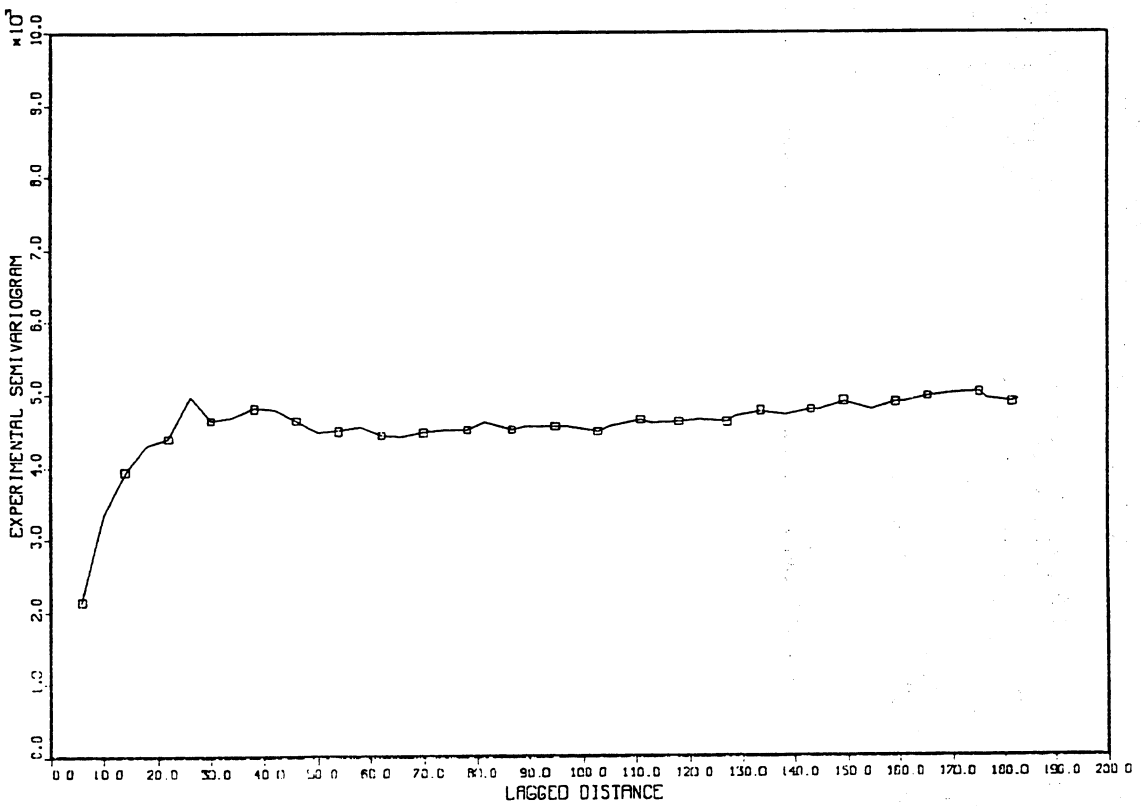

Figure II-19. Three dimensional semivariogram of the vug size.

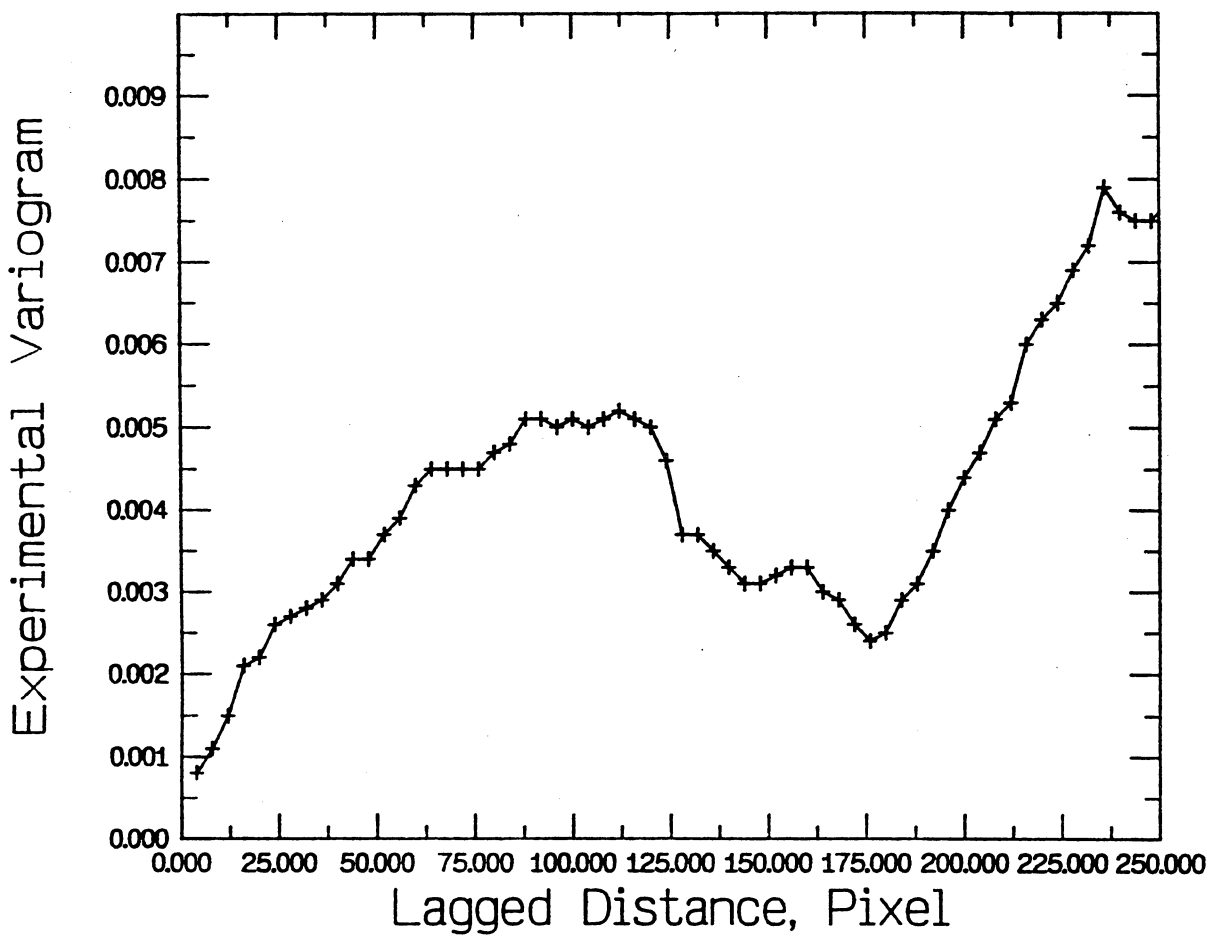

Figure II-20. Semivariogram of the local vug density.

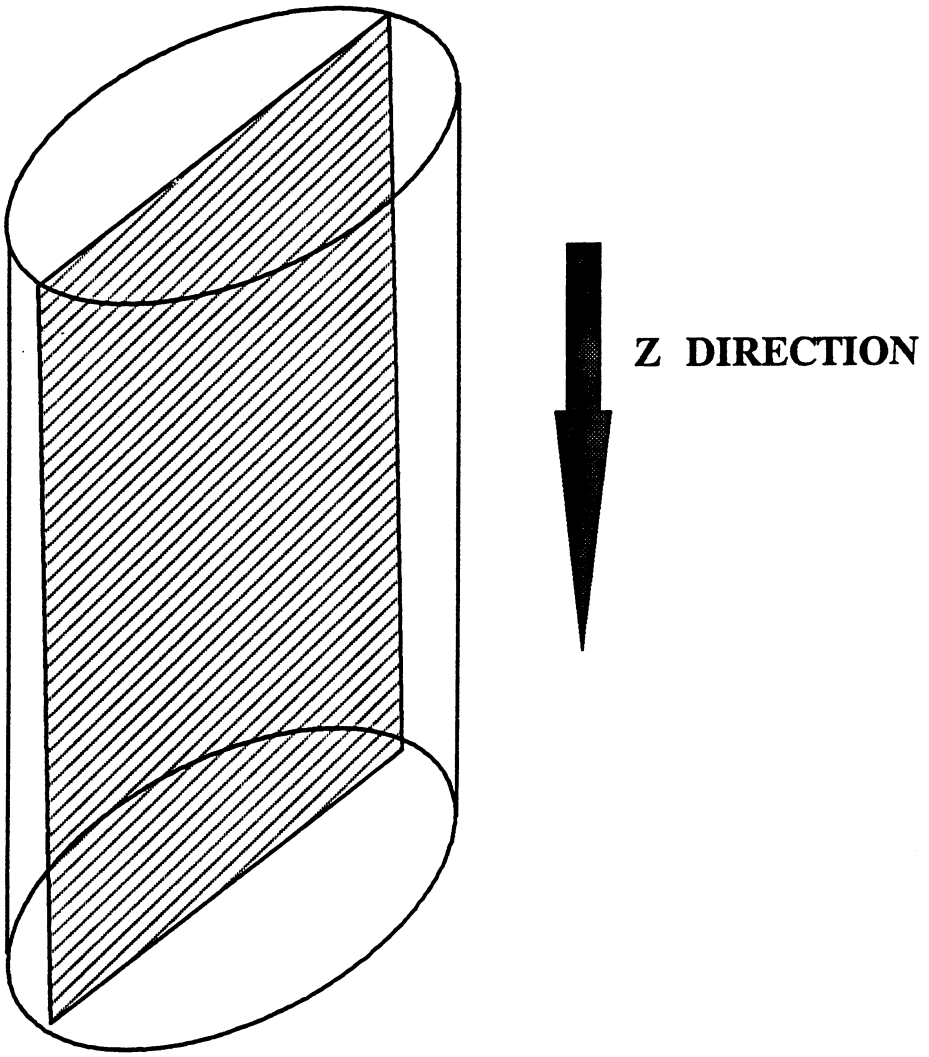

Figure II-21. Schematic view of the synthesized cross-section in the Z direction.

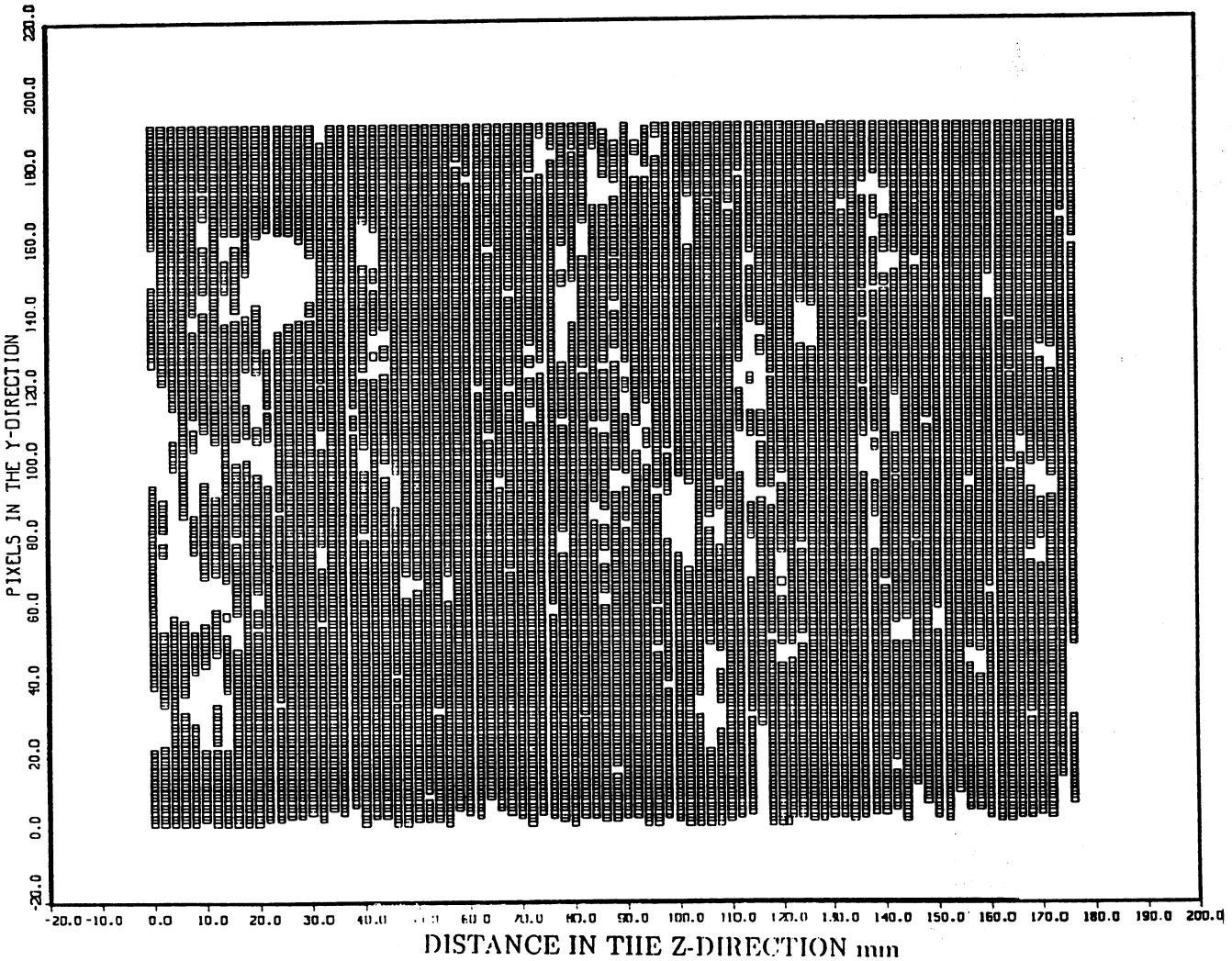

Figure II-22. Synthesized cross-section showing the vug distribution.

consists of 91 strips, each of which represents the intersection of the cross-section plane with the CT-scanned image at 91 locations. The strip thickness is equivalent to the thickness of a CT-scanned image slice. The main assumptions used in the construction of the cross-section are that the size of vugs remained unchanged throughout the thickness of the slice, and the CT-scanned images were positioned as accurately as possible without any angular rotation during the photographing.

The white areas in Fig. II-22 represent the vugs while the shaded area represent the matrix. For distance less than 30 mm from the left end of the core, the density of vugs is high. The vug sizes are relatively large and they are close together. However, the vug density drops dramatically in the next segment (30mm < distance < 60mm). In the second region, the vug size is small, and they are isolated and concentrated in the upper part of the figure. The lower part of this segment is almost devoid of vugs. In general, the vugs in the cross-sectional plane are mostly isolated, particularly in the vertical direction (along the sample length). However, the extension of the vugs along the x direction (perpendicular to the plane of the lengthwise section) is expected to be a function of the vug size on this figure. The larger the vug, the larger it is in the x direction.

The distribution of the vugs and their incomplete connectivity in the cross-section raises an important question about the role of the matrix in enabling fluid flow among the vugs. The 2-D synthesized cross-section presented in Fig. II-23 is similar to the one in Fig. II-22 in showing the vugs themselves, except that it also includes the regions of the matrix, which would be expected to have high porosity. The low light intensity region (light intensity less than 5) is expected to represent a high porosity matrix, and is expected also to be a region of high local permeability. The white areas in this cross-section represent both the vug and the high porosity matrix. Direct comparison between both the cross-sections (Figs. II-22 and II-23) indicates, as expected, that the white areas are expanded in the latter figure. Such expansion indicates that the high matrix porosity areas are located adjacent to the vug areas. This observation is supported by Fig. II-24, where the local vug density frequencies were plotted against the local frequency of the matrix pixels having low light intensity (0 < light intensity < 5) less than 5) for all images. Despite the scatter in the data, there is clear evidence that as the frequency of a high porosity matrix increases, the local vug density increases as well. This supports the observation as seen in the cross-section, that most of the matrix porosity matrix regions are very close to and adjacent to the vug areas.

Figure II-25 is the same synthesized cross-section in which the white areas represent the vugs and the regions of the matrix that possess light intensity up to 20 units. As observed in the previous cross-section, the additional porous matrix generally surround the vugs, and depending on their permeability, they may act to provide significant communication between the vugs. Visual observation of the figure suggests that possible communication through the porous matrix is more likely in the vertical direction than in the direction along the sample length. Furthermore, comparison of the cross-sections indicates that the area without vugs, or with very low vug density, would be less porous and likely to be less permeable. For instance, the lower left portion of the cross-section in Fig. II-22 is almost free of the vugs. The matrix of the same area is relatively tight as indicated in the other cross-sections (Figs. II-23 and II-25). This observation supports the idea that most of the more porous matrix areas are adjacent to the vugs.

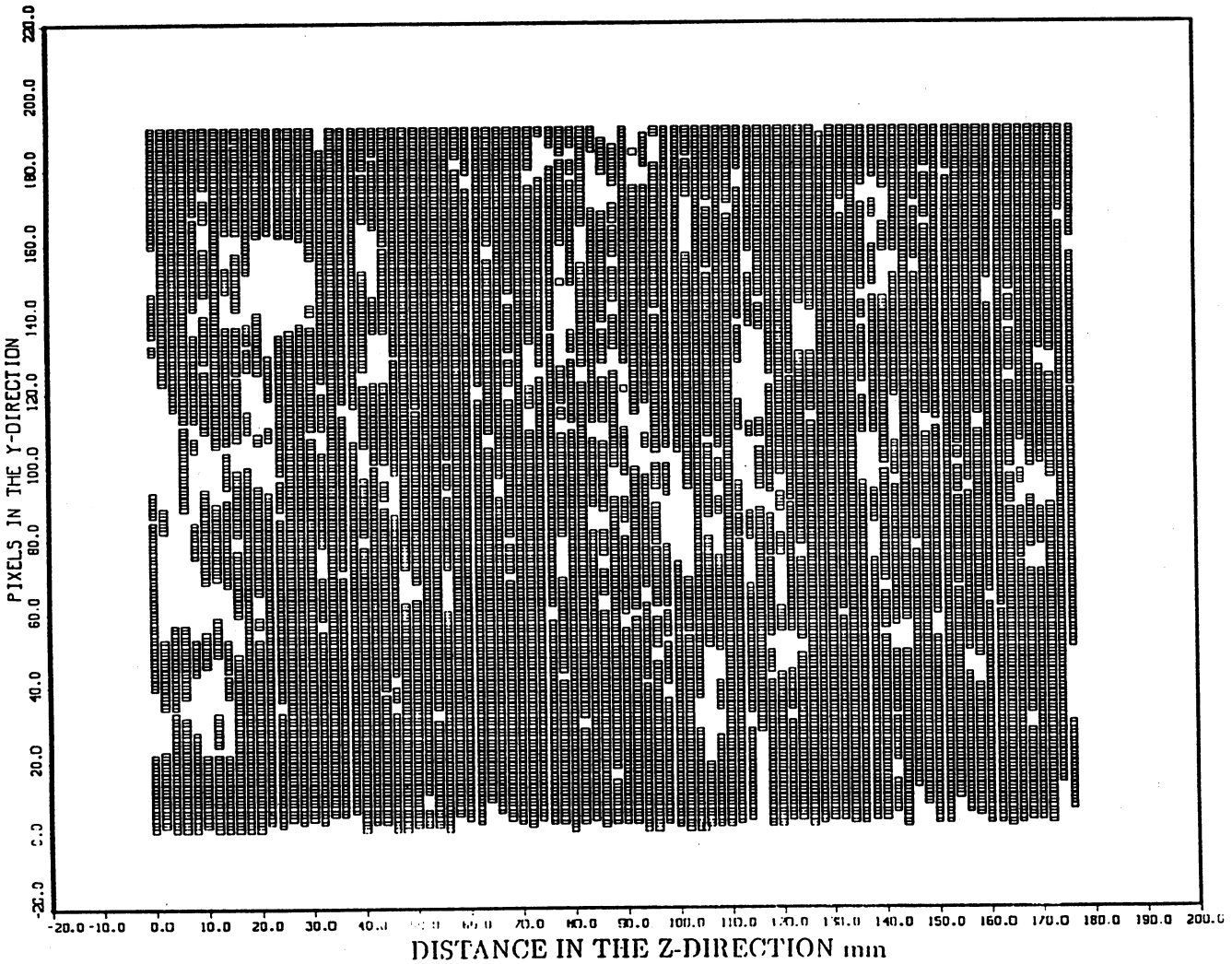

Figure II-23. Synthesized cross-section showing vugs and high porosity matrix regions (light intensity < 5).

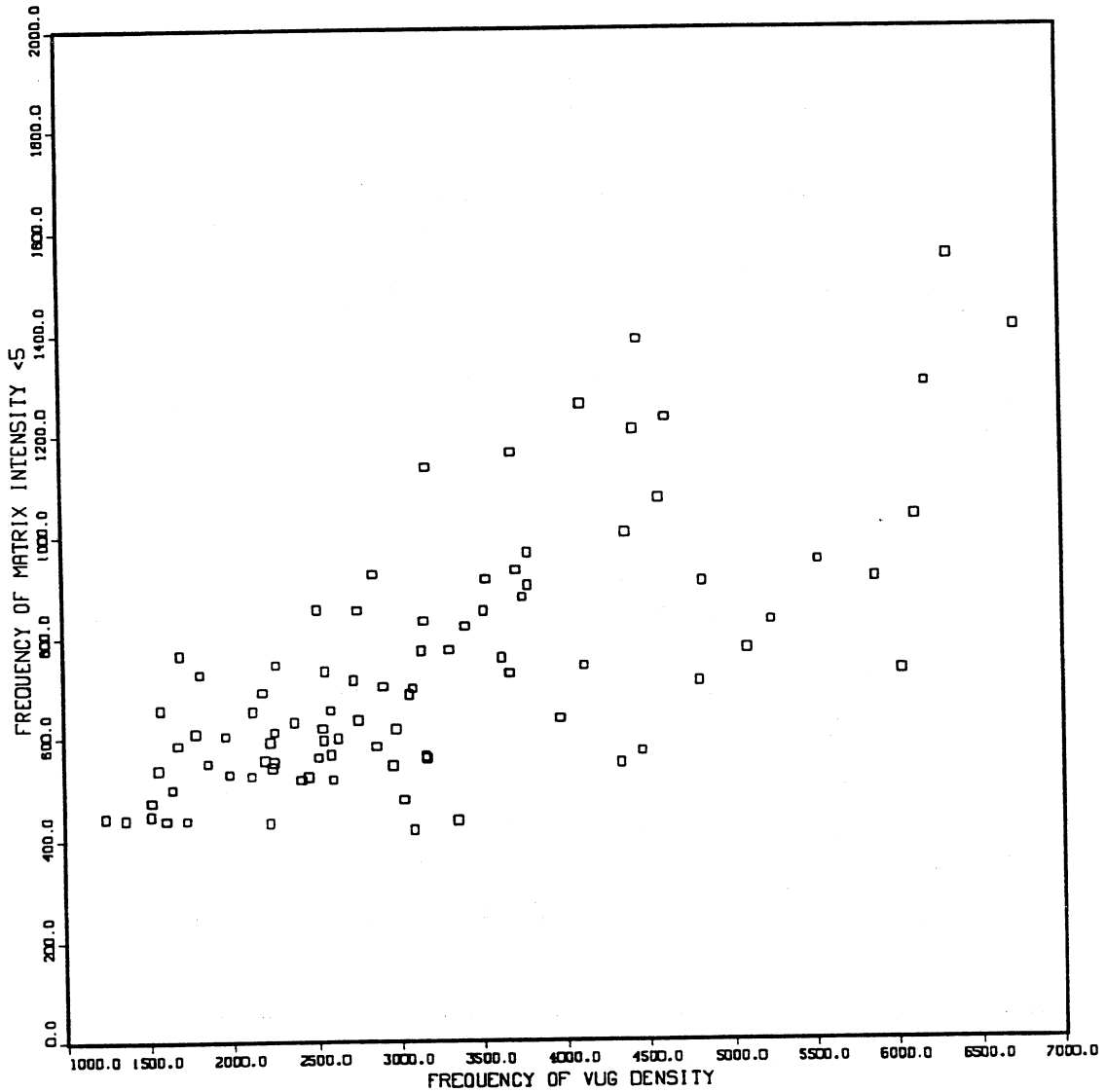

Figure II-24. Relationship of the local vug density and high porosity matrix.

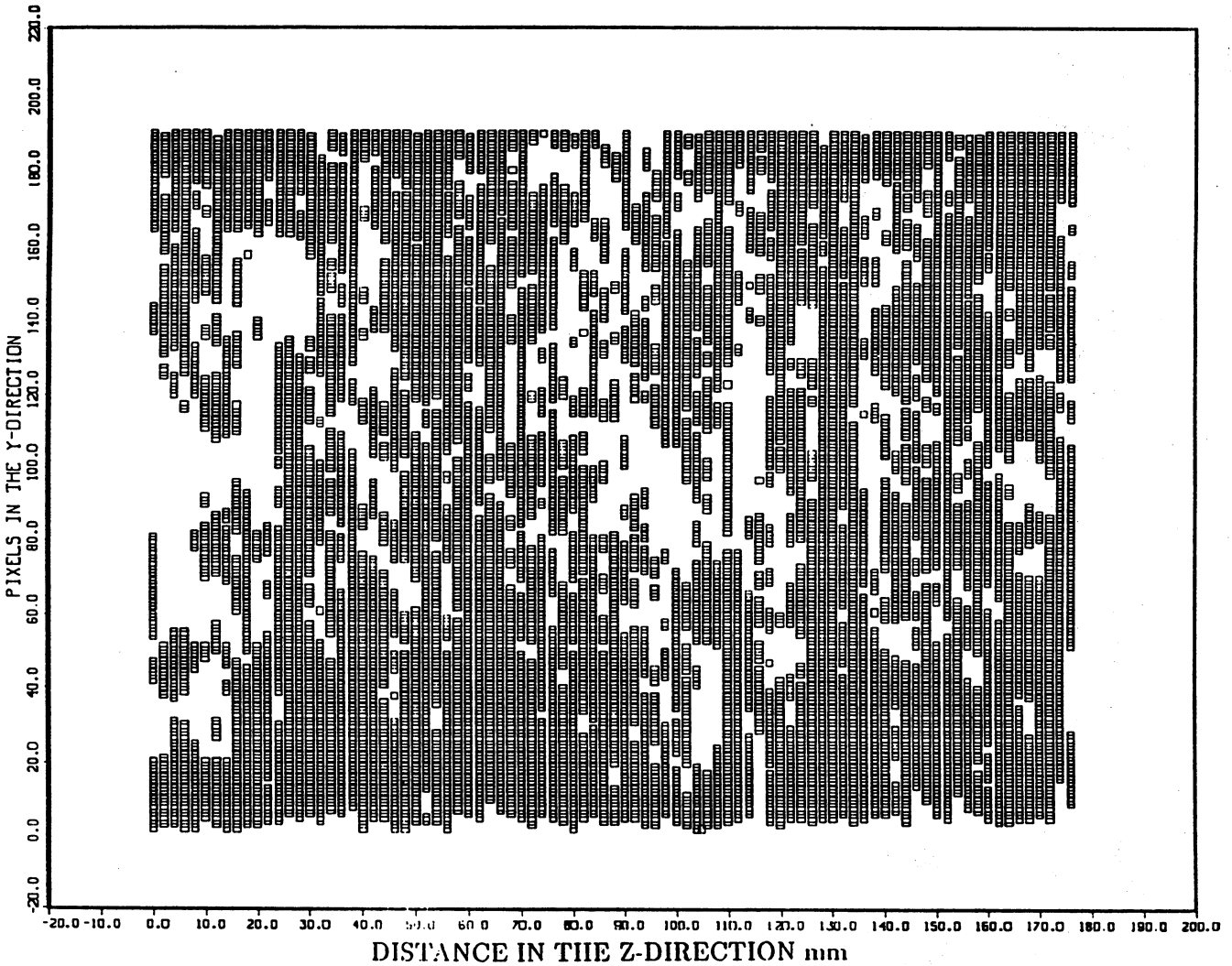

Figure II-25. Synthesized cross-section showing vugs and matrix region having light intensity < 20.

4. Mobility Control

The topic of flow nonuniformities in CO_2 and other miscible floods has been divided, in this project, according to what are considered its underlying causes. These are, of course, the nonuniformity of permeability of the rock itself, and the occurrence and growth of frontal instabilities. These causes can operate independently as well as in concert. The most costly type of flow nonuniformity (from the point of view of displacement efficiency) occurs when the regions of higher or lower flow velocity are *correlated* in the direction of flow. It is in this circumstance that the production engineer will encounter early breakthrough of displacing fluid and poor long-term displacement efficiency, the two negative outcomes that can occur in any flooding program.

As has been discussed, this correlation of higher or lower velocity in the direction of flow is found all too often when heterogeneities in the rock permeability are themselves so distributed. Another cause for such uneven and costly displacement behavior is also prevalent, however. Whenever the mobility of the displacing fluid is much less than that of the displaced fluid, the front becomes *unstable*. Any small nonparallelism between the direction of flow and the vector gradient of concentration (or saturation) will become larger during the course of flow. The situation leads to the growth of *fingers* on the front. Their growth rate is greater if the mobility ratio is large. Although the fingers can start at any location along the front, the simultaneous presence of correlated permeability heterogeneities is an especially unfortunate combination. The preferential flow in the higher permeability *channels* is faster and the fingers can be more rapidly extended to the production wells in this case.

In this project, our concern with this problem is centered on means to counter the effects of frontal instability in CO_2 floods. We have spent a great deal of research effort in the development of two different methods by which this problem can be attacked, and the severity of instability reduced in CO_2 floods. In both methods, our efforts have been to effectively *thicken* the injected CO_2. In the first of the research efforts, CO_2-soluble substances have been sought that will form high viscosity polymeric solutions in the dense gas. In the second effort to be described, we have made an effort to understand and control the properties of mixtures of dense CO_2 and aqueous surfactant solution so that advantage can be taken of the unusual properties of this so-called foam in the reservoir rock.

Our work in these areas are discussed in detail in the two major sections below.

B. DEVELOPMENT OF DIRECT THICKENERS

1. Introduction

In our continuing search of direct thickeners for the mobility control of dense CO_2 floods, our research efforts this year have been particularly focussed on the development of associative polymers of significantly improved properties. These polymers have potential use in a number of Enhanced Oil Recovery (EOR) applications. Such associative polymers, referred to as Method II *ionomers*, rely on ion-pair interactions and manifest both *intra-* and *inter ionic* associations to develop desired thickening properties in nonpolar solvents. During the past year, we have devoted particular attention to *telechelic* polymers and ionomers in which the functional groups are attached at the ends of the polymer molecules. Based on carefully prepared model ionomers, an understanding of structure/solution property interrelationships is rapidly emerging.

a. Research Objectives

Our research program seeks to identify and synthesize the dense CO_2-soluble polymers that can viscosify the solvent to increase volumetric sweep efficiency of fluid displacement in EOR processes. A principle objective of this research is to develop polymers that have the potential for field use as mobility control additives. Other objectives are to design the necessary equipment and to develop procedures for the laboratory evaluation of thickeners.

b. Research Accomplishments

All major objectives of our search for prospective direct thickeners, as outlined in the proposal, have been investigated. Our research is documented in project reports as well as in a number of publications. We have also been performing extensive studies to develop ionomers and to better understand their solution properties. Significant accomplishments of our work to date are outlined below.

- The design and construction of a high-pressure solubility measuring apparatus for polymers/compounds in gases such as dense and supercritical CO_2, propane, butane, etc. With a slight modification, the same apparatus can be used for measuring viscosity of the resulting solution. This equipment can also be used to test the effectiveness of small samples of prospective direct thickeners of the order of one gram or less.

- Both symmetrical and unsymmetrical trialkyltin fluorides and novel trialkylsilyltin fluorides have been developed and extensively characterized by modern spectroscopic methods such as FTIR, ^1H, ^{13}C-NMR, and X-ray diffraction studies. Evaluation of solution properties of these types of compounds in nonpolar solvents demonstrated their ability to thicken light hydrocarbons such as propane, butane, etc.

- A high-pressure capillary tube viscometer has been designed and constructed to evaluate the effectiveness of prospective polymers as direct thickeners by measuring viscosity of liquid and supercritical CO_2 in combination with a cosolvent.

- Most recently, we have also developed a few new polyfunctional aromatic, aliphatic, and alicyclic initiators for the living carbocationic polymerization of a hydrocarbon monomer, isobutylene.

- We also investigated the use of new electron-pair donors for the living carbocationic polymerization of isobutylene in conjunction with aromatic as well as aliphatic initiators.

2. Overview

Our research on the development of direct thickeners over the past six years is covered in five sections of this report. The initially defined directions of our search for direct thickeners were expanded into three main methods to cover other types of viscosifiers called associative polymers. The following sections of the report summarize the experimental aspects and the results of these methods.

The first section of this report briefly recapitulates the experimental results of our earlier work on Method I polymers. The second section presents a brief description of syntheses, characterization, and evaluation of solution properties of the Method III associative trialkyltin fluorides and novel trialkylsilyltin fluorides.

The third section is segregated into two subsections to include two entirely different types of ionomers. The first subsection deals with the ionomers in which the ionic groups are randomly distributed. These Method II ionomers were prepared by the conversion of some of the Method I hydrocarbon copolymers by sulfonation and neutralization. The syntheses of copolymers and ionomers, characterization, measurements of solubility of copolymers and ionomers in CO_2, and of their solution behavior in hexane are also reported. The second subsection deals with promising new types of associative ionomers referred to as *telechelic* ionomers. The major progress of the past year has been the syntheses of telechelic (terminally functionalized) polymers by a living electron-pair donor (ED) stabilized carbocationic polymerization of isobutylene, using different types of polyfunctional *ini*tiator trans*fer* (*inifer*) reagents in conjunction with coinitiators such as BCl_3 and $TiCl_4$ in polar diluents. Chemical characterization of these polymers includes FTIR, ^1H and ^{13}C-NMR spectroscopic methods, while their physical characterization was done by gel permeation chromatography (GPC), vapor pressure osmometry (VPO), and their solution viscosity behavior in hexane by dilution viscometry. The syntheses of polymers of different molecular weight and of narrow molecular weight distribution (MWD), and the investigation of new EDs are the two topical subjects. Also presented are the solubility data of some of these polymers in dense CO_2.

The fourth section of this report summarizes the modified version of a high-pressure solubility measurement apparatus, emphasizing the recent improvement on it to work with various cosolvents. Also reported are the solubility data of certain polymers in dense CO_2 with and without cosolvents.

In the fifth section, we describe the design and operation of the high pressure capillary tube viscometer. This section also includes the recently generated results of viscosity measurements of thickened CO_2 with a commercial polymethylhydrosiloxane using toluene as a cosolvent.

3. Method I Polymers

Method I has dealt with our initial efforts to find conventional polymers that are soluble in CO_2, and that might increase the viscosity of the CO_2 sufficiently to retard frontal instabilities during displacement. Our earlier experimental measurements[13] on commercially available polymers indicated that atactic hydrocarbon polymers would make good candidates for achieving higher solubility in CO_2.

Accordingly, we synthesized different types of homo- and copolymers of α-olefins using both Ziegler-Natta and cationic polymerization techniques and obtained their solubility in CO_2 and other nonpolar solvents such as *n*-butane, *n*-pentane, etc.[14] Most of these polymers showed some solubility, but not significantly enough to increase the viscosity of CO_2.

It is well known that the solubility of a polymer in a given solvent decreases with an increase in molecular weight. This phenomenon, however, was more pronounced in the case of a polymer-CO_2 system, despite the high density of the solvent. We had anticipated that introduction of branching and atacticity in α-olefinic polymers would increase their entropy, resulting in higher solubility. While our choice of the polymer molecular structure may have helped to achieve increased entropy of the polymer,

and thus, keep its solubility parameter (cohesive energy density)[15] low, the increase in polymer molecular weight certainly would have contributed to raising that parameter, causing lower solubility in CO_2.

It has become evident that Method I will not succeed in CO_2 viscosification unless polymers of very high molecular weight and very low solubility parameters ($\delta = 6$) are used. According to Hildebrand and Scott,[16] the rule of thumb is that a solution results when the solubility parameters of solute and solvent are matched. Certain commercial polymers that fit in this range are polysiloxanes and polytetrafluoroethylenes as described in the Fifth Annual Report of this project.[17] More recently, Bae and Irani[18] showed the use of polydimethylsiloxane in combination with a cosolvent such as toluene to thicken dense CO_2.

A versatile approach of *associative viscosification*, which differs from the conventional way of viscosifying solvents (as a result of solute-solvent interactions), is by virtue one of strong interactions between solute-solute and has become our principal goal. Associative viscosification, occurs as a result of associations between the solute molecules themselves. These interactions could either be ionic or electrostatic, which would form polymer clusters or transient chains, respectively, to markedly thicken the solution. It is expected that the number of such clusters or chains existing at any given moment should depend on the solute concentration to some power higher than one. We synthesized two types of such molecules, which we expected to show associative viscosification under the general designations, Method II and Method III.

4. Method III Organotin Fluorides

Our initial work in Method III, dealt with syntheses, characterization, solubility measurements in CO_2, and evaluation of solution behavior of certain trialkyltin fluorides in various hydrocarbons such as *n*-propane, *n*-butane, etc.

Dandge *et al.*[19] and Taylor[20] found that increasing the alkyl chain beyond C_4 in trialkyltin fluorides substantially increased their solubility in most organic solvents. Furthermore, viscosification of nonpolar solvents by these trialkyltin fluorides, which ranged from triamyl to tridecyltin fluorides, was as effective as that by tributyltin fluoride or even better. The transient polymeric chains, resulting from dipole-dipole interactions because of the large difference in the electronegativity of Sn and F atoms as shown in Fig. II-26, are responsible for the increase in solvent viscosity, which becomes almost vertical above a certain concentration. The synthesis and characterization of symmetric trialkyltin fluorides and the results of this work were documented in two papers[19,21] and a patent.[22] More extensive results of these trialkyltin fluorides appeared in Craig Taylor's master's thesis.[20]

The exploratory work on tri-*n*-alkyltin fluorides (R_3SnF) indicated that increasing the alkyl chain length in these compounds increased both their solubilities and viscosities in hydrocarbons such as propane and butane.[19,22] On the other hand, their solubility in CO_2 did not show a considerable increase. Taking these observations into consideration, we decided to synthesize silicon-substituted trialkyltin fluorides in order to increase the solubility of these compounds in CO_2.

Two novel silicon-containing tin fluorides, tris(trimethylsilylpropyl)tin fluoride (PTF) and dibutyl(trimethylsilylpropyl)tin fluoride (BTF), were synthesized according to the Schemes a and b, respectively, shown in Fig II-27. Another known tris(trimethylsilylmethyl)tin fluoride (MTF)[23] was also synthesized for comparison of solution properties. Extensive characterization of these compounds by X-

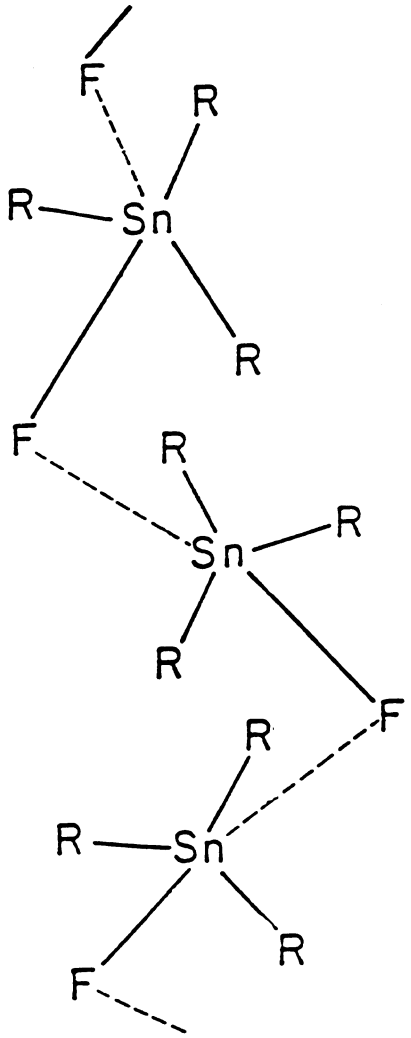

Figure II-26. Schematic representation of the formation of chains of trialkyltin fluoride through penta coordination of tin in nonpolar solvents.

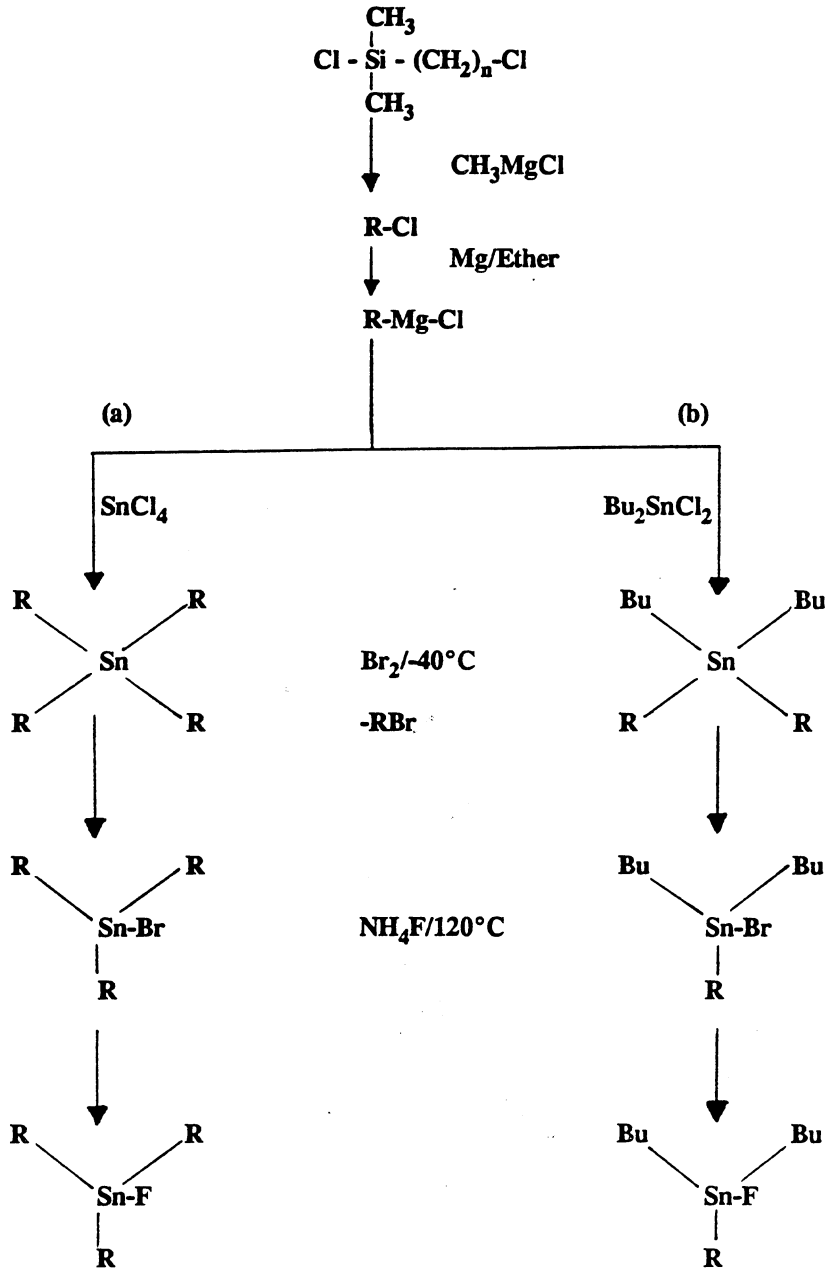

n = 3, R = $-(CH_2)_3Si(CH_3)_3$ = PTF

n = 3, R = $-(CH_2)_3Si(CH_3)_3$ = BTF

n = 1, R = $-CH_2Si(CH_3)_3$ = MTF

Figure II-27. Schematic of syntheses of silylorganotin fluorides.

ray diffraction,[24] FTIR, ^1H, and ^{13}C-NMR spectroscopy were documented in Pradeep Singh's master's thesis.[25]

The solubilities of MTF, PTF, and BTF in various common organic solvents including CO_2 are listed in Table II-1. It has been found that the substitution of a trimethylsilyl group for a methyl group enhanced the solubility of these compounds in nonpolar solvents. This is well-reflected in the marked higher solubility of these compounds in CO_2 as shown in Table II-1. The higher rates of dissolution of PTF and BTF in nonpolar solvents than in the corresponding tri-*n*-alkyltin fluorides indicate that the introduction of a trimethylsilyl group at the end of each chain, and somewhat away from the Sn-F bond, imparts higher solubility as well as higher dissolution rates.

The solutions of PTF and BTF in nonpolar solvents, such as *n*-hexane, exhibit nonlinear concentrations vs. viscosity curves as shown in Fig. II-28. It is obvious from these curves that the critical concentration for these two compounds is above 0.7%, while analogous tri-*n*-alkyltin fluorides showed a critical concentration of less than 0.4%.[20] This difference may be attributed to the presence of bulky $(CH_3)_3Si$-groups nearer to the Sn-F bond, which offers some steric hinderance to auto-association. Another important contribution of this study is that the introduction of a trimethylsilyl group increased the solubility of these compounds in nonpolar solvents. But this increase in solubility slightly decreased the ability of these compounds to viscosify hydrocarbon solvents. The effect of concentration of PTF on the viscosity of dense CO_2 at 25°C is shown in Fig. II-29. The observed 50% increase in viscosity is not sufficient for EOR operations.

5. Method II Ionomers

We investigated two different types in the Method II ionomers. These method types deal with ion-containing polymers and are reported in two subsections.

A literature survey on ion-containing polymers showed that the introduction of ionic groups into polymers having unsaturation (double bonds) has resulted in substantial changes in the physical properties[26] because of the ability of ionic associations to provide physical cross-links as depicted in Fig. II-30. A direct consequence of these ion-pair interactions is the thickening behavior of ionomers in the semi-dilute polymer regime as compared to their nonionic counterparts.

a. Exploratory Work

In an exploratory work for the synthesis of Method II ionomers that might be capable of thickening the solvent CO_2, we have undertaken the synthesis of Method II CO_2-soluble ionomers using Method I copolymer precursors as described in a Quarterly Report of 1990.[27] This method involved the initial preparation of a base copolymer that contained about 3-15% of unsaturation, derived from a diene comonomer by cationic copolymerization. The resulting copolymer was functionalized by sulfonation, followed by neutralization, with either metal acetate or metal hydroxide, into the corresponding sulfonated ionomers.

TABLE II-1. SOLUBILITIES OF SILICON-CONTAINING TRIORGANOTIN FLUORIDES AT 25°C

SOLVENT	SOLVENT SOLUBILITY PARAMETER $(cal/cm^3)^{1/2}$	DIPOLE MOMENT (D)	DIELECTRIC CONSTANT (ε)	SOLVENT VISCOSITY (CP)	MTF	PTF	BTF
carbon dioxide*	6.0	0	1.60	0.07		4.46§	4.14§
ethane*	6.0	0		0.16			
propane*	6.4	0.854	1.61	0.22 (25°C)			
butane	6.8	0.05		0.27	O	X+	X+
pentane	7.0	0	1.84	0.4	O	X+	X+
hexane	7.3	0.08	1.89 (25°C)	0.4	X	X+	X+
heptane	7.4	0	1.92 (20°C)	0.6	O	X+	X+
decane	8.0	0	1.99	1.26			
cyclohexane	8.2	0	2.02	1.3 (17°C)	X		
carbon tetrachloride	8.6	0	2.24	0.5	X	X+	X+
toluene	8.9	0.36	2.38	0.6 (30°C)	X+	X+	X+
benzene	9.2	0	2.275	0.7	X	X+	X+
chloroform	9.3	1.0	4.80	0.3	X	X+	X+

§ = in g/l
O = insoluble
X = solubility at least 0.2 g/dl
X+ = solubility >> 0.4%

*Conditions used for solubility determinations

Pressure PSI		Temp. °C
CO_2	= 2500	25
ethane	= 1200	25
propane	= 1200	25

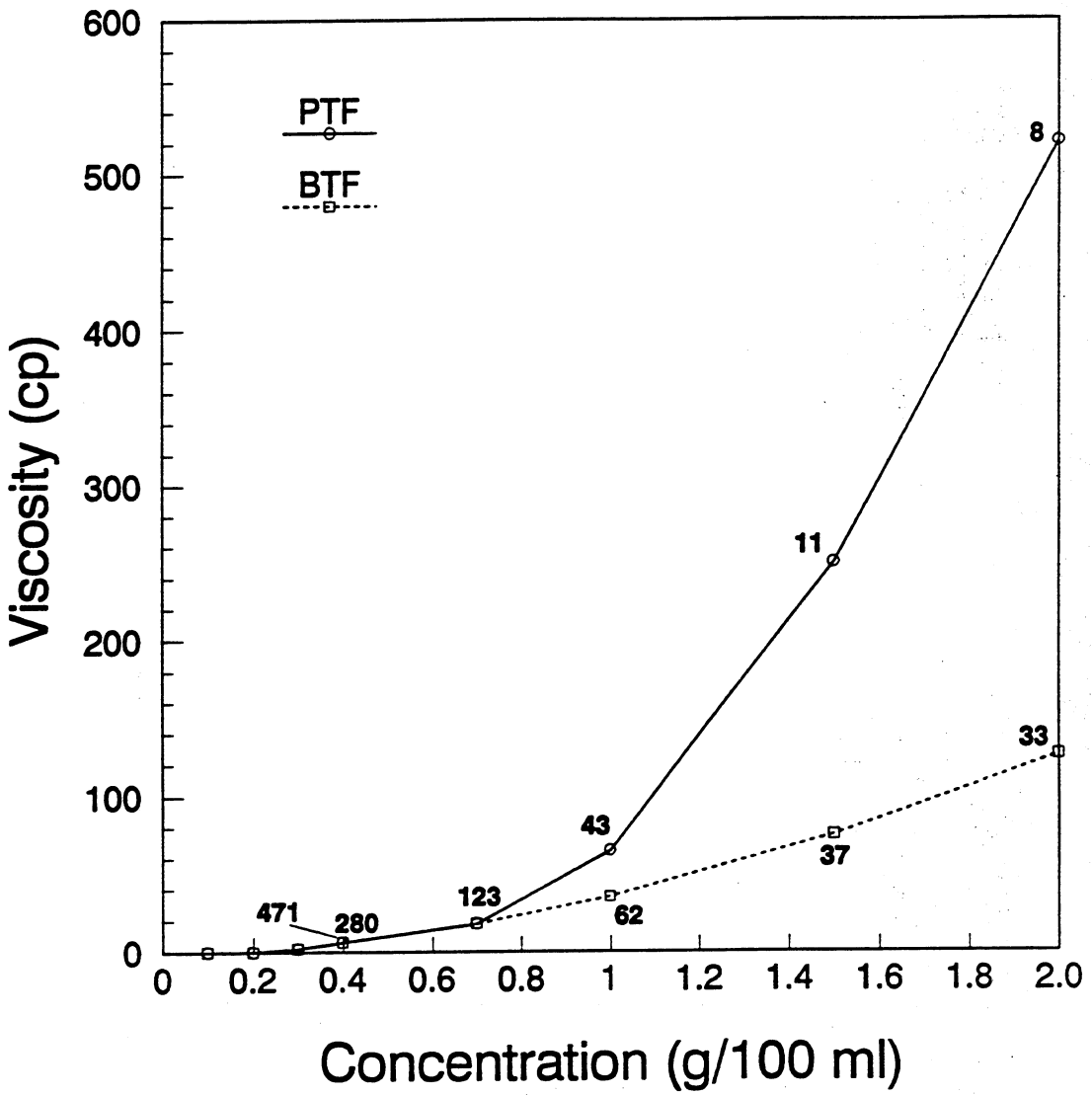

Figure II-28. Viscosity as a function of concentration of tris(trimethylsilylpropyl)tin fluoride (PTF) and of dibutyl(trimethylsilylpropyl)tin fluoride (BTF) in *n*-hexane at 25°C (The number at each data point indicates approximate shear rate at the wall).

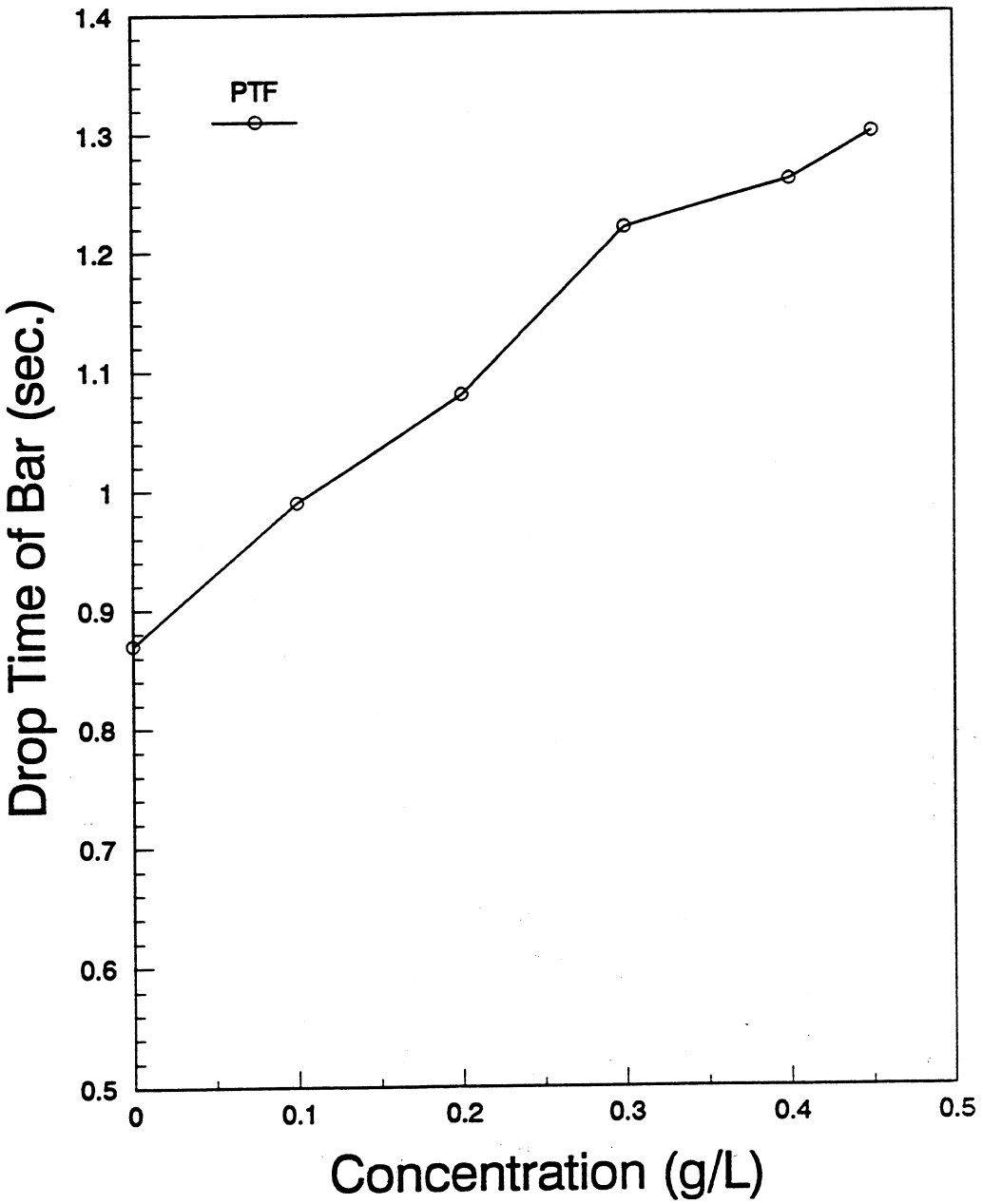

Figure II-29. Viscosity of solutions of tris(trimethylsilylpropyl)tin fluoride (PTF) in CO_2.

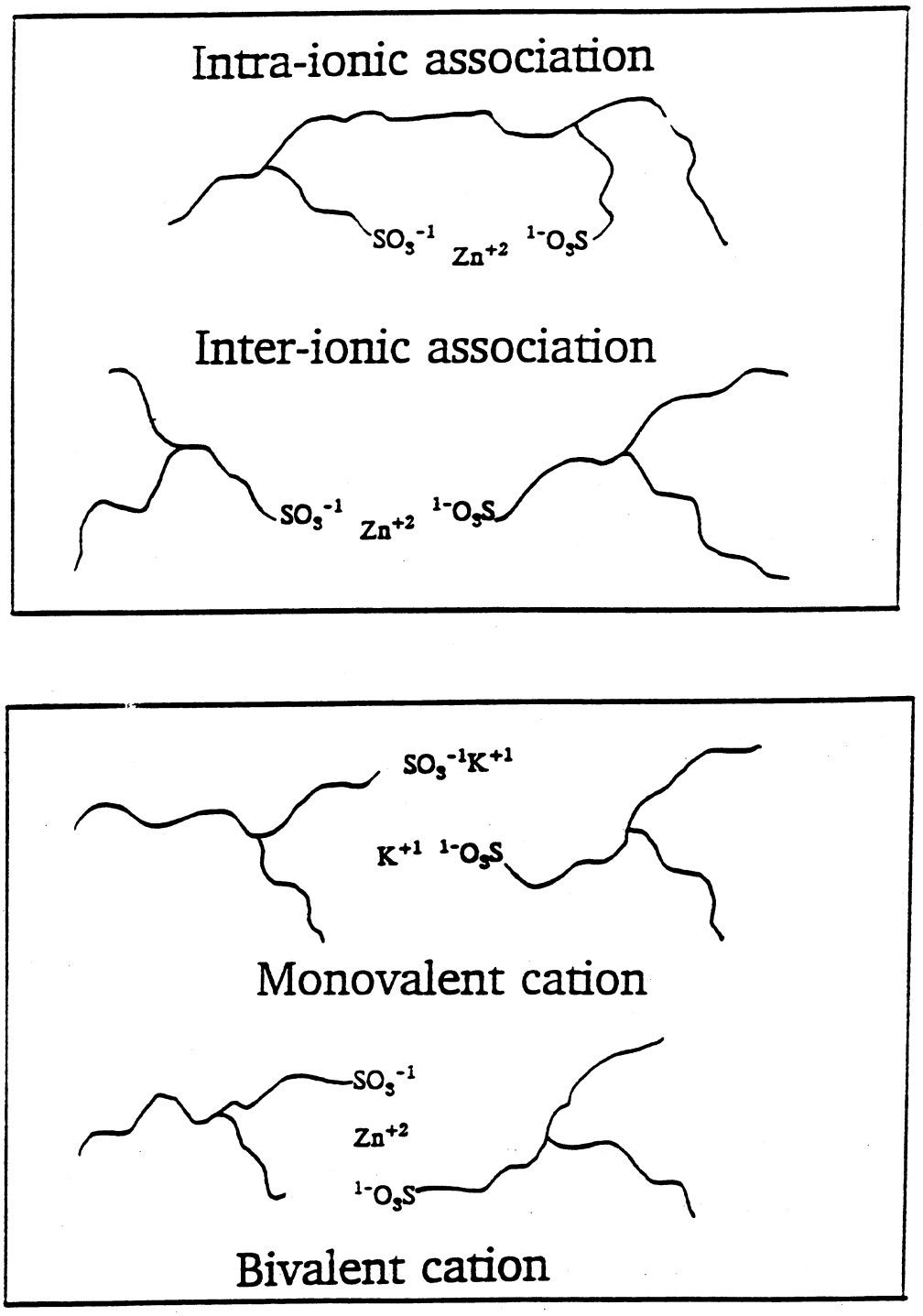

Figure II-30. Types of ionic associations in ionomers.

i. Experimental Procedures and Characterization

The preparation of Method II ionomers for our purposes began with the initial synthesis of nonionic copolymer precursors containing about 3-10% of unsaturation. We have considered the cationic copolymerization of 1-hexene with 1,4-hexadiene comonomer with $AlCl_3$ catalyst. The experimental conditions of copolymerization of 1-hexene with 1,4-hexadiene and the solubilities measurements of poly(1-hexene-co-1,4-hexadiene)s in dense CO_2 are given in Table II-2.

Heterogeneous sulfonation[16] was performed to introduce sulfonic acid groups into the copolymers and was carried out in hexanes solution by premixed acetic anhydride and sulfuric acid mixture. In a typical procedure of sulfonation, the copolymer (1g in 25 mL of hexane) was added to the sulfonating reagent at room temperature and stirred vigorously for about two hours. Stirring was stopped and the layers were allowed to separate. The lower acid layer was discarded and the hexane solution was subsequently added drop-wise into rapidly stirred, boiling distilled water. Precipitation of the sulfonated copolymer into water efficiently removed the residual sulfuric acid. The precipitated sulfonated copolymer was washed free of acid with distilled water and dried *in vacuo* at room temperature overnight.

The characterization of sulfonated copolymers was done by FTIR analysis. The analysis of sulfonated copolymer confirmed the introduction of sulfonic acid groups, which could be easily noticed by comparing the IR spectra of the copolymer and the corresponding sulfonated copolymer as shown in Figs. II-31 and II-32. The SO_3H group exhibited a broad absorption band between 1255-1280 cm^{-1} and sharp absorptions at 1168 cm^{-1} and 1049 cm^{-1}. The absorbance at 1168 cm^{-1} resulted from the symmetric stretching vibration of two $(S=O)_2$ bonds, while the absorption at 1049 cm^{-1} resulted from the symmetric stretching vibration of the -S-O(H) bond. The broad absorption band between 1255-1330 cm^{-1} was due to the asymmetric stretching of the two $(S=O)_2$ bonds of the sulfonic acid. Additionally, an absorption resulting from the stretching vibration of the S-O could be noticed at 893 cm^{-1}. Also, the appearance of hydroxyl absorption ranging from 3150-3400 cm^{-1} confirmed the presence of sulfonic acid groups.

Both the sulfonated and the base polymers showed some common absorptions, which correspond to the asymmetric and the symmetric stretching vibrations of methylene and methyl groups between 2955-2875 cm^{-1}. The presence of methylenes and methyl groups was further supported by the appearance of a methylene bending vibration at 1455 cm^{-1} and by the rocking vibration at 735 cm^{-1}, while the methyl bending absorption could be seen at 1375 cm^{-1}.

The viscosity profiles of the sulfonated copolymer and of the base copolymer in hexane are shown in Fig. II-33 for comparison. The slight increase in viscosity of the sulfonated copolymer is attributed to association of sulfonic acid groups as a result of hydrogen bonding.

Neutralization of the sulfonated copolymers was performed, using both monovalent and bivalent cations in order to observe the effect of the cation type on the associative nature of the resulting ionomers. This procedure was similar to that reported by Makowski *et al.* for the sulfonated EPDM polymers.[28]

A representative neutralization procedure is as follows. The excess amount of metal salt was dissolved in tetrahydrofuran/ethanol (95/5, v/v), followed by the addition of sulfonated copolymer in THF solution. After stirring for a few minutes, the solvents were distilled off under reduced pressure and steam stripped to remove the unreacted neutralizing agent. The resulting ionomer was then extracted with hexanes and dried *in vacuo* at 45°C overnight. Following the same procedure, potassium, zinc, and

TABLE II-2. REACTION CONDITIONS OF CATIONIC COPOLYMERIZATION OF 1-HEXANE WITH 1,4-HEXADIENE

POLYMER CODE	HEXENE (mole%)	DIENE (mole%)	CATALYST (mole%)	REACTION (hr)	TEMP (°C)	YIELD (%)	SOLUBILITY (g/L) IN DENSE CO_2 AT 2500 PSI AND 25°C
Copolymer-10	90	10	1.0	4	24	90	3.50
Copolymer-3	97	3	1.5	4	24	95	3.78

Comonomer = 1,4-Hexadiene (10 and 3%)

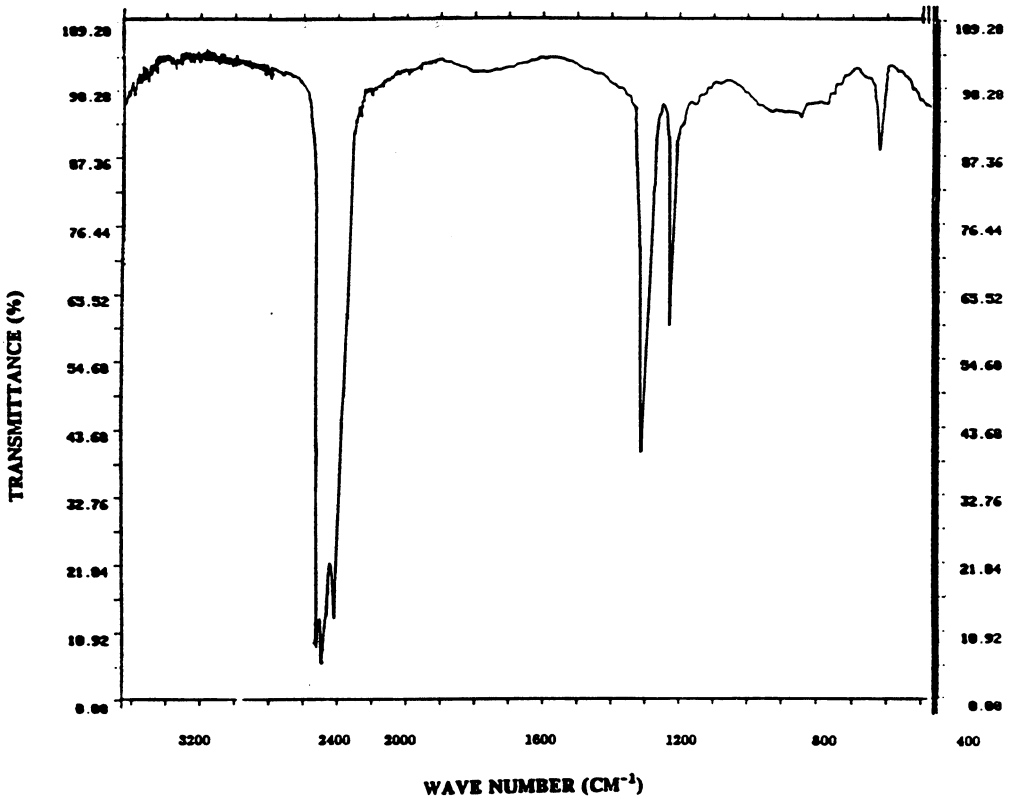

Figure II-31. FTIR spectrum of poly(1-hexene-co-1,4-hexadiene).

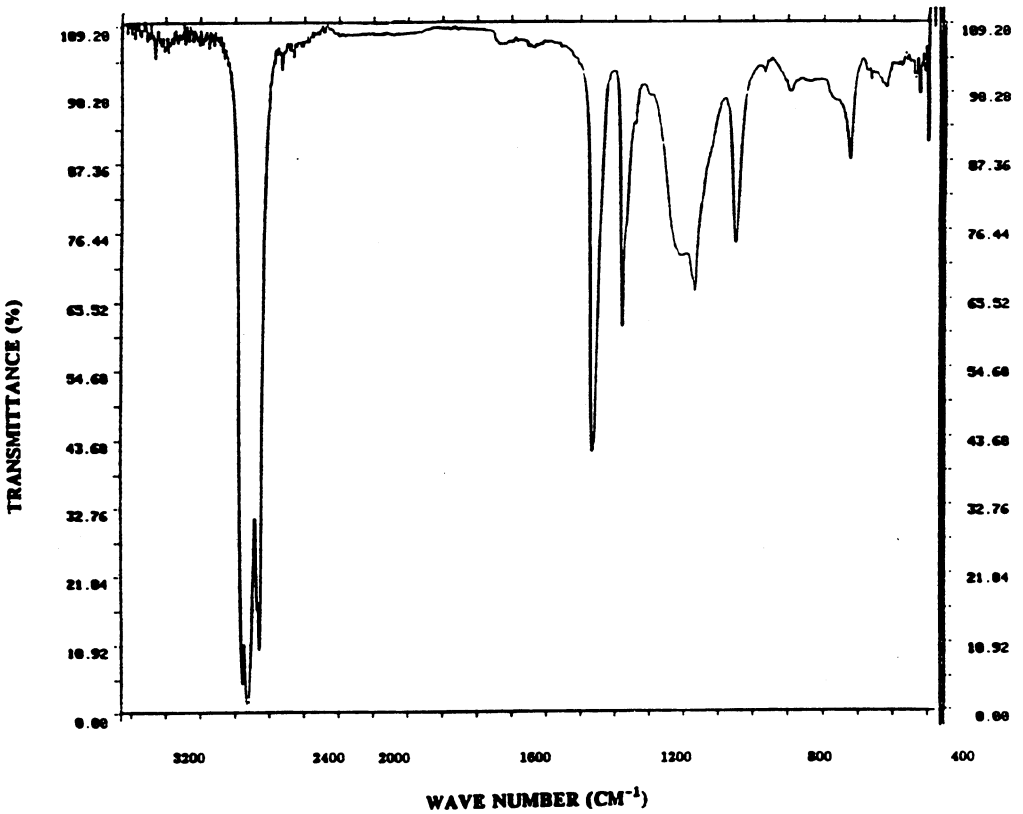

Figure II-32. FTIR spectrum of sulfonated poly(1-hexene-co-1,4-hexadiene).

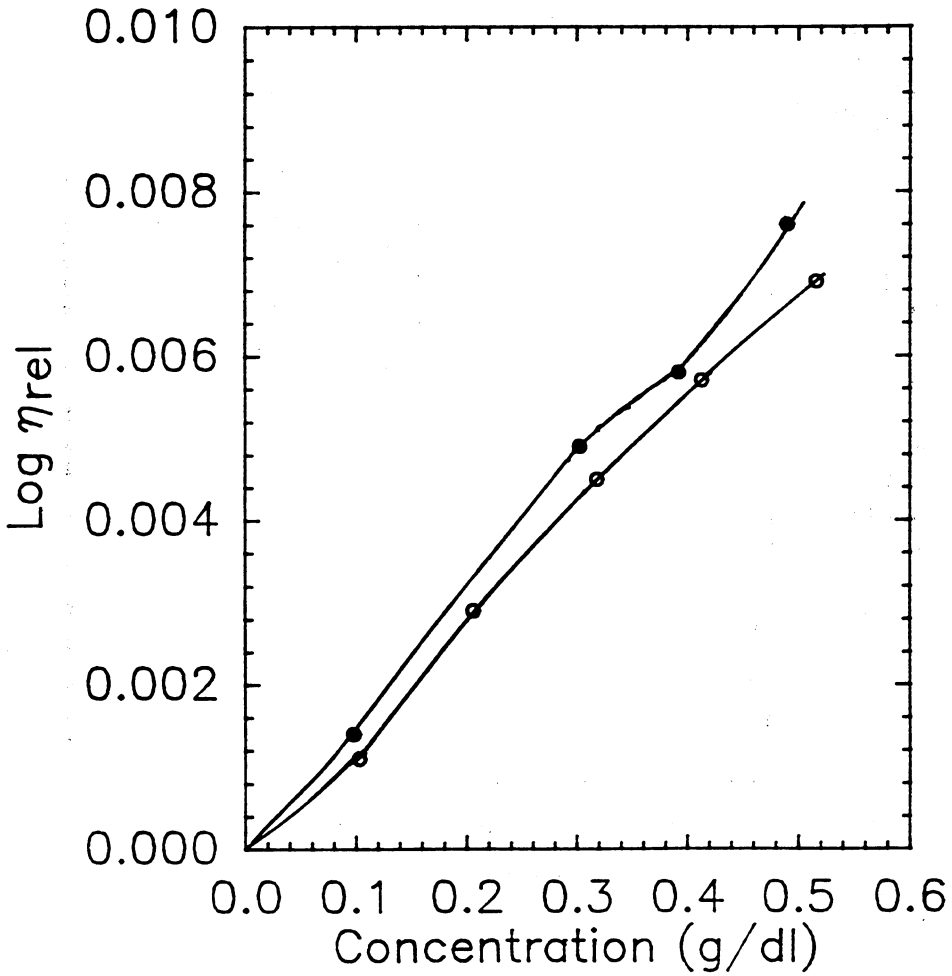

Figure II-33. Effect of sulfonation upon relative viscosity for (○) poly(1-hexene-co-1,4-hexadiene) and (●) sulfonated poly(1-hexene-co-1,4-hexadiene).

barium ionomers were synthesized and characterized by FTIR spectroscopy and solution viscosity measurements.

Characterization of the potassium, zinc, and barium ionomers has been primarily done with FTIR as shown in Figs. II-34, II-35, and II-36, respectively. For the potassium ionomer, the symmetric stretching vibration of the SO_3^{-1} anion appeared at 1043 cm^{-1} while the asymmetric stretching vibration of SO_3^{-1} appeared as a broad band at 1202 cm^{-1}. Noteworthy in monovalent ionomers, such as the potassium ionomer, is that the second absorption as a result of the asymmetric stretch of the SO_3^{-1} could not be distinguished. It appears, however, that the absorbance at 1168 cm^{-1} in the sulfonated polymer might include a contribution from this vibration. In contrast to this, Zn^{2+} ionomer showed different effects, presumably because of the strong interactions of the d-electrons with the SO_3^{-1} group. The broad absorption between 1210-1230 cm^{-1} was due to the SO_3^{-1} anion in the Zn^{2+} ionomer. The symmetric stretching vibration of the SO_3^{-1} appeared as a shoulder peak at 1175 cm^{-1}. The lower intensity of the sulfonate absorptions in the barium ionomer is attributed to the low concentration ($\sim$3%) of the ionic groups.

ii. Solubility Measurements of Copolymers and Ionomers in Dense CO_2

The solubility measurements of the ionomers and of the base copolymer were measured in dense CO_2 at 2500 psig and 25°C. The design of the solubility apparatus and the method of determination of solubility are described in detail in previous Annual Reports.[13,17,29] The results of solubilities of the base copolymer and of the ionomers are listed in Table II-2.

The zinc ionomer was found to be more soluble than either the potassium or the barium ionomers. Both potassium and barium form bonds that are more ionic in character; consequently, the corresponding ionomers showed less solubility than did the ionomer prepared with a transition metal such as zinc, which forms bonds of a more covalent character. This is evidenced by the higher solubility of the zinc ionomer in dense CO_2.

iii. Solution Properties of Copolymer and Ionomers

Finally, the solution properties of these three ionomers, as well as of a nonionic copolymer, have been measured in hexane using a standard Ubbelohde viscometer at 25°C. Solution properties include measurements of their relative viscosities (defined as $\eta_{rel}=\eta/\eta_0$) and of reduced viscosities or viscosity numbers (η-$\eta_0/\eta_0 c$), where η is the viscosity of polymer solution, η_0 is viscosity of the pure solvent, and c is the concentration of polymer.

Figures II-37 and II-38 represent viscosity profiles of the potassium, zinc, and barium ionomers, and that of the base copolymer. The ionomers show a *nonlinear* increase in reduced viscosities, while the nonionic copolymer precursor shows a *linear* increase in reduced viscosity with increasing concentration of the polymer. The trend of viscosity increase of these ionomers indicates that they do indeed associate at a higher polymer concentration. However, the extent of increase in viscosity depends largely on the associative nature of the cation used to neutralize the acid precursor. Two important variables that may affect the properties of ionomers are the *type* and *ionic potential* (q/a, where q = charge and a = ionic radius) of the cation. The increase in relative viscosity or reduced viscosity of the zinc ionomer was found to be more than that of the potassium ionomer. Since potassium is monovalent,

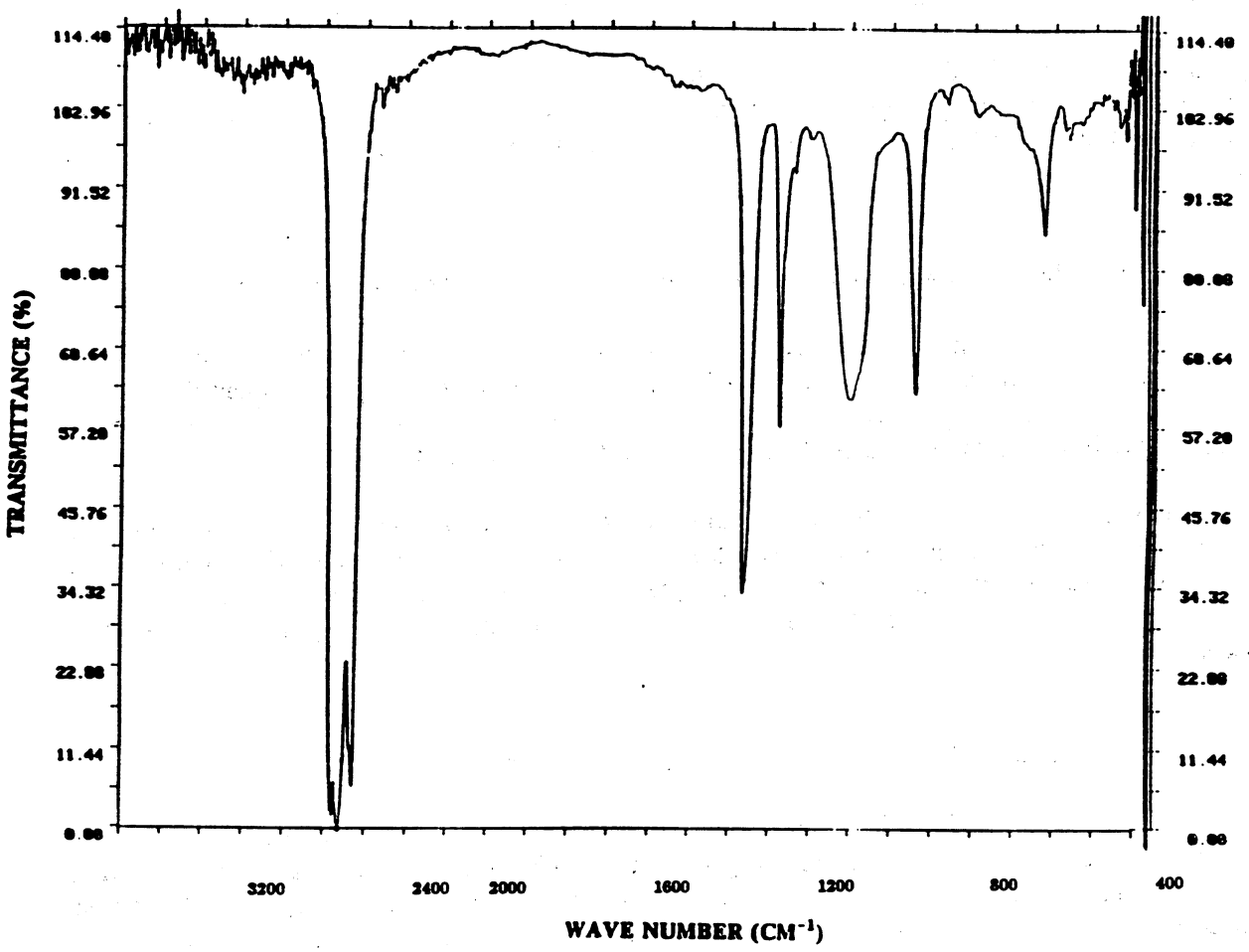

Figure II-34. FTIR spectrum of potassium ionomer.

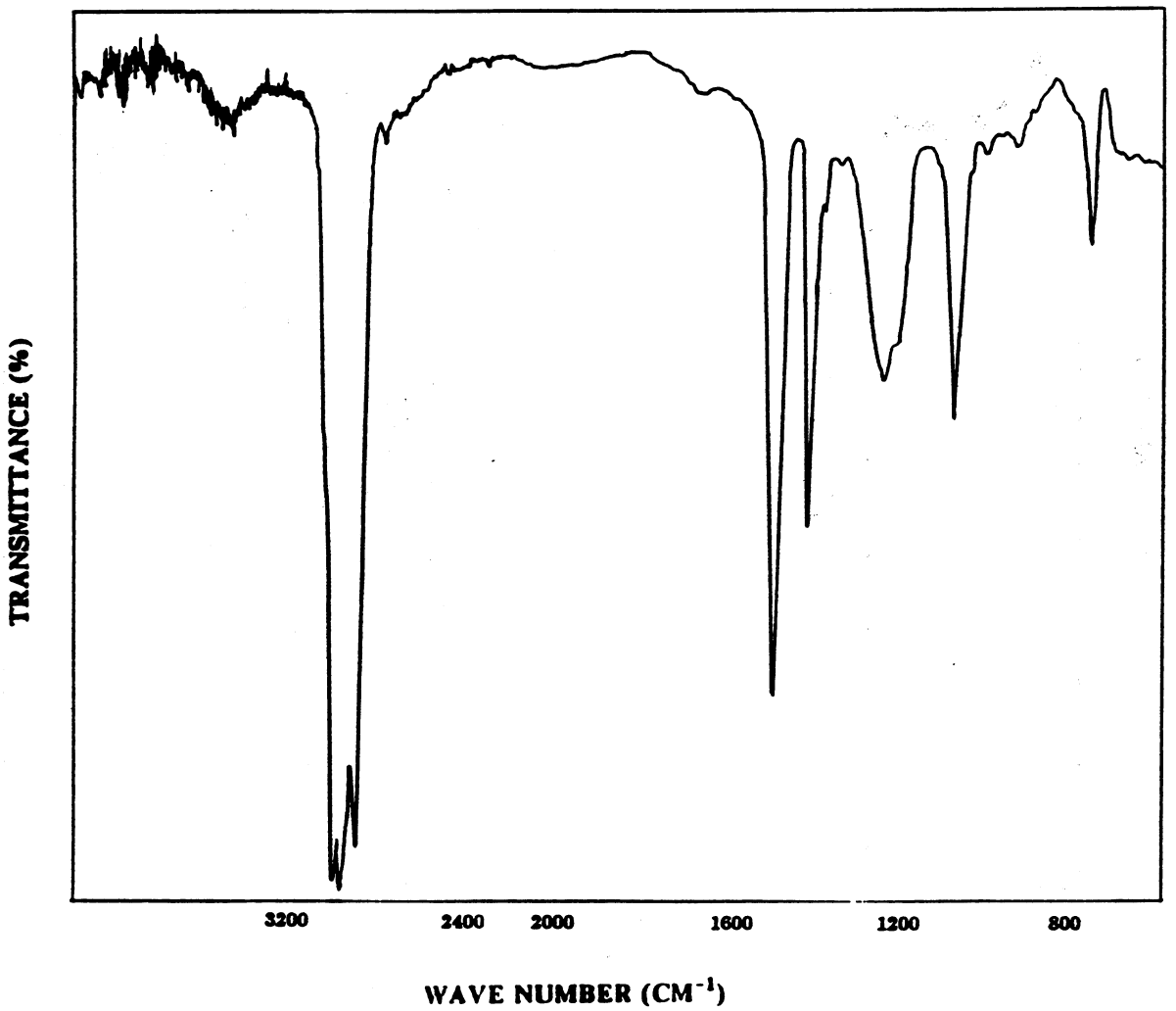

Figure II-35. FTIR spectrum of zinc ionomer.

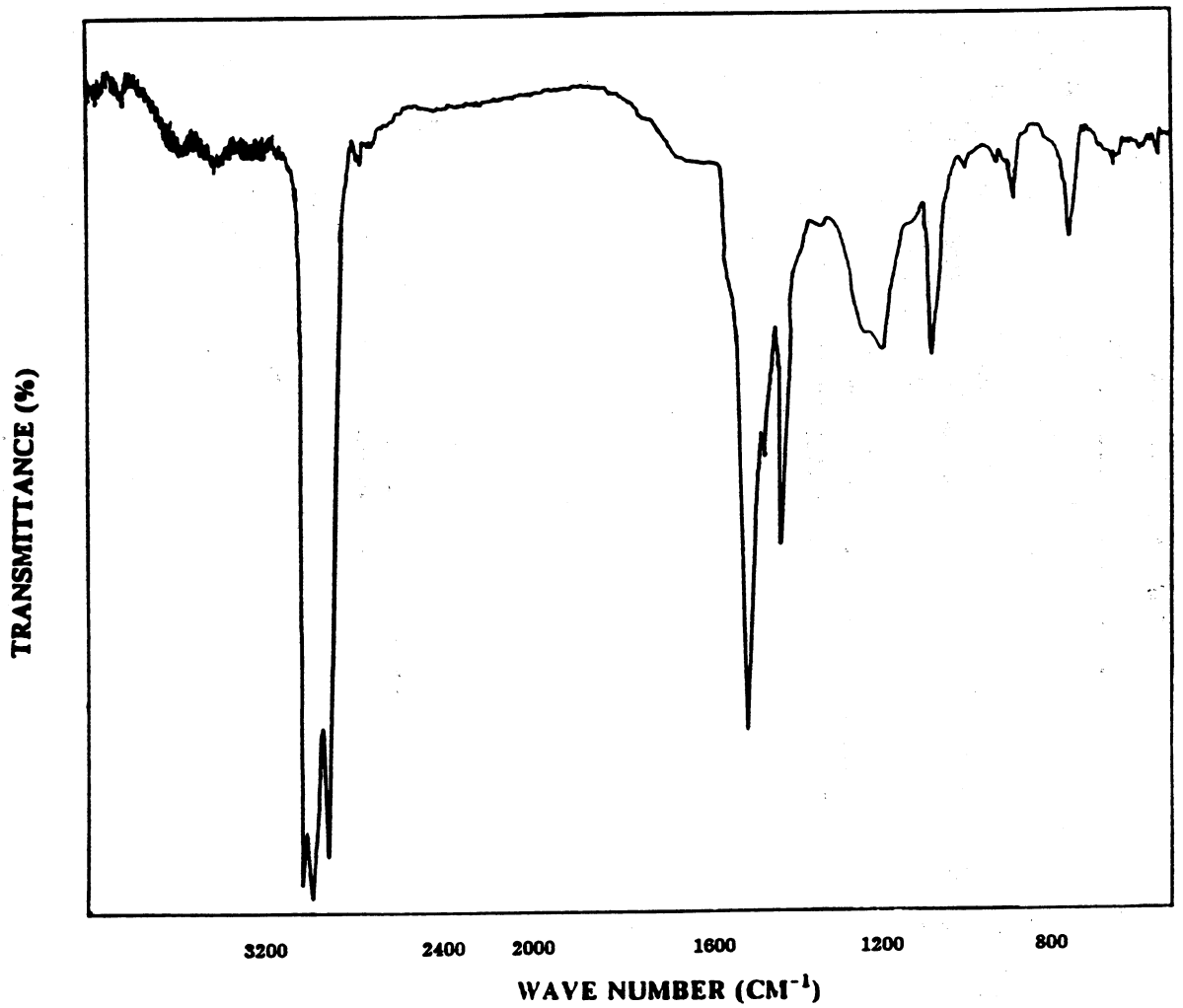

Figure II-36. FTIR spectrum of barium ionomer.

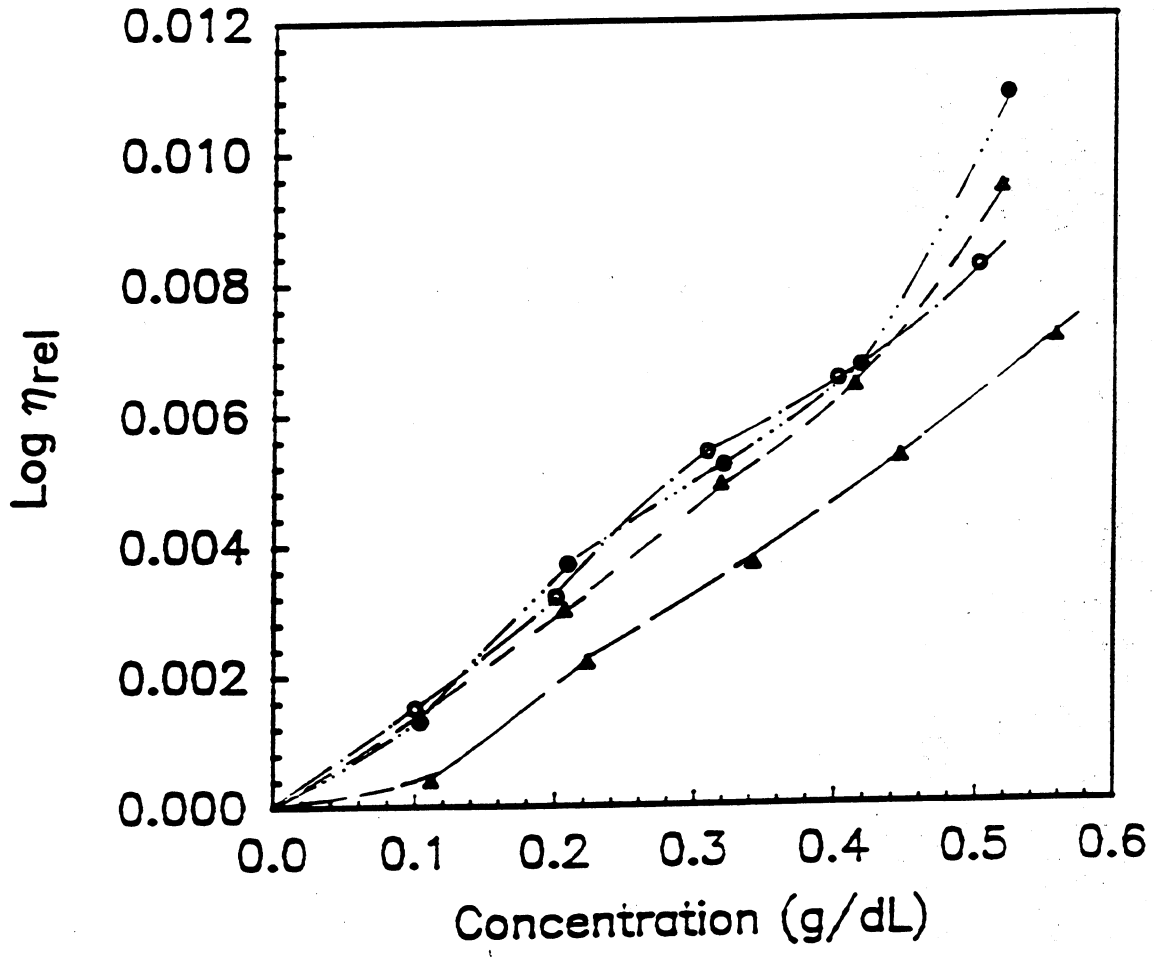

Figure II-37. Comparison of relative viscosities of poly(1-hexene-co-1,4-hexadiene) (▲), potassium ionomer (○), zinc ionomer (●), and barium ionomer (△) in *n*-hexane at 25°C.

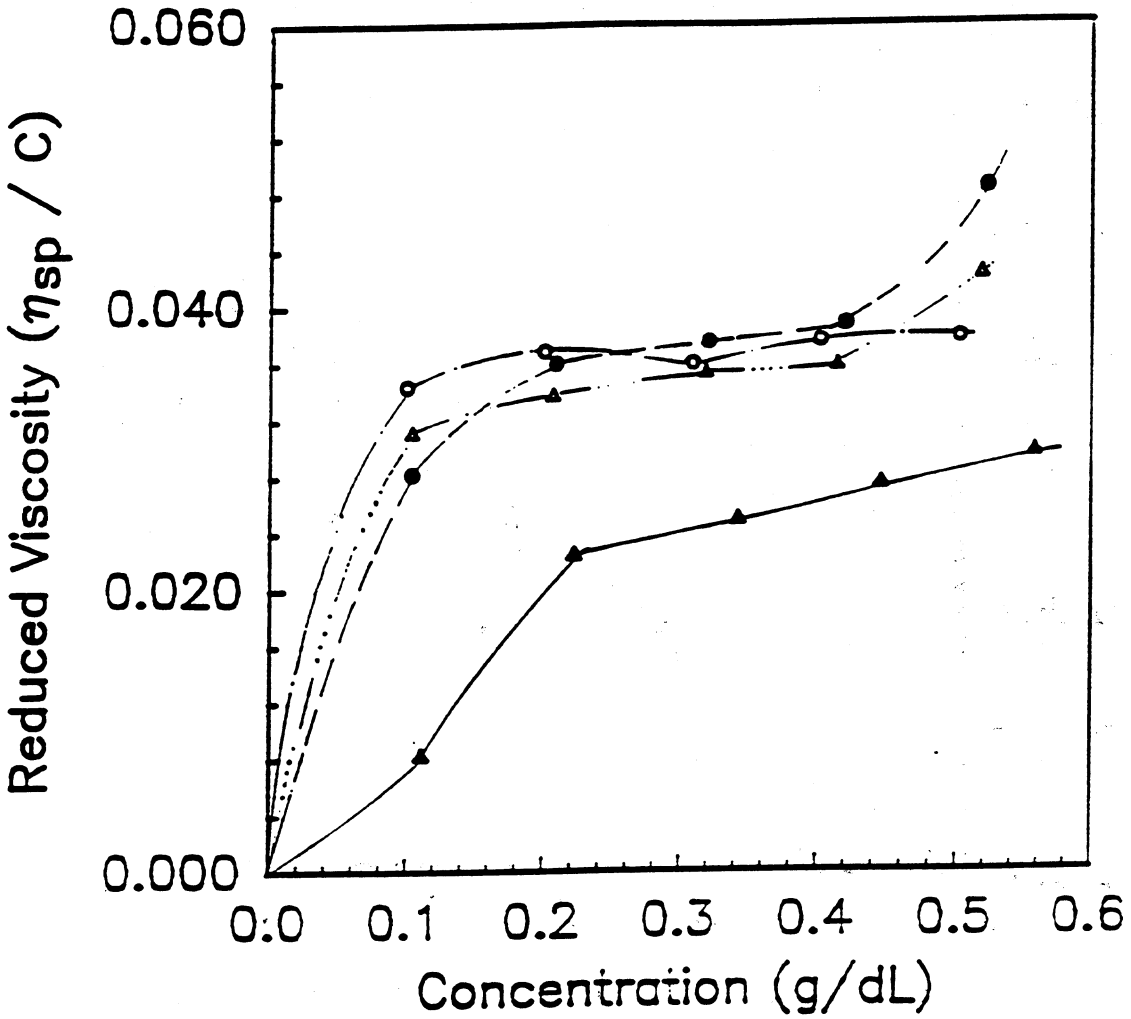

Figure II-38. Comparison of reduced viscosities of poly(1-hexene-co-1,4-hexadiene) (▲), potassium ionomer (○), zinc ionomer (●), and barium ionomer (△) in *n*-hexane at 25°C.

it can only associate with one sulfonate group and exhibits first order ion-pair associations of the type shown in Fig. II-26. In contrast, the bivalent zinc ion can associate with two sulfonate groups. This leads to a greater increase in the viscosity as a result of higher order associations caused by the formation of triplets and multiplets, also shown in Fig. II-26.

Of the three ionomers, the zinc ionomer increased the viscosity more than the barium ionomer did. Although both of these cations are bivalent, zinc can apparently associate more than barium can. This can be rationalized by considering the ionic potential (*q/a = charge of the cation/ionic radius*) of the cations. The smaller size and higher ionic potential of zinc account for the observed results. Higher visocification of the solvent could have been observed if the ionomer concentration was more than 4-5%.

In summary, three different types of CO_2-soluble Method II ionomers were prepared, characterized, and evaluated for their viscosity behavior in hexane. Although higher solubilities were achieved, viscosification was not sufficiently high. Based on this work, we have investigated other types of versatile ionomers called telechelic ionomers.

b. Rationale of Method II-Telechelic Ionomers

Perhaps the most promising of our approaches for the development of direct thickeners is that based on ion-containing polymers, identified as the Method II ionomers. Another particular development this year was on the design and development of a special group of ionomers called *telechelic ionomers*. In these polymeric molecules, unlike those in other conventional ionomers, the ionic groups are selectively placed only at the ends of polymer chains. These ionomers have attributes that, we believe, may prove them superior to the other polymers. Such systems have been envisioned and initiated earlier for different applications such as elastomers.[30] Recent discoveries in our laboratories and elsewhere have demonstrated the feasibility of synthesis of such ionomers.

The presence of a low concentration of ionic groups on nonpolar polymers (usually $<15\%$) significantly influences the properties of the polymers because of ion aggregation.[31] This aggregation leads to a two-phase morphology in which the ion aggregates serve as physical cross-links. These ionic cross-links, resulting from intra- and inter-ionic associations, have a substantial effect upon the solution behavior of the ionomers. This leads to the potential application of telechelic ionomers as viscosity building agents for EOR.

The design of the Method II telechelic ionomers with specific desirable properties demands the controlled synthesis of well-defined polymers that can be modified into ionomers as outlined in Fig. II-39. Precisely defined networks can be obtained, as described in earlier reports, by end-linking the prepolymers using polyfunctional initiators called *ini*tiator trans*fer* (*inifer*) agents. The use of such reagents in the carbocationic polymerization of isobutylene, well established by Kennedy *et al.*,[32] leads to the synthesis of polyisobutylenes end-capped with chloro functional groups. The subsequent dehydrochlorination of these polymers yields polymers with terminal double bonds that direct the selective placement of sulfonic acid groups. The neutralization of sulfonic acid groups with either metal hydroxide or metal acetate yields sulfonated telechelic ionomers.

The more significant polymer properties, which affect their solubility in dense CO_2, are their molecular weight and molecular weight distribution (MWD). As dense CO_2 is capable of extracting the lighter hydrocarbon fractions,[33] it is likely that CO_2 fractionates the polymers of relatively large

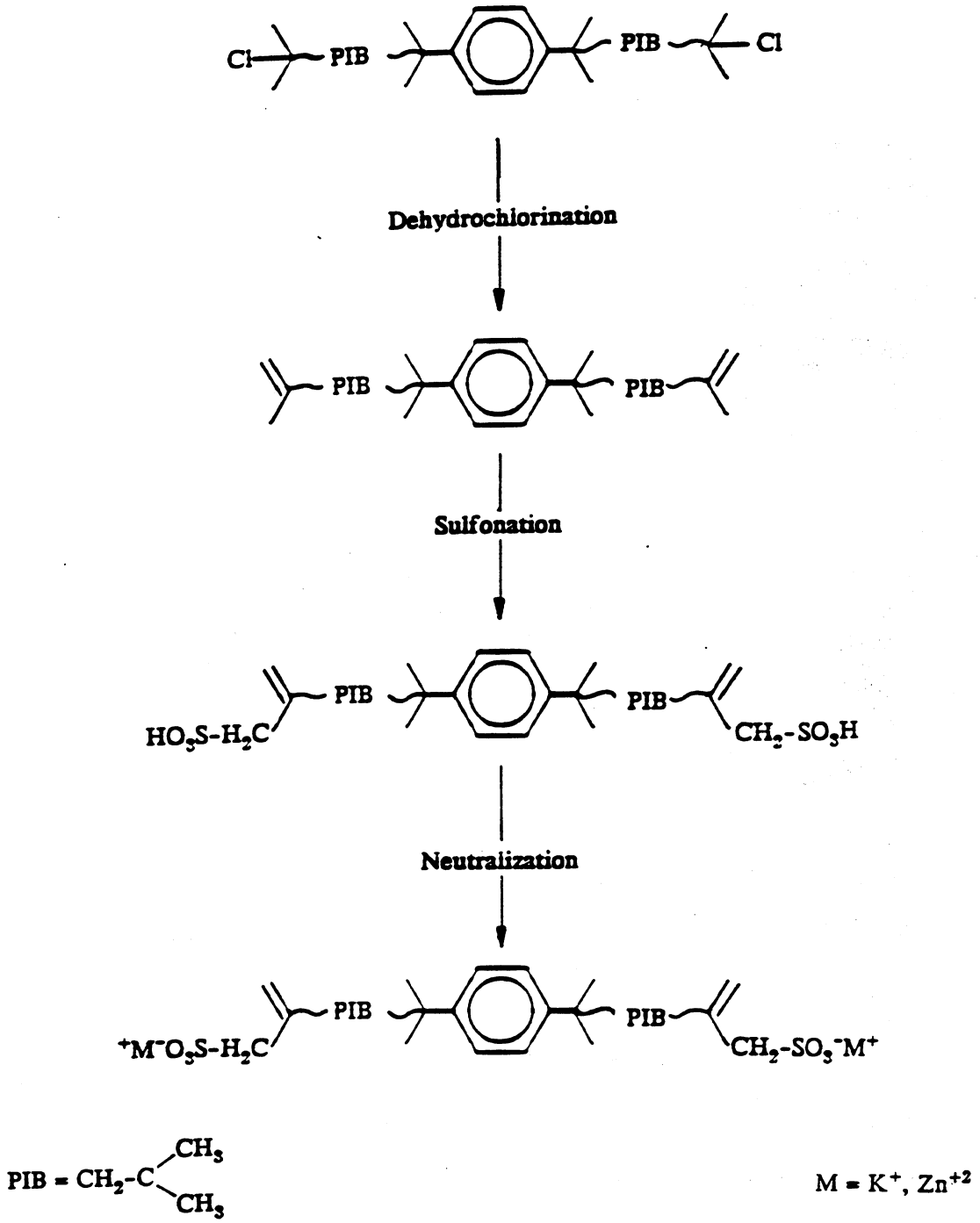

Figure II-39. Synthesis of two-arm linear sulfonated polyisobutylene telechelic ionomers with *binifers*.

polydispersity (i.e., wide MWD). It has therefore been thought worthwhile to synthesize near-monodisperse networks of ionomers using living carbocationic polymerization techniques for the synthesis of the prepolymers. Living polymerization is an effective method to control both molecular weight and MWD of polymers. Truly living polymerization (i.e., polymerization that proceeds in the absence of termination and chain transfer) are of great scientific and industrial importance.[34,35] By living polymerization techniques, it is possible to achieve fairly high solubility of carefully prepared narrow MWD polymers.

Our preliminary synthetic efforts have demonstrated the promise of such ionomers as potential viscosifiers. Syntheses, characterization, and solution properties of model synthetic ionomers are currently in progress. Instrumental techniques including FTIR, NMR, GPC, VPO, and dilute solution viscometry are being used to characterize the polymers that are synthesized in our laboratory, and to probe molecular interactions and solution viscosity behavior.

We have chosen isobutylene monomer for our studies for several reasons. First of all, its structural feature, which generates a stable carbocation during the carbocationic polymerization, is relatively simple to work with. Secondly, isobutylene is one of the most economically available commercial hydrocarbon monomers.[36] Supplemental to this, the polymers produced using this monomer are mostly amorphous. As the solubility of polymer depends on its tacticity, reported in our earlier paper,[14] amorphous polymers are preferred for our purposes. Moderate molecular weight polyisobutylene was one of the first viscosity-index modifiers for lubricants.[36] Additionally, polyisobutylenes are considered to have no chronic hazard associated with exposure under normal industrial use.[36]

Isobutylene (IB, Aldrich) was used as received by condensing it under dry nitrogen. 1,4-Dicumyl alcohol, used as an initiator for isobutylene polymerization, was obtained through the courtesy of the GoodYear Tire and Rubber Co. 1-Methyl-1-cyclohexanol, *tert*-butanol, and *tert*-amyl alcohol, 2-chloro-2-methylbutane were distilled before use. Boron trichloride (BCl_3), titanium chloride ($TiCl_4$), anhydrous N,N-dimethyl acetamide (DMA), anhydrous 1-methyl-2-pyrrolidinone (M-Pyrol), potassium *tert*-butoxide (*t*-BuOK), lithium aluminum hydride (LAH), acetic anhydride (Ac_2O), triethylamine (Et_3N), 4-dimethylaminopyridine (DMAP), *n*-hexane, methanol (all Aldrich) were used as received. Methylene chloride (CH_2Cl_2) was distilled over CaH_2, tetrahydrofuran (THF) was distilled over LAH, and toluene was distilled before use. Methyl chloride (CH_3Cl, Matheson) was used as received.

i. Preliminary Experiments of Living Polymerization of Isobutylene

As indicated before, the design and development of near-monodisperse telechelic ionomers demands careful and controlled synthetic techniques. One such technique has been that of *Living Polymerization*. Truly living polymerizations proceed in the absence of termination and chain transfer. Great efforts have since been made to find conditions under which a living carbocationic polymerization could be achieved. The instability of the propagating carbocations of olefins in the carbocationic polymerization usually leads to chain transfer to the monomer, and to termination reactions.

A conventional nonliving carbocationic polymerization can be rendered living by the use of a proper electron-pair donor (ED) that eliminates undesirable side reactions such as uncontrolled initiation by protic impurities, chain transfer, irreversible chain termination, etc. This concept has been substantially investigated by Hagashimura *et al.* for vinyl ethers[37] and by Kennedy *et al.* for isobutylene[32] polymerization using a classical *inifer* method. According to these investigators, the presence of an ED

in these polymerizations apparently stabilizes and reduces the high intrinsic reactivity of unstable growing polymerization-active carbocations and yields polymers of narrow MWD.

We have performed initial polymerizations with BCl_3 alone in the absence of any *tert*-alcohol. The extremely low yield of polyisobutylene prompted the use of the *inifer* concept,[32] which led to convenient synthetic routes for the preparation of telechelic polyisobutylenes.

In our scouting synthetic efforts, we have used a BCl_3 coinitiator in conjunction with a *binifer*, 1,4-dicumyl alcohol. The use of this initiating system resulted in a polymer of wide MWD. On the other hand, we have produced a polymer with a very narrow MWD using an externally added ED such as DMA. These observations can be well appreciated if one observes the GPC traces of α,ω-di(*tert*-chloro)polyisobutylenes as shown in Fig. II-40 (a), polymer obtained in the absence of any ED, and Fig. II-40 (b) in the presence of DMA using 1,4-dicumyl alcohol in both instances. The figure caption details the experimental conditions for polymers (a) and (b). Inasmuch as dense CO_2 fractionates the polymers of high polydispersity (wide MWD), it has been thought worthwhile to prepare a near-monodisperse network of ionomers. It appears from this that the polymer with narrow MWD is certainly more advantageous for our purposes than the one with wide MWD.

We then focussed our attention on the synthesis of new asymmetric and symmetric telechelic polysiobutylenes. Significant progress has since been made in the syntheses of telechelic polysiobutylenes. We have recently identified a few *m*onofunctional *ini*tiator trans*fer* agents (*minifers*) such as aliphatic, alicyclic, and aromatic tertiary alcohols. Among the bifunctional initiators (*binifers*), both aliphatic and aromatic tertiary alcohols have been successfully explored for the living polymerization of isobutylene. Two synthetic procedures, incremental monomer addition (IMA) and all-monomer-in (AMI) techniques, have been used for isobutylene polymerization.[38] The following sections of the report describe these techniques.

ii. Incremental Monomer Addition (IMA) Technique

Owing to the high reactivity of carbocations in isobutylene polymerization, the IMA technique has been used to modulate the high reactivity of cations by the addition of strong EDs. About three to five flasks were charged with initiator in a mixture of methylene chloride and ED in a low temperature bath. Detailed polymerization conditions are given in tables and in figure captions. BCl_3 was added to the *tert*-alcohol in methylene chloride and allowed to stir for about 10-15 minutes. Then the monomer was slowly added to the initiating system. After a predetermined polymerization time ($\sim$30 minutes), polymerization was stopped in the first reactor by the addition of prechilled methanol, whereas an additional amount of isobutylene was charged to all the remaining flasks. After 30 minutes, the reaction in the second flask was quenched and a further quantity of monomer was charged to the rest of the flasks. This procedure was continued until all the charges in the series had been quenched with methanol. Solvents were evaporated, polymer was dissolved in *n*-hexane, washed with distilled water until neutral, dried over Na_2SO_4, and filtered. Polymer was recovered by evaporating the solvent using rotavap and dried *in vacuo*. However, minute losses of the polymer were unavoidable. One of the advantages of this method is that it is possible to control the molecular weights of the polymers by controlling the concentration ratio $[M_0]/[I_0]$, where $[M_0]$ and $[I_0]$ are the initial concentrations of monomer and of the initiator, respectively.

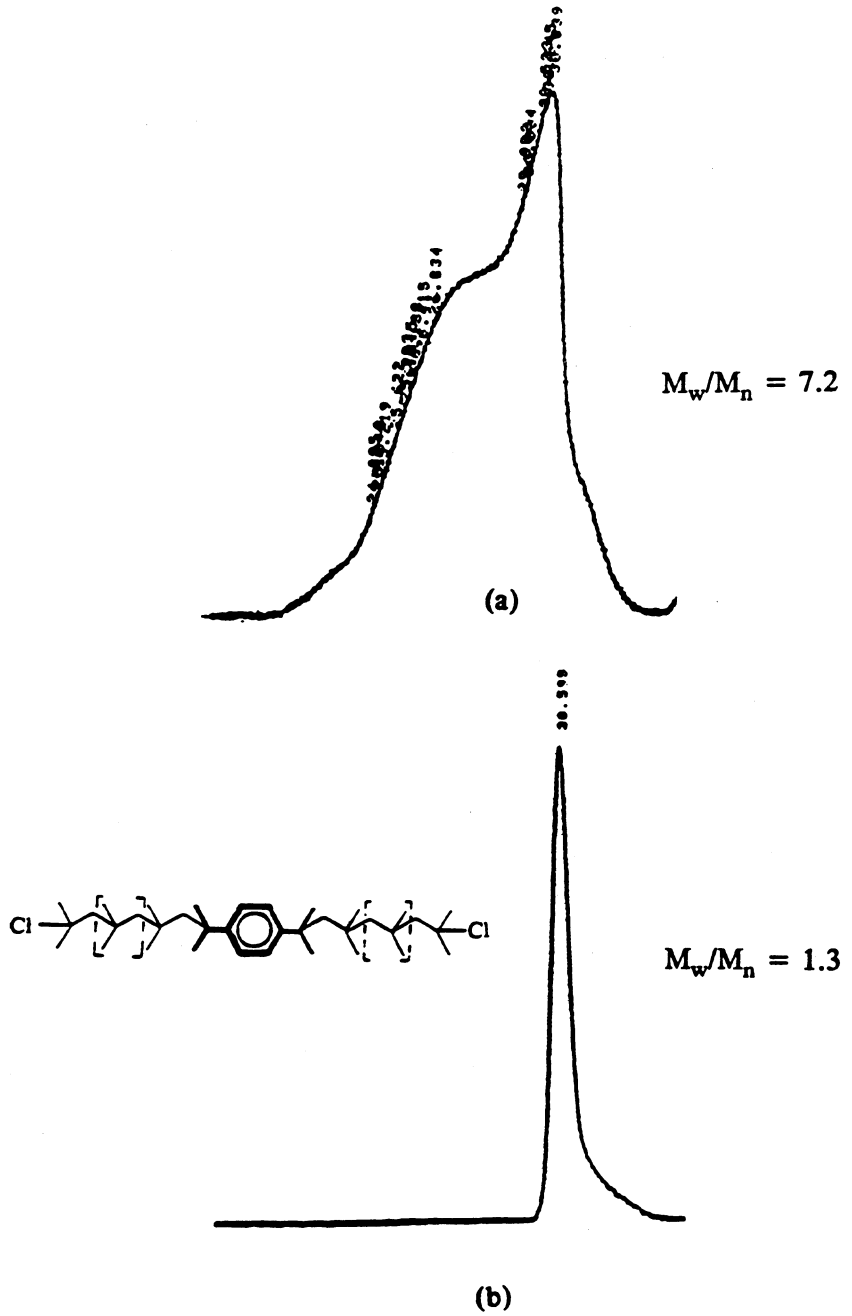

Figure II-40. GPC traces of α,ω-Di(*tert*-chloro)polyisobutylenes using 1,4-bis(1-hydroxy-1-methylethyl)benzene (DiCumOH)/IB/BC_3/CH_2Cl_2 at -65°C for 15 minutes: (a) In the absence of electron-pair donor: [DiCumOH] = 0.00178 moles/L, [IB] = 0.06675 moles/L, [BCl_3] = 0.0224 moles/L and (b) In the presence of electron-pair donor: [DiCumOH] = 0.00143 moles/L, [IB] = 0.0534 moles/L, [BCl_3] = 0.0179 moles/L, and [DMA] = 0.00286 moles/L.

iii. All-Monomer-In (AMI) Technique

In this method, monomer is added to the *inifer* recipe and the polymerization is terminated after a predetermined time. The first IMA experiment is also referred to as AMI method.

iv. Inifer Methods

A variety of tertiary alcohols have been investigated for their efficient use as *inifers* for the living polymerization of isobutylene. We have performed scouting experiments with *tert*-amyl alcohol and 1-methyl-1-cyclohexanol (which have not been investigated before for this purpose) in conjunction with BCl_3 and DMA in a polar diluent methylene chloride. The encouraging preliminary results led to the extensive experimentation to synthesize polymers of different molecular weights.

A new initiating system, *tert*-amyl alcohol/BCl_3/DMA, has been investigated for polymerization of isobutylene. Adopting the IMA technique, a series of low molecular weight asymmetric telechelic polyisobutylenes carrying an ethyl head group and a *tert*-chloro end group was prepared using a *tert*-amyl alcohol/IB/BCl_3/DMA system at -40°C. The experimental conditions are listed in Table II-3. All polymerizations were carried out in dry culture tubes fitted with screw caps and magnetic stirrers under a dry nitrogen atmosphere in a low temperature bath. The resulting polymers were characterized by FTIR, GPC, and VPO.

Definite proofs for the living nature of this polymerization were obtained by a linear plot, passing through the origin, of number average molecular weight (M_n) vs. amount of polymer (W_p) formed and by a horizontal N (number of PIB molecules) vs. W_p plot. The M_n of these polymers were evaluated by VPO method. These measured M_n values are close to the theoretical M_n values as shown in Fig. II-41 and the values of M_n as well as the weight of polymers increase with an increasing monomer addition. This suggests the growing ability of the living species that persist throughout the experiment and clearly demonstrates the living nature of these polymers.

In view of the significant advances in living carbocationic polymerizations, especially with the use of EDs such as DMA or DMSO for isobutylene (by Kennedy *et al.*),[39] we have investigated the potential use of another ED, 1-methyl-2-pyrrolidinone, in conjunction with *tert*-amyl alcohol and BCl_3 in methylene chloride for isobutylene polymerization for the first time. This resulted in a well-defined polyisobutylene end-capped with a *tert*-chloro group.

A series of new asymmetric telechelic α-ethyl-ω-(*tert*-chloro)polyisobutylenes has been prepared using a *tert*-amyl alcohol/IB/BCl_3/1-methyl-2-pyrrolidinone initiating (*minifer*) system by the IMA method as shown in Fig. II-42.

The nature of the head and end groups has been characterized by FTIR and ^{1}H-NMR spectroscopy. The living nature of these polymers was determined by GPC. Also definite proofs of their living nature were obtained by a linear plot of M_n vs. the amount of polymer (W_p) formed and by a horizontal plot of N (number of polyisobutylene chains formed, g/M_n) vs. W_p. The results of this new system have been documented in a paper, "Living Carbocationic Polymerization of Isobutylene by *tert*-Amyl alcohol/BCl_3/1-Methyl-2-pyrrolidinone Initiating System," which was recently accepted for publication in the *Journal of Applied Polymer Science*.[40]

TABLE II-3. POLYMERIZATION OF ISOBUTLEYNE BY THE *TERT*-AMYL ALCOHOL/BCl_3/DMA/CH_2Cl_2 SYSTEM

SAMPLE	WT. OF THE POLYMER (g)	M_n*	Mw/M_n**	I_{eff} (%)	REMARKS
1.	0.54	845	1.94	89.4	Telechelic
2.	1.27	1920	1.42	92.5	Telechelic
3.	2.90	4900	1.59	82.7	Telechelic

[*tert*-Amyl alcohol] = 0.00715 moles/L
[IB] = 0.0267 moles/L
[BCl_3] = 0.00896 moles/L
[DMA] = 0.000715 moles/L
Temperature = -40°C; 15 minutes premixing of catalyst with BCl_3

*Mn = Determined by VPO
**Mw/Mn = Determined by GPC

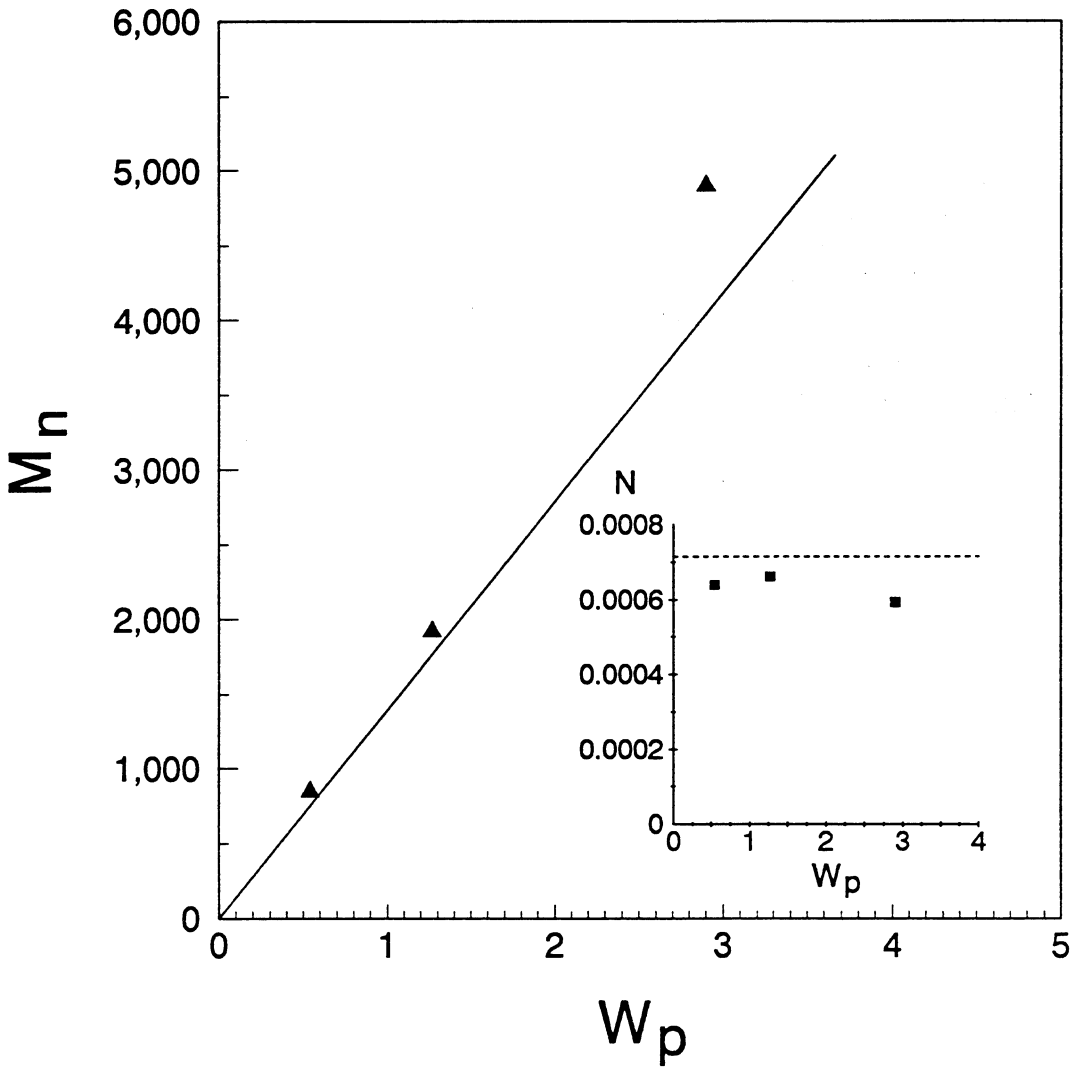

Figure II-41. M_n vs. weight W_p and N vs. W_p plots of α-ethyl-ω-(*tert*-chloro)polyisobutylenes formed using *tert*-amyl alcohol/IB/BCl_3/DMA/CH_2Cl_2 system at -40°C by IMA technique [(a), (b), and (c) refer to three incremental monomer additions]. Solid line indicates the theoretical values.

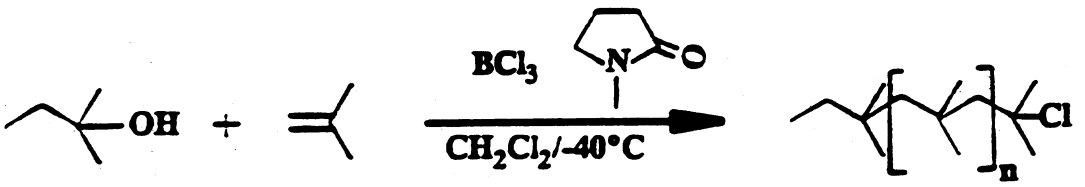

Figure II-42. Synthesis of α-ethyl-ω-(*tert*-chloro)polyisobutylenes using *tert*-amyl alcohol/IB/BCl_3/1-methyl-2-pyrrolidinone initiating system.

v. New Initiators

Two new monofunctional initiators, 2-chloro-2-methylbutane and 1-methyl-1-cyclohexanol, have also been successfully used for the living polymerizations of isobutylene. The results of a 2-chloro-2-methylbutane/IB/BCl_3/1-methyl-2-pyrrolidinone initiating system for the living polymerization of isobutylene are documented in another paper, "A New Initiating (Minifer) System for the Living Polymerization of Isobutylene," which was submitted to the *Journal of Chemical Society: Chemical Communications*.[41]

For comparison, we have also conducted the isobutylene polymerization separately with 2-chloro-2-methylbutane, 1-methyl-1-cyclohexanol, and *tert*-butanol adopting the AMI technique at -40°C. The polymerization conditions for these systems are listed in Table II-4. The monomer was added to an inifer recipe and the polymerization was terminated after a predetermined time.

In addition to the above *minifer* systems, we have also identified an aliphatic bifunctional tertiary alcohol, 2,4-dimethyl-2,4-pentanediol. This initiator, which mimics the groups derived from the monomer in the resulting polyisobutylene, has effectively initiated isobutylene polymerization in conjunction with either BCl_3 or $TiCl_4$ yielding *tert*-chloro end groups. The experimental conditions and the composition of the binifer recipes with two coinitiators are listed in Table II-5.

In order to see the effect of the coinitiator, we performed polymerization of isobutylene with two Lewis acid coinitiators, BCl_3 and $TiCl_4$, in conjunction with 1,4-dicumyl alcohol. The polymerization conditions are listed in Table II-6. We have observed that the polymerization of isobutylene with $TiCl_4$ was much faster than with BCl_3, even in the presence of an ED such as DMA at the same temperature.

The use of 1-methyl-2-pyrrolidinone has also been extended to an aromatic initiator, 1,4-dicumyl acetate, for the synthesis of linear, living α,ω-di(*tert*-chloro)polyisobutylenes. The initiator, required for the synthesis of these polymers, has been prepared in a quantitative yield by the acetylation of 1,4-dicumyl alcohol as shown in Fig. II-43.

It has been characterized by both ^{13}C-NMR and ^{1}H-NMR, as well as by ^{13}C-^{1}H-NMR COrrelation SpectroscopY (COSY), as shown in Fig. II-44.

Cycloalkylation, a side reaction often encountered with the use of cumyl-type initiators, leads to the formation of undesirable indanyl (a) and diindane (b) end groups as shown below.

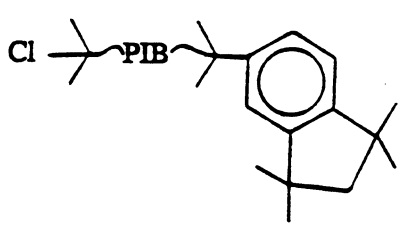

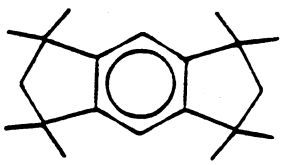

These side reactions hamper the clean synthesis of perfect telechelic polymers. A series of polymers was prepared using 1,4-dicumyl acetate/IB/BCl_3/1-methyl-2-pyrrolidinone in CH_2Cl_2 at -60°C. The resulting polymers were analyzed and characterized by GPC and FTIR. In order to verify the effect of M-pyrol, a similar kind of noncyclic ED, DMA, was also used with this initiator. The use of M-pyrol

TABLE II-4. POLYMERIZATION OF ISOBUTYLENE WITH MINIFERS

INITIATOR (mol)	BCl_3 (mol)	DMA (mol)	ISOBUTYLENE (mol)	CONVERSION (%)	REMARKS
2-Chloro-2-methylbutane (0.000715)	0.00896	0.000715	0.0267	52	Telechelic
1-Methyl-1-cyclohexanol (0.00143)	0.00896	0.00143	0.0534	57	Telechelic
tert-Butanol (0.00143)	0.0179	0.00143	0.0534	60	Telechelic

Time = 30 min
Temp = -40°C
CH_2Cl_2 = 20 ml
AMI Technique

TABLE II-5. LIVING POLYMERIZATION OF ISOBUTYLENE WITH 2,4-DIMETHYL-2,4-PENTANEDIOL/BCl_3 OR $TiCl_4$/DMA INITIATING SYSTEMS

INITIATOR (mol)	CO-INITIATOR (mol)	DMA (mol)	ISOBUTYLENE (mol)	CONVERSION (%)	REMARKS
0.002529	BCl_3 (0.0303)	0.002523	0.177	67	Telechelic
0.002529	$TiCl_4$ (0.0303)	0.002523	0.177	85	Telechelic, Fast Polymerization

Time = 30 min
Temp = -40°C
CH_2Cl_2 Solvent
AMI Technique

TABLE II-6. LIVING POLYMERIZATION OF ISOBUTYLENE WITH 1,4-DICUMYL ALCOHOL/BCl_3 OR $TiCl_4$/DMA INITIATING SYSTEMS

1,4-DICUMYL ALCOHOL (mol)	CO-INITIATOR (mol)	ISOBUTYLENE (mol)	DMA (mol)	CONVERSION (%)	REMARKS
0.00178	BCl_3 (0.0262)	0.067	0.00179	80	Telechelic
0.00178	$TiCl_4$ (0.0262)	0.067	0.00179	92	Telechelic, Fast Polymerization

Time = 30 min
Temp = -60°C
CH_2Cl_2 Solvent
AMI Technique

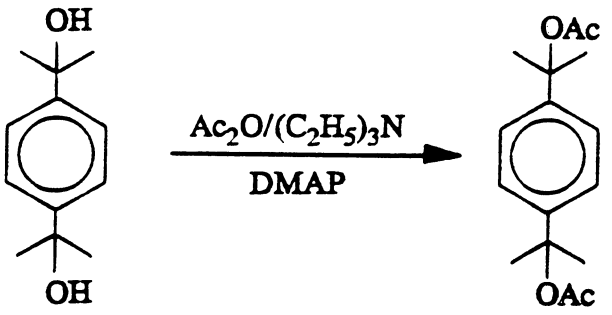

Figure II-43. Synthesis of 1,4-di(2-propyl-2-acetate)benzene.

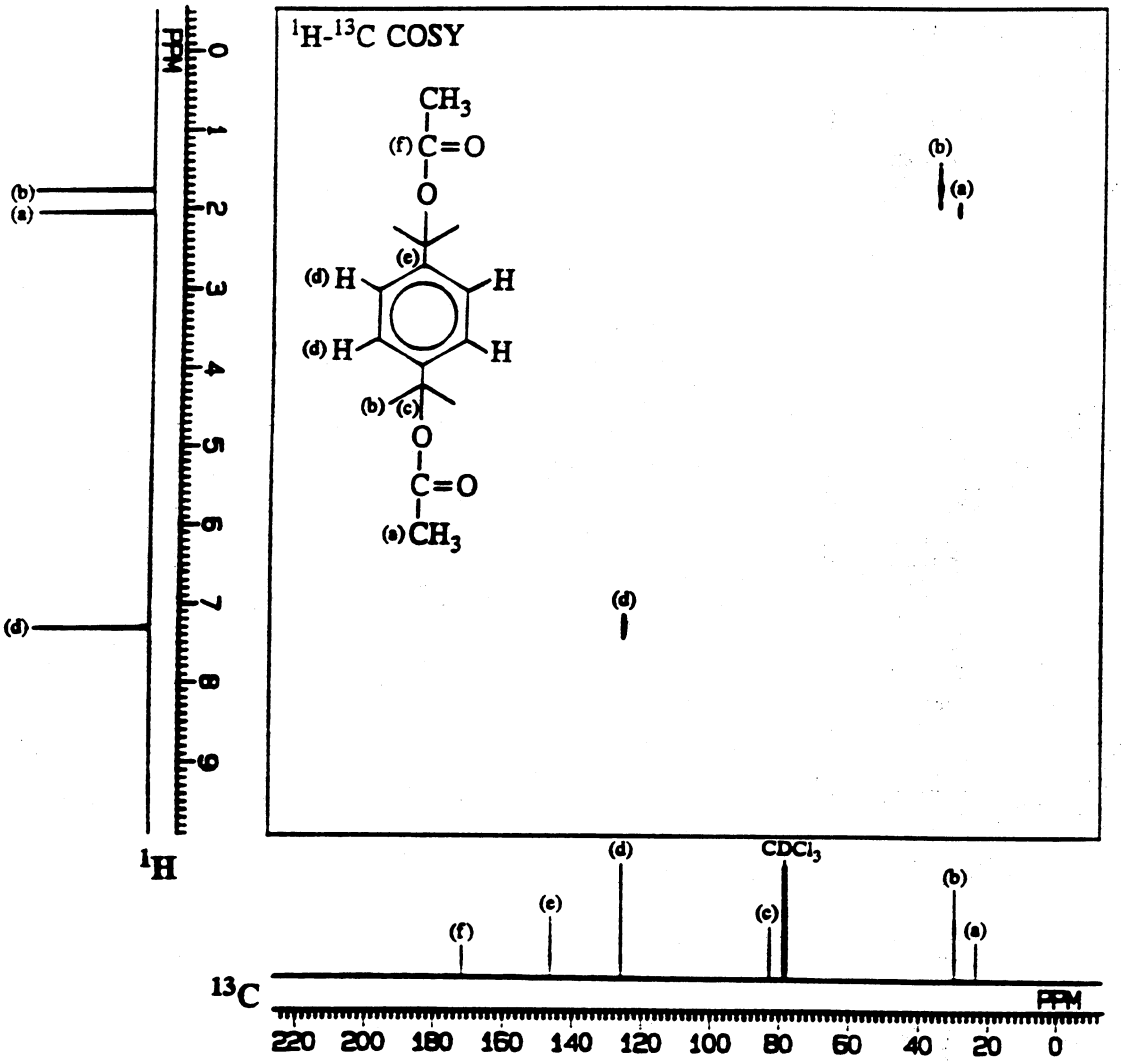

Figure II-44. ^{1}H, ^{13}C-NMR and ^{1}H-^{13}C COSY of 1,4-di(2-propyl-2-acetate)benzene.

suppressed the formation of the cyclic indanyl side products. The effects of these EDs on the suppression cycloalkylation and MWD have been determined independently by FTIR and GPC. All of these observations are presented in a note, "Electron-Pair Donors in Carbocationic Polymerization: Synthesis of Linear Living α,ω-Di(*tert*-chloro)polyisobutylenes," submitted to the *Journal of Polymer Science: Part A: Polymer Chemistry*.[42]

vi. Polymer Characterization

The telechelic polymers synthesized with various initiating systems have been extensively characterized by FTIR. The following sections describe the different methods used to evaluate the living nature of these telechelic polymers by GPC and VPO, respectively, to determine MWD and M_n. Also, their chemical composition in all the instances has been primarily done with FTIR spectroscopy, and in some cases, by ^1H and ^{13}C-NMR spectroscopy.

The MWD of the polymers synthesized with various initiators was determined by GPC using a liquid chromatograph (Waters Associates Model 264) with a separation system consisting of three columns in a series, packed with Lichrogel PS400, PS40, and PS1 (E. Merck, Darmstadt, FRG) of particle size 10 μm. THF was used as the mobile phase with a flow rate of 1 mL/min. A differential refractometer (Waters Associates Model 401) with a sensitivity of 16x, was used for detection. Fifty-μL samples of 1% solutions in degassed THF were injected into the columns following filtration through a 5.0 μm filter. The speed of the chart recorder was 0.5 cm/min.

With the recently developed computer software at the Petroleum Recovery Research Center,[43] we could reduce the data obtained with this system, according to ASTM D 3593, of both the weight average molecular weight (M_w), number average molecular weight (M_n), and polydispersity (M_w/M_n) for the polymers synthesized.

The GPC traces of the polymers, synthesized with *tert*-amyl alcohol/BCl_3/DMA system by the IMA method, are shown in Fig. II-45. The narrow MWD, for instance, of the third monomer addition explicitly demonstrates the observation that the polydispersity values of these polymers decreased with an increasing addition of monomer. MWD was greater in the case of the first polymer and became narrower with the progressive addition of monomer. It has also been observed that MWD decreases while the molecular weight of the resulting polymer increases with increasing monomer additions. The method of IMA is a good technique to control both molecular weight and MWD of the telechelic polymers.

Figure II-46 shows the GPC traces of the telechelic polyisobutylenes, α-methyl-ω-(*tert*-chloro) polyisobutylene, α-methyl cyclohexyl-ω-(*tert*-chloro)polyisobutylene, and α-ethyl-ω-(*tert*-chloro)polyisobutylene, synthesized with *tert*-butanol, 1-methyl-1-cylcohexanol, and *tert*-amyl alcohol, respectively. From these data, all three initiators are found to be efficient initiators for the living carbocationic polymerization of isobutylene.

A narrow MWD of α,ω-di(*tert*-chloro)polyisobutylene was also obtained with the aliphatic 2,4-dimethyl-2,4-pentanediol/BCl_3/DMA initiating system for isobutylene polymerization as shown by the GPC trace of this polymer in Fig. II-47. On the contrary, the same initiator in conjunction with $TiCl_4$ yielded a wider MWD as shown in Fig. II-48. It seems that the polymerization with the $TiCl_4$ coinitiator is rather sensitive to the traces of moisture as seen by the wide MWD.

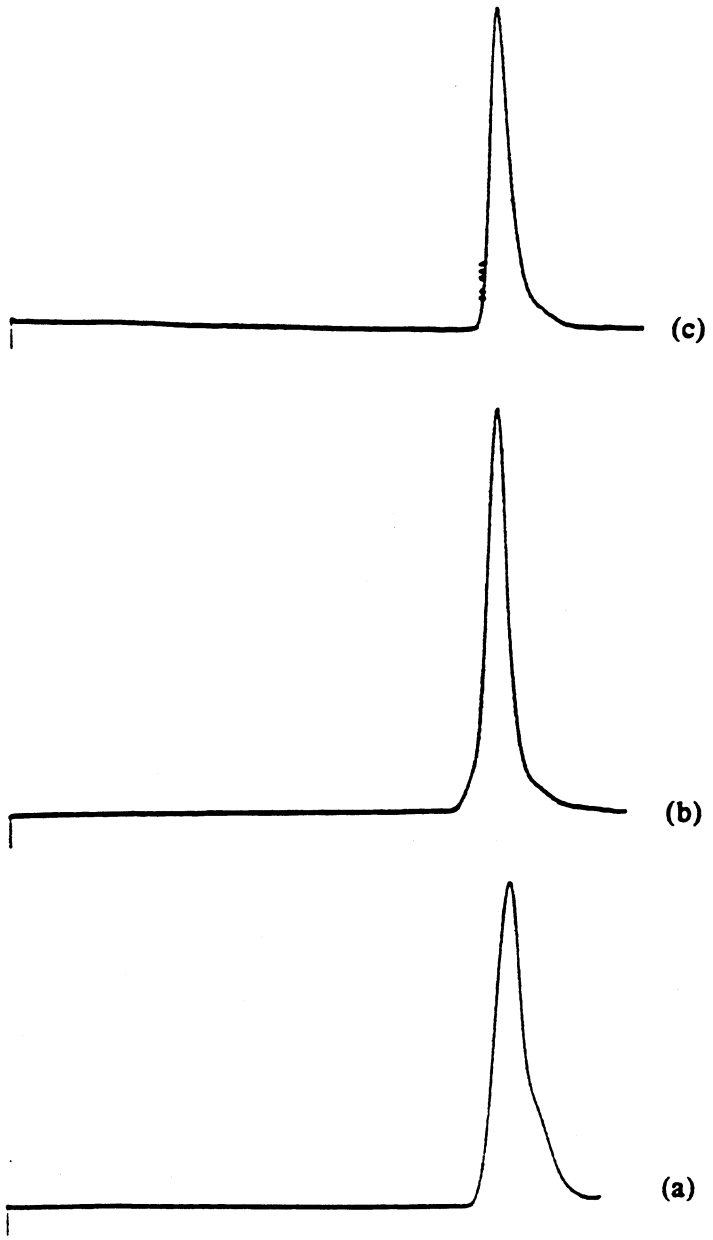

Figure II-45. GPC traces if α-ethyl-ω-(*tert*-chloro)polyisobutylenes [(a), (b), and (c) indicate the polymers formed by three incremental additions of monomer by IMA technique, see Fig. II-16].

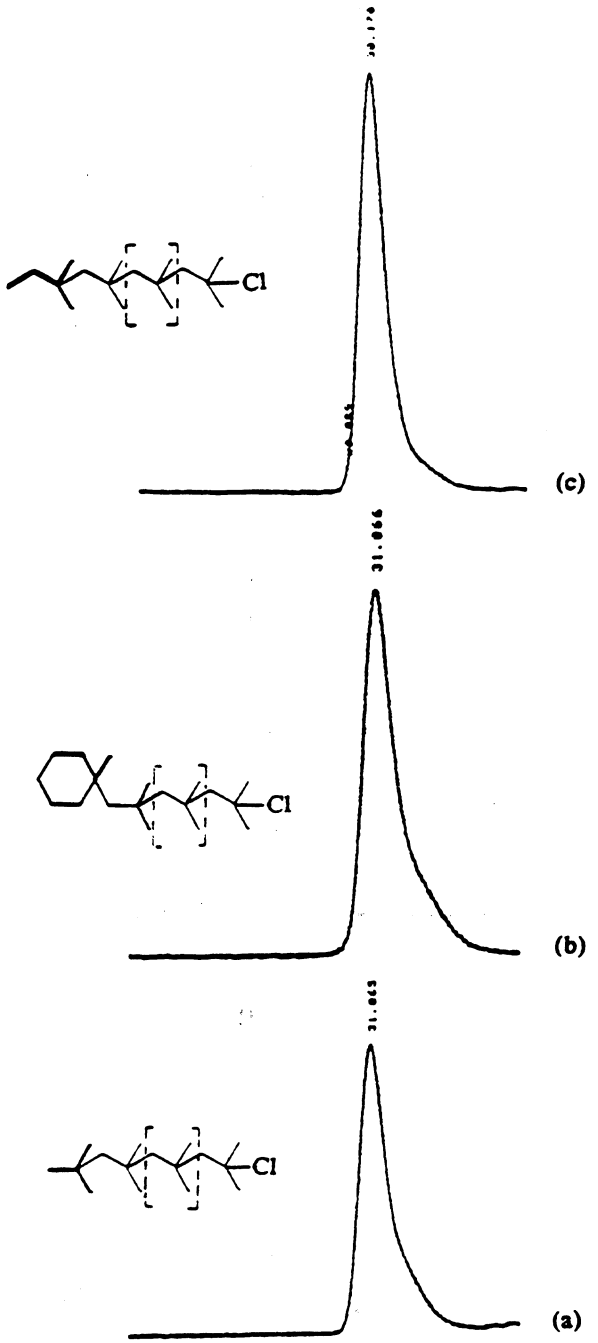

Figure II-46. GPC traces of (a) α-methyl-ω-(*tert*-chloro)polyisobutylene formed in the *tert*-butanol/IB/BCl_3/CH_2Cl_2 system at -40°C, (b)α-methyl cyclohexyl-ω-(*tert*-chloro) polyisobutylene formed in the 1-methylcylohexanol/IB/BCl_3/DMA/CH_2Cl_2 system at -40°C, and (c) α-ethyl-ω-(*tert*-chloro)polyisobutylene formed in the *tert*-amyl alcohol/IB/BCl_3/DMA/CH_2Cl_2 system at -40°C.

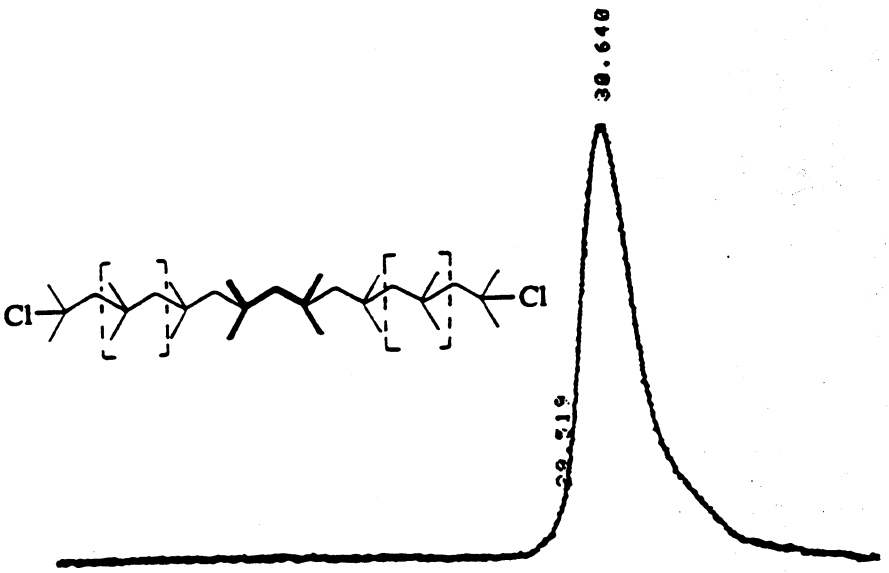

Figure II-47. GPC trace of α,ω-di(*tert*-chloro)polyisobutylene formed in the 2,4-dimethyl-2,4-pentanediol/IB/BCl3/DMA/CH_2Cl_2 system at -40°C.

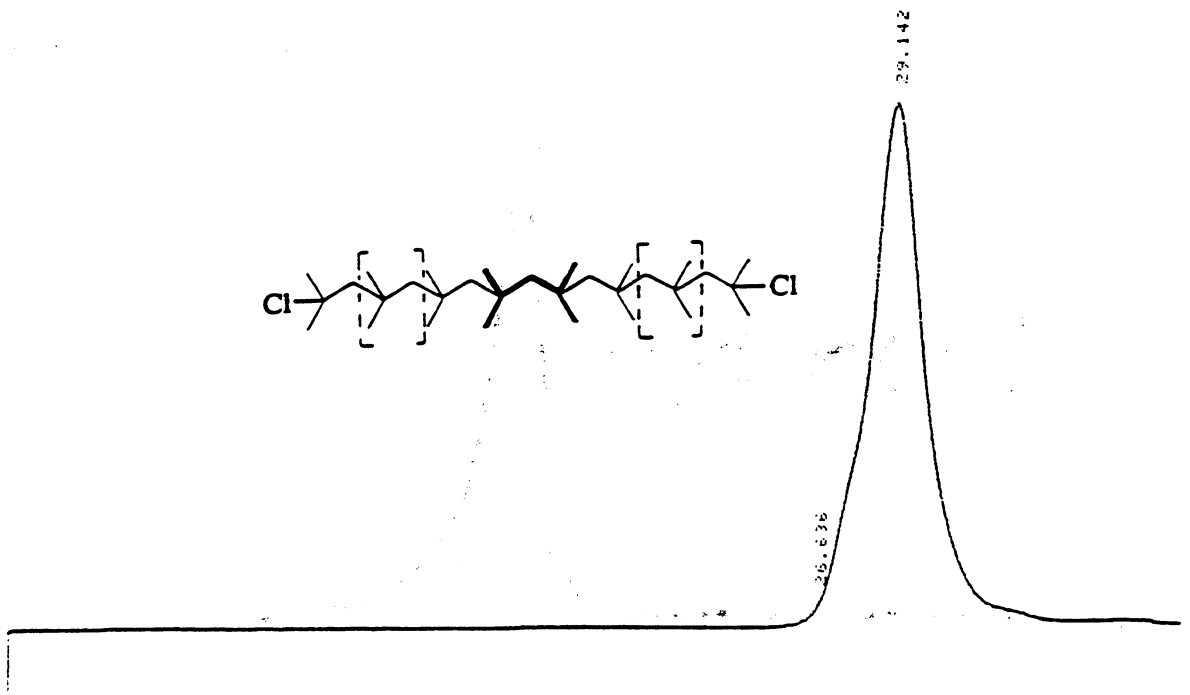

Figure II-48. GPC trace of α,ω-di(*tert*-chloro)polyisobutylene formed in the 2,4-dimethyl-2,4-pentanediol/IB/$TiCl_4$/DMA/CH_2Cl_2 system at -40°C.

The number average molecular weights (M_n) of the polymers were also determined—as and when required—by an indirect measurement of vapor-pressure lowering in toluene by VPO using a Wescan Instruments Vapor-Phase Osmometer (Model 232A) calibrated with sucrose octa-acetate. Measurement is made of the small temperature difference resulting from different rates of solvent evaporation from, and condensation onto, droplets of pure solvent and of polymer solutions that are maintained at a constant temperature in an atmosphere of solvent vapor. The basis of the method is that this temperature difference is proportional to the vapor-pressure lowering of the polymer solution at equilibrium and, thus, to the number average molecular weight.

The infrared spectra were recorded on a Perkin Elmer Fourier Transform Infrared Spectrometer (Model 1710) using the dried samples. Figure II-49 shows a representative FTIR spectrum of the living telechelic α-ethyl-ω-(*tert*-chloro)polyisobutylene. These polymers showed a weak absorption at 744 cm^{-1} corresponding to the chloro groups, while another very weak absorption at 1264 cm^{-1} (which is characteristic of chloro groups) could have submerged with the broad methylene bending absorption ranging between 1175-1280 cm^{-1}. All of these polymers showed two common characteristic strong absorptions corresponding to the bending absorptions of the tertiary methyl groups at 1390 cm^{-1} and 1367 cm^{-1}, followed by another doublet absorption at 951 cm^{-1} and 924 cm^{-1}. This is characteristic of both methyl and methylene groups in polyisobutylene in addition to the strong asymmetric and symmetric stretching vibrations. A typical FTIR spectrum of α-methyl-ω-(*tert*-chloro)polyisobutylene (synthesized with *tert*-butanol/BCl_3/DMA initiating system) as shown in Fig. II-50 also displayed similar absorption peaks characteristic of these telechelic polymers. Figure II-51 shows the representative FTIR spectrum of α,ω-di(*tert*-chloro)polyisobutylene, prepared with 2,4-dimethyl-2,4-pentanediol/BCl_3/DMA initiating system. The FTIR results of this polymer are similar to those observed for α-ethyl-ω-(*tert*-chloro)polyisobutylene and confirm the presence of chloro, methylenes, and methyl groups of polyisobutylene.

Figures II-52 and II-53 are the FTIR spectra of the linear, living, two-arm telechelic α,ω-di(*tert*-chloro)polyisobutylenes, obtained with the use of a 1,4-dicumyl alcohol/BCl_3/DMA initiating system. In contrast to the telechelic polyisobutylenes obtained with aliphatic initiators, noticeable aromatic ring absorptions derived from the initiator can be seen at 1660 cm^{-1} and 1030 cm^{-1}, in addition to a strong aromatic absorption at 831 cm^{-1}. The appearance and intensity of the absorption at 1660 cm^{-1}, which corresponds to aromatic ring C-C stretching vibration, depend on the concentration of the ring moiety derived from the initiator by comparing the spectra of α,ω-di(*tert*-chloro)polyisobutylenes labelled #1 and #2 as shown in Figs. II-52 and II-53, respectively. It can be deduced from the intensity of the aromatic absorptions that polymer #1 is of relatively lower molecular weight than the polymer #2. These two spectra showed two common, characteristic, strong bending doublet absorptions corresponding to methyl and methylene groups like those in other polyisobutylenes, in addition to the weak absorptions corresponding to the chloro groups at 744 cm^{-1} and 585 cm^{-1}.

vii. Dehydrochlorination

The second step in the synthesis of telechelic ionomers is a simple chemical modification referred to as dehydrochlorination of the chlorinated prepolymers, end-capped with tertiary chloro groups. These chlorinated polymers can be effectively dehydrochlorinated with a strong base such as potassium *tert*-butoxide. A brief description of the procedure is described in the following paragraph.

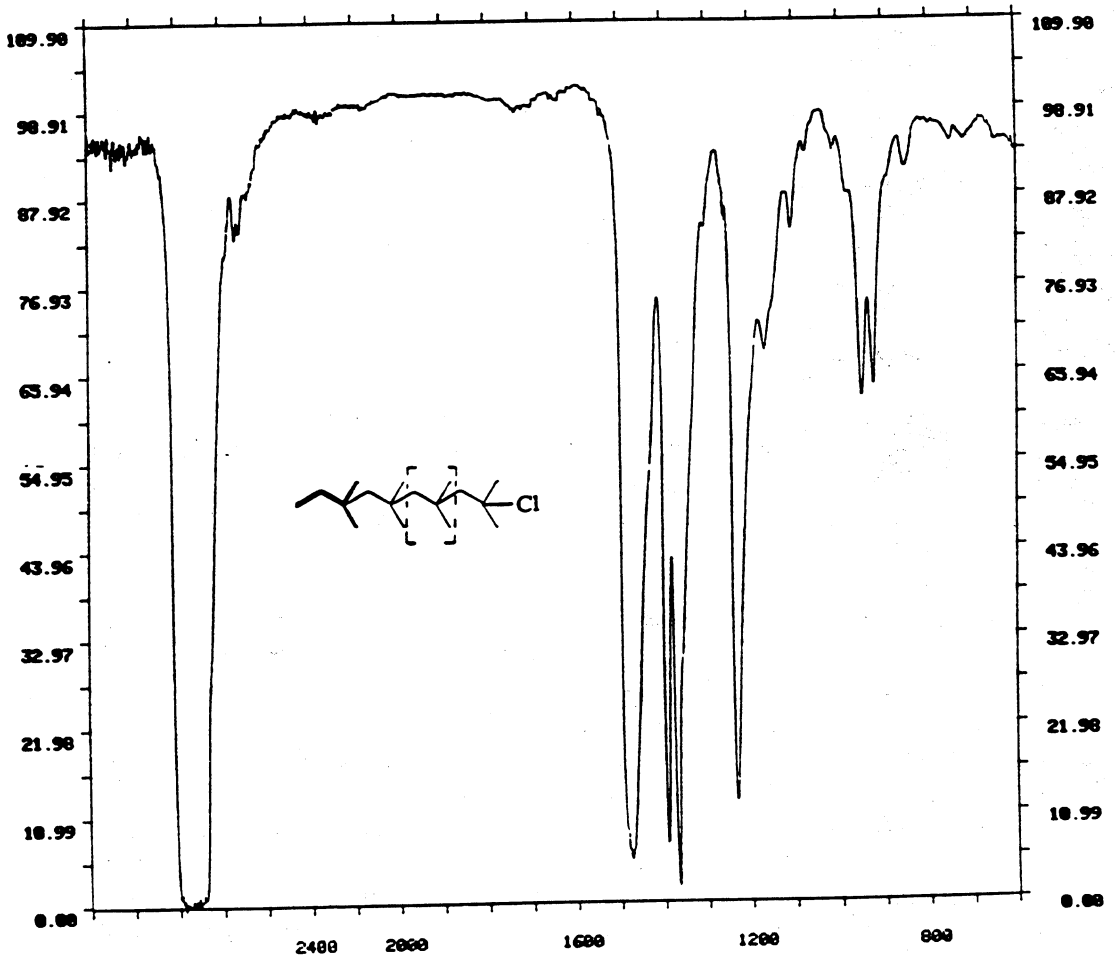

Figure II-49. FTIR spectrum of α-ethyl-ω-(*tert*-chloro)polyisobutylene.

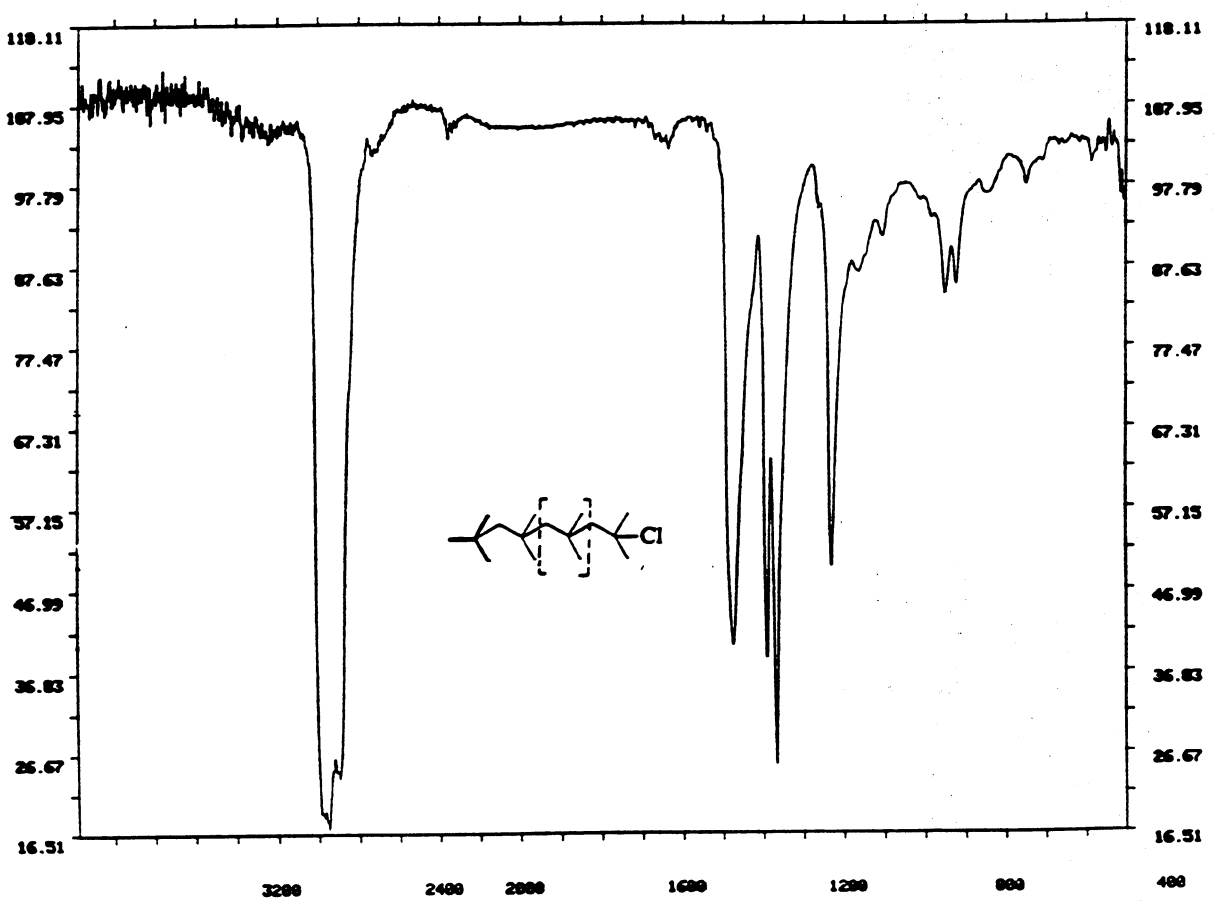

Figure II-50. FTIR spectrum of α-methyl-ω-(*tert*-chloro)polyisobutylene.

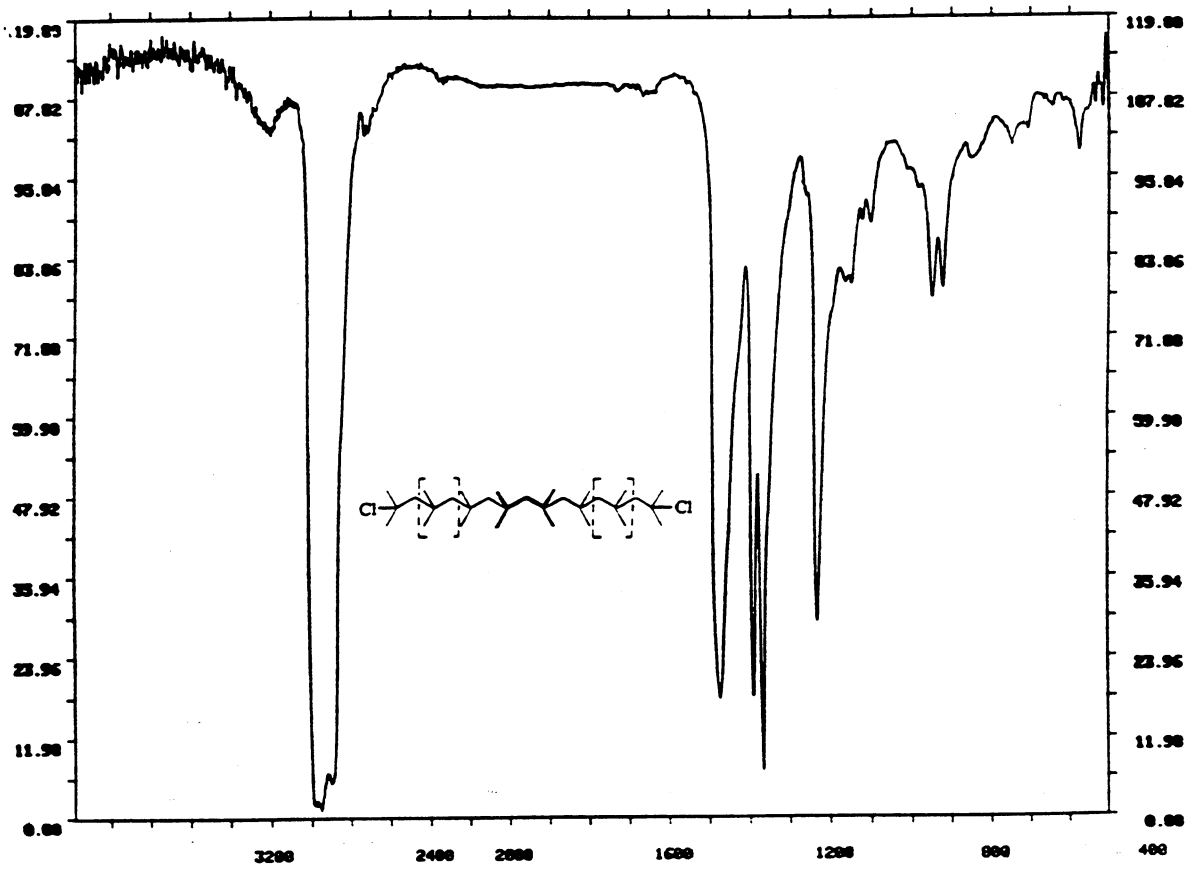

Figure II-51. FTIR spectrum of α,ω-di(*tert*-chloro)polyisobutylene formed in the 2,4-dimethyl-2,4-pentanediol/IB/BCl_3/DMA/CH_2Cl_2 system at -40°C.

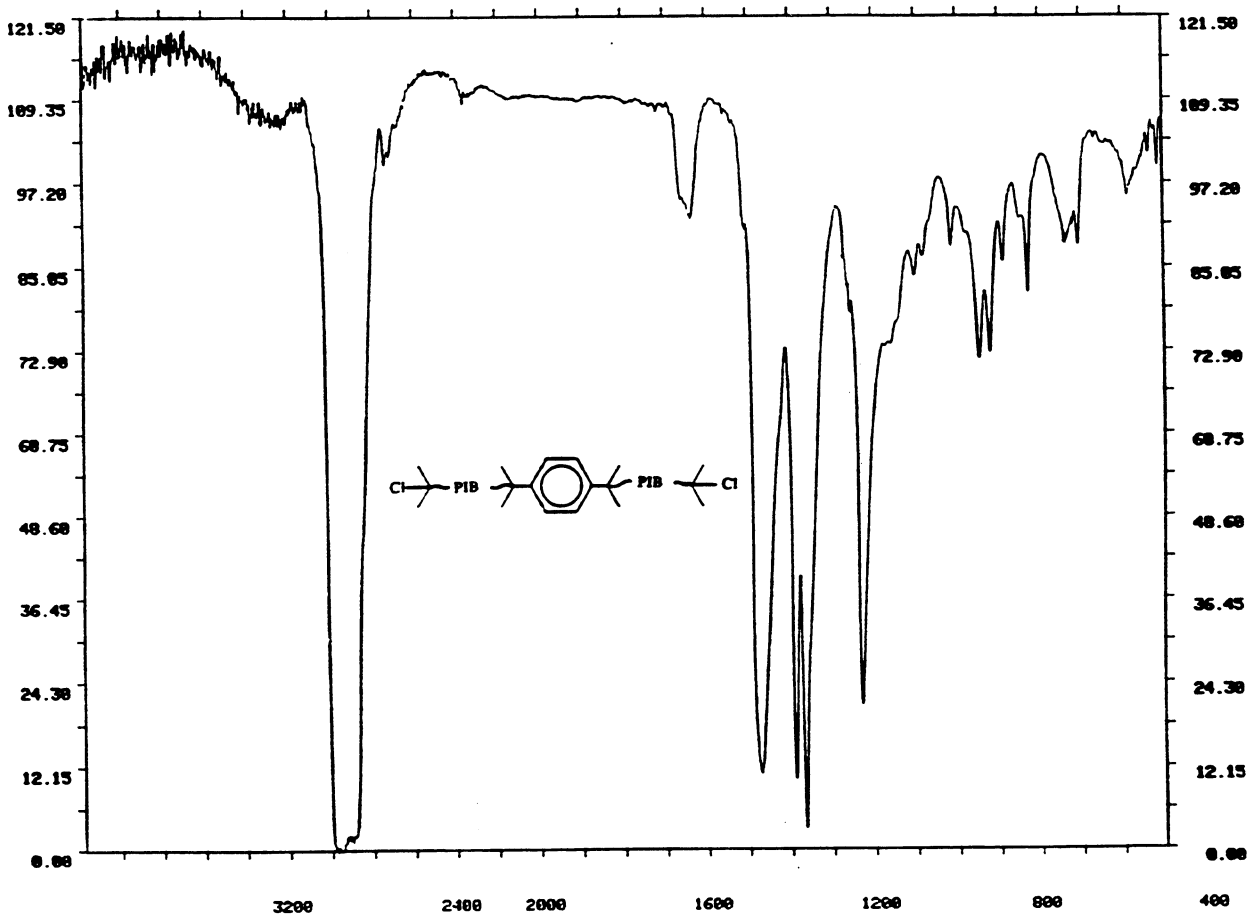

Figure II-52. FTIR spectrum of α,ω-di(*tert*-chloro)polyisobutylene (polymer #1) formed in the 1,4-dicumyl alcohol/IB/BCl3/DMA/CH_2Cl_2 system at -60°C.

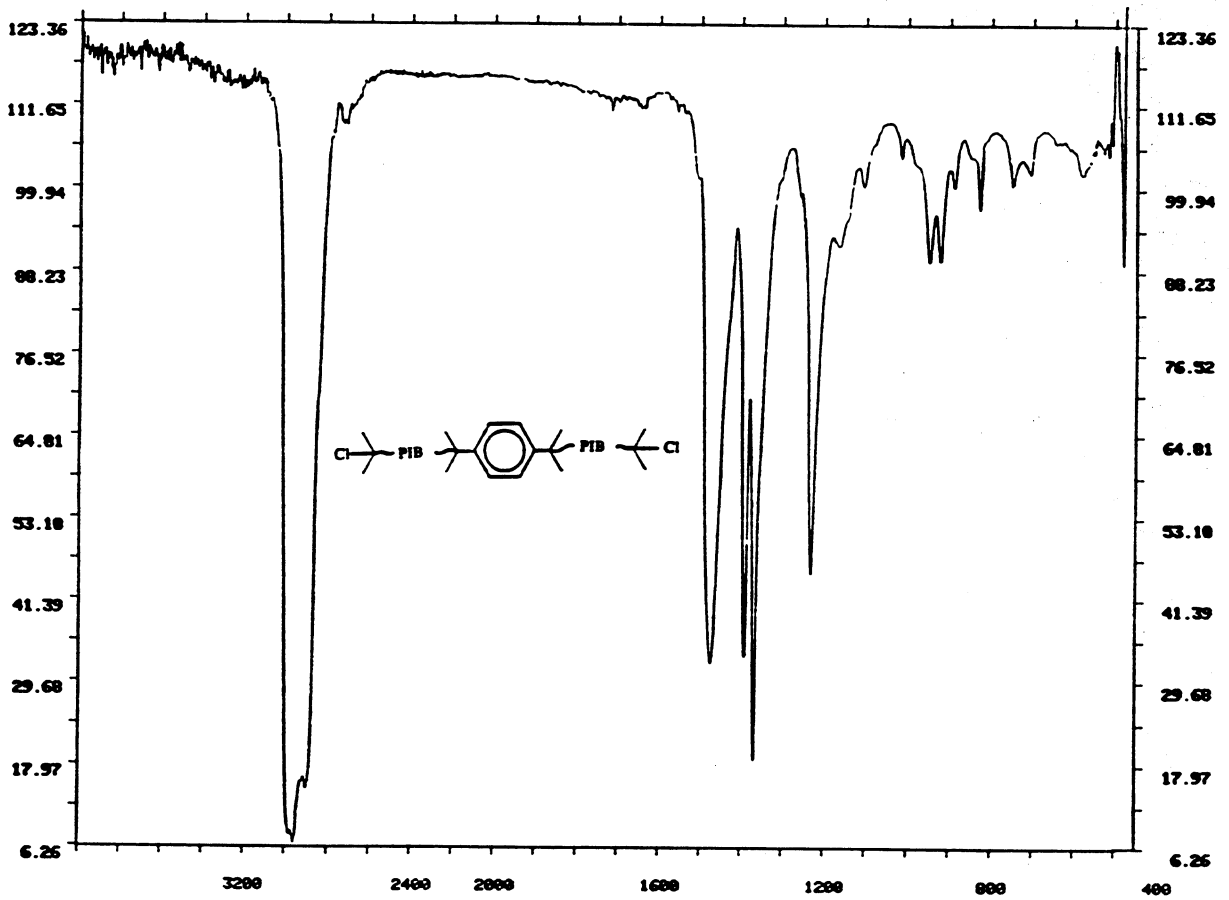

Figure II-53. FTIR spectrum of α,ω-di(*tert*-chloro)polyisobutylene (polymer #2) formed in the 1,4-dicumyl alcohol/IB/BCl3/DMA/CH_2Cl_2 system at -60°C.

In a typical procedure of dehydrochlorination, a prepolymer, (α,ω-di(*tert*-chloro)polyisobutylene obtained with 1,4-dicumyl alcohol/BCl_3/DMA system), was first dissolved in dry THF. This polymer solution was slowly added to a solution of potassium *tert*-butoxide in THF at about 40°C. After refluxing for about 20 hrs, the reaction was stopped with the addition of water and the dehydrochlorinated polymer was extracted with hexane. The hexane extract was washed free of the base with water. Evaporation of the solvent in this case left α,ω-di(isopropenyl)polyisobutylene. Dehydrochlorination of other prepolymers, synthesized with various initiating systems, was performed in a similar manner.

The generation of double bonds by dehydrochlorination was primarily confirmed by the characterization of dehydrochlorinated polymers by FTIR analysis. The presence of double bonds was confirmed by the appearance of several characteristic olefinic absorptions. A typical IR spectrum of α,ω-di(isopropenyl)polyisobutylene, obtained with the 1,4-dicumyl alcohol binifer system, is shown in Fig. II-54. The loss of absorptions corresponding to chloro groups and the simultaneous appearance of olefinic absorptions, comprising weak asymmetric and medium symmetric stretching vibrations at 3078 cm^{-1} and 1641 cm^{-1}, respectively, and a strong doublet at 1049 cm^{-1} and 1011 cm^{-1} together with a medium out-of-plane stretching vibration at 851 cm^{-1}, confirm the presence of substituted terminal double bonds in the dehydrochlorinated polymer. Other absorptions are similar to those seen in the prepolymer.

Also shown in Fig. II-55 is the corresponding α,ω-di(isopropenyl)polyisobutylene, obtained by the dehydrochlorination of the prepolymer prepared with 2,4-dimethyl-2,4-pentanediol/BCl_3/DMA system. Figure II-56 is the representative FTIR spectrum of the dehydrochlorinated polymer, α-ethyl-ω-di(isopropenyl)polyisobutylene(obtained with 2-chloro-2-methylbutane). All dehydrochlorinated polymers showed similar characteristic olefinic absorptions as described above.

viii. Sulfonation of Dehydrochlorinated Polyisobutylenes

Sulfonation of the terminal double bonds, generated by dehydrochlorination of the prepolymer, is performed by a heterogeneous sulfonation. Sulfonation of macro olefins by acetyl sulfate is a simple and convenient method of polymer modification. Acetyl sulfate is a mild sulfonating reagent and has advantages over sulfur trioxide. The use of acetyl sulfate not only precludes the handling of gaseous sulfur trioxide, but it also makes the reaction feasible at room temperature. In the present study, we have adopted the procedure developed by Makowski *et al.*[28] for sulfonation of macro olefins using acetyl sulfate at room temperature.

A representative sulfonation procedure involved premixing of acetic anhydride and sulfuric acid in an equimolar ratio at room temperature, and in a quantity based on the amount of unsaturation in the dehydrochlorinated polymer to be used. The sulfonating reagent(CH_3-CO-SO_3H) was prepared by slowly adding sulfuric acid to a cooled acetic anhydride solution, stirring constantly. After stirring for about five minutes, the dehydrochlorinated polymer, dissolved in hexanes (olefin-free), was slowly added to the sulfonating reagent at room temperature under a nitrogen atmosphere. After stirring vigorously (heterogeneous) for about two hours, the reaction was stopped and the layers were allowed to separate. The use of two liquid phases (heterogeneous sulfonation) in this process makes it possible to remove most of the unbound acid impurities from the polymer. Our attempts to purify the sulfonated polymer by washing the hexane solution with water failed because the uptake of water was so great that the polymer started precipitating from solution. The presence of sulfonic acid end groups rendered the polymer very hydrophilic. In an alternative procedure, hexanes were distilled off with rotavap and the sulfonated polymer was slowly added to a rapidly stirred distilled water at ~ 30°C to remove the acid impurities

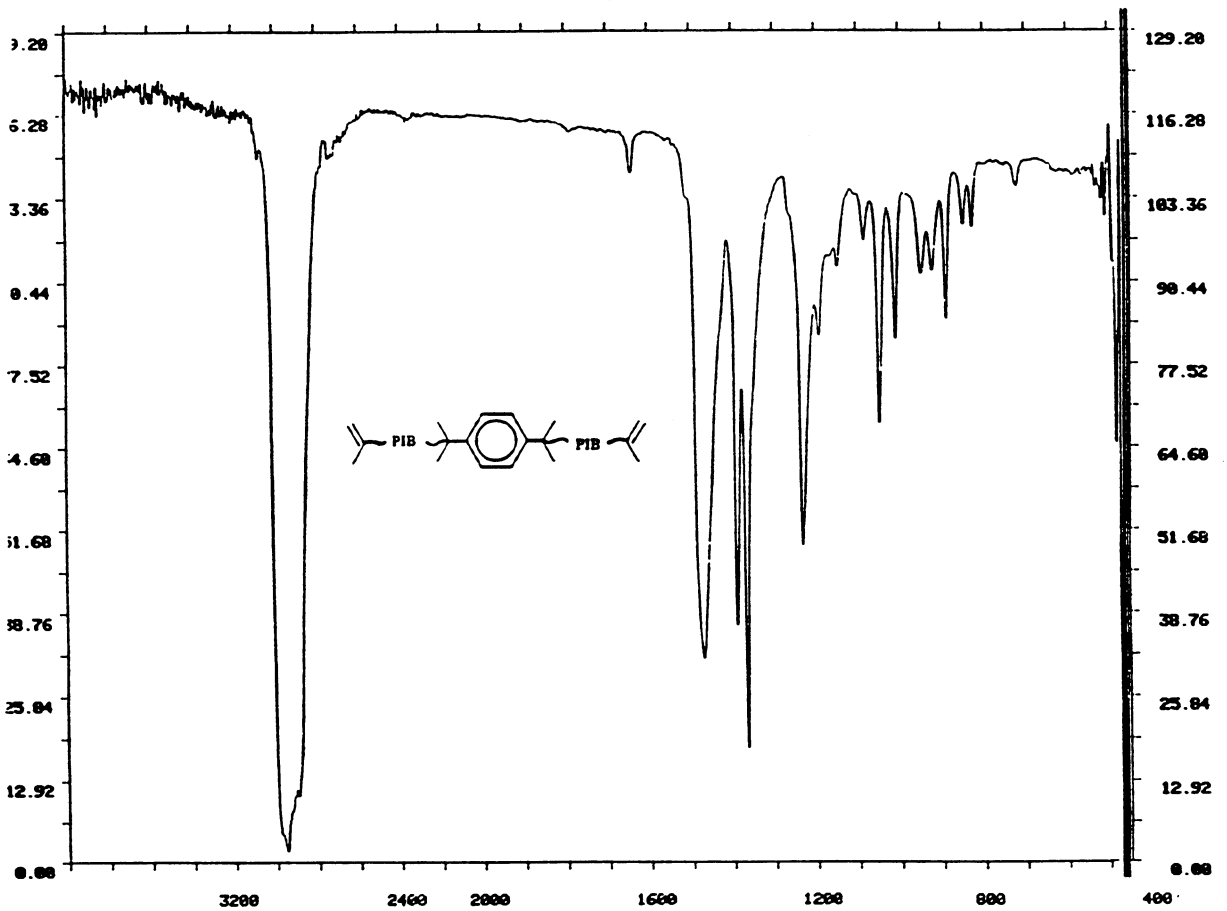

Figure II-54. FTIR spectrum of α,ω-di(isopropenyl)polyisobutylene.

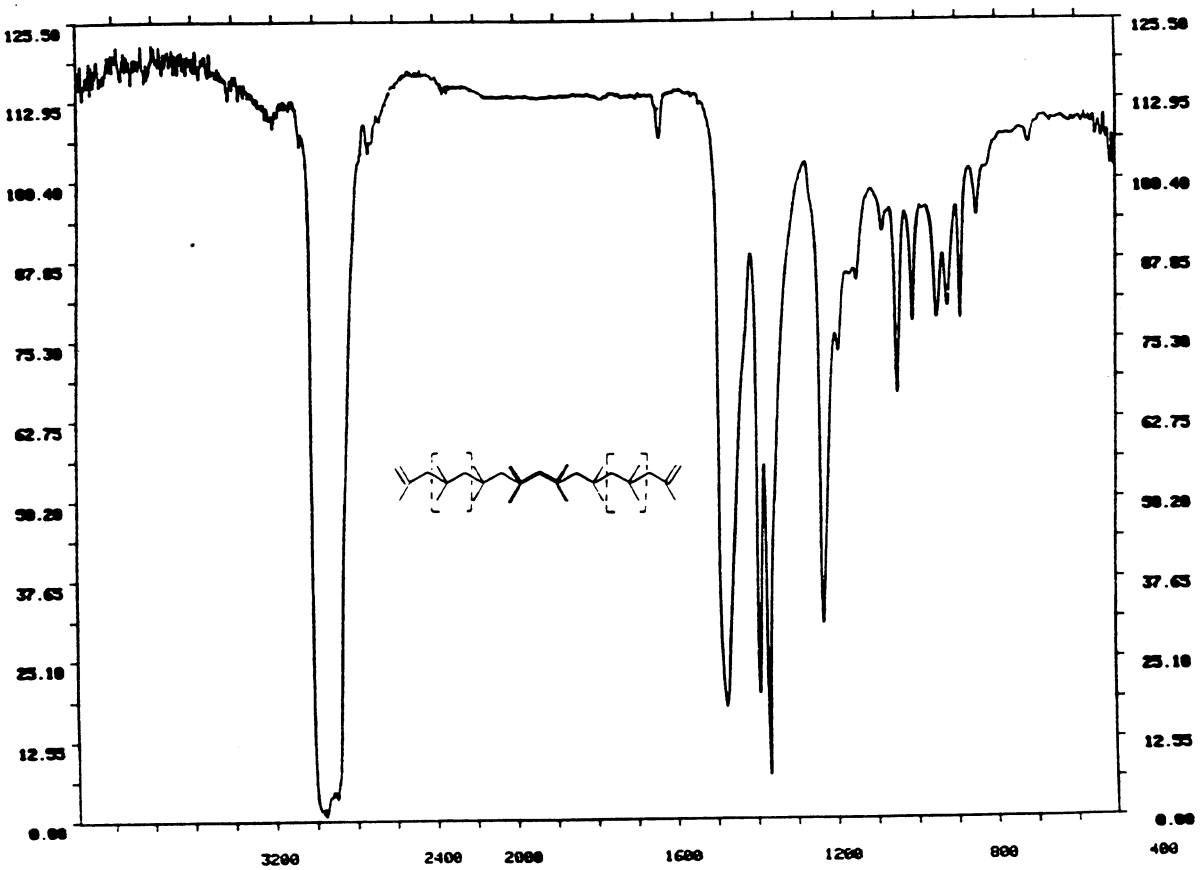

Figure II-55. FTIR spectrum of α,ω-di(isopropenyl)polyisobutylene (obtained by the dehydrochlorination of the prepolymer formed in the 2,4-dimethyl-2,4-pentanediol/IB/BCl_3/DMA/CH_2Cl_2 system).

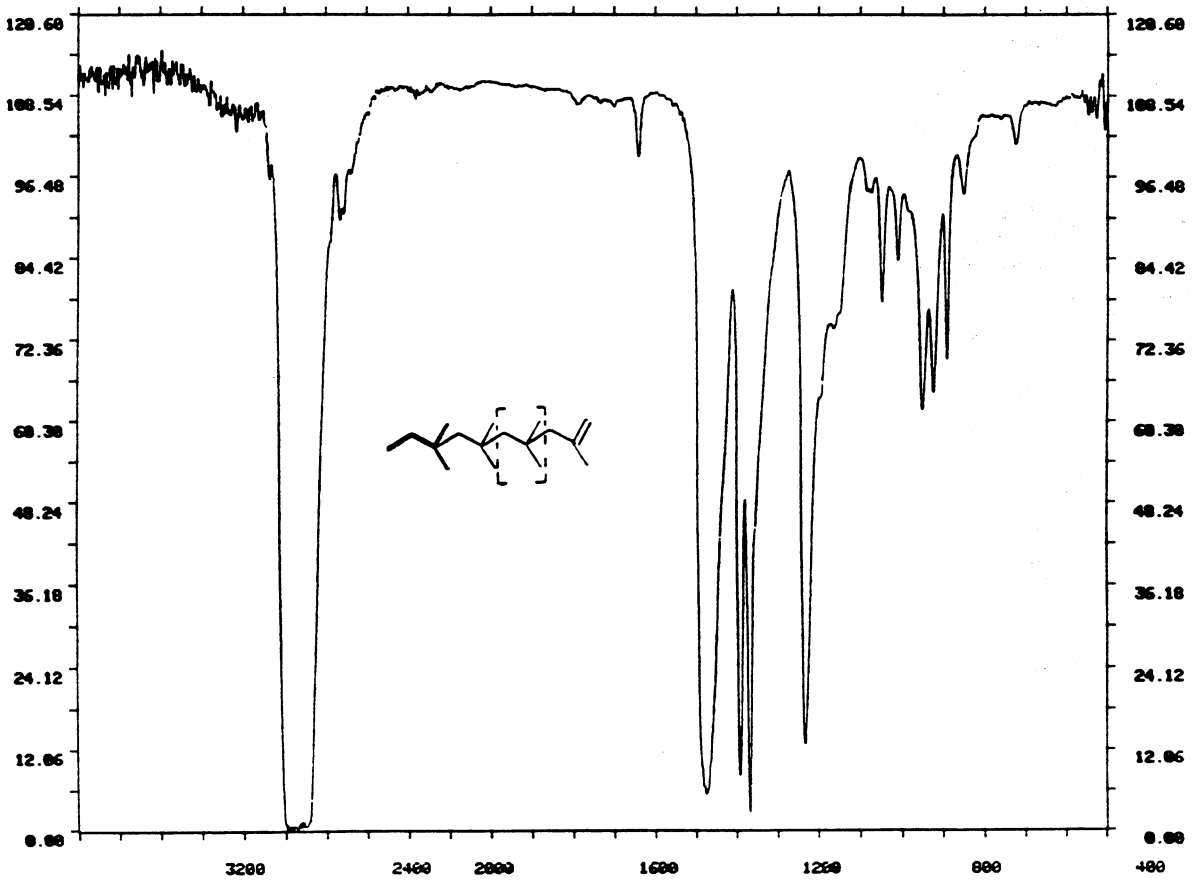

Figure II-56. FTIR spectrum of α-ethyl-ω-(isoprepenyl)polyisobutylene.

and the sulfonating reagent, if any. The resulting precipitate was then washed repeatedly with distilled water. The moist crumb was kneaded in acetone or methanol to remove water. It was then dried *in vacuo* at room temperature overnight.

Structural analysis of the sulfonated telechelic polymer was essentially done by FTIR spectroscopy using the steam-stripped and dried samples. Noteworthy in the IR spectrum of sulfonated polymer (as shown in Fig. II-57), is the appearance of new absorptions arising from the asymmetric and symmetric stretching vibrations of the sulfonic acid groups. The absorptions at 1176 cm^{-1} are characteristic of the symmetric stretch of two S=O bonds, while the strong absorption at 1040 cm^{-1} is due to the symmetric stretching vibration of the S-(OH) bond. The broad absorption ranging from 1230-1330 cm^{-1} includes the asymmetric stretching of the two $(S=O)_2$ bonds of the $-SO_3H$ groups. The hydroxyl group of the sulfonic acid appeared in the range of 3100-3400 cm^{-1}.

Sulfonated telechelic polyisobutylenes are soluble in both aliphatic and a variety of aromatic solvents. THF is a good solvent for the sulfonated telechelic polyisobutylenes. These polymers display considerable end group association—which is obvious from its bulk viscosity—as a result of hydrogen bonding, but it is not associated to the same extent as the ionomer to be produced from it.

ix. Neutralization of Sulfonated Telechelic Polyisobutylenes by Acid-Base Titration

Neutralization of the sulfonated telechelic polyisobutylenes was performed similarly to that reported by Makowski *et al.* for the sulfonated EPDM polymers.[28] Both monovalent and bivalent cations have been considered for neutralization in order to observe the effect of cation types on the associative nature of the resulting ionomers. The procedure for neutralization with metal acetate is similar to that with metal hydroxide.

A representative neutralization procedure is as follows. Dried sulfonated polyisobutylene was dissolved (2.0 wt%) in THF and titrated with an ethanolic KOH solution (0.5N) to a faint pink or light blue, using ethanolic alizarin and thymolphthalein indicator solution. The solution was stirred for a few minutes and the solvents were removed under reduced pressure. The resulting ionomer was steam stripped by pouring it into boiling distilled water to remove the excess neutralizing reagent, if any. The polymer crumbs were filtered, kneaded in acetone, and dried in a vacuum oven at 70°C for one day.

The characterization of ionomers was primarily done by FTIR. This analysis of ionomers showed a symmetric stretching vibration of the SO_3^{-1} anion at 1047 cm^{-1} together with the asymmetric stretch of SO_3^{-1}, which appeared as a broad absorption at 1226 cm^{-1}. Figure II-58 shows the typical FTIR spectrum of the potassium ionomer. The loss of a hydroxyl peak also confirms the neutralization of sulfonic acid groups.

x. Solution Viscosity Behavior of Mono Telechelic Prepolymers

Relative viscosity (defined as $\eta_{rel}=\eta/\eta_0$, where η is the viscosity of the polymer solution, and η_0 is the viscosity of the pure solvent) measurements of hexane solutions vs. concentration profiles of α-methyl-ω-(*tert*-chloro)polyisobutylene, α-ethyl-ω-(*tert*-chloro)polyisobutylene, and α-methyl cyclohexyl-ω-(*tert*-chloro)polyisobutylene are shown in Fig. II-59. Among these polymers, maximum viscosity was obtained with α-methyl cyclohexyl-ω-(*tert*-chloro)polyisobutylene. The

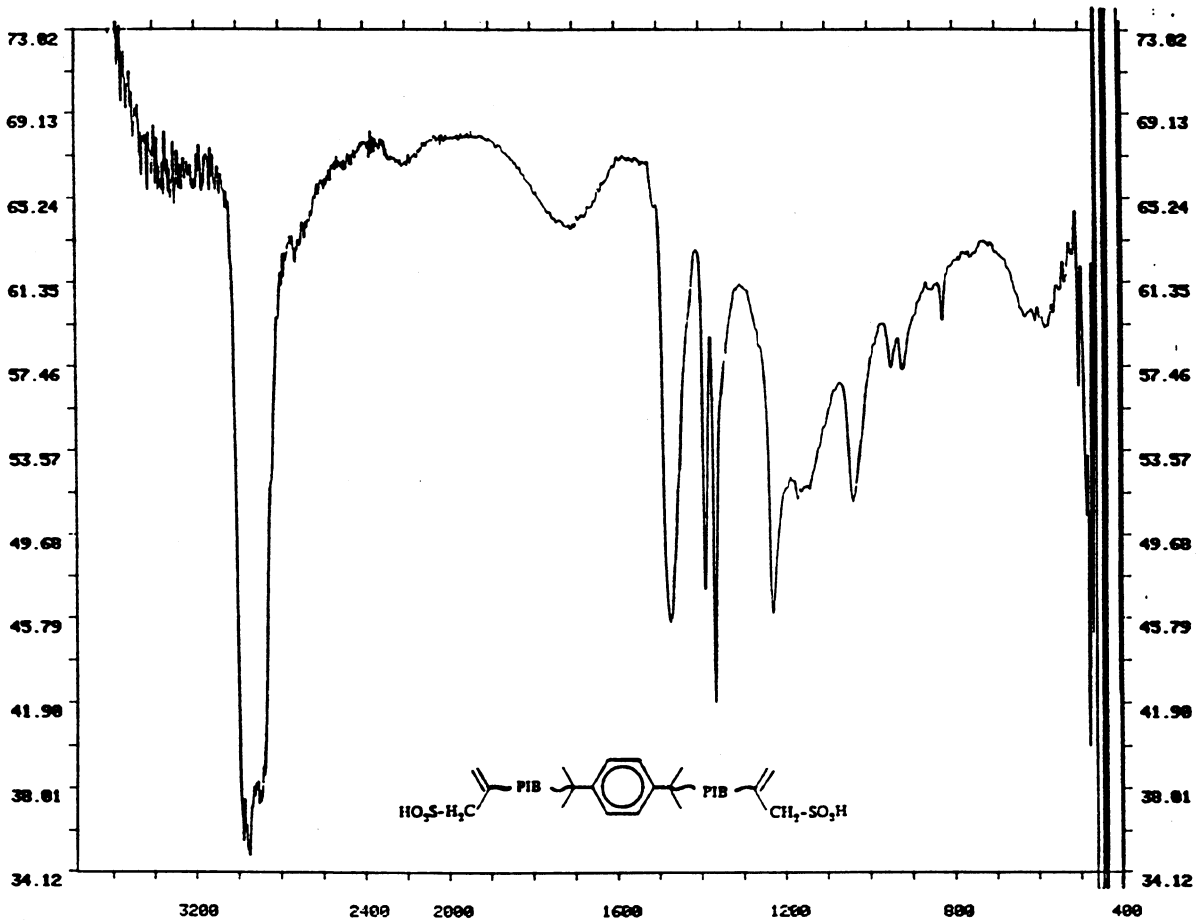

Figure II-57. FTIR spectrum of sulfonated telechelic polyisobutylene (obtained by the sulfonation of α,ω-di(isopropenyl)polyisobutylene).

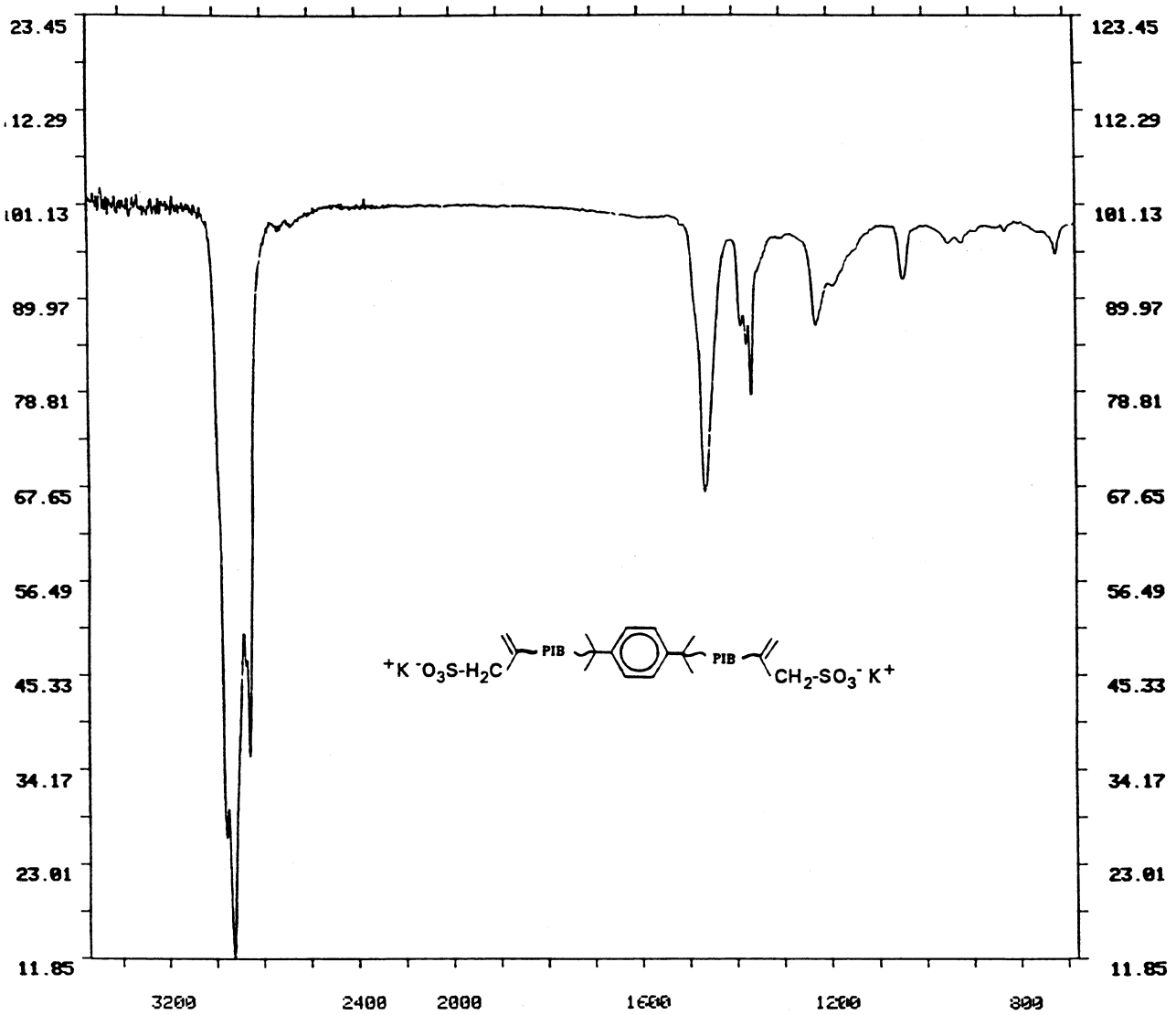

Figure II-58. FTIR spectrum of sulfonated telechelic potassium ionomer.

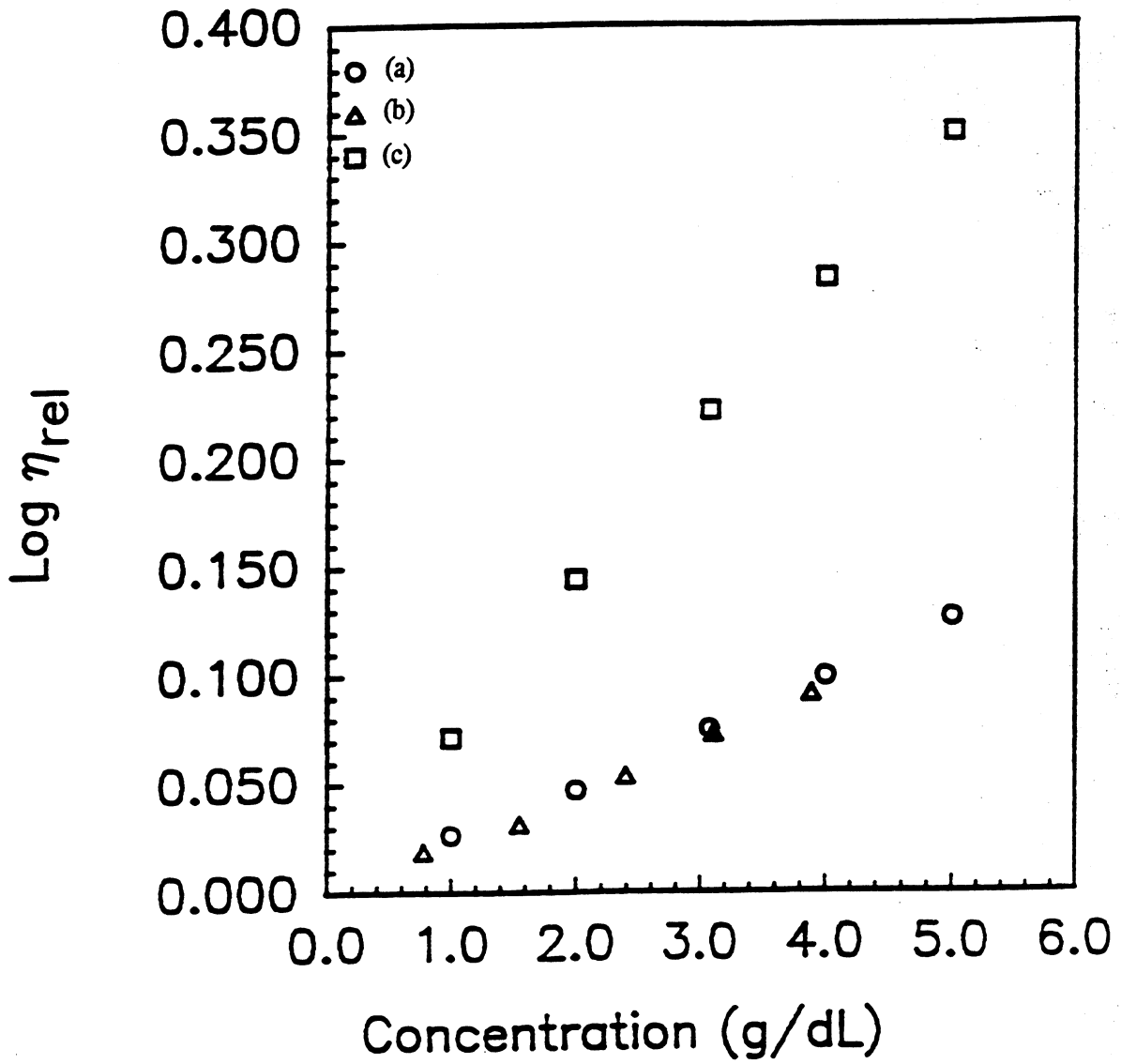

Figure II-59. Relative viscosity vs. concentration profiles of (a) α-methyl-ω-(*tert*-chloro) polyisobutylene, (b) α-ethyl-ω-(*tert*-chloro)polyisobutylene, and (c) α-methyl cyclohexyl-ω-(*tert*-chloro)polyisobutylene in *n*-hexane at 25°C.

viscosities of solutions of both α-ethyl-ω-(*tert*-chloro)polyisobutylene and that of α-methyl-ω-(*tert*-chloro)polyisobutylene are able to increase the solution viscosity by only about 35%. Although these three polymers differ in the extent of viscosification, their viscosity behavior (linear increase) is the same in all the cases. It also reflects the fact that these polymers could be further derivatized into ionomers, which could exhibit higher viscosification.

Figure II-60 shows the comparative profiles of relative viscosity measurements for solutions of the α,ω-di(isopropenyl)polyisobutylene and of the sulfonated telechelic polyisobutylene, derivatized from the α,ω-di(*tert*-chloro)polyisobutylene prepolymer that was formed in the 1,4-dicumyl alcohol/IB/ BCl_3/ DMA initiating system. A *nonlinear* increase in relative viscosity with the increasing concentration of the sulfonated polymer, compared to the *linear* increase in the case of the dehydrochlorinated polymer, demonstrates the extent to which these sulfonated polymers do indeed associate. This increase in relative viscosity is attributed to the hydrogen bonding in the case of sulfonated polymer.

In addition to these three polymers, we also performed the viscosity measurements of α,ω-di(*tert*-chloro)polyisobutylene, α,ω-di(isopropenyl)polyisobutylene (synthesized with an aliphatic binifer system), sulfonated telechlelic polymer, and the corresponding potassium ionomer. The viscosity measurements of hexane solutions of these polymers are shown in Fig. II-61. We observed a nonlinear increase in viscosity with the zinc ionomer and a linear increase with the prepolymer.

Figure II-62 represents the relative viscosity vs. concentration profiles of α,ω-di(isopropenyl)polyisobutylene (synthesized with the aromatic binifer system), the sulfonated telechelic polymer, and of the potassium ionomer. The viscosity measurements of the above polymers were measured in hexane to determine the effects of sulfonation and neutralization on the prepolymer. While the dehydrochlorinated polymer showed a linear increase in relative viscosity with an increase in concentration of the polymer, both the sulfonated and the potassium ionomer derivatized from the corresponding dehydrochlorinated polymer by sulfonation and neutralization, respectively, showed a nonlinear increase in relative viscosity with an increase in concentration of the polymer. Nevertheless, the extent of increase in the observed trend of relative viscosity behavior is greater in the case of the ionomer due to the ionic associations than in the corresponding sulfonated polyisobutylene as a result of hydrogen bonding. This observation indicates that the ionomer associates to a greater extent, depending on the nature of the neutralizing cation, than either the corresponding sulfonated polymer or the dehydrochlorinated polymer. In the present instance, as it is a monovalent potassium cation, it can only associate with one sulfonate group. However, these associations may be increased more by neutralizing with multivalent cations. Based on this analogy, one can expect higher relative viscosity values with multivalent neutralizing cations such as zinc, magnesium, barium, calcium, aluminium, etc., which are being considered for increasing the viscosity. These observations indicate the possibility of their use as viscosity building agents for nonpolar solvents.

6. High-pressure Solubility Measuring Apparatus

We have made significant progress with the use of cosolvents, in addition to the syntheses of living telechelic polymers. The concept of adding cosolvents or entrainers has recently received considerable attention.[44,45] The use of a cosolvent for the solubility enhancement of polymers in dense CO_2 has now been established to a considerable degree,[18] and such use in dense CO_2, in order to increase the viscosity of the solvent, has also become an increasing and promising contributor to enhanced oil recovery (EOR).

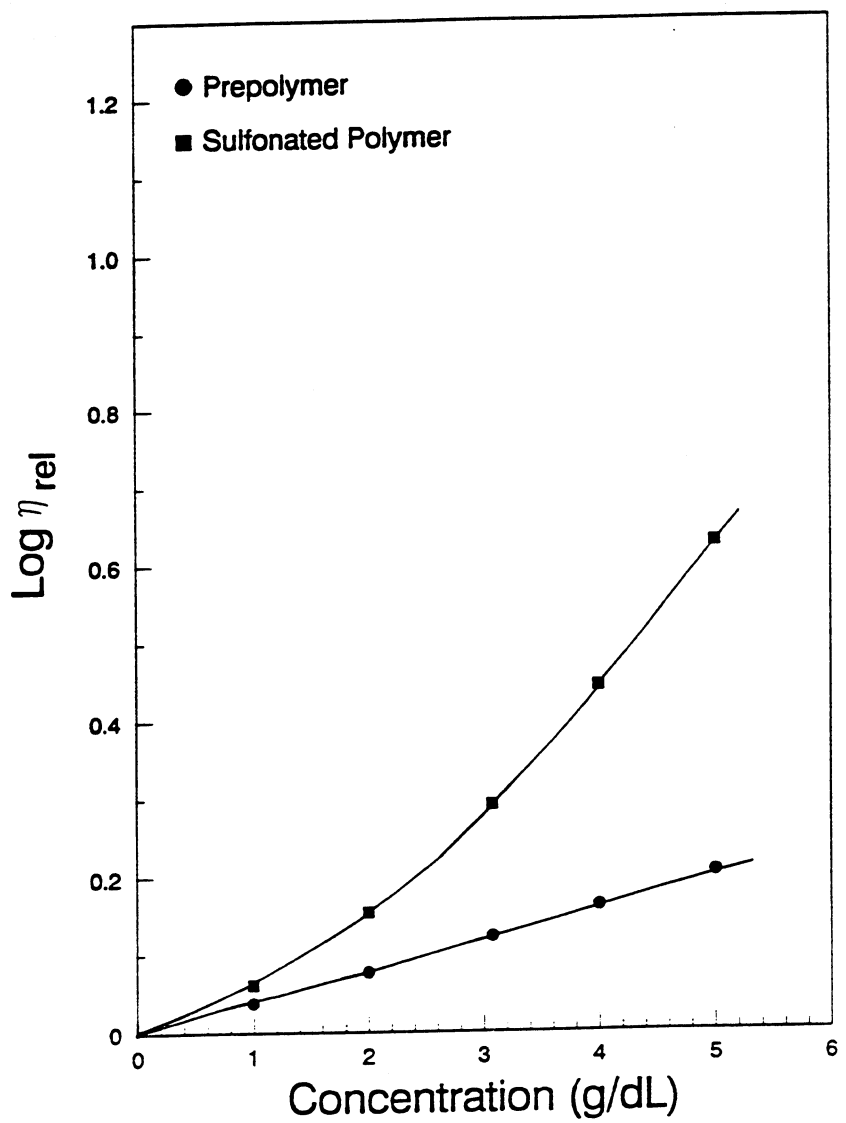

Figure II-60. Effect of sulfonation upon relative viscosity for α,ω-di(isopropenyl)polyisobutylene (formed in the 1,4-dicumyl alcohol binifer system) in *n*-hexane at 25°C.

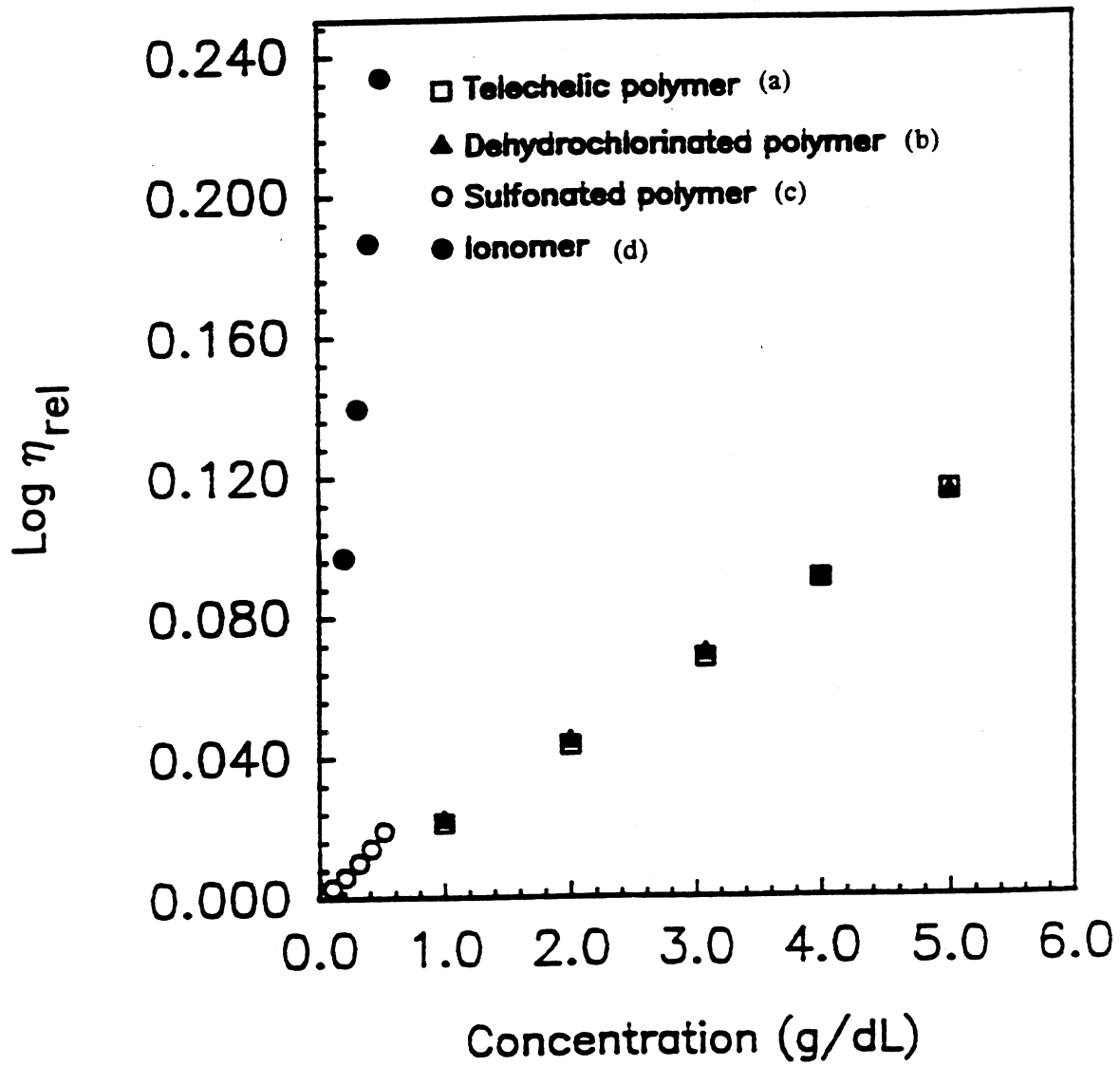

Figure II-61. Relative viscosity vs. concentration profiles of (a) α,ω-di(*tert*-chloro)polyisobutylene (formed in the 2,4-dimethyl-2,4-pentanediol binifer system), (b) α,ω-di (isopropenyl)polyisobutylene, (c) sulfonated α,ω-di(isopropenyl)polyisobutylene, and (d) zinc ionomer of sulfonated telechelic polyisobutylene in *n*-hexane at 25°C.

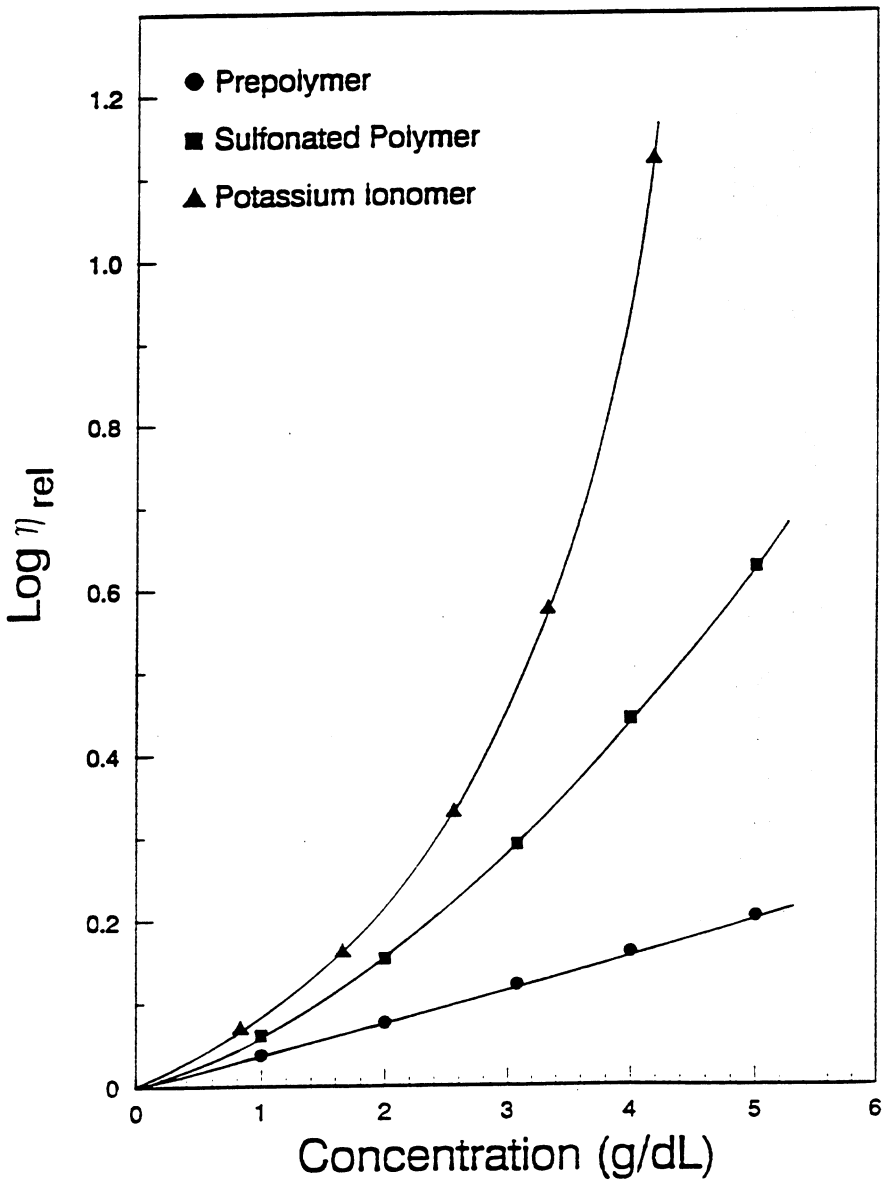

Figure II-62. Effect of sulfonation and KOH neutralization upon relative viscosity for (a) α,ω-di(*tert*-chloro)polyisobutylene (formed in the 1,4-dicumyl alcohol, *binifer*, system), (b) α,ω-di(isopropenyl)polyisobutylene, (c) sulfonated α,ω-di(isopropenyl)polyisobutylene, and (d) potassium ionomer of sulfonated telechelic polyisobutylene in *n*-hexane at 25°C.

The choice of a cosolvent is based on the polymer-solvent interaction parameter (χ), which serves as a good indication of solubility.[26] Values of χ, 0.5, or less indicate good solubility for a polymer-solvent system. Amorphous polyisobutylenes are readily soluble in a variety of nonpolar solvents. For instance, the value of χ for cyclohexane and n-pentane are close to 0.5. Hence, these solvents can act as good cosolvents for polyisobutylenes.

Recently, we have taken advantage of the solubility apparatus for the use of cosolvents as shown in Fig. II-63. The descriptions of the solubility apparatus and the method of determination of solubility have been adequately described in the previous Annual Reports.[13,17,29]

We have quantitatively measured the solubility enhancement using hydrocarbon solvents such as hexane, isooctane, cyclohexane, and toluene as cosolvents to increase the solubility of some of the telechelic polymers that have been synthesized in our laboratory. Solubility enhancement measurements of a slightly soluble (higher M_n) α-ethyl-ω-(*tert*-chloro)polyisobutylene were determined using these hydrocarbon cosolvents at 25°C and 2500 psig, and the results are listed in Table II-7. From these results, hexane seems to the best cosolvent for isobutylene based polymers.

Listed in Table II-8 are the solubility measurements in dense CO_2 of a series of α-ethyl-ω-(*tert*-chloro)polyisobutylenes, prepared by the IMA technique using the *tert*-amyl alcohol/BCl_3/1-methyl-2-pyrrolidinone initiating system. These results are in agreement with the observation that solubility of a given polymer decreases while increasing its molecular weight.

7. The High-pressure Capillary Tube Viscometer

The high-pressure capillary tube viscometer has undergone additional modifications[17] to allow a quicker screening of the polymers being tested and to reduce the mixing problems associated with the previous design.

Figure II-64 represents a newly-modified version of the high pressure capillary tube viscometer. The recent change enables both the dissolution of the polymer in dense CO_2 at the test run temperature, and the use of two alternative flow paths for pure CO_2 and polymer-saturated CO_2. The alternate flow paths can be accessed by the operation of Whitey three-way ball valves. The first of these valves is located on the outlet port of the ISCO pump containing the dense CO_2. This three-way valve can divert the flow into either of two 3" long, 3/8" OD stainless steel tubes filled with cotton and with screens. One of the tubes will be used for pure dense CO_2 to make the base-line adjustment. The other tube will contain a small amount (~0.1-0.5 g) of the polymer to be tested. After flowing through one of these cotton-containing tubes, the second three-way valve enables the dense CO_2 to be directed to the capillary tube. The pressure drop across this tube is monitored with a sensitive pressure transducer that has been placed at the combined outlets of the sample holder and the other tube. An evacuation outlet is also provided at the entry of the capillary tube. The viscosity of a saturated polymer solution can be measured by allowing the CO_2 flow path to pass through the polymer-containing sample holder. The viscosities of pure CO_2 and polymer in CO_2 can be compared, and the viscosity of the polymer solution determined by use of the tabulated values of dense CO_2 properties.

Although the ease of testing different concentrations of a polymer is lost, the new flow path will enable us to perform the viscosity measurements more quickly. This alternate flow path also eliminates

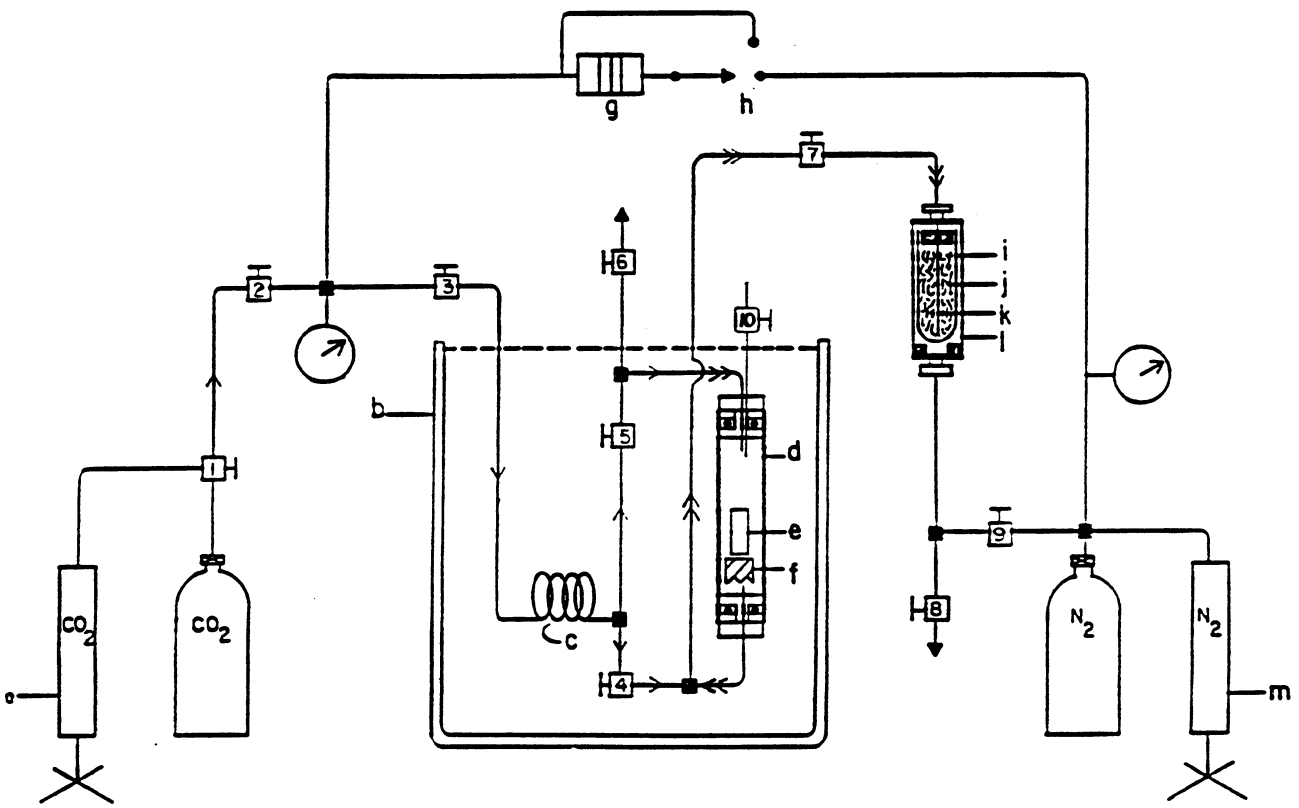

Figure II-63. Modified high-pressure solubility measuring apparatus (a) CO_2 syringe pump, (b) thermostated water bath, (c) tubing to achieve temperature equilibrium, (d) sapphire mixing tube chamber (e) magnet, (f) spiral extension, (g) pressure transducer, (h) Whitey 3-way valve, (i) test tube, (j) cotton, (k) needle tube, (l) assay chamber, and (m) N_2 syringe pump, and valve (10 allows the addition of cosolvent).

TABLE II-7. SOLUBILITY MEASUREMENTS OF A SLIGHTLY SOLUBLE α-ETHYL-ω-(*TERT*-CHLORO) POLYISOBUTYLENE* WITH COSOLVENTS IN DENSE CO_2

COSOLVENT (5%)	SOLUBILITY IN g/L AT 25°C AND 2500 PSIG
None	0.90
Hexane	5.75
Cyclohexane	3.61
Octane	3.50
Isooctane	2.21
Toluene	2.70

*Polymer obtained with the 3rd incremental monomer addition.

TABLE II-8. SOLUBILITY MEASUREMENTS OF α-ETHYL-ω-(*TERT*-CHLORO) POLYISOBUTYLENES IN DENSE CO_2

POLYMER (IMA TECHNIQUE)	M_n	SOLUBILITY (g/L) IN DENSE CO_2 AT 25°C, 2500 PSIG
(1)	1095	3.83
(2)	2790	1.89
(3)	4790	0.90
(4)	5810	0.10

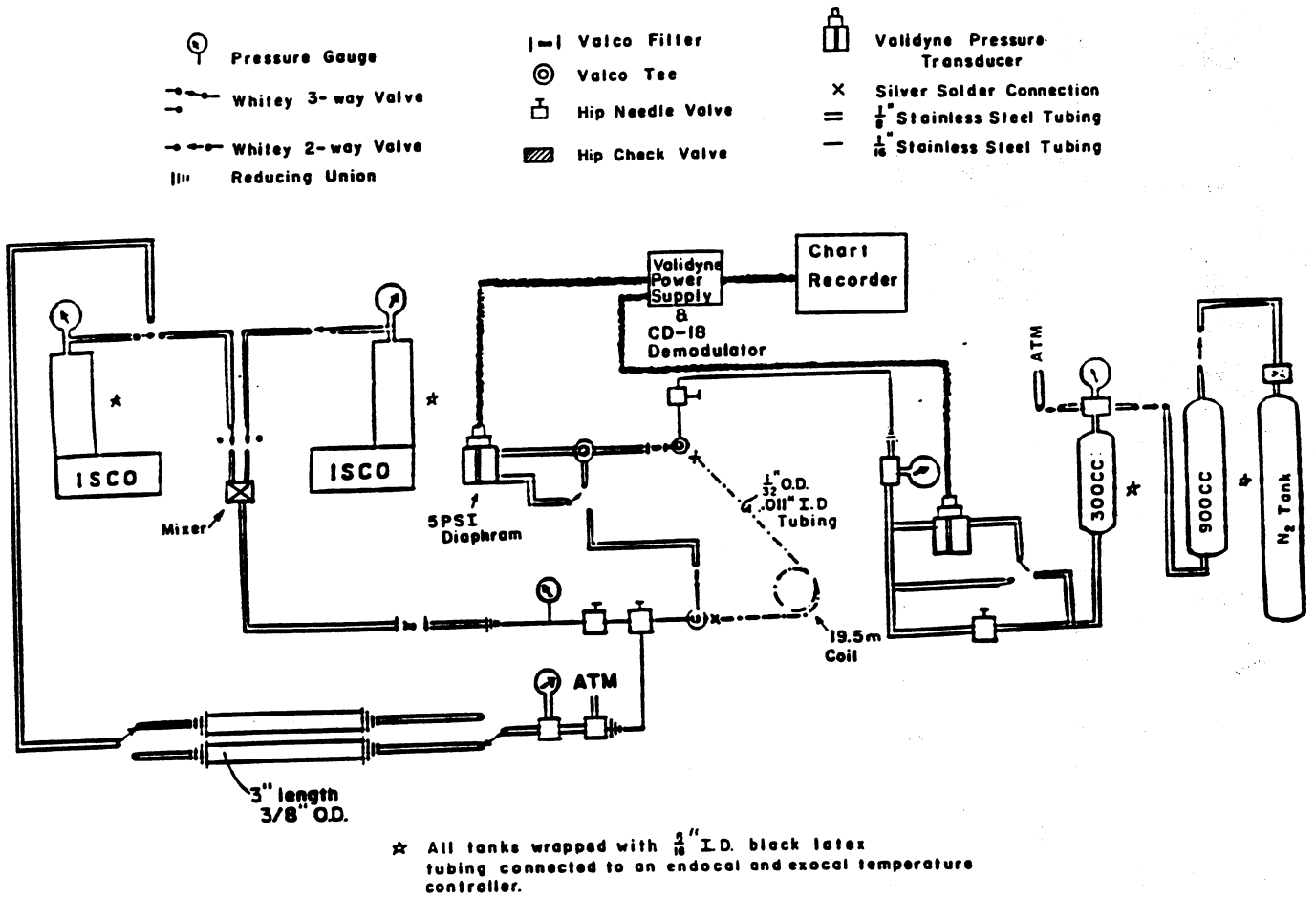

Figure II-64. Modified high-pressure capillary tube viscometer.

the necessity of mixing the polymer with dense CO_2 in a separate ISCO pump. Initial pressure testing has been completed and a variety of polymers are being tested.

Viscosity measurements of dense CO_2 have been performed with a commercial polymethylhydrosiloxane (5%) using toluene as the cosolvent (5%) to test the usefulness of our high-pressure capillary tube viscometer. These results indicated that this polymer system has thickened the dens CO_2 by 5.5 times.

8. Conclusions

Progress this past year, has particularly been on the syntheses of telechelic (terminally functionalized) polymers by *electron-pair donor stabilized living carbocationic polymerization* of isobutylene using a variety of aliphatic, aromatic, and alicyclic polyfunctional *inifers* in the presence of two coinitiators, BCl_3 and $TiCl_4$, in polar diluent. Some of these telechelic prepolymers were derivatized into telechelic ionomers by sulfonation and neutralization. The solubility data of these polymers in dense CO_2 and their solution viscosity behavior in hexane were also measured.

Our work this past year led to the following conclusions:

a. Syntheses and identification of aliphatic, alicyclic, and aromatic polyfunctional *inifers* for the preparation of near-monodisperse telechelic polymers by electron-pair donor stabilized living carbocationic polymerization of isobutylene.

b. With the *incremental monomer addition technique*, we could achieve the syntheses of polymers of theoretical M_n and polydispersities by controlling the concentration ratio, $[M_0]/[I_0]$, where $[M_0]$ and $[I_0]$ are the initial concentrations of monomer and initiator, respectively.

c. We have found for the first time, the use of 1-methyl-2-pyrrolidinone as an ED, in conjunction with both aliphatic and aromatic initiators for the preparation of living polyisobutylenes of theoretical (low) polydispersities.

d. The synthesis of ionomers based on the *inifer* method led to interesting polymers, which can find be applied in EOR.

e. The most significant use of our approach with Method II telechelic ionomers is that higher viscosification (power-law type increase) of nonpolar solvents can be achieved with extremely *low* polymer concentrations.

f. The use of hydrocarbon cosolvents has been investigated.

g. Our in-house high-pressure solubility measuring apparatus has been successfully modified and used to measure solubility of polymers in conjunction with various cosolvents.

h. We also completed the design and development of another in-house apparatus, the high-pressure capillary tube viscometer, for the evaluation of polymers as direct thickeners.

i. An automatic timer for viscosity measurements of dilute solutions has been designed and developed.

j. Computer software for the calculations of M_w, M_n, and polydispersity of polymers has also been developed.

In future work, we plan to prepare different molecular weight ionomers with multivalent cations such as Zn, Ca, Mg, Ca, and Al in addition to the monovalent cations. We will be investigating the thickening behavior of these ionomers and their solubilities in dense CO_2.

These recent developments, particularly with the telechelic ionomers, offer much promise for the discovery of many prospective direct thickeners.

C. MOBILITY CONTROL BY USE OF CO_2 FOAMS

CO_2 flooding is a promising enhanced oil recovery technique in which CO_2 can mobilize the residual oil in a reservoir by generating a developed-miscibility zone, if the CO_2 exists as a dense enough fluid at reservoir conditions. The use of dense CO_2 by itself as a displacing fluid, however, will cause frontal instability because of the viscosity difference between the CO_2 and the displaced oil. The fingering caused by the frontal instability leads to an early breakthrough of displacing fluid and results in an inefficient recovery. Furthermore, the nonuniform flow can be enhanced when there is a stratification or heterogeneities in the reservoir. This can be solved by modifying the flow mechanism by changing the structure of the displacing fluid at the pore level. One way to do this is to produce bubble-films or lamellae within the pore space by injecting an aqueous solution of foaming agent (surfactant) with the dense CO_2. When the foam is formed in the porous media, the lamellae tend to impede the flow of CO_2 such that the apparent viscosity of the foam is increased. The degree of thickening depends on the properties of the rock. It has been confirmed by our study that the apparent viscosity of foam is greater in more permeable rock. Therefore, the nonuniform displacement caused by the permeability heterogeneities can be lessened and a higher volumetric sweep efficiency can be achieved by means of a CO_2-foam flooding process.

For a surfactant to be effective in mobility control, it is necessary for the lamellae to have some degree of durability when foam flows through the pore space. It is impossible to observe the persistence of the foam flow inside the rock sample, however. The alternative to screening the surfactant under such circumstances is performing foamability tests to observe the percent foam generated, as well as the persistence of foam under static conditions after its formation. In the Fifth Annual Report,[17] we reported an innovative design for a new foam durability test. This new apparatus has enabled us to perform CO_2-foam durability tests at reservoir conditions in a much more reliable and efficient way. Although we are unable to specify the optimum extent of foam durability or survival for the purpose of mobility control, we believe that the information gained from this test is still one of the most effective ways to assure the surfactant's suitability for the CO_2-foam displacement process. This test also enables us to determine the interfacial tension (IFT) between brine and dense CO_2 at reservoir conditions, as well as the critical micelle concentration (CMC).

In addition to the need for a surfactant to form durable lamellae with dense CO_2 at reservoir conditions, a successful foamant must not be adsorbed excessively during flow of the foam in the reservoir. Because of its amphipatic nature, however, the surfactant tends to adsorb onto all of the

surfaces or interfaces of the system, and some losses onto the rock are inevitable. The major concern in a dynamic process is that the permanent adsorption should not be so great as to become a major economic or supply burden. Therefore, the aim of our dynamic adsorption experiments is to evaluate the magnitude of the adsorption of the surfactant. One other factor, the chromatographic delay that measures the slope of the overall adsorption isotherm, is also evaluated in this experiment.

Our research during this past year can be divided into three parts: (1) the measurements of CO_2-foam mobility, (2) the measurements of foam durability, and (3) the development of dynamic adsorption measurements.

In foam mobility measurements, we directed our efforts towards the enlargement of our database of CO_2-foam mobility measurements. Our work, therefore, was extended to measuring the mobility of dense CO_2 and surfactant-free solution on three rock systems: Rock Creek sandstone, Baker dolomite, and San Andres dolomite. In addition, the mobility of CO_2-foam at surfactant concentrations far below CMC value was also investigated.

In foam durability experiments, we continued to perform surfactant screening at reservoir conditions. The IFT between dense CO_2 and the surfactant itself, as well as the durability of CO_2-foams with several surfactants, were conducted at a high pressure and temperature. Moreover, a new series of surfactant-aging experiments was also carried out for two specific surfactants, Chevron CD1040 and CD1050, to test the surfactant's ability to withstand thermal decomposition over time.

In support of the dynamic adsorption experiments, we worked on improving the experimental setup. Considerable time was spent improving the modified drop-weight method (MDWM) apparatus and perform preliminary testing.

1. CO_2-Foam Mobility Measurements

As was mentioned earlier, the displacement of oil by dense CO_2 is accomplished in the frontal region where most of the miscibility is developed. If this frontal zone can be stabilized against nonuniform flow during the displacement, a much larger fraction of the oil in the reservoir can be recovered. In the field, the stabilization of the front requires mobility control of the large region lying between the front and the injection well. Therefore, it is necessary for the experimental situation to simulate that portion of the reservoir in a region that lies behind a stable displacement front during a CO_2 flood. Because most of the oil in this region will be displaced, and because the saturation of aqueous surfactant solution and dense CO_2 are no longer changing appreciably, a steady-state experiment is appropriate for measuring mobility.

We added a transfer vessel to the flow apparatus that we constructed last year for measuring foam mobility. The transfer vessel was installed to contain the brine and thus protect the ISCO pump from corrosion. For convenience, Figs. II-65 and II-66, which respectively show a simplified schematic and a more detailed representation of the flow apparatus, are presented here. In operation, brine/surfactant solution flows simultaneously with dense CO_2, first through a foam generator (consisting of a short section of the test rock) and then through a sample of the same rock being tested. The brine/surfactant solution is driven at a known rate from the transfer vessel, which displaces it with oil from the ISCO pump. The dense CO_2 comes directly from the temperature controlled RUSKA pump. Although the

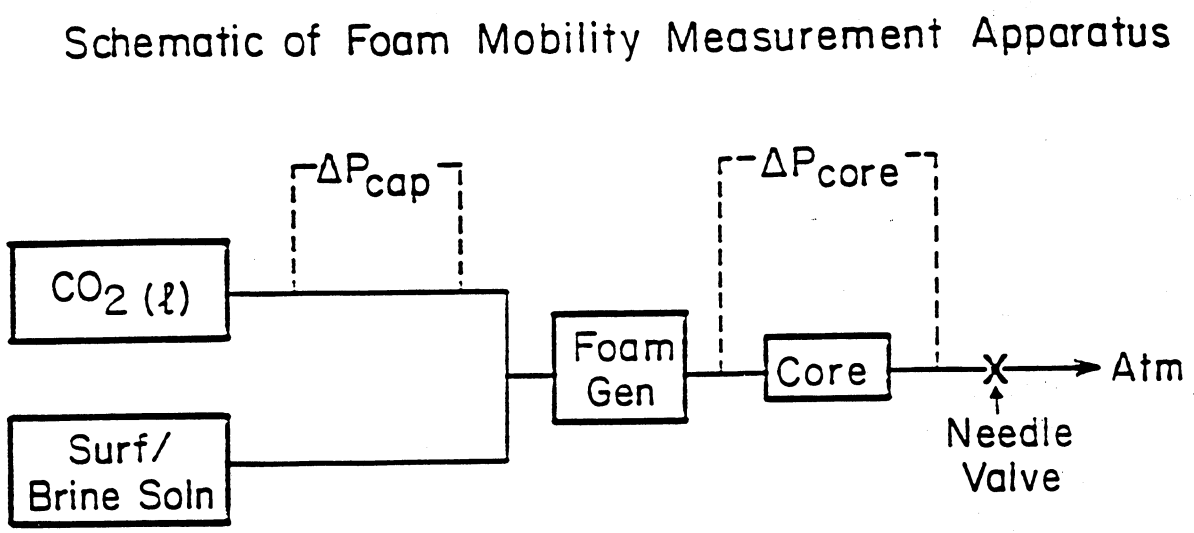

Figure II-65. Simplified diagram of the apparatus for measuring steady-state/CO_2 mobility.

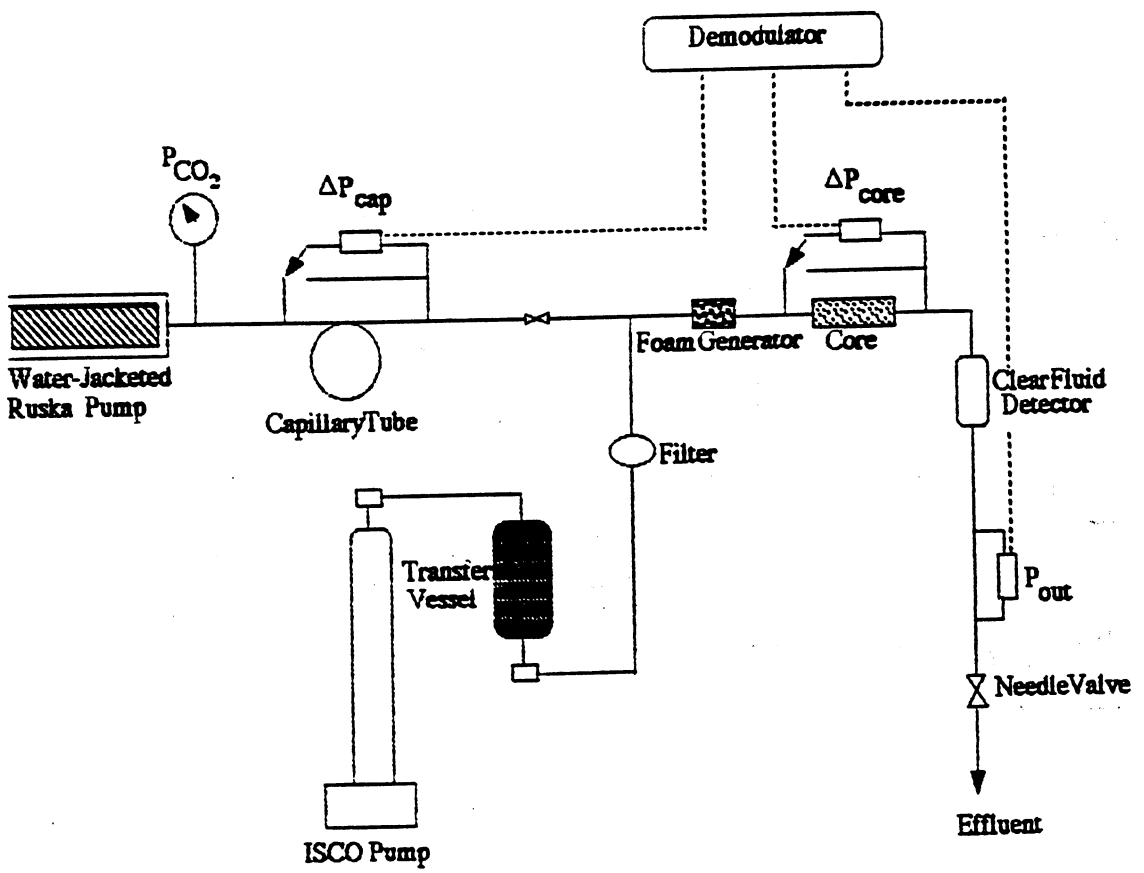

Figure II-66. Foam mobility measurement system.

motor drive rate of the RUSKA can be set precisely, the short-term rate of efflux of the CO_2 is also monitored by measuring the pressure drop across a capillary tube.

The mobility of the rock sample is calculated from measured values of the pressure drop, the total flow rate in the experiment, and from the dimensions of the sample. The mobility is the ratio of the Darcy or superficial velocity of the foam (treating it, for calculation, as a single fluid) to the average pressure gradient along the sample. The units of mobility are millidarcies/centipoise.

Most of the mobility measurements were completed in 1989. The results reported in the Fifth Annual Report[17] and by Lee and Heller[46] lead to several conclusions, which indicate that the application of CO_2-foam in the field is promising. The main conclusion that they reach is that the apparent viscosity of CO_2-foam in reservoir rock is dependent not only on surfactant type, concentration, and volumetric flowing fraction of CO_2, but also to a minor extent on the flow rate and to a large extent on the permeability of the rock sample. It was found that the apparent viscosity of foam is greater in rocks of higher permeability, which is in the proper direction for reducing the effects of reservoir heterogeneity. But the dependence of the apparent viscosity of foam on the rock is nonlinear; it approaches asymptotic values at both high and low rock permeabilities. This means that the frontal smoothing effect based on the thickening of the displacing fluid will only be effective over a certain range of permeabilities. The limiting values of apparent viscosity have been measured for a certain surfactant, but may well differ for others. Concerning this effect, we shall obtain more experimental data by using core material and surfactants appropriate to particular oil fields.

This past year, we also continued a few mobility measurements. Three rocks—Baker dolomite, Rock Creek sandstone, and San Andres dolomite—were used as tested core samples. Three different surfactants—Enordet X2001 from Shell Chemicals, Witcolate 1276 from Witco, and Chevron Chaser CD1050 from Chevron Chemical—were used as the foamant. In the following discussions, some of the previous results will be included wherever it is appropriate.

a. Effect of Rock Permeability

The differences between mobility measurements made on the different kinds of rock are presented as the effect of rock permeability. In different rock samples, this effect is illustrated in terms of the apparent viscosity of the foam to the rock permeability. This means that the foam is considered as a single-phase fluid that saturates the pore space. The reciprocal of the relative mobility, a ratio of the measured absolute mobility of foam to the rock permeability, is recognized as the apparent viscosity of the foam.

Figure II-67 is a log-log plot that indicates the relationship between the apparent viscosity of foam and rock permeability. As indicated from this plot, the apparent viscosity of foam increases with the rock permeability. All four data points were obtained under the same experimental conditions—where Baker dolomite was used as the tested sample and Enordet X2001 was used as the surfactant. Among these data points, two (at permeability of 99.4 md) were obtained from a series of experiments recently performed while the foam generator was changed to Rock Creek sandstone. The slight change of the foam generator is needed because the short piece of Baker dolomite core used in the foam generator was damaged within a short period of time on several occasions. A deformed rock structure on the inlet surface of the damaged foam generator, after dismounting, is normally observed. The damage resulted, most likely, because of the dissolution of the mineral in the presence of the CO_2 at testing condition.

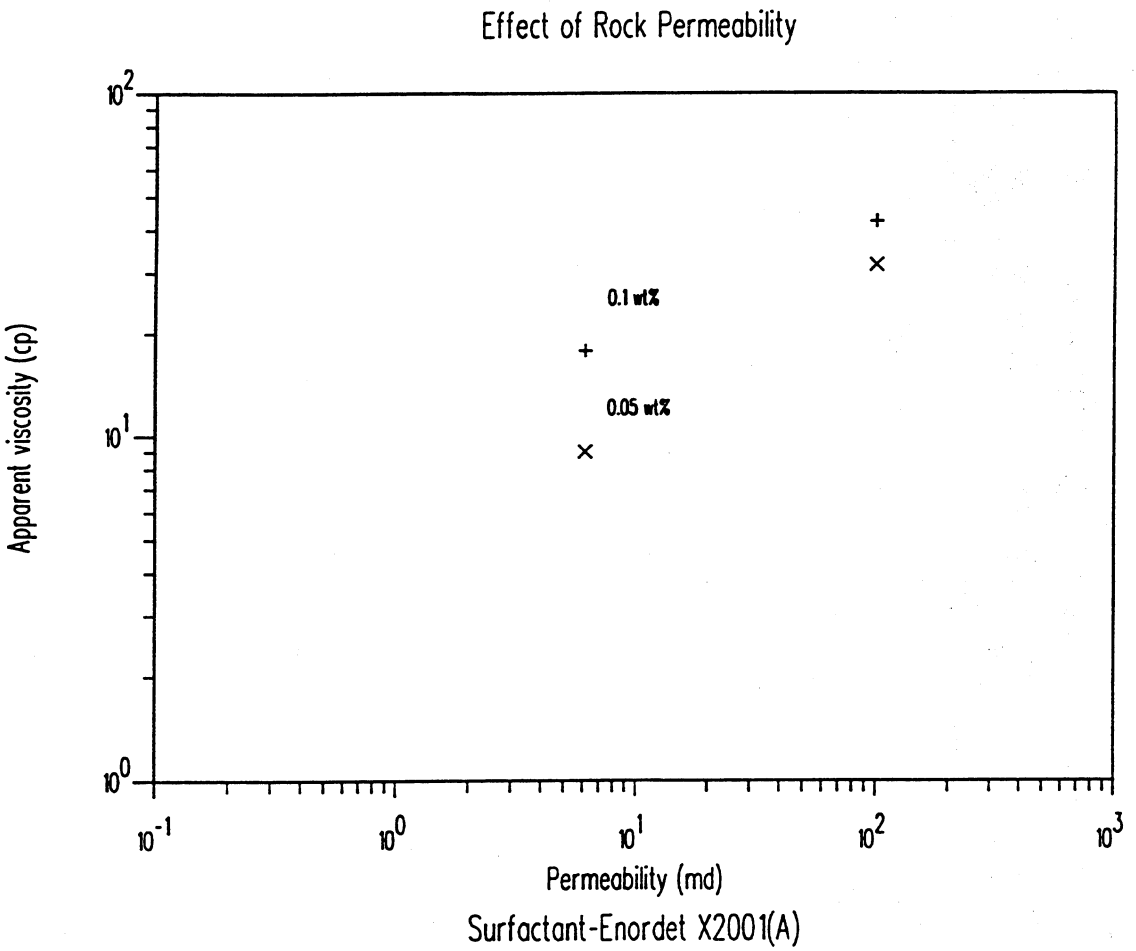

Figure II-67. Apparent viscosity of CO_2-foam for different rock permeabilities.

b. Effect of Surfactant Concentration

The variation of the foam mobility with the surfactant concentration for Witcolate 1276 is shown in Fig. II-68 for three different samples of Rock Creek sandstone. The lowest surfactant concentration shown here is 0.001 wt%, or only 10 ppm of active surfactant. As indicated in this plot, the mobility tends to level off at lower surfactant concentrations. The maximum mobility asymptote that occurs at low-end concentrations is the combined mobility of surfactant-free brine and dense CO_2, which is approximately at 2.0 md/cp measured with the 13.1 md sample. Moreover, the decreasing trend for the foam mobility with the increase of surfactant concentration indicates another characteristic of the surfactant, which changes the population of the lamellae that composes the foam and, thus, impedes to an increasing extent the free motion of CO_2 through the rock.

This characteristic is also found in two other plots. The results shown in Fig. II-69 present the mobility variation with the surfactant Chevron CD1050 for a San Andres dolomite core of permeability 1.6 md; whereas Fig. II-70 shows another set of data with the surfactant Enordet X2001 for Baker dolomite cores of different permeabilities. The mobility for surfactant-free brine and dense CO_2 is 0.5 md/cp for San Andres dolomite and 31.5 md/cp for a Baker dolomite of permeability 99.4 md. In the results shown in Fig. II-69, no noticeable change of mobility reduction was found when the surfactant concentration was increased from 0 to 25 ppm. It was also found that the mobility of CO_2-foam did not decrease even at 50 ppm of surfactant concentration in the other mobility measurement with a core of permeability 1.8 md (which is not shown here). The results from our foam durability measurement show that at these two surfactant concentrations, 25 and 50 ppm, the foamabilities are low and the CO_2-foam does not last longer than 15 minutes.

Using a concentration of surfactant below its CMC in a foam application has been suggested by Kuhlman and Falls[47] (they address the problems associated with injectivity and the surfactant front's propagation), and it is obviously advantageous from our economic standpoint to keep the concentrations of surfactant as low as possible. But there is still a need to justify the range of suitable concentrations of surfactant for mobility control. Figure II-70 shows an example, which indicates that the mobility reduction may be sufficient to successfully stabilize a displacement front at surfactant concentrations above 50 ppm and below 5000 ppm (its CMC value) but apparently will fail at concentrations below 50 ppm. Therefore, it is important to consider all the parameters involved in the design of a CO_2-foam operation.

c. Effect of Flow Rate

The effect of flow rate on the measured mobilities is shown in Fig. II-71. As in previous results, some 'shear thinning' behavior is observed; the foam mobilities increase as the velocities are moderately raised. The rather moderate increase of mobility with increase of velocity can be understood in terms of the decrease of the stable population of lamellae or bubble-films in the pores of the rock at greater flow rates.

The results obtained from the mobility measurements taken this past year have supported the previous findings of our study. We are now using the core material obtained from the field and the likely appropriate surfactants to continue our research in this area.

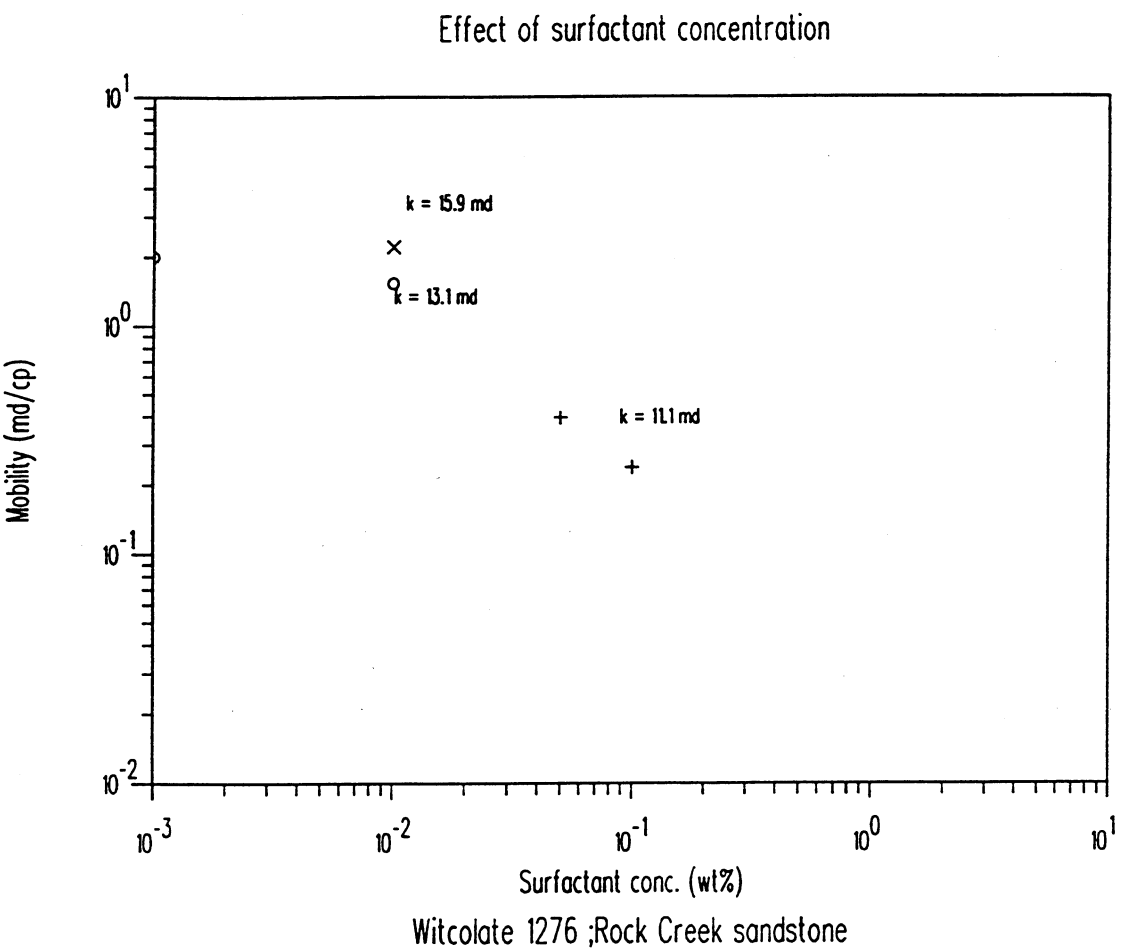

Figure II-68. Effect of surfactant concentration (Witcolate 1276) on CO_2-foam mobility.

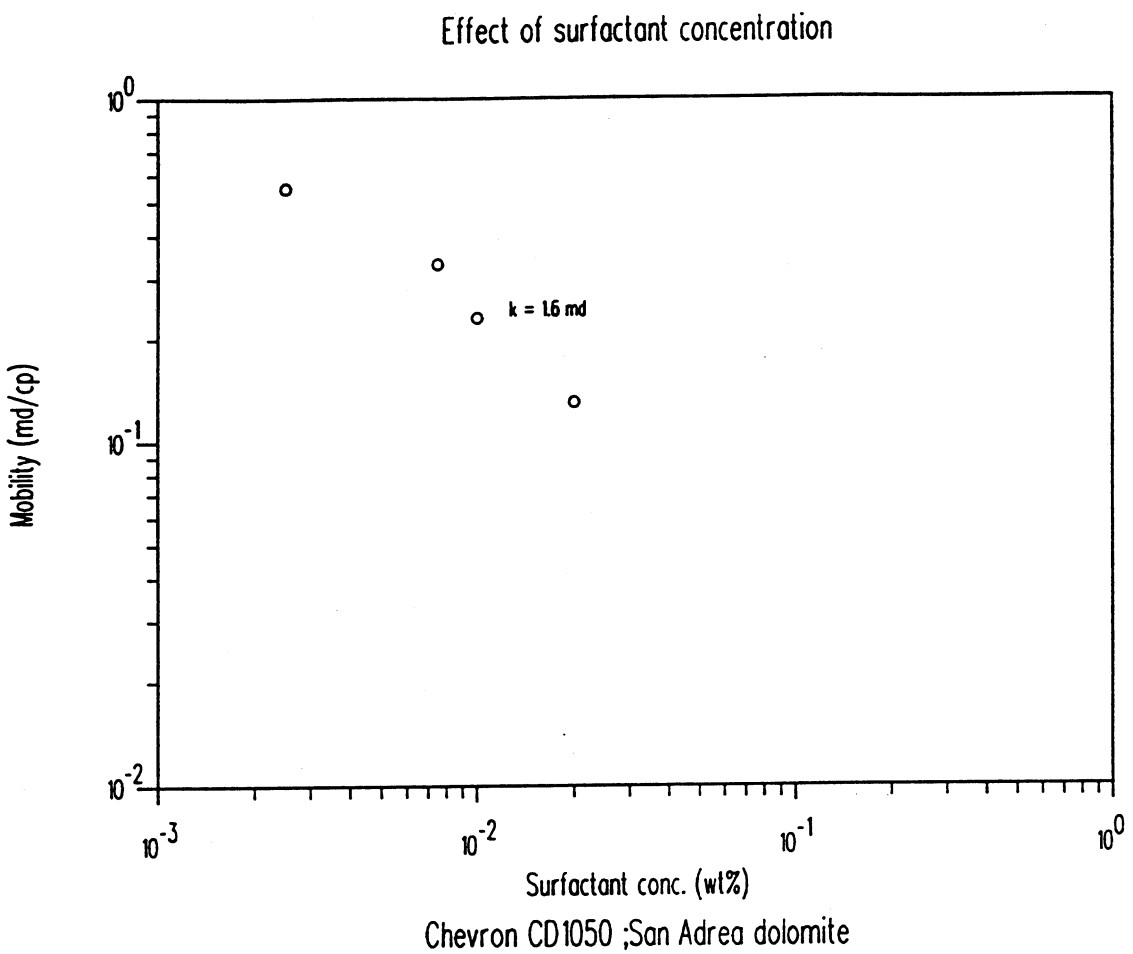

Figure II-69. Effect of surfactant concentration (Chevron CD1050) on CO_2-foam mobility.

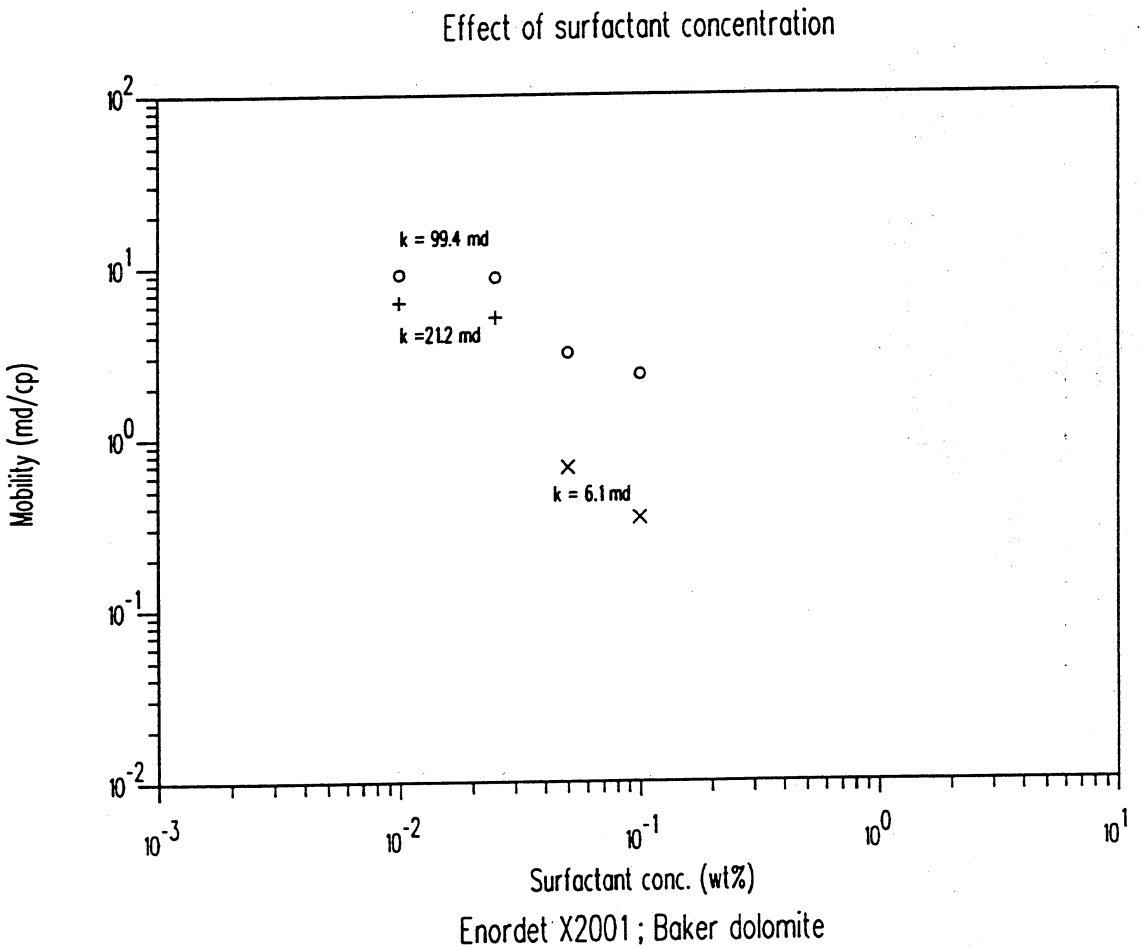

Figure II-70. Effect of surfactant concentration (Enordet X2001) on CO_2-foam mobility.

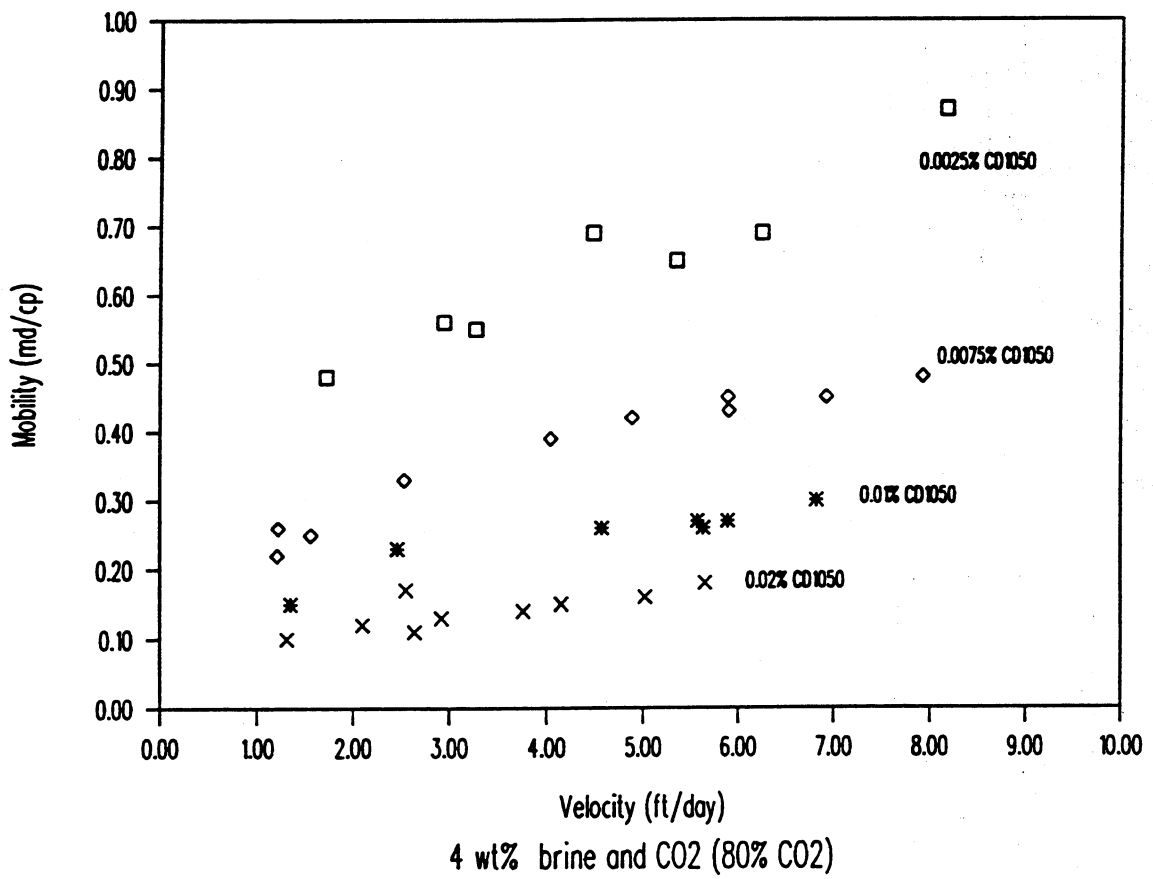

Figure II-71. Effect of flow rate on CO_2-foam mobility.

2. Foam Durability Experiment

The foam durability apparatus is a device that is used for testing surfactant properties at high pressure, thus, allowing the evaluation of these surfactants for reservoir use. The schematic view of the entire apparatus is shown in Fig. II-72, and an enlarged view of the sapphire tube high-pressure cell is shown in Fig. II-73. Basically, there is only one minor change of the apparatus from the design shown in the Fifth Annual Report.[17] The change was found to be important in eliminating the possible contamination of CO_2 caused by a small quantity of oil which remained in the tubing connected to the transfer tank. The modification was made by repositioning the Validyne transducer and adding a 7 cm^3 volume cylinder to protect the CO_2 tank from the possibility of any contamination.

During the experiment, dense CO_2 is introduced through a needle at the lower end of the cell, and CO_2-foam is collected one bubble at a time at the upper end of a sapphire tube, which is initially full of surfactant solution. Then, depending on the effectiveness of the surfactant, the bubbles will either collect into a layer of 'foam-like dispersion' at the top of the tube or coalesce quickly into a clear layer of dense CO_2. After a standard volume of CO_2 (1.75 cm^3) has been drawn into the sapphire cell by running the Ruska pump backwards, the persistence of any foam that has been formed is observed.

Several results can be obtained from the foam durability apparatus. First, it is possible to observe and measure the lifetime of static CO_2-foam at reservoir conditions of temperature and pressure. These lifetimes are determined by the times of drainage (of the bulk aqueous liquid, from the lamellae into their plateau boundaries, and then through a network into the bulk phase) and by the critical minimum thicknesses the films can maintain. The durability of a CO_2-foam is measured in terms of foam decay. This is accomplished by using a cathetometer to measure the change of CO_2-foam height and the overall height of the CO_2 in the sapphire cell, which is reported as 'percent foam.'

The second set of results obtainable from the apparatus includes measurements of the interfacial tension (IFT). The calculation of the measurements are analogous to those of the drop-weight method. Because the rate of entry of the dense CO_2 is known from the pump setting, and because the individual drops are counted and timed, the volume and radius of each drop can be calculated. The radius of the needle from which the bubbles emerge, the density of the surfactant, and the density of the CO_2 are also known. The following equation is used to calculate the IFT:

$$\frac{4}{3}\pi R^3(\rho_{surf} - \rho_{co_2})g = 2\pi r \gamma f \qquad \text{(II-7)}$$

where

R is the average radius of the bubbles,
r is the radius of the needle from which the bubbles emerge,
γ is the interfacial tension (IFT) between dense CO_2 and surfactant solution, and
f is a dimensionless correction factor.

The correction factor is that cited by Adamson;[48] it is necessary because a portion of the CO_2 remains on the tip of the needle after the bubble is released.

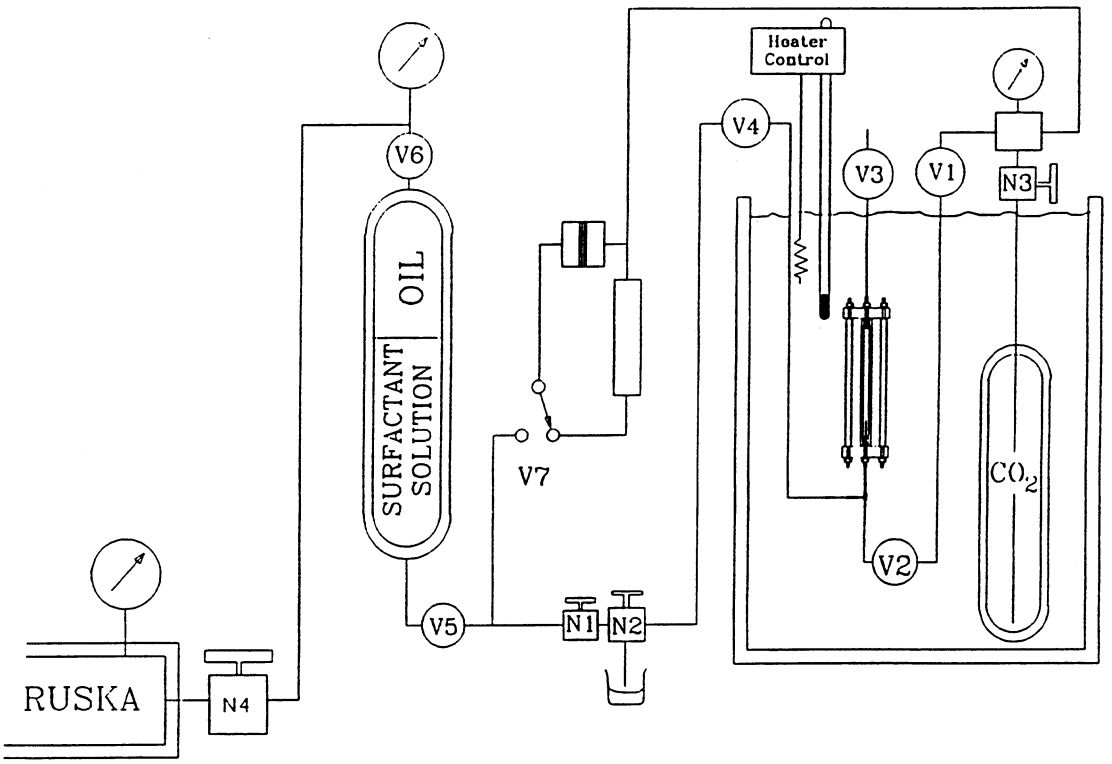

Figure II-72. Foam durability test system.

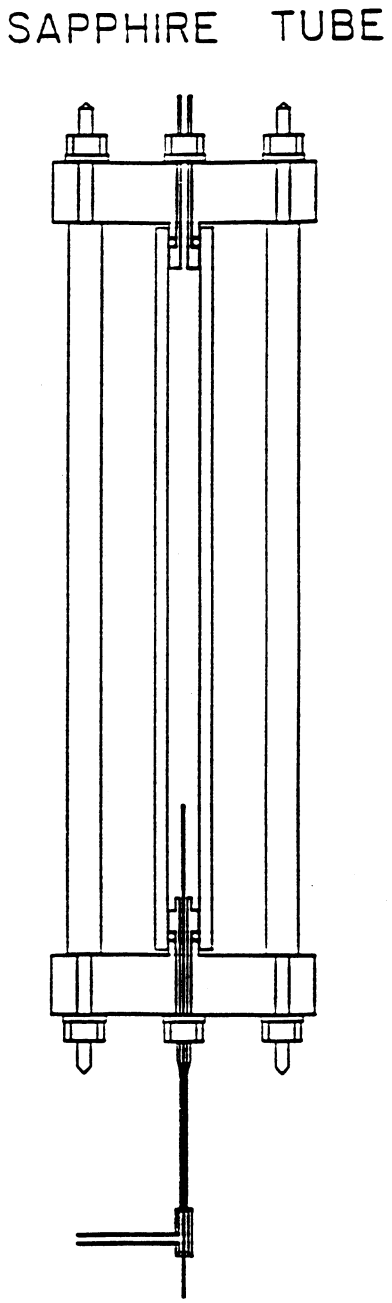

Figure II-73. High-pressure cell for foam durability test.

The last result of the experiment is the determination of the critical micelle concentration (CMC) of a surfactant, which can be determined graphically from a plot of surfactant concentration vs. IFT.

Five surfactants have been tested using the foam durability apparatus. The first two surfactants, Witcolate 1259 and Witcolate 1276, are anionic alcohol ether sulfates manufactured by Witco Chemical Corporation. The third surfactant is Enordet X2001, an anionic surfactant manufactured by Shell Chemical Company. The last two surfactants are manufactured by Chevron Chemical Company. Chevron Chaser CD1040, a brine-tolerant sulfonate, is designed for use in sandstone reservoirs, and Chevron Chaser CD1050 is designed specifically for carbonate reservoir CO_2 flood.

Measurements of the interfacial tension between surfactant solutions and dense CO_2 were conducted under two conditions; at 25°C and 1500 psig and at 40°C and 2500 psig. Two compositions of brine were used. The first brine was a 1 wt% brine containing 0.5wt% NaCl and 0.5wt% $CaCl_2$. The composition of the second brine is listed in Table II-9. Figures II-74 through II-80 show graphs of the IFT between different surfactants and dense CO_2 . The CMC values estimated from these plots and the IFT at each CMC are also summarized in Table II-10. In general, the CMC values for these surfactants do not change with temperature and pressure. The IFT values at CMC are generally higher at conditions of lower temperature and pressure. The only exception occurs for CD1050, which has lower CMC at lower temperature. Furthermore, the two surfactants, CD1040 and CD1050, were tested with two different brines. It is found that the CMC value decreases for surfactant CD1040 as the electrolyte concentration increased in the brine. For surfactant CD1050, however, the CMC value was found to increase with brine concentration at conditions of low temperature and pressure, but no change at all was observed when it was tested at conditions of high temperature and pressure.

The decay of foam as a function of time for these surfactants is also illustrated in Figs. II-81 through II-87. The foamability and durability are also summarized in Table II-10. The foamability in this table is defined as the percent foam generated when the surfactant initially contacted the CO_2 during the first hour; whereas the durability is defined as the subsequent persistence of the foam bubbles. The values shown for the foamability are the percent foam and the corresponding surfactant concentration; whereas the values shown for the durability are the lifetime of the foam bubbles and the related surfactant concentration. It was observed that the greatest amount of foam was present at or above the CMC. The persistence of foam varies considerably for different concentrations of surfactant; however, the most durable foam was also found to occur at or above the CMC. In general, the amount of foam formed and the persistence of the foam bubbles are greater at lower temperatures and pressures. For the same surfactant, the concentration that produces the greatest amount of foam is not necessarily the one that produces the most durable foam.

Regarding the foamability and durability of a surfactant, Witcolate 1276 is a better foamer than Witcolate 1259; whereas Chevron CD1050 is better than CD1040. In addition to Enordet X2001, Witcolate 1276 and CD1050 have also shown promising mobility measurements. But a standard for determining the optimum condition for a surfactant applied to CO_2-foam mobility reduction is not yet completed. Nevertheless, the minimum requirements for a qualified surfactant for mobility control should be that it needs to be a good foamer and it should not allow the CO_2 bubbles to coalesce immediately upon contact with each other.

Some results obtained from a designated surfactant aging experiment are also included in Table II-10. Details of these results are shown in Figs. II-88 through II-93. This surfactant aging experiment was conducted to test the surfactant's ability to withstand thermal decomposition over time. Two

TABLE II-9. COMPOSITION OF 4 WT% BRINE

COMPONENT	IN 1000.0 gm SOLUTION (gm)
NaCl	30.628
KCl	0.290
$CaCl_2H_2O$	4.769
$MgCl_26H_2O$	2.594
Na_2SO_4	2.957
H_2O	958.762

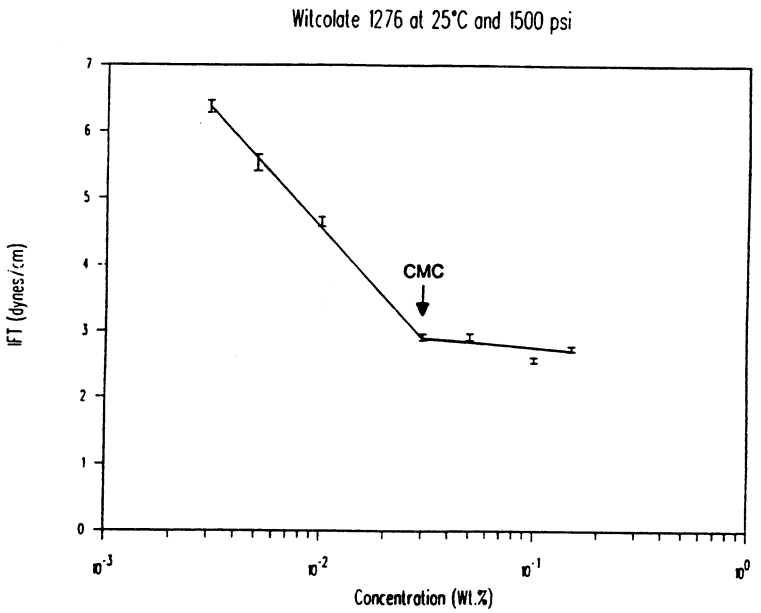

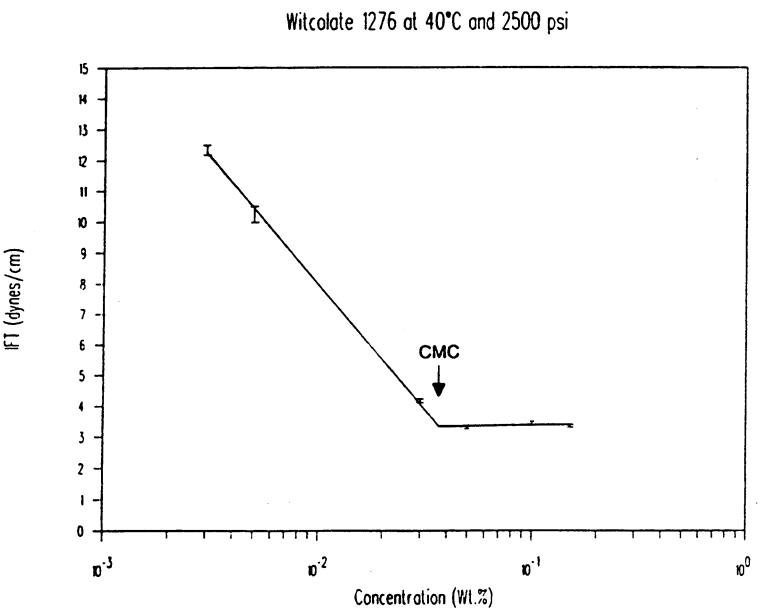

Figure II-74. Interfacial tension between dense CO_2 and Witcolate 1276/1 wt% brine solution.

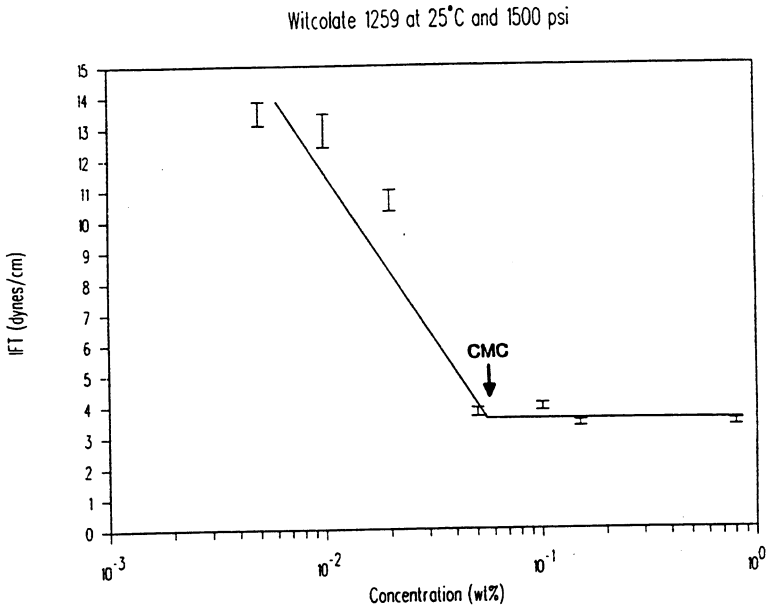

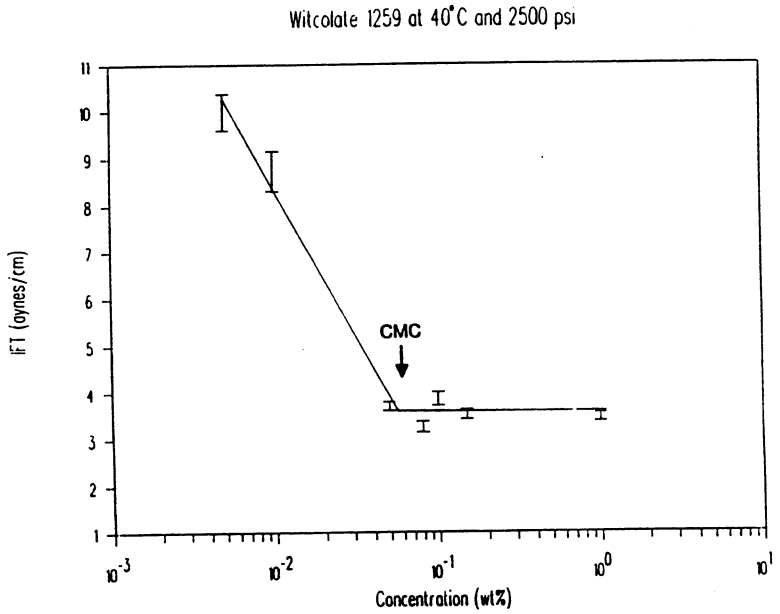

Figure II-75. Interfacial tension between dense CO_2 and Witcolate 1259/1 wt% brine solution.

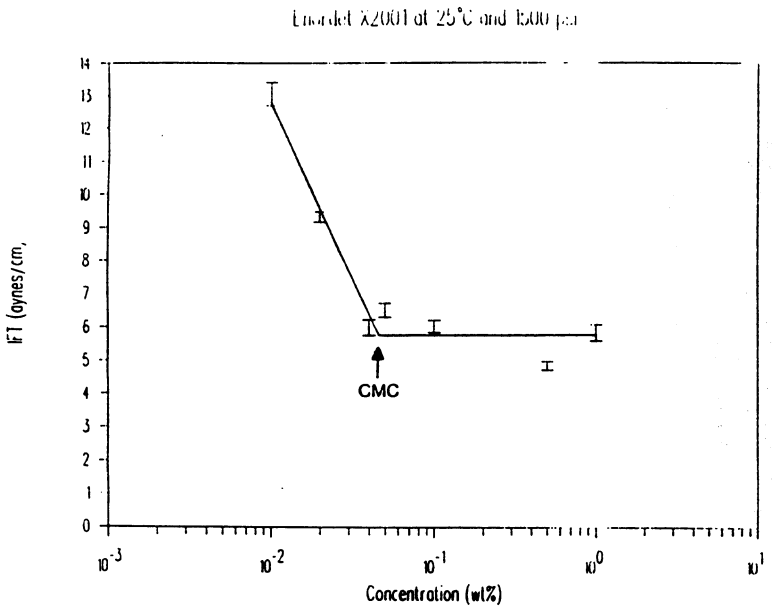

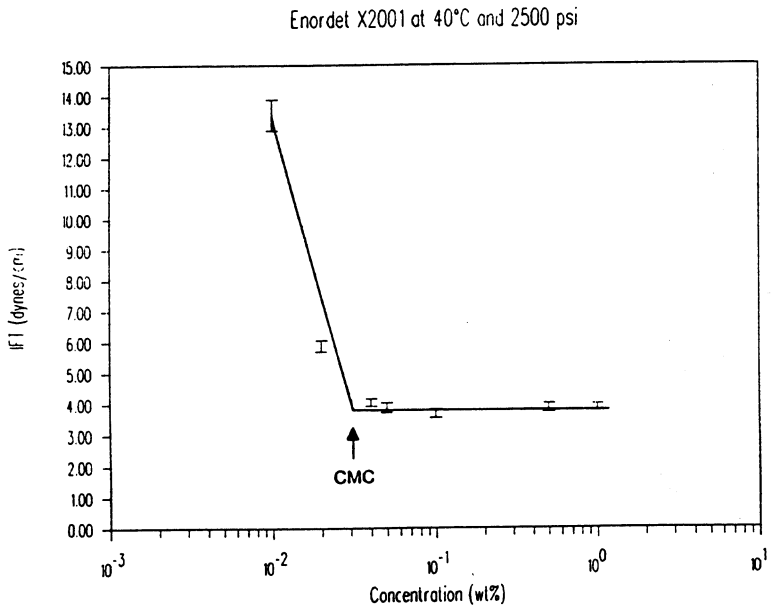

Figure II-76. Interfacial tension between dense CO_2 and Enordet X2001/1 wt% brine solution.

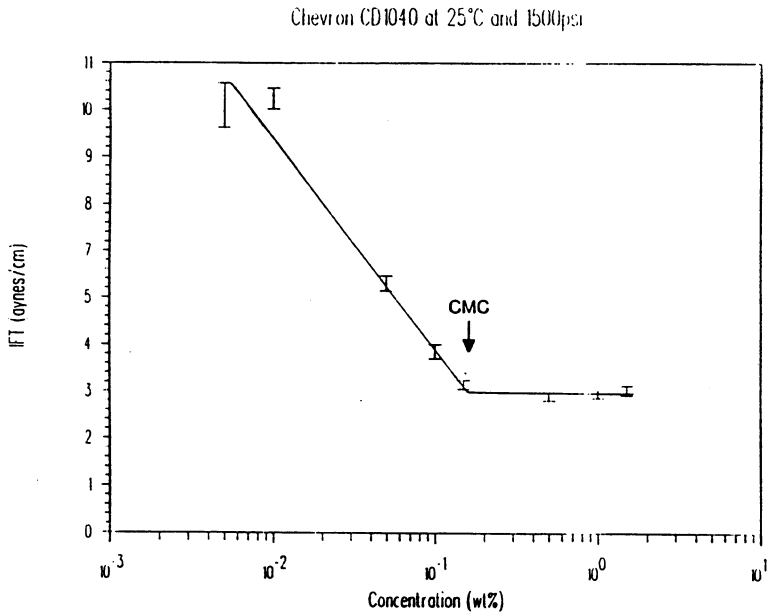

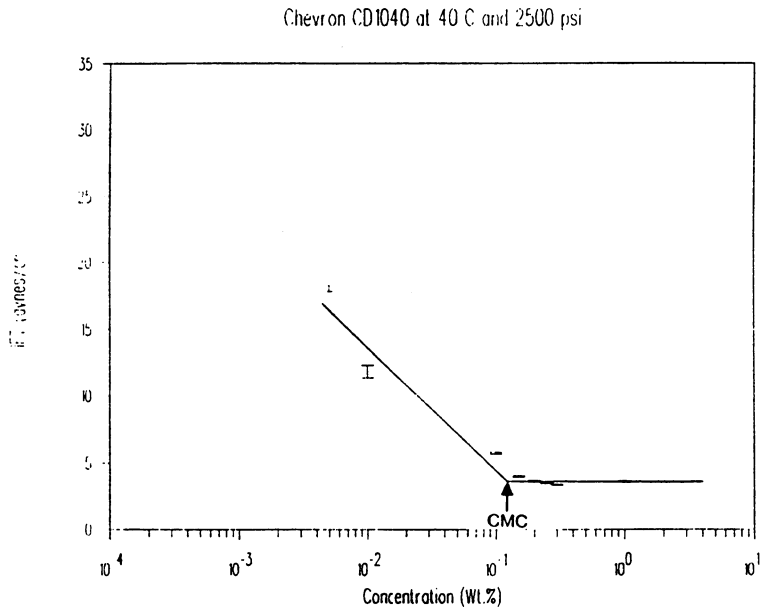

Figure II-77. Interfacial tension between dense CO_2 and Chevron CD1040/1 wt% brine solution.

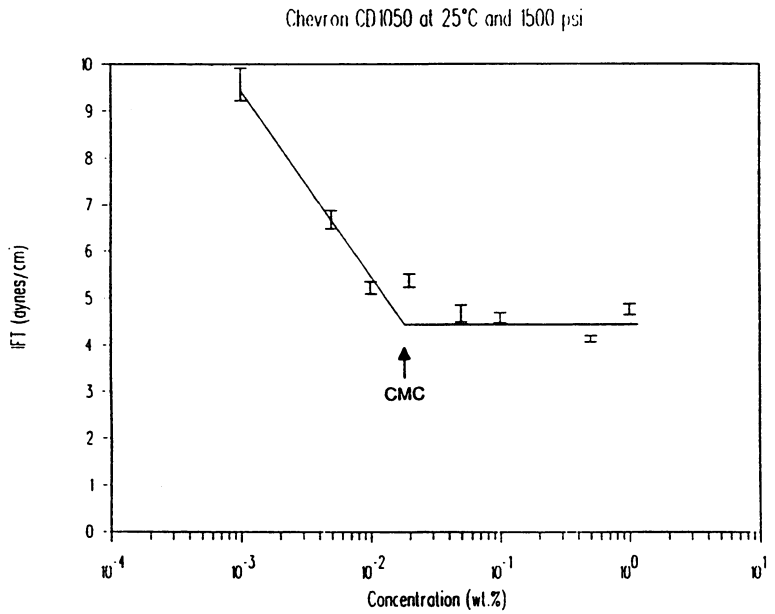

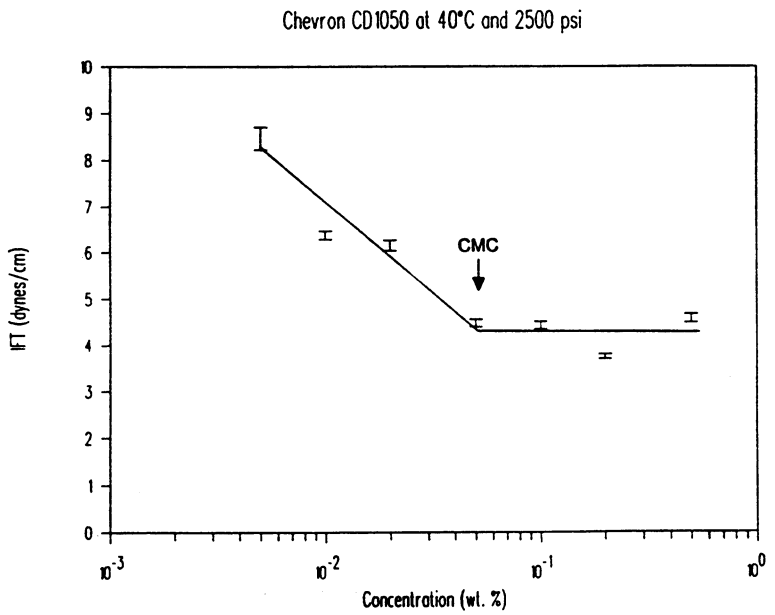

Figure II-78. Interfacial tension between dense CO_2 and Chevron CD1050/1 wt% brine solution.

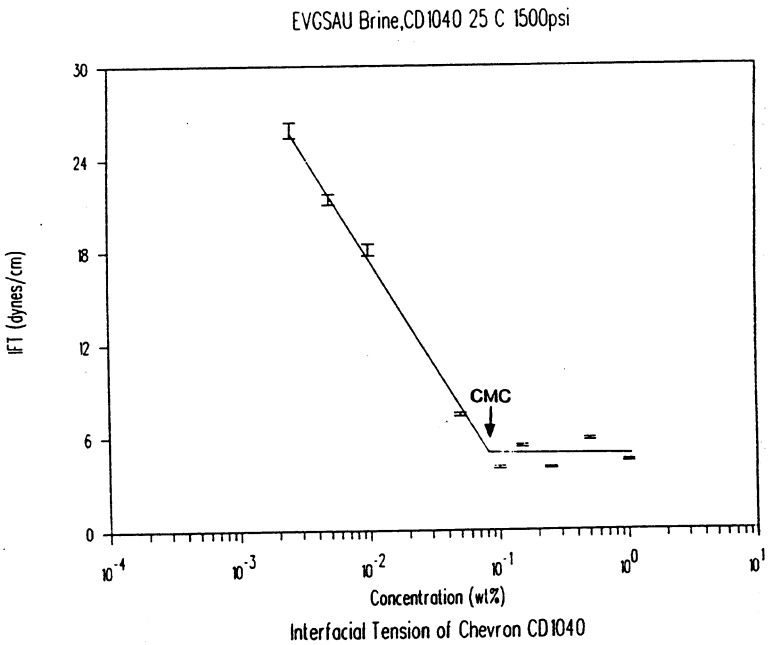

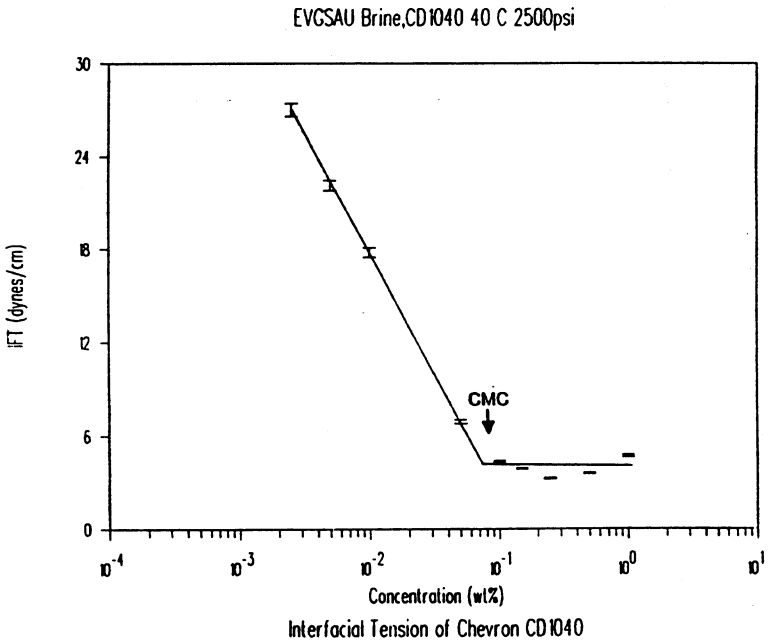

Figure II-79. Interfacial tension between dense CO_2 and Chevron CD1040/4 wt% brine solution.

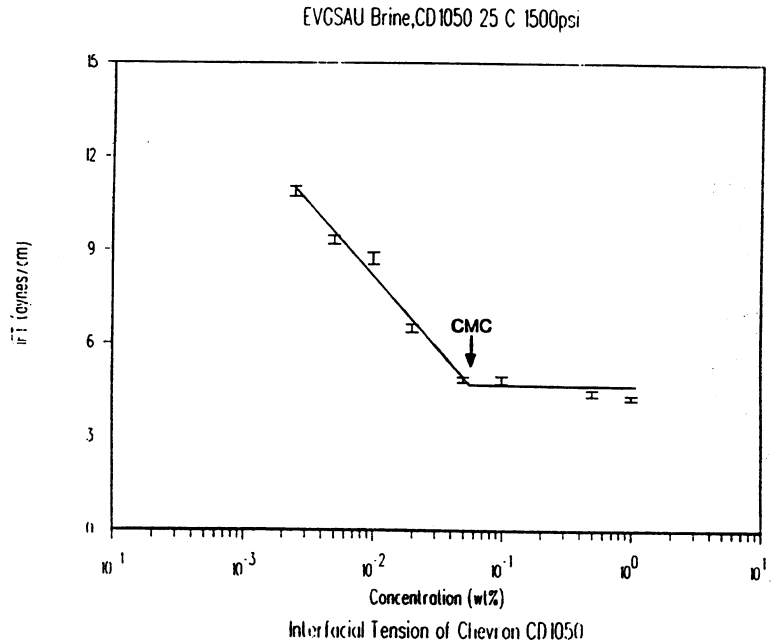

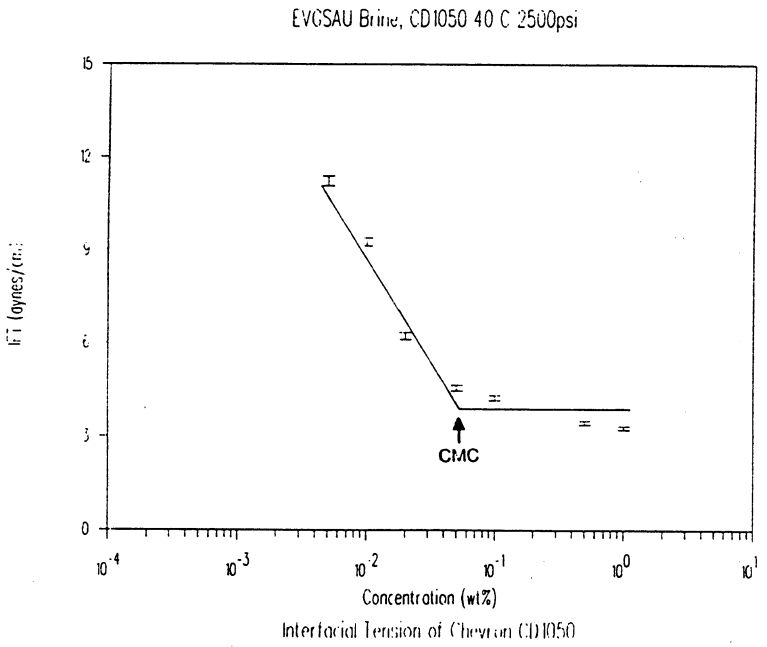

Figure II-80. Interfacial tension between dense CO_2 and Chevron CD1050/4 wt% brine solution.

TABLE II-10. SUMMARY OF THE FOAM DURABILITY EXPERIMENT

SURFACTANT NAME	TEST CONDITION		BRINE (wt%)	CMC (wt%)	IFT @ CMC (dyne/cm)	FOAMABILITY (%foam/wt%)		DURABILITY (hours/wt%)	
	T (°C)	P (psig)				HIGHEST	LOWEST	LONGEST	SHORTEST
Witcolate 1276	25	1500	1	0.03	3.0	36/0.5	0/0.005	9/0.05	0/0.005
Witcolate 1276	40	2500	1	0.03	3.0	50/0.05	25/0.03	2.75/0.05	0.3/0.03
Witcolate 1259	25	1500	1	0.05	3.5	28/0.8	11/0.1	0.3/0.8	0.2/0.1
Witcolate 1259	40	2500	1	0.05	3.5	36/0.05	0/0.005	0.01/0.08	0.005/0.05
Enordet X2001	25	1500	1	0.05	5.5	79/1.0	0/0.01	2/1.0	0/0.01
Enordet X2001	40	2500	1	0.02	4.0	14/0.05	0/0.01	0.3/1.0	0/0.01
Chevron CD1040	25	1500	1	0.15	3.2	63/0.05	0/0.005	>6/0.05	0/0.005
Chevron CD1040	40	2500	1	0.15	3.2	32/0.1	0/0.01	0.5/0.1	0/0.01
Chevron CD1040	25	1500	4	0.08	4.8	16/0.05	0/0.01	0.12/0.05	0/0.01
Chevron CD1040	40	2500	4	0.08	4.2	12/0.05	0/0.01	0.12/0.05	0/0.01
Chevron CD1040	40 DA	2500 DA	1	0.15	3.2	87/0.1	0/0.01	3.5/0.1	0/0.01
Chevron CD1040	40 OA	2500 OA	1	0.15	3.5	67/0.1	0/0.01	2.0/0.1	0/0.01
Chevron CD1040	40 FA	2500 FA	1	0.15	3.6	38/0.1	0/0.1	0.67/0.1	0/0.01
Chevron CD1050	25	1500	1	0.02	4.5	100/0.5	0/0.001	>45/0.5	0/0.001
Chevron CD1050	40	2500	1	0.05	4.5	85/0.5	7/0.005	5.6/0.05	0.3/0.005
Chevron CD1050	25	1500	4	0.05	4.2	100/0.05	8/0.005	1.8/0.05	0.2/0.005
Chevron CD1050	40	2500	4	0.05	4.0	22/1.0	7/0.005	0.5/1.0	0.5/0.005
Chevron CD1050	40 DA	2500 DA	1	0.05	4.2	78/1.0	0/0.001	3.0/1.0	0/0.001
Chevron CD1050	40 DA	2500 OA	1	0.03	4.0	94/1.0	0/0.005	3.5/1.0	0/0.005
Chevron CD1050	40 FA	2500 FA	1	0.04	4.2	46/0.05	0/0.001	1.7/1.0	0/0.001

DA: desktop-aged
OA: oven-aged
FA: fresh-acidified

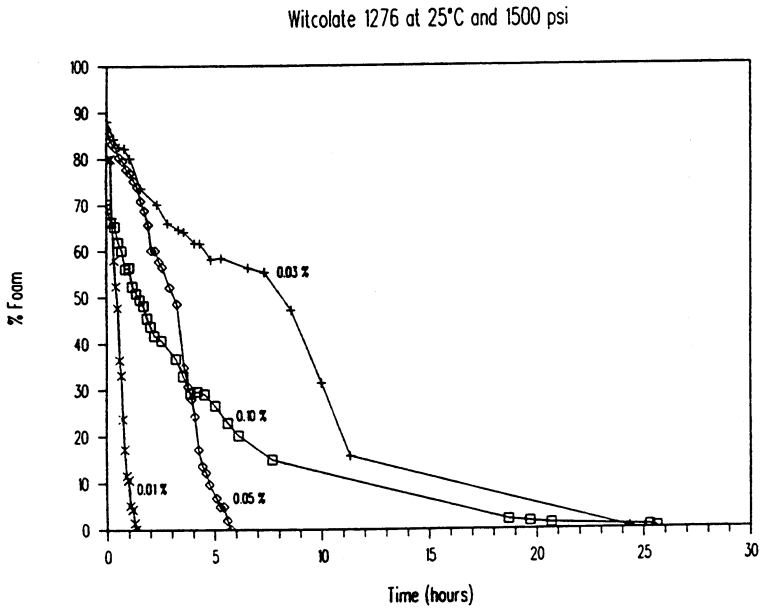

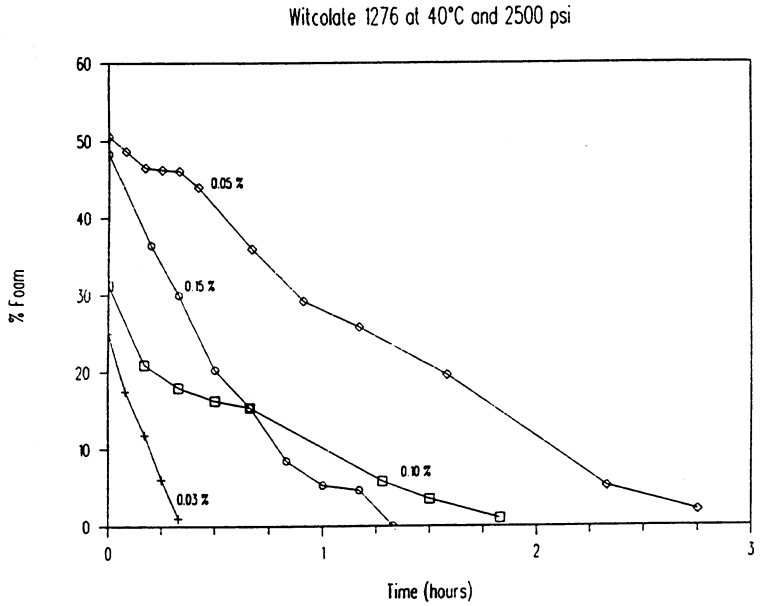

Figure II-81. Foam decay of Witcolate 1276/1 wt% brine in dense CO_2.

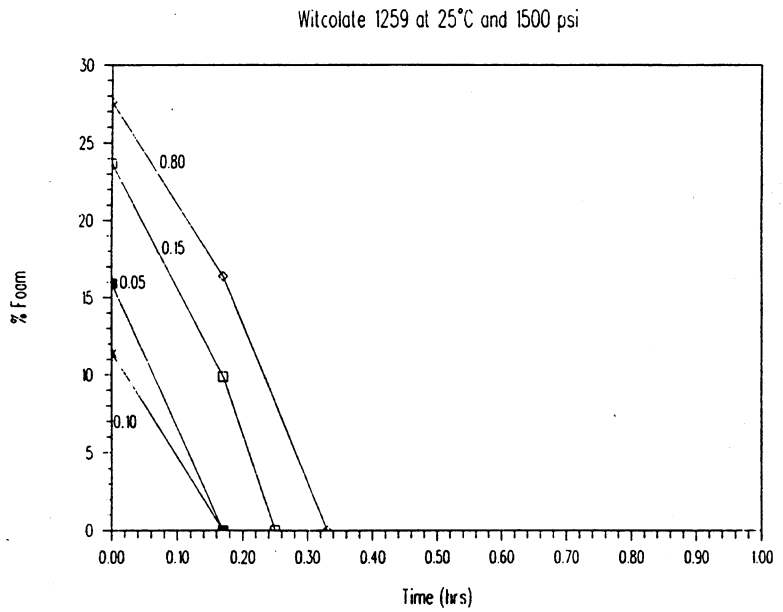

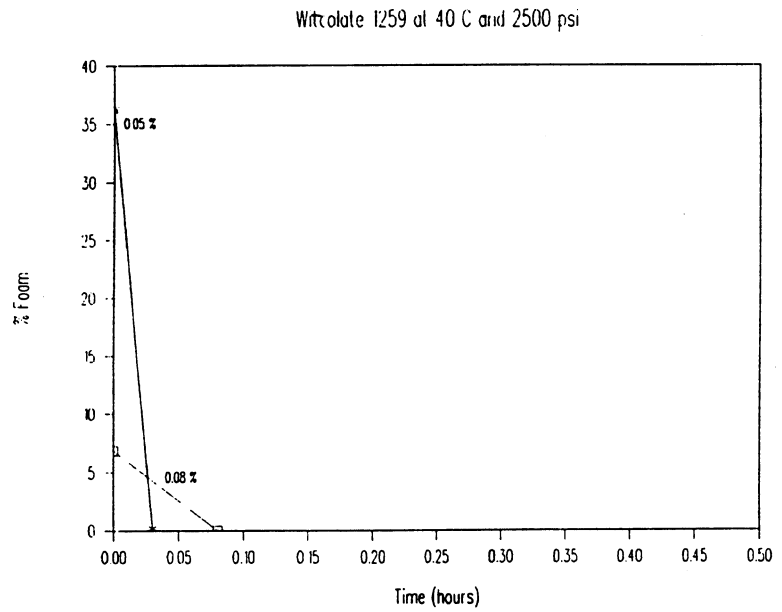

Figure II-82. Foam decay of Witcolate 1259/1 wt% brine in dense CO_2.

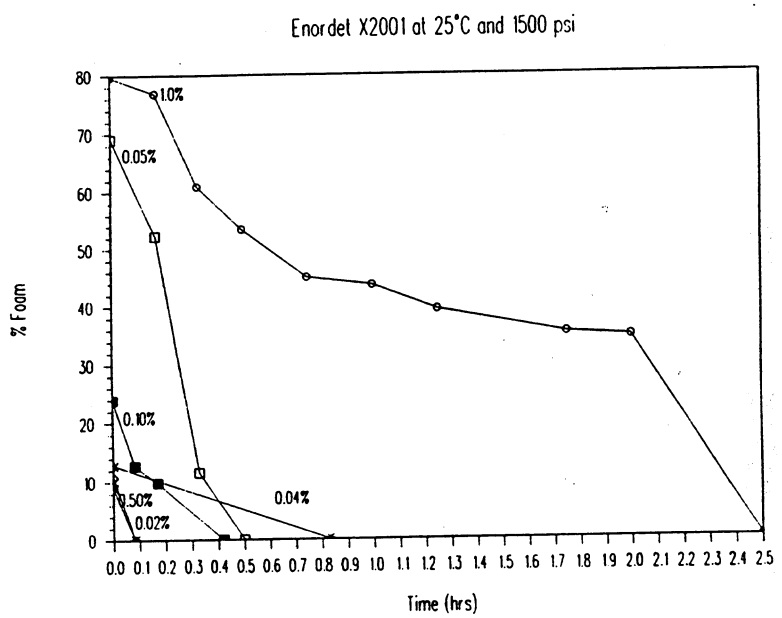

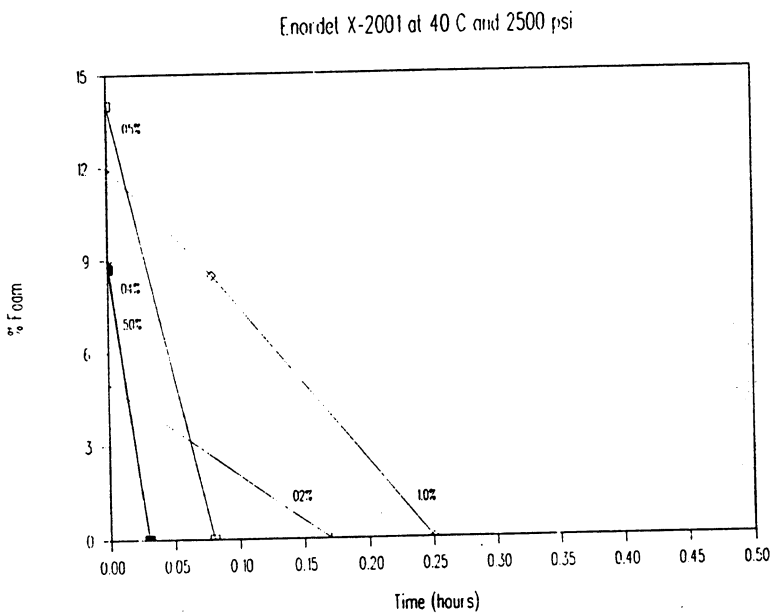

Figure II-83. Foam decay of Enordet X2001/1 wt% brine in dense CO_2.

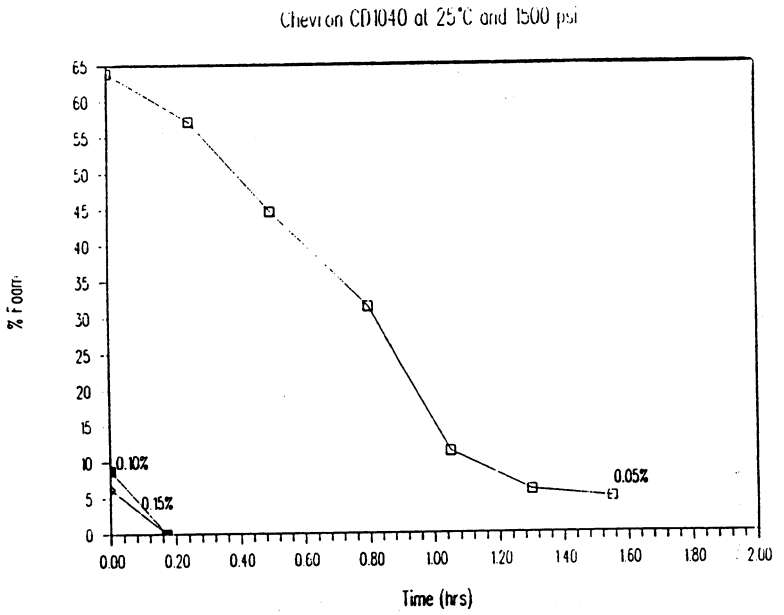

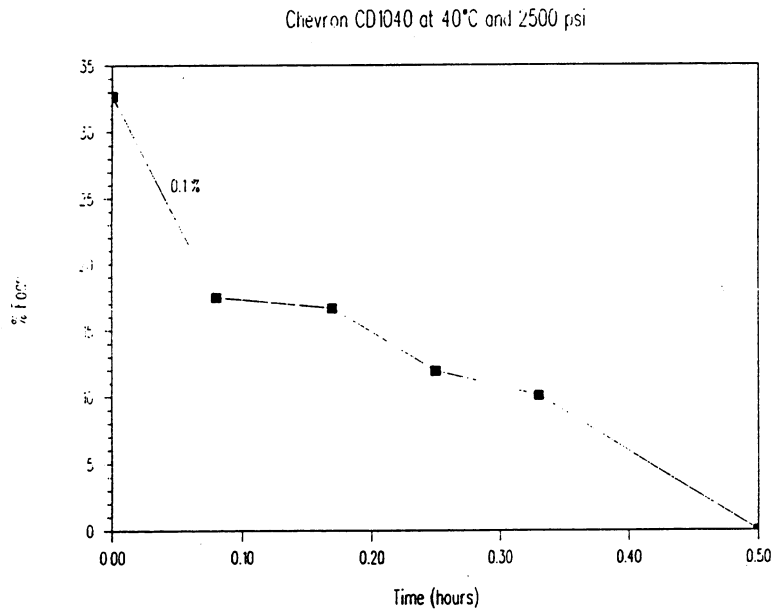

Figure II-84. Foam decay of Chevron CD1040/1 wt% brine in dense CO_2.

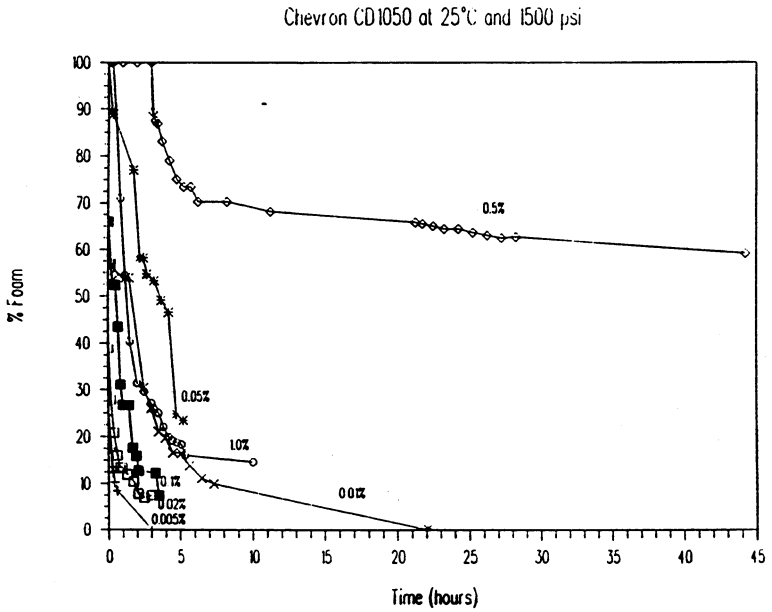

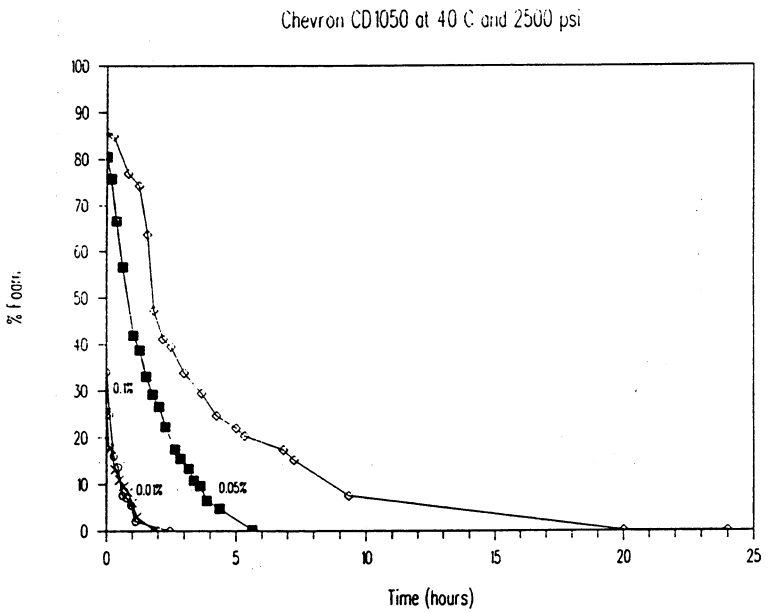

Figure II-85. Foam decay of Chevron CD1050/1 wt% brine in dense CO_2.

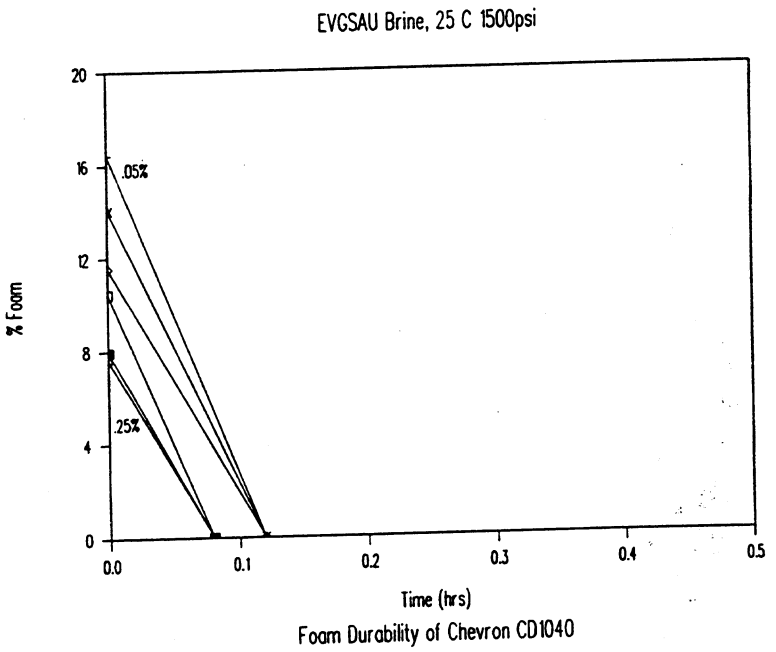

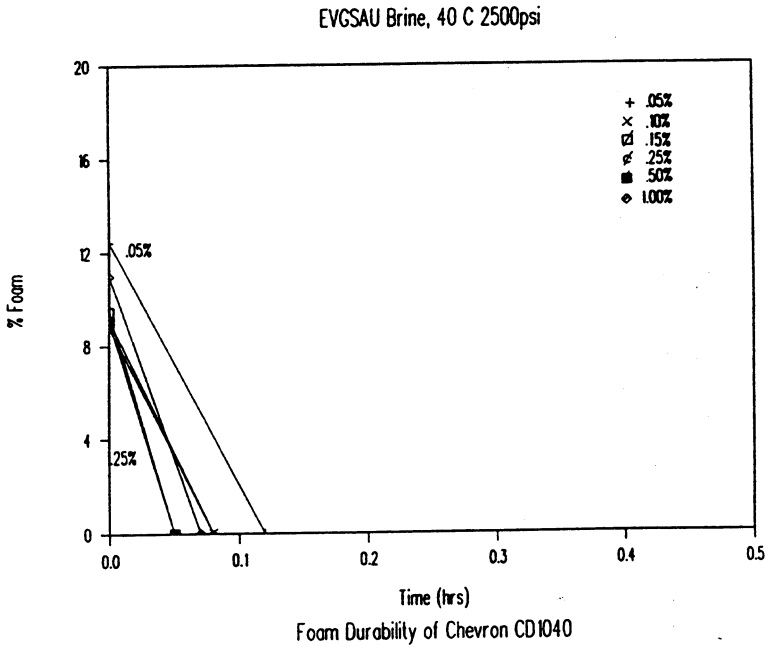

Figure II-86. Foam decay of Chevron CD1040/4 wt% brine in dense CO_2.

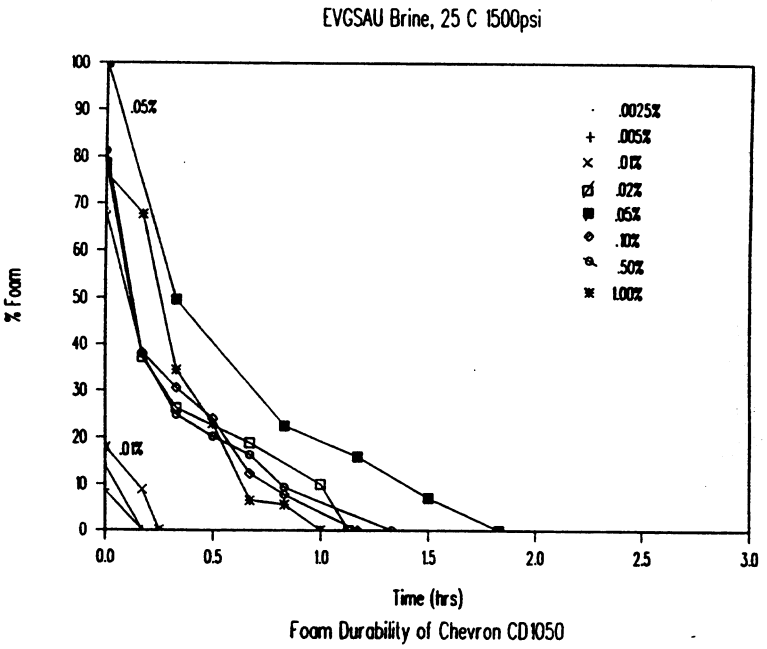

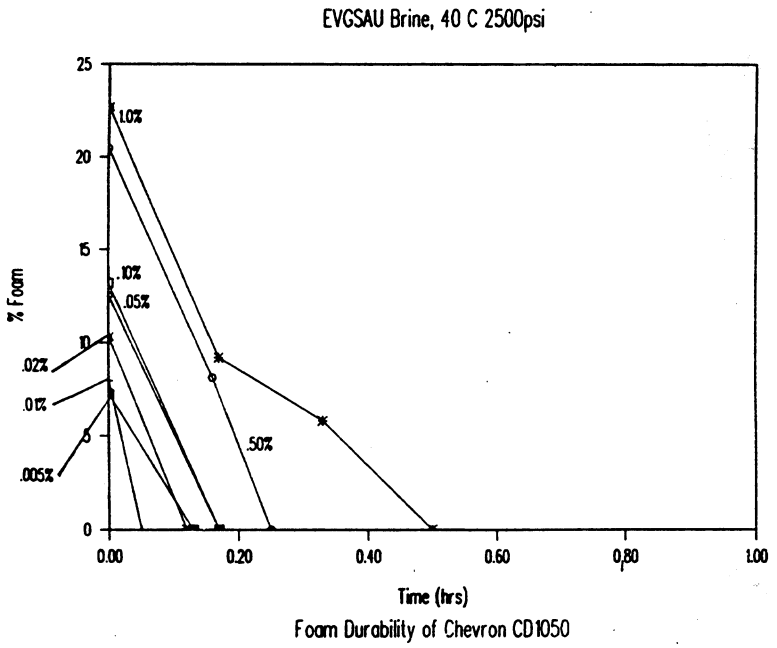

Figure II-87. Foam decay of Chevron CD1050/4 wt% brine in dense CO_2.

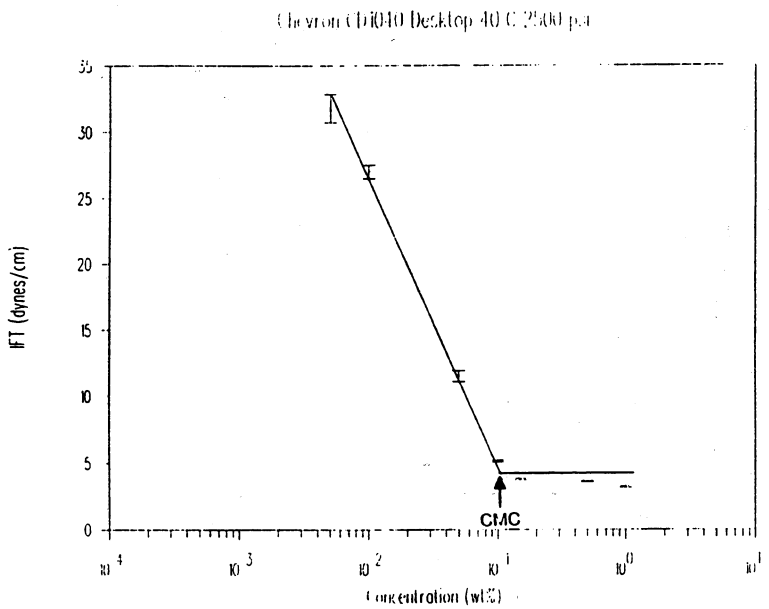

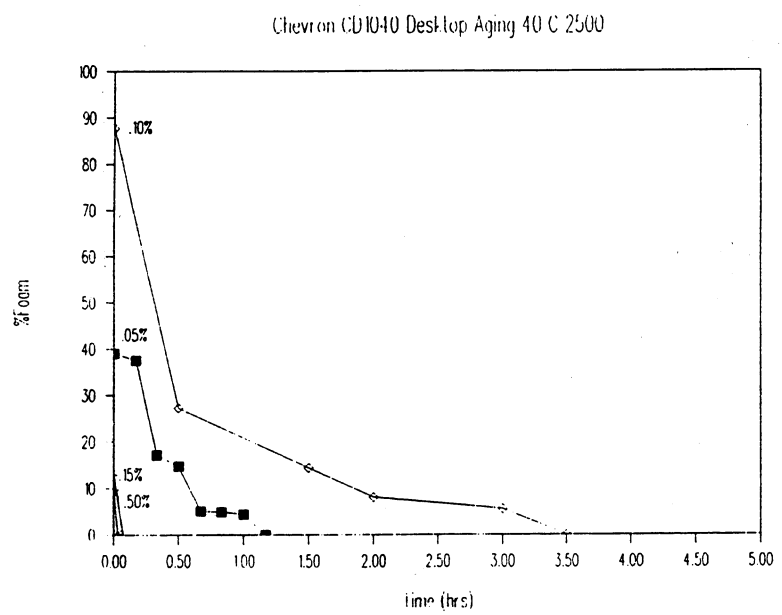

Figure II-88. Interfacial tension and foam decay of a Chevron CD1040 desktop-aged sample in dense CO_2.

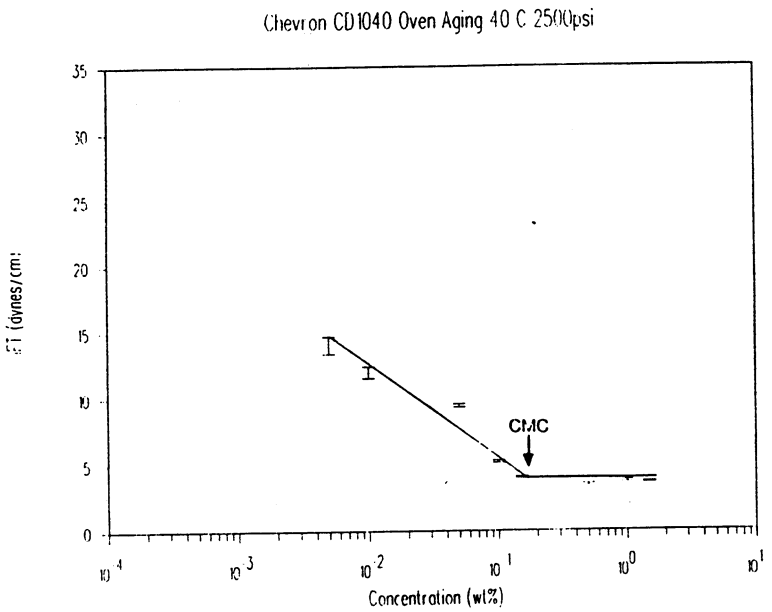

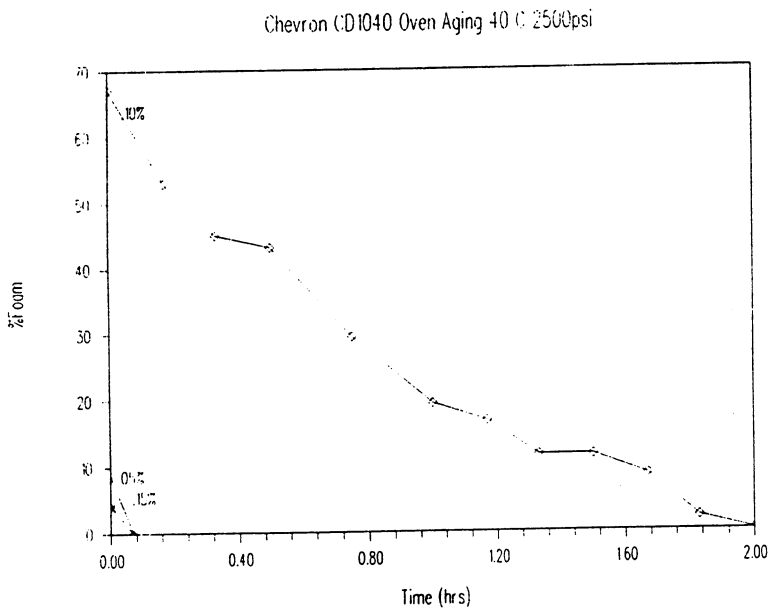

Figure II-89. Interfacial tension and foam decay of a Chevron CD1040 oven-aged sample in dense CO_2.

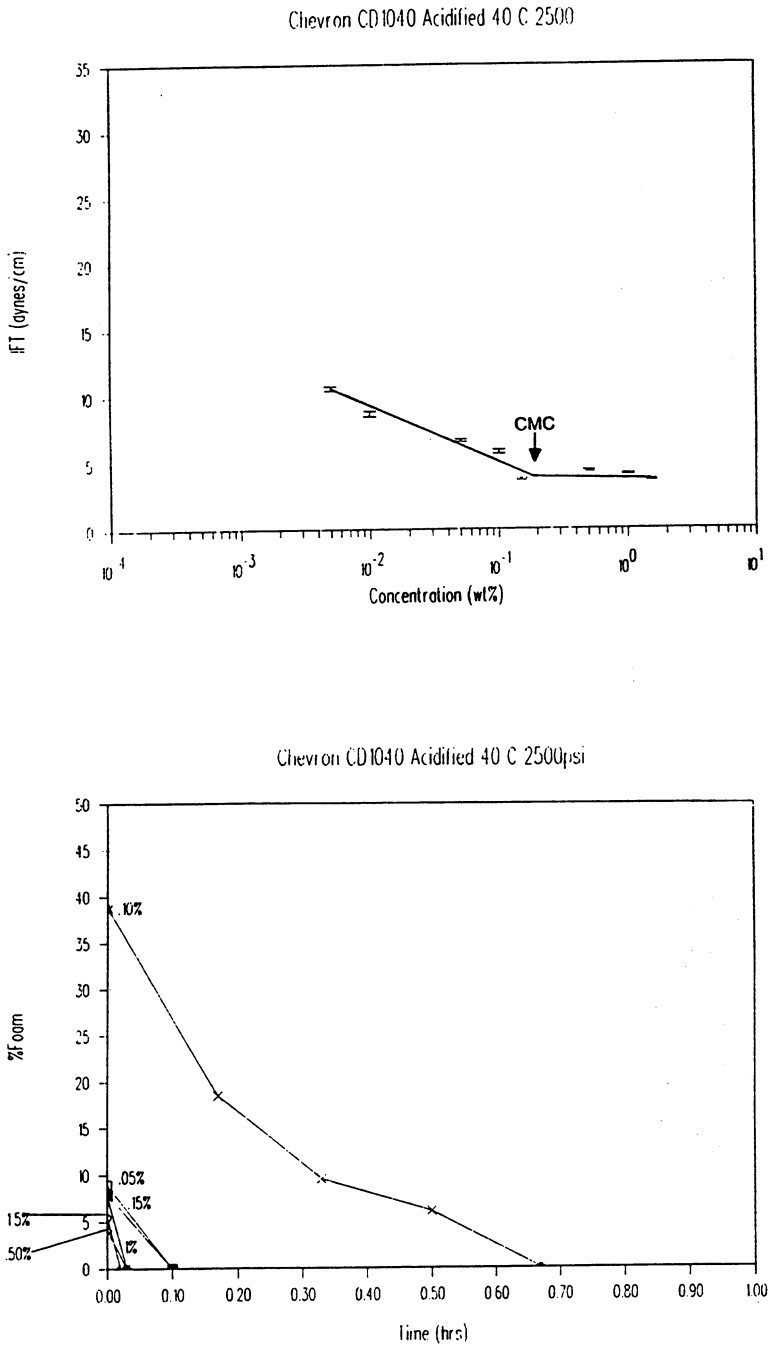

Figure II-90. Interfacial tension and foam decay of a Chevron CD1040 fresh-acidified sample in dense CO_2.

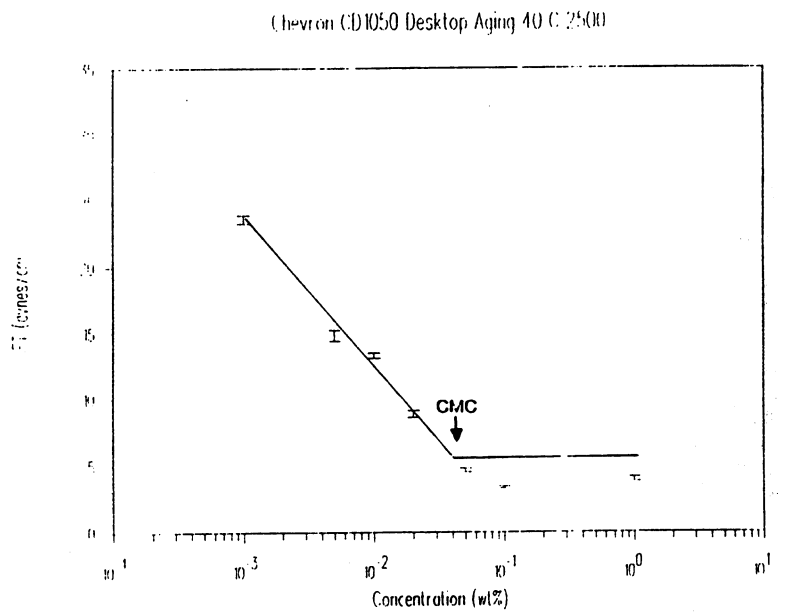

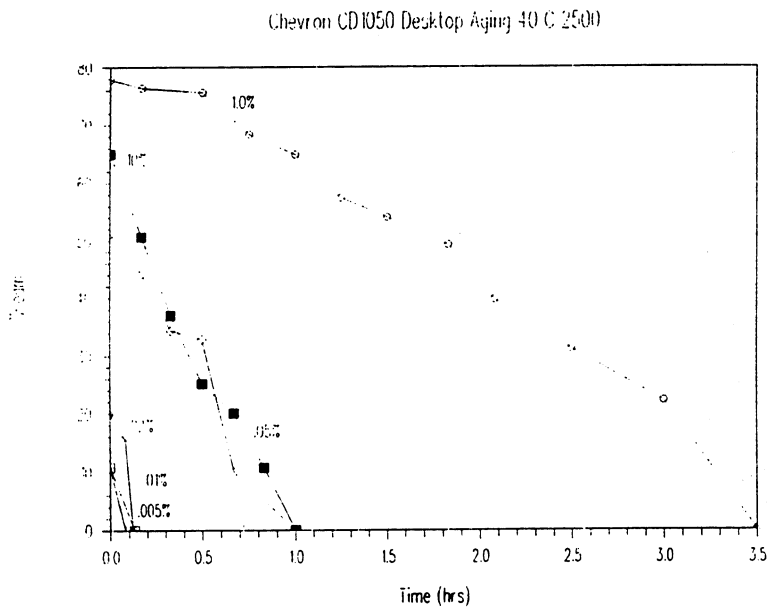

Figure II-91. Interfacial tension and foam decay of a Chevron CD1050 desktop-aged sample in dense CO_2.

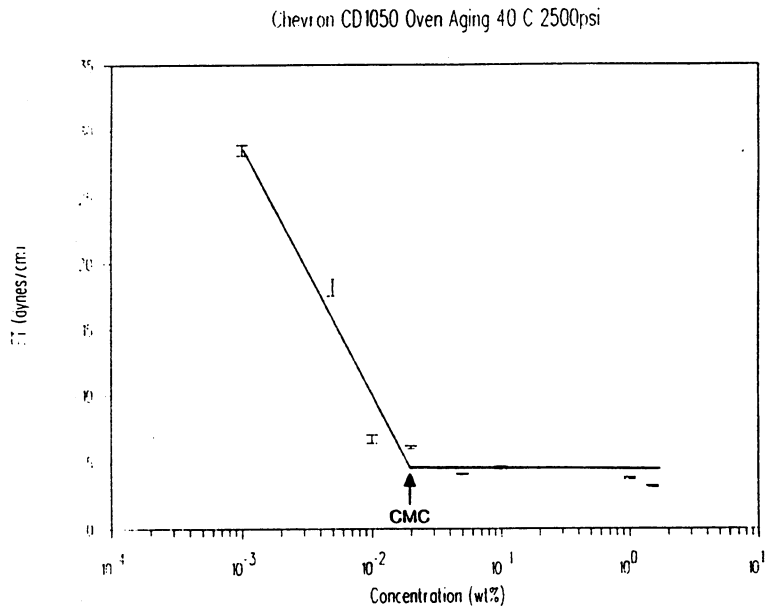

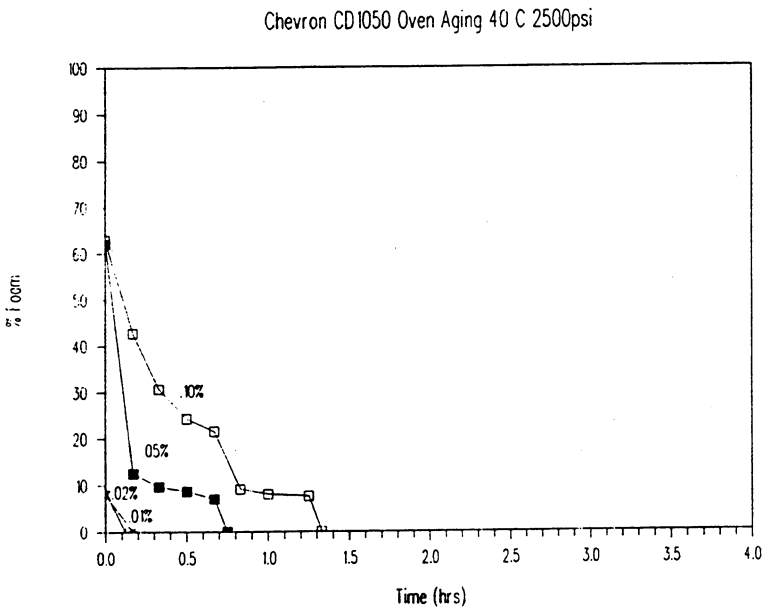

Figure II-92. Interfacial tension and foam decay of a Chevron CD1050 oven-aged sample in dense CO_2.

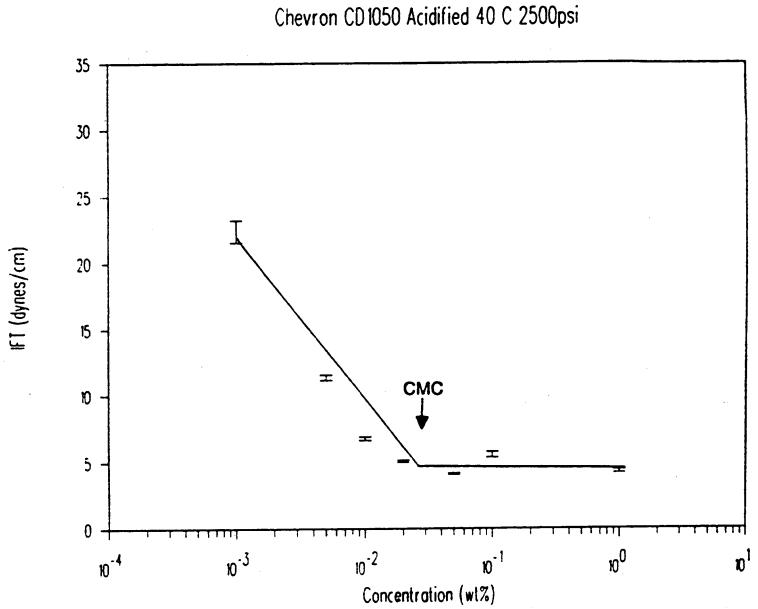

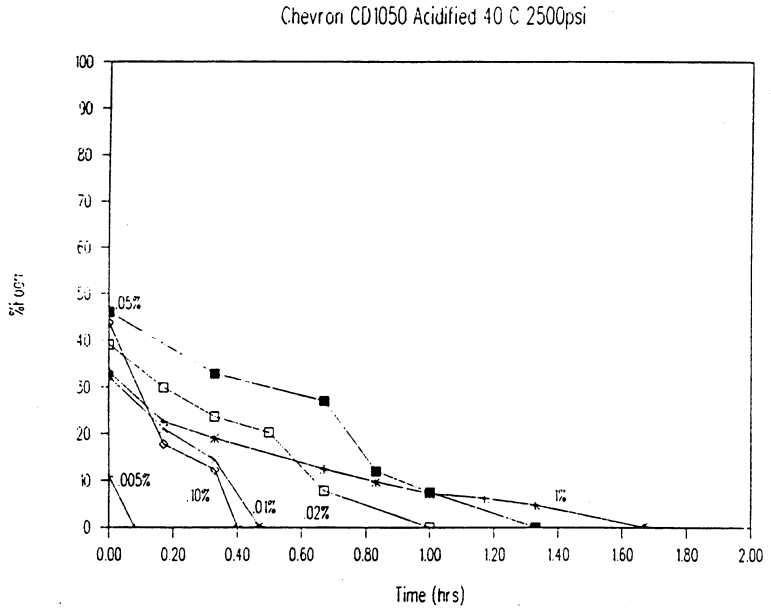

Figure II-93. Interfacial tension and foam decay of a Chevron CD1050 fresh-acidified sample in dense CO_2.

surfactants, Cheveron CD1040 and CD1050, were tested. Each surfactant was first acidified to a pH of 3.0 at room temperature and then separated into two batches. The desktop sample was aged at room temperature for 30 days; whereas the other sample was aged in the oven at 50°C for 30 days. Following the 30 days of aging time, a foam durability test and interfacial tension measurements for the dense CO_2 and each sample were conducted at conditions of 40°C and 2500 psig. In addition, a batch of fresh, acidified, but unaged sample was also prepared and tested to allow comparison.

For most of the aged samples, the pH value did not change significantly after 30 days of aging time. The CMC value of CD1040 also showed no evidence of change for the three samples (all were 0.15 wt%). On the other hand, the CMC value for the desktop-aged CD1050 was 0.05 wt%. The CMC value was found to decline to 0.04 wt% for a fresh, acidified sample and to 0.03 wt% for an oven-aged sample.

For the CD1040 surfactant, a greater amount of durable foam was formed among the aged samples in comparison to the fresh sample. But for the CD1050 surfactant, no significant difference in the foamablity and durability was found for the fresh and aged samples. Therefore, these two surfactants can sustain temperature changes over a 30-day period without affecting their foamability and durability.

In summary, several surfactants were tested in the foam durability experiments. It was proven that the foam durability apparatus is a useful device for the fairly rapid screening of surfactants at reservoir conditions. Although we have not had a standard to connect the durability of foam in this experiment and the effectiveness of the surfactant in the reservoir, the results from these experiments should strongly support other measurements in our study.

3. Dynamic Adsorption Experiment

Because of the nature of the foamant surfactant, it tends to be adsorbed onto the pore surfaces of the reservoir. The amount of surfactant adsorbed and retained on the rock within the time frame of the flood is, therefore, critical to the effectiveness of a mobility control operation. In addition, some of the surfactant desorbed from the rock will result in a chromatographic delay and affect the flow of the surfactant front. These two parameters, the chromatographic delay and the quantity of surfactant irreversibly adsorbed at a given flow rate, are important for the design of a field application of CO_2-foam. Therefore, we set up a dynamic adsorption experiment to determine these two parameters at reservoir flow rates.

In previous years, we have used a differential refractometer for in-line detection of surfactant concentration for conducting dynamic adsorption experiments. Although this instrument had sufficient sensitivity and was convenient to use, questions have been raised about results obtained with it because the use of the differential refractometer is not specific for a given surfactant. Early last year, the feasibility of two alterative in-line surfactant detection techniques, the photometric method and the drop-weight method, was studied. Since the photometric method can only be applied to specific surfactants having chromophores, much time was spent on the development of a much more general method—a modified drop-weight method, which enables the measurement of the surface tension of the output fluid.

The main device used for the modified drop-weight method is a standard slot-type edge detector that is a LED/phototransistor pair mounted below the tube on which the drops are formed. This device is wired into a simple circuit that sends out a signal when a drop passes between the light source and the detector. This signal is fed into a convenient input port of a PC computer so that the drop can be

observed. A computer program continually polls this input and records the successive time intervals between drops.

In the modified drop-weight method, the surface-tension values are calculated by measuring the time between drops rather than the weight of each drop. Therefore, a constant rate for the delivery of the fluid is required. To attain a constant rate delivery source, we have tried several devices.

A hydrostatic head was first adapted as a driving force for fluid flow in the very early stages of this study. But it was adequate only when the resistance of flow in a system was very small. Installing a hydrostatic head large enough to conduct flowing experiments in a core was not used because it would have been inconvenient and impractical. The second method used was to implement a constant pressure driving force in conjunction with a micro-needle valve to adjust the required fluid rate. Unfortunately, the instantaneous flow rate resulting from such a setup has an unexpected variation. This problem has been addressed in our Third Quarterly Report.[49] Finally, a constant rate pump was used in conjunction with a device designed to smooth out short-term variations in the motor drive rate. The constancy of the fluid delivery rate of an ISCO pump by itself was evaluated. Figure II-94 presents a 1 wt% brine effluent profile emerging from the drops detector. The inter-drop time intervals (represented as 54.925 ms. ticks between drops) showed a short-term variation. The average time interval in this case was 1620 (or 88.98 seconds) with a relative standard deviation of 1.3%. This variation was considered too high to be tolerated for use in the measurement of surface tension. As a consequence, a pulse dampener was constructed to modify and smooth the fluid delivery rate. Figure II-95 shows evidence of improvement, where the inter-drop time intervals are more consistent than shown in Fig. II-94: the relative standard variation has been decreased from 1.3% to approximately 0.3%.

4. Description of the Experiment and Apparatus

The setup of this experiment has gradually changed because of the modifications that we have done to the fluid delivery method, so experiments in this area are not yet complete. Nevertheless, the method of analysis and some of the preliminary results are described below.

The schematic of the latest experimental apparatus is shown in Fig. II-96. An ISCO pump is used to deliver fluid at a constant rate. Soltrol-130 oil is used as a buffer solution to displace the brine solution in a transfer vessel. The pulse dampener, between the transfer vessel and a Rheodyne sampling valve, is used to smooth the fluid flow as needed. The two sampling valves used are the type designed for liquid chromatography (LC). One is used for loading the surfactant sample by way of syringe injection. Another one is used to direct the fluid flow through either a capillary tube or a core sample. The fluid flowing through the system emerges from the drop detector, and the inter-drop time intervals are measured and recorded.

The core sample is put into a rubber sleeve inside a core holder where overburden pressure is applied outside of the sleeve with distilled water. The core is degassed and completely saturated with the brine solution before it is used in the experiment.

To completely measure adsorption of a given rock sample, we plan to conduct three experiments. The first experiment (Experiment A) is a nonadsorption experiment in which flow through the capillary tube is used. Different concentrations of surfactant solution prepared in brine will be loaded into the

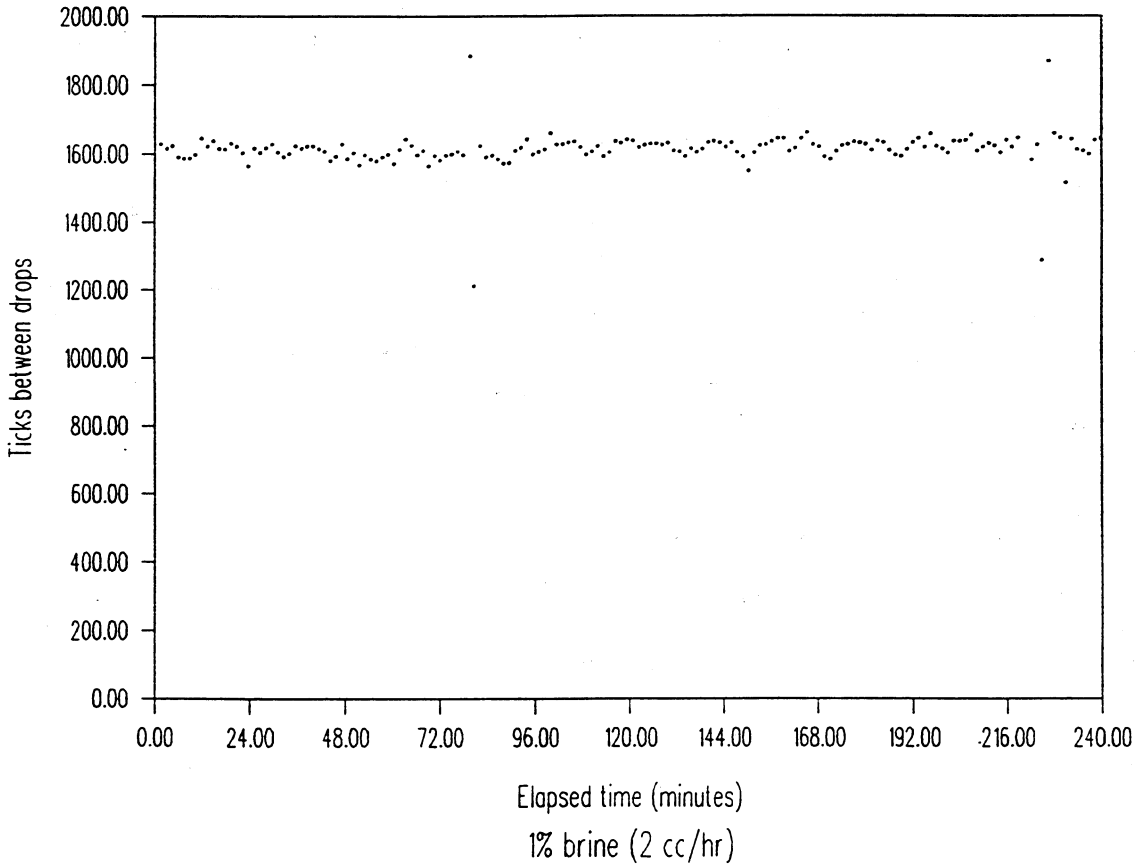

Figure II-94. Effluent profile of 1 wt% brine solution without a pulse dampener.

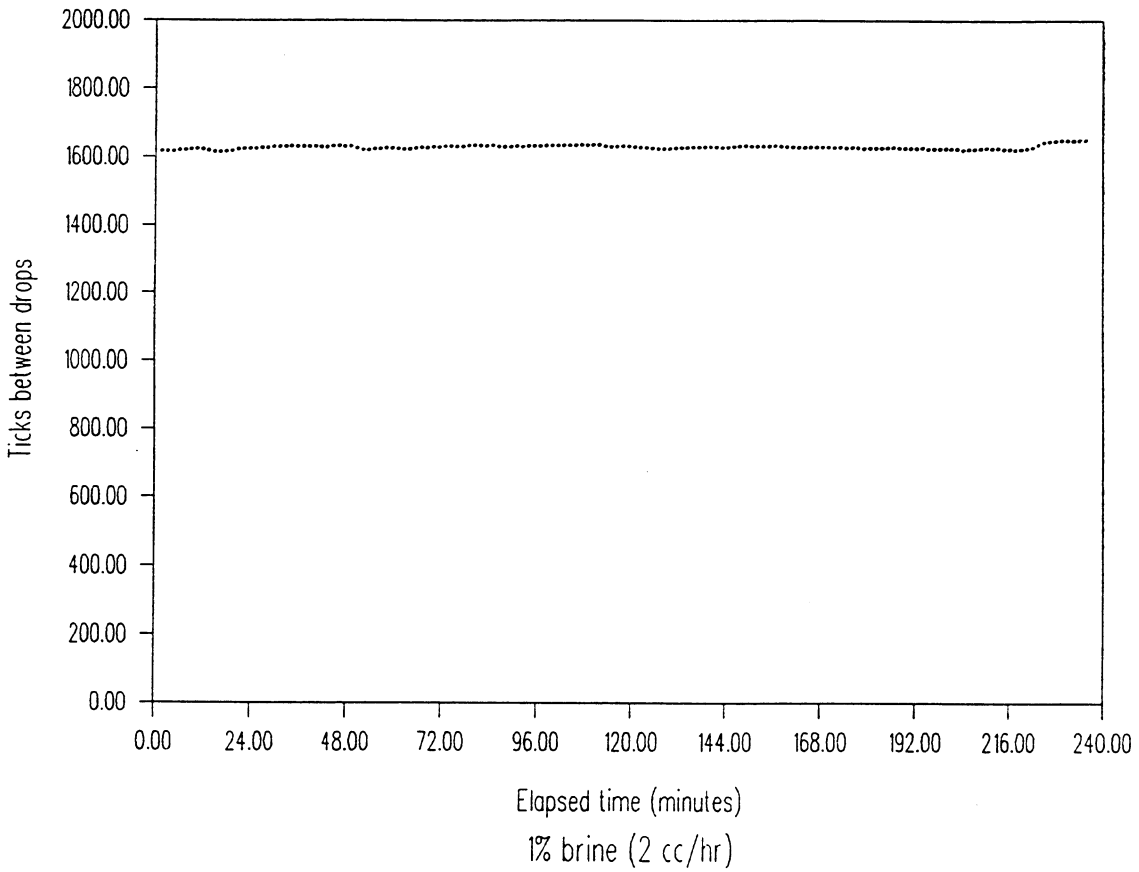

Figure II-95. Effluent profile of 1 wt% brine solution with a pulse dampener.

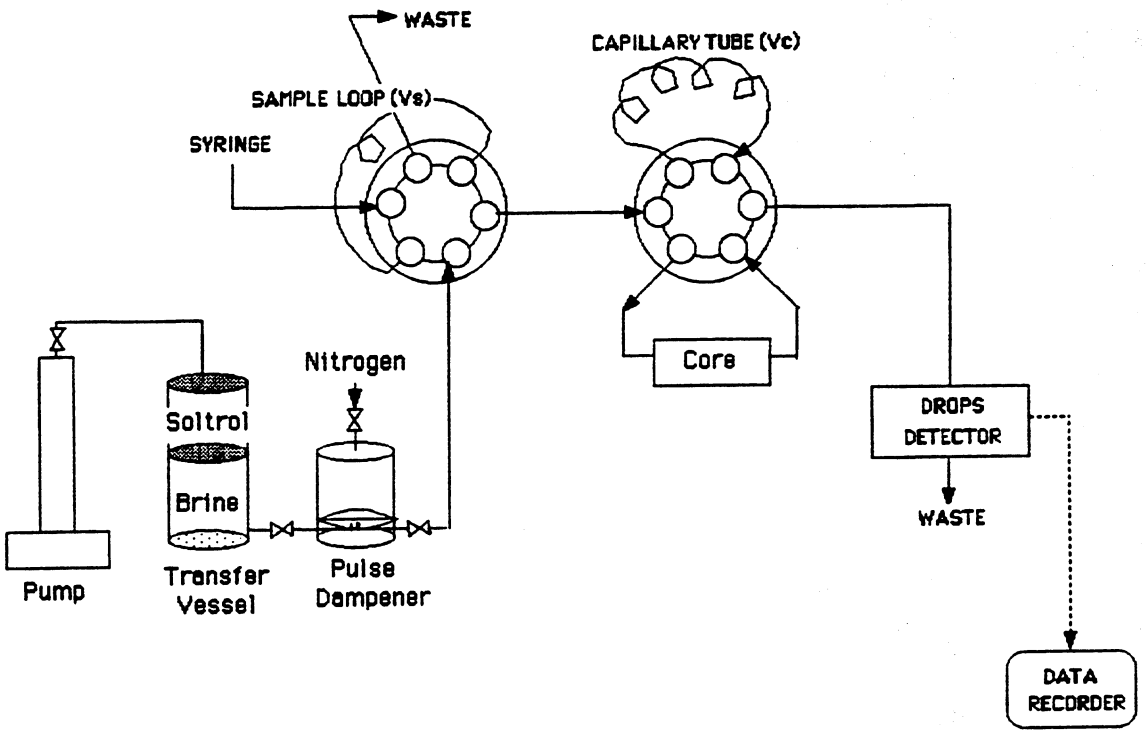

Figure II-96. Schematic of the modified drop-weight method apparatus.

sample loop (its sample volume is about 1 cm^3) in a sequence for obtaining the calibration curve of that certain type of surfactant.

The calibration curve is important to the remaining analysis of this adsorption experiment. Conventionally, a well known equation[50]

$$\gamma = \frac{Mg}{2\pi rF} \tag{II-8}$$

where

γ is the surface tension of the liquid,
M is the mass of the drop,
g is the gravitational acceleration constant,
r is the radius of the tip, and
F is the correction factor

used to determine the surface tension of a liquid.

By substituting the mass of each drop, M, with the volume of each drop, V, and density of the liquid, ρ, in Eq. (II-8), we will have

$$\gamma = \frac{\rho Vg}{2\pi rF} \tag{II-9}$$

and if the rate of delivery Q is constant,

$$Q\Delta t = V \tag{II-10}$$

where Δt represents the inter-drop time interval, then Eq. (II-9) becomes

$$\gamma = \frac{\rho gQ\Delta t}{2\pi rF} \tag{II-11}$$

Equation (II-11) implies that the surface tension of any liquid-air is proportional to the density of the liquid, ρ, the flow rate, Q, and the time intervals between each drop, Δt. This method can also be used for solutions, but it is not well suited to systems that slowly establish their equilibrium surface tension,[51] which means the flow rate, Q, should be limited to some extent such that the equilibrium surface tension of the solution can be reached.

In this modified drop-weight method, we will measure the time interval between drops as the fluid emerges from the drop detector. If there is only one liquid medium flowing through the system, the time interval for each drop should be constant. Any change of inter-drop time interval will be caused by the change of surface tension of the fluid at a given constant rate. As a consequence, when a slug of surfactant flows with the liquid medium brine and if the size of the slug is big enough, two constant sections of Δt will be observed in the effluent profile. Since

$$\gamma_s = \frac{\rho_s g Q \Delta t_s}{2\pi r F_s} \tag{II-12}$$

$$\gamma_b = \frac{\rho_b g Q \Delta t_b}{2\pi r F_b} \tag{II-13}$$

where the subscripts stand for surfactant and brine, respectively. The relation between the two surface tensions (γ_s and γ_b) can be established as a product of density ratio, correction factor's ratio, and the inter-drop time interval's ratio between two fluid such as:

$$\frac{\gamma_s}{\gamma_b} = \frac{\rho_s}{\rho_b}\frac{F_b}{F_s}\frac{\Delta t_s}{\Delta t_b} \tag{II-14}$$

Assuming the densities of these two fluids are equal, Eq. (II-14) finally becomes

$$\frac{\gamma_s}{\gamma_b} = \frac{F_b}{F_s}\frac{\Delta t_s}{\Delta t_b} \tag{II-15}$$

It is adequate to say that the surface tension derived from Eq. (II-15) is a pseudo surface tension of the fluid tested because of the involvement of the correction factors. According to our estimation, when the ratio of two inter-drop intervals varies from 1.0 to 0.4, the variation of $\frac{F_b}{F_s}$ is in the range of 1.0 to 1.07. Therefore, even though the correction factor, F, is a function of the drop volume and the tip size in use, the variation of the F ratio is insignificant compared to the variation of the Δts. In addition, because the calibration curve is established against the same sample medium brine, different values of the inter-drop time interval ratio (or the normalized rate) will have the same basis and should represent different concentrations of surfactant. Furthermore, the inherent variation of correction factor F will vanish when the surfactant concentration in the effluent is analyzed against the calibration curve.

Two calibration curves for surfactant solutions, Enordet X2001 in 1% brine and Chevron Chaser CD1050 in 4% brine, have been established. Figure II-97 shows the calibration curve for Enordet X2001, which is conducted at a flow rate of 2 cm^3/hr. The CMC value calculated from this plot is approximately 600 ppm. Since the relation between the normalized rate and surfactant concentration is almost linear in a semi-log plot, the capability of using this curve to interpret any other surfactant effluent profile as derived in the latter adsorption experiment is expected to extend to 10 ppm. Figure II-98 shows another calibration curve for CD1050 surfactant. Two similar curves represent the calibration curves at flow rates of 2 cm^3/hr and 3 cm^3/hr. The CMC value calculated from this curve is approximately at 200 ppm.

Once we have established the calibration curve, we need to conduct two other types of experiments to complete the adsorption experiment. The second type of experiment (Experiment B) is also a nonadsorption experiment. A presumably nonadsorbed tracer will be loaded into the sample loop and directed so that it flows through the core sample. The retention time of this slug of tracer will be measured by recording the time required before its peak is observed.

The last type of experiment (Experiment C) is designed to yield information on the amount of surfactant that is actually adsorbed onto the rock. The variation of surfactant concentration at the outlet of the core sample is measured after the injection of a "slug" of surfactant. The experiment is dynamic because the equilibrium level of adsorption at any point along the rock sample is a function of the concentration of the slug in the solution, which depends on the slug's position along the core and on time.

Although no type-C experiments have been completed thus far, the following results are expected. The surfactant concentration will be proportional to the measured peak height or the peak area in an effluent profile. The peak area of surfactant after flowing through the core in Experiment C will be smaller than the one after flowing through the tube in Experiment A. The ratio of the former peak area to the latter one is expected to indicate the amount of surfactant permanently or irreversibly adsorbed on the rock within the time frame of the experiment.

Furthermore, the time required to observe a peak after surfactant flow through the core should be longer than that measured in Experiment B using the nonadsorbed tracer through the same core. This indicates chromatographic delay or a reversible adsorption. The reversible adsorption means that the surfactant adsorbed onto the rock can be desorbed as well, within the times determined by the flow rates. This information provides the expected chromatographic delay of the surfactant front in the reservoir.

Despite the fact that this experiment is not yet complete, the feasibility of the modified drop-weight method has been proven to be practical in the application of dynamic adsorption experiments. Further laboratory work will be conducted to determine the amount of surfactant adsorbed and the chromatographic delay in different rock samples so that more information can be provided for field applications.

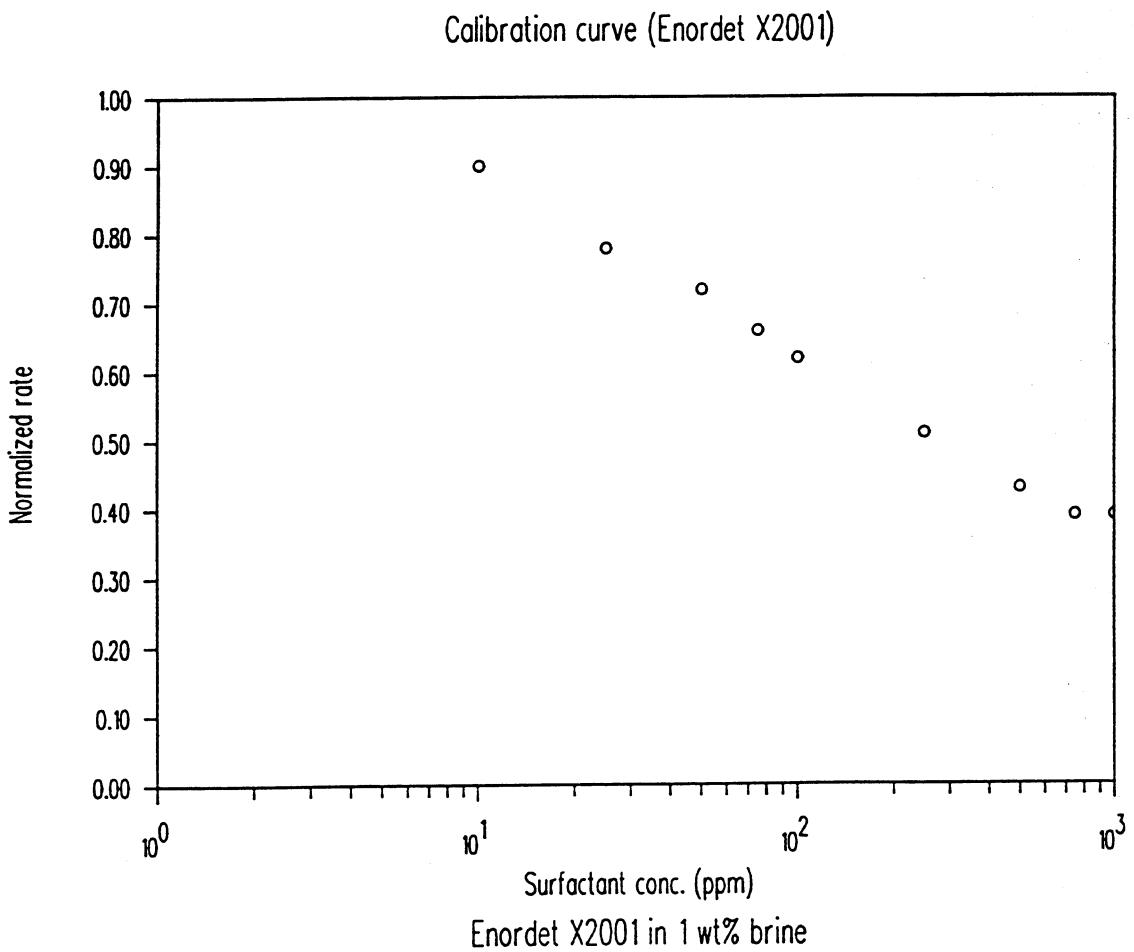

Figure II-97. The calibration curve for Enordet X2001/1 wt% brine solution.

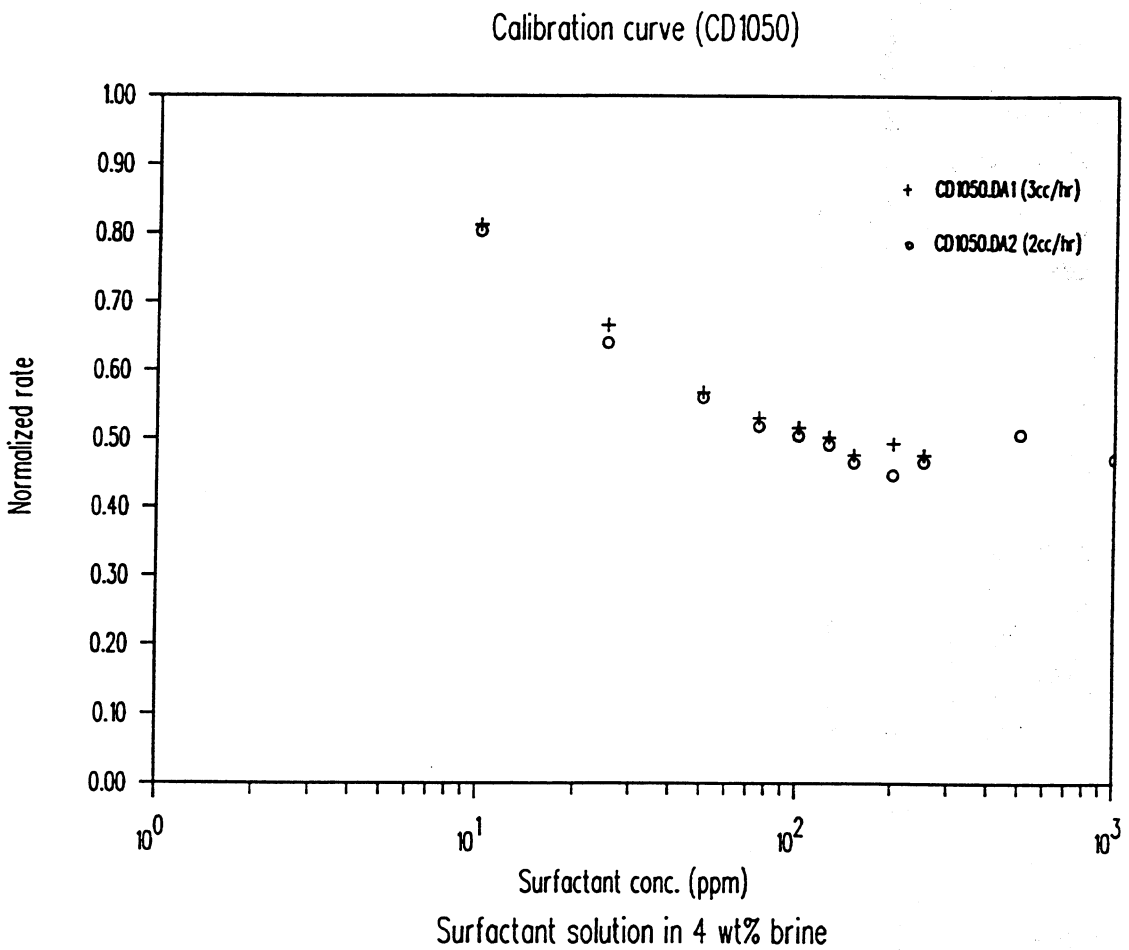

Figure II-98. The calibration curve for Chevron CD1050/4 wt% brine solution.

D. FOLLOW-ON PROJECT—FIELD VERIFICATION OF CO_2 FOAM

This project is supported by the Department of Energy, the New Mexico Research and Development Institute, and a number of companies with interest in the application of CO_2-foam for EOR in the Permian Basin of New Mexico and Texas. Its objectives are:

- to conduct reservoir studies, laboratory tests, simulation runs, and field tests to evaluate the use of foam for mobility control or fluid diversion in a New Mexico CO_2 flood,

- to evaluate the concept of CO_2-foam in the field by using a reservoir where CO_2 flooding is ongoing, characterizing the reservoir, modeling the process, and verifying the effectiveness.

Seven tasks were identified for the successful completion of this four-year project.

(1) Evaluate and select a field site.
(2) Develop an initial site-specific plan.
(3) Conduct laboratory CO_2-foam mobility tests.
(4) Perform reservoir simulations.
(5) Design the foam slug.
(6) Implement a field test.
(7) Evaluate the results.

By evaluating information from candidate CO_2 floods, a suitable field in New Mexico, the East Vacuum Grayburg/San Andres Unit (EVGSAU) has been identified as an appropriate site for the work. This field is operated by the Phillips Petroleum Company for a number of interest owners, including several other major oil companies. The initial site-specific plan was developed and submitted to the Unit Working Interest Owners at a meeting in Odessa, Texas, on May 21, 1990. The operator submitted ballots for project approval and after their due consideration, a sufficient number of Unit Working Interest Owners voted in favor of the project. It was approved on June 25, 1990. To date, Task 1 and most of Task 2 have been completed.

The first batch of representative cores (recovered from a well in a nearby pattern) have been received from Phillips Petroleum Company, and initial tests have been performed on them in our laboratories. Plugs were cut from these cores and tested. The only tests completed so far are CO_2-foam mobility tests, using several of the surfactants that have been proposed for use. We have also performed some geological examinations and minipermeameter measurements and plan to commence surfactant adsorption tests shortly.

A Joint Project Advisory Team, consisting of engineering representatives from Phillips, interested Interest Owners (Arco, Chevron, Exxon, Marathon, Mobil, Oxy, and Texaco), the Department of Energy, and PRRC, has been organized. This team has held three technical meetings, at which numerous details of the project were discussed and decided. A suitable pattern in EVGSAU has been selected, and design considerations have been discussed. The advisory team has agreed that an observation well in the pattern area would be desirable for providing cores and logs to improve reservoir characterization as well as for monitoring foam performance. The pattern selection was based on the criterion that the production there was typical of that from other patterns, and that the well's record of CO_2 breakthrough does not differ greatly from the rest of the field.

Phillips, as operator of the field, will perform all onsite operations pertaining to the drilling, completion and operation of the observation well to be drilled, and the well is to be owned by EVGSAU. The observation well will be located approximately 150 feet to the west of the CO_2-foam injection well of the chosen pattern. This location is such that the observation well will be situated to the north of a direct line from the injector to the producer with the worst history of the pattern for rapid CO_2 breakthrough. Approximately 450 feet of core is proposed to be cut through the San Andres interval, with approximately 120 feet being sponge core to recover some of the residual fluids expelled from the core during its trip to the surface. Detailed plans have also been made for the initial logging program to secure geological and fluid saturation information.

The Field Verification project is proceeding and making good progress. We expect that with the continued cooperation and support from the sponsoring agencies and companies, much can be learned about the use of the research that has been performed. Furthermore, we expect that a successful demonstration of CO_2-foam in this project will enable other operators to make use of this technology to increase the production efficiency of CO_2 floods in other areas as well.

E. SUMMARY AND CONCLUSIONS

Enhanced, or Improved, Oil Recovery by CO_2 flooding has a promising future. As a result of the research presented in this report, as well as that performed at other institutions, ways are being developed by which additional recovery can be obtained from many fields that have been waterflooded extensively. The Nation seems prepared to abandon its major oil reserve, which is trapped in known fields. Although much of this unrecovered oil has been considered unrecoverable, the object of our research has been to show that this diagnosis is too pessimistic, at least for oil in reservoirs where CO_2 can be used. Not all of the unrecovered oil is susceptible to recovery by CO_2 flooding, of course, by virtue of its composition and the depth at which it is located.[52] Furthermore, the fields that contain much of the suitable oil are too far from economically available sources of CO_2, for advantage to be taken of this materials unique properties.

We anticipate, though, that for reservoirs in the Permian Basin and other locations where CO_2 is both available and effective, the results presented can be directly applicable.

In this research, we have:

- Designed and constructed a system by which the properties of reservoir mixtures can be measured, rapidly and continuously, at near equilibrium conditions;
- Defined more closely the pressure, temperature, and composition conditions that define the phase behavior of many mixtures of dense CO_2 with crude oils and natural gas;
- Measured the viscosity, density, and composition of the phases described above that occur during displacement of crude oil by CO_2 in reservoirs;
- Defined a new and more extensive viscosity correlation for use in simulations of CO_2 floods;
- Constructed and tested a mechanistic foam simulator to predict the results of CO_2 floods;

- Constructed and utilized high-pressure micromodels for the observation of CO_2-foam and its interaction with water and crude oil;

- Designed and constructed special apparatus to measure the mobility of CO_2-foam;

- Measured the mobility of CO_2-foam under reservoir conditions, with different surfactants at different concentrations and in different kinds of porous rock;

- Observed and measured the interfacial tension and coalescence time of CO_2-foam at reservoir conditions in a visual high-pressure cell, as a function of temperature and surfactant concentration at high CO_2 density, for different surfactants;

- Studied a number of polymers and other compounds that can make high-viscosity polymeric solutions in dense CO_2 and other nonpolar solvents, utilizing equipment designed and constructed in our laboratory;

- Identified a very promising class of ionomers that raise the viscosity of nonpolar fluids by molecular association, which should prove useful as direct thickeners in CO_2 floods;

- Investigated experimentally and theoretically the effect of the lateral dimension of an unstable miscible displacement on the growth of instability patterns;

- Investigated the effects of reservoir heterogeneity on the outcome of oil displacement by CO_2 and other miscible fluids and of the relevance of geostatistical description of the field to displacement efficiency;

- Developed and refined a method by which the geostatistical parameters of the distribution of effective permeability can be deduced from the results of a well-to-well tracer test;

- Constructed computer code by which a random field, generated to given specifications of correlation length and variance, can be conditioned to conform to the permeability at known data points;

- Investigated the small-scale heterogeneity of samples of porous rock, showing that the variabilities of permeability of both Berea and reservoir samples are sufficient to influence many common laboratory experiments; and

- In addition, many other research results have been presented in formal reports of this project and in published papers and presentations. A separate listing of these is included as an appendix to this report.

It is certainly true that more research on the general topic of CO_2 flooding remains. In addition, the research and engineering work required to tailor materials and procedures to particular fields is substantial. Nevertheless, we believe we have shown that stabilized CO_2 floods can be effective in reaching higher recovery efficiency. In particular, they can produce a larger fraction of the light oil that remains in known reservoirs that have been waterflooded to near their economic limit than can be done by more-conventional CO_2 flooding procedures.

In conclusion, we recommend the following as areas for further research:

a. Further measurements of the properties of mixtures of crude oil and CO_2, in the presence of Methane and Nitrogen.

b. Integration of geological knowledge with geostatistical description.

c. Integration of small and larger scale measurements of the variability of rock properties, with more measurements at both ends of the scale.

d. Investigation of the limits of fractal and other geostatistical description of reservoirs.

e. Further development of direct thickeners for CO_2. During this last year of our project, a very promising series of ionomers have been discovered. We will hopefully be able to continue with this work under a separate research project, a proposal for which has already been sent to the Department of Energy. We are also soliciting industry support for it.

f. Further examination of fundamental problems in the use of CO_2-foam. These include research into the more fundamental chemical description of the attributes needed by an effective surfactant. CO_2-foam promises a partial, but immediately available solution to Improved Oil Recovery. A demonstration project, entitled the Field Verification of CO_2-Foam, is now being pursued in collaboration with a number of interested oil companies, the Department of Energy, and the New Mexico Research and Development Institute. A brief description of this project is given in a separate section of this Report.

F. REFERENCES

1. Heravi, N.E.: "Five-Spot Displacement at Unit Mobility Ratio in Reservoirs with Heterogeneous Permeability," MS thesis, New Mexico Inst. of Mining and Technology, Socorro, NM (Sept. 1988).

2. Abdalla, E.: "Numerical Simulation of Pattern Miscible Displacement in a Heterogeneous Formaton with Varied Well Position," MS thesis, New Mexico Inst. of Mining and Technology, Socorro, NM (Dec. 1990).

3. Gutjahr, A.: Professor of Mathematics, New Mexico Inst. of Mining and Technology, Socorro, NM, personal conversation, Oct. 1990.

4. Sultan, A.J. and Heller, J.P.: "Rock Heterogeneity and Geostatistical Methods," PRRC Report No. 89-9 (1989).

5. Journel, A.G. and Huijbregts, C.J.: *Mining Geostatistics*, Academic Press (1978).

6. Heller, J.P.: "Observations of Mixing and Diffusion in Porous Media," Fundamentals of Transport Phenomena in Porous Media, *Proc.*, Second Symposium, IAHR-ISSS, Guelph, Ontario (1972) 1-26.

7. Matheron, G.: "The Intrinsic Random Function and their Applications," *Advan. Appl. Prob.* (1973) 5, 439-468.

8. Montoglou, A. and Wilson, J.L.: "The Turning Bands Method for Simulation of Random Fields Using Line Generation by a Spectral Method," *Water Resour. Res.* (1982) 18, 5.

9. Gutjahr, A.L.: "Fast Fourier Transforms for Random Field Generation," New Mexico Tech Project Report, LANL Contract 4-R58-2690R (1989).

10. Sultan, A.J, Heller, J.P., and Gutjahr, A.L.: "Generation and Testing of Random Fields and the Conditional Simulation of Reservoirs," presented at the International Technical Meeting, Calgary, CIM/SPE 90-98 (1990).

11. Desbarats, A.J.: "Spatial Averaging of Transmissivity," Geological Survey of Canada (1990).

12. McCaffery, F.G., Sigmund, P.M., and Fosti, J.C.: "Pore Space and Displacement Characteristics of Carbonate Reservoir Rocks," paper presented at the 6th Formation Evaluation Symposium of the Canadian Well Logging Society, Calgary, Oct. 1977.

13. Heller, J.P., Dandge, D.K., Donaruma, L.G., and Card, R.G.: "Direct Thickeners for Mobility Control of CO_2 Floods," *SPEJ* (Oct. 1985) 679-686.

14. Dandge, D.K. and Heller, J.P.: "Polymers for Mobility Control in CO_2 Floods," paper *SPE* 16271 presented at the 1987 *SPE* International Symposium on Oil-Field Chemistry, San Antonio, Feb. 4-6.

15. Barton, A.F.M.: *Handbook of Solubility Parameters and Other Cohesion Parameters,* CRC Press, Boca Raton, FL (1983).

16. Hildebrand, J.H. and Scott, R.L.: *Solubility of Non-Electrolytes*, 3rd Ed., Reinhold Publishing Corporation, New York (1950).

17. Heller, J.P. and Kovarik, F.S.: "Improvement of CO_2 Flood Performance," Fifth Annual Report, DOE/MC/21136-21, (July 1989).

18. Bae, J.H. and Irani, C.A.: "A Laboratory Investigation of Thickened CO_2 Process," paper *SPE* 20467 presented at the 65th Annual Technical Conference of *SPE*, New Orleans, Sept. 23-26, (1990).

19. Dandge, D.K., Taylor, C., and Heller, J.P.: "Associative Organotin Polymers. I. Symmetric Trialkyltin Fluorides: Synthesis and Properties," *J. Polym. Sci: Part A: Polymer Chemistry* (1989) Vol. 27, 1053-1063.

20. Taylor, C.: "Synthesis, Characterization, and Solution Properties of Trialkyltin Fluorides," MS thesis, New Mexico Institute of Mining and Technology, Socorro, NM (1987).

21. Dandge, D.K., Taylor,C., Heller, J.P., Wilson, K.V., and Brumley, N.: "Associative Organotin Polymers. 2. Solution Properties of Symmetric Trialkyltin Fluorides," *J. Macromol. Sci.-Chem.* (1989) **A26** (10) 1451-1464.

22. Heller, J.P. and Dandge, D.K.: "Topical Viscosity Control for Light Hydrocarbon Displacing Fluids in Petroleum Recovery and in Fracturing Fluids for Well Stimulation," U.S. Patent No. 4,607,696 (1986).

23. Seyferth, D.J.: "Neopentyl Group Analog. I. The Preparation and Some Cleavage Reactions of Trimethylsilyl Methyl-Substituted Tin Compounds," *J. Am. Chem. Soc.* (1957) **79**, 5881.

24. Dandge, D.K., Singh, P.K., and Heller, J.P.: "Associative Organotin Polymers: Triorgano Fluorides in Miscible Gas Enhanced Oil Recovery," presented at the 1988 Symposium on Advances in Oil-Field Chemistry, Division of Petroleum Chemistry, Inc., Am. Chem. Soc., Toronto, June 5-11, *ACS Symposium Series* (1989) **396**, Chapter 29, 529-546.

25. Singh, P.K.: "Synthesis, Characterization, and Solution Properties of 5 Triorganotin Fluorides," MS thesis, New Mexico Institute of Mining and Technology, Socorro, NM (1987).

26. Agarwal, P.K., Makowski, H.S., and Lundburg, R.D.: "Viscoelastic behavior of Sulfonated Polymers: Sulfonated Ethylene-Propylene Terpolymer," *Macromolecules* (1980) **13**, 1679-1687.

27. Heller, J.P. and Martin, F.D.: "Improvement of CO_2 Flood Performance," Quarterly Report to DOE, NMRDI, and Industry (Oct.-Dec. 1989) PRRC Report No. 90-17 (April 1990).

28. Makowski, H.S. Lundberg, R.D., Singhal, G.H.: "Flexible Polymeric Compositions Comprising a Normally Plastic Polymer Sulfonated to about 0.2 to about 10 mole% Sulfonate," U.S. Patent No. 3,870,841 (March 11, 1975).

29. Heller, J.P. and Taber, J.T.: "Development of Mobility Control Methods to Improve Oil Recovery by CO_2," NMERDI 2-69-3307 (Feb. 1984).

30. Kovarik, F.S. and Heller, J.P.: "Improvement of CO_2 Flood Performance," Fifth Annual Report Oct. 1, 1988-Sept. 30, 1989, PRRC Report No. 89-22, New Mexico Petroleum Recovery Research Center, Feb. 1990.

31. Goethals, E.J.: *Telechelic Polymers: Synthesis and Applications*, CRC Press, Inc., Boca Raton, FL (1989).

32. Eisenberg, A. and Bailey, F.E.: "Coulombic Interactions in Macromolecular Systems," *ACS Symposium Series* (1986) **302**, ACS, Washington, DC.

33. Kennedy, J.P. and Smith, R.A.: "New Telechelic Polymers and Sequential Copolymers by Polyfunctional *Ini*tiator-Trans*fer* Agents (Inifers). II. Synthesis and Characterization of α,ω-Di(*tert*-chloro)polyisobutylenes," *J. Polym. Sci.* (1980) Vol. **18**, 1523-1537.

34. Holm, L.W. and Josendal, V.A.: "Mechanisms of Oil Displacement By Carbon Dioxide," *JPT* (Dec. 1974) 1427-1436.

35. Szwarc, M.: "Living Polymers," *Nature* (Nov. 1956) Vol. **178**, 1168-1169.

36. "Living Polymer Systems," *Encyclopedia of Polymer Science: Supplement* (1987) 380-445.

37. Kresge, E.D., Schatz, R.H., and Wang, H-C.: "Isobutylene Polymers," *Encyclopedia of Polymer Science* (1987) Vol. **8**, 423-448.

38. Hagashimura, T., Miyamoto, M., and Sawamoto, M.: "Mechanism of Living Polymerization of Vinyl Ethers by the Hydrogen Iodide/Iodine Initiating System," *Macromolecules* (1985) **18**, 611-616.

39. Faust, R. and Kennedy, J.P.: "Living Carbocationic Polymerization: III. Demonstration of Living Polymerization of Isobutylene," *Polym. Bull.* (1986) **15**, 317-323.

40. Kaszas, G., Puskas, J.E., Chen, C.C., and Kennedy, J.P.: "Electron-pair Donors in Carbocationic Polymerization. I. Introduction into the Synthesis of Narrow Molecular Weight Distribution Polysiobutylenes," *Polym. Bull.* (1988) **20**, 413-419.

41. Pratap, G., Mustafa, S.M., Hollis, W.K., and Heller, J.P.: "Living Carbocationic Polymerization of Isobutylene by *tert*-Amyl alcohol/BCl_3/1-Methyl-2-pyrrolidinone Initiating System," *J. Appl. Polym. Sci.*, (in Press) PRRC Report No. 90-51 (1990).

42. Pratap, G. and Heller, J.P.: "A New Initiating (*Minifer*) System for the Living Polymerization of Isobutylene," *J. Chem. Soc.: Chem. Commun.*, (under review) PRRC Report No. 90-39 (1990).

43. Pratap, G. and Heller, J.P.: "Electron-pair Donors in Carbocationic Polymerization: Synthesis of Linear Living α,ω-Di(*tert*-chloro)polyisobutylenes," *J. Polym. Sci.: Part A: Polym. Chem.*, (communicated) PRRC Report No. 90-48.

44. Heller, J.P.: "Computer Software for Gel Permeation Chromatography for Polymer Analysis," PRRC, Socorro, NM (1990).

45. Schmitt, W.J. and Reid, R.C.: "Solubility of Monofunctional Organic Solids in Chemically Diverse Supercritical Fluids," *J. Chem. Eng. Data* (1986) **31**, 204-212.

46. Dobbs, J.M., Wong, J.M., and Johnston, K.P.: "Nonpolar Co-Solvents for Solubility Enhancement in Supercritical Fluid Carbon Dioxide, *J. Chem. Eng. Data* (1986) **31**, 303-308.

47. Martin, F.D. and Heller, J.P.: "Improvement of CO_2 Flood Performance," Fifth Annual Report (Oct. 1988-Sept. 1989) PRRC Report No. 89-22 (Feb. 1990).

48. Lee, H.O. and Heller, J.P.: "Change in Apparent Viscosity of CO_2-Foam with Rock Permeability," paper SPE/DOE 20194 presented at the Seventh Symposium on Enhanced Oil Recovery, Tulsa, Apr. 22-25, 1990.

49. Kuhlman, M.I. and Falls, A.H.:"Carbon Dioxide Foam with Surfactants Used Below Their Critical Micelle Concentrations," paper SPE/DOE 20192 presented at the Seventh Symposium on Enhanced Oil Recovery, Tulsa, Apr. 22-25, 1990.

50. Adamson, A.W.: *Physical Chemistry of Surfaces*, Fifth Edition, John Wiley & Sons, Inc. (1990).

51. Martin, F.D. and Heller, J.P.: "Improvement of CO_2 Flood Performance," 3rd Quarterly Report to DOE, NMRDI, and Industry (Apr.-Jun. 1990) PRRC Report No. 90-34 (Sept. 1990).

52. Harkins, W.D. and Brown, F.E.: *J. Amer. Chem. Soc.* (1919) **41**, 499.

53. Jho, C. and Burke, R.: "Drop Weight Technique for the Measurement of Dynamic Surface Tension," *J. Coll. and Interface Sci.* (Sept. 1983) **95**, No. 1, 61-71.

54. Heller, J.P. and Taber, J.J.: "Improvement of CO_2 Flood Performance," Annual Report to the U.S. Dept. of Energy, No. DOE/MC/21136-6 (DE 86000283) Jun. 1986.

APPENDIX A

MFS 2.1:

MECHANISTIC FOAM SIMULATOR

Model Description and User's Manual

by

Shih-Hsien Chang

March, 1990

PRRC No. 90-7

NEW MEXICO PETROLEUM RECOVERY RESEARCH CENTER
NEW MEXICO INSTITUTE OF MINING AND TECHNOLOGY

Socorro, New Mexico

TABLE OF CONTENTS

I. MODEL DESCRIPTION 1

A. Introduction 1

B. Mathematical Formulation 1

C. Numerical Solution 7

D. Code Description 12

II. USER'S MANUAL 15

A. System Requirements 15

B. Setup of Parameter Values 15

C. Input and Output Files 15

D. Input Description for Input Data File 17

E. Input Description for Control File 24

F. Sample Problems 25

1. One-Dimensional Problem 25

2. Two-Dimensional Problem 29

NOMENCLATURE 62

REFERENCES 64

I. MODEL DESCRIPTION

A. Introduction

MFS, a two-dimensional mechanistic foam simulator, has been developed and is described in this report. This simulator is able to model many of the processes associated with channel blockage by foam and diversion of flow into the bypassed oil matrix. Foam is generated by the following mechanisms:[1,2] snap-off, lamella division, and leave-behind, all of which are included in the simulator. In addition, foam coalescence and trapping mechanisms are incorporated in the model.

The MFS is formulated by adding a conservation equation for the surfactant and a population balance equation[3] for the foam texture, one of the key variables governing foam mobility, to the usual three-phase conservation equations. The solution technique is implicit in pressure and explicit in saturation, surfactant concentration, and bubble density.

This report discusses the physics included in the MFS, describes the numerical solution, includes a user's guide, and presents sample problems.

B. Mathematical Formulation

The assumptions used in the model are as follows:

1. There are four components: oil, gas, water, and surfactant; and three phases: oil, gas, and water.
2. The amount of surfactant in the oil and gas phases is negligible.
3. Loss of surfactant by foam formation is negligible.
4. Surfactant concentration adsorbed on the rock (Γ) is in equilibrium with the surfactant concentration in the water phase (C_s).
5. Surfactant does not affect the mobility of the water phase.
6. Foam affects only the gas-phase mobility.
7. Darcy's law applies for the gas phase in the presence of foam.
8. Foam can not exist if the oil saturation (S_o) is larger than a limiting oil saturation (S_o^{lim}) or if the surfactant concentration (C_s) is less than a limiting surfactant concentration (C_s^{lim}).
9. Snap-off or lamella division only occurs above a critical gas velocity (V_c).
10. The flowing and trapped foams do not discriminate between pores of different size.

11. The process of foam trapping is instantaneous, and the bubble density of trapped foam (n_s) is in equilibrium with the bubble density of flowing foam (n_f).
12. The mass transfer among the bubbles has a negligible effect on the average bubble density.
13. Dispersion is negligible.

Some of the assumptions used in this model have been defined by others.[4,5]

The mass balance equation for each phase is

$$-\nabla \cdot (\rho_\ell \mathbf{U}_\ell) + q_\ell = \frac{\partial}{\partial t}(\rho_\ell \phi S_\ell) \tag{1}$$

where

$$\mathbf{U}_\ell = -\frac{k k_{r\ell}}{\mu_\ell}(\nabla P_\ell - \rho_\ell \mathbf{g}) \tag{2}$$

Here $\mathbf{g}$ is the gravitational acceleration vector, ϕ is the porosity, k is the absolute permeability, $\mathbf{U}$ is the Darcy's velocity, ρ is the mass density, S is the saturation, q is the production/injection rate per unit reservoir volume, μ is the viscosity, P is the pressure, k_r is the relative permeability, and the subscript ℓ refers to the phases, with $\ell = o$ for oil phase, $\ell = w$ for water phase, and $\ell = g$ for gas phase.

To track the surfactant concentration in the water phase (C_s), the following mass balance is included:

$$-\nabla \cdot (C_s \rho_w \mathbf{U}_w) + \hat{C}_s q_w = \frac{\partial}{\partial t}[C_s \rho_w \phi S_w + \rho_r (1-\phi)\delta\Gamma] \tag{3}$$

where

$$\hat{C}_s = \begin{cases} C_{sI} & \text{at injection} \\ C_s & \text{at production} \end{cases} \tag{4}$$

Here C_{sI} is the injected surfactant concentration, ρ_r is the mass density of rock, δ is the rock surface area per unit mass, and the surfactant concentration adsorbed on the rock (Γ) is given as:

$$\Gamma = \frac{K_s A_s C_s}{1 + K_s C_s} \tag{5}$$

where K_s is the adsorption equilibrium constant and A_s is the maximum surfactant concentration adsorbed on the rock.

Foam texture, the average bubble size, is one of the most important variables governing foam mobility.[6] To account for changes in foam texture, the population balances for the flowing and trapped foams are used. In view of the above assumptions, the bubble population balances can be combined as follows:

$$-\nabla \cdot (n_f \mathbf{U}_g) + G_f - C_f + \hat{n}_f \hat{q}_g = \frac{\partial}{\partial t}[X_f n_f \phi S_g + (1 - X_f) n_s \phi S_g] \tag{6}$$

where

$$\hat{q}_g = \frac{q_g}{\rho_g} \tag{7}$$

$$\hat{n}_f = \begin{cases} n_{fI} & \text{at injection} \\ n_f & \text{at production} \end{cases} \tag{8}$$

Here n_f is the bubble density of the flowing foam, n_s is the bubble density of the trapped foam, n_{fI} is the injected bubble density, X_f is the fraction of gas that is flowing, G_f is the bubble generation rate per unit reservoir volume, and C_f is the bubble coalescence rate per unit reservoir volume. The equilibrium relationship between n_s and n_f is described by[5]

$$n_s = \frac{K_f A_f n_f}{1 + K_f n_f} \tag{9}$$

where A_f and K_f are the bubble trapping parameters. The rate of bubble consumption by coalescence is modeled as follows:

$$C_f = K_2 n_f \left(\frac{C_{sref}}{C_s}\right)^{e_2} \left(\frac{|\mathbf{U}_g|}{U_{ref2}}\right)^{c_2} \tag{10}$$

where K_2 is the coalescence rate constant and $|\mathbf{U}_g|$ is the magnitude of $\mathbf{U}_g$. Equation (10) is motivated by the work of Khatib *et al.*[7] which indicates that the limiting capillary pressure for coalescence varies with gas velocity. In addition, the rate of coalescence is proportional to the number of bubbles, and the higher the surfactant concentration, the more stable the bubbles. In the region where foam can not exist, the rate of coalescence is infinite. The rate of bubble generation is given as:

$$G_f = K_1 \left[1 + \left(\frac{n_f}{n_c}\right)^{e_1}\right]^{-1} \left(\frac{|\mathbf{U}_g|}{U_{ref1}}\right)^{c_1} \tag{11}$$

where K_1 is the generation rate constant and n_c is the critical bubble density such that the generation rate approaches zero when n_f is much larger than n_c. The use of the velocity term in Equation (11) is motivated by the studies of others[5,8]

which indicate that steady foam flow resistance decreases with increasing gas velocity and by Equation (10) which indicates that the coalescence rate is a function of gas velocity. When the critical velocity is not exceeded, the rate of generation is zero. The critical velocity is calculated according to[5]

$$V_c = \frac{d}{{F_w}^e} \tag{12}$$

where F_w is the injected liquid volume fraction.

The gas-phase mobility is modified in the simulator according to the flow diagram shown in Figure 1. The basic concept is outlined below.

The first decision is whether or not foam is flowing. If foam is flowing, the gas-phase mobility is modified according to[4,5]

$$\mu_g^{(e)} = \mu_g K_3 n_f k^{1.5} \left(\frac{U_{ref3}}{|\mathbf{U}_g|} \right)^{c_3} \tag{13}$$

$$k_{rg}^{(e)} = X_f k_{rg} \tag{14}$$

where K_3 is a geometric factor. If the calculated viscosity falls below the gas viscosity, it is reset to the gas viscosity. The next decision is whether or not foam can occur. In order for foam to occur, the following conditions must be satisfied: $S_g > 0$, $S_o < S_o^{lim}$, and $C_s > C_s^{lim}$. If any of these conditions are not met, the gas-phase mobility is not modified. If foam can occur, the conditions to generate the static and flowing foams are checked. For leave-behind lamellae to occur, surfactant must be present in the water phase before gas invades that location in the porous medium. If this case occurs, the gas-phase relative permeability is modified according to[5]

$$k_{rg}^{(e)} = \frac{k_{rg}}{a} \tag{15}$$

where a is a reduction factor which is modeled as

$$a = 1 + bS_g \tag{16}$$

For flowing foam to occur, the gas velocity should be above a critical value. No distinction between the mechanisms of snap-off and lamella division is made here. If the gas velocity is above the critical value, the gas-phase mobility is modified according to Equations (13) and (14). When both static and flowing foams occur, the modification method yielding the lowest mobility is selected. When both static and flowing foams can not occur, no modification is made.

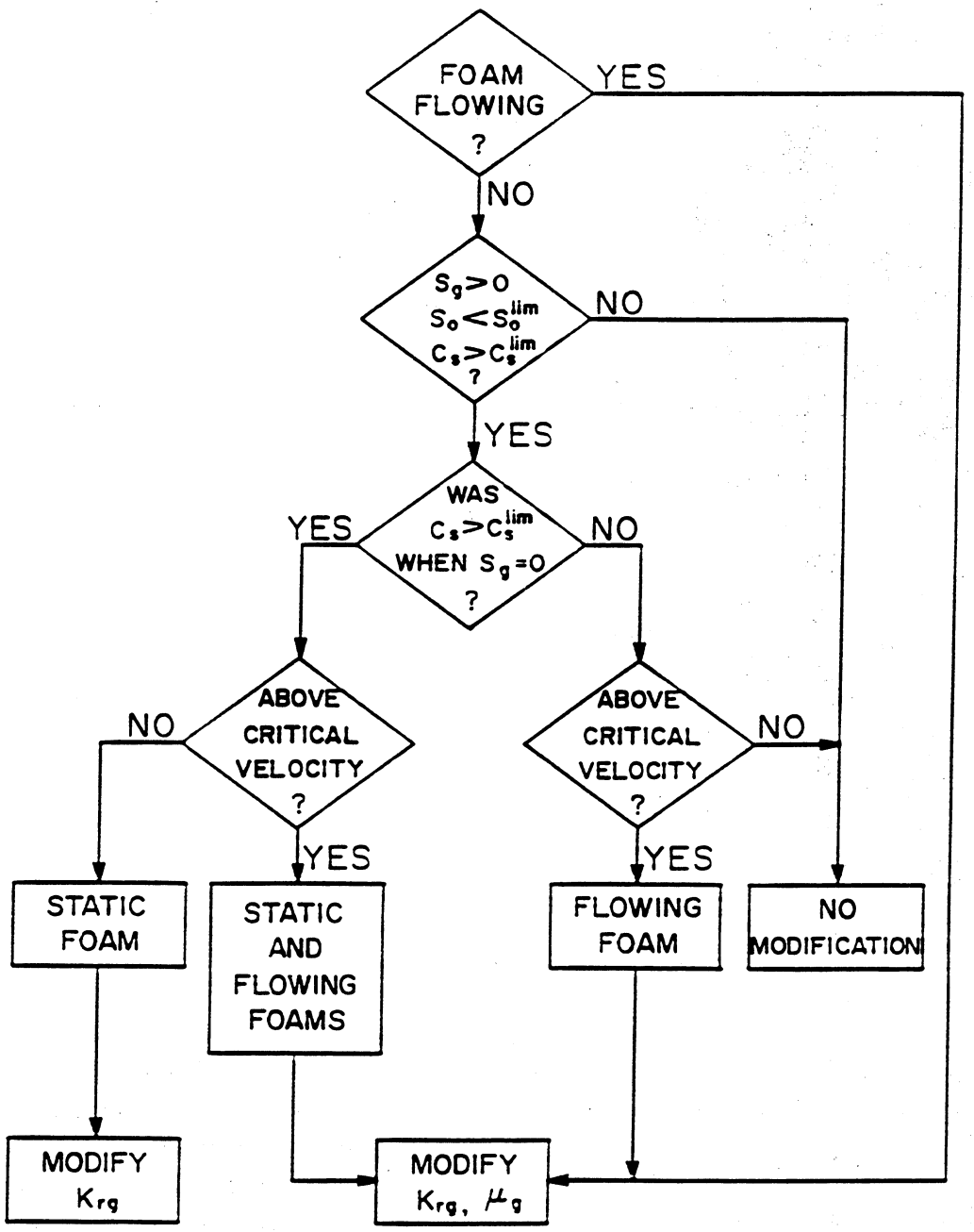

Figure 1. Flow diagram for the modification of gas-phase mobility.

Equations (1), (3), and (6) represent a system of nonlinear partial differential equations (PDEs) in space and time. To solve this set of PDEs, the following constraints are used:

$$S_o + S_g + S_w = 1 \tag{17}$$

$$P_{cgo} = P_g - P_o \tag{18}$$

$$P_{cow} = P_o - P_w \tag{19}$$

This set of PDEs is solved numerically, as described in Section C below.

In three-phase relative permeability calculations, the modified Stone method is used to calculate the oil-phase relative permeability as[9]

$$k_{ro} = \frac{1}{k_{rocw}}(k_{row} + k_{rw})(k_{rog} + k_{rg}) - (k_{rw} + k_{rg}) \tag{20}$$

where

$$k_{rocw} = k_{row}(S_w = S_{wc}) = k_{rog}(S_g = 0) \tag{21}$$

Here S_{wc} is the irreducible water saturation, k_{row} is the oil-phase relative permeability in an oil-water system, and k_{rog} is the oil-phase relative permeability in an oil-gas system. Equation (21) indicates that an oil-water system at S_{wc} and an oil-gas system at $S_g = 0$ are physically identical. This implies that the gas-oil data are measured in the presence of irreducible water.

All real reservoirs are, of course, three-dimensional; it is, however, possible in many practical situations to assume that flow in one of the three coordinate directions is negligible compared to flow in the other two directions. In this model, we consider only two-dimensional rectangular systems. If the fluids are injected into the left side of the system, we call this side the injection boundary and the right side of the system becomes the production boundary. The boundary conditions imposed are: (1) constant pressure at the production boundary, and (2) constant flow rate at the injection boundary. Both the water and gas phases are being injected simultaneously into the system at a constant flow rate. The surfactant is introduced into the system through the water phase. The top and bottom sides of the system are impermeable to the fluids.

C. Numerical Solution

The system of nonlinear PDEs, Equations (1), (3), and (6), are discretized using standard finite difference techniques.[10,11]

Expanding Equation (1) in Cartesian coordinates, we have

$$\frac{\partial}{\partial x}\left(\lambda_\ell \frac{\partial P_\ell}{\partial x}\right) + \frac{\partial}{\partial y}\left(\lambda_\ell \frac{\partial P_\ell}{\partial y}\right) + q_\ell = \frac{\partial}{\partial t}(\rho_\ell \phi S_\ell) \tag{22}$$

where

$$\lambda_\ell \equiv \frac{k k_{r\ell} \rho_\ell}{\mu_\ell} \tag{23}$$

for each phase ℓ. The variations in z-direction and the effect of gravity are not considered in this model.

In this model, the block-centered grid method is used to construct the grid system. The total system is divided into a number of grid blocks of equal size, and the grid points are placed in the center of the blocks. The grid block (i,j) corresponds to the grid point (x,y) where $x = \mathrm{i}\Delta x$ and $y = \mathrm{j}\Delta y$. Here, Δx is the length of the grid block, and Δy is the width of the grid block. In this model, the use of irregular grid size is not implemented. The finite-difference approximation to Equation (22), for each grid block (i,j) and for each phase ℓ, is

$$\begin{aligned}
&T_{\ell x}{}^{\mathrm{n}}_{\mathrm{i}+\frac{1}{2},\mathrm{j}}(P_{\ell}{}^{\mathrm{n+1}}_{\mathrm{i+1,j}} - P_{\ell}{}^{\mathrm{n+1}}_{\mathrm{i,j}}) - T_{\ell x}{}^{\mathrm{n}}_{\mathrm{i}-\frac{1}{2},\mathrm{j}}(P_{\ell}{}^{\mathrm{n+1}}_{\mathrm{i,j}} - P_{\ell}{}^{\mathrm{n+1}}_{\mathrm{i-1,j}}) \\
&+T_{\ell y}{}^{\mathrm{n}}_{\mathrm{i,j}+\frac{1}{2}}(P_{\ell}{}^{\mathrm{n+1}}_{\mathrm{i,j+1}} - P_{\ell}{}^{\mathrm{n+1}}_{\mathrm{i,j}}) - T_{\ell y}{}^{\mathrm{n}}_{\mathrm{i,j}-\frac{1}{2}}(P_{\ell}{}^{\mathrm{n+1}}_{\mathrm{i,j}} - P_{\ell}{}^{\mathrm{n+1}}_{\mathrm{i,j-1}}) + Q_{\ell}{}^{\mathrm{n+1}}_{\mathrm{i,j}} \\
&= \frac{\Delta V}{\Delta t}\phi_{\mathrm{i,j}}\rho_{\ell}{}^{\mathrm{n}}_{\mathrm{i,j}}(S_{\ell}{}^{\mathrm{n+1}}_{\mathrm{i,j}} - S_{\ell}{}^{\mathrm{n}}_{\mathrm{i,j}}) + \frac{\Delta V}{\Delta t}\phi_{\mathrm{i,j}} S_{\ell}{}^{\mathrm{n}}_{\mathrm{i,j}} \overline{\rho}_{\ell}{}^{\mathrm{n}}_{\mathrm{i,j}}(P_{\ell}{}^{\mathrm{n+1}}_{\mathrm{i,j}} - P_{\ell}{}^{\mathrm{n}}_{\mathrm{i,j}})
\end{aligned} \tag{24}$$

where

$$T_{\ell x}{}^{\mathrm{n}}_{\mathrm{i}+\frac{1}{2},\mathrm{j}} \equiv \frac{\Delta V}{(\Delta x)^2}\lambda_{\ell}{}^{\mathrm{n}}_{\mathrm{i}+\frac{1}{2},\mathrm{j}} \tag{25}$$

$$T_{\ell y}{}^{\mathrm{n}}_{\mathrm{i,j}+\frac{1}{2}} \equiv \frac{\Delta V}{(\Delta y)^2}\lambda_{\ell}{}^{\mathrm{n}}_{\mathrm{i,j}+\frac{1}{2}} \tag{26}$$

$$Q_{\ell}{}^{\mathrm{n+1}}_{\mathrm{i,j}} = q_{\ell}{}^{\mathrm{n+1}}_{\mathrm{i,j}}\Delta V \tag{27}$$

$$\triangle V \equiv \triangle x \triangle y \triangle z \tag{28}$$

$$\overline{\rho}_\ell \equiv \frac{d\rho_\ell}{dP_\ell} \tag{29}$$

Here, $\triangle z$ is the thickness of the system, $\triangle t$ is the time step, and the superscripts indicate the time level at which a quantity is to be evaluated. The transmissibilities, $T_{\ell x}$ and $T_{\ell y}$, are evaluated at time level n and at the block boundary (i,j$\pm\frac{1}{2}$) or (i$\pm\frac{1}{2}$,j); i.e., they are computed explicitly at the block boundary. In order to calculate the transmissibility, each quantity in Equation (23) must also be evaluated explicitly at the block boundary. Either the single-point upstream weighting method or the two-point upstream weighting method can be used to calculate the relative permeability in this model. The absolute permeability is computed as a harmonic average of two neighboring blocks. Both viscosity and density are calculated by averaging between two adjacent blocks.

The implicit pressure explicit saturation (IMPES) method is used in this model. The essential feature is the approximation of the capillary pressures at time level n+1 by their value at time level n. The phase equations, Equation (24) for each phase ℓ, can be combined into a single pressure equation as follows:

$$T_{xp}{}^{\mathrm{n}}_{\mathrm{i}+\frac{1}{2},\mathrm{j}}(P_{o}{}^{\mathrm{n+1}}_{\mathrm{i+1,j}} - P_{o}{}^{\mathrm{n+1}}_{\mathrm{i,j}}) - T_{xm}{}^{\mathrm{n}}_{\mathrm{i}-\frac{1}{2},\mathrm{j}}(P_{o}{}^{\mathrm{n+1}}_{\mathrm{i,j}} - P_{o}{}^{\mathrm{n+1}}_{\mathrm{i-1,j}})$$

$$+T_{yp}{}^{\mathrm{n}}_{\mathrm{i,j}+\frac{1}{2}}(P_{o}{}^{\mathrm{n+1}}_{\mathrm{i,j+1}} - P_{o}{}^{\mathrm{n+1}}_{\mathrm{i,j}}) - T_{ym}{}^{\mathrm{n}}_{\mathrm{i,j}-\frac{1}{2}}(P_{o}{}^{\mathrm{n+1}}_{\mathrm{i,j}} - P_{o}{}^{\mathrm{n+1}}_{\mathrm{i,j-1}})$$

$$= F^{\mathrm{n}}_{\mathrm{i,j}}(P_{o}{}^{\mathrm{n+1}}_{\mathrm{i,j}} - P_{o}{}^{\mathrm{n}}_{\mathrm{i,j}}) - C^{\mathrm{n}}_{\mathrm{i,j}} - Q_{T}{}^{\mathrm{n+1}}_{\mathrm{i,j}} \tag{30}$$

where

$$T_{xp}{}^{\mathrm{n}}_{\mathrm{i}+\frac{1}{2},\mathrm{j}} \equiv T_{ox}{}^{\mathrm{n}}_{\mathrm{i}+\frac{1}{2},\mathrm{j}} + \beta^{\mathrm{n}}_{\mathrm{i,j}} T_{gx}{}^{\mathrm{n}}_{\mathrm{i}+\frac{1}{2},\mathrm{j}} + \gamma^{\mathrm{n}}_{\mathrm{i,j}} T_{wx}{}^{\mathrm{n}}_{\mathrm{i}+\frac{1}{2},\mathrm{j}} \tag{31}$$

$$T_{xm}{}^{\mathrm{n}}_{\mathrm{i}-\frac{1}{2},\mathrm{j}} \equiv T_{ox}{}^{\mathrm{n}}_{\mathrm{i}-\frac{1}{2},\mathrm{j}} + \beta^{\mathrm{n}}_{\mathrm{i,j}} T_{gx}{}^{\mathrm{n}}_{\mathrm{i}-\frac{1}{2},\mathrm{j}} + \gamma^{\mathrm{n}}_{\mathrm{i,j}} T_{wx}{}^{\mathrm{n}}_{\mathrm{i}-\frac{1}{2},\mathrm{j}} \tag{32}$$

$$T_{yp}{}^{\mathrm{n}}_{\mathrm{i,j}+\frac{1}{2}} \equiv T_{oy}{}^{\mathrm{n}}_{\mathrm{i,j}+\frac{1}{2}} + \beta^{\mathrm{n}}_{\mathrm{i,j}} T_{gy}{}^{\mathrm{n}}_{\mathrm{i,j}+\frac{1}{2}} + \gamma^{\mathrm{n}}_{\mathrm{i,j}} T_{wy}{}^{\mathrm{n}}_{\mathrm{i,j}+\frac{1}{2}} \tag{33}$$

$$T_{ym}{}^{\mathrm{n}}_{\mathrm{i,j}-\frac{1}{2}} \equiv T_{oy}{}^{\mathrm{n}}_{\mathrm{i,j}-\frac{1}{2}} + \beta^{\mathrm{n}}_{\mathrm{i,j}} T_{gy}{}^{\mathrm{n}}_{\mathrm{i,j}-\frac{1}{2}} + \gamma^{\mathrm{n}}_{\mathrm{i,j}} T_{wy}{}^{\mathrm{n}}_{\mathrm{i,j}-\frac{1}{2}} \tag{34}$$

$$F^{\mathrm{n}}_{\mathrm{i,j}} \equiv \frac{\triangle V}{\triangle t}\phi_{\mathrm{i,j}}(S_{o}{}^{\mathrm{n}}_{\mathrm{i,j}}\overline{\rho}_{o}{}^{\mathrm{n}}_{\mathrm{i,j}} + \beta^{\mathrm{n}}_{\mathrm{i,j}} S_{g}{}^{\mathrm{n}}_{\mathrm{i,j}}\overline{\rho}_{g}{}^{\mathrm{n}}_{\mathrm{i,j}} + \gamma^{\mathrm{n}}_{\mathrm{i,j}} S_{w}{}^{\mathrm{n}}_{\mathrm{i,j}}\overline{\rho}_{w}{}^{\mathrm{n}}_{\mathrm{i,j}}) \tag{35}$$

$$Q_{T_{i,j}}^{n+1} \equiv Q_{o_{i,j}}^{n+1} + \beta_{i,j}^{n} Q_{g_{i,j}}^{n+1} + \gamma_{i,j}^{n} Q_{w_{i,j}}^{n+1} \tag{36}$$

$$\begin{aligned} C_{i,j}^{n} \equiv \beta_{i,j}^{n}[&T_{gx_{i+\frac{1}{2},j}^{n}}(P_{cgo_{i+1,j}^{n}} - P_{cgo_{i,j}^{n}}) - T_{gx_{i-\frac{1}{2},j}^{n}}(P_{cgo_{i,j}^{n}} - P_{cgo_{i-1,j}^{n}}) \\ &+T_{gy_{i,j+\frac{1}{2}}^{n}}(P_{cgo_{i,j+1}^{n}} - P_{cgo_{i,j}^{n}}) - T_{gy_{i,j-\frac{1}{2}}^{n}}(P_{cgo_{i,j}^{n}} - P_{cgo_{i,j-1}^{n}})] \\ -\gamma_{i,j}^{n}[&T_{wx_{i+\frac{1}{2},j}^{n}}(P_{cow_{i+1,j}^{n}} - P_{cow_{i,j}^{n}}) - T_{wx_{i-\frac{1}{2},j}^{n}}(P_{cow_{i,j}^{n}} - P_{cow_{i-1,j}^{n}}) \\ &+T_{wy_{i,j+\frac{1}{2}}^{n}}(P_{cow_{i,j+1}^{n}} - P_{cow_{i,j}^{n}}) - T_{wy_{i,j-\frac{1}{2}}^{n}}(P_{cow_{i,j}^{n}} - P_{cow_{i,j-1}^{n}})] \end{aligned} \tag{37}$$

$$\beta_{i,j}^{n} \equiv \frac{\rho_{o_{i,j}^{n}}}{\rho_{g_{i,j}^{n}}} \tag{38}$$

$$\gamma_{i,j}^{n} \equiv \frac{\rho_{o_{i,j}^{n}}}{\rho_{w_{i,j}^{n}}} \tag{39}$$

The iterative alternating direction implicit (ADI) scheme is used to find the pressure solution. The iterative ADI formulation of Equation (30) is

$$\begin{aligned} -T_{xm_{i-\frac{1}{2},j}^{n}} g_{i-1,j} + (T_{xp_{i+\frac{1}{2},j}^{n}} + T_{xm_{i-\frac{1}{2},j}^{n}} + F_{i,j}^{n} + D^{(k)}) g_{i,j} \\ -T_{xp_{i+\frac{1}{2},j}^{n}} g_{i+1,j} = R_{i,j} \end{aligned} \tag{40}$$

$$\begin{aligned} -T_{ym_{i,j-\frac{1}{2}}^{n}} h_{i,j-1} + (T_{yp_{i,j+\frac{1}{2}}^{n}} + T_{ym_{i,j-\frac{1}{2}}^{n}} + F_{i,j}^{n} + D^{(k)}) h_{i,j} \\ -T_{yp_{i,j+\frac{1}{2}}^{n}} h_{i,j+1} = (F_{i,j}^{n} + 2D^{(k)}) g_{i,j} \end{aligned} \tag{41}$$

where

$$\begin{aligned} R_{i,j} \equiv T_{xp_{i+\frac{1}{2},j}^{n}}(P_{o_{i+1,j}}^{(k)} - P_{o_{i,j}}^{(k)}) - T_{xm_{i-\frac{1}{2},j}^{n}}(P_{o_{i,j}}^{(k)} - P_{o_{i-1,j}}^{(k)}) - F_{i,j}^{n}(P_{o_{i,j}}^{(k)} - P_{o_{i,j}^{n}}) \\ +T_{yp_{i,j+\frac{1}{2}}^{n}}(P_{o_{i,j+1}}^{(k)} - P_{o_{i,j}}^{(k)}) - T_{ym_{i,j-\frac{1}{2}}^{n}}(P_{o_{i,j}}^{(k)} - P_{o_{i,j-1}}^{(k)}) + C_{i,j}^{n} + Q_{T_{i,j}}^{(k)} \end{aligned} \tag{42}$$

$$g \equiv P_o^{(k+\frac{1}{2})} - P_o^{(k)} \tag{43}$$

$$h \equiv P_o^{(k+1)} - P_o^{(k)} \tag{44}$$

$$D^{(k)} \equiv \sigma^{(k)}(T_{xp}{}^{n}_{i+\frac{1}{2},j} + T_{xm}{}^{n}_{i-\frac{1}{2},j} + T_{yp}{}^{n}_{i,j+\frac{1}{2}} + T_{ym}{}^{n}_{i,j-\frac{1}{2}}) \tag{45}$$

Here, the superscript k indicates the iteration level and $\sigma^{(k)}$ is an iteration parameter.[11] To check the convergence of the solution and stop the iteration, the following closure criterion is used:

$$\epsilon_p = \sum_{i,j} |R_{i,j}| \tag{46}$$

Usually $\epsilon_p \leq 0.0001$ is satisfactory for closure. After the pressure has been advanced in time implicitly, the saturations are updated explicitly. The surfactant concentration and foam bubble density from the previous time step are used to modify the gas-phase mobility. After the solution converges, the surfactant and population balance equations are solved for the current time. The iterative formulations for these two equations are described below.

Expanding the surfactant and population balance equations, Equations (3) and (6), in Cartesian coordinates, we obtain

$$\begin{aligned} &-\frac{\partial}{\partial x}(C_s\rho_w U_{wx}) - \frac{\partial}{\partial y}(C_s\rho_w U_{wy}) + \hat{C}_s q_w \\ &= \rho_r(1-\phi)\delta\frac{\partial\Gamma}{\partial t} + \phi\frac{\partial}{\partial t}(C_s\rho_w S_w) \end{aligned} \tag{47}$$

$$\begin{aligned} &-\frac{\partial}{\partial x}(n_f U_{gx}) - \frac{\partial}{\partial y}(n_f U_{gy}) + G_f - C_f + \hat{n}_f\hat{q}_g \\ &= \phi X_f\frac{\partial}{\partial t}(n_f S_g) + \phi(1-X_f)\frac{\partial}{\partial t}(n_s S_g) \end{aligned} \tag{48}$$

The finite-difference approximations to Equations (47) and (48), for each grid block (i,j), are written as follows:

$$\begin{aligned} &-\frac{\Delta V}{\Delta x}(C_{s}{}^{n+1}_{i+\frac{1}{2},j}\rho_{w}{}^{n+1}_{i+\frac{1}{2},j}U_{wx}{}^{n+1}_{i+\frac{1}{2},j} - C_{s}{}^{n+1}_{i-\frac{1}{2},j}\rho_{w}{}^{n+1}_{i-\frac{1}{2},j}U_{wx}{}^{n+1}_{i-\frac{1}{2},j}) \\ &-\frac{\Delta V}{\Delta y}(C_{s}{}^{n+1}_{i,j+\frac{1}{2}}\rho_{w}{}^{n+1}_{i,j+\frac{1}{2}}U_{wy}{}^{n+1}_{i,j+\frac{1}{2}} - C_{s}{}^{n+1}_{i,j-\frac{1}{2}}\rho_{w}{}^{n+1}_{i,j-\frac{1}{2}}U_{wy}{}^{n+1}_{i,j-\frac{1}{2}}) \\ &= \rho_r\delta\frac{\Delta V}{\Delta t}(1-\phi_{i,j})(\Gamma^{n+1}_{i,j} - \Gamma^{n}_{i,j}) - \hat{C}_{s}{}^{n+1}_{i,j}Q_{w}{}^{n+1}_{i,j} \\ &+\frac{\Delta V}{\Delta t}\phi_{i,j}(C_{s}{}^{n+1}_{i,j}\rho_{w}{}^{n+1}_{i,j}S_{w}{}^{n+1}_{i,j} - C_{s}{}^{n}_{i,j}\rho_{w}{}^{n}_{i,j}S_{w}{}^{n}_{i,j}) \end{aligned} \tag{49}$$

$$-\frac{\Delta V}{\Delta x}(n_{f_{i+\frac{1}{2},j}}^{n+1} U_{gx_{i+\frac{1}{2},j}}^{n} - n_{f_{i-\frac{1}{2},j}}^{n+1} U_{gx_{i-\frac{1}{2},j}}^{n}) - \frac{\Delta V}{\Delta y}(n_{f_{i,j+\frac{1}{2}}}^{n+1} U_{gy_{i,j+\frac{1}{2}}}^{n} - n_{f_{i,j-\frac{1}{2}}}^{n+1} U_{gy_{i,j-\frac{1}{2}}}^{n})$$

$$= \frac{\Delta V}{\Delta t}\phi_{i,j} X_f (S_{g_{i,j}}^{n+1} n_{f_{i,j}}^{n+1} - S_{g_{i,j}}^{n} n_{f_{i,j}}^{n}) - G_{f_{i,j}}^{n}\Delta V + C_{f_{i,j}}^{n}\Delta V - \hat{n}_{f_{i,j}}^{n+1}\hat{Q}_{g_{i,j}}^{n+1}$$

$$+\frac{\Delta V}{\Delta t}\phi_{i,j}(1 - X_f)(S_{g_{i,j}}^{n+1} n_{s_{i,j}}^{n+1} - S_{g_{i,j}}^{n} n_{s_{i,j}}^{n}) \tag{50}$$

where

$$\hat{Q}_{g_{i,j}}^{n+1} \equiv \hat{q}_{g_{i,j}}^{n+1}\Delta V \tag{51}$$

The iterative scheme is used to find the solutions. The iterative formulations of Equations (49) and (50) are

$$\frac{\Delta V}{\Delta t}\left(\phi_{i,j}\rho_{w_{i,j}}^{n+1} S_{w_{i,j}}^{n+1} + \frac{\rho_r \delta K_s A_s (1 - \phi_{i,j})}{(1 + K_s C_{s_{i,j}}^{(k)})^2}\right)(C_{s_{i,j}}^{(k+1)} - C_{s_{i,j}}^{(k)}) = R_{si,j} \tag{52}$$

$$\frac{\Delta V}{\Delta t}\phi_{i,j}\left(X_f + \frac{K_f A_f (1 - X_f)}{(1 + K_f n_{f_{i,j}}^{(k)})^2}\right) S_{g_{i,j}}^{n+1}(n_{f_{i,j}}^{(k+1)} - n_{f_{i,j}}^{(k)}) = R_{ni,j} \tag{53}$$

where

$$R_{si,j} \equiv -\frac{\Delta V}{\Delta x}(C_{s_{i+\frac{1}{2},j}}^{(k)}\rho_{w_{i+\frac{1}{2},j}}^{n+1} U_{wx_{i+\frac{1}{2},j}}^{n+1} - C_{s_{i-\frac{1}{2},j}}^{(k)}\rho_{w_{i-\frac{1}{2},j}}^{n+1} U_{wx_{i-\frac{1}{2},j}}^{n+1})$$

$$-\frac{\Delta V}{\Delta y}(C_{s_{i,j+\frac{1}{2}}}^{(k)}\rho_{w_{i,j+\frac{1}{2}}}^{n+1} U_{wy_{i,j+\frac{1}{2}}}^{n+1} - C_{s_{i,j-\frac{1}{2}}}^{(k)}\rho_{w_{i,j-\frac{1}{2}}}^{n+1} U_{wy_{i,j-\frac{1}{2}}}^{n+1})$$

$$+\rho_r \delta\frac{\Delta V}{\Delta t}(1 - \phi_{i,j})(\Gamma_{i,j}^{n} - \Gamma_{i,j}^{(k)}) + \hat{C}_{s_{i,j}}^{(k)} Q_{w_{i,j}}^{n+1}$$

$$+\frac{\Delta V}{\Delta t}\phi_{i,j}(C_{s_{i,j}}^{n}\rho_{w_{i,j}}^{n} S_{w_{i,j}}^{n} - C_{s_{i,j}}^{(k)}\rho_{w_{i,j}}^{n+1} S_{w_{i,j}}^{n+1}) \tag{54}$$

$$R_{ni,j} \equiv -\frac{\Delta V}{\Delta t}\phi_{i,j} X_f (S_{g_{i,j}}^{n+1} n_{f_{i,j}}^{(k)} - S_{g_{i,j}}^{n} n_{f_{i,j}}^{n}) + G_{f_{i,j}}^{n}\Delta V$$

$$-\frac{\Delta V}{\Delta x}(n_{f_{i+\frac{1}{2},j}}^{(k)} U_{gx_{i+\frac{1}{2},j}}^{n} - n_{f_{i-\frac{1}{2},j}}^{(k)} U_{gx_{i-\frac{1}{2},j}}^{n}) - C_{f_{i,j}}^{n}\Delta V$$

$$-\frac{\Delta V}{\Delta y}(n_{f_{i,j+\frac{1}{2}}}^{(k)} U_{gy_{i,j+\frac{1}{2}}}^{n} - n_{f_{i,j-\frac{1}{2}}}^{(k)} U_{gy_{i,j-\frac{1}{2}}}^{n}) + \hat{n}_{f_{i,j}}^{(k)} \hat{Q}_{g_{i,j}}^{n+1}$$

$$-\frac{\Delta V}{\Delta t}\phi_{i,j}(1 - X_f)(S_{g_{i,j}}^{n+1} n_{s_{i,j}}^{(k)} - S_{g_{i,j}}^{n} n_{s_{i,j}}^{n}) \tag{55}$$

Note that the nonlinear terms Γ and n_s at the $(k+1)$th iteration level have been linearized using a Newton-Raphson procedure. The single-point upstream weighting method is used to compute the quantities C_s, ρ_w, and n_f at the block boundary. To check the convergences of the solutions, the following closure criteria are used:

$$\epsilon_s = \sum_{i,j} |R_{si,j}| \tag{56}$$

$$\epsilon_n = \sum_{i,j} |R_{ni,j}| \tag{57}$$

Usually, $\epsilon_s \leq 0.0001$ and $\epsilon_n \leq 0.0001$ are satisfactory for closure.

D. Code Description

This section describes the structure and logic used in the MFS code. The FORTRAN code listing is reproduced on the floppy disk accompanying this manual in ASCII format. The hierarchy for the MFS is presented in Figure 2. This diagram identifies the relationships between the various routines. The functions of MFS's main program and subroutines are:

MAIN: This routine is the driver for the simulator.

FOAM: This routine modifies both the viscosity and relative permeability of the gas phase.

INPUT: This routine reads the input data and does the initialization.

LOOKUP: This routine does the table lookup.

OUTPUT: This routine prints out the results.

POP: This routine solves the population balance equation.

PRESS: This routine solves the pressure equation and updates the saturations and the production rates.

REREAD: This routine reads data from the restart file.

SLOPE: This routine calculates the first derivatives from tabular data.

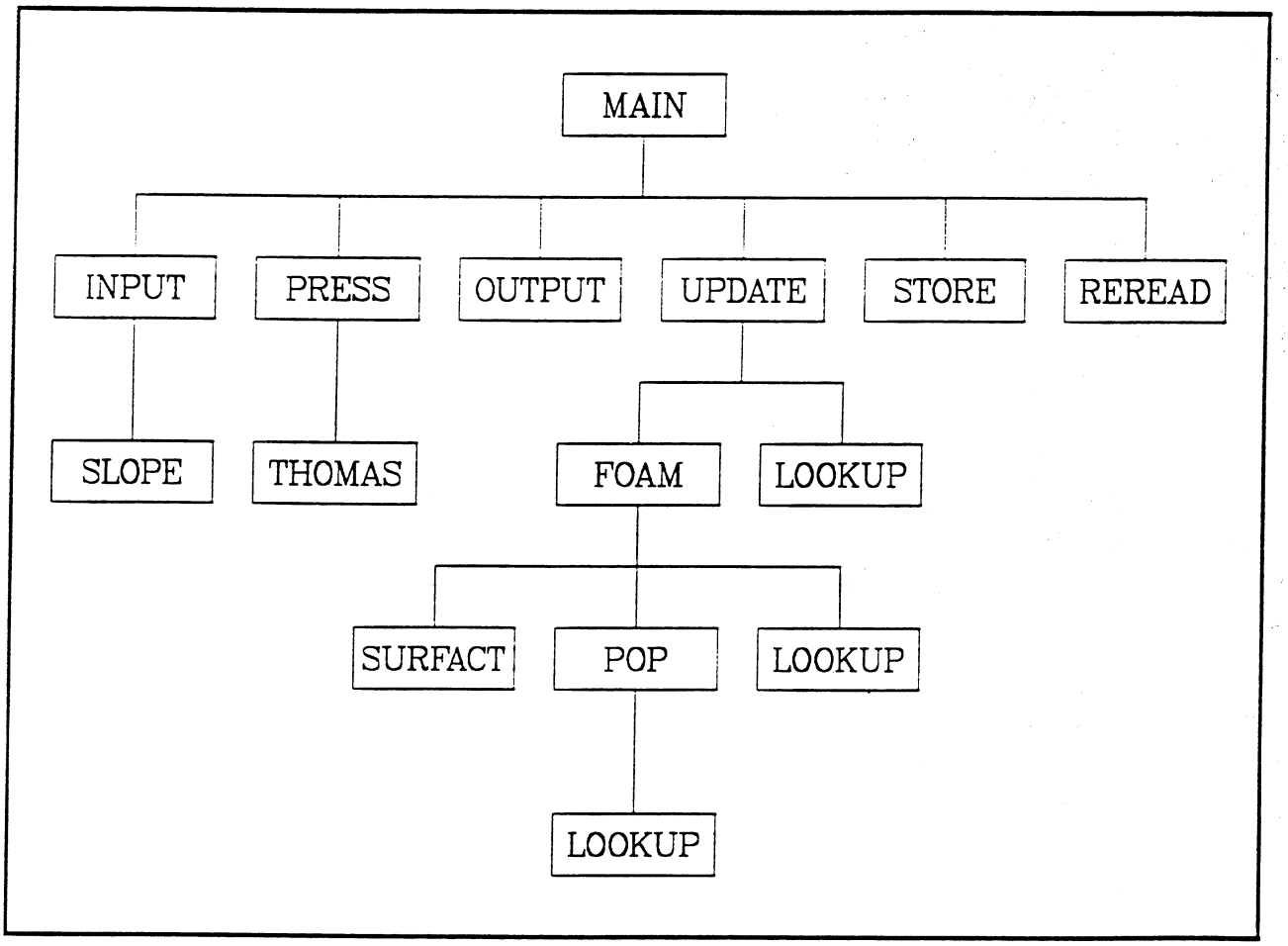

Figure 2. Hierarchy of mechanistic foam simulator.

STORE: This routine stores the images in the common block to the dump file.

SURFACT: This routine solves the surfactant equation.

THOMAS: This routine solves the tridiagonal matrix using the Thomas method.

UPDATE: This routine updates the transmissibilities and calculates the material balance errors for each phase and for the surfactant and the population balance error.

II. USER'S MANUAL

A. System Requirements

The MFS was developed on a Hewlett-Packard computer system (HP 9000 Series 835) and was written in standard FORTRAN 77. The simulator should run with minor or no modification on machines designed to handle standard FORTRAN 77.

B. Setup of Parameter Values

Dimensions are set with symbolic names in PARAMETER statements when the code is compiled. The symbolic names are:

- MNI: maximum number of grid blocks in the x-direction
- MNJ: maximum number of grid blocks in the y-direction
- MAXIJ: maximum of MNI and MNJ
- MNCPG: maximum number of entries in the viscosity-pressure and density-pressure tables for the gas phase
- MNCPW: maximum number of entries in the viscosity-pressure and density-pressure tables for the water phase
- MNCPO: maximum number of entries in the viscosity-pressure and density-pressure tables for the oil phase
- MNCG: maximum number of entries in the gas-oil relative permeability and capillary pressure tables
- MNCW: maximum number of entries in the water-oil relative permeability and capillary pressure tables

To allow efficient computer usage and successful simulations, the PARAMETER statements may need to be changed.

C. Input and Output Files

The MFS requires two input files and generates three output files. The first input file is the control file which tells the computer what the file names are for the output data file, dump file, and input data file. The control file also tells the computer whether the run is a continuation or not. If this run is a continuation, the time step, number of time steps, and diagnostic interval for output can be changed by using the control file. The word *read5* is reserved for the name of the control file. The FORTRAN unit number for this file is 5.

The second input file is the input data file. The FORTRAN unit number for this file is 20. The data descriptions for the input data file and the control file are given in Sections D and E below.

The first output file is the output data file. This file includes the following results:

- Elapsed time, sec
- Pore volumes injected
- Current time step, sec
- Current time step number
- Cumulative material balance of oil phase, %
- Cumulative material balance of water phase, %
- Cumulative material balance of gas phase, %
- Cumulative material balance of surfactant, %
- Cumulative bubble population balance, %
- Pressure drop across the system, atm
- Oil recovery, %
- Cumulative mass of surfactant injected into the system, g
- Cumulative oil production, cm^3
- Cumulative water injection, cm^3
- Cumulative water production, cm^3
- Cumulative gas injection, cm^3
- Cumulative gas production, cm^3
- Oil injection and production rates, g/sec
- Water injection and production rates, g/sec
- Gas injection and production rates, g/sec
- Saturation of oil phase
- Saturation of water phase
- Saturation of gas phase
- Pressure of oil phase, atm
- Pressure of water phase, atm
- Pressure of gas phase, atm
- X-component of oil velocity at the block boundary $(i \pm \frac{1}{2}, j)$, cm/sec
- Y-component of oil velocity at the block boundary $(i, j \pm \frac{1}{2})$, cm/sec
- X-component of water velocity at the block boundary $(i \pm \frac{1}{2}, j)$, cm/sec
- Y-component of water velocity at the block boundary $(i, j \pm \frac{1}{2})$, cm/sec
- X-component of gas velocity at the block boundary $(i \pm \frac{1}{2}, j)$, cm/sec

- Y-component of gas velocity at the block boundary $(i, j \pm \frac{1}{2})$, cm/sec
- Surfactant concentration, g/g
- Bubble density for flowing foam, $\#/cm^3$

These results are printed at time steps specified by the user. This file also echoes the input data from the input data file and prints the time at which foams first occur. The FORTRAN unit number for this file is 21.

The second output file is the dump file. This file is generated at the end of each run and can be used as a restart file. This permits the user to perform the simulation for a short period of time, then stop to examine the results before continuing. The FORTRAN unit number for this file is 22.

The third file is the monitoring file. The elapsed time, pore volumes injected, and number of iterations are printed at every time step. The number of iterations is not printed if it is not greater than 2. The absolute residual is printed if the number of iterations is greater than the maximum number of iterations. The cumulative material balance errors for each phase and for the surfactant and the cumulative bubble population balance error are printed if they are greater than 0.1%. Based on this information, we can adjust the time step to an optimal value. The automatic time step control option is not supported in this version. This file also echoes the input data from the control file and input data file. The word *write6* is reserved for the name of the monitoring file. The FORTRAN unit number for this file is 6.

D. Input Description for Input Data File

All data are free-formatted. This means that for each READ statement, it is only necessary to leave a blank space between data elements. Note that the first data element for a given READ statement must be on a new line in the file. Subsequent data elements for that read statement can span as many lines as necessary.

The following is a list of variables as they are read by the MFS. The variable names appear in all-caps on a single line in the order that they are read by the program. Every list of variables is followed by a description of each variable, by the corresponding unit, and by the possible values, if applicable. All of the variables listed below will be read by the program unless otherwise noted; therefore, a dummy value will be read by the program for variables not pertinent to the problem being run.

1. Read TITLE (A78).

   TITLE: title and/or run description (78 characters per line)

2. Read TITLE (A78).

3. Read TITLE (A78).

4. Read DT, NTSTPS, IDIAG, IOUW, IOUG, IOUS, IOUB.

   DT: time step, sec
   NTSTPS: number of time steps for the current run
   IDIAG: diagnostic interval for output
   IOUW: output control code for the water phase
   IOUG: output control code for the gas phase
   IOUS: output control code for the surfactant concentration
   IOUB: output control code for the bubble density

   If code = 0, no output will be printed.
   If code = 1, output will be printed.

5. Read TITLE (A78).

6. Read MAXITER, EPSP, EPSC, EPSN, ITWO.

   MAXITER: maximum number of iterations
   EPSP: tolerance for pressure convergence
   EPSC: tolerance for surfactant concentration convergence
   EPSN: tolerance for bubble density convergence
   ITWO: numerical control code

   If ITWO = 0, one-point upstream weighting method is used.
   If ITWO = 1, two-point upstream weighting method is used.

7. Read TITLE (A78).

8. Read XLENG, YLENG, DZ.

   XLENG: length of the system, cm
   YLENG: width of the system, cm
   DZ: thickness of the system, cm

9. Read TITLE (A78).

10. Read NI, NJ.

    NI: number of grid blocks in the x-direction
    NJ: number of grid blocks in the y-direction

    Note that NI $\leq$ MNI and NJ $\leq$ MNJ.

11. Read TITLE (A78).

12. Read IFI, IPKO.

IFI: code for porosity input type

IPKO: code for absolute permeability input type

If code = 0, a single value is read for all grid blocks.

If code = 1, an individual value must be read for each grid block.

13. Read TITLE (A78).

14. If IFI = 0, read FIH.

    If IFI = 1, read FI(I,J) I = 1 ... NI for NJ times.

    FIH: porosity for the system

    FI(I,J): porosity for grid block (I,J)

15. Read TITLE (A78).

16. If IPKO = 0, read PKOH.

    If IPKO = 1, read PKO(I,J) I = 1 ... NI for NJ times.

    PKOH: absolute permeability for the system, darcy

    PKO(I,J): absolute permeability for grid block (I,J), darcy

17. Read TITLE (A78).

18. Read IRO, IMU.

    IRO: code for density input type

    IMU: code for viscosity input type

    If code = 0, a single value is read (independent of pressure).

    If code = 1, a table format is read (function of pressure).

19. Read TITLE (A78).

20. If IRO = 0, read ROG0, ROW0, ROO0.

    If IRO = 1, then

    1) Read NDO, NDW, NDG.
    2) Read TITLE (A78).
    3) Read XPDO, YDO for NDO times in the order of increasing XPDO.
    4) Read TITLE (A78).
    5) Read XPDW, YDW for NDW times in the order of increasing XPDW.
    6) Read TITLE (A78).
    7) Read XPDG, YDG for NDG times in the order of increasing XPDG.

    ROG0: density of gas phase, g/cm^3

    ROW0: density of water phase, g/cm^3

    ROO0: density of oil phase, g/cm^3

    NDO: number of entries in density-pressure table for oil phase

NDW: number of entries in density-pressure table for water phase
NDG: number of entries in density-pressure table for gas phase
XPDO: pressure of oil phase, atm
YDO: density of oil phase, g/cm^3
XPDW: pressure of water phase, atm
YDW: density of water phase, g/cm^3
XPDG: pressure of gas phase, atm
YDG: density of gas phase, g/cm^3

Note that $2 \leq$ NDO $\leq$ MNCPO, $2 \leq$ NDW $\leq$ MNCPW and $2 \leq$ NDG $\leq$ MNCPG.

21. Read TITLE (A78).

22. If IMU = 0, read VMUG0, VMUW0, VMUO0.
If IMU = 1, then
1) Read NVO, NVW, NVG.
2) Read TITLE (A78).
3) Read XPO, YVO for NVO times in the order of increasing XPO.
4) Read TITLE (A78).
5) Read XPW, YVW for NVW times in the order of increasing XPW.
6) Read TITLE (A78).
7) Read XPG, YVG for NVG times in the order of increasing XPG.

VMUG0: viscosity of gas phase, cp
VMUW0: viscosity of water phase, cp
VMUO0: viscosity of oil phase, cp
NVO: number of entries in viscosity-pressure table for oil phase
NVW: number of entries in viscosity-pressure table for water phase
NVG: number of entries in viscosity-pressure table for gas phase
XPO: pressure of oil phase, atm
YVO: viscosity of oil phase, cp
XPW: pressure of water phase, atm
YVW: viscosity of water phase, cp
XPG: pressure of gas phase, atm
YVG: viscosity of gas phase, cp

Note that $2 \leq$ NVO $\leq$ MNCPO, $2 \leq$ NVW $\leq$ MNCPW and $2 \leq$ NVG $\leq$ MNCPG.

23. Read TITLE (A78).

24. Read NW, NG.

    NW: number of entries in water-oil relative permeability table

    NG: number of entries in gas-oil relative permeability table

    Note that $2 \leq NW \leq MNCW$ and $2 \leq NG \leq MNCG$.

25. Read TITLE (A78).

26. Read XW, YW, YWO for NW times in the order of increasing XW.

    XW: water saturation

    YW: water relative permeability

    YWO: oil relative permeability

    Note that YWO(1) = YGO(1) is required because of the assumption that the gas-oil data are measured in the presence of irreducible water.

27. Read TITLE (A78).

28. Read XG, YG, YGO for NG times in the order of increasing XG.

    XG: gas saturation

    YG: gas relative permeability

    YGO: oil relative permeability

29. Read TITLE (A78).

30. Read NENW, NENG.

    NENW: number of entries in water-oil capillary pressure table

    NENG: number of entries in gas-oil capillary pressure table

    Note that $2 \leq NENW \leq MNCW$ and $2 \leq NENG \leq MNCG$.

31. Read TITLE (A78).

32. Read XPCOW, YPCOW for NENW times in the order of increasing XPCOW.

    XPCOW: water saturation

    YPCOW: oil-water capillary pressure, atm

33. Read TITLE (A78).

34. Read XPCGO, YPCGO for NENG times in the order of increasing XPCGO.

    XPCGO: gas saturation

    YPCGO: gas-oil capillary pressure, atm

35. Read TITLE (A78).

36. Read IIP, IIC.

IIP: code for the type of initial pressure

IIC: code for the type of initial saturation/concentration

If code = 0, a single value is read for all grid blocks.

If code = 1, an individual value must be read for each grid block.

37. Read TITLE (A78).

38. If IIP = 0, read PO0.

    If IIP = 1, read PO(I,J) I = 1 ... NI for NJ times.

    PO0: pressure for the system, atm

    PO(I,J): pressure for grid block (I,J), atm

39. Read TITLE (A78).

40. If IIC = 0, read SO0, SG0, SW0, CS0.

    If IIC = 1, then

    1) Read SO(I,J) I = 1 ... NI for NJ times.
    2) Read TITLE (A78).
    3) Read SG(I,J) I = 1 ... NI for NJ times.
    4) Read TITLE (A78).
    5) Read SW(I,J) I = 1 ... NI for NJ times.
    6) Read TITLE (A78).
    7) Read CS(I,J) I = 1 ... NI for NJ times.

    SO0: oil saturation for the system

    SG0: gas saturation for the system

    SW0: water saturation for the system

    CS0: surfactant concentration for the system

    SO(I,J): oil saturation for grid block (I,J)

    SG(I,J): gas saturation for grid block (I,J)

    SW(I,J): water saturation for grid block (I,J)

    CS(I,J): surfactant concentration for grid block (I,J)

41. Read TITLE (A78).

42. Read VQMG, VQMW, PB.

    VQMG: injected gas volumetric flow rate, cm^3/sec

    VQMW: injected water volumetric flow rate, cm^3/sec

    PB: production pressure, atm

43. Read TITLE (A78).

44. Read CSI.

CSI: injected surfactant concentration, g/g

45. Read TITLE (A78).

46. Read ROR, DELTA, CKS, AS.

    ROR: mass density of rock, g/cm^3

    DELTA: rock surface area per unit mass, cm^2/g

    CKS: adsorption equilibrium constant, g/g

    AS: maximum surfactant concentration adsorbed on the rock, g/cm^2

47. Read TITLE (A78).

48. Read SOLIM, CSLIM.

    SOLIM: limiting oil saturation

    CSLIM: limiting surfactant concentration

49. Read TITLE (A78).

50. Read VCD, VCE.

    VCD: constant d in Equation (12), cm/sec

    VCE: exponent e in Equation (12)

51. Read TITLE (A78).

52. Read BK1, BNC, VREF1, E1, C1.

    BK1: generation rate constant, $\#/cm^3/sec$

    BNC: critical bubble density, $\#/cm^3$

    VREF1: reference velocity U_{ref1} in Equation (11), cm/sec

    E1: exponent e_1 in Equation (11)

    C1: exponent c_1 in Equation (11)

53. Read TITLE (A78).

54. Read CK2, CSREF, VREF2, E2, C2.

    CK2: coalescence rate constant, $cm^3/sec/cm^3$

    CSREF: reference surfactant concentration, g/g

    VREF2: reference velocity U_{ref2} in Equation (10), cm/sec

    E2: exponent e_2 in Equation (10)

    C2: exponent c_2 in Equation (10)

55. Read TITLE (A78).

56. Read BNFI.

BNFI: injected bubble density, #/cm^3

57. Read TITLE (A78).

58. Read BKF, AF.

    BKF: bubble trapping parameter, cm^3/#

    AF: bubble trapping parameter, #/cm^3

59. Read TITLE (A78).

60. Read XF.

    XF: fraction of gas that is flowing

61. Read TITLE (A78).

62. Read B, AK3, VREF3, C3.

    B: constant b in Equation (16)

    AK3: geometric factor

    VREF3: reference velocity U_{ref3} in Equation (13), cm/sec

    C3: exponent c_3 in Equation (13)

E. Input Description for Control File

The following is a list of variables as they are read by MFS.

1. Read OUTFILE (A15).

   OUTFILE: name of the output data file (up to 15 characters)

2. Read DUMP (A15).

   DUMP: name of the dump file

3. Read KK.

   KK: flag for restart problem

   If KK = 0, this run is a first run problem.

   If KK = 1, this run is a restart problem.

4. If KK = 0, read INFILE (A15).

   If KK = 1, then

   1) Read REFILE (A15).

   2) Read KT.

      a) If KT = 1, read DT.

   3) Read KN.

a) If KN = 1, read NTSTPS.

4) Read KI.

a) If KI = 1, read IDIAG.

INFILE: name of the input data file

REFILE: name of the restart file

KT: flag for changing time step

KN: flag for changing number of time steps

KI: flag for changing diagnostic interval for output

If flag = 0, no change is made.

If flag = 1, change to new value is made.

F. Sample Problems

This section includes two sample problems to help the user learn to properly construct an input data file for a MFS application. The input data file is included for each example, along with an explanation of the problem setup and the variables used. A section of the output data file is also included.

1. One-Dimensional Problem

For this example, the simulator is used to perform a history match on the results of a coreflood experiment.[12] The core was a 15.16-cm long Berea sandstone core with a diameter of 3.88 cm and was initially saturated with water phase (1% NaCl brine). The experiment was conducted at 100°F and 1000 psig with a flow rate of 75 cm^3/hr. The gas (CO_2) and water (surfactant solution) phases were injected simultaneously into the core with a volumetric ratio of 2:1. The surfactant solution was 1% Alipal CD-128 surfactant in 1% NaCl brine.

The input data file for this example is shown in Table 1. The number of time steps (NTSTPS = 180360) can be calculated based on the time step, on the pore volume of the system, on the injected flow rates for water and gas phases, and on how many pore volumes of fluids are to be injected. The results are printed at every 0.2 pore volumes injected (IDIAG = 4008). The two-point upstream weighting method is used (ITWO = 1). The system is divided into 20 grid blocks. The values assigned to the width and thickness of the system are equal to the square root of the cross-sectional area of the core. Dummy values are used for all the quantities related to the oil phase because no oil was involved in this experiment. In the case of no oil, PKROW and PKROG are best set equal to -10 or a large negative value. For the values of PCOW and PCGO, however, one can be set equal to 0 and the other can be set equal to the water-gas capillary

TABLE 1. INPUT DATA FILE FOR EXAMPLE 1

```
*** #V96-41-26-c2: Gas and S.S. into Brine *** (CO2SS8)
        ***        Example 1          ***
 DT [SEC], NTSTPS, IDIAG, IOUW, IOUG, IOUS, IOUB
0.1 180360 4008 1 1 1 1
 MAXITER, EPSP, EPSC, EPSN, ITWO
700 1.0E-09 1.0E-08 1.0E-05 1
 XLENG [CM], YLENG [CM], DZ [CM]
15.16 3.438 3.438
 NI, NJ
20 1
 IFI, IPKO
0 0
 FIH
0.233
 PKOH [DARCY]
0.242
 IRO, IMU
1 1
 NDO, NDW, NDG
2 2 6
 PO [ATM], ROO [G/CM^3]
50  0.834
100 0.834
 PW [ATM], ROW [G/CM^3]
67.705 0.8536
76.892 0.8537
 PG [ATM], ROG [G/CM^3]
67.705 0.1955
69.407 0.2062
71.448 0.2205
73.149 0.2338
74.85  0.2499
76.892 0.2737
 NVO, NVW, NVG
2 2 6
 PO [ATM], VMUO [CP]
50  2.8
100 2.8
 PW [ATM], VMUW [CP]
67.705 0.9771
76.892 0.9780
 PG [ATM], VMUG [CP]
67.705 0.0203
69.407 0.0207
71.448 0.0212
```

TABLE 1 (continued)

```
73.149 0.0217
74.85  0.0224
76.892 0.0235
 NW, NG
8 8
 SW, PKRW, PKROW
     .40       .00       -10.0
     .55       .03       -10.0
     .65       .08       -10.0
     .70       .12       -10.0
     .75       .30       -10.0
     .80       .53       -10.0
     .85       .80       -10.0
     .90      1.00       -10.0
 SG, PKRG, PKROG
     .10       .0000     -10.0
     .15       .0003     -10.0
     .20       .001      -10.0
     .25       .007      -10.0
     .30       .010      -10.0
     .35       .025      -10.0
     .45       .15       -10.0
     .60       .8        -10.0
 NENW, NENG
8 2
 SW, PCOW [ATM]
0.40 0.578
0.55 0.102
0.65 0.034
0.70 0.027
0.75 0.017
0.80 0.010
0.85 0.007
0.90 0.003
 SG, PCGO [ATM]
0.10 0.0
0.60 0.0
 IIP, IIC
0 0
 POO [ATM]
69.046
 SOO, SGO, SWO, CSO [G/G]
0.0 0.0 1.0 0.0
 VQMG [CM^3/SEC], VQMW [CM^3/SEC], PB [ATM]
1.389E-02 6.944E-03 69.046
```

TABLE 1 (continued)

```
 CSI [G/G]
0.01
 ROR [G/CM^3], DELTA [CM^2/G], CKS [G/G], AS [G/CM^2]
2.66 3000.0 793.0 2.52E-07
 SOLIM, CSLIM [G/G]
1.0 0.00999
 VCD [CM/SEC], VCE
5.5E-05 1.54
 BK1 [#/CM^3/SEC], BNC [#/CM^3], VREF1 [CM/SEC], E1, C1
1.0218E06 2.0E06 0.03916 5.0 0.333333333
 CK2 [CM^3/SEC/CM^3], CSREF [G/G], VREF2 [CM/SEC], E2, C2
2.0436E-02 0.01 0.03916 1.4 1.0
 BNFI [#/CM^3]
0.0
 BKF [CM^3/#], AF [#/CM^3]
1.0E-04 7.5E06
 XF
0.175
 B, AK3, VREF3 [CM/SEC], C3
25.345 1.9E08 0.03916 0.29
```

pressure. Three sections of the output data file for this example are shown in Table 2. In addition to the input data, the length, width, and volume of the grid block (DX, DY, DV), the pore volume of the system (PVOL), the slopes or first derivatives of the density-pressure data (ROOBAR, ROWBAR, ROGBAR), the volume of original fluids in the system (VSO0, VSW0, VSG0), and the injected liquid volume fraction (BLVF) are printed in the first section. The second section shows the time at which foams first occur. The computational results at 3 pore volumes injected are shown in the last section. Figure 3 shows the matching results.

2. Two-Dimensional Problem

For this example, the MFS is used to demonstrate the blockage and diversion of flow by foam. Figure 4 is the layout of a hypothetical system that we used for this demonstration. This system is 6.8 cm in length, 5 cm in width, and 0.0221 cm in thickness. A high-permeability zone which has been labeled as PFP, preferential flow path, is located in the center portion of the system. When foam occurs in the PFP, the blockage and diversion of flow can be observed. The fluids are injected into the system from the left side of the system (injection boundary) and are produced at the right side of the system (production boundary). The other two sides of the system are impermeable to the fluids. The boundary conditions are constant flow rates at the injection boundary and constant pressure at the production boundary. The fluid properties are independent of pressure. The water and gas phases are being simultaneously injected into the system saturated with oil at connate water. The injection rates for the water and gas phases are 0.060 and 0.081 cm^3/hr, respectively.

The input data file for this example is shown in Table 3. In this example, a total of one pore volume of fluids is injected into the system (NTSTPS = 384290), and the results are printed at every 0.1 pore volume injected (IDIAG = 38429). The one-point upstream weighting method is used (ITWO = 0). The grid system is 20×20. The fluid properties are not functions of pressure in this example. Therefore, we can set PB = 0 and PO0 = 0. The surfactant is introduced to the system through the water phase with a concentration of 0.01 g/g. The initial conditions are 74% oil and 26% water. To start the foam generation earlier, we set SOLIM = 0.6 in order to shorten the simulation time. A section of the output data file for this example is shown in Table 4.

To demonstrate the blockage and diversion of flow by foam, the gas velocity field for different times is shown in Figures 5-7. The region enclosed by the dotted line is the PFP. The length of the arrow represents the magnitude of the gas velocity and the direction the arrow is pointed in is the flow direction. For the case without foam, high gas flow through the PFP is inevitable. For the case

TABLE 2. SAMPLE OUTPUT DATA FILE FOR EXAMPLE 1

```
*** #V96-41-26-c2: Gas and S.S. into Brine *** (CO2SS8)
        ***        Example 1          ***
DT [SEC], NTSTPS, IDIAG, IOUW, IOUG, IOUS, IOUB                <--- Section 1
.1 180360 4008 1 1 1 1
MAXITER, EPSP, EPSC, EPSN, ITWO
700 1.000000000000000E-09 1.000000000000000E-08
1.000000000000000E-05 1
XLENG [CM], YLENG [CM], DZ [CM]
15.16 3.438 3.438
NI, NJ
20 1
      ===================================
      DX [CM] =  .758
      DY [CM] =  3.438
      DV [CM^3] =  8.959441752
      ===================================
IFI, IPKO
0 0
FIH
.233
      ===================================
      PVOL [CM^3] =  41.75099856432
      ===================================
PKOH [DARCY]
.242
IRO, IMU
1 1
NDO, NDW, NDG
2 2 6
 PO [ATM], ROO [G/CM^3]        ROOBAR [G/CM^3/ATM]
50.0 .834          .0
100.0 .834          .0
 PW [ATM], ROW [G/CM^3]        ROWBAR [G/CM^3/ATM]
67.705 .8536          1.088494611951551E-05
76.892 .8537          1.088494611951551E-05
 PG [ATM], ROG [G/CM^3]        ROGBAR [G/CM^3/ATM]
67.705 .1955          6.286721504112807E-03
69.407 .2062          6.646545465432207E-03
71.448 .2205          7.412649733951919E-03
73.149 .2338          8.641975308641979E-03
74.85 .2499          1.056013026847721E-02
76.892 .2737          1.165523996082270E-02
NVO, NVW, NVG
2 2 6
PO [ATM], VMUO [CP]
```

TABLE 2 (continued)

```
50.0 2.8
100.0 2.8
PW [ATM], VMUW [CP]
67.705 .9771
76.892 .978
PG [ATM], VMUG [CP]
67.705 2.030000000000000E-02
69.407 2.070000000000000E-02
71.448 2.120000000000000E-02
73.149 2.170000000000000E-02
74.85 2.240000000000000E-02
76.892 2.350000000000000E-02
NW, NG
8 8
SW, PKRW, PKROW
.4 .0 -10.0
.55 3.000000000000000E-02 -10.0
.65 8.000000000000000E-02 -10.0
.7 .12 -10.0
.75 .3 -10.0
.8 .53 -10.0
.85 .8 -10.0
.9 1.0 -10.0
SG, PKRG, PKROG
.1 .0 -10.0
.15 2.999999999999999E-04 -10.0
.2 1.000000000000000E-03 -10.0
.25 7.000000000000000E-03 -10.0
.3 1.000000000000000E-02 -10.0
.35 2.500000000000000E-02 -10.0
.45 .15 -10.0
.6 .8 -10.0
NENW, NENG
8 2
SW, PCOW [ATM]
.4 .578
.55 .102
.65 3.400000000000000E-02
.7 2.700000000000000E-02
.75 1.700000000000000E-02
.8 1.000000000000000E-02
.85 7.000000000000000E-03
.9 3.000000000000000E-03
SG, PCGO [ATM]
.1 .0
```

TABLE 2 (continued)

```
.6 .0
IIP, IIC
0 0
POO [ATM]
69.046
SOO, SGO, SWO, CSO [G/G]
.0 .0 1.0 .0
      ====================================
      VSOO [CM^3] =  .0
      VSWO [CM^3] =  41.75099856431999
      VSGO [CM^3] =  .0
      ====================================
VQMG [CM^3/SEC], VQMW [CM^3/SEC], PB [ATM]
1.389000000000000E-02 6.944000000000000E-03 69.046
      ====================================
      BLVF =  .3333013343573005
      ====================================
CSI [G/G]
1.000000000000000E-02
ROR [G/CM^3], DELTA [CM^2/G], CKS [G/G], AS [G/CM^2]
2.66 3000.0 793.0 2.520000000000000E-07
SOLIM, CSLIM [G/G]
1.0 9.990000000000000E-03
VCD [CM/SEC], VCE
5.500000000000000E-05 1.54
BK1 [#/CM^3/SEC], BNC [#/CM^3], VREF1 [CM/SEC], E1, C1
1021800.0 2000000.0 3.916000000000000E-02 5.0 .333333333
CK2 [CM^3/SEC/CM^3], CSREF [G/G], VREF2 [CM/SEC], E2, C2
2.043600000000000E-02 1.000000000000000E-02 3.916000000000000E-02 1.4
1.0
BNFI [#/CM^3]
.0
BKF [CM^3/#], AF [#/CM^3]
1.000000000000000E-04 7500000.0
XF
.175
B, AK3, VREF3 [CM/SEC], C3
25.345 190000000.0 3.916000000000000E-02 .29
 ********** END OF INPUT DATA ************
 ##########################################

 ------------------------------------------                    <--- Section 2
 FLOWING FOAM FIRST OCCURRED AT  TIME =  1899.099999999368 [SEC]
 ------------------------------------------
```

TABLE 2 (continued)

```
==========================================                    <--- Section 3
ELAPSED TIME [SEC] =  6012.000000004339
==========================================
PORE VOLUMES INJECTED =  3.00002424629746
CURRENT TIME STEP [SEC] =  .1
CURRENT TIME STEP NUMBER =  60120
****************************************
MATERIAL BALANCE OF OIL PHASE [%] =  .0
MATERIAL BALANCE OF WATER PHASE [%] =  -1.941058303689402E-03
MATERIAL BALANCE OF GAS PHASE [%] =  1.589036516691510E-03
MATERIAL BALANCE OF SURFACTANT [%] =  -2.066951720891552E-07
BUBBLE POPULATION BALANCE [%] =  -2.620126338115369E-12
****************************************
PRESSURE DROP [ATM] =  2.88221866892957
OIL RECOVERY [%] = .0
CUM. SURFACTANT INJECTION [G] =  .3563665588648413
****************************************
CUM. OIL PRODUCTION [CM^3] =  .0
CUM. WATER INJECTION [CM^3] =  41.74732800003013
CUM. WATER PRODUCTION [CM^3] =  60.23078715166764
CUM. GAS INJECTION [CM^3] =  83.50668000006029
CUM. GAS PRODUCTION [CM^3] =  67.47549438536661
****************************************
OIL INJECTION AND PRODUCTION [G/SEC]
.000E+00  .000E+00
****************************************
WATER INJECTION AND PRODUCTION [G/SEC]
.593E-02 -.643E-02
****************************************
GAS INJECTION AND PRODUCTION [G/SEC]
.311E-02 -.300E-02
****************************************
SATURATION OF OIL PHASE
.000E+00  .000E+00  .000E+00  .000E+00  .000E+00  .000E+00  .000E+00  .000E+00  .000E+00  .000E+00
.000E+00  .000E+00  .000E+00  .000E+00  .000E+00  .000E+00  .000E+00  .000E+00  .000E+00  .000E+00
****************************************
SATURATION OF WATER PHASE
.444E+00  .442E+00  .441E+00  .441E+00  .440E+00  .440E+00  .440E+00  .441E+00  .441E+00  .445E+00
.460E+00  .505E+00  .657E+00  .697E+00  .715E+00  .721E+00  .725E+00  .732E+00  .745E+00  .773E+00
****************************************
SATURATION OF GAS PHASE
.556E+00  .558E+00  .559E+00  .559E+00  .560E+00  .560E+00  .560E+00  .559E+00  .559E+00  .555E+00
.540E+00  .495E+00  .343E+00  .303E+00  .285E+00  .279E+00  .275E+00  .268E+00  .255E+00  .227E+00
****************************************
PRESSURE OF OIL PHASE [ATM]
```

TABLE 2 (continued)

```
.719E+02  .717E+02  .715E+02  .713E+02  .711E+02  .708E+02  .706E+02  .704E+02  .702E+02  .700E+02
.697E+02  .694E+02  .692E+02  .691E+02  .691E+02  .691E+02  .691E+02  .691E+02  .691E+02  .691E+02
****************************************
PRESSURE OF WATER PHASE [ATM]
.715E+02  .713E+02  .711E+02  .708E+02  .706E+02  .704E+02  .702E+02  .700E+02  .697E+02  .695E+02
.693E+02  .692E+02  .691E+02  .691E+02  .691E+02  .691E+02  .691E+02  .691E+02  .691E+02  .691E+02
****************************************
PRESSURE OF GAS PHASE [ATM]
.719E+02  .717E+02  .715E+02  .713E+02  .711E+02  .708E+02  .706E+02  .704E+02  .702E+02  .700E+02
.697E+02  .694E+02  .692E+02  .691E+02  .691E+02  .691E+02  .691E+02  .691E+02  .691E+02  .691E+02
****************************************
X-COMPONENT OF OIL VELOCITY [CM/SEC]
.000E+00  .000E+00  .000E+00  .000E+00  .000E+00  .000E+00  .000E+00  .000E+00  .000E+00  .000E+00
.000E+00  .000E+00  .000E+00  .000E+00  .000E+00  .000E+00  .000E+00  .000E+00  .000E+00  .000E+00
.000E+00
****************************************
Y-COMPONENT OF OIL VELOCITY [CM/SEC]
.000E+00  .000E+00  .000E+00  .000E+00  .000E+00  .000E+00  .000E+00  .000E+00  .000E+00  .000E+00
.000E+00  .000E+00  .000E+00  .000E+00  .000E+00  .000E+00  .000E+00  .000E+00  .000E+00  .000E+00
.000E+00  .000E+00  .000E+00  .000E+00  .000E+00  .000E+00  .000E+00  .000E+00  .000E+00  .000E+00
.000E+00  .000E+00  .000E+00  .000E+00  .000E+00  .000E+00  .000E+00  .000E+00  .000E+00  .000E+00
****************************************
X-COMPONENT OF WATER VELOCITY [CM/SEC]
.000E+00  .587E-03  .587E-03  .587E-03  .587E-03  .587E-03  .587E-03  .588E-03  .588E-03  .588E-03
.588E-03  .588E-03  .589E-03  .589E-03  .590E-03  .594E-03  .600E-03  .610E-03  .621E-03  .631E-03
.000E+00
****************************************
Y-COMPONENT OF WATER VELOCITY [CM/SEC]
.000E+00  .000E+00  .000E+00  .000E+00  .000E+00  .000E+00  .000E+00  .000E+00  .000E+00  .000E+00
.000E+00  .000E+00  .000E+00  .000E+00  .000E+00  .000E+00  .000E+00  .000E+00  .000E+00  .000E+00
.000E+00  .000E+00  .000E+00  .000E+00  .000E+00  .000E+00  .000E+00  .000E+00  .000E+00  .000E+00
.000E+00  .000E+00  .000E+00  .000E+00  .000E+00  .000E+00  .000E+00  .000E+00  .000E+00  .000E+00
****************************************
X-COMPONENT OF GAS VELOCITY [CM/SEC]
.000E+00  .118E-02  .119E-02  .120E-02  .121E-02  .121E-02  .122E-02  .123E-02  .124E-02  .125E-02
.126E-02  .127E-02  .128E-02  .129E-02  .129E-02  .128E-02  .128E-02  .127E-02  .126E-02  .125E-02
.000E+00
****************************************
Y-COMPONENT OF GAS VELOCITY [CM/SEC]
.000E+00  .000E+00  .000E+00  .000E+00  .000E+00  .000E+00  .000E+00  .000E+00  .000E+00  .000E+00
.000E+00  .000E+00  .000E+00  .000E+00  .000E+00  .000E+00  .000E+00  .000E+00  .000E+00  .000E+00
.000E+00  .000E+00  .000E+00  .000E+00  .000E+00  .000E+00  .000E+00  .000E+00  .000E+00  .000E+00
.000E+00  .000E+00  .000E+00  .000E+00  .000E+00  .000E+00  .000E+00  .000E+00  .000E+00  .000E+00
****************************************
SURFACTANT CONCENTRATION [G/G]
```

TABLE 2 (continued)

```
.100E-01  .100E-01  .100E-01  .100E-01  .100E-01  .100E-01  .100E-01  .100E-01  .100E-01  .100E-01
.100E-01  .100E-01  .998E-02  .981E-02  .928E-02  .762E-02  .348E-02  .434E-03  .345E-04  .260E-05
****************************************
FLOWING-FOAM BUBBLE DENSITY [#/CM^3]
.407E+07  .477E+07  .495E+07  .499E+07  .500E+07  .500E+07  .500E+07  .500E+07  .499E+07  .499E+07
.498E+07  .498E+07  .000E+00  .000E+00  .000E+00  .000E+00  .000E+00  .000E+00  .000E+00  .000E+00
****************************************
########################################
```

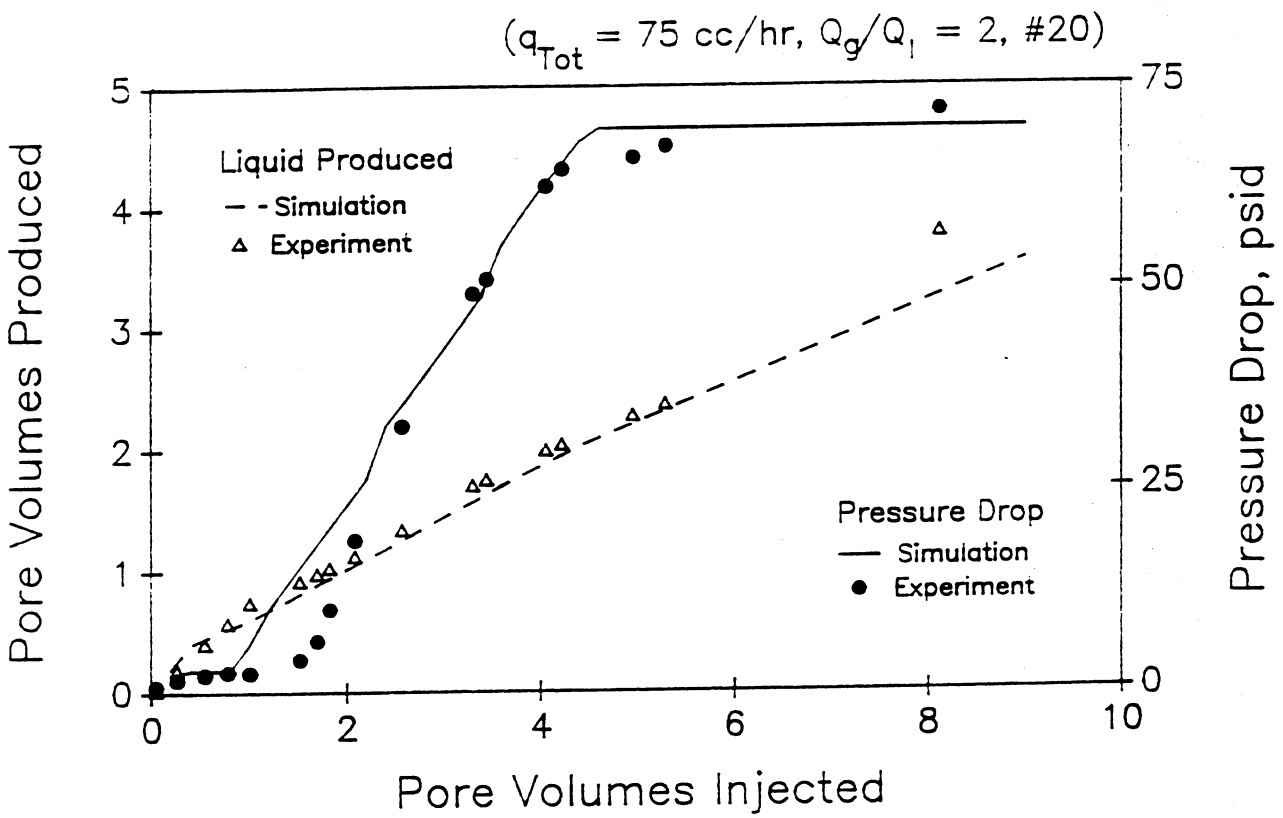

Figure 3. History match of liquid production and pressure drop.

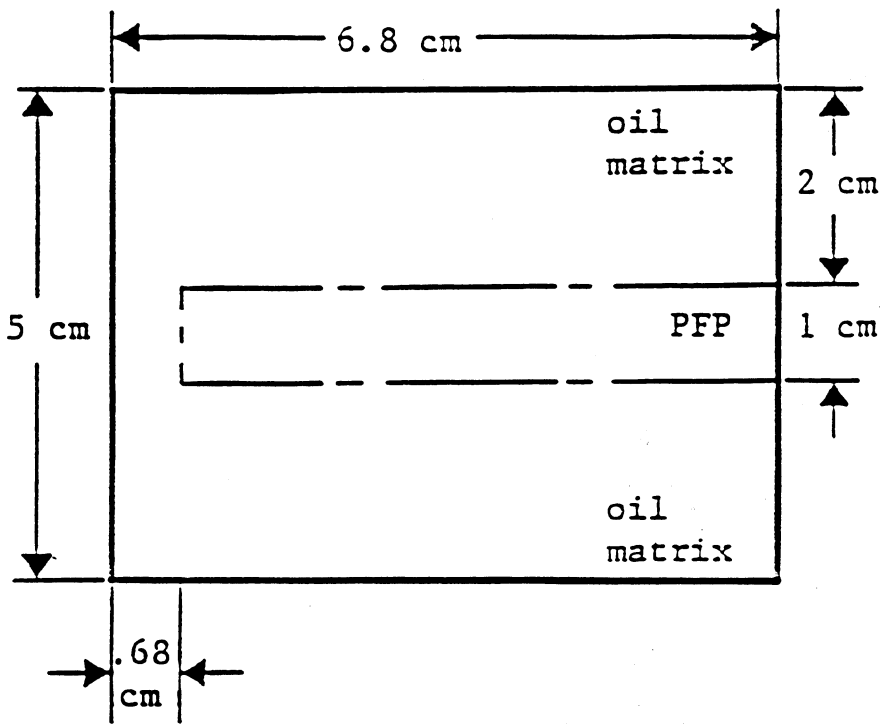

Figure 4. Layout of a hypothetical system.

TABLE 3. INPUT DATA FILE FOR EXAMPLE 2

```
 *** CASE # 14  ***
*****       Example 2      *****
 DT [SEC], NTSTPS, IDIAG ,IOUW, IOUG, IOUS, IOUB
0.01 384290 38429 1 1 1 1
 MAXITER, EPSP, EPSC, EPSN, ITWO
700 0.00000001 0.00000001 0.00001 0
 XLENG [CM], YLENG [CM], DZ [CM]
6.8 5.0 0.0221
 NI, NJ
20 20
 IFI, IPKO
0 1
 FIH
0.2
 PKO [DARCY]
0.01 0.01 0.01 0.01 0.01 0.01 0.01 0.01 0.01 0.01
0.01 0.01 0.01 0.01 0.01 0.01 0.01 0.01 0.01 0.01
0.01 0.01 0.01 0.01 0.01 0.01 0.01 0.01 0.01 0.01
0.01 0.01 0.01 0.01 0.01 0.01 0.01 0.01 0.01 0.01
0.01 0.01 0.01 0.01 0.01 0.01 0.01 0.01 0.01 0.01
0.01 0.01 0.01 0.01 0.01 0.01 0.01 0.01 0.01 0.01
0.01 0.01 0.01 0.01 0.01 0.01 0.01 0.01 0.01 0.01
0.01 0.01 0.01 0.01 0.01 0.01 0.01 0.01 0.01 0.01
0.01 0.01 0.01 0.01 0.01 0.01 0.01 0.01 0.01 0.01
0.01 0.01 0.01 0.01 0.01 0.01 0.01 0.01 0.01 0.01
0.01 0.01 0.01 0.01 0.01 0.01 0.01 0.01 0.01 0.01
0.01 0.01 0.01 0.01 0.01 0.01 0.01 0.01 0.01 0.01
0.01 0.01 0.01 0.01 0.01 0.01 0.01 0.01 0.01 0.01
0.01 0.01 0.01 0.01 0.01 0.01 0.01 0.01 0.01 0.01
0.01 0.01 0.01 0.01 0.01 0.01 0.01 0.01 0.01 0.01
0.01 0.01 0.01 0.01 0.01 0.01 0.01 0.01 0.01 0.01
0.01 0.01 0.01 0.01 0.01 0.01 0.01 0.01 0.01 0.01
0.01 0.01 0.50 0.50 0.50 0.50 0.50 0.50 0.50 0.50
0.50 0.50 0.50 0.50 0.50 0.50 0.50 0.50 0.50 0.50
0.01 0.01 0.50 0.50 0.50 0.50 0.50 0.50 0.50 0.50
0.50 0.50 0.50 0.50 0.50 0.50 0.50 0.50 0.50 0.50
0.01 0.01 0.50 0.50 0.50 0.50 0.50 0.50 0.50 0.50
0.50 0.50 0.50 0.50 0.50 0.50 0.50 0.50 0.50 0.50
0.01 0.01 0.50 0.50 0.50 0.50 0.50 0.50 0.50 0.50
0.50 0.50 0.50 0.50 0.50 0.50 0.50 0.50 0.50 0.50
0.01 0.01 0.01 0.01 0.01 0.01 0.01 0.01 0.01 0.01
0.01 0.01 0.01 0.01 0.01 0.01 0.01 0.01 0.01 0.01
0.01 0.01 0.01 0.01 0.01 0.01 0.01 0.01 0.01 0.01
0.01 0.01 0.01 0.01 0.01 0.01 0.01 0.01 0.01 0.01
0.01 0.01 0.01 0.01 0.01 0.01 0.01 0.01 0.01 0.01
0.01 0.01 0.01 0.01 0.01 0.01 0.01 0.01 0.01 0.01
```

TABLE 3 (continued)

```
0.01 0.01 0.01 0.01 0.01 0.01 0.01 0.01 0.01 0.01
0.01 0.01 0.01 0.01 0.01 0.01 0.01 0.01 0.01 0.01
0.01 0.01 0.01 0.01 0.01 0.01 0.01 0.01 0.01 0.01
0.01 0.01 0.01 0.01 0.01 0.01 0.01 0.01 0.01 0.01
0.01 0.01 0.01 0.01 0.01 0.01 0.01 0.01 0.01 0.01
0.01 0.01 0.01 0.01 0.01 0.01 0.01 0.01 0.01 0.01
0.01 0.01 0.01 0.01 0.01 0.01 0.01 0.01 0.01 0.01
0.01 0.01 0.01 0.01 0.01 0.01 0.01 0.01 0.01 0.01
0.01 0.01 0.01 0.01 0.01 0.01 0.01 0.01 0.01 0.01
0.01 0.01 0.01 0.01 0.01 0.01 0.01 0.01 0.01 0.01
 IRO, IMU
0 0
 ROGO [G/CM^3], ROWO [G/CM^3], ROOO [G/CM^3]
0.743 1.0 0.834
 VMUGO [CP], VMUWO [CP], VMUOO [CP]
0.064 1.0 2.8
 NW, NG
9 8
 SW, PKRW, PKROW
0.26 0.0    1.0
0.3  0.0004  0.98
0.35 0.0011  0.77
0.40 0.0020  0.51
0.45 0.0035  0.3
0.50 0.0052  0.16
0.55 0.0080  0.09
0.60 0.0113  0.06
0.71 0.0143  0.00
 SG, PKRG, PKROG
0.0  0.00   1.00
0.05 0.02   0.63
0.10 0.05   0.46
0.15 0.07   0.26
0.20 0.15   0.16
0.25 0.16   0.08
0.30 0.22   0.03
0.38 0.26   0.0
 NENW, NENG
9 8
 SW, PCOW [ATM]
0.26 0.340
0.30 0.170
0.35 0.102
0.40 0.0749
0.45 0.0544
```

TABLE 3 (continued)

```
0.50 0.0408
0.55 0.0272
0.60 0.0204
0.71 0.0136
 SG, PCGO [ATM]
0.0  0.0
0.05 0.136
0.10 0.340
0.15 0.544
0.20 0.749
0.25 1.021
0.30 1.361
0.38 1.701
 IIP, IIC
0 0
 POO [ATM]
0.0
 SOO, SGO, SWO, CSO [G/G]
0.74 0.0 0.26 0.0
 VQMG [CM^3/SEC], VQMW [CM^3/SEC], PB [ATM]
2.2436e-5 1.667e-5 0.0
 CSI [G/G]
0.01
 ROR [G/CM^3], DELTA [CM^2/G], CKS [G/G], AS [G/CM^2]
2.66 3000.0 793.0 1.68E-08
 SOLIM, CSLIM [G/G]
0.6 0.0001
 VCD [CM/SEC], VCE
5.5E-05 1.54
 BK1 [#/CM^3/SEC], BNC [#/CM^3], VREF1 [CM/SEC], E1, C1
1.0218E07 2.0E07 0.03916 5.0 0.333333333
 CK2 [CM^3/SEC/CM^3], CSREF [G/G], VREF2 [CM/SEC], E2, C2
2.0436E-03 0.01 0.03916 1.4 1.0
 BNFI [#/CM^3]
0.0
 BKF [CM^3/#], AF [#/CM^3]
1.0E-05 7.5E07
 XF
0.15
 B, AK3, VREF3 [CM/SEC], C3
25.345 1.9E07 0.03916 0.29
```

TABLE 4. SAMPLE OUTPUT DATA FILE FOR EXAMPLE 2

```
==========================================
ELAPSED TIME [SEC] =  1537.159999998746
==========================================
PORE VOLUMES INJECTED =  .4000011908434321
CURRENT TIME STEP [SEC] =  1.000000000000000E-02
CURRENT TIME STEP NUMBER =  153716
****************************************
MATERIAL BALANCE OF OIL PHASE [%] =  -1.357994863671052E-04
MATERIAL BALANCE OF WATER PHASE [%] =  1.491029522071585E-10
MATERIAL BALANCE OF GAS PHASE [%] =  -1.254182434551331E-03
MATERIAL BALANCE OF SURFACTANT [%] =  -1.306066366169034E-10
BUBBLE POPULATION BALANCE [%] =  1.143529715363911E-12
****************************************
PRESSURE DROP [ATM] =  3.02373594419125
OIL RECOVERY [%] = 29.41949440275701
CUM. SURFACTANT INJECTION [G] =  2.562445720003069E-04
****************************************
CUM. OIL PRODUCTION [CM^3] =  3.271648938962562E-02
CUM. WATER INJECTION [CM^3] =  2.562445719997910E-02
CUM. WATER PRODUCTION [CM^3] =  .0
CUM. GAS INJECTION [CM^3] =  3.448772175997187E-02
CUM. GAS PRODUCTION [CM^3] =  2.739608504040351E-02
****************************************
OIL INJECTION AND PRODUCTION [G/SEC]
.000E+00 -.216E-06
.000E+00 -.212E-06
.000E+00 -.204E-06
.000E+00 -.191E-06
.000E+00 -.173E-06
.000E+00 -.151E-06
.000E+00 -.126E-06
.000E+00 -.971E-07
.000E+00 -.377E-05
.000E+00 -.375E-05
.000E+00 -.375E-05
.000E+00 -.377E-05
.000E+00 -.971E-07
.000E+00 -.126E-06
.000E+00 -.151E-06
.000E+00 -.173E-06
.000E+00 -.191E-06
.000E+00 -.204E-06
.000E+00 -.212E-06
.000E+00 -.216E-06
```

TABLE 4 (continued)

```
****************************************
WATER INJECTION AND PRODUCTION [G/SEC]
.833E-06  .000E+00
.833E-06  .000E+00
.833E-06  .000E+00
.833E-06  .000E+00
.833E-06  .000E+00
.833E-06  .000E+00
.833E-06  .000E+00
.833E-06  .000E+00
.833E-06  .000E+00
.833E-06  .000E+00
.833E-06  .000E+00
.833E-06  .000E+00
.833E-06  .000E+00
.833E-06  .000E+00
.833E-06  .000E+00
.833E-06  .000E+00
.833E-06  .000E+00
.833E-06  .000E+00
.833E-06  .000E+00
.833E-06  .000E+00
.833E-06  .000E+00
****************************************
GAS INJECTION AND PRODUCTION [G/SEC]
.833E-06 -.361E-06
.833E-06 -.350E-06
.833E-06 -.328E-06
.833E-06 -.296E-06
.833E-06 -.253E-06
.833E-06 -.202E-06
.833E-06 -.143E-06
.833E-06 -.798E-07
.833E-06 -.232E-05
.833E-06 -.228E-05
.833E-06 -.228E-05
.833E-06 -.232E-05
.833E-06 -.798E-07
.833E-06 -.143E-06
.833E-06 -.202E-06
.833E-06 -.253E-06
.833E-06 -.296E-06
.833E-06 -.328E-06
.833E-06 -.350E-06
.833E-06 -.361E-06
****************************************
```

TABLE 4 (continued)

SATURATION OF OIL PHASE

.292E+00	.295E+00	.297E+00	.299E+00	.300E+00	.305E+00	.349E+00	.525E+00	.660E+00	.685E+00
.687E+00	.689E+00	.692E+00	.696E+00	.700E+00	.705E+00	.709E+00	.715E+00	.720E+00	.728E+00
.292E+00	.295E+00	.298E+00	.299E+00	.301E+00	.306E+00	.351E+00	.530E+00	.661E+00	.685E+00
.687E+00	.689E+00	.692E+00	.696E+00	.701E+00	.705E+00	.710E+00	.715E+00	.721E+00	.728E+00
.292E+00	.296E+00	.298E+00	.301E+00	.303E+00	.310E+00	.356E+00	.540E+00	.663E+00	.685E+00
.687E+00	.689E+00	.693E+00	.697E+00	.701E+00	.706E+00	.711E+00	.716E+00	.721E+00	.728E+00
.292E+00	.296E+00	.300E+00	.304E+00	.308E+00	.315E+00	.365E+00	.556E+00	.666E+00	.685E+00
.687E+00	.689E+00	.693E+00	.698E+00	.703E+00	.707E+00	.712E+00	.717E+00	.722E+00	.729E+00
.292E+00	.299E+00	.306E+00	.311E+00	.315E+00	.323E+00	.377E+00	.574E+00	.667E+00	.683E+00
.687E+00	.690E+00	.694E+00	.699E+00	.704E+00	.709E+00	.714E+00	.718E+00	.723E+00	.730E+00
.292E+00	.306E+00	.317E+00	.323E+00	.328E+00	.335E+00	.393E+00	.581E+00	.649E+00	.664E+00
.674E+00	.683E+00	.692E+00	.700E+00	.707E+00	.712E+00	.716E+00	.721E+00	.725E+00	.731E+00
.292E+00	.315E+00	.334E+00	.343E+00	.348E+00	.352E+00	.403E+00	.530E+00	.585E+00	.605E+00
.623E+00	.643E+00	.661E+00	.679E+00	.698E+00	.711E+00	.718E+00	.723E+00	.727E+00	.732E+00
.292E+00	.320E+00	.362E+00	.364E+00	.364E+00	.362E+00	.374E+00	.400E+00	.432E+00	.458E+00
.484E+00	.514E+00	.550E+00	.596E+00	.643E+00	.675E+00	.695E+00	.711E+00	.722E+00	.729E+00
.292E+00	.331E+00	.327E+00	.312E+00	.311E+00	.312E+00	.307E+00	.304E+00	.305E+00	.308E+00
.314E+00	.336E+00	.378E+00	.441E+00	.511E+00	.575E+00	.633E+00	.665E+00	.689E+00	.699E+00
.292E+00	.331E+00	.324E+00	.298E+00	.297E+00	.302E+00	.303E+00	.303E+00	.303E+00	.302E+00
.303E+00	.313E+00	.362E+00	.439E+00	.505E+00	.570E+00	.630E+00	.663E+00	.688E+00	.698E+00
.292E+00	.331E+00	.324E+00	.298E+00	.297E+00	.302E+00	.303E+00	.303E+00	.303E+00	.302E+00
.303E+00	.313E+00	.362E+00	.439E+00	.505E+00	.570E+00	.630E+00	.663E+00	.688E+00	.698E+00
.292E+00	.331E+00	.327E+00	.312E+00	.311E+00	.312E+00	.307E+00	.304E+00	.305E+00	.308E+00
.314E+00	.336E+00	.378E+00	.441E+00	.511E+00	.575E+00	.633E+00	.665E+00	.689E+00	.699E+00
.292E+00	.320E+00	.362E+00	.364E+00	.364E+00	.362E+00	.374E+00	.400E+00	.432E+00	.458E+00
.484E+00	.514E+00	.550E+00	.596E+00	.643E+00	.675E+00	.695E+00	.711E+00	.722E+00	.729E+00
.292E+00	.315E+00	.334E+00	.343E+00	.348E+00	.352E+00	.403E+00	.530E+00	.585E+00	.605E+00
.623E+00	.643E+00	.661E+00	.679E+00	.698E+00	.711E+00	.718E+00	.723E+00	.727E+00	.732E+00
.292E+00	.306E+00	.317E+00	.323E+00	.328E+00	.335E+00	.393E+00	.581E+00	.649E+00	.664E+00
.674E+00	.683E+00	.692E+00	.700E+00	.707E+00	.712E+00	.716E+00	.721E+00	.725E+00	.731E+00
.292E+00	.299E+00	.306E+00	.311E+00	.315E+00	.323E+00	.377E+00	.574E+00	.667E+00	.683E+00
.687E+00	.690E+00	.694E+00	.699E+00	.704E+00	.709E+00	.714E+00	.718E+00	.723E+00	.730E+00
.292E+00	.296E+00	.300E+00	.304E+00	.308E+00	.315E+00	.365E+00	.556E+00	.666E+00	.685E+00
.687E+00	.689E+00	.693E+00	.698E+00	.703E+00	.707E+00	.712E+00	.717E+00	.722E+00	.729E+00
.292E+00	.296E+00	.298E+00	.301E+00	.303E+00	.310E+00	.356E+00	.540E+00	.663E+00	.685E+00
.687E+00	.689E+00	.693E+00	.697E+00	.701E+00	.706E+00	.711E+00	.716E+00	.721E+00	.728E+00
.292E+00	.295E+00	.298E+00	.299E+00	.301E+00	.306E+00	.351E+00	.530E+00	.661E+00	.685E+00
.687E+00	.689E+00	.692E+00	.696E+00	.701E+00	.705E+00	.710E+00	.715E+00	.721E+00	.728E+00
.292E+00	.295E+00	.297E+00	.299E+00	.300E+00	.305E+00	.349E+00	.525E+00	.660E+00	.685E+00
.687E+00	.689E+00	.692E+00	.696E+00	.700E+00	.705E+00	.709E+00	.715E+00	.720E+00	.728E+00

****

SATURATION OF WATER PHASE

.651E+00	.657E+00	.664E+00	.664E+00	.662E+00	.656E+00	.606E+00	.423E+00	.284E+00	.261E+00
.260E+00	.260E+00	.260E+00	.260E+00	.260E+00	.260E+00	.260E+00	.260E+00	.260E+00	.260E+00

TABLE 4 (continued)

.651E+00	.657E+00	.663E+00	.663E+00	.660E+00	.653E+00	.602E+00	.418E+00	.283E+00	.261E+00
.260E+00	.260E+00	.260E+00	.260E+00	.260E+00	.260E+00	.260E+00	.260E+00	.260E+00	.260E+00
.651E+00	.656E+00	.661E+00	.659E+00	.655E+00	.647E+00	.595E+00	.406E+00	.281E+00	.260E+00
.260E+00	.260E+00	.260E+00	.260E+00	.260E+00	.260E+00	.260E+00	.260E+00	.260E+00	.260E+00
.650E+00	.654E+00	.656E+00	.652E+00	.645E+00	.636E+00	.582E+00	.389E+00	.277E+00	.260E+00
.260E+00	.260E+00	.260E+00	.260E+00	.260E+00	.260E+00	.260E+00	.260E+00	.260E+00	.260E+00
.649E+00	.648E+00	.644E+00	.636E+00	.630E+00	.621E+00	.565E+00	.368E+00	.275E+00	.261E+00
.260E+00	.260E+00	.260E+00	.260E+00	.260E+00	.260E+00	.260E+00	.260E+00	.260E+00	.260E+00
.647E+00	.633E+00	.621E+00	.611E+00	.604E+00	.600E+00	.541E+00	.359E+00	.293E+00	.281E+00
.273E+00	.268E+00	.263E+00	.261E+00	.260E+00	.260E+00	.260E+00	.260E+00	.260E+00	.260E+00
.641E+00	.609E+00	.579E+00	.563E+00	.561E+00	.566E+00	.522E+00	.410E+00	.357E+00	.340E+00
.325E+00	.310E+00	.296E+00	.284E+00	.273E+00	.266E+00	.262E+00	.261E+00	.260E+00	.260E+00
.628E+00	.565E+00	.481E+00	.478E+00	.502E+00	.532E+00	.541E+00	.534E+00	.511E+00	.488E+00
.465E+00	.442E+00	.408E+00	.369E+00	.336E+00	.308E+00	.291E+00	.277E+00	.269E+00	.266E+00
.606E+00	.484E+00	.551E+00	.596E+00	.621E+00	.635E+00	.645E+00	.651E+00	.653E+00	.651E+00
.645E+00	.621E+00	.586E+00	.538E+00	.479E+00	.415E+00	.357E+00	.327E+00	.304E+00	.297E+00
.593E+00	.460E+00	.556E+00	.616E+00	.643E+00	.653E+00	.654E+00	.653E+00	.653E+00	.657E+00
.656E+00	.645E+00	.606E+00	.546E+00	.486E+00	.419E+00	.360E+00	.328E+00	.305E+00	.297E+00
.593E+00	.460E+00	.556E+00	.616E+00	.643E+00	.653E+00	.654E+00	.653E+00	.653E+00	.657E+00
.656E+00	.645E+00	.606E+00	.546E+00	.486E+00	.419E+00	.360E+00	.328E+00	.305E+00	.297E+00
.606E+00	.484E+00	.551E+00	.596E+00	.621E+00	.635E+00	.645E+00	.651E+00	.653E+00	.651E+00
.645E+00	.621E+00	.586E+00	.538E+00	.479E+00	.415E+00	.357E+00	.327E+00	.304E+00	.297E+00
.628E+00	.565E+00	.481E+00	.478E+00	.502E+00	.532E+00	.541E+00	.534E+00	.511E+00	.488E+00
.465E+00	.442E+00	.408E+00	.369E+00	.336E+00	.308E+00	.291E+00	.277E+00	.269E+00	.266E+00
.641E+00	.609E+00	.579E+00	.563E+00	.561E+00	.566E+00	.522E+00	.410E+00	.357E+00	.340E+00
.325E+00	.310E+00	.296E+00	.284E+00	.273E+00	.266E+00	.262E+00	.261E+00	.260E+00	.260E+00
.647E+00	.633E+00	.621E+00	.611E+00	.604E+00	.600E+00	.541E+00	.359E+00	.293E+00	.281E+00
.273E+00	.268E+00	.263E+00	.261E+00	.260E+00	.260E+00	.260E+00	.260E+00	.260E+00	.260E+00
.649E+00	.648E+00	.644E+00	.636E+00	.630E+00	.621E+00	.565E+00	.368E+00	.275E+00	.261E+00
.260E+00	.260E+00	.260E+00	.260E+00	.260E+00	.260E+00	.260E+00	.260E+00	.260E+00	.260E+00
.650E+00	.654E+00	.656E+00	.652E+00	.645E+00	.636E+00	.582E+00	.389E+00	.277E+00	.260E+00
.260E+00	.260E+00	.260E+00	.260E+00	.260E+00	.260E+00	.260E+00	.260E+00	.260E+00	.260E+00
.651E+00	.656E+00	.661E+00	.659E+00	.655E+00	.647E+00	.595E+00	.406E+00	.281E+00	.260E+00
.260E+00	.260E+00	.260E+00	.260E+00	.260E+00	.260E+00	.260E+00	.260E+00	.260E+00	.260E+00
.651E+00	.657E+00	.663E+00	.663E+00	.660E+00	.653E+00	.602E+00	.418E+00	.283E+00	.261E+00
.260E+00	.260E+00	.260E+00	.260E+00	.260E+00	.260E+00	.260E+00	.260E+00	.260E+00	.260E+00
.651E+00	.657E+00	.664E+00	.664E+00	.662E+00	.656E+00	.606E+00	.423E+00	.284E+00	.261E+00
.260E+00	.260E+00	.260E+00	.260E+00	.260E+00	.260E+00	.260E+00	.260E+00	.260E+00	.260E+00

****

SATURATION OF GAS PHASE

.572E-01	.478E-01	.391E-01	.374E-01	.377E-01	.385E-01	.450E-01	.517E-01	.553E-01	.546E-01
.531E-01	.511E-01	.481E-01	.441E-01	.398E-01	.352E-01	.305E-01	.255E-01	.197E-01	.124E-01
.573E-01	.480E-01	.395E-01	.381E-01	.389E-01	.400E-01	.464E-01	.524E-01	.555E-01	.547E-01
.531E-01	.511E-01	.479E-01	.438E-01	.394E-01	.348E-01	.301E-01	.251E-01	.194E-01	.122E-01
.574E-01	.485E-01	.406E-01	.400E-01	.417E-01	.432E-01	.492E-01	.537E-01	.560E-01	.549E-01

TABLE 4 (continued)

.531E-01	.509E-01	.475E-01	.432E-01	.387E-01	.340E-01	.293E-01	.244E-01	.189E-01	.118E-01
.578E-01	.499E-01	.433E-01	.443E-01	.472E-01	.485E-01	.530E-01	.554E-01	.566E-01	.551E-01
.531E-01	.506E-01	.468E-01	.423E-01	.375E-01	.327E-01	.281E-01	.233E-01	.180E-01	.112E-01
.588E-01	.533E-01	.501E-01	.523E-01	.550E-01	.551E-01	.586E-01	.574E-01	.573E-01	.554E-01
.529E-01	.502E-01	.458E-01	.409E-01	.357E-01	.308E-01	.262E-01	.216E-01	.167E-01	.104E-01
.613E-01	.604E-01	.618E-01	.661E-01	.681E-01	.651E-01	.659E-01	.593E-01	.580E-01	.555E-01
.526E-01	.492E-01	.446E-01	.392E-01	.332E-01	.280E-01	.235E-01	.194E-01	.149E-01	.931E-02
.670E-01	.760E-01	.874E-01	.939E-01	.904E-01	.815E-01	.750E-01	.600E-01	.582E-01	.553E-01
.522E-01	.475E-01	.432E-01	.372E-01	.291E-01	.237E-01	.197E-01	.162E-01	.125E-01	.784E-02
.798E-01	.115E+00	.157E+00	.158E+00	.134E+00	.106E+00	.847E-01	.656E-01	.572E-01	.540E-01
.510E-01	.443E-01	.424E-01	.357E-01	.214E-01	.168E-01	.143E-01	.119E-01	.931E-02	.586E-02
.102E+00	.185E+00	.122E+00	.923E-01	.676E-01	.535E-01	.480E-01	.444E-01	.422E-01	.414E-01
.410E-01	.426E-01	.356E-01	.209E-01	.101E-01	.106E-01	.101E-01	.880E-02	.702E-02	.446E-02
.115E+00	.209E+00	.120E+00	.855E-01	.597E-01	.455E-01	.432E-01	.436E-01	.432E-01	.410E-01
.407E-01	.420E-01	.319E-01	.154E-01	.974E-02	.104E-01	.992E-02	.871E-02	.696E-02	.442E-02
.115E+00	.209E+00	.120E+00	.855E-01	.597E-01	.455E-01	.432E-01	.436E-01	.432E-01	.410E-01
.407E-01	.420E-01	.319E-01	.154E-01	.974E-02	.104E-01	.992E-02	.871E-02	.696E-02	.442E-02
.102E+00	.185E+00	.122E+00	.923E-01	.676E-01	.535E-01	.480E-01	.444E-01	.422E-01	.414E-01
.410E-01	.426E-01	.356E-01	.209E-01	.101E-01	.106E-01	.101E-01	.880E-02	.702E-02	.446E-02
.798E-01	.115E+00	.157E+00	.158E+00	.134E+00	.106E+00	.847E-01	.656E-01	.572E-01	.540E-01
.510E-01	.443E-01	.424E-01	.357E-01	.214E-01	.168E-01	.143E-01	.119E-01	.931E-02	.586E-02
.670E-01	.760E-01	.874E-01	.939E-01	.904E-01	.815E-01	.750E-01	.600E-01	.582E-01	.553E-01
.522E-01	.475E-01	.432E-01	.372E-01	.291E-01	.237E-01	.197E-01	.162E-01	.125E-01	.784E-02
.613E-01	.604E-01	.618E-01	.661E-01	.681E-01	.651E-01	.659E-01	.593E-01	.580E-01	.555E-01
.526E-01	.492E-01	.446E-01	.392E-01	.332E-01	.280E-01	.235E-01	.194E-01	.149E-01	.931E-02
.588E-01	.533E-01	.501E-01	.523E-01	.550E-01	.551E-01	.586E-01	.574E-01	.573E-01	.554E-01
.529E-01	.502E-01	.458E-01	.409E-01	.357E-01	.308E-01	.262E-01	.216E-01	.167E-01	.104E-01
.578E-01	.499E-01	.433E-01	.443E-01	.472E-01	.485E-01	.530E-01	.554E-01	.566E-01	.551E-01
.531E-01	.506E-01	.468E-01	.423E-01	.375E-01	.327E-01	.281E-01	.233E-01	.180E-01	.112E-01
.574E-01	.485E-01	.406E-01	.400E-01	.417E-01	.432E-01	.492E-01	.537E-01	.560E-01	.549E-01
.531E-01	.509E-01	.475E-01	.432E-01	.387E-01	.340E-01	.293E-01	.244E-01	.189E-01	.118E-01
.573E-01	.480E-01	.395E-01	.381E-01	.389E-01	.400E-01	.464E-01	.524E-01	.555E-01	.547E-01
.531E-01	.511E-01	.479E-01	.438E-01	.394E-01	.348E-01	.301E-01	.251E-01	.194E-01	.122E-01
.572E-01	.478E-01	.391E-01	.374E-01	.377E-01	.385E-01	.450E-01	.517E-01	.553E-01	.546E-01
.531E-01	.511E-01	.481E-01	.441E-01	.398E-01	.352E-01	.305E-01	.255E-01	.197E-01	.124E-01

****

PRESSURE OF OIL PHASE [ATM]

.286E+01	.246E+01	.199E+01	.152E+01	.107E+01	.666E+00	.323E+00	.134E+00	.105E+00	.913E-01
.789E-01	.673E-01	.564E-01	.464E-01	.375E-01	.295E-01	.224E-01	.160E-01	.102E-01	.492E-02
.284E+01	.243E+01	.197E+01	.149E+01	.105E+01	.653E+00	.316E+00	.133E+00	.105E+00	.914E-01
.790E-01	.672E-01	.562E-01	.461E-01	.371E-01	.291E-01	.220E-01	.157E-01	.100E-01	.482E-02
.280E+01	.239E+01	.192E+01	.145E+01	.102E+01	.627E+00	.304E+00	.130E+00	.105E+00	.918E-01
.791E-01	.671E-01	.557E-01	.454E-01	.363E-01	.283E-01	.212E-01	.151E-01	.960E-02	.462E-02
.274E+01	.232E+01	.185E+01	.139E+01	.966E+00	.590E+00	.286E+00	.128E+00	.106E+00	.924E-01
.794E-01	.669E-01	.550E-01	.444E-01	.350E-01	.269E-01	.200E-01	.141E-01	.897E-02	.430E-02

TABLE 4 (continued)

.265E+01	.222E+01	.176E+01	.130E+01	.895E+00	.540E+00	.264E+00	.127E+00	.107E+00	.935E-01
.799E-01	.666E-01	.540E-01	.427E-01	.330E-01	.250E-01	.183E-01	.128E-01	.810E-02	.388E-02
.255E+01	.211E+01	.162E+01	.118E+01	.804E+00	.482E+00	.241E+00	.128E+00	.109E+00	.949E-01
.806E-01	.661E-01	.523E-01	.403E-01	.302E-01	.222E-01	.161E-01	.111E-01	.701E-02	.336E-02
.243E+01	.197E+01	.144E+01	.102E+01	.691E+00	.421E+00	.227E+00	.134E+00	.112E+00	.967E-01
.815E-01	.653E-01	.498E-01	.366E-01	.261E-01	.186E-01	.132E-01	.910E-02	.572E-02	.275E-02
.231E+01	.181E+01	.111E+01	.743E+00	.516E+00	.342E+00	.226E+00	.161E+00	.130E+00	.106E+00
.854E-01	.638E-01	.454E-01	.309E-01	.201E-01	.136E-01	.958E-02	.671E-02	.427E-02	.210E-02
.220E+01	.161E+01	.377E+00	.329E+00	.292E+00	.255E+00	.218E+00	.181E+00	.147E+00	.115E+00
.852E-01	.593E-01	.382E-01	.243E-01	.152E-01	.101E-01	.711E-02	.510E-02	.331E-02	.164E-02
.215E+01	.153E+01	.368E+00	.324E+00	.289E+00	.253E+00	.217E+00	.182E+00	.148E+00	.115E+00
.854E-01	.585E-01	.365E-01	.234E-01	.149E-01	.992E-02	.704E-02	.506E-02	.329E-02	.163E-02
.215E+01	.153E+01	.368E+00	.324E+00	.289E+00	.253E+00	.217E+00	.182E+00	.148E+00	.115E+00
.854E-01	.585E-01	.365E-01	.234E-01	.149E-01	.992E-02	.704E-02	.506E-02	.329E-02	.163E-02
.220E+01	.161E+01	.377E+00	.329E+00	.292E+00	.255E+00	.218E+00	.181E+00	.147E+00	.115E+00
.852E-01	.593E-01	.382E-01	.243E-01	.152E-01	.101E-01	.711E-02	.510E-02	.331E-02	.164E-02
.231E+01	.181E+01	.111E+01	.743E+00	.516E+00	.342E+00	.226E+00	.161E+00	.130E+00	.106E+00
.854E-01	.638E-01	.454E-01	.309E-01	.201E-01	.136E-01	.958E-02	.671E-02	.427E-02	.210E-02
.243E+01	.197E+01	.144E+01	.102E+01	.691E+00	.421E+00	.227E+00	.134E+00	.112E+00	.967E-01
.815E-01	.653E-01	.498E-01	.366E-01	.261E-01	.186E-01	.132E-01	.910E-02	.572E-02	.275E-02
.255E+01	.211E+01	.162E+01	.118E+01	.804E+00	.482E+00	.241E+00	.128E+00	.109E+00	.949E-01
.806E-01	.661E-01	.523E-01	.403E-01	.302E-01	.222E-01	.161E-01	.111E-01	.701E-02	.336E-02
.265E+01	.222E+01	.176E+01	.130E+01	.895E+00	.540E+00	.264E+00	.127E+00	.107E+00	.935E-01
.799E-01	.666E-01	.540E-01	.427E-01	.330E-01	.250E-01	.183E-01	.128E-01	.810E-02	.388E-02
.274E+01	.232E+01	.185E+01	.139E+01	.966E+00	.590E+00	.286E+00	.128E+00	.106E+00	.924E-01
.794E-01	.669E-01	.550E-01	.444E-01	.350E-01	.269E-01	.200E-01	.141E-01	.897E-02	.430E-02
.280E+01	.239E+01	.192E+01	.145E+01	.102E+01	.627E+00	.304E+00	.130E+00	.105E+00	.918E-01
.791E-01	.671E-01	.557E-01	.454E-01	.363E-01	.283E-01	.212E-01	.151E-01	.960E-02	.462E-02
.284E+01	.243E+01	.197E+01	.149E+01	.105E+01	.653E+00	.316E+00	.133E+00	.105E+00	.914E-01
.790E-01	.672E-01	.562E-01	.461E-01	.371E-01	.291E-01	.220E-01	.157E-01	.100E-01	.482E-02
.286E+01	.246E+01	.199E+01	.152E+01	.107E+01	.666E+00	.323E+00	.134E+00	.105E+00	.913E-01
.789E-01	.673E-01	.564E-01	.464E-01	.375E-01	.295E-01	.224E-01	.160E-01	.102E-01	.492E-02

****

PRESSURE OF WATER PHASE [ATM]

.284E+01	.244E+01	.197E+01	.150E+01	.105E+01	.649E+00	.303E+00	.687E-01	-.132E+00	-.246E+00
-.261E+00	-.273E+00	-.284E+00	-.294E+00	-.303E+00	-.311E+00	-.318E+00	-.324E+00	-.330E+00	-.335E+00
.283E+01	.242E+01	.195E+01	.148E+01	.104E+01	.636E+00	.296E+00	.650E-01	-.137E+00	-.246E+00
-.261E+00	-.273E+00	-.284E+00	-.294E+00	-.303E+00	-.311E+00	-.318E+00	-.324E+00	-.330E+00	-.335E+00
.279E+01	.237E+01	.190E+01	.144E+01	.100E+01	.610E+00	.283E+00	.580E-01	-.148E+00	-.246E+00
-.261E+00	-.273E+00	-.284E+00	-.295E+00	-.304E+00	-.312E+00	-.319E+00	-.325E+00	-.330E+00	-.335E+00
.272E+01	.230E+01	.183E+01	.137E+01	.948E+00	.572E+00	.263E+00	.471E-01	-.161E+00	-.246E+00
-.261E+00	-.273E+00	-.285E+00	-.296E+00	-.305E+00	-.313E+00	-.320E+00	-.326E+00	-.331E+00	-.336E+00
.263E+01	.221E+01	.174E+01	.128E+01	.877E+00	.521E+00	.238E+00	.347E-01	-.168E+00	-.241E+00
-.259E+00	-.273E+00	-.286E+00	-.297E+00	-.307E+00	-.315E+00	-.322E+00	-.327E+00	-.332E+00	-.336E+00
.253E+01	.209E+01	.160E+01	.116E+01	.784E+00	.462E+00	.212E+00	.309E-01	-.888E-01	-.157E+00

TABLE 4 (continued)

-.202E+00	-.242E+00	-.273E+00	-.295E+00	-.309E+00	-.318E+00	-.324E+00	-.329E+00	-.333E+00	-.337E+00
.241E+01	.195E+01	.142E+01	.997E+00	.666E+00	.396E+00	.192E+00	.629E-01	.137E-01	-.195E-01
-.549E-01	-.915E-01	-.136E+00	-.202E+00	-.260E+00	-.298E+00	-.319E+00	-.329E+00	-.334E+00	-.337E+00
.229E+01	.179E+01	.107E+01	.697E+00	.475E+00	.310E+00	.197E+00	.130E+00	.918E-01	.621E-01
.351E-01	.608E-02	-.264E-01	-.610E-01	-.101E+00	-.146E+00	-.200E+00	-.259E+00	-.297E+00	-.315E+00
.218E+01	.156E+01	.350E+00	.308E+00	.273E+00	.237E+00	.200E+00	.164E+00	.130E+00	.975E-01
.676E-01	.402E-01	.160E-01	-.627E-02	-.313E-01	-.589E-01	-.913E-01	-.129E+00	-.162E+00	-.182E+00
.213E+01	.148E+01	.341E+00	.304E+00	.271E+00	.236E+00	.200E+00	.164E+00	.130E+00	.983E-01
.685E-01	.409E-01	.164E-01	-.499E-02	-.298E-01	-.571E-01	-.894E-01	-.126E+00	-.160E+00	-.180E+00
.213E+01	.148E+01	.341E+00	.304E+00	.271E+00	.236E+00	.200E+00	.164E+00	.130E+00	.983E-01
.685E-01	.409E-01	.164E-01	-.499E-02	-.298E-01	-.571E-01	-.894E-01	-.126E+00	-.160E+00	-.180E+00
.218E+01	.156E+01	.350E+00	.308E+00	.273E+00	.237E+00	.200E+00	.164E+00	.130E+00	.975E-01
.676E-01	.402E-01	.160E-01	-.627E-02	-.313E-01	-.589E-01	-.913E-01	-.129E+00	-.162E+00	-.182E+00
.229E+01	.179E+01	.107E+01	.697E+00	.475E+00	.310E+00	.197E+00	.130E+00	.918E-01	.621E-01
.351E-01	.608E-02	-.264E-01	-.610E-01	-.101E+00	-.146E+00	-.200E+00	-.259E+00	-.297E+00	-.315E+00
.241E+01	.195E+01	.142E+01	.997E+00	.666E+00	.396E+00	.192E+00	.629E-01	.137E-01	-.195E-01
-.549E-01	-.915E-01	-.136E+00	-.202E+00	-.260E+00	-.298E+00	-.319E+00	-.329E+00	-.334E+00	-.337E+00
.253E+01	.209E+01	.160E+01	.116E+01	.784E+00	.462E+00	.212E+00	.309E-01	-.888E-01	-.157E+00
-.202E+00	-.242E+00	-.273E+00	-.295E+00	-.309E+00	-.318E+00	-.324E+00	-.329E+00	-.333E+00	-.337E+00
.263E+01	.221E+01	.174E+01	.128E+01	.877E+00	.521E+00	.238E+00	.347E-01	-.168E+00	-.241E+00
-.259E+00	-.273E+00	-.286E+00	-.297E+00	-.307E+00	-.315E+00	-.322E+00	-.327E+00	-.332E+00	-.336E+00
.272E+01	.230E+01	.183E+01	.137E+01	.948E+00	.572E+00	.263E+00	.471E-01	-.161E+00	-.246E+00
-.261E+00	-.273E+00	-.285E+00	-.296E+00	-.305E+00	-.313E+00	-.320E+00	-.326E+00	-.331E+00	-.336E+00
.279E+01	.237E+01	.190E+01	.144E+01	.100E+01	.610E+00	.283E+00	.580E-01	-.148E+00	-.246E+00
-.261E+00	-.273E+00	-.284E+00	-.295E+00	-.304E+00	-.312E+00	-.319E+00	-.325E+00	-.330E+00	-.335E+00
.283E+01	.242E+01	.195E+01	.148E+01	.104E+01	.636E+00	.296E+00	.650E-01	-.137E+00	-.246E+00
-.261E+00	-.273E+00	-.284E+00	-.294E+00	-.303E+00	-.311E+00	-.318E+00	-.324E+00	-.330E+00	-.335E+00
.284E+01	.244E+01	.197E+01	.150E+01	.105E+01	.649E+00	.303E+00	.687E-01	-.132E+00	-.246E+00
-.261E+00	-.273E+00	-.284E+00	-.294E+00	-.303E+00	-.311E+00	-.318E+00	-.324E+00	-.330E+00	-.335E+00

****

PRESSURE OF GAS PHASE [ATM]

.302E+01	.259E+01	.210E+01	.162E+01	.117E+01	.771E+00	.445E+00	.277E+00	.262E+00	.246E+00
.228E+00	.208E+00	.187E+00	.166E+00	.146E+00	.125E+00	.105E+00	.852E-01	.639E-01	.386E-01
.301E+01	.256E+01	.207E+01	.160E+01	.116E+01	.762E+00	.443E+00	.278E+00	.263E+00	.247E+00
.228E+00	.208E+00	.187E+00	.165E+00	.144E+00	.124E+00	.104E+00	.840E-01	.629E-01	.380E-01
.297E+01	.252E+01	.203E+01	.156E+01	.113E+01	.745E+00	.438E+00	.281E+00	.266E+00	.248E+00
.228E+00	.207E+00	.185E+00	.163E+00	.142E+00	.121E+00	.101E+00	.814E-01	.609E-01	.368E-01
.291E+01	.245E+01	.197E+01	.151E+01	.109E+01	.722E+00	.434E+00	.286E+00	.269E+00	.249E+00
.228E+00	.205E+00	.182E+00	.159E+00	.137E+00	.116E+00	.964E-01	.774E-01	.578E-01	.349E-01
.282E+01	.237E+01	.189E+01	.145E+01	.105E+01	.697E+00	.434E+00	.293E+00	.273E+00	.251E+00
.228E+00	.203E+00	.179E+00	.154E+00	.130E+00	.109E+00	.896E-01	.717E-01	.534E-01	.322E-01
.273E+01	.229E+01	.181E+01	.138E+01	.101E+01	.680E+00	.442E+00	.302E+00	.278E+00	.253E+00
.227E+00	.200E+00	.174E+00	.147E+00	.120E+00	.984E-01	.801E-01	.638E-01	.475E-01	.287E-01
.263E+01	.221E+01	.173E+01	.134E+01	.992E+00	.685E+00	.465E+00	.310E+00	.282E+00	.254E+00
.226E+00	.194E+00	.167E+00	.138E+00	.105E+00	.830E-01	.669E-01	.533E-01	.398E-01	.241E-01

TABLE 4 (continued)

.257E+01	.221E+01	.169E+01	.132E+01	.996E+00	.707E+00	.504E+00	.361E+00	.295E+00	.259E+00
.226E+00	.184E+00	.161E+00	.128E+00	.784E-01	.594E-01	.484E-01	.392E-01	.296E-01	.180E-01
.255E+01	.229E+01	.808E+00	.638E+00	.500E+00	.405E+00	.348E+00	.302E+00	.261E+00	.227E+00
.197E+00	.175E+00	.135E+00	.812E-01	.426E-01	.390E-01	.345E-01	.290E-01	.224E-01	.138E-01
.255E+01	.233E+01	.789E+00	.604E+00	.464E+00	.377E+00	.335E+00	.300E+00	.265E+00	.227E+00
.196E+00	.173E+00	.123E+00	.652E-01	.414E-01	.383E-01	.340E-01	.287E-01	.222E-01	.137E-01
.255E+01	.233E+01	.789E+00	.604E+00	.464E+00	.377E+00	.335E+00	.300E+00	.265E+00	.227E+00
.196E+00	.173E+00	.123E+00	.652E-01	.414E-01	.383E-01	.340E-01	.287E-01	.222E-01	.137E-01
.255E+01	.229E+01	.808E+00	.638E+00	.500E+00	.405E+00	.348E+00	.302E+00	.261E+00	.227E+00
.197E+00	.175E+00	.135E+00	.812E-01	.426E-01	.390E-01	.345E-01	.290E-01	.224E-01	.138E-01
.257E+01	.221E+01	.169E+01	.132E+01	.996E+00	.707E+00	.504E+00	.361E+00	.295E+00	.259E+00
.226E+00	.184E+00	.161E+00	.128E+00	.784E-01	.594E-01	.484E-01	.392E-01	.296E-01	.180E-01
.263E+01	.221E+01	.173E+01	.134E+01	.992E+00	.685E+00	.465E+00	.310E+00	.282E+00	.254E+00
.226E+00	.194E+00	.167E+00	.138E+00	.105E+00	.830E-01	.669E-01	.533E-01	.398E-01	.241E-01
.273E+01	.229E+01	.181E+01	.138E+01	.101E+01	.680E+00	.442E+00	.302E+00	.278E+00	.253E+00
.227E+00	.200E+00	.174E+00	.147E+00	.120E+00	.984E-01	.801E-01	.638E-01	.475E-01	.287E-01
.282E+01	.237E+01	.189E+01	.145E+01	.105E+01	.697E+00	.434E+00	.293E+00	.273E+00	.251E+00
.228E+00	.203E+00	.179E+00	.154E+00	.130E+00	.109E+00	.896E-01	.717E-01	.534E-01	.322E-01
.291E+01	.245E+01	.197E+01	.151E+01	.109E+01	.722E+00	.434E+00	.286E+00	.269E+00	.249E+00
.228E+00	.205E+00	.182E+00	.159E+00	.137E+00	.116E+00	.964E-01	.774E-01	.578E-01	.349E-01
.297E+01	.252E+01	.203E+01	.156E+01	.113E+01	.745E+00	.438E+00	.281E+00	.266E+00	.248E+00
.228E+00	.207E+00	.185E+00	.163E+00	.142E+00	.121E+00	.101E+00	.814E-01	.609E-01	.368E-01
.301E+01	.256E+01	.207E+01	.160E+01	.116E+01	.762E+00	.443E+00	.278E+00	.263E+00	.247E+00
.228E+00	.208E+00	.187E+00	.165E+00	.144E+00	.124E+00	.104E+00	.840E-01	.629E-01	.380E-01
.302E+01	.259E+01	.210E+01	.162E+01	.117E+01	.771E+00	.445E+00	.277E+00	.262E+00	.246E+00
.228E+00	.208E+00	.187E+00	.166E+00	.146E+00	.125E+00	.105E+00	.852E-01	.639E-01	.386E-01

****

X-COMPONENT OF OIL VELOCITY [CM/SEC]

.000E+00	.000E+00	.000E+00	.000E+00	.900E-06	.319E-05	.877E-05	.339E-04	.756E-04	.841E-04
.799E-04	.756E-04	.718E-04	.673E-04	.632E-04	.592E-04	.553E-04	.519E-04	.492E-04	.475E-04
.000E+00									
.000E+00	.000E+00	.000E+00	.000E+00	.936E-06	.331E-05	.921E-05	.335E-04	.758E-04	.843E-04
.804E-04	.765E-04	.727E-04	.682E-04	.639E-04	.596E-04	.553E-04	.515E-04	.485E-04	.467E-04
.000E+00									
.000E+00	.000E+00	.000E+00	.000E+00	.108E-05	.362E-05	.982E-05	.330E-04	.761E-04	.847E-04
.816E-04	.783E-04	.748E-04	.701E-04	.654E-04	.603E-04	.551E-04	.506E-04	.472E-04	.451E-04
.000E+00									
.000E+00	.000E+00	.000E+00	.000E+00	.120E-05	.349E-05	.954E-05	.331E-04	.781E-04	.858E-04
.838E-04	.815E-04	.782E-04	.733E-04	.677E-04	.612E-04	.547E-04	.491E-04	.450E-04	.425E-04
.000E+00									
.000E+00	.000E+00	.000E+00	.000E+00	.216E-06	.194E-05	.959E-05	.321E-04	.820E-04	.877E-04
.872E-04	.865E-04	.835E-04	.781E-04	.710E-04	.622E-04	.537E-04	.467E-04	.417E-04	.388E-04
.000E+00									
.000E+00	.000E+00	.000E+00	.000E+00	.000E+00	.000E+00	.801E-05	.350E-04	.836E-04	.887E-04
.907E-04	.935E-04	.919E-04	.849E-04	.753E-04	.627E-04	.514E-04	.428E-04	.373E-04	.341E-04

TABLE 4 (continued)

.000E+00									
.000E+00	.000E+00	.000E+00	.000E+00	.000E+00	.000E+00	.452E-05	.363E-04	.596E-04	.698E-04
.793E-04	.922E-04	.991E-04	.919E-04	.792E-04	.615E-04	.467E-04	.368E-04	.312E-04	.282E-04
.000E+00									
.000E+00	.000E+00	.000E+00	.000E+00	.000E+00	.000E+00	.355E-06	.848E-05	.120E-04	.159E-04
.220E-04	.327E-04	.409E-04	.488E-04	.553E-04	.473E-04	.354E-04	.266E-04	.231E-04	.211E-04
.000E+00									
.000E+00	.000E+00	.000E+00	.000E+00	.000E+00	.000E+00	.000E+00	.292E-05	.728E-05	.195E-04
.406E-04	.735E-04	.149E-03	.252E-03	.390E-03	.536E-03	.640E-03	.718E-03	.765E-03	.801E-03
.000E+00									
.000E+00	.000E+00	.000E+00	.000E+00	.000E+00	.000E+00	.000E+00	.123E-05	.425E-05	.750E-05
.108E-04	.156E-04	.525E-04	.199E-03	.351E-03	.478E-03	.596E-03	.689E-03	.749E-03	.791E-03
.000E+00									
.000E+00	.000E+00	.000E+00	.000E+00	.000E+00	.000E+00	.000E+00	.123E-05	.425E-05	.750E-05
.108E-04	.156E-04	.525E-04	.199E-03	.351E-03	.478E-03	.596E-03	.689E-03	.749E-03	.791E-03
.000E+00									
.000E+00	.000E+00	.000E+00	.000E+00	.000E+00	.000E+00	.000E+00	.292E-05	.728E-05	.195E-04
.406E-04	.735E-04	.149E-03	.252E-03	.390E-03	.536E-03	.640E-03	.718E-03	.765E-03	.801E-03
.000E+00									
.000E+00	.000E+00	.000E+00	.000E+00	.000E+00	.000E+00	.355E-06	.848E-05	.120E-04	.159E-04
.220E-04	.327E-04	.409E-04	.488E-04	.553E-04	.473E-04	.354E-04	.266E-04	.231E-04	.211E-04
.000E+00									
.000E+00	.000E+00	.000E+00	.000E+00	.000E+00	.000E+00	.452E-05	.363E-04	.596E-04	.698E-04
.793E-04	.922E-04	.991E-04	.919E-04	.792E-04	.615E-04	.467E-04	.368E-04	.312E-04	.282E-04
.000E+00									
.000E+00	.000E+00	.000E+00	.000E+00	.000E+00	.000E+00	.801E-05	.350E-04	.836E-04	.887E-04
.907E-04	.935E-04	.919E-04	.849E-04	.753E-04	.627E-04	.514E-04	.428E-04	.373E-04	.341E-04
.000E+00									
.000E+00	.000E+00	.000E+00	.000E+00	.216E-06	.194E-05	.959E-05	.321E-04	.820E-04	.877E-04
.872E-04	.865E-04	.835E-04	.781E-04	.710E-04	.622E-04	.537E-04	.467E-04	.417E-04	.388E-04
.000E+00									
.000E+00	.000E+00	.000E+00	.000E+00	.120E-05	.349E-05	.954E-05	.331E-04	.781E-04	.858E-04
.838E-04	.815E-04	.782E-04	.733E-04	.677E-04	.612E-04	.547E-04	.491E-04	.450E-04	.425E-04
.000E+00									
.000E+00	.000E+00	.000E+00	.000E+00	.108E-05	.362E-05	.982E-05	.330E-04	.761E-04	.847E-04
.816E-04	.783E-04	.748E-04	.701E-04	.654E-04	.603E-04	.551E-04	.506E-04	.472E-04	.451E-04
.000E+00									
.000E+00	.000E+00	.000E+00	.000E+00	.936E-06	.331E-05	.921E-05	.335E-04	.758E-04	.843E-04
.804E-04	.765E-04	.727E-04	.682E-04	.639E-04	.596E-04	.553E-04	.515E-04	.485E-04	.467E-04
.000E+00									
.000E+00	.000E+00	.000E+00	.000E+00	.900E-06	.319E-05	.877E-05	.339E-04	.756E-04	.841E-04
.799E-04	.756E-04	.718E-04	.673E-04	.632E-04	.592E-04	.553E-04	.519E-04	.492E-04	.475E-04
.000E+00									

****

Y-COMPONENT OF OIL VELOCITY [CM/SEC]

TABLE 4 (continued)

.000E+00	.000E+00	.000E+00	.000E+00	.000E+00	.000E+00	.000E+00	.000E+00	.000E+00	.000E+00
.000E+00	.000E+00	.000E+00	.000E+00	.000E+00	.000E+00	.000E+00	.000E+00	.000E+00	.000E+00
.000E+00	.000E+00	.000E+00	.579E-07	.187E-06	.453E-06	.159E-05	.462E-05	-.162E-05	-.140E-05
-.603E-06	.564E-06	.186E-05	.300E-05	.386E-05	.424E-05	.409E-05	.346E-05	.249E-05	.131E-05
.000E+00	.000E+00	.000E+00	.121E-06	.393E-06	.955E-06	.300E-05	.833E-05	-.378E-05	-.316E-05
-.138E-05	.115E-05	.393E-05	.636E-05	.814E-05	.886E-05	.845E-05	.709E-05	.507E-05	.265E-05
.000E+00	.000E+00	.000E+00	.214E-06	.657E-06	.155E-05	.473E-05	.963E-05	-.727E-05	-.560E-05
-.249E-05	.182E-05	.652E-05	.105E-04	.134E-04	.143E-04	.134E-04	.111E-04	.781E-05	.405E-05
.000E+00	.000E+00	.000E+00	.338E-06	.892E-06	.211E-05	.640E-05	.586E-05	-.115E-04	-.879E-05
-.410E-05	.268E-05	.101E-04	.162E-04	.203E-04	.211E-04	.192E-04	.154E-04	.107E-04	.550E-05
.000E+00	.000E+00	.000E+00	.862E-07	.675E-06	.273E-05	.712E-05	-.626E-05	-.150E-04	-.122E-04
-.627E-05	.395E-05	.152E-04	.243E-04	.299E-04	.299E-04	.260E-04	.202E-04	.137E-04	.691E-05
.000E+00	.000E+00	.000E+00	.000E+00	.000E+00	.277E-05	.594E-05	-.213E-04	-.180E-04	-.133E-04
-.671E-05	.785E-05	.248E-04	.367E-04	.436E-04	.413E-04	.340E-04	.251E-04	.164E-04	.807E-05
.000E+00	.000E+00	.000E+00	.000E+00	.000E+00	.250E-05	.512E-06	-.143E-04	-.163E-04	-.136E-04
-.806E-05	.127E-04	.414E-04	.593E-04	.669E-04	.583E-04	.441E-04	.301E-04	.187E-04	.874E-05
.000E+00	.000E+00	.000E+00	.000E+00	.000E+00	.712E-06	.301E-05	-.221E-06	-.553E-06	-.620E-06
.546E-06	.269E-04	.641E-04	.906E-04	.958E-04	.829E-04	.609E-04	.406E-04	.250E-04	.123E-04
.000E+00	.000E+00	.000E+00	.000E+00	.000E+00	.000E+00	.487E-07	-.102E-06	-.275E-06	-.254E-06
-.142E-06	.736E-05	.430E-04	.498E-04	.408E-04	.460E-04	.349E-04	.247E-04	.138E-04	.765E-05
.000E+00	.000E+00	.000E+00	.000E+00	.000E+00	.000E+00	.524E-20	.141E-19	-.877E-20	-.409E-19
-.329E-19	.675E-19	-.143E-18	-.391E-18	.452E-18	.000E+00	.821E-18	.498E-18	.281E-18	.588E-18
.000E+00	.000E+00	.000E+00	.000E+00	.000E+00	.000E+00	-.487E-07	.102E-06	.275E-06	.254E-06
.142E-06	-.736E-05	-.430E-04	-.498E-04	-.408E-04	-.460E-04	-.349E-04	-.247E-04	-.138E-04	-.765E-05
.000E+00	.000E+00	.000E+00	.000E+00	.000E+00	-.712E-06	-.301E-05	.221E-06	.553E-06	.620E-06
-.546E-06	-.269E-04	-.641E-04	-.906E-04	-.958E-04	-.829E-04	-.609E-04	-.406E-04	-.250E-04	-.123E-04
.000E+00	.000E+00	.000E+00	.000E+00	.000E+00	-.250E-05	-.512E-06	.143E-04	.163E-04	.136E-04
.806E-05	-.127E-04	-.414E-04	-.593E-04	-.669E-04	-.583E-04	-.441E-04	-.301E-04	-.187E-04	-.874E-05
.000E+00	.000E+00	.000E+00	.000E+00	.000E+00	-.277E-05	-.594E-05	.213E-04	.180E-04	.133E-04
.671E-05	-.785E-05	-.248E-04	-.367E-04	-.436E-04	-.413E-04	-.340E-04	-.251E-04	-.164E-04	-.807E-05
.000E+00	.000E+00	.000E+00	-.862E-07	-.675E-06	-.273E-05	-.712E-05	.626E-05	.150E-04	.122E-04
.627E-05	-.395E-05	-.152E-04	-.243E-04	-.299E-04	-.299E-04	-.260E-04	-.202E-04	-.137E-04	-.691E-05
.000E+00	.000E+00	.000E+00	-.338E-06	-.892E-06	-.211E-05	-.640E-05	-.586E-05	.115E-04	.879E-05
.410E-05	-.268E-05	-.101E-04	-.162E-04	-.203E-04	-.211E-04	-.192E-04	-.154E-04	-.107E-04	-.550E-05
.000E+00	.000E+00	.000E+00	-.214E-06	-.657E-06	-.155E-05	-.473E-05	-.963E-05	.727E-05	.560E-05
.249E-05	-.182E-05	-.652E-05	-.105E-04	-.134E-04	-.143E-04	-.134E-04	-.111E-04	-.781E-05	-.405E-05
.000E+00	.000E+00	.000E+00	-.121E-06	-.393E-06	-.955E-06	-.300E-05	-.833E-05	.378E-05	.316E-05
.138E-05	-.115E-05	-.393E-05	-.636E-05	-.814E-05	-.886E-05	-.845E-05	-.709E-05	-.507E-05	-.265E-05
.000E+00	.000E+00	.000E+00	-.579E-07	-.187E-06	-.453E-06	-.159E-05	-.462E-05	.162E-05	.140E-05
.603E-06	-.564E-06	-.186E-05	-.300E-05	-.386E-05	-.424E-05	-.409E-05	-.346E-05	-.249E-05	-.131E-05
.000E+00	.000E+00	.000E+00	.000E+00	.000E+00	.000E+00	.000E+00	.000E+00	.000E+00	.000E+00
.000E+00	.000E+00	.000E+00	.000E+00	.000E+00	.000E+00	.000E+00	.000E+00	.000E+00	.000E+00

****

X-COMPONENT OF WATER VELOCITY [CM/SEC]

.000E+00	.149E-03	.178E-03	.182E-03	.171E-03	.155E-03	.131E-03	.791E-04	.159E-04	.818E-06

TABLE 4 (continued)

.289E-08	.621E-11	.127E-13	.231E-16	.000E+00	.000E+00	.000E+00	.000E+00	.000E+00	.000E+00
.000E+00									
.000E+00	.152E-03	.177E-03	.180E-03	.169E-03	.152E-03	.127E-03	.773E-04	.150E-04	.738E-06
.257E-08	.563E-11	.117E-13	.216E-16	.000E+00	.000E+00	.000E+00	.000E+00	.000E+00	.000E+00
.000E+00									
.000E+00	.156E-03	.176E-03	.178E-03	.165E-03	.147E-03	.121E-03	.724E-04	.132E-04	.596E-06
.203E-08	.462E-11	.100E-13	.188E-16	.000E+00	.000E+00	.000E+00	.000E+00	.000E+00	.000E+00
.000E+00									
.000E+00	.157E-03	.175E-03	.174E-03	.158E-03	.139E-03	.111E-03	.644E-04	.110E-04	.427E-06
.141E-08	.381E-11	.111E-13	.159E-16	.000E+00	.000E+00	.000E+00	.000E+00	.000E+00	.000E+00
.000E+00									
.000E+00	.159E-03	.174E-03	.167E-03	.147E-03	.127E-03	.989E-04	.537E-04	.849E-05	.328E-06
.736E-08	.162E-08	.324E-09	.322E-10	.855E-12	.271E-15	.333E-19	.000E+00	.000E+00	.000E+00
.000E+00									
.000E+00	.163E-03	.174E-03	.154E-03	.129E-03	.108E-03	.829E-04	.399E-04	.446E-05	.667E-06
.277E-06	.157E-06	.707E-07	.219E-07	.441E-08	.605E-09	.586E-10	.273E-11	.124E-14	.128E-18
.000E+00									
.000E+00	.168E-03	.180E-03	.123E-03	.863E-04	.694E-04	.544E-04	.246E-04	.334E-05	.120E-05
.991E-06	.803E-06	.702E-06	.710E-06	.400E-06	.142E-06	.346E-07	.585E-08	.742E-09	.107E-09
.000E+00									
.000E+00	.179E-03	.191E-03	.493E-04	.289E-04	.258E-04	.233E-04	.147E-04	.797E-05	.506E-05
.380E-05	.342E-05	.311E-05	.227E-05	.170E-05	.118E-05	.815E-06	.531E-06	.194E-06	.468E-07
.000E+00									
.000E+00	.210E-03	.324E-03	.494E-03	.572E-03	.632E-03	.664E-03	.666E-03	.639E-03	.602E-03
.557E-03	.505E-03	.423E-03	.340E-03	.269E-03	.182E-03	.116E-03	.670E-04	.375E-04	.135E-04
.000E+00									
.000E+00	.207E-03	.252E-03	.455E-03	.577E-03	.643E-03	.673E-03	.668E-03	.639E-03	.602E-03
.564E-03	.520E-03	.450E-03	.361E-03	.283E-03	.190E-03	.122E-03	.697E-04	.392E-04	.139E-04
.000E+00									
.000E+00	.207E-03	.252E-03	.455E-03	.577E-03	.643E-03	.673E-03	.668E-03	.639E-03	.602E-03
.564E-03	.520E-03	.450E-03	.361E-03	.283E-03	.190E-03	.122E-03	.697E-04	.392E-04	.139E-04
.000E+00									
.000E+00	.210E-03	.324E-03	.494E-03	.572E-03	.632E-03	.664E-03	.666E-03	.639E-03	.602E-03
.557E-03	.505E-03	.423E-03	.340E-03	.269E-03	.182E-03	.116E-03	.670E-04	.375E-04	.135E-04
.000E+00									
.000E+00	.179E-03	.191E-03	.493E-04	.289E-04	.258E-04	.233E-04	.147E-04	.797E-05	.506E-05
.380E-05	.342E-05	.311E-05	.227E-05	.170E-05	.118E-05	.815E-06	.531E-06	.194E-06	.468E-07
.000E+00									
.000E+00	.168E-03	.180E-03	.123E-03	.863E-04	.694E-04	.544E-04	.246E-04	.334E-05	.120E-05
.991E-06	.803E-06	.702E-06	.710E-06	.400E-06	.142E-06	.346E-07	.585E-08	.742E-09	.107E-09
.000E+00									
.000E+00	.163E-03	.174E-03	.154E-03	.129E-03	.108E-03	.829E-04	.399E-04	.446E-05	.667E-06
.277E-06	.157E-06	.707E-07	.219E-07	.441E-08	.605E-09	.586E-10	.273E-11	.124E-14	.128E-18
.000E+00									
.000E+00	.159E-03	.174E-03	.167E-03	.147E-03	.127E-03	.989E-04	.537E-04	.849E-05	.328E-06

TABLE 4 (continued)

```
.736E-08  .162E-08  .324E-09  .322E-10  .855E-12  .271E-15  .333E-19  .000E+00  .000E+00  .000E+00
.000E+00
.000E+00  .157E-03  .175E-03  .174E-03  .158E-03  .139E-03  .111E-03  .644E-04  .110E-04  .427E-06
.141E-08  .381E-11  .111E-13  .159E-16  .000E+00  .000E+00  .000E+00  .000E+00  .000E+00  .000E+00
.000E+00
.000E+00  .156E-03  .176E-03  .178E-03  .165E-03  .147E-03  .121E-03  .724E-04  .132E-04  .596E-06
.203E-08  .462E-11  .100E-13  .188E-16  .000E+00  .000E+00  .000E+00  .000E+00  .000E+00  .000E+00
.000E+00
.000E+00  .152E-03  .177E-03  .180E-03  .169E-03  .152E-03  .127E-03  .773E-04  .150E-04  .738E-06
.257E-08  .563E-11  .117E-13  .216E-16  .000E+00  .000E+00  .000E+00  .000E+00  .000E+00  .000E+00
.000E+00
.000E+00  .149E-03  .178E-03  .182E-03  .171E-03  .155E-03  .131E-03  .791E-04  .159E-04  .818E-06
.289E-08  .621E-11  .127E-13  .231E-16  .000E+00  .000E+00  .000E+00  .000E+00  .000E+00  .000E+00
.000E+00
****************************************
Y-COMPONENT OF WATER VELOCITY [CM/SEC]
.000E+00  .000E+00  .000E+00  .000E+00  .000E+00  .000E+00  .000E+00  .000E+00  .000E+00  .000E+00
.000E+00  .000E+00  .000E+00  .000E+00  .000E+00  .000E+00  .000E+00  .000E+00  .000E+00  .000E+00
.815E-05  .129E-04  .124E-04  .110E-04  .916E-05  .679E-05  .309E-05  .392E-06  .526E-07  .295E-10
-.439E-13  .998E-16  .637E-18  .000E+00  .000E+00  .000E+00  .000E+00  .000E+00  .000E+00  .000E+00
.194E-04  .248E-04  .242E-04  .220E-04  .182E-04  .133E-04  .592E-05  .708E-06  .950E-07  .296E-10
-.807E-13  .186E-15  .124E-17  .000E+00  .000E+00  .000E+00  .000E+00  .000E+00  .000E+00  .000E+00
.329E-04  .355E-04  .359E-04  .331E-04  .271E-04  .191E-04  .876E-05  .957E-06  .112E-06  -.750E-11
-.116E-12  .244E-15  .175E-17  .000E+00  .000E+00  .000E+00  .000E+00  .000E+00  .000E+00  .000E+00
.442E-04  .480E-04  .491E-04  .449E-04  .359E-04  .248E-04  .101E-04  .889E-06  .437E-07  -.309E-08
-.314E-09  -.213E-11  .211E-17  .000E+00  .000E+00  .000E+00  .000E+00  .000E+00  .000E+00  .000E+00
.537E-04  .591E-04  .665E-04  .594E-04  .447E-04  .282E-04  .956E-05  .217E-06  -.105E-05  -.698E-06
-.304E-06  -.957E-07  -.174E-07  -.957E-09  .849E-16  .176E-19  .000E+00  .000E+00  .000E+00  .000E+00
.594E-04  .680E-04  .888E-04  .768E-04  .542E-04  .296E-04  .579E-05  -.296E-05  -.502E-05  -.523E-05
-.439E-05  -.322E-05  -.199E-05  -.881E-06  -.250E-06  -.450E-07  -.418E-08  -.157E-10  .394E-19  .000E+00
.594E-04  .745E-04  .139E-03  .106E-03  .666E-04  .313E-04  -.124E-05  -.191E-04  -.181E-04  -.156E-04
-.144E-04  -.127E-04  -.975E-05  -.812E-05  -.570E-05  -.309E-05  -.145E-05  -.485E-06  -.134E-06  -.498E-07
.522E-04  .818E-04  .255E-03  .135E-03  .842E-04  .401E-04  -.334E-05  -.337E-04  -.378E-04  -.352E-04
-.320E-04  -.318E-04  -.346E-04  -.314E-04  -.246E-04  -.166E-04  -.104E-04  -.790E-05  -.477E-05  -.381E-05
.243E-04  .149E-04  .141E-03  .842E-04  .451E-04  .193E-04  -.326E-05  -.185E-04  -.224E-04  -.222E-04
-.224E-04  -.177E-04  -.105E-04  -.199E-04  -.145E-04  -.878E-05  -.502E-05  -.401E-05  -.209E-05  -.195E-05
-.769E-18  -.204E-18  .935E-18  .130E-17  .138E-17  .707E-18  .709E-18  .000E+00  -.708E-18  -.143E-17
-.356E-18  -.174E-18  .159E-18  .323E-18  .327E-19  -.143E-18  -.713E-19  .000E+00  .000E+00  -.187E-18
-.243E-04  -.149E-04  -.141E-03  -.842E-04  -.451E-04  -.193E-04  .326E-05  .185E-04  .224E-04  .222E-04
.224E-04  .177E-04  .105E-04  .199E-04  .145E-04  .878E-05  .502E-05  .401E-05  .209E-05  .195E-05
-.522E-04  -.818E-04  -.255E-03  -.135E-03  -.842E-04  -.401E-04  .334E-05  .337E-04  .378E-04  .352E-04
.320E-04  .318E-04  .346E-04  .314E-04  .246E-04  .166E-04  .104E-04  .790E-05  .477E-05  .381E-05
-.594E-04  -.745E-04  -.139E-03  -.106E-03  -.666E-04  -.313E-04  .124E-05  .191E-04  .181E-04  .156E-04
.144E-04  .127E-04  .975E-05  .812E-05  .570E-05  .309E-05  .145E-05  .485E-06  .134E-06  .498E-07
-.594E-04  -.680E-04  -.888E-04  -.768E-04  -.542E-04  -.296E-04  -.579E-05  .296E-05  .502E-05  .523E-05
```

TABLE 4 (continued)

.439E-05	.322E-05	.199E-05	.881E-06	.250E-06	.450E-07	.418E-08	.157E-10	-.394E-19	.000E+00
-.537E-04	-.591E-04	-.665E-04	-.594E-04	-.447E-04	-.282E-04	-.956E-05	-.217E-06	.105E-05	.698E-06
.304E-06	.957E-07	.174E-07	.957E-09	-.849E-16	-.176E-19	.000E+00	.000E+00	.000E+00	.000E+00
-.442E-04	-.480E-04	-.491E-04	-.449E-04	-.359E-04	-.248E-04	-.101E-04	-.889E-06	-.437E-07	.309E-08
.314E-09	.213E-11	-.211E-17	.000E+00	.000E+00	.000E+00	.000E+00	.000E+00	.000E+00	.000E+00
-.329E-04	-.355E-04	-.359E-04	-.331E-04	-.271E-04	-.191E-04	-.876E-05	-.957E-06	-.112E-06	.750E-11
.116E-12	-.244E-15	-.175E-17	.000E+00	.000E+00	.000E+00	.000E+00	.000E+00	.000E+00	.000E+00
-.194E-04	-.248E-04	-.242E-04	-.220E-04	-.182E-04	-.133E-04	-.592E-05	-.708E-06	-.950E-07	-.296E-10
.807E-13	-.186E-15	-.124E-17	.000E+00	.000E+00	.000E+00	.000E+00	.000E+00	.000E+00	.000E+00
-.815E-05	-.129E-04	-.124E-04	-.110E-04	-.916E-05	-.679E-05	-.309E-05	-.392E-06	-.526E-07	-.295E-10
.439E-13	-.998E-16	-.637E-18	.000E+00	.000E+00	.000E+00	.000E+00	.000E+00	.000E+00	.000E+00
.000E+00	.000E+00	.000E+00	.000E+00	.000E+00	.000E+00	.000E+00	.000E+00	.000E+00	.000E+00
.000E+00	.000E+00	.000E+00	.000E+00	.000E+00	.000E+00	.000E+00	.000E+00	.000E+00	.000E+00

****

X-COMPONENT OF GAS VELOCITY [CM/SEC]

.000E+00	.179E-03	.121E-03	.921E-04	.805E-04	.767E-04	.820E-04	.100E-03	.142E-03	.173E-03
.192E-03	.199E-03	.195E-03	.185E-03	.168E-03	.149E-03	.129E-03	.113E-03	.999E-04	.916E-04
.000E+00									
.000E+00	.170E-03	.119E-03	.920E-04	.812E-04	.781E-04	.845E-04	.103E-03	.148E-03	.179E-03
.198E-03	.203E-03	.199E-03	.187E-03	.169E-03	.148E-03	.128E-03	.110E-03	.973E-04	.890E-04
.000E+00									
.000E+00	.162E-03	.118E-03	.932E-04	.836E-04	.820E-04	.903E-04	.109E-03	.162E-03	.193E-03
.209E-03	.213E-03	.206E-03	.191E-03	.171E-03	.147E-03	.124E-03	.106E-03	.920E-04	.836E-04
.000E+00									
.000E+00	.165E-03	.122E-03	.980E-04	.901E-04	.909E-04	.101E-03	.125E-03	.186E-03	.215E-03
.227E-03	.227E-03	.216E-03	.198E-03	.174E-03	.145E-03	.118E-03	.977E-04	.838E-04	.756E-04
.000E+00									
.000E+00	.169E-03	.132E-03	.108E-03	.104E-03	.110E-03	.125E-03	.166E-03	.226E-03	.245E-03
.250E-03	.246E-03	.228E-03	.207E-03	.179E-03	.141E-03	.109E-03	.864E-04	.725E-04	.648E-04
.000E+00									
.000E+00	.179E-03	.153E-03	.131E-03	.131E-03	.142E-03	.176E-03	.281E-03	.286E-03	.280E-03
.276E-03	.271E-03	.238E-03	.218E-03	.191E-03	.134E-03	.939E-04	.706E-04	.579E-04	.515E-04
.000E+00									
.000E+00	.202E-03	.232E-03	.218E-03	.222E-03	.247E-03	.308E-03	.373E-03	.344E-03	.311E-03
.301E-03	.311E-03	.238E-03	.234E-03	.222E-03	.119E-03	.702E-04	.495E-04	.403E-04	.361E-04
.000E+00									
.000E+00	.233E-03	.495E-03	.518E-03	.512E-03	.475E-03	.401E-03	.245E-03	.102E-03	.616E-04
.508E-04	.585E-04	.193E-03	.256E-03	.324E-03	.749E-04	.340E-04	.242E-04	.210E-04	.198E-04
.000E+00									
.000E+00	.203E-03	.173E-04	.126E-04	.974E-05	.663E-05	.440E-05	.433E-05	.681E-05	.158E-04
.237E-04	.368E-04	.683E-04	.512E-04	.399E-04	.340E-03	.442E-03	.500E-03	.537E-03	.557E-03
.000E+00									
.000E+00	.178E-03	.280E-04	.191E-04	.168E-04	.168E-04	.193E-04	.226E-04	.242E-04	.233E-04
.286E-04	.382E-04	.655E-04	.742E-04	.652E-04	.280E-03	.408E-03	.481E-03	.524E-03	.547E-03
.000E+00									

TABLE 4 (continued)

```
.000E+00  .178E-03  .280E-04  .191E-04  .168E-04  .168E-04  .193E-04  .226E-04  .242E-04  .233E-04
.286E-04  .382E-04  .655E-04  .742E-04  .652E-04  .280E-03  .408E-03  .481E-03  .524E-03  .547E-03
.000E+00
.000E+00  .203E-03  .173E-04  .126E-04  .974E-05  .663E-05  .440E-05  .433E-05  .681E-05  .158E-04
.237E-04  .368E-04  .683E-04  .512E-04  .399E-04  .340E-03  .442E-03  .500E-03  .537E-03  .557E-03
.000E+00
.000E+00  .233E-03  .495E-03  .518E-03  .512E-03  .475E-03  .401E-03  .245E-03  .102E-03  .616E-04
.508E-04  .585E-04  .193E-03  .256E-03  .324E-03  .749E-04  .340E-04  .242E-04  .210E-04  .198E-04
.000E+00
.000E+00  .202E-03  .232E-03  .218E-03  .222E-03  .247E-03  .308E-03  .373E-03  .344E-03  .311E-03
.301E-03  .311E-03  .238E-03  .234E-03  .222E-03  .119E-03  .702E-04  .495E-04  .403E-04  .361E-04
.000E+00
.000E+00  .179E-03  .153E-03  .131E-03  .131E-03  .142E-03  .176E-03  .281E-03  .286E-03  .280E-03
.276E-03  .271E-03  .238E-03  .218E-03  .191E-03  .134E-03  .939E-04  .706E-04  .579E-04  .515E-04
.000E+00
.000E+00  .169E-03  .132E-03  .108E-03  .104E-03  .110E-03  .125E-03  .166E-03  .226E-03  .245E-03
.250E-03  .246E-03  .228E-03  .207E-03  .179E-03  .141E-03  .109E-03  .864E-04  .725E-04  .648E-04
.000E+00
.000E+00  .165E-03  .122E-03  .980E-04  .901E-04  .909E-04  .101E-03  .125E-03  .186E-03  .215E-03
.227E-03  .227E-03  .216E-03  .198E-03  .174E-03  .145E-03  .118E-03  .977E-04  .838E-04  .756E-04
.000E+00
.000E+00  .162E-03  .118E-03  .932E-04  .836E-04  .820E-04  .903E-04  .109E-03  .162E-03  .193E-03
.209E-03  .213E-03  .206E-03  .191E-03  .171E-03  .147E-03  .124E-03  .106E-03  .920E-04  .836E-04
.000E+00
.000E+00  .170E-03  .119E-03  .920E-04  .812E-04  .781E-04  .845E-04  .103E-03  .148E-03  .179E-03
.198E-03  .203E-03  .199E-03  .187E-03  .169E-03  .148E-03  .128E-03  .110E-03  .973E-04  .890E-04
.000E+00
.000E+00  .179E-03  .121E-03  .921E-04  .805E-04  .767E-04  .820E-04  .100E-03  .142E-03  .173E-03
.192E-03  .199E-03  .195E-03  .185E-03  .168E-03  .149E-03  .129E-03  .113E-03  .999E-04  .916E-04
.000E+00
****************************************
Y-COMPONENT OF GAS VELOCITY [CM/SEC]
.000E+00  .000E+00  .000E+00  .000E+00  .000E+00  .000E+00  .000E+00  .000E+00  .000E+00  .000E+00
.000E+00  .000E+00  .000E+00  .000E+00  .000E+00  .000E+00  .000E+00  .000E+00  .000E+00  .000E+00
.113E-04  .831E-05  .600E-05  .470E-05  .358E-05  .249E-05  .143E-05 -.199E-04 -.165E-04 -.869E-05
-.145E-05  .464E-05  .925E-05  .122E-04  .134E-04  .128E-04  .108E-04  .792E-05  .482E-05  .186E-05
.235E-04  .155E-04  .116E-04  .922E-05  .701E-05  .490E-05  .271E-05 -.426E-04 -.332E-04 -.168E-04
-.214E-05  .101E-04  .193E-04  .252E-04  .277E-04  .264E-04  .220E-04  .161E-04  .970E-05  .374E-05
.368E-04  .218E-04  .169E-04  .137E-04  .104E-04  .728E-05  .268E-05 -.709E-04 -.497E-04 -.236E-04
-.127E-05  .173E-04  .307E-04  .396E-04  .438E-04  .414E-04  .341E-04  .245E-04  .147E-04  .562E-05
.489E-04  .277E-04  .220E-04  .183E-04  .136E-04  .907E-05 -.344E-06 -.106E-03 -.643E-04 -.275E-04
.194E-05  .272E-04  .438E-04  .558E-04  .630E-04  .589E-04  .474E-04  .334E-04  .197E-04  .747E-05
.579E-04  .339E-04  .268E-04  .215E-04  .145E-04  .824E-05 -.141E-04 -.141E-03 -.713E-04 -.268E-04
.774E-05  .419E-04  .580E-04  .733E-04  .879E-04  .802E-04  .621E-04  .425E-04  .245E-04  .921E-05
.611E-04  .362E-04  .348E-04  .232E-04  .124E-04 -.562E-05 -.745E-04 -.136E-03 -.608E-04 -.197E-04
```

TABLE 4 (continued)

.140E-04	.666E-04	.704E-04	.892E-04	.125E-03	.107E-03	.776E-04	.509E-04	.288E-04	.107E-04
.492E-04	-.172E-05	.372E-04	.172E-04	-.575E-05	-.441E-04	-.111E-03	-.107E-03	-.310E-04	-.844E-05
.896E-05	.119E-03	.703E-04	.921E-04	.196E-03	.140E-03	.914E-04	.573E-04	.319E-04	.119E-04
.140E-04	-.211E-03	.898E-05	.801E-05	.624E-05	.510E-05	.277E-05	.111E-05	.202E-05	.248E-05
.465E-05	.193E-04	.215E-04	.293E-04	.376E-03	.168E-03	.976E-04	.593E-04	.328E-04	.123E-04
-.142E-05	-.919E-04	.205E-05	.340E-05	.387E-05	.453E-05	.255E-05	.433E-06	-.216E-05	.524E-06
.906E-06	.640E-05	.156E-04	.181E-04	.157E-03	.935E-04	.543E-04	.320E-04	.174E-04	.646E-05
-.119E-17	.000E+00	.121E-18	.160E-18	-.193E-18	-.147E-18	.141E-17	.345E-17	.541E-18	-.688E-18
-.111E-17	.264E-17	.103E-17	-.135E-17	-.253E-17	-.181E-17	-.172E-17	-.755E-18	-.603E-18	-.192E-18
.142E-05	.919E-04	-.205E-05	-.340E-05	-.387E-05	-.453E-05	-.255E-05	-.433E-06	.216E-05	-.524E-06
-.906E-06	-.640E-05	-.156E-04	-.181E-04	-.157E-03	-.935E-04	-.543E-04	-.320E-04	-.174E-04	-.646E-05
-.140E-04	.211E-03	-.898E-05	-.801E-05	-.624E-05	-.510E-05	-.277E-05	-.111E-05	-.202E-05	-.248E-05
-.465E-05	-.193E-04	-.215E-04	-.293E-04	-.376E-03	-.168E-03	-.976E-04	-.593E-04	-.328E-04	-.123E-04
-.492E-04	.172E-05	-.372E-04	-.172E-04	.575E-05	.441E-04	.111E-03	.107E-03	.310E-04	.844E-05
-.896E-05	-.119E-03	-.703E-04	-.921E-04	-.196E-03	-.140E-03	-.914E-04	-.573E-04	-.319E-04	-.119E-04
-.611E-04	-.362E-04	-.348E-04	-.232E-04	-.124E-04	.562E-05	.745E-04	.136E-03	.608E-04	.197E-04
-.140E-04	-.666E-04	-.704E-04	-.892E-04	-.125E-03	-.107E-03	-.776E-04	-.509E-04	-.288E-04	-.107E-04
-.579E-04	-.339E-04	-.268E-04	-.215E-04	-.145E-04	-.824E-05	.141E-04	.141E-03	.713E-04	.268E-04
-.774E-05	-.419E-04	-.580E-04	-.733E-04	-.879E-04	-.802E-04	-.621E-04	-.425E-04	-.245E-04	-.921E-05
-.489E-04	-.277E-04	-.220E-04	-.183E-04	-.136E-04	-.907E-05	.344E-06	.106E-03	.643E-04	.275E-04
-.194E-05	-.272E-04	-.438E-04	-.558E-04	-.630E-04	-.589E-04	-.474E-04	-.334E-04	-.197E-04	-.747E-05
-.368E-04	-.218E-04	-.169E-04	-.137E-04	-.104E-04	-.728E-05	-.268E-05	.709E-04	.497E-04	.236E-04
.127E-05	-.173E-04	-.307E-04	-.396E-04	-.438E-04	-.414E-04	-.341E-04	-.245E-04	-.147E-04	-.562E-05
-.235E-04	-.155E-04	-.116E-04	-.922E-05	-.701E-05	-.490E-05	-.271E-05	.426E-04	.332E-04	.168E-04
.214E-05	-.101E-04	-.193E-04	-.252E-04	-.277E-04	-.264E-04	-.220E-04	-.161E-04	-.970E-05	-.374E-05
-.113E-04	-.831E-05	-.600E-05	-.470E-05	-.358E-05	-.249E-05	-.143E-05	.199E-04	.165E-04	.869E-05
.145E-05	-.464E-05	-.925E-05	-.122E-04	-.134E-04	-.128E-04	-.108E-04	-.792E-05	-.482E-05	-.186E-05
.000E+00	.000E+00	.000E+00	.000E+00	.000E+00	.000E+00	.000E+00	.000E+00	.000E+00	.000E+00
.000E+00	.000E+00	.000E+00	.000E+00	.000E+00	.000E+00	.000E+00	.000E+00	.000E+00	.000E+00

****

SURFACTANT CONCENTRATION [G/G]

.995E-02	.965E-02	.874E-02	.695E-02	.452E-02	.218E-02	.647E-03	.820E-04	.147E-05	.719E-09
.698E-15	.104E-23	.253E-35	.954E-50	.000E+00	.000E+00	.000E+00	.000E+00	.000E+00	.000E+00
.995E-02	.965E-02	.873E-02	.694E-02	.450E-02	.215E-02	.629E-03	.772E-04	.131E-05	.575E-09
.497E-15	.670E-24	.152E-35	.536E-50	.000E+00	.000E+00	.000E+00	.000E+00	.000E+00	.000E+00
.995E-02	.965E-02	.873E-02	.692E-02	.445E-02	.209E-02	.591E-03	.676E-04	.102E-05	.359E-09
.243E-15	.270E-24	.524E-36	.161E-50	.000E+00	.000E+00	.000E+00	.000E+00	.000E+00	.000E+00
.995E-02	.965E-02	.873E-02	.690E-02	.437E-02	.198E-02	.531E-03	.539E-04	.678E-06	.166E-09
.787E-16	.492E-21	.572E-33	.598E-48	.000E+00	.000E+00	.000E+00	.000E+00	.000E+00	.000E+00
.995E-02	.965E-02	.875E-02	.688E-02	.425E-02	.182E-02	.443E-03	.369E-04	.345E-06	.256E-09
.144E-10	.498E-12	.535E-14	.722E-17	.663E-27	.109E-40	.855E-59	.000E+00	.000E+00	.000E+00
.995E-02	.967E-02	.880E-02	.685E-02	.403E-02	.153E-02	.309E-03	.184E-04	.783E-06	.238E-06
.547E-07	.807E-08	.666E-09	.244E-10	.303E-12	.113E-14	.111E-17	.232E-23	.449E-37	.136E-54
.995E-02	.970E-02	.891E-02	.671E-02	.338E-02	.910E-03	.158E-03	.851E-04	.476E-04	.214E-04
.780E-05	.207E-05	.358E-06	.398E-07	.233E-08	.595E-10	.837E-12	.436E-14	.868E-17	.133E-19

TABLE 4 (continued)

.995E-02	.974E-02	.908E-02	.593E-02	.199E-02	.706E-03	.107E-02	.120E-02	.868E-03	.512E-03
.252E-03	.994E-04	.267E-04	.452E-05	.499E-06	.285E-07	.103E-08	.212E-10	.172E-12	.825E-15
.996E-02	.982E-02	.932E-02	.817E-02	.689E-02	.616E-02	.586E-02	.553E-02	.495E-02	.402E-02
.278E-02	.149E-02	.539E-03	.127E-03	.209E-04	.218E-05	.132E-06	.445E-08	.694E-10	.426E-12
.996E-02	.988E-02	.948E-02	.899E-02	.849E-02	.803E-02	.753E-02	.685E-02	.590E-02	.465E-02
.318E-02	.175E-02	.685E-03	.173E-03	.294E-04	.313E-05	.194E-06	.663E-08	.108E-09	.670E-12
.996E-02	.988E-02	.948E-02	.899E-02	.849E-02	.803E-02	.753E-02	.685E-02	.590E-02	.465E-02
.318E-02	.175E-02	.685E-03	.173E-03	.294E-04	.313E-05	.194E-06	.663E-08	.108E-09	.670E-12
.996E-02	.982E-02	.932E-02	.817E-02	.689E-02	.616E-02	.586E-02	.553E-02	.495E-02	.402E-02
.278E-02	.149E-02	.539E-03	.127E-03	.209E-04	.218E-05	.132E-06	.445E-08	.694E-10	.426E-12
.995E-02	.974E-02	.908E-02	.593E-02	.199E-02	.706E-03	.107E-02	.120E-02	.868E-03	.512E-03
.252E-03	.994E-04	.267E-04	.452E-05	.499E-06	.285E-07	.103E-08	.212E-10	.172E-12	.825E-15
.995E-02	.970E-02	.891E-02	.671E-02	.338E-02	.910E-03	.158E-03	.851E-04	.476E-04	.214E-04
.780E-05	.207E-05	.358E-06	.398E-07	.233E-08	.595E-10	.837E-12	.436E-14	.868E-17	.133E-19
.995E-02	.967E-02	.880E-02	.685E-02	.403E-02	.153E-02	.309E-03	.184E-04	.783E-06	.238E-06
.547E-07	.807E-08	.666E-09	.244E-10	.303E-12	.113E-14	.111E-17	.232E-23	.449E-37	.136E-54
.995E-02	.965E-02	.875E-02	.688E-02	.425E-02	.182E-02	.443E-03	.369E-04	.345E-06	.256E-09
.144E-10	.498E-12	.535E-14	.722E-17	.663E-27	.109E-40	.855E-59	.000E+00	.000E+00	.000E+00
.995E-02	.965E-02	.873E-02	.690E-02	.437E-02	.198E-02	.531E-03	.539E-04	.678E-06	.166E-09
.787E-16	.492E-21	.572E-33	.598E-48	.000E+00	.000E+00	.000E+00	.000E+00	.000E+00	.000E+00
.995E-02	.965E-02	.873E-02	.692E-02	.445E-02	.209E-02	.591E-03	.676E-04	.102E-05	.359E-09
.243E-15	.270E-24	.524E-36	.161E-50	.000E+00	.000E+00	.000E+00	.000E+00	.000E+00	.000E+00
.995E-02	.965E-02	.873E-02	.694E-02	.450E-02	.215E-02	.629E-03	.772E-04	.131E-05	.575E-09
.497E-15	.670E-24	.152E-35	.536E-50	.000E+00	.000E+00	.000E+00	.000E+00	.000E+00	.000E+00
.995E-02	.965E-02	.874E-02	.695E-02	.452E-02	.218E-02	.647E-03	.820E-04	.147E-05	.719E-09
.698E-15	.104E-23	.253E-35	.954E-50	.000E+00	.000E+00	.000E+00	.000E+00	.000E+00	.000E+00

****

FLOWING-FOAM BUBBLE DENSITY [#/CM^3]

.334E+08	.558E+08	.535E+08	.517E+08	.503E+08	.467E+08	.294E+08	.000E+00	.000E+00	.000E+00
.000E+00	.000E+00	.000E+00	.000E+00	.000E+00	.000E+00	.000E+00	.000E+00	.000E+00	.000E+00
.384E+08	.569E+08	.537E+08	.519E+08	.505E+08	.469E+08	.289E+08	.000E+00	.000E+00	.000E+00
.000E+00	.000E+00	.000E+00	.000E+00	.000E+00	.000E+00	.000E+00	.000E+00	.000E+00	.000E+00
.450E+08	.575E+08	.539E+08	.522E+08	.511E+08	.473E+08	.274E+08	.000E+00	.000E+00	.000E+00
.000E+00	.000E+00	.000E+00	.000E+00	.000E+00	.000E+00	.000E+00	.000E+00	.000E+00	.000E+00
.451E+08	.575E+08	.542E+08	.530E+08	.521E+08	.474E+08	.252E+08	.000E+00	.000E+00	.000E+00
.000E+00	.000E+00	.000E+00	.000E+00	.000E+00	.000E+00	.000E+00	.000E+00	.000E+00	.000E+00
.452E+08	.577E+08	.574E+08	.555E+08	.535E+08	.472E+08	.206E+08	.000E+00	.000E+00	.000E+00
.000E+00	.000E+00	.000E+00	.000E+00	.000E+00	.000E+00	.000E+00	.000E+00	.000E+00	.000E+00
.453E+08	.579E+08	.645E+08	.617E+08	.585E+08	.476E+08	.125E+08	.000E+00	.000E+00	.000E+00
.000E+00	.000E+00	.000E+00	.000E+00	.000E+00	.000E+00	.000E+00	.000E+00	.000E+00	.000E+00
.455E+08	.578E+08	.642E+08	.622E+08	.575E+08	.363E+08	.606E+07	.000E+00	.000E+00	.000E+00
.000E+00	.000E+00	.000E+00	.000E+00	.000E+00	.000E+00	.000E+00	.000E+00	.000E+00	.000E+00
.456E+08	.576E+08	.620E+08	.594E+08	.501E+08	.295E+08	.221E+08	.183E+08	.301E+06	.302E+03
.301E+00	.000E+00	.000E+00	.000E+00	.000E+00	.000E+00	.000E+00	.000E+00	.000E+00	.000E+00
.453E+08	.571E+08	.462E+08	.379E+08	.254E+08	.144E+08	.953E+07	.673E+07	.212E+07	.172E+07

TABLE 4 (continued)

.878E+06	.452E+06	.114E+07	.121E+07	.000E+00	.000E+00	.000E+00	.000E+00	.000E+00	.000E+00
.451E+08	.567E+08	.398E+08	.263E+08	.123E+08	.264E+07	.196E+07	.118E+07	.191E+07	.158E+07
.673E+06	.755E+06	.131E+07	.351E+06	.000E+00	.000E+00	.000E+00	.000E+00	.000E+00	.000E+00
.451E+08	.567E+08	.398E+08	.263E+08	.123E+08	.264E+07	.196E+07	.118E+07	.191E+07	.158E+07
.673E+06	.755E+06	.131E+07	.351E+06	.000E+00	.000E+00	.000E+00	.000E+00	.000E+00	.000E+00
.453E+08	.571E+08	.462E+08	.379E+08	.254E+08	.144E+08	.953E+07	.673E+07	.212E+07	.172E+07
.878E+06	.452E+06	.114E+07	.121E+07	.000E+00	.000E+00	.000E+00	.000E+00	.000E+00	.000E+00
.456E+08	.576E+08	.620E+08	.594E+08	.501E+08	.295E+08	.221E+08	.183E+08	.301E+06	.302E+03
.301E+00	.000E+00	.000E+00	.000E+00	.000E+00	.000E+00	.000E+00	.000E+00	.000E+00	.000E+00
.455E+08	.578E+08	.642E+08	.622E+08	.575E+08	.363E+08	.606E+07	.000E+00	.000E+00	.000E+00
.000E+00	.000E+00	.000E+00	.000E+00	.000E+00	.000E+00	.000E+00	.000E+00	.000E+00	.000E+00
.453E+08	.579E+08	.645E+08	.617E+08	.585E+08	.476E+08	.125E+08	.000E+00	.000E+00	.000E+00
.000E+00	.000E+00	.000E+00	.000E+00	.000E+00	.000E+00	.000E+00	.000E+00	.000E+00	.000E+00
.452E+08	.577E+08	.574E+08	.555E+08	.535E+08	.472E+08	.206E+08	.000E+00	.000E+00	.000E+00
.000E+00	.000E+00	.000E+00	.000E+00	.000E+00	.000E+00	.000E+00	.000E+00	.000E+00	.000E+00
.451E+08	.575E+08	.542E+08	.530E+08	.521E+08	.474E+08	.252E+08	.000E+00	.000E+00	.000E+00
.000E+00	.000E+00	.000E+00	.000E+00	.000E+00	.000E+00	.000E+00	.000E+00	.000E+00	.000E+00
.450E+08	.575E+08	.539E+08	.522E+08	.511E+08	.473E+08	.274E+08	.000E+00	.000E+00	.000E+00
.000E+00	.000E+00	.000E+00	.000E+00	.000E+00	.000E+00	.000E+00	.000E+00	.000E+00	.000E+00
.384E+08	.569E+08	.537E+08	.519E+08	.505E+08	.469E+08	.289E+08	.000E+00	.000E+00	.000E+00
.000E+00	.000E+00	.000E+00	.000E+00	.000E+00	.000E+00	.000E+00	.000E+00	.000E+00	.000E+00
.334E+08	.558E+08	.535E+08	.517E+08	.503E+08	.467E+08	.294E+08	.000E+00	.000E+00	.000E+00
.000E+00	.000E+00	.000E+00	.000E+00	.000E+00	.000E+00	.000E+00	.000E+00	.000E+00	.000E+00

****

##

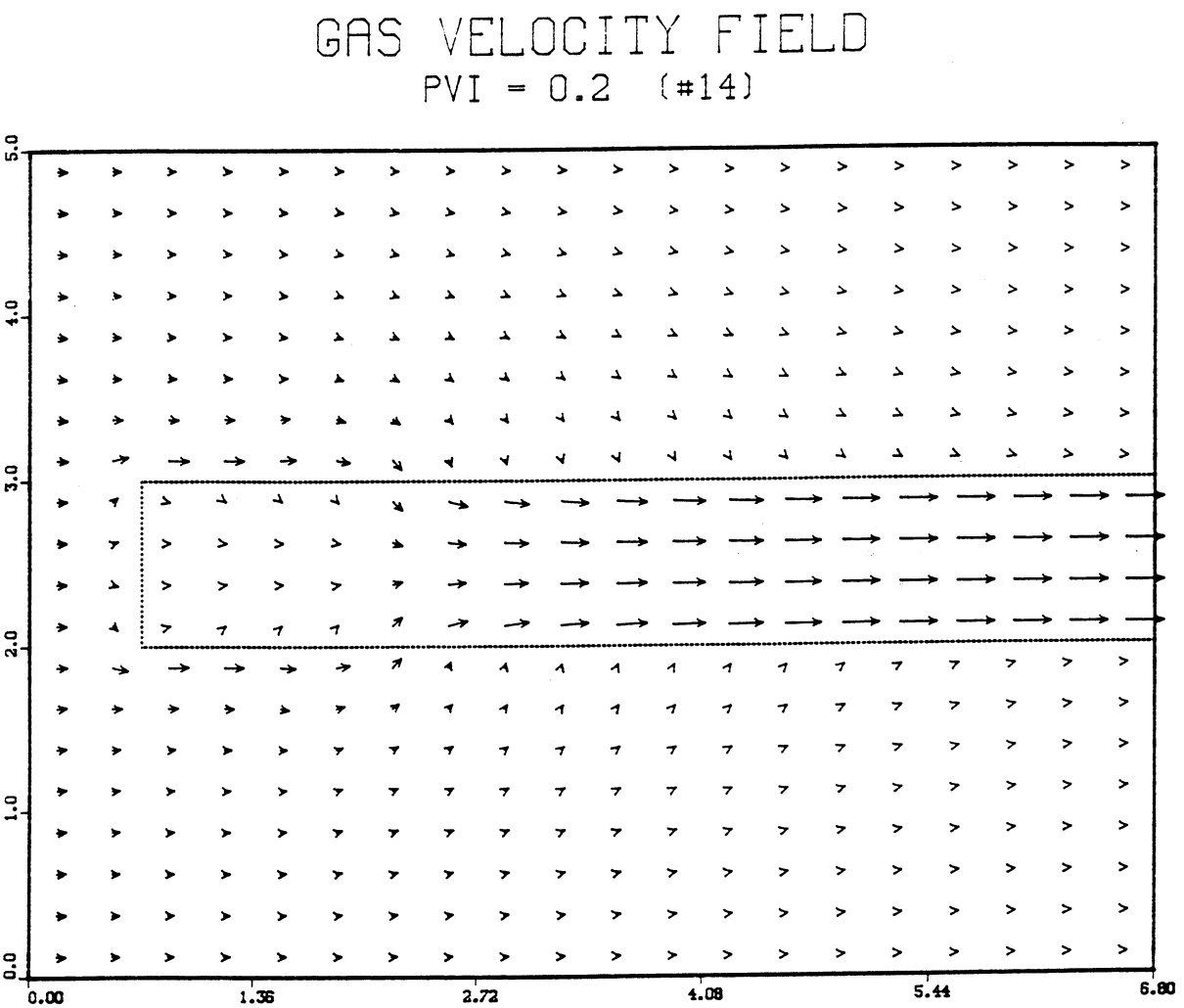

Figure 5. Gas velocity field at 0.2 pore volumes injected.

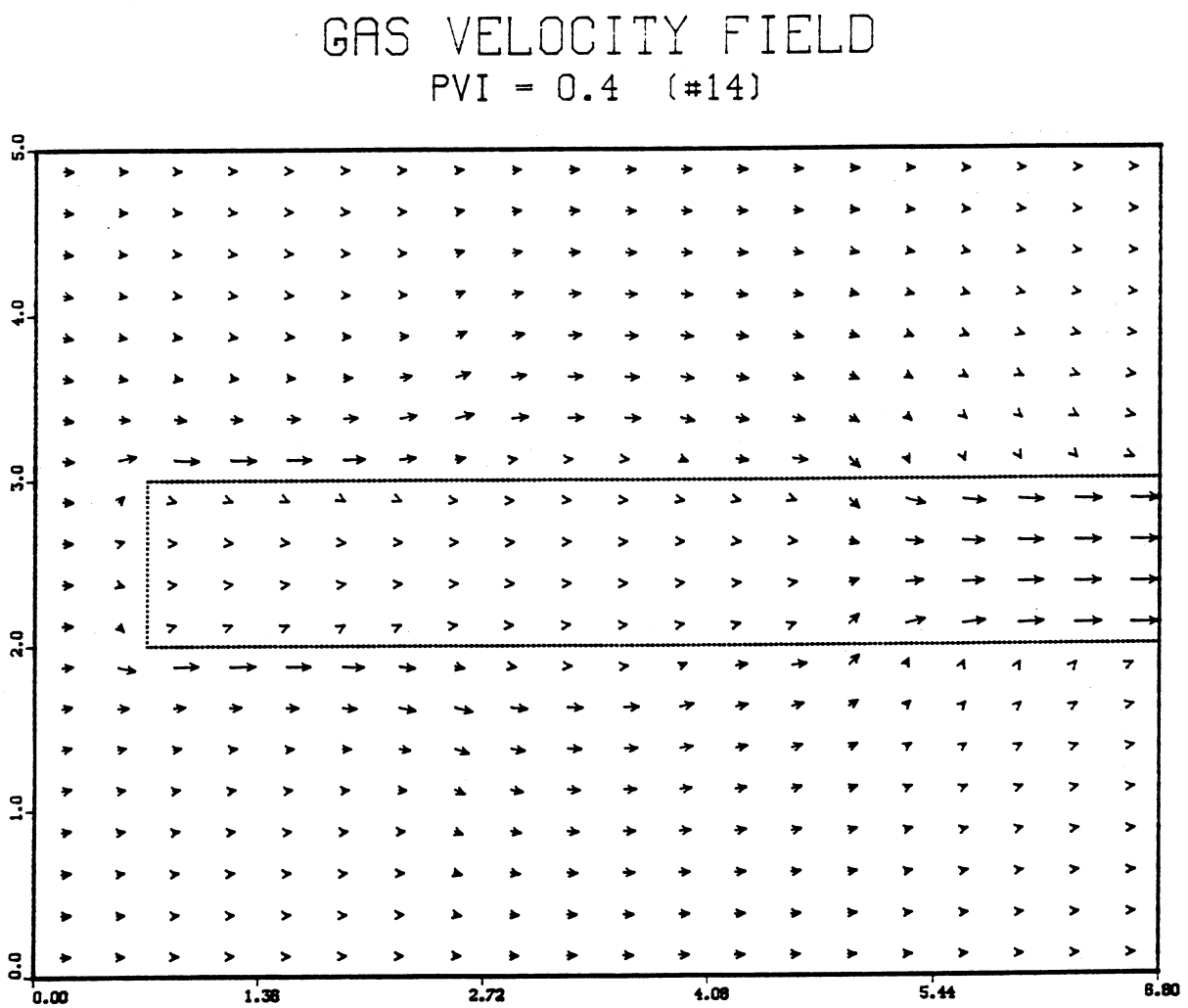

Figure 6. Gas velocity field at 0.4 pore volumes injected.

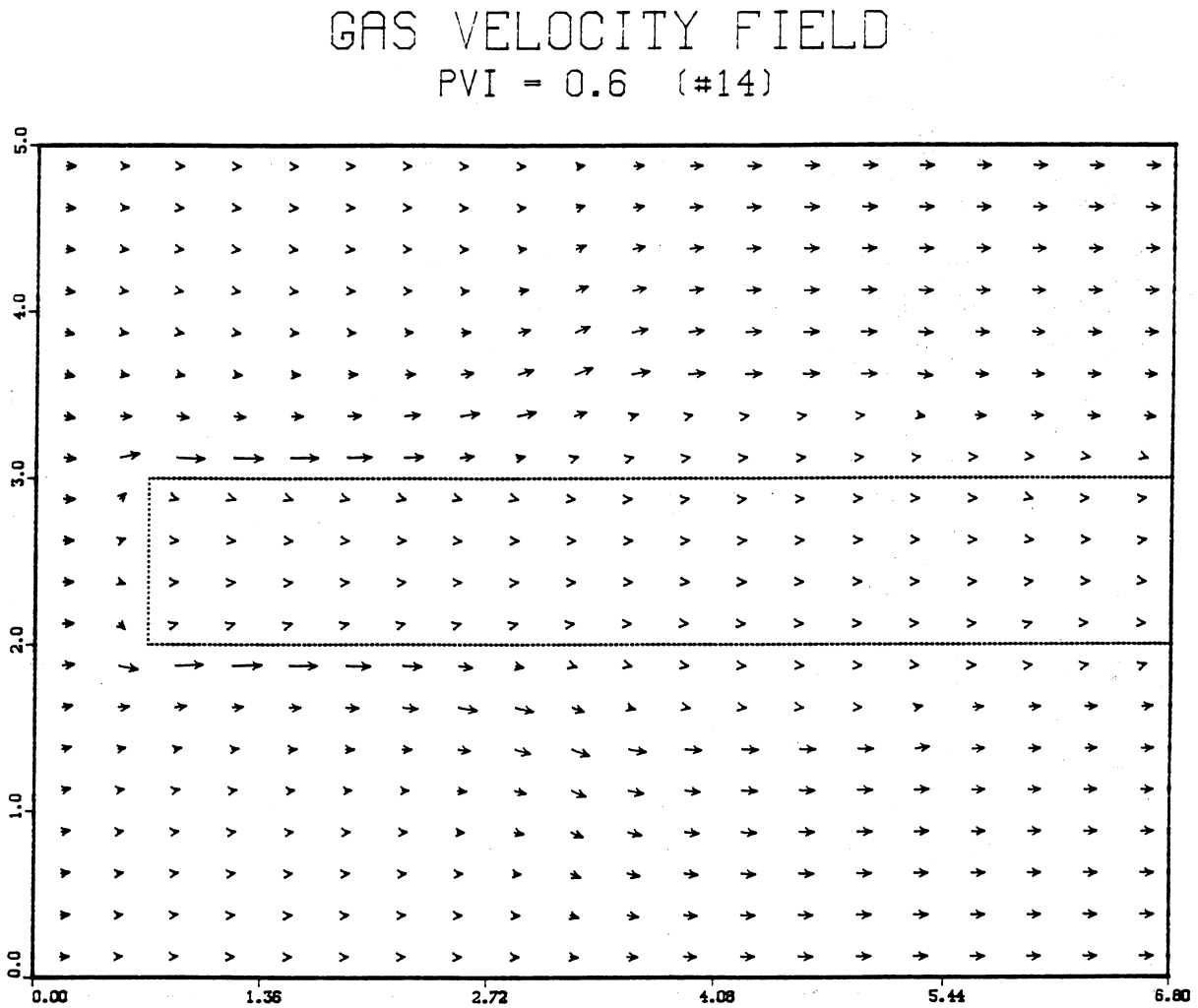

Figure 7. Gas velocity field at 0.6 pore volumes injected.

with foam (Figures 5-7), it is clear that the flow was blocked and diverted into the oil matrix and that trapped oil was recovered. Note that before the whole PFP is blocked, high gas flow through the PFP still can be seen (Figures 5 and 6).

NOMENCLATURE

A_f = bubble trapping parameter, #/cm^3
A_s = constant in the Langmuir model, g/cm^2
a = reduction factor
b = parameter in Equation (16)
C_f = bubble coalescence rate per unit reservoir volume, #/sec/cm^3
C_s = surfactant concentration, g/g
C_{sI} = injected surfactant concentration, g/g
C_s^{lim} = minimum surfactant concentration for which foam can exist, g/g
C_{sref} = reference surfactant concentration, g/g
c_1 = exponent in Equation (11)
c_2 = exponent in Equation (10)
c_3 = exponent in Equation (13)
d = constant in Equation (12), cm/sec
e = exponent in Equation (12)
e_1 = exponent in Equation (11)
e_2 = exponent in Equation (10)
F_w = injected liquid volume fraction
G_f = bubble generation rate per unit reservoir volume, #/sec/cm^3
$\mathbf{g}$ = gravitational acceleration vector
K_f = bubble trapping parameter, cm^3/#
K_s = equilibrium constant in the Langmuir model, g/g
K_1 = generation rate constant, #/sec/cm^3
K_2 = coalescence rate constant, cm^3/sec/cm^3
K_3 = geometric factor
k = absolute permeability, darcy
$k_{rg}^{(e)}$ = effective relative permeability of the gas phase when foam exists
$k_{r\ell}$ = relative permeability of phase ℓ
k_{rog} = oil-phase relative permeability in an oil-gas system
k_{row} = oil-phase relative permeability in an oil-water system
n_c = critical bubble density above which the generation rate

approaches zero, $\#/cm^3$

n_f = bubble density of the flowing foam, $\#/cm^3$

n_{fI} = injected bubble density, $\#/cm^3$

n_s = bubble density of the trapped foam, $\#/cm^3$

P_{cgo} = gas-oil capillary pressure, atm

P_{cow} = oil-water capillary pressure, atm

P_ℓ = pressure of phase ℓ, atm

q_ℓ = injection/production rate of phase ℓ per unit reservoir volume, $g/sec/cm^3$

S_ℓ = saturation of phase ℓ

S_o^{lim} = maximum oil saturation for which foam can exist

S_{wc} = irreducible water saturation

t = time, sec

U_ℓ = Darcy's velocity of phase ℓ, cm/sec

$U_{ref1}, U_{ref2}, U_{ref3}$ = reference gas velocities, cm/sec

V_c = critical gas velocity above which flowing foam can be generated, cm/sec

X_f = fraction of gas that is flowing

Greek

Γ = adsorbed surfactant concentration, g/cm^2

δ = rock surface area per unit mass, cm^2/g

$\mu_g^{(e)}$ = effective viscosity of gas phase when foam exists, cp

μ_ℓ = viscosity of phase ℓ, cp

ρ_ℓ = mass density of phase ℓ, g/cm^3

ρ_r = mass density of rock, g/cm^3

ϕ = porosity

REFERENCES

1. Ransohoff, T. C. and Radke, C. J.: "Mechanisms of Foam Generation in Glass-Bead Packs," *SPERE* (May 1988) 573-585.

2. Huh, D. G., Cochrane, T. D., and Kovarik, F. S.: "The Effect of Microscopic Heterogeneity on CO_2-Foam Mobility: Part 1 - Mechanistic Study," *JPT* (August 1989) 872-879.

3. Patzek, T. W.: "Description of Foam Flow in Porous Media by the Population Balance Method," *Surfactant-Based Mobility Control*, D. H. Smith, (ed.), ACS Symposium Series #373, Washington, D. C. (1988) 326-341.

4. Falls, A. H., Hirasaki, G. J., Patzek, T. W., Gauglitz, D. A., Miller, D. D., and Ratulowski, T.: "Development of a Mechanistic Foam Simulator: The Population Balance and Generation by Snap-off," *SPERE* (August 1988) 884-892.

5. Friedmann, F., Chen, W. H., and Gauglitz, P. A.: "Experimental and Simulation Study of High-Temperature Foam Displacement in Porous Media," paper SPE/DOE 17357 presented at the 1988 SPE/DOE Enhanced Oil Recovery Symposium, Tulsa, April 17-20.

6. Hirasaki, G. J. and Lawson, J. B.: "Mechanisms of Foam Flow in Porous Media: Apparent Viscosity in Smooth Capillaries," *SPEJ* (April 1985) 176-190.

7. Khatib, Z. I., Hirasaki, G. J., and Falls, A. H.: "Effects of Capillary Pressure on Coalescence and Phase Mobilities in Foams Flowing Through Porous Media," *SPERE* (August 1988) 919-926.

8. Persoff, P., Radke, C. J., Benson, S. M., and Witherspoon, P. A.: "A Laboratory Investigation of Foam Flow in Sandstone at Elevated Pressure," paper SPE 18781 presented at the 1989 SPE California Regional Meeting, Bakersfield, April 5-7.

9. Dietrich, J. K. and Bondor, P. L.: "Three-Phase Oil Relative Permeability Models," paper SPE 6044 presented at the 1976 SPE Annual Technical Conference and Exhibition, New Orleans, October 3-6.

10. Aziz, K. and Settari, A.: *Petroleum Reservoir Simulation*, Elsevier Applied Science Publishers, London (1979).

11. Thomas, G. W.: *Principles of Hydrocarbon Reservoir Simulation*, International Human Resources Development Corporation, Boston (1981).

12. Chang, S. H., Owusu, L. A., French, S. B., and Kovarik, F. S.: "The Effect of Microscopic Heterogeneity on CO_2-Foam Mobility: Part 2 - Mechanistic

Foam Simulation," paper SPE/DOE 20191 presented at the 1990 SPE/DOE Enhanced Oil Recovery Symposium, Tulsa, April 22-25.

APPENDIX B

Reports, Presentations and Published Papers from "Improvement of CO_2 Flood Performance"

The following is a list of publications, presentations, and reports that have been produced by members of the PRRC research team on the subjects in this report. Most of the documents included were written during, and as part of, the project "Improvement of CO_2 Flood Performance." A few additional titles written in the immediately preceding research projects have also been included where especially relevant. There may also be a few accidental omissions, for which we apologize in advance. All of these documents are available from the Information and Publications Section at PRRC for a small handling charge.

Heller, J.P., Donaruma, L.G., and Dandge, D.K.: "Measuring Solubilities of Polymers in Dense CO_2," *Polymer Preprints*, New York City (Aug. 1981) **22**, No. 2, 59-60.

Silva, M.K., Lien, C.L., Pelletier, M.T., Franklin, J.C., Linert, S.M., and Orr, F.M., Jr.: "Phase Compositions and Densities of Mixtures of CO_2 with a Synthetic Oil Consisting of iC_5, iC_{10}, iC_{16}, and C_{30} at 100°F and 1300 psia," PRRC Report 83-10, Petroleum Recovery Research Center, Socorro, NM (Mar. 1983).

Silva, M.K., Lien, C.L., Shelly, F.C., Rosacker, P.A., and Orr, F.M., Jr.: "Phase Compositions and Densities of Mixtures of CO_2 with a Synthetic Oil Consisting of a Blend of Soltrols and C_{30} at 100°F and 1300 psia," PRRC Report 83-25, Petroleum Recovery Research Center, Socorro, NM (July 1983).

Campbell, B.T. and Orr, F.M., Jr.: "Flow Visualization for CO_2/Crude Oil Displacements," paper SPE 11958 presented at 1983 Annual Technical Conference, San Francisco, Oct. 5-8.

Silva, M.K., Larsen, L.L., Lien, C.L., and Orr, F.M., Jr.: "Measured Phase Compositions and Densities for CO_2-C_1-C_4-C_{10} Systems at 160°F and 1250 psia and Phase Compositions and Densities by Peng-Robinson EOS for Systems at 160°F and Pressures from 750 to 2250 psia," PRRC Report 83-24, Petroleum Recovery Research Center, Socorro, NM (Dec. 1983).

Lien, C.L.: "Crude Oil Analysis by HP5880 Gas Chromatograph," PRRC Report 83-32, Petroleum Recovery Research Center, Socorro, NM (Dec. 1983).

Campbell, B.T. and Orr, F.M., Jr: "Flow Visualization for CO_2-Crude Oil Experiments," presented at the International Energy Agency Workshop on Enhanced Oil Recovery, Vienna, Austria (1983).

Orr, F.M., Jr.: "Recovery of Oil by Miscible Flooding," presented at the American Institute of Chemical Engineering Diamond Jubilee Meeting, Washington, D.C. (1983).

Orr, F.M., Jr., Heller, J.P., and Taber, J.J.: "Carbon Dioxide Flooding for Enhanced Oil Recovery: Promise and Problems," *J. of American Chemical Society*, **59** (1983) 810A-17A.

Orr, F.M., Jr., Heller, J.P., Taber, J.J., and Card, R.J.: "CO_2 as a Solvent for Oil Recovery," *CHEMTECH*, **13** (1983) 482-87.

Silva, M.K., Lien, C.L., Romero, F.A., and Orr, F.M., Jr.: "Phase Compositions and Densities of Mixtures of CO_2 with A Synthetic Oil Consisting of Aromatic Hydrocarbons (C_6, C_{10} and C_{16}) and Squalane at 100°F and 1300 psia," PRRC Report 84-3, Petroleum Recovery Research Center, Socorro, NM (Feb. 1984).

Taylor, M.A.: "Effects of 10% N_2 Contamination in CO_2 on the Phase Behavior of Wasson Crude Oil-CO_2 Mixtures," PRRC Report 84-6, Petroleum Recovery Research Center, Socorro, NM (March 1984).

Hutter, C.E., Franklin, J.C., Pelletier, M.T., Silva, M.K., and Orr, F.M., Jr.: "Operation and Control of the Continuous Multiple Contact Experiment by the HP87XM Microcomputer," PRRC Report 84-7, Petroleum Recovery Research Center, Socorro, NM (March 1984).

Pande, P.K. and Heller, J.P.: "Economic Model of Mobility Control Methods for CO_2 Flooding," paper SPE 12753 presented at the 1984 California Regional Meeting, Long Beach, CA, April 11-13.

Heller, J.P.: "Reservoir Application of Mobility Control Foams in CO_2 Floods," paper SPE 12644 presented at the 1984 SPE/DOE Fourth Symposium on Enhanced Oil Recovery, Tulsa, OK, April 15-18.

Silva, M.K., Lien, C.L., Hutter, C.E., and Orr, F.M., Jr.: "Phase Compositions and Densities of Mixtures of CO_2 with A Western Oklahoma Separator Oil at 100°F and 1300 psia," PRRC Report 84-16, Petroleum Recovery Research Center, Socorro, NM (May 1984).

Pande, P.K. and Heller, J.P.: "Economics and Potential for Mobility Control Methods for CO_2 Floods in the Rocky Mountain Region," paper SPE 12928 presented at the 1984 Rocky Mountain Regional Meeting, Casper, WY, May 21-23.

Taylor, M.A.: "Calibration of the PVT System Viscometer at 100°F at 1500 psia and 100 psia," PRRC Report 84-11, Petroleum Recovery Research Center, Socorro, NM (June 1984).

Taylor, M.A., Silva, M.K., and Orr, F.M., Jr.: "Measurement of the Density of CO_2-Tetradecane Mixtures at 160°F," PRRC Report 84-21, Petroleum Recovery Research Center, Socorro, NM (July 1984).

Heller, J.P. and Orr, F.M., Jr.: "Improvement of CO_2 Flood Performance," Quarterly Technical Progress Report to company consortium, April 1 to June 30, 1984, PRRC Report 84-22, Petroleum Recovery Research Center, Socorro, NM (July 1984).

Heller, J.P., Lien, C.L., and Kuntamukkula, M.S.: "Foamlike Dispersions for Mobility Control in CO_2 Floods," paper SPE 11233, published in *SPEJ* (Aug. 1984).

Taylor, M.A.: "Volumetric Calibration of the PVT System - A Guide for Understanding How it Works," PRRC Report 84-24, Petroleum Recovery Research Center, Socorro, NM (Sept. 1984).

Heller, J.P., Dandge, D.K., Card, R.J., and Donaruma, L.G.: "Direct Thickeners for Mobility Control of CO_2," paper SPE 11789, published in *SPEJ* (Sept. 1984).

Heller, J.P. and Orr, F.M., Jr.: "Improvement of CO_2 Flood Performance," Quarterly Technical Progress Report to the U.S. Department of Energy, the New Mexico Energy Research and Development Institute and company consortium, July 1 to September 30, 1984, PRRC Report 84-26, Petroleum Recovery Research Center, Socorro, NM (Oct. 1984).

Silva, M.K., Taylor, M.A., Hutter, C.E., and Orr, F.M., Jr.: "Measured Compositions and Densities for the CO_2-C_1-C_{16} System at 90°F," PRRC Report 84-28, Petroleum Recovery Research Center, Socorro, NM (Dec. 1984).

Taylor, M.A. and Orr, F.M., Jr.: "Phase Behavior of CO_2 Hexadecane and CO_2 Squalane Mixtures," PRRC Report 84-30, Petroleum Recovery Research Center, Socorro, NM (Dec. 1984).

Silva, M.K., Taber, J.J., and Orr, F.M., Jr: "Minimum Miscibility Pressure: Effects of Crude Oil Composition," presented at the 1984 International Energy Agency Workshop on EOR, Trondheim, Norway.

Heller, J.P. and Orr, F.M., Jr.: "Improvement of CO_2 Flood Performance," Quarterly Technical Progress Report to the U.S. Department of Energy, the New Mexico Energy Research and Development Institute and company consortium, October 1 to December 31, 1984, PRRC Report 85-2, Petroleum Recovery Research Center, Socorro, NM (Jan. 1985).

Silva, M.K., Dandge, D.K., Lien, C.L., Hutter, C.E., Heller, J.P., and Orr, F.M., Jr.: "Measured Phase Compositions and Densities of Mixtures of CO_2 with a Multicomponent Synthetic Oil at 100°F and 1300 psia," PRRC Report 85-3, Petroleum Recovery Research Center, Socorro, NM (Jan. 1985).

Bretz, R.E. and Orr, F.M., Jr.: "Comparison of Analytical and Explicit Finite Difference Solutions of the Convection-Dispersion Equation," PRRC Report 85-6, Petroleum Recovery Research Center, Socorro, NM (Jan. 1985).

Bretz, R.E., Specter, R.M., and Orr, F.M., Jr.: "Mixing During Single-Phase Flow in Reservoir Rocks: Models, Effects of Pore Structure and Interpretation of Experiments," PRRC Report 85-5, Petroleum Recovery Research Center, Socorro, NM (Feb. 1985).

Silva, M.K., Hutter, C.E., and Lien, C.L.: "Phase Compositions and Densities of Mixtures of CO_2 with Maljamar Separator Oil at 160°F and 3000 psia," PRRC Report 85-7, Petroleum Recovery Research Center, Socorro, NM (Feb. 1985).

Silva, M.K., Hutter, C.E., and Lien, C.L.: "Phase Compositions and Densities of Mixtures of CO_2 with Maljamar Separator Oil at 160°F and 2000 psia," PRRC Report 85-8, Petroleum Recovery Research Center, Socorro, NM (March 1985).

Silva, M.K., Hutter, C.E., and Lien, C.L.: "Phase Compositions and Densities of Mixtures of CO_2 with Maljamar Separator Oil at 160°F and 1600 psia," PRRC Report 85-11, Petroleum Recovery Research Center, Socorro, NM (April 1985).

Silva, M.K., Hutter, C.E., and Lien, C.L.: "Phase Compositions and Densities of Mixtures of CO_2 with Ganado Stock Tank Oil at 160°F and 3000 psia," PRRC Report 85-12, Petroleum Recovery Research Center, Socorro, NM (April 1985).

Heller, J.P. and Orr, F.M., Jr.: "Improvement of CO_2 Flood Performance," Quarterly Technical Progress Report to the U.S. Department of Energy, the New Mexico Energy Research and Development Institute and company consortium, January 1 to March 31, 1985, PRRC Report 85-15, Petroleum Recovery Research Center, Socorro, NM (April 1985).

Silva, M.K. and Hutter, C.E.: "Crude Oil Analysis for MMP Correlation," PRRC Report 85-24, Petroleum Recovery Research Center, Socorro, NM (May 1985).

Silva, M.K., Larsen, L.L., and Orr, F.M., Jr.: "CO_2-Hydrocarbon Phase Behavior in Model Systems - Part 1: CO_2-C_1-C_4-C_{10}," PRRC Report 85-31, Petroleum Recovery Research Center, Socorro, NM (June 1985).

Larsen, L.L., Taylor, M.A., and Orr, F.M., Jr.: "CO_2-Hydrocarbon Phase Behavior in Model Systems - Part 2: CO_2-C_3-C_{16}," PRRC Report 85-32, Petroleum Recovery Research Center, Socorro, NM (June 1985).

Larsen, L.L., Silva, M.K., and Orr, F.M., Jr.: "CO_2-Hydrocarbon Phase Behavior in Model Systems - Part 3: CO_2-C_1-C_{16}," PRRC Report 85-33, Petroleum Recovery Research Center, Socorro, NM (June 1985).

Dandge, D.K., Heller, J.P., and Wilson, K.V.: "Poly 1-Hexene, Synthesis and Solubility in Dense Carbon Dioxide," PRRC Report 85-37, Petroleum Recovery Research Center, Socorro, NM (July 1985).

Heller, J.P.: "Improvement of CO_2 Flood Performance," Quarterly Technical Progress Report to the U.S. Department of Energy, the NMERDI, and company consortium, April 1 to June 30, 1985, PRRC Report PRRC Report 85-39, Petroleum Recovery Research Center, Socorro, NM (Aug. 1985).

Bahralolom, I., Bretz, R.E., and Orr, F.M., Jr.: "Experimental Investigation of the Interaction of Phase Behavior with Microscopic Heterogeneity in a CO_2 Flood," paper SPE 14147 presented at the 1985 Annual Technical Conference and Exhibition of the Society of Petroleum Engineers held in Las Vegas, NV, Sept. 22-25.

Heller, J.P., Lien, C., Wilson, K.V., and Dandge, D.K.: "Kinetics of 1-Hexene Polymerization," PRRC Report 85-43, Petroleum Recovery Research Center, Socorro, NM (Oct. 1985).

Silva, M.K., Taber, J.J., and Orr, F.M., Jr: "Pressures Required for Miscible Displacement of Crude Oils by CO_2." presented at the International Energy Agency Workshop on EOR, Tokyo, Japan (1985).

Taber, J.J. and Martin, F.D.: "Technical and Economic Criteria for Selecting Methods and Materials for Enhanced Oil Recovery (or Why CO_2 Fills the Bill in the Permian Basin of New Mexico and Texas)," *Proc.* of the 1985 Southwestern Petroleum Short Course, Lubbock.

Dandge, D.K., Heller, J.P., and Wilson, K.V.: "Structure Solubility Correlations: Organic Compounds an Dense Carbon Dioxide Binary Systems," I&EC: Product Research & Development (1985) **24**, 162.

Morrow, N.R. and Heller, J.P.: "Fundamentals of Enhanced Oil Recovery," chapter 3 in *Enhanced Oil Recovery—I. Developments in Petroleum Science*, 17A, E.C. Donaldson, G.V. Chilingarian and T.F. Yen, Editors, Elsevier Science Publishers (1985).

Heller, J.P. and Kovarik, F.S.: "Improvement of CO_2 Flood Performance," Quarterly Report, October 1 to December 31, 1985, PRRC Report 86-1, Petroleum Recovery Research Center, Socorro, NM (Jan. 1986).

Heller, J.P. and Taber, J.J.: "Improvement of CO_2 Flood Performance," Annual Report to the U.S. Department of Energy, the NMERDI, and company consortium, April 1, 1984 to September 30, 1985, PRRC Report 85-44, Petroleum Recovery Research Center, Socorro, NM (March 1986).

Taylor, C., Dandge, D.K., and Heller, J.P.: "Review of the Literature on Trialkyltin Fluoride," PRRC Report 86-5, Petroleum Recovery Research Center, Socorro, NM (March 1986).

Heller, J.P. and Taber, J.J.: "Influence of Reservoir Depth on Enhanced Oil Recovery by CO_2 Flooding," paper SPE 15001 presented at the 1986 Permian Basin Oil and Gas Recovery Conference, Midland, March 13-14.

Bahralolom, I.M. and Orr, F.M., Jr.: "Solubility and Extraction in Multiple-Contact Miscible Displacements: Comparison of N_2 and CO_2 Flow Visualization Experiments," paper SPE 15079 presented at the 1986 California Regional Meeting of the Society of Petroleum Engineers held in Oakland, CA, April 2-4.

Heller, J.P. and Kovarik, F.S.: "Improvement of CO_2 Flood Performance," Quarterly Report, January 1, 1986 to March 31, 1986, PRRC Report 86-7, Petroleum Recovery Research Center, Socorro, NM (May 1986).

Bretz, R.E. and Welch, S.L.: "Two-Phase, Steady-State Displacements in Berea Sandstone," PRRC Report 86-9, Petroleum Recovery Research Center, Socorro, NM (June 1986).

Welch, S.L., Bretz, R.E., and Mueller, T.: "Two-Phase, Steady-State Displacements in Rock Creek Sandstone," PRRC Report 86-10, Petroleum Recovery Research Center, Socorro, NM (June 1986).

Heller, J.P. and Kovarik, F.S.: "Improvement of CO_2 Flood Performance," Quarterly Report, April 1 to June 30, 1986, PRRC Report 86-14, Petroleum Recovery Research Center, Socorro, NM (Aug. 1986).

Taber, J.J.: "Carbon Dioxide Field Projects in the U.S.A.," presented at the 1986 International Energy Agency Workshop on EOR, Hanover, Germany (Sept.).

Dandge, D.K. and Heller, J.P.: "The Search For Polymers Useful as Direct Thickeners in CO_2 Floods," presented by Joseph J. Taber at the 1986 Enhanced Oil Recovery Symposium of the International Energy Agency Collaborative Research Program, Hannover, Germany, Sept. 16-19.

Heller, J.P. and Kovarik, F.S.: "Improvement of CO_2 Flood Performance," Annual Report to the U.S. Department of Energy, the NMRDI, and company consortium, October 1985 to October 1986, PRRC Report 86-18, Petroleum Recovery Research Center, Socorro, NM (Nov. 1986).

Dandge, D.K., Heller, J.P., Lien, C.L., and Wilson, K.V.: "Kinetics of Higher α-Olefin Polymerization," presented at the ACS Meeting, April 1986, *Polymer Preprints* (1986) **27**, No. 1, 273-74.

Dandge, D.K., Heller, J.P., and Wilson, K.V.: "Poly-1-Hexane, Synthesis and Solubility in Dense Carbon Dioxide," *J. of App. Poly. Sci.* (1986) **32**, 3775-81.

Dandge, D.K., Heller, J.P., Lien, C.L., and Wilson, K.V.: "Kinetics of 1-Hexane Polymerization," *J. of App. Poly. Sci.* (1986) **32**, 5373-84.

Taylor, M.A., Heller, J.P., and Hutter, C.: "Design and Application of the Torsional Quartz Viscometer for the Continuous Phase Equilibrium Apparatus," PRRC Report 87-2, Petroleum Recovery Research Center, Socorro, NM (Feb. 1987) Not Available.

Dandge, D.K. and Heller, J.P.: "Polymers for Mobility Control in CO_2 Floods," paper SPE 16271 presented at the 1987 SPE Conference on Oilfield Chemistry, San Antonio, Feb. 7-9.

Taber, J.J.: "Current Status of the Use of CO_2 for EOR," presented at the 1987 Recovery and Use of Waste CO_2 in Enhanced Oil Recovery Meeting (sponsored by Argonne National Labs), Denver, Colorado, March 18-20.

Heller, J.P. and Kovarik, F.S, "Improvement of CO_2 Flood Performance," Quarterly Report to U.S. Department of Energy and New Mexico Research and Development Institute, October 1, 1986 to January 31, 1987, PRRC Report 87-6, Petroleum Recovery Research Center, Socorro, NM (April 1987).

Heller, J.P. and Kovarik, F.S.: "Improvement of CO_2 Flood Performance," Quarterly Report to U.S. Department of Energy and New Mexico Research and Development Institute, February 1 to April 30, 1987, PRRC Report 87-8, Petroleum Recovery Research Center, Socorro, NM (June 1987).

Sultan, A.J.: "Simulation of Matched Viscosity Miscible Displacement in a Heterogeneous Porous Medium," M.S. Thesis, New Mexico Institute of Mining and Technology, Petroleum Engineering Department, Socorro, NM (July 1987).

Taber, J.J.: "More Oil and Less Acid Rain—Prospects for Using Waste CO_2 for Enhanced Oil Recovery," 1987 Symposium of the International Energy Agency Collaborative Research Program, Sydney, Australia, Sept. 28-Oct. 2.

Heller, J.P. and Kovarik, F.S.: "Improvement of CO_2 Flood Performance," Annual Report to U.S. Department of Energy, New Mexico Research and Development Institute, and industrial consortium, October 1, 1986 to September 30, 1987, DOE/MC/21136-17 (DE89000720), NMRDI 2-75-5340, PRRC Report 87-9, Petroleum Recovery Research Center, Socorro, NM (Nov. 1987).

Kovarik, F.S. and M.A. Taylor: "Viscosity Measurements of High-Pressure CO_2/Hydrocarbon Mixtures," presented at the 1987 AIChE Annual Meeting, New York, Nov. 15-20.

Heller, J.P. and Kuntamukkula, M.S.: "A Critical Review of the Foam Rheology Literature," *Industrial & Engineering Chemistry Research* (1987) **26**, 318-25.

Heller, J.P. and Kovarik, F.S.: "Improvement of CO_2 Flood Performance," Quarterly Report to U.S. Department of Energy, New Mexico Research and Development Institute, and industrial consortium, October to December 1987, PRRC Report 88-1, Petroleum Recovery Research Center, Socorro, NM (Jan. 1988).

Lee, H.O. and Heller, J.P.: "Laboratory Measurements of CO_2-Foam Mobility," paper SPE 17363 presented at the 1988 SPE/DOE Enhanced Oil Recovery Symposium, Tulsa, OK, April 17-20.

Kovarik, F.D. and Heller, J.P.: "Improvement of CO_2 Flood Performance," Quarterly Report to U.S. Department of Energy and Industrial Consortium, January to March, 1988, PRRC Report 88-4, Petroleum Recovery Research Center, Socorro, NM (May 1988).

Kovarik, F.S. and Heller, J.P.: "Improvement of CO_2 Flood Performance," Quarterly Report to the New Mexico Research and Development Institute, April to June, 1988, PRRC Report 88-8, Petroleum Recovery Research Center, Socorro, NM (Aug. 1988).

Huh, D.G., Chang, S.H., and Kovarik, F.S.: "Effect of Pore-Level Heterogeneity on High-Pressure Gas/Foam Flow Through an Oil-Saturated Porous Media," presented at the 1988 AIChE Annual Meeting, Washington, D.C., Nov. 27-Dec. 2.

Lee, H.O. and Heller, J.P.: "Carbon Dioxide—Foam Mobility Measurements at High Pressure," Duane H. Smith (ed.), ACS Symposium Series No. 373, Copyright 1988, American Chemical Society.

Ghori, S.G.: "Numerical Simulation of Miscible Displacement of Tracer Flow in a Homogeneous Five-Spot Pattern," M.S. Thesis, New Mexico Institute of Mining and Technology, Petroleum Engineering Deptartment, Socorro, NM (1988).

Heravi, N.E.: "Five-Spot Displacement in a Heterogeneous Reservoir at Unit Mobility Ratio," M.S.Thesis, New Mexico Institute of Mining and Technology, Petroleum Engineering Department, Socorro, NM (1988).

Kovarik, F.S. and Heller, J.P.: "Improvement of CO2 Flood Performance," Fourth Annual Report to the New Mexico Research and Development Institute, October to September, 1988, PRRC Report 88-11, Petroleum Recovery Research Center, Socorro, NM (Feb. 1989).

Kovarik, F.S. and Huh, D.G.: "Modeling Multiphase Flow in Oil Reservoirs," presented at the 1989 Eastern Simulation Multi-Conference, Tampa, March 27-31.

Heller, J.P.: "Evaluation and Improvement of Flow Uniformity," Quarterly Report, October-December 1988 (Task II), PRRC Report 88-13, Petroleum Recovery Research Center, Socorro, NM (April 1989).

Kovarik, F.S., Huh, D.G., Lansangan, R., Taylor, M., Smith, J., and Yahya, F.A.: "Miscible Hydrocarbon Gas Flooding the Shuaiba Reservoir in Abu Dhabi: Optimal Phase Behavior and Fluid Property Conditions," presented at the 1989 European Symposium on Improved Oil Recovery, Budapest, April 25-27.

Kovarik, F.S. and Heller, J.P.: "Improvement of CO_2 Flood Performance," Quarterly Report, October-December 1988, submitted to DOE, NMRDI, and Industry, PRRC Report 88-14, Petroleum Recovery Research Center, Socorro, NM (April 1989).

Kovarik, F.S.: "Displacements With Pure and Impure CO_2," Quarterly Report, October-December 1988, (Task I), PRRC Report 88-15, Petroleum Recovery Research Center, Socorro, NM (April 1989).

Kovarik, F.S. and Heller, J.P.: "Improvement of CO_2 Flood Performance," Quarterly Report, January-March, 1989, submitted to DOE, NMRDI, and Industry, PRRC Report 89-2, Petroleum Recovery Research Center, Socorro, NM (June 1989).

Kovarik, F.S.: Quarterly - Task I, PRRC Report 89-3, Petroleum Recovery Research Center, Socorro, NM (June 1989).

Heller, J.P.: Quarterly - Task II, PRRC Report 89-4, Petroleum Recovery Research Center, Socorro, NM (June 1989).

Sultan, J.A. and Heller, J.P.: "Rock Heterogeneity and Geostatistical Methods," (included with PRRC 89-15), PRRC Report 89-9, Petroleum Recovery Research Center, Socorro, NM (Sept. 1989).

Heller, J.P.: "Improvement of CO_2 Flood Performance - Task II," April-June 1989 Quarterly, PRRC Report 89-12, Petroleum Recovery Research Center, Socorro, NM (Sept. 1989).

Kovarik, F.S.: "Improvement of CO_2 Flood Performance - Task I," April-June 1989 Quarterly, PRRC Report 89-13, Petroleum Recovery Research Center, Socorro, NM (Sept. 1989).

Gullapalli, P., Hollis, W.K., and Heller, J.P.: "Cationic Polymerization of α-Olefins I: Synthesis of Poly(α-Olefin)s and Their Solubility in Dense CO2," unsolicited manuscript sent to *J. of Polymer Sci.: Part A*, PRRC Report 89-14, Petroleum Recovery Research Center, Socorro, NM (Sept. 1989).

Kovarik, F.S. and Heller, J.P.: "Improvement of CO_2 Flood Performance." Quarterly Report, April-June 1989, submitted to DOE, NMRDI, and Industry, PRRC Report 89-15, Petroleum Recovery Research Center, Socorro, NM (Sept. 1989).

Dandge, D.K., Taylor, C., and Heller, J.P.: "Associative Organotin Polymers. 1. Symmetric Trialkyltin Fluorides: Synthesis and Properties," *J. of Polymer Sci: Part A: Polymer Chemistry* (1989) **27**, 1053-63.

Dandge, D.K., Taylor, C., Heller, J.P., Wilson, K.V., and Brumley, N.: "Associative Organotin Polymers. 2. Solution Properties of Symmetric Trialkyltin Fluorides," *J. Macromol. Sci.-Chem.*, (1989) **A26** (10) 1451-64.

Dandge, D.K., Singh, P.K., and Heller, J.P.: "Associative Organotin Polymers: 5. Triorganotin Fluorides in Miscible Gas Enhanced Oil Recovery," chapter 29 of *Oil-Field Chemistry: Enhanced Recovery and Production Stimulation*, John K. Borchardt and Teh Fu Yen (eds.), Copyright 1989, American Chemical Society.

Lee, H.O. and Heller, J.P.: "Mobility of CO_2 and Surfactant Adsorption in Porous Rocks," ACS Symposium Series 396, Oilfield Chemistry: Enhanced Recovery and Production Simulation, Chapter 27, pp. 502-17, John K. Borchardt and Teh Fu Yen (eds.), Copyright 1989, American Chemical Society.

Kovarik, F.S., (F.D. Martin) and Heller, J.P. "Improvement of CO_2 Flood Performance," Fifth Annual Report to the New Mexico Research and Development Institute, DOE, and Industry, October 1988 to September 1989, PRRC Report 89-22, Petroleum Recovery Research Center, Socorro, NM (Feb. 1990).

Heller, J.P. "Improvement of CO_2 Flood Performance: Task Area II," Annual Report to Mobil Research and Development Corporation, PRRC Report 89-24, Petroleum Recovery Research Center, Socorro, NM (Feb. 1990).

Chang, S-H.: "MSF 2.1: Mechanistic Foam Simulator—Model Description and User's Manual," PRRC No. 90-7 Petroleum Recovery Research Center, Socorro, NM (March 1990).

Sultan, A.J. and Heller, J.P.: "Rock Heterogeneity and Geostatistical Methods in Reservoirs and Source Rocks," *Proc.* of the 1990 Workshop: Source Rocks, Generation and Migration of Hydrocarbons and Other Fluids in the Southern Midcontinent, Norman, OK, February 6-7.

Martin, F.D. and Heller, J.P.: "Improvement of CO_2 Flood Performance," 1st Quarterly Report for the Period of October to December 1989, PRRC Report 90-17, Petroleum Recovery Research Center, Socorro, NM (April 1990).

Chang, S-H., Owusu, L.A., and French, S.B.: "The Effect of Microscopic Heterogeneity on CO_2-Foam Mobility: Part 2—Mechanistic Foam Simulation," paper SPE/DOE 20191 presented at the 1990 SPE/DOE Seventh Symposium on Enhanced Oil Recovery, Tulsa, OK, April 22-25.

Lansangan, R.M., Taylor, M.A., Smith, J.L., and Kovarik, F.S.: "An Improved Viscosity Correlation for CO_2/Reservoir Systems," paper SPE/DOE 20209 presented at the 1990 SPE/DOE Seventh Symposium on Enhanced Oil Recovery, Tulsa, OK, April 22-25.

Lee, H.O., Heller, J.P., and Hoefer, A.M.W.: "Change in Apparent Viscosity of CO_2-Foam with Rock Permeability," paper SPE/DOE 20194 presented at the 1990 SPE/DOE Seventh Symposium on Enhanced Oil Recovery, Tulsa, OK, April 22-25.

Bahralolom, I. and Heller, J.P.: "Core Sample Heterogeneity From Laboratory Flow Experiments," *Proc.*, Second International Res. Char. Tech. Conf., Dallas, June 25-28, 1989; PRRC Report 90-22, Petroleum Recovery Research Center, Socorro, NM (May 1990).

Heller, J.P., and Ghori, S.G.: "Quantifying Permeability Heterogeneity Using an Improved Numerical Simulation of a Field Tracer Test," American Geophysical Union, Baltimore, MD (May 1990).

Ghori, S.G., and Heller, J.P.: "Quantifying Permeability Heterogeneity Using an Improved Numerical Simulation of a Field Tracer Test," presented at the 1990 American Geophysical Union Spring Meeting, Baltimore, May 29-June 1.

Sultan, A.J., Heller, J.P. and Gutjahr, A.: "Generation and Testing of Random Fields and the Conditional Simulation of Reservoirs," paper CIM/SPE 90-98, presented at the 1990 International Technical Meeting Jointly Hosted by the Petroleum Society of the CIM and the Society of Petroleum Engineers, Calgary, June 10-13.

Martin, F.D. and Heller, J.P.: "Improvement of CO_2 Flood Performance," 2nd Quarterly Report to DOE, NMRDI, and Industry, January - March 1990, PRRC Report 90-20, Petroleum Recovery Research Center, Socorro, NM (June 1990).

Sultan, J.A., Heller, J.P., and Gutjahr, A.: "Generation and Testing of Random Fields and the Conditional Simulation of Reservoirs," CIM/SPE 90-98, presented at the 1990 CIM/SPE International Technical Meeting, Calgary, Canada (June).

Heller, J.P.: "Uniformity of Displacement in Porous Media." Sent to *Geophysical Research Letters* for possible publication in 6/90; sent to *Water Resources Research* for possible publication in 9/89; PRRC Report 90-28, Petroleum Recovery Research Center, Socorro, NM (July 1990).

Martin F.D. and Heller J.P.: "Improvement of CO_2 Flood Performance," 3rd Quarterly Report (and Technical Summary to DOE & NMRDI) to DOE, NMRDI, and Industry, April-June 1990, PRRC Report 90-34, Petroleum Recovery Research Center, Socorro, NM (Aug. 1990).

Ghori, S.G. and Heller, J.P.: "Computed Effect of Heterogeneity of Well-to Well Tracer Results," for presentation at the 5th Canadian/American Conference on Hydrogeology, Calgary, Alberta, Canada, Sept. 18-20, 1990; PRRC Report 90-33, Petroleum Recovery Research Center, Socorro, NM (Sept. 1990).

Gullapalli, P. and Heller, J.P.: "A New Initiating (Minifer) System for the Living Polymerization of Isobutylene," submitted for publication in *J. of Chem. Soc.: Chem. Communications*; PRRC Report 90-39, Petroleum Recovery Research Center, Socorro, NM (Oct. 1990).

Gullapalli, P. and Heller, J.P.: "Electron-Pair Donors in Carbocationic Polymerizations and Synthesis of Linear Living α,ω-Di-(Tert Chloro) Polyisobutylene," submitted to *J. of Polymer Sci.: Part A: Polym. Chem.*; PRRC Report 90-48, Petroleum Recovery Research Center, Socorro, NM (Nov. 1990).

Heller, J.P. and Martin, F.D. "Improvement of CO_2 Flood Performance," Fourth Quarterly Report to DOE, NMRDI, and Industry, July 1, 1990-Sept. 30, 1990, PRRC Report 90-49, Petroleum Recovery Research Center, Socorro, NM (Nov. 1990).

Gullapalli, P., Mustafa, S.A., Hollis, W.K. and Heller, J.P: "Living Carbocationic Polymerization of Isobutylene by Tert-Amyl Alcohol/BCl_3/1-Methyl-2-Pyrrolidinone Initiating System," PRRC Report 90-51 (Dec. 1990); submitted to *J. of App. Poly. Sci.* In press.

Lansangan, R.M. and Smith, J.L.: "Viscosity, Density, and Composition Measurements of Certain CO_2/West Texas Oil Systems," paper SPE 21017 presented at the 1991 SPE International Symposium on Oilfield Chemistry, Anaheim, CA, February 20-22.